UNIVERSITAT POLITÈCNICA DE VALÈNCIA

Instituto Universitario Mixto de Tecnología Química

(UPV-CSIC)

Heterogeneous Metal Catalysis: From Single Atoms to Metal Clusters and Nanoparticles

TESIS DOCTORAL

Presentada por:

Lichen Liu

Dirigida por:

Prof. Avelino Corma

Valencia, Septiembre, 2018

To My Grandmother

Acknowledgements

To close my PhD thesis, I would like to show my sincerest acknowledgements to my supervisor, Prof. Avelino Corma and my colleagues in ITQ. Without their tremendous support on me, I cannot complete the work presented in this thesis.

About six years ago, I met Avelino in Nanjing University during his visit to my home university. At that time, I was still an undergraduate student and after a short discussion with him, he invited me to come to Valencia to work with him as a PhD student. To be honest, I didn't know anything about Valencia City at that time and I just knew that Avelino is a world-leading scientist on heterogeneous catalysis, although I just had read several of his papers. Before meeting him, I had never considered to go to Spain to for a PhD degree. But I made up my mind on the second day after the meeting with Avelino and decided to pursue a PhD on Sustainable Chemistry with him in ITQ. As a chemist, I believe in the natural laws. However, I have to say that, a man's life track is always influenced by some unexpected factors. To some extent, it can be called destiny. At least, it was what happened to me during the transition period after my graduation from Nanjing University six years ago. When I arrived in Valencia in 2013, Avelino gave me two projects (preparation of small Cu nanoparticles and encapsulation of Pt in MWW zeolite), which initiated my research in ITQ. Thanks to Avelino's thoughtful arrangements and kind help from the ITQ administration staff, I became used to the working environment in ITQ in short time. Since then, my PhD journey kicked off.

During the last five years of PhD study with Avelino, his encouragements, inspirations on the scientific projects and passion for doing research has been always providing me the driving force to move forward. Doing research is always dealing with tough problems. When I get lost in those difficulties, Avelino can always point a way out of the chaos for me and drag me back to the right track. Certainly, he has also "created" plenty of challenges during my PhD study and set a high bar for me to cross over. In those situations, he is always trying to push me to my limit. When I have prepared some new materials, he will ask me to make them in a more controllable and practical way. When I show him some nice TEM images, he will ask whether I can tell the information

of the materials at atomic level. When I present the catalytic results to him, he will ask about the reaction mechanism and the structure-reactivity correlation. Under his requests, I have to carry out lots of experiments to clarify his questions and to convince him, especially when I have some new discoveries. After the five-year training with him, I start to understand his "tough" requirements, which is of absolute necessity to unveil the scientific issues behand the raw data. carry out high-level research works. My understanding on heterogeneous catalysis has improved significantly during the "back and forth" process when working together with Avelino. Without his guidance and encouragement, I may be still out of the threshold of heterogeneous catalysis and material science.

In the film <Whiplash>, the "tough" instructor Terence Fletcher tried to push the young drummer Andrew Neiman to his limit by all means, just in order to make Neiman achieve the height beyond his expectation. To some extent, Avelino is playing a role as a strict supervisor on the scientific aspect, but much better than Fletcher. He is always trying to take care of me and cares a lot about my personal life. Leaving my home country to Valencia, sometimes I miss a lot about my family. When I ask for some vacation to see my family and friends, Avelino is always willing to approve that and wishes me to enjoy the time there. During my communication with Avelino and Brisa, they convey the concept that work and life should be kept in a good balance to me. Knowing Avelino and Brisa is a big fortune to me in my life and they have set an excellent example to me on both working on science and living a life.

In ITQ, we are working link a team. All my research works have been carried out within the framework of collaboration with scientists and technicians from different aspects. When I have questions on preparation of zeolites, Dr. Urbano Diaz is always patient to provide me helpful suggestions. When I need to perform characterizations on my catalysts, Dra. Patricia Concepcion is always trying her best to do the spectroscopic measurements and those efforts contribute a lot to clarify the catalyst structures and reaction mechanism. When I have problems with the fix-bed reactors, Dr. Joaquín Martinez and Dra. Cristina Martinez can always help me to solve the problems and make the reactors and instruments running well. I need to show my thanks to Dr. Antonio Leyva since I have leant a lot from him on application of heterogeneous metal

catalysts for organic reactions. The collaboration with Dra. Mercedes Boronat on theoretical calculations provides very helpful insights on the reaction mechanism to explain my experimental results. Of course, the technician team in ITQ (Jose Miguel, Dolo, David, Mariam, Adelina, Javier, Jose Gaona…) and the microscope service of UPV (Manuel, Alicia, Mercha, Ximo, Jose Luis) have always given the best support they have for me which makes me focused my concentration on the scientific issues without worrying about the technical problems. Heterogeneous catalysis is a field which requires multidisciplinary knowledge covering analytic chemistry, material chemistry, organic chemistry and chemical engineering. The collaborative atmosphere and working style has greatly impressed me and implanted that concept into my mind.

During the daily work time in ITQ, I have got tremendous support from my colleagues (Tomas, Dr. Jiuxing Jiang, Miguel, Chengeng, Lu, Qintong, Alberto, Christian, Francine, Elisa, Manuel, Ivan, Pilar, Luismi, Jose Maria, Marta, Raquel, Judit, Jose Ramon, Javier, Victor……). Their selfless help and humorous sense make my time in ITQ so pleasant and efficient. Of course, my other friends in Valencia (Xuehua, Teng, Zi, Rui, Lixin, Yue…) also bring me so much joy and make my life in Valencia colorful, especially when after a tired week of working in the lab without progress.

To gain more insights on the catalyst structure and to study the reaction mechanism under reaction conditions, I need to go outside and collaborate with researchers in other universities and institutes (Dr. Raul Arenal from Zaragoza University, Dra. Virginia Pérez-Dieste and Dra. Laura Simonelli from ALBA Synchrotron, Dr. Dmitri Zakharov and Dr. Eric A. Stach from Brookhaven National Lab, Dr. Juan C. Hernandez, Dr. Miguel Haro and Prof. Jose J. Calvino from Cadiz University and Dr. Giovanni Agostini and Dra. Debora Motta-Meira from European Synchrotron Radiation Facility). Those advanced characterizations have significantly improved the depth of my research work and my visits to them has broadened my horizon, showing me those amazing state-of-art tools to study materials and catalysis at molecular and atomic level. With their patient and strong support, our fruitful collaborations have turned out into several research papers and I am sure our collaboration will continue to produce more significant results.

I have to confess that I cannot remember all the meaningful moments in the

last five years. However, on some specific occasion, some memories jump out into my mind (like this moment…), which remind me the people I encountered, the experiences I had, the choices I made, the thoughts I had… When standing in ITQ at this moment and looking back into the last five years, I still remember the afternoon on September 22nd, 2013 when I arrived the Joaquín Sorolla train station. It was Zhibin Li who picked me up there and showed me how to live in Valencia. And I feel so lucky for myself and sincerely appreciate the generous help I have received from my supervisor and colleagues in ITQ and UPV, as well as my friends in Valencia.

Life is like the energy profiles of a catalytic reaction, which is usually not straight forward but with twisted pathways. In most of the time, it is like climbing countless mountains (energy barriers). Over the mountains, still mountains. To curiosity for the scenery and people behind the next mountain attracts us to climb it, even though we have to sacrifice something valuable in some cases. If treating one individual person as an active site for reaction, then the people we have met are the reactants in contact with the active sites. Every person we have encountered in our life has an impact, large or small, on our growth or evolution. The chemical principle for solubility between different compounds tells us that, compounds with similar polarity have stronger affinity to each other. I feel so lucky to come to this city and to work in this institute. After staying in Valencia for five years, I have to say, ITQ and Valencia is a perfect reaction medium for me to interact with different people and making strong bonding with them. The enthusiasm and optimism of the Spanish friends, the sunshine and delicious food in Valencia, the beautiful landscapes, the colorful life in Europe as well as the scientific journey in ITQ has deeply influenced my body and my mind. I have just realized that I have changed so much during my PhD period, from outside to inside. Comparing to the 20 kg loss on my weight and the loss of my hair (jajajajaja…), the five-year time in ITQ and Valencia has left a more profound imprint on my mind and my life concepts, which is definitely an incredible fortune to me!

I have also to thank Avelino for providing me the opportunities to travel around the world, from Europe to United States to Australia, to do experiments in various institutes or universities and participate academic conferences. Those experiences have greatly broadened my horizon and prompted myself to be

involved into the international catalysis community. If treating my personal character as an evolution, the friends I have met during my journeys have definitely influenced my evolution dynamics, to some content, which is probably more than you imaged. I should thank them all. ☺

Herein, I prefer to quote the philosophy concept from Wang Guowei, in which he describes the three stages for doing research.

"昨夜西风凋碧树。独上高楼，望尽天涯路。" 此第一境界也。

"衣带渐宽终不悔，为伊消得人憔悴。" 此第二境界也。

"众里寻他千百度，蓦然回首，那人却在灯火阑珊处。此第三境界也。

Certainly, I am still in the first stage. What I am thinking now at the end of my PhD period is the future direction that heading for. The truth is, I am still not determined on my next move. However, the PhD experience has taught me how to judge and evaluate the influence of my behavior and work.

I would like to thank Prof. Lin Dong, Dr. Fei Gao, Dr. Chuanzhi Sun and Dr. Changjin Tang. They are my enlightenment mentor when I was still an undergraduate student in Nanjing University. They took me into the world of material chemistry and heterogeneous catalysis. Without their recommendation, I would not have the opportunity to know Avelino and to join ITQ as a PhD student. Lab mates from Nanjing University (Annai, Weixin, Jiangfang…) are also greatly thanked.

At last, I have to show my deep appreciation for my family. Being far away from my family for five years, I have owed them so much, especially to my dearest grandmother. Without their understanding and strong supports, I cannot concentrate myself on my research in ITQ. They give plant the most powerful faith in my mind and it is always my most efficient driving force. I have also received very strong support from the friends who grew up together with me since middle school (Fangjie, Siqi, Haigen, Guangcai,…) in my hometown and my close friends in Nanjing University (Hao, Linsen, Jinping, Mufan…). They have given me countless inspirations, encouragements, happiness and unforgettable memories.

!Muchas Gracias!

谢谢大家!

UNIVERSITAT POLITÈCNICA DE VALÈNCIA

ESCOLA DE DOCTORAT

Authorization of no doctor co-authors for the inclusion of articles in a doctoral thesis made by publications.

The doctoral thesis developed by *Lichen Liu*, with title *Heterogeneous Catalysis: From Single Atoms to Nanoclusters and Nanoparticles*, is presented by compendium of articles.

The doctorate declares that all co-authors of the articles are PhD degree ☐
(In case of completing this option it is not necessary to complete the following lists)

The doctoral student declares that the following co-authors of the articles included in the thesis hold a PhD degree:

Name and Surname
Alberto V Puga
Patricia Concepcion
Virginia Pérez-Dieste
Hermenegildo García
Avelino Corma
Dmitri N Zakharov
Raul Arenal
Eric A Stach
Giovanni Agostini
Toshiyuki Matsushita
Antonio Leyva-Pérez

Add as many lines as needed

The doctoral student declares that the following co-authors of the articles included in the thesis do not hold a PhD degree:

Name and Surname	Home University
Jorge Cored	*Universitat Politècnica de València*

Add as many lines as needed

In compliance with the regulation of Doctoral Studies at the Universitat Politècnica de València, the authorizations of the co-authors listed in the previous table are attached, stating their agreement for the inclusion of the articles in which they participate in the aforementioned

doctoral thesis, together with their resignation to use the same article as part of another thesis.

In Valencia, at *11-07-2018*

Signed: *Doctoral student author of the thesis*

Lichen Liu

Lichen Liu

The doctoral thesis developed by **Lichen Liu**, with title *Heterogeneous Catalysis: From Single Atoms to Nanoclusters and Nanoparticles*, is presented by compendium of articles.

Mr./Ms. **Jorge Cored** *appears as co-author of the publication(s) listed below:*

- *Sunlight-assisted Hydrogenation of CO_2 into ethanol and C2+ Hydrocarbons by Sodium-promoted Co@C Nanocomposites*

And so declares his/her acceptance to the inclusion of this articles in the aforementioned doctoral thesis, together with his/her resignation to use the same article as part of another thesis.

Place and date of signature

Valencia, 11-07-18

JORGE CORED BANDRÉS

Signed: *Co-author*

Index

This chapter is reused from the following publication:

Metal Catalysts for Heterogeneous Catalysis: From Single Atoms to Nanoclusters and Nanoparticles, *Chemical Reviews*, L. Liu and A. Corma, 2018, *118*, 4981–5079.

Chapter 1

Background

1. Background
1.1 Introduction

With the actual explosion of work on nanoscience and more specially on nanomaterials, one cannot avoid to look back in time and to see that nanomaterials were already prepared and regularly used for heterogeneous catalysis more than 60 years ago.[1,2] Indeed, supported metal catalysts were based on metal crystallites close to the nanometer size, and catalytic reactions with zeolitic materials occurred in nanopores with a dimension below 1 nm, in where strong confinement effects impacted the reactivity.[3]

In the first case, i.e. metal catalysts, previous researchers were already able to establish structure-reactivity correlations with the techniques available, such as transmission electron microscopy and chemisorption of gases. They discovered the different relative activity shown by metal atoms located at crystal edges, corners and facets during different catalytic reactions and they classified reactions on metal catalysts as structure-sensitive and non-structure-sensitive reactions.[4] As a consequence of those studies, it was possible to rationalize the impact of the size of supported metal nanoparticles on their catalytic reactivity.[5]

It is obvious that, with the resolution of the characterization techniques available at that time, it was not possible to visualize metal particles below 1 nm. Nevertheless, one could already infer that the electronic properties of metal particles should strongly change when going below 1 nm (see **Figure 1.1**). So, it could be expected that, the subnanometric metal particles would interact differently with reactants, showing distinct reactivity with respect to larger nanoparticles.[6] Today, it is possible to see single metal atoms and subnanometric metal clusters formed by a few atoms, by means of the aberration-corrected electron microscopy.[7] These achievements can now be, not only visualized by electron microscopy but also can be studied by X-ray absorption spectroscopy (XAS) on their coordination environment of those metal species under reaction conditions.[8] By using these new advanced techniques, it is possible to directly correlate the atomic structures of heterogeneous metal catalysts with their catalytic behavior, providing more insights on how metal species participate in the surface reaction and how to design more efficient metal catalysts.
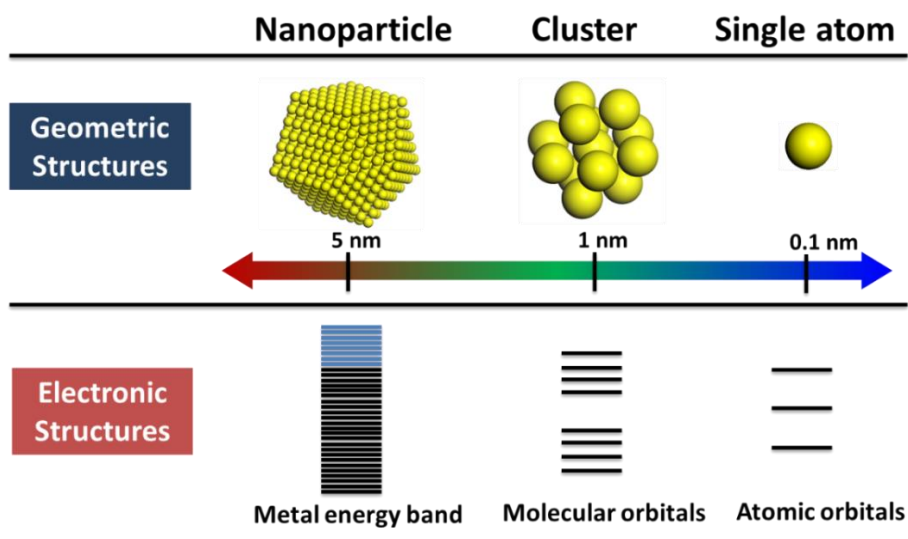
Figure 1.1. Geometric and electronic structures of single atom, clusters and nanoparticles.

In recent years, great attention has been shifted from nanoparticulate metal catalysts to subnanometric regime, which includes single atoms and clusters supported on solid carriers. It has already been shown in the literature that, these subnanometric metal species can show unique catalytic behavior compared to their nanoparticulate counterparts.[9] Those size-dependent properties can extend the well-established size effects based on nanoparticulate metal catalysts from nanoscale regime to subnanometric regime, which is associated with single atoms and metal clusters. However, there are still some important issues related with the catalytic properties of single-atom metal catalysts and metal clusters are still not clear . For instance, although single-atom metal catalysts have been reported as active and efficient catalysts for various reactions, including CO oxidation, selective hydrogenation, selective oxidation and electrocatalytic reactions.[10] However, in most of previous works, the catalytic performance of single-atom catalysts has not been compared with the other counterparts (metal clusters and nanoparticles) under the same conditions. Besides, it is already well-known that, the atomic structures of metal nanoparticles under reaction

conditions will change with the reaction conditions. The structural transformation of single atoms and clusters under reaction conditions are barely studied. Therefore, it is necessary to carry out systematic studies on comparing the catalytic behavior of single atoms, clusters and nanoparticles under comparative conditions, which can provide reliable insights and understanding on the role of single-atom catalysts.

Regarding subnanometric metal clusters, it has been well demonstrated in the literature that, metal clusters with a few atoms are quite flexible when interacting with reactants. And more importantly, their reactivity is strongly related with their atomicity (which will be further discussed later in the **Part 1.5 Catalytic applications of metal clusters**). Considering their instability, it is of great importance to develop efficient synthetic methodologies to stabilize metal clusters under reaction conditions. It has been reported in the literature that, by using organic ligands, it is possible to stabilize metal clusters against sintering. However, those ligands also block the surface sites of metal clusters, which has significant influence on their reactivity. It should be emphasized that, a catalytically promising methodology for the generation of active metal clusters should leave the surface of metal clusters exposed to reactants. Nevertheless, considering the practical applications of metal clusters for industrial-relevant applications, it is vital to develop synthetic approaches to stabilize those tiny particles under high-temperature oxidation-reduction processes, which is currently still a challenging task.

On the other hand, although the synthesis, characterizations and catalytic applications of metal nanoparticles for heterogeneous catalysis have been well established. However, most of previous works are based on noble metals (Au, Pt, Pd, Ru, Rh etc.). From a sustainable point of view, development of non-noble metal catalysts (Fe, Co, Ni, Cu etc.) as substitutes for noble metal catalysts has attracted much attention in recent years. There is already some significant progress in this field, showing the possibility of using non-noble metal catalysts for some heterogeneous reactions that usually performed with noble metal catalysts.[11,12] However, the reactivity of the non-noble metal catalysts is still much lower when compared with the noble metal catalysts and the reaction mechanism on non-noble metal catalysts are still not clear.

In the following chapter, the different electronic and geometric structures

between different types of metal entities (from single atoms to nanoclusters and nanoparticles) will be discussed. Then, an overview of the recent progress on the catalytic application of subnanometric metal catalysts (including supported single atoms and metal clusters) will be presented. Moreover, the recent developments on non-noble metal catalysts as substitutes for noble metal catalysts will also be summarized.

1.2 Electronic and geometric structures of different metal species
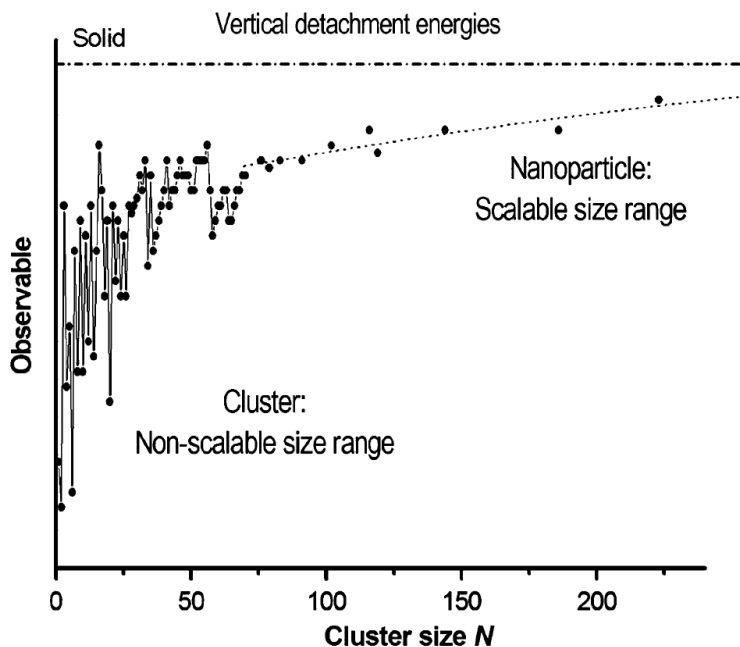
Figure 1.2. Work function obtained from ultraviolet photoelectron spectroscopy (UPS) of Au clusters with different atomicty. Adapted with permission from ref **15**. Copyright 1992 AIP Publishing LLC.

Before starting the discussion on the catalytic properties of different types of metal species, the size effects on the electronic and geometric structures of metal species will be briefly discussed. For mononuclear metal complex, their electronic structures are strongly related with their coordination environment, being especially dependent on the ligands and solvent, and they have already been intensively studied and clearly defined.[13,14] However, in the case of metal

clusters and nanoparticles, the situation becomes much more complicated due to the orbital overlapping between metal atoms. Taking Au as an example (see **Figure 1.2**), the work function of Au species with different atomicity are strongly dependent on the particle size.[15] For Au clusters with less than 30 atoms, the work function varies greatly with the atomicity, while when the atomicity increases above 70 atoms (>1.5 nm), the work function almost remains constant and slowly increases with the growth of particle size. If one considers the orbital structures of Au nanoclusters with less than 40 atoms, the size-dependent electronic structures is more significant.[16] As shown in **Figure 1.3**, the frontier orbitals of planar Au_n clusters (n≤7) consist of several lobes localized on the Au atoms with unsaturated coordination environment. Moreover, those frontier orbitals are fully accessible for the interaction with molecules through the overlap of electronic orbitals. However, when the atomicity increases above 8, the geometric structure of the Au nanocluster will change from planar to 3D.[17] In that case, the coordination number of the surface atoms increases and the contribution of the atoms inside the particle to the composition of the frontier orbitals becomes more important. As a consequence, orbital overlap with substrate molecules would be less efficient if compared with smaller clusters with fully accessible orbital structures.

When the atomicity of metal particles increases to >40 (with particle size >1 nm), the bandgap between HOMO and LUMO becomes smaller than those in subnanometric metal clusters. For larger metal nanoparticles (>2 nm), a continuous energy level will form.[18] Specially, for metal nanoparticles like Au, Ag and Cu, their size-dependent electronic structures will be reflected on their plasmonic properties.[19] As a result, their optical properties will also vary with the particle size, which will further affect their catalytic behavior in photocatalysis.
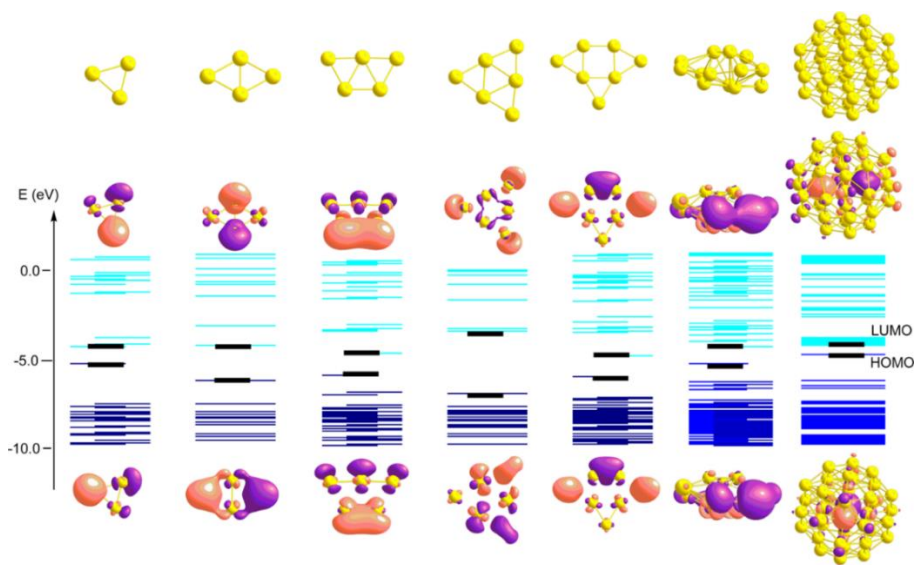
Figure 1.3. Electronic structures of Au clusters according to theoretical calculations. Optimized structure (top) and calculated isosurfaces of the lowest unoccupied molecular orbital (LUMO, center) and highest occupied molecular orbital (HOMO, bottom) of Au_3, Au_4, Au_5, Au_6, Au_7, Au_{13}, and Au_{38} clusters, together with molecular orbital energy levels in blue. Obtained at the B3LYP/LANL2DZ level using the Gaussian09 program. Adapted with permission from ref **16**. Copyright 2014 American Chemical Society.

In the case of supported single atoms, they can be stabilized by the support by chemical bonding, especially when single atoms are anchored on inorganic supports like transition metal oxides and zeolites. Thus, those single atoms may show limited geometric transformation under reaction conditions. However, when single atoms are supported on organic polymers with functional groups (like amine, carbonyl groups, thiol, etc.), they may adapt their coordination environment under reaction conditions due to the interaction between single atoms with substrate molecules. On the other hand, when the particle size reaches the cluster region (less than 20 atoms), the geometric structures of those clusters are quite flexible and can be strongly affected by the environment. One metal cluster with specific atomicity can have several possible geometric configurations, which depends on the support, reactant and reaction conditions.

The geometric structure of a metal cluster is also related with its charge. For instance, theoretical calculations show that the geometric configuration of Au_3 cluster can change from linear to triangular when the charge changes from Au_3^- to Au_3^+.[20] Then, during redox reactions, the charge of metal clusters may change during the catalytic cycles, implying that the geometric configuration may also show a dynamic transformation under reaction conditions. That complexity will be reflected on their catalytic behavior, as will be shown in the following section when discussing the catalytic applications of metal clusters.

In the case of metal nanoparticles (>1 nm, usually with more than 40 atoms), their geometric structures are less sensitive, and usually the geometric structure of one metal nanoparticle is relatively stable, although the geometric configuration of exposed surface atoms (facet, corner, edge, metal-support interface etc.) may change due to the environment.[21,22] Furthermore, the strain effects and lattice defects in metal nanoparticles are also important factors when considering the influences of geometric structures on catalytic properties.[23]

1.3 Influence of particle size on the metal-support and metal-reactant interaction

1.3.1 Metal-support interaction on different types of metal species
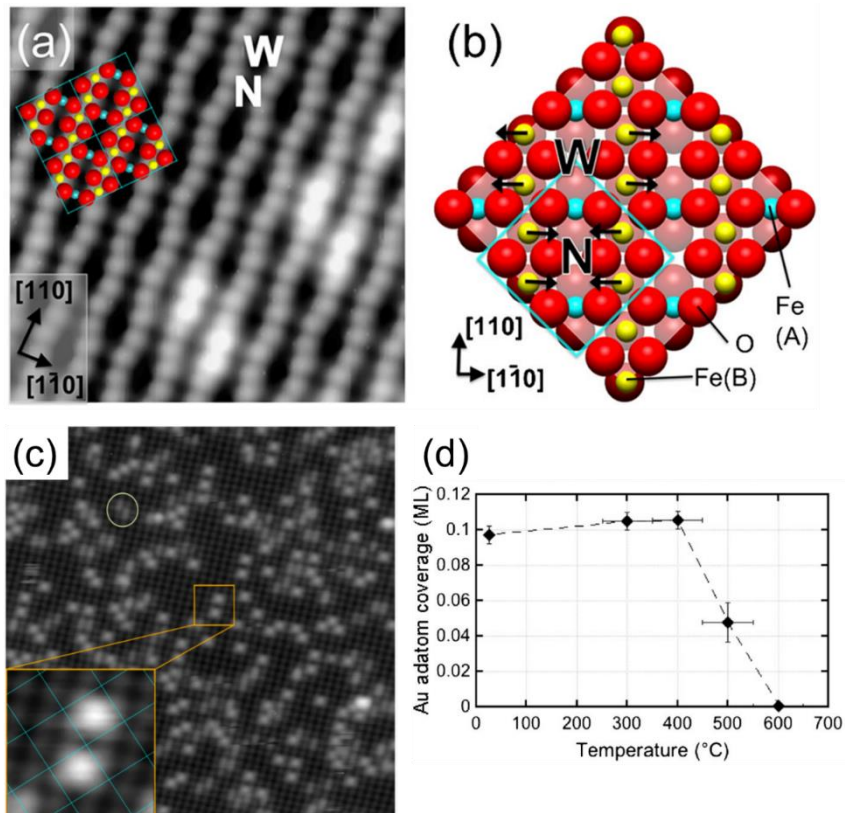
Figure 1.4. (a) STM image (6 nm × 6 nm) of the clean $Fe_3O_4(001)$ surface. The bright double protrusions located on the Fe(B) rows correspond to hydroxyl species. (b) Top view of the $Fe_3O_4(001)$ surface. Alternate pairs of surface Fe(B) cations (yellow) relax perpendicular to the Fe(B) row (relaxation indicated by blue arrows), creating two types of hollow sites within the reconstructed surface cell; wide (W) and narrow (N). (c) STM image (30 nm × 30 nm) of 0.12 ML Au deposited on $Fe_3O_4(001)$ surface at room temperature. Au adatoms are located between the surface Fe(B) rows, in the center of the cell, i.e., at the narrow sites. (d) Coverage of single Au adatoms after annealing 0.1 ML Au to various temperatures. The decrease of surface coverage of Au adatoms is caused by the sintering of single Au atoms into clusters. Adapted with

permission from ref **26**. Copyright 2012 American Physical Society.

The importance of the interaction between metal species and the support has been recognized since 1970s through the concept of strong metal-support interaction (SMSI).[24] The realistic situation in practical supported metal catalysts are too complicated to elucidate the fundamental mechanism behind. Therefore, the metal-support interaction has been studied by surface science techniques to understand the structures and properties of supported metal species at atomic level. When metal species are deposited on a solid carrier, it can be expected that their locations are related with the local surface structure of the carrier. As a model surface, rutile(110) surface can provide three types of anchoring sites for single Pt atoms, including the Ti rows, O rows and O-vacancy sites. It has been observed that, only Pt atoms located at the O-vacancy sites are stabilized while Pt atoms on the other sites are mobile at room temperature. Electron transfer from Pt to TiO_2 has also been observed since Pt atoms located at the O-vacancies are in contact with Ti atoms.[25] In some more complicated systems, different types of O-vacancy sites may exist on one surface. It has been shown that, Au single atoms are exclusively stabilized in the "narrow" hollow sites instead of the "wide" hollow sites on $Fe_3O_4(001)$ surface, which is caused by the electronic difference between the two types of surface hollow sites (see **Figure 1.4**).[26] It should also be mentioned that, for a given support, different metals may show distinct behavior. When Au is deposited on anatase $TiO_2(101)$ surface, Au clusters are preferentially formed on the edge sites while Pt clusters are formed both on terrace and edge sites.[27] The electronic interaction between Au-TiO_2 and Pt-TiO_2 may cause their different stability and mobility on anatase surface, which further influence their spatial distributions. These results from surface science studies indicate that, the structures and electronic properties of the support has significant influence on the spatial location and stability of metal species. It can also be speculated that, they will also further influence the catalytic behavior of metal species.
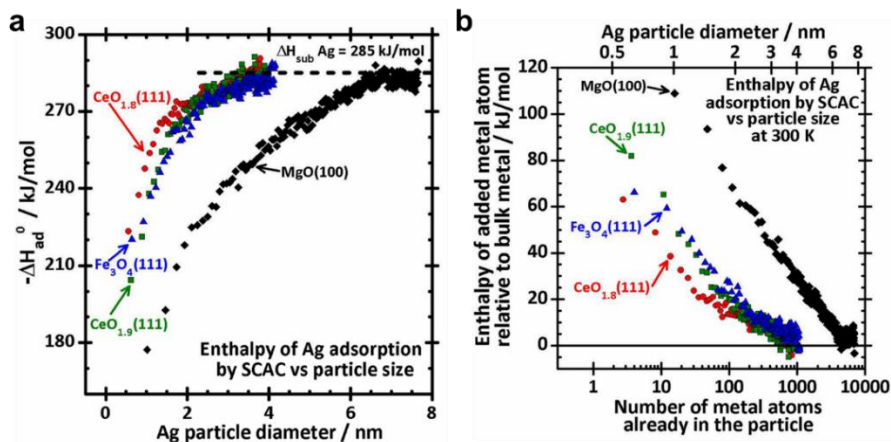
Figure 1.5. (a) Size-dependent adsorption heat of Ag atom when Ag is vapor deposited onto different metal oxide surfaces at 300 K for growing Ag nanoparticles on the surface. (b) Size-dependent partial molar enthalpy of Ag atoms in Ag nanoparticles on different oxide surfaces. Adapted with permission from ref **27**. Copyright 2013 American Chemical Society.
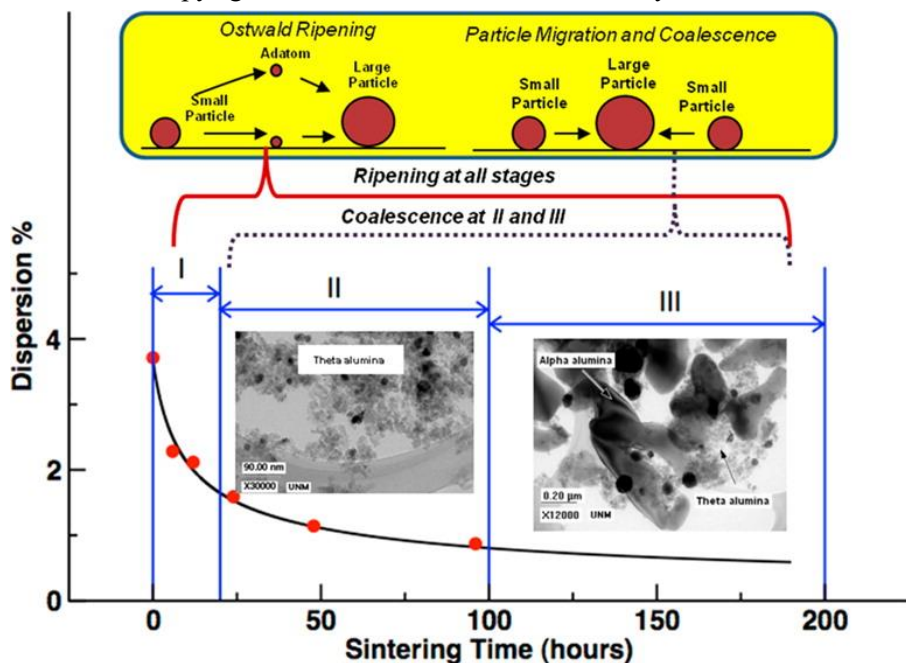

Figure 1.6. Schematic illustration of Ostwald ripening and particle migration

and coalescence during the sintering process. Adapted with permission from ref **31**. Copyright 2013 American Chemical Society.

In supported metal catalysts, one of the important roles of the support is to stabilize the metal species from sintering, being a quite common phenomenon during the preparation and application of metal catalysts. However, it is difficult to model the sintering process in a quantitative way. In the last years, based on concepts from surface chemistry, Campbell *et al.* have studied the influence of particle size on the stability of supported metal species.[28,29] Considering the physical models for sintering, the adsorption heat of metal atoms onto a metal particle is used as parameter to describe the size effect on thermal stability of metal species. According to their work, the thermal stability of metal species will dramatically increase when increasing the particle size in the range from 1 to 6 nm. When the particle size is as large as 6 nm, metal nanoparticles become relatively stable towards sintering. Using similar concepts, Campell *et al.* have also studied the effects of supports on the thermal stability of metal species.[30] As shown in **Figure 1.5**, regardless of the support, the thermal stability of metal species also increases when increasing the particle size. However, if there are oxygen vacancies in the metal oxide support (for instance, CeO_{2-x}), Ag nanoparticles with sizes of 2-3 nm can show excellent stability.

Basically, the sintering of metal species can be described by the Ostwald ripening and particle migration and coalescence models. As illustrated in **Figure 1.6**, the sintering of small metal nanoparticles can be divided into three stages.[31] In the first stage, rapid loss of activity and agglomeration of small metal particles will occur through an Ostwald ripening mechanism, as has been investigated by *in situ* transition electron microscopy.[32,33] For that process, the driving force is the different surface diffusion energy of metal particles with different sizes. Therefore, the Ostwald ripening process can be significantly suppressed if the size of metal particles can be controlled in a narrow range. Indeed, in a recent work, Wettergren *et al.* have produced highly stable size-selected Pt nanoclusters by precisely controlling the particle size distribution in a narrow range.[34] Pt nanoclusters with a broad size distribution will show significant Ostwald ripening during thermal treatment, while if the size of Pt nanoclusters has been well controlled, both Pt_{22} and Pt_{68} clusters will show good

stability against sintering through Ostwald ripening.
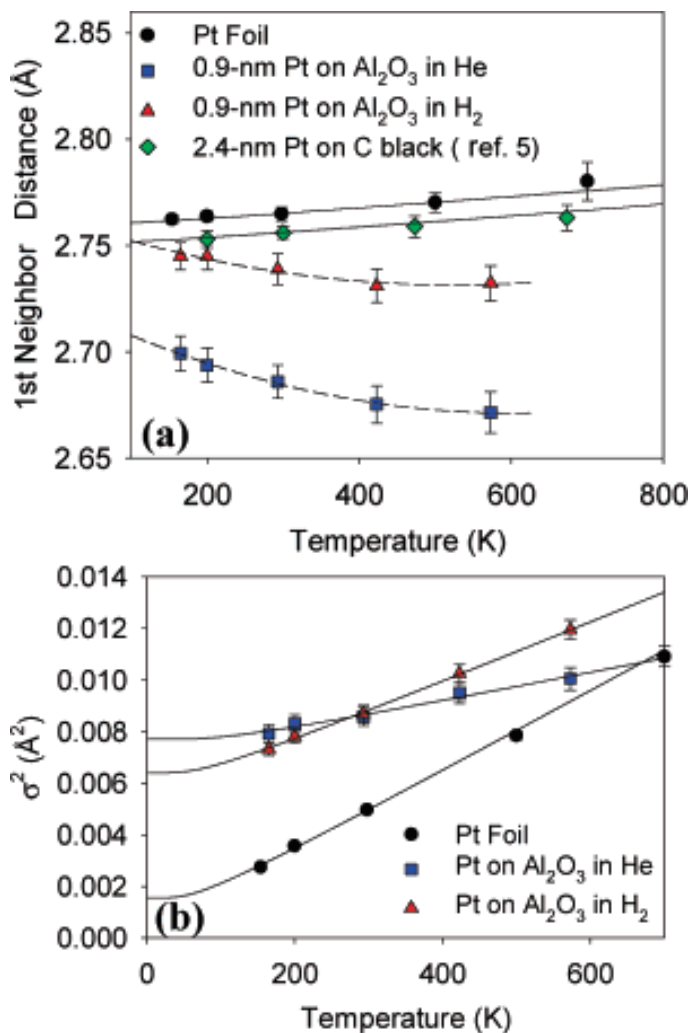
Figure 1.7. Evolution of Pt-Pt coordination parameters in supported Pt/γ-Al$_2$O$_3$ catalyst with 1 wt% of Pt and a Pt foil reference. (a) Temperature-dependent Pt-Pt first-neighbor distances of the Pt nanoclusters supported on γ-Al$_2$O$_3$ (ca. 0.9 nm), Pt nanoparticles (ca. 2.4 nm) supported on carbon black, and a Pt foil reference. (b) The mean-square relative displacement of the supported Pt clusters and Pt foil standard as a function of temperature. Adapted with permission from ref **35**. Copyright 2006 American Chemical Society.

The size-dependent properties on the metal-support interaction can also be reflected on the evolution of geometric structures of metal species during thermal treatments. Frenkel *et al.* have found an unusual contraction of surface Pt-Pt bonds in Pt nanoclusters supported on γ-Al₂O₃ (ca. 0.9 nm) during *in situ* X-ray absorption measurements.[35] As shown in **Figure 1.7**, the lattice distance of Pt-Pt bonds decreases when increasing the temperature, which is contrary to conventional supported Pt nanoparticles (like Pt/C sample). Furthermore, the size effects on the Pt-Pt bond dynamics has also been investigated by *in situ* EXAFS. When the size of Pt particles supported on γ-Al₂O₃ increases from ca. 0.9 to ca. 2.9 nm, such abnormal negative thermal expansion will disappear, and Pt particles will show positive thermal expansion coefficient, indicating that only Pt particles with very small sizes can show the nonbulk-like properties.[36]

1.3.2 Electronic interaction between metal species and the support

Electron transfer between the support and metal species is a result of the balancing between the Fermi energy level of the metal species and the support. The electron transfer will affect the charge density and distribution of metal species, which will further affect the catalytic properties.[37] Considering that the electronic structures will be dependent on the particle size, the metal-support interaction by electron-transfer process will also be dependent on the particle size.

In 2008, the electronic transfer between subnanometric Au clusters and alumina film has been studied by STM imaging and theoretical modelling. Nilius *et al.* have shown that, three electrons are transferred from the alumina support to Au_5 and Au_7 clusters, respectively.[38] When the atomicity of Au clusters increases to 18, four electrons transferred from MgO to Au clusters was observed. It should be noted that, the number of transferred electrons between Au clusters and the support is less on 2D Au clusters than 1D Au clusters, which should be related with their different electronic structures.[39]

In a recent work, Libuda *et al.* have measured the size effects of metal species, ranging from subnanometric clusters to nanoparticles, on the electronic metal-support interaction (EMSI) between Pt and CeO_2.[40] As shown in **Figure 1.8**, the electronic states of Pt species measured by resonant photoemission

spectroscopy are strongly dependent on the particle size. Pt nanoparticles with about 30-70 atoms show the highest positive charge on each Pt atoms, which indicates the strongest electronic metal-support interaction. To explain the size effects on the charge transfer process between Pt and CeO_2, density functional calculations have been performed. According to the DFT calculations, the particle size of Pt, the density of Pt species on CeO_2 surface and the concentration of surface Ce^{3+} on the CeO_2 surface can be the reasons accounting for the experimental results. Looking into those results from another viewpoint, in many experimental works, the sizes of supported Pt species (the supports vary from metal oxides to carbon or other materials) in the high-performance catalysts are usually in the range of 1-3 nm, which is consistent with the above work.[41-43] Such coincidence implies that the electronic interaction between the metal and support and the catalytic performances of metal particles can be correlated.
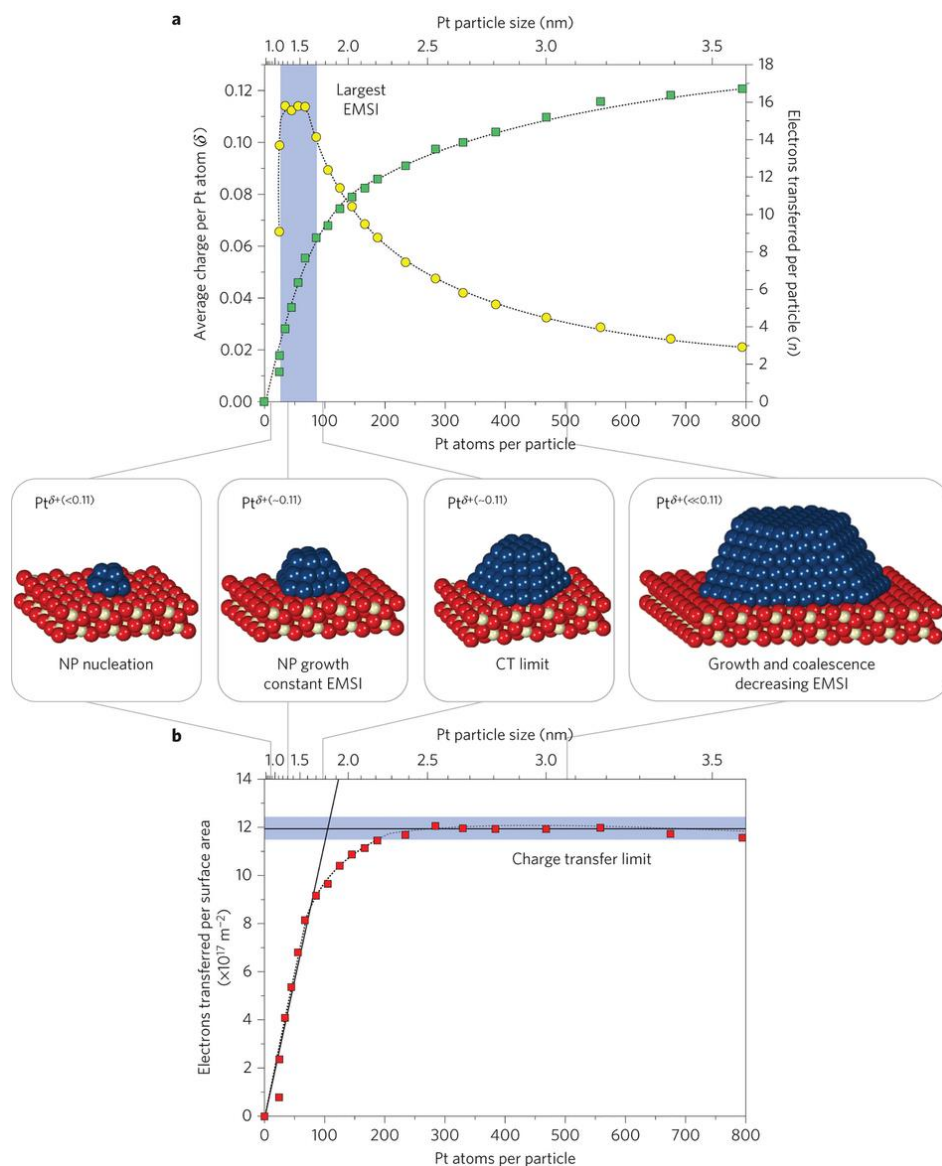
Figure 1.8. (a) The average charge on each Pt atom in Pt particles with different sizes measured by resonant photo-emission spectroscopy. The partial charge on each Pt atom reaches a maximum for Pt nanoparticles with 30 to 70 atoms. (b) The relationship between electrons transferred per surface area and the size of Pt deposited on CeO_2. At higher Pt coverage, the total amount of transferred electrons approaches a charge-transfer limit. Schematic models of Pt/CeO_2

samples with different size of Pt species are also shown in this figure. Adapted with permission from ref **40**. Copyright 2016 Macmillan Publishers Limited, part of Springer Nature.

Nevertheless, the electron transfer between metal and the support is also affected by the geometric location of the metal species on the support. As a typical example, Au atoms are found to be negatively charged when deposited on thin MgO(100) film with 3-layer thickness.[44] In the case of Pd atoms, they remain neutral on the same support, which is in line with theoretical calculations.[45] Interestingly, when the support is FeO(111)/Pt(111) surface, it has been found that Au atoms are positively charged while Pd atoms remain neutral. Au atoms show preferential binding to the hcp hollow positions of FeO(111)/Pt(111) surface, while Pd atoms show a randomly distribution on the same surface and still remain neutral.[46] By comparing the results obtained from different systems, it is proposed that, the charge states of Au atoms are related with the positions occupied by Au atoms on different surface.[47]

In a recent work, Vajda *et al.* have investigated the structural evolution of subnanometric Co clusters under oxidation conditions.[48] Size-selected Co_n clusters (n=4, 7, and 27) were firstly deposited on amorphous alumina and ultra-nanocrystalline diamond (UNCD) surfaces before being oxidized by exposure to ambient atmosphere. Grazing incidence X-ray absorption near-edge spectroscopy (GIXANES) and near-edge X-ray absorption fine structure (NEXAFS) were used to characterize the clusters to get information about their structural evolution by oxidative treatment. Most of Co^0 species were oxidized to Co^{2+} in all samples regardless of the size and the support. However, XANES analysis of Co clusters on UNCD showed that ~10% fraction of a Co^0 phase remained and resisted the oxidative conditions for all three Co clusters. Moreover, about 30%, 27% and 12% fraction of a Co^{3+} phase in Co_4, Co_7, and Co_{27} clusters were detected, respectively. In the alumina-supported clusters, metallic Co^0 species were not observed and it was proposed that the dominating Co^{2+} species could be attributed to the formation of cobalt aluminate due to the strong binding of Co^{2+} to the support. NEXAFS showed that their structures also follow the tetrahedral morphology of the support.[49]

For simplicity, the electronic interaction between metal species and the

support can be modeled as metal-semiconductor junction.[50,51] Therefore, the electronic energy level will reach an equilibrium state at the metal-support interface, being the equilibrium energy level structure dependent on both the metal species and the support. For metal species supported on a specific solid carrier, the electronic structure of the metal-support junction is related with the atomicity of metal species. Basically, for supported large metal nanoparticles, they prefer to be in metallic state, especially for noble metal nanoparticles (such as Au, Ag, Pt, etc.). It has been observed in many systems that, metal clusters prefer to be positively charged, which is a medium state between metallic nanoparticles and isolated atoms. Besides, for electron-donor support, metal species may prefer to be electron-rich state compared to those supported on electron-acceptor support. For instance, when Ru nanoparticles supported on electride compound, the electron density in Ru nanoparticles is higher than those supported on conventional supports, and the Ru/electride catalysts show higher activity for ammonia synthesis.[52,53]
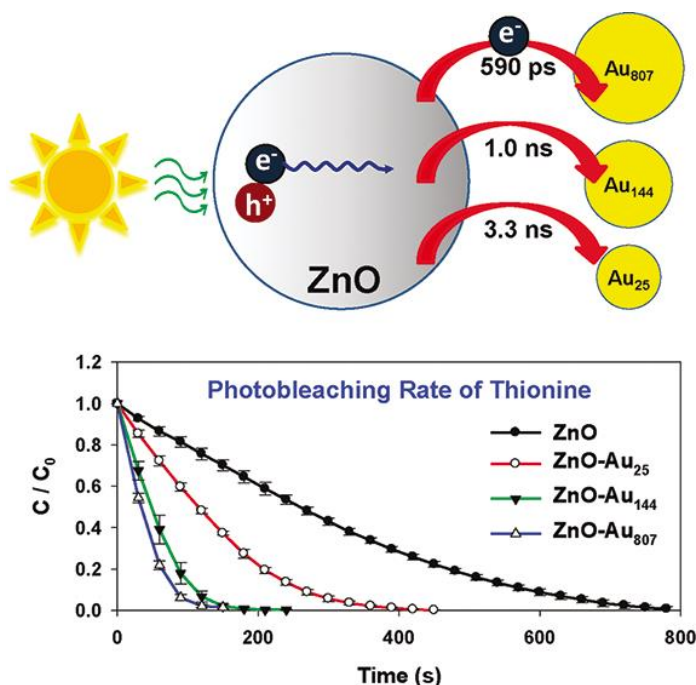

Figure 1.9. Schematic illustration of charge-transfer between ZnO nanoparticle and Au particles with different sizes. The kinetic curves of photocatalytic

degradation of thionine (a model dye molecule) is also presented to show the kinetic of the recombination of photo-generated electrons and holes in ZnO nanoparticles. With faster charge-transfer process between Au particles and ZnO nanoparticles, the photocatalytic degradation of thionine will be faster. Adapted with permission from ref **56**. Copyright 2011 American Chemical Society.

Moreover, the charge-transfer process between metal and support also plays an important role with working catalysts. A typical example is the separation of photo-generated electrons and holes at the interface of metal-semiconductor interface.[54] An electronic equilibrium will be established once the contact of metal and semiconductor is formed. Since the electronic structures of the semiconductor support is usually constant, the electronic structures of metal species have significant influence on the electronic structures of the metal-semiconductor junction. When photo-generated electrons are produced in the semiconductor, they will probably be transferred to the metal particles through Schottky barrier.[55] As shown in **Figure 1.9**, the charge-transfer rates between ZnO nanoparticles and Au particles with different sizes have been measured by ultrafast spectroscopy. When the particle size increases from ca. <1 nm (Au_{25}) to ca. 3.5 nm (Au_{807}), the charge-transfer rate also increases, leading to higher photocatalytic activity for thionine degradation.[56]

1.3.3 Metal-reactants interaction on different types of metal species

When molecules are absorbed by metal species, orbital hybridization between metal and the adsorbed molecules will occur. Since CO is usually used as probe molecule to study the electronic and geometric structures of metal species, Sitja *et al.* have measured the CO adsorption energy on Pd particles with different sizes ranging from 0.6 to 6 nm, as shown in **Figure 1.10**.[57] When the size of Pd particles is larger than 1.8 nm, the CO adsorption energy shows a gradual increase when increasing the particle size. However, for Pd particles below 2 nm, the CO adsorption energy shows irregular oscillation, since according to DFT calculations, electronic and geometric structures of metal clusters strongly depend on the atomicity.[58] The variations in the CO adsorption energy indicate the transition of metal species from non-metallic to metallic

when changing the particle size from molecule-like state (below 1 nm) to bulk-like state (nanoparticles larger than 2 nm). The same tendency was observed when CO molecules are adsorbed on Au particles with different sizes. Lowest adsorption energy was observed on Au nanoparticles of ~2 nm, which corresponds to the transition of non-metallic to metallic properties.[59]
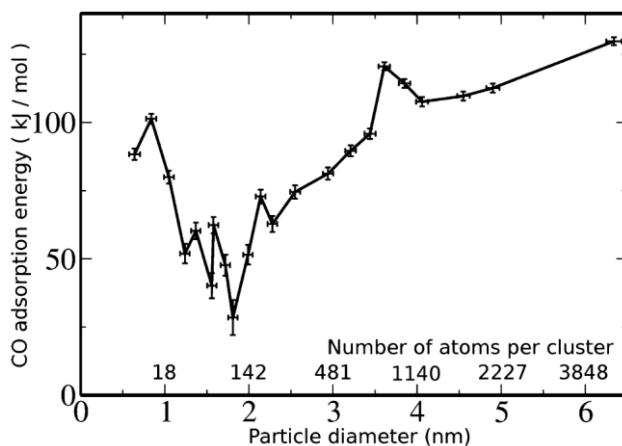

Figure 1.10. Size-dependent CO adsorption energy on Pd species from subnanometric clusters to nanoparticles. Adapted with permission from ref **57**. Copyright 2013 American Chemical Society.

When small molecules are adsorbed on metal species, the geometric deformation will also be dependent on the particle size. Lei *et al.* have studied the structural changes in Pt nanoparticles of 1-3 nm when interacting with small molecules. Thus, significant relaxation of Pt-Pt bonds can be observed in Pt nanoparticles of ~1 nm when H_2 and CO is adsorbed on the surface, as a consequence of orbital hybridization between the metal species and molecules. When the size increases to 2-3 nm, the adsorbate-induced lattice relaxation of Pt nanoparticles is much smaller, which can be ascribed to its lower fraction of surface unsaturated-coordinated Pt atoms.[60]

Due to the interaction between metal species and molecules, different types of metal species can suffer dynamic transformations under various treatments. It has been found that, by consecutive treatment with CO and NO, Pd nanoparticles can show dynamic size and shape transformations under different atmosphere.[61,62] In oxidative atmosphere (such as O_2, NO), Pd nanoparticles

will disintegrate into smaller particles or even subnanometric species. After reductive treatment with CO or H_2, Pd species will agglomerate into larger particles. Tracking by *in situ* EXAFS, it has been demonstrated that, the dynamics for the above redispersion-agglomeration behavior is strongly related with the particle size of metal species. In this sense, we have recently reported the reversible transformation of Pt nanoclusters (~1 nm) into single Pt atoms in high-silica CHA zeolite.[63] As shown in **Figure 1.11**, the size of Pt species in the chabazite can go from single atoms to small Pt nanoparticles (1-2 nm) by controlling the temperature and atmosphere.
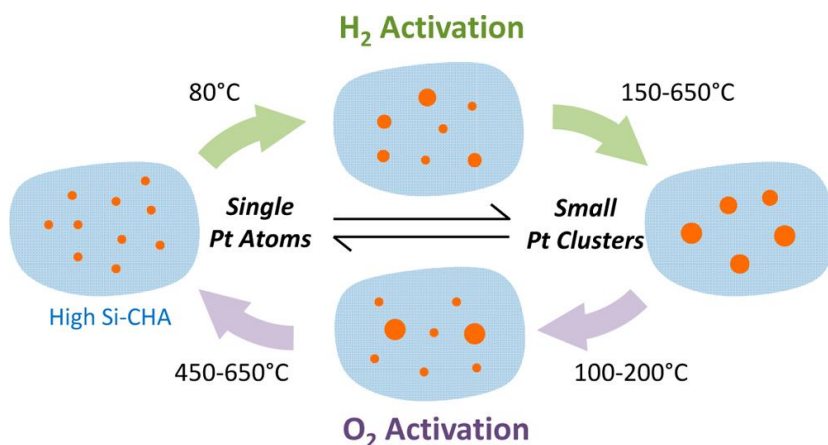

Figure 1.11. Reversible transformation between single Pt atoms and Pt nanoclusters (~1 nm) confined in CHA zeolite under reduction-oxidation treatments. Adapted with permission from ref **53**. Copyright 2017 American Chemical Society.

Such dynamic structural transformation of supported metal species has also been found on other metals like Au and Cu when the metal species interact with molecules.[64,65] Understanding such dynamic processes can help to control the size of metal species at a precise level and provide an alternative approach for generation of supported metal catalysts or can serve as a strategy for the regeneration of deactivated catalyst.[66,67] In the above discussion, we have presented some factors that can affect the size, shape and electronic characteristics of metal catalysts. They will be useful to explain the reactivity of the supported metal catalysts

1.4   Catalytic applications of supported single atoms

1.4.1 CO oxidation

Au single atoms for CO oxidation

   Since the pioneering work from Haruta, the application of Au catalysts for low-temperature CO oxidation has attracted plenty of attention and great effort has been made to develop Au catalysts with new structures and to identify the active sites.[68] Although it has been well demonstrated that Au nanoparticles (~2 nm) can be very active for low-temperature CO oxidation, there is still debate on the catalytic role of subnanometric Au species, including Au clusters and single Au atoms. Zhang *et al.* have reported two examples of supported single Au atoms for CO oxidation. In one report, Au/FeOx catalysts with very low Au loading (0.03 wt% to 0.09%) exhibited high activity and excellent stability for CO oxidation. From high-resolution STEM images, the presence of highly dispersed Au single atoms in the Au/FeOx sample with 0.03 wt% of Au was confirmed. Nevertheless, in the Au/FeOx sample with Au loading of 0.09 wt% , a small amount of Au clusters and nanoparticles could also be observed.[69,70] In another work, Au/CeO$_2$ with low Au loading amount (0.05 wt%, containing singly dispersed Au atoms) was prepared and used for oxidation of CO in the presence of H$_2$ (CO-PROX).[71] It was reported that, the Au single atoms supported on CeO$_2$ show higher selectivity to oxidation of CO, with very low selectivity to oxidation of H$_2$ at 80 $^\circ$C, than Au/CeO$_2$ samples containing Au clusters and nanoparticles, making the single-atom Au/CeO$_2$ an excellent catalyst for CO-PROX reaction. Unfortunately, no information about how CO and O$_2$ are activated and how they react on supported single Au atoms was reported. This could be an interesting research to investigate if it is the cooperative effect between Au and CeO$_2$ that should be responsible for the observed activity. If this is so, then the catalytic active site would not be a single atom, but an association of Au and Ce/O.

Pt single atoms for CO oxidation

   In the case of Pt, Zhang et al. reported that it was possible to prepare single Pt atoms dispersed on FeOx by a co-precipitation method, and the catalytic properties of Pt single atoms were studied for the CO oxidation reaction.[72] As shown in **Table 1**, the Pt$_1$/FeOx (sample A) with Pt single atoms show higher

specific rate and higher TOF than Pt/FeOx catalyst containing Pt clusters and nanoparticles (sample B), indicating that singly dispersed Pt atoms supported on FeOx can be efficient catalyst for both CO oxidation and CO-PROX under mild conditions. DFT calculations show that O_2 is activated at the neighboring O-vacancy site of the Pt atom in FeOx support. The partially vacant 5d orbitals of the positively charged Pt atoms can adsorb and activate CO with lower barrier energy than Pt clusters, which makes Pt single atoms more active for CO oxidation.

Table 1 Catalytic performance of Pt/FeOx catalysts (Sample A and Sample B) in comparison with Au/Fe_2O_3 from World Gold Council. Sample A with low Pt loading contains Pt single atoms while Sample B with high Pt loading mainly contains Pt clusters and nanoparticles. Adapted with permission from ref **72**. Copyright 2014 Macmillan Publishers Limited, part of Springer Nature.

	Metal loading (wt %)	Reaction	Temp. (°C)	Specific rate× 10^2 (mol_{CO} h^{-1} g_{metal}^{-1})	TOF $\times 10^2$ [b]
Sample A	0.17	CO+O_2	27	43.5	13.6
Sample B	2.5	CO+O_2	27	17.7	8.01
Au/Fe_2O_3[a]	4.4	CO+O_2	27	21.7	4.76
Sample A	0.17	CO-PROX	27	67.6	21.2
Sample B	2.5	CO-PROX	27	20.3	9.15
Au/Fe_2O_3 [a]	4.4	CO-PROX	27	39.3	8.60
Sample A	0.17	CO-PROX	80	99.2	31.1
Sample B	2.5	CO-PROX	80	35.8	16.2
Au/Fe_2O_3 [a]	4.4	CO-PROX	80	80.3	17.6

[a] The Au/Fe_2O_3 sample was provided by the World Gold Council. [b] TOFs were calculated based on the metal dispersion in the catalysts. For Pt/FeOx samples, the metal dispersion was measured by CO chemisorption. For Au/Fe_2O_3 sample, the dispersion was estimated by the average particle size.

According to theoretical calculations, it appears that the FeOx support in the

Pt_1/FeOx catalyst participates in the catalytic pathways for CO oxidation. It should be then interesting to study the behavior of single Pt atoms dispersed on inert supports (like Al_2O_3, SiO_2, TiO_2 etc.). Following that, Narula *et al.* studied the catalytic properties of Pt single atoms supported on an inert support (θ-Al_2O_3) for CO oxidation and the results were compared with those obtained with Pt nanoparticles (~1 nm) supported on θ-Al_2O_3.[73] It was found that singly dispersed Pt atoms can catalyzed the CO oxidation reaction. However, the TOF at 200 °C for Pt nanoparticles was nearly four-fold higher than that for Pt/θ-Al_2O_3 with singly dispersed Pt atoms, indicating that Pt nanoparticles were intrinsically more active than Pt single atoms for CO oxidation when supported on θ-Al_2O_3.

In the case of TiO_2, Christopher *et al.* reported the generation of stable single Pt atoms on TiO_2 by strong electrostatic adsorption of very low amount of Pt on TiO_2 (0.025-0.05 wt%). The activity was compared with a Pt/TiO_2 sample (1.0 wt% of Pt) containing Pt nanoparticles (~1 nm). Kinetic studies showed that, both Pt single atoms and nanoparticles followed the same reaction mechanism and the rate-limiting step was related with O_2 activation. The catalytic results indicated that, single Pt atoms showed 4- to 6-fold more active than Pt nanoparticles (~1 nm) on the basis of activity normalized to Pt mass. It is suggested by the authors that, the Pt-TiO_2 interface is the active site for CO oxidation and the rate-limiting step involves the migration of atomic oxygen from TiO_2 to isolated Pt atoms or interfacial Pt species in the Pt/TiO_2 sample containing Pt nanoparticles.[74] However, the catalytic behavior of subnanometric Pt clusters were not studied and it seems that part of the isolated Pt atoms sintered into Pt clusters according to the IR spectra during the CO oxidation test in a fix-bed reactor.

Furthermore, it has been reported that Pt single atoms within a zeolite can catalyze CO oxidation at 150 °C with a moderate activity.[75] Unfortunately, no direct activity comparison between single Pt atoms and Pt clusters or nanoparticles was performed in that work.

Since water plays a critical role on the activity and selectivity of Au nanoparticles for CO oxidation reaction and CO-PROX,[76,77] its potential role on catalytic properties of Pt single atoms has been recently studied. Single Pt atoms were generated on CeO_2 by atomic layer deposition (ALD) and the role

of water in CO oxidation was studied.[78] By kinetic and isotopic studies together with theoretical calculations, it was proposed that CO oxidation can be significantly improved by a water-mediated Mars−van Krevelen mechanism instead of the previously reported Langmuir−Hinshelwood mechanism on Au catalysts. Notably, transformation of part of the single Pt atoms into Pt clusters after the CO oxidation reaction at 90-100 $^{\circ}$C was observed by high-resolution STEM. Therefore, it can still be discussed if the active species are the single Pt atoms or the Pt clusters and Pt nanoparticles formed under reaction conditions.

The stability of single atoms is a critical issue due to their strong trend to agglomerate into clusters or nanoparticles, especially in the presence of CO. Recently, it has been found that Pt atoms can evaporate from Pt nanoparticles during a high-temperature treatment of Pt/La-Al$_2$O$_3$ catalyst in air at 800 $^{\circ}$C and trapped by CeO$_2$ nanocrystals.[79] Those trapped Pt atoms on CeO$_2$ were stable up to 800 $^{\circ}$C in air and the addition of CeO$_2$ can significantly improve the stability of Pt/La-Al$_2$O$_3$ catalyst during the high-temperature aging treatment. However, the activity of those Pt single atoms for CO oxidation reaction is much lower than other reported Pt/CeO$_2$ catalysts containing Pt nanoparticles. Besides, it has also been reported that, mesoporous Al$_2$O$_3$ can serve as the support to stabilize Pt single atoms, even after H$_2$ reduction treatment at 400 $^{\circ}$C.[80] It is claimed that those Pt single atoms are highly stable during the CO oxidation reaction up to 400 $^{\circ}$C.
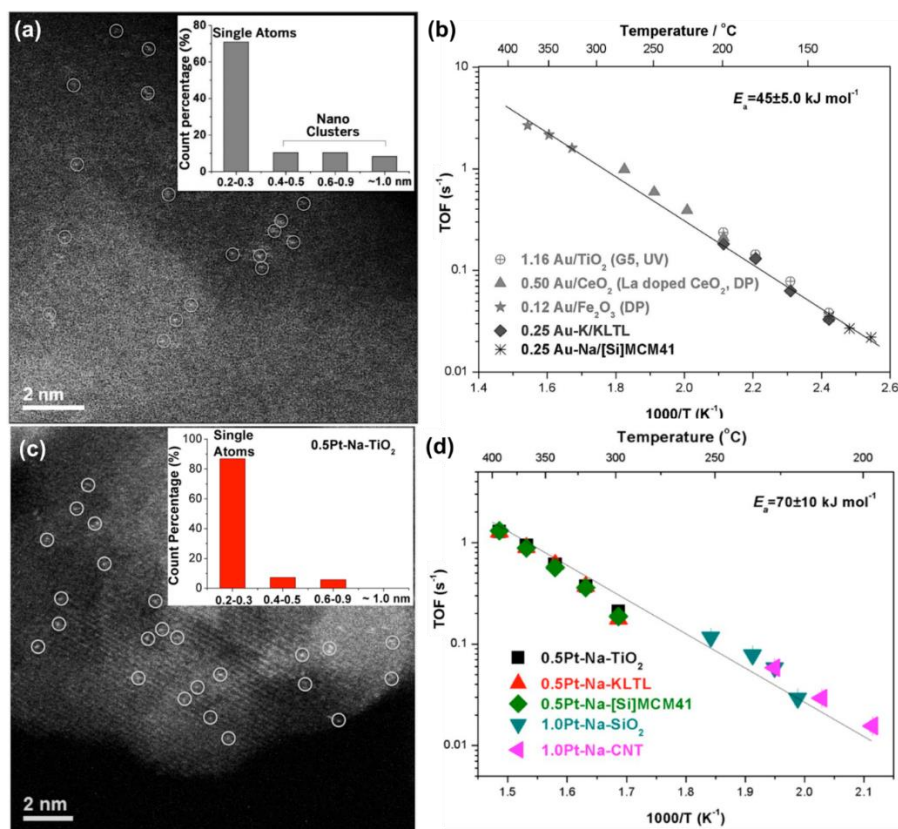
Figure 1.12. (a) High-resolution STEM image and the corresponding size distribution of Au species in Au-Na/[Si]MCM41 catalyst with 0.25 wt% of Au. (b) TOF values of atomically dispersed Au species on different supports. The TOF values are obtained under the same reaction conditions. Adapted with permission from ref **90**. Copyright 2014 Association for the Advancement of Science. (c) High-resolution STEM image and the corresponding size distribution of Pt species in Pt-Na/TiO$_2$ catalyst with 0.5 wt% of Pt. (d) TOF values of atomically dispersed Pt species on different supports. The TOF values are obtained under the same reaction conditions. Adapted with permission from ref **91**. Copyright 2015 American Chemical Society.

1.4.2 Water-gas shift

Like CO oxidation, water-gas shift (WGS) is also a widely-used model reaction. In 2003, Flytzani-Stephanopoulos *et al.* pointed out the important role

of non-metallic Au and Pt species on CeO_2-based catalysts for WGS reaction.[81] After chemical leaching of the metallic nanoparticles in conventional Au/CeO_2 and Pt/CeO_2 catalysts containing a large number of metallic nanoparticles, their activity is almost not affected, implying that those residual non-metallic Au and Pt are the active species. In following work, the authors have further demonstrated that, atomically dispersed Pt stabilized by alkali ions are the active sites for WGS reactions.[82] The introduction of alkali ions can generate partially oxidized Pt-alkali-Ox(OH)y sites, which are able to catalyze the WGS reaction at low temperature range (200-300 °C). According to their latest works, not only single Au and Pt atoms supported on CeO_2, but also single atoms supported on other oxides (like TiO_2, FeO_x, SiO_2, zeolites, etc.) are proposed to be the active sites in WGS reaction.[83,84] It is also found that, atomically dispersed metal species (both Pt and Au) supported on various supports show almost the same apparent activation energy (see **Figure 1.12b** and **Figure 1.12d**), implying that a common single-site species exist in different catalysts for the WGS reaction.[85]

In the above works, alkali ions are required to stabilize Au and Pt single atoms. In a recent work, Zhang *et al.* reported the utilization of single Ir atoms for WGS reaction without the addition of alkali ions.[86] By decreasing the Ir loading to 0.01 wt%, it was possible to generate isolated Ir sites on FeO_x and those Ir single atoms show higher TOFs for WGS reaction at 300 °C compared with Ir clusters and nanoparticles.

The size of metal species will also affect the product distributions in WGS reaction. The high activity and suppressed selectivity to methanation product (CH_4) has been reported on atomically Rh species supported on TiO_2 during WGS reaction.[87] At 300 °C, the selectivity to CH_4 was almost zero on Rh/TiO_2 catalysts containing Rh single atoms as the dominant species, while Rh nanoparticles gave ~50% selectivity to CH_4. Based on spectroscopic characterizations, it is proposed that H_2 dissociation is not favorable on isolated Rh atoms, and this leads to low CO_2 methanation activity.
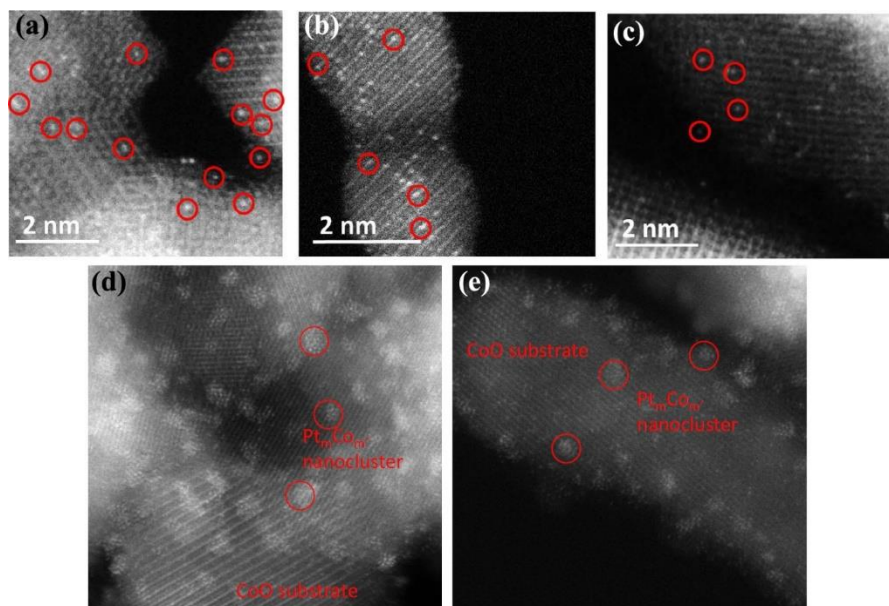
Figure 1.13. (a-c) High-resolution STEM images of singly dispersed Pt atoms on Co_3O_4 nanorods. Pt atoms are indicated by red circles. (d, e) High-resolution STEM images of Pt_mCo_n/CoO sample after WGS reaction at 350 °C. Pt_mCo_m clusters are indicated by red circles. Adapted with permission from ref **88**. Copyright 2013 American Chemical Society.

Nevertheless, it should be taken into consideration that when working with single atoms, metal clusters and nanoparticles can also be present and metal species may undergo dynamic structural transformation (including morphological and chemical transformation) under reaction conditions. It is then crucial when studying the catalytic behavior of single atoms to investigate their state under reaction conditions. Along this line, in a recent work, Pt single atoms supported on Co_3O_4 nanorods were used as catalyst for WGS reaction.[88] It was observed that in the fresh catalyst, single Pt atoms were dispersed on Co_3O_4 nanorods and they were stable after calcination in air. However, after catalyzing WGS reaction at 350 °C, single Pt atoms aggregated and formed Pt_mCo_n bimetallic clusters, as determined by STEM images (**Figure 1.13**). Interestingly, the activation energy of Pt_mCo_n clusters for WGS reaction was lower than that of single Pt atoms. This work illustrates that metal atoms or

clusters may have strong interaction with the supports and they can show dynamic structural transformations during the reactions.

Such transformation of metal species under reaction conditions was also confirmed by *in situ* TEM techniques.[89] It was observed that subnanometric Au clusters were generated from singly dispersed Au atoms under WGS reaction conditions. However, the whole evolution process of Au species was not clearly demonstrated, probably due to the instrument limitation. The contrast between Au species and the CeO_2 support is not high enough for studying such process when working under bright-field transmission mode. Similar agglomeration of subnanometric Au species into Au nanoparticles has also been observed on $Au/CeZrO_4$ catalyst by *in situ* TEM.[90] This is an interesting phenomenon and we believe that the dynamic evolution of subnanometric metal species could be studied with high-resolution HAADF-STEM and XANES-EXAFS spectroscopy to detect the potential structural transformation under reaction conditions.

1.4.3 Oxidation of alcohols

Selective oxidation of alcohols has wide applications in transformation of biomass platform molecules and fine chemicals. It has been presented that metal nanoparticles (such as Pt, Au, Pd, etc.) show excellent activity and selectivity for selective oxidation of alcohols under mild conditions.[91,92] In recent years, it has been reported that single atoms can also serve as the active sites for oxidation of alcohols. In 2007, Hackett *et al.* reported the generation and application of single Pd atoms supported on mesoporous alumina for selective oxidation of allylic alcohols.[93] As shown in **Figure 1.14**, Pd species (from single Pd atoms to clusters to nanoparticles) showed strong size effects on the TOFs in oxidation of crotyl alcohol. With smaller Pd species, the TOF value became higher and reach the maximum with Pd single atoms while the high selectivity was also preserved. The selective oxidation of allylic alcohols can also be catalyzed by supported Au nanoparticles, giving very high selectivity (99%) to α,β-unsaturated carbonyl compounds.[94] Compared with the state-of-art supported Au catalysts (538 h^{-1} at 120 ^{o}C), Pd single atoms supported on mesoporous alumina show even higher TOF (4400 h^{-1} at 60 ^{o}C),

although the selectivity to α,β-unsaturated carbonyl compound is lower (~90%). The life time of the nanoparticulate Au catalysts for selective oxidation of allylic alcohols were very long, however, the lifetime of the Pd single atoms during the oxidation of alcohols was not mentioned.
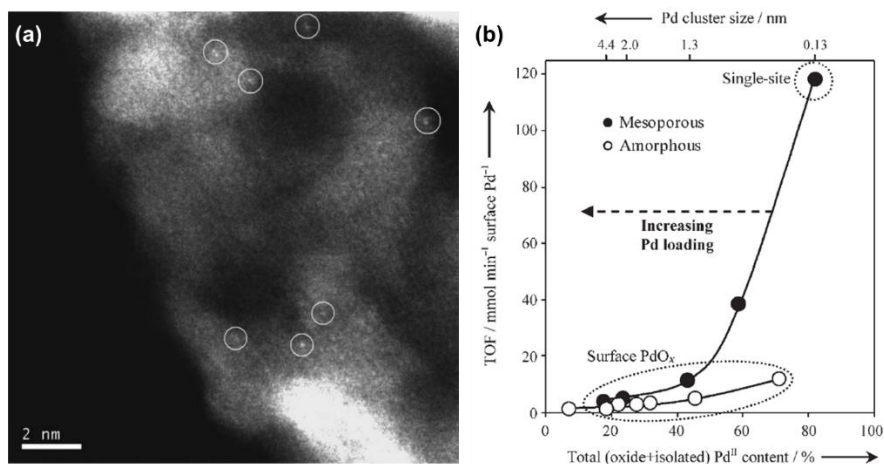

Figure 1.14. (a) High-resolution STEM image of Pd/Al$_2$O$_3$ sample containing 0.03 wt% of Pd. (b) Relationships between the TOFs of surface Pd species for aerobic oxidation of crotyl alcohol and the particle size and chemical states of Pd in various Pd/Al$_2$O$_3$ catalysts. Adapted with permission from ref **93**. Copyright 2007 Wiley-VCH Verlag GmbH & Co. KGaA, Weinheim.

In the last few years, the development of non-noble metal catalysts as substitute for noble metals is emerging in heterogeneous catalysis. Recently, it has been widely reported that single transition metal atoms (such as Co, Fe, etc.) can be stabilized by N-doped carbon. Beller *et al.* reported the application of Co-N-C and Fe-N-C catalysts for oxidative esterification of alcohols and oxidative dehydrogenation of N-heterocycles.[95,96] With the help of high-resolution STEM, it was revealed that the active sites for these selective oxidation reactions may be associated with the atomically dispersed metal species embedded in the carbon support while the residual nanoparticles are not active.[97] A series of catalysts containing transition metal atoms stabilized by N-doped carbon have been studied for selective oxidation of alcohols.[98] It was found that beside Co-N-C and Fe-N-C, Cu-N-C, Ni-N-C and Cr-N-C are also

active for the oxidation of benzyl alcohol to benzyl aldehyde. Among them, Cu-N-C sample shows the best performance, which is only one-order of magnitude lower than Pt-based catalyst. However, these atomically dispersed metal species show poor activity for oxidation of aliphatic alcohols. Isotopic studies show that, the β-H elimination is a key step in oxidation of benzyl alcohol. Deeper understanding of the catalytic mechanism in these systems is necessary to further improve the performance and stability of those catalysts for substituting noble metal catalysts.

1.4.4 Selective hydrogenation
Pt-group single-atom catalysts for hydrogenation reactions

Pt-group metals are widely used industrially for hydrogenation reactions. In those industrial catalysts, Pt-group metals mainly exist as nanoparticles. In recent years, new methodologies have been developed to generate single-site Pt-group metals and these single-atom catalysts have shown promising catalytic performances for hydrogenation reactions.

A series of Pt/FeOx catalysts were prepared by a co-precipitation method and Pt species with different particle size ranging from single atoms to nanoparticles were generated by tuning the loading of Pt (see **Figure 1.15**).[99] The catalytic performances of various Pt/FeOx catalysts are exhibited in **Table 2**. Interestingly, all the Pt/FeOx catalysts show excellent selectivity for the chemoselective hydrogenation of 3-nitrostyrene, and the TOFs based on all the Pt atoms in the catalyst almost keep constant when the Pt loading increases from 0.08 wt% to 0.75 wt%, although the size distribution of Pt species varies with the loading amount of Pt. The Pt single atoms in the 0.08%Pt/FeOx-R200 sample show a remarkable TOF of 1494 h^{-1}, which is nearly 20 times higher than Pt/TiO$_2$ (containing Pt nanoparticles). Notably, subnanometric Pt clusters can also be observed in the 0.08%Pt/FeOx-R250 sample, which exhibits the highest TOF, implying that Pt clusters may also play a role in the hydrogenation of nitroarenes.

Table 2. Chemoselective hydrogenation of 3-nitrostyrene on different Pt/FeOx catalysts.^{a} Adapted with permission from ref **99**. Copyright 2014 Macmillan Publishers Limited, part of Springer Nature.

Entry	Catalyst	Time (min)	Conv. (%)	Sel. (%)	TOF (h^{-1})^d
1	0.08%Pt/FeOx-R200	49	95.6	98.4	1494
2	0.08%Pt/FeOx-R250	50	96.5	98.6	1514
3^b	0.08%Pt/FeOx-R250	7	88.8	91.1	11064
4	0.31%Pt/FeOx-R250	67	95.8	94.4	1506
5	0.75%Pt/FeOx-R250	73	96.7	92.6	1324
6	2.73%Pt/FeOx-R250	110	97.8	92.9	933
7^c	4.30%Pt/FeOx-R250	34	94.2	92.7	762
8	0.2%Pt/TiO$_2$-R450	840	96.8	94.0	88
9	0.08%Pt/SiO$_2$	65	87.9	46.9	-
10	0.08%Pt/Al$_2$O$_3$	158	87.3	27.8	-
11	Fe$_3$O$_4$	210	-	-	-
12	Fe$_2$O$_3$	240	-	-	-

^{a}Reaction conditions: Pt/substrate=0.08%, 40 ^{o}C and 3 bar of H$_2$; 5 mL reaction mixture: 0.5 mmol 3-nitrostyrene, toluene as solvent and o-xylene as internal standard. ^{b}Reaction performed at 80 ^{o}C with 10 bar of H$_2$. ^{c}Pt/Substrate=0.45%. ^{d}The TOFs were calculated based on the total amount of Pt species in the catalysts.

Compared with conventional Pt nanoparticles, Pt single atoms may show different selectivity in hydrogenation of different molecules.[100] Stabilized on phosphomolybdic acid, Pt single atoms show higher TOFs in hydrogenation of polar groups like -NO$_2$ and C=O compared with Pt nanoparticles supported on carbon. However, in the case of hydrogenation of C=C and C≡C groups, Pt single atoms are less active, indicating that the reactivity of different types of Pt species is dependent on the substrate molecules.

Different reactivity of single atoms will cause unique selectivity in hydrogenation reactions. For instance, Pd single atoms supported on graphene showed high selectivity to 1-butene during selective hydrogenation of 1,3-butadiene, while Pd nanoparticles gave higher selectivity to cis-2-butene and trans-2-butene and less full hydrogenation products, as shown in **Figure 1.16**.[101] Moreover, when the hydrogenation of 1,3-butadiene is performed in the presence of 70% propene in the feed gas, Pd single atoms show negligible

propene conversion while Pd nanoparticles will react much more with propene. Unique selectivity of Pd single atoms have also been reported for hydrogenation of alkynes.[102] Pd atoms stabilized by C_3N_4 show excellent selectivity (~90%) in hydrogenation of 1-hexyne to 1-hexene. However, there are still some arguments on the catalytic properties of single Pd atoms. For instance, Rossell *et al.* have reported that single Pd atoms supported on Fe_3O_4 show no activity in hydrogenation of alkenes while Pd clusters and nanoparticles are active.[103]
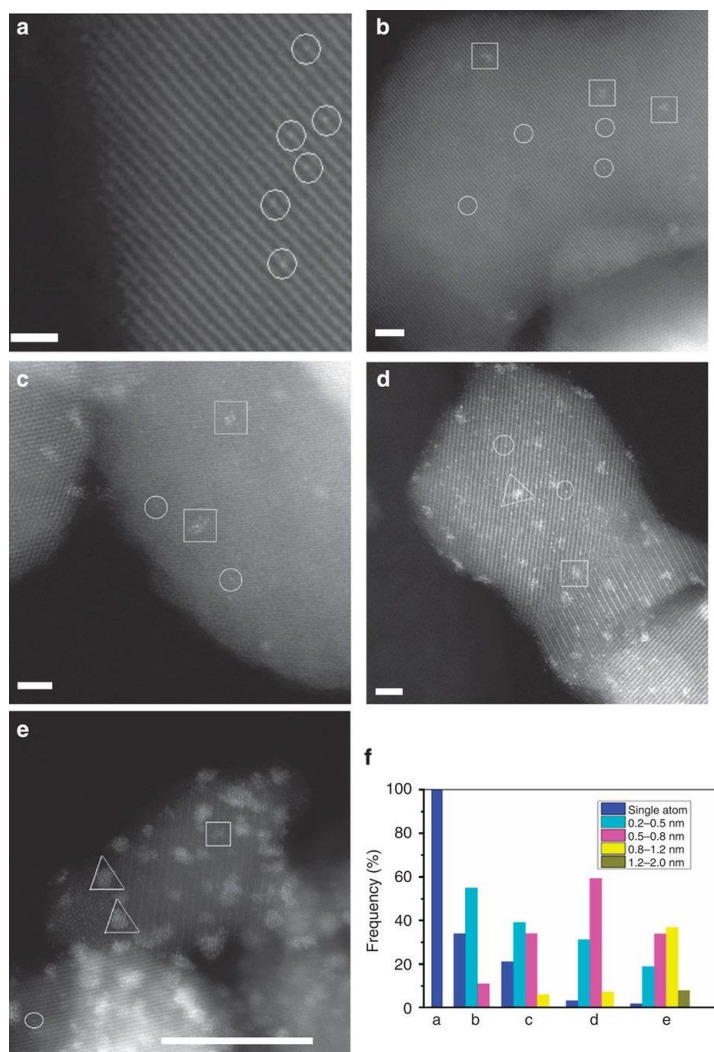
Figure 1.15. STEM images of various Pt/FeOx catalysts with different Pt

loading. (a) Pt/FeOx with 0.08 wt% of Pt and reduced by H_2 at 200 °C. (b) Pt/FeOx with 0.08 wt% of Pt and reduced by H_2 at 250 °C. (c) Pt/FeOx with 0.31 wt% of Pt and reduced by H_2 at 250 °C. (d) Pt/FeOx with 0.75 wt% of Pt and reduced by H_2 at 250 °C. (e) Pt/FeOx with 4.30 wt% of Pt and reduced by H_2 at 250 °C. The circles, squares and triangles in the above images correspond to single Pt atoms, two-dimensional Pt clusters and three-dimensional Pt nanoparticles, respectively. Adapted with permission from ref **99**. Copyright 2014 Macmillan Publishers Limited, part of Springer Nature.
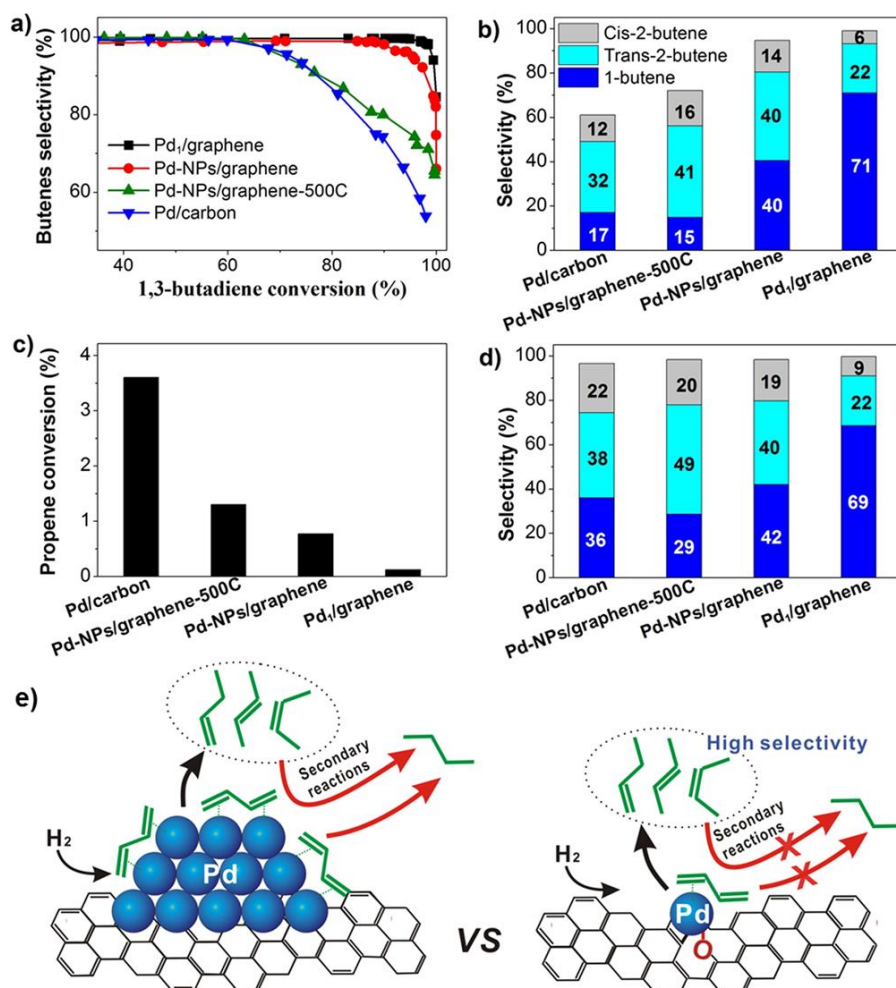
Figure 1.16. Catalytic performances of Pd$_1$/graphene, Pd-NPs/graphene, Pd-

NPs/graphene-500C, and Pd/carbon samples for selective hydrogenation of 1,3-butadiene. (a) Selectivity to butenes as a function of butadiene conversion by changing the reaction temperatures; (b) Distribution of butene products at 95% conversion of butadiene. Conversion of propene (c) and the distribution of butene products at 98% conversion of butadiene in the presence of 70% of propene in the feed gas. (e) Schematic illustration of the reactivity of 1,3-butadiene on Pd nanoparticles and Pd single atoms, showing different chemoselectivity. Adapted with permission from ref **101**. Copyright 2015 American Chemical Society.

Non-noble single-atom metal catalysts for hydrogenation reactions
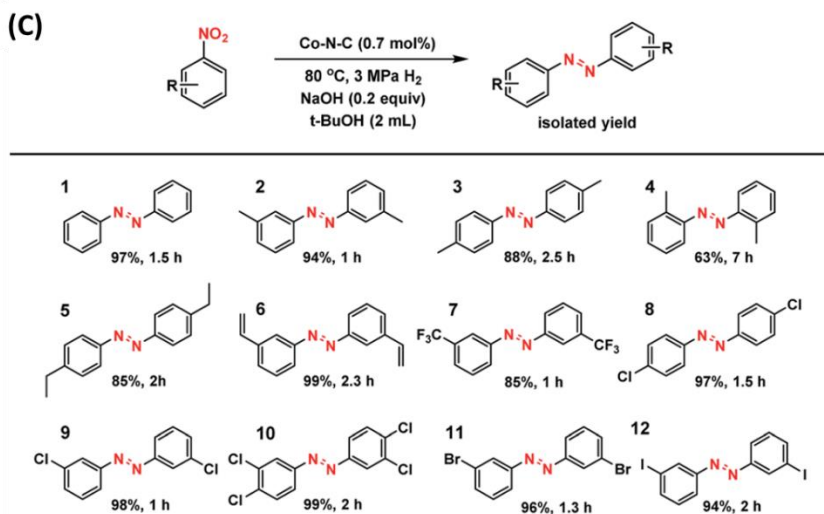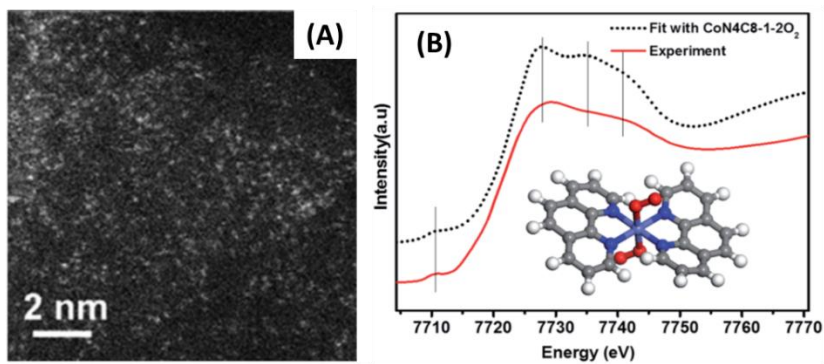
Figure 1.17. (A) High-resolution STEM image of singly dispersed Co atoms stabilized by N-doped carbon matrix (Co-N-C catalyst). (B) Determination of the coordination structure of Co-N-C catalyst according to the fitting and simulation of XANES spectrum. (C) Hydrogenation of nitroarenes to corresponding azo products using Co-N-C catalyst. Adapted with permission from ref **129**. Copyright 2016 The Royal Society of Chemistry.

In recent years, non-noble metal catalysts have attracted great attention and shown promising catalytic performances for substituting noble metal catalysts for selective hydrogenation reactions. For instance, Co nanoparticles covered by thin carbon layers have been reported as active and selective catalyst for chemoselective hydrogenation of nitroarenes to corresponding anilines.[104] The active sites are proved to be the surface of metallic Co nanoparticles and the role of the thin carbon layers is to protect Co nanoparticles from deep oxidation.[105,106] Recently, a facile method to generate a Co-N-C catalyst containing singly dispersed Co atoms on N-doped carbon matrix has been presented.[107] As shown in **Figure 1.17**, Co atoms were clearly observed by high-resolution STEM and their local coordination structure has also been clarified by EXAFS and XANES. The Co-N-C catalyst showed excellent activity and selectivity in hydrogenation of nitroarenes to corresponding azo products in the presence of strong base (NaOH), but the activity of Co-N-C catalysts was also lower than supported Au nanoparticles.[108,109] In another work, using MOF as precursor, Co-N-C catalyst containing atomically dispersed CoNx species was prepared and tested for selective hydrogenation of nitroarenes to corresponding anilines.[110] However, there is no direct comparison study on the catalytic performance of single-site Co catalysts and nanoparticulate Co catalysts.

Figure 1.18. Schematic illustration of immobilization of single-site Co catalyst in porous metal-organic framework and its catalytic applications for hydrogenation reactions. The metal centers in MOF is Zr or Hf and the organic linker is *p*-biphenylcarboxylate. The single-site Co catalyst is stabilized by the secondary building unites. Adapted with permission from ref **111**. Copyright 2016 American Chemical Society.

MOFs, as a versatile family of porous materials, can serve as tunable support for single-site non-noble metals. Taking advantage of the coordination interaction between the framework nodes and mononuclear metal complex, single-site Co catalyst can be generated and stabilized in MOFs. Single-site Co catalyst in MOFs can be applied for hydrogenation of unsaturated bonds, such as alkenes, imines, carbonyls and heterocycles (see **Figure 1.18**).[111] High turn-over numbers and stability can be achieved in those reactions, due to the open structure of MOFs and stabilization effects of single-site Co on the nodes. Besides, single-site Ni catalyst can also be prepared and show promising catalytic performances for hydrogenation of alkenes.[112] It can be expected that, the preparation and reactivity of single-site metal species in MOFs will expand the scope of single-site metal catalysts.[113]

1.4.5 Dehydrogenation and reforming reactions

Non-oxidative activation of CH_4 and selective transformation into olefins and aromatics are desired for utilization of natural gas resource. However,

traditional Mo-based catalysts are limited by a fast catalyst deactivation under non-oxidative reaction conditions.[114] Bao and his co-workers have developed a supported Fe©SiO$_2$ catalyst, showing remarkable activity and selectivity for direct non-oxidative conversion of methane to ethylene, aromatics and H$_2$.[115] In the Fe©SiO$_2$ catalyst after activation in CH$_4$/N$_2$ at 1173 K, atomically dispersed Fe species are confined in the matrix of SiO$_2$ through Fe-Si and Fe-C bonding, according to the *in situ* XAS analysis and high-resolution STEM (see **Figure 1.19E**). As shown in **Figure 1.19**, only Fe©SiO$_2$ catalyst containing atomically Fe sites can selectively transform CH$_4$ into desired products without the formation of coke, and give high selectivity to ethylene (~52.7% at 1293 K). Excellent stability has also been achieved at 1293 K with no obvious changes in conversion and selectivity.
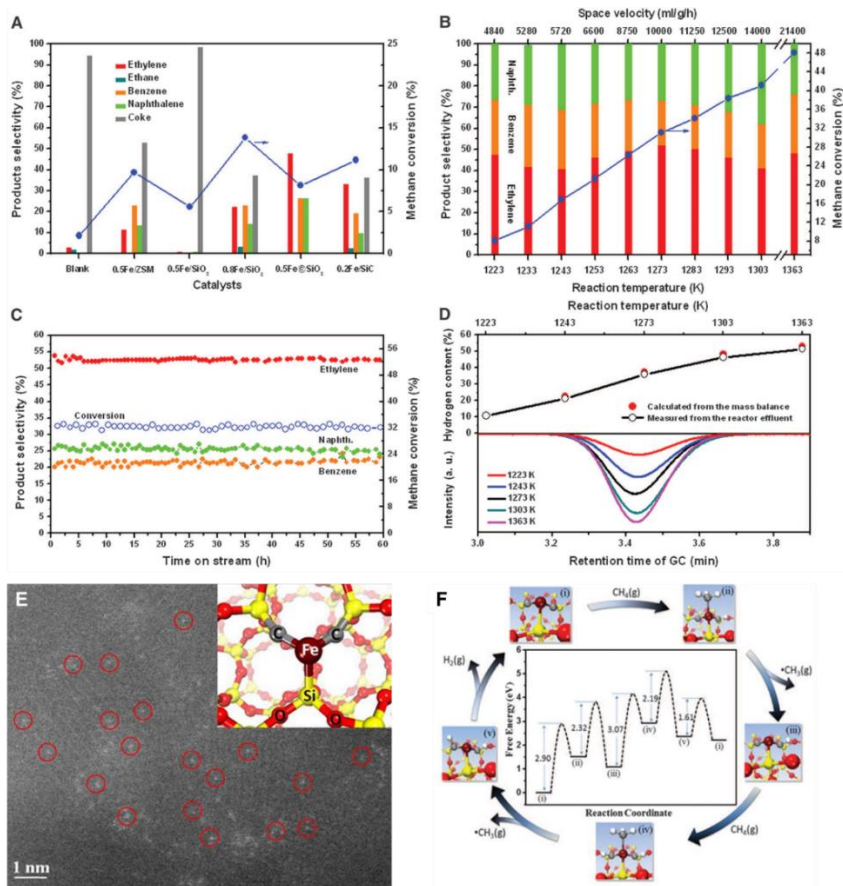
Figure 1.19. (A) Product distributions on various Fe-based catalysts. (B) Activity and distributions of the products on Fe@SiO$_2$ (with 0.5% of Fe) at different reaction conditions and space velocities. (C) Long-term stability test of Fe@SiO$_2$ (with 0.5% of Fe) at 1293 K. (D) Amount of H$_2$ produced at different temperature on Fe@SiO$_2$ (with 0.5% of Fe) catalyst. (E) High-resolution STEM image of Fe@SiO$_2$ (with 0.5% of Fe) catalyst after the reaction. (F) Schematic illustration of the catalytic mechanism of CH$_4$ activation on single-site Fe species confined in the SiO$_2$ matrix according to theoretical calculations. Adapted with permission from ref **115**. Copyright 2014 The American Association for the Advancement of Science.

By *in situ* spectroscopic characterizations and theoretical calculations, the activation of CH$_4$ on single-site Fe catalyst is proposed as described in **Figure 1.19F**. CH$_4$ is activated on Fe atoms and gives CH$_3$· radicals and H$_2$. Then, CH$_3$· radicals in the gas phase will form ethylene and aromatics. In this work, the unique geometric and electronic structures of single-site Fe catalysts can efficiently break the C-H bonds in CH$_4$ without formation of coke. The concept of Fe©SiO$_2$ catalyst has further been applied for non-oxidative activation of CH$_4$ in hydrogen-permeable tubular membrane reactor.[116] By adding H$_2$ in the feed gas into the membrane reactor, 30% conversion of CH$_4$ and 99% selectivity to C2 products (acetylene and ethylene) can be achieved with good stability at 1303 K.
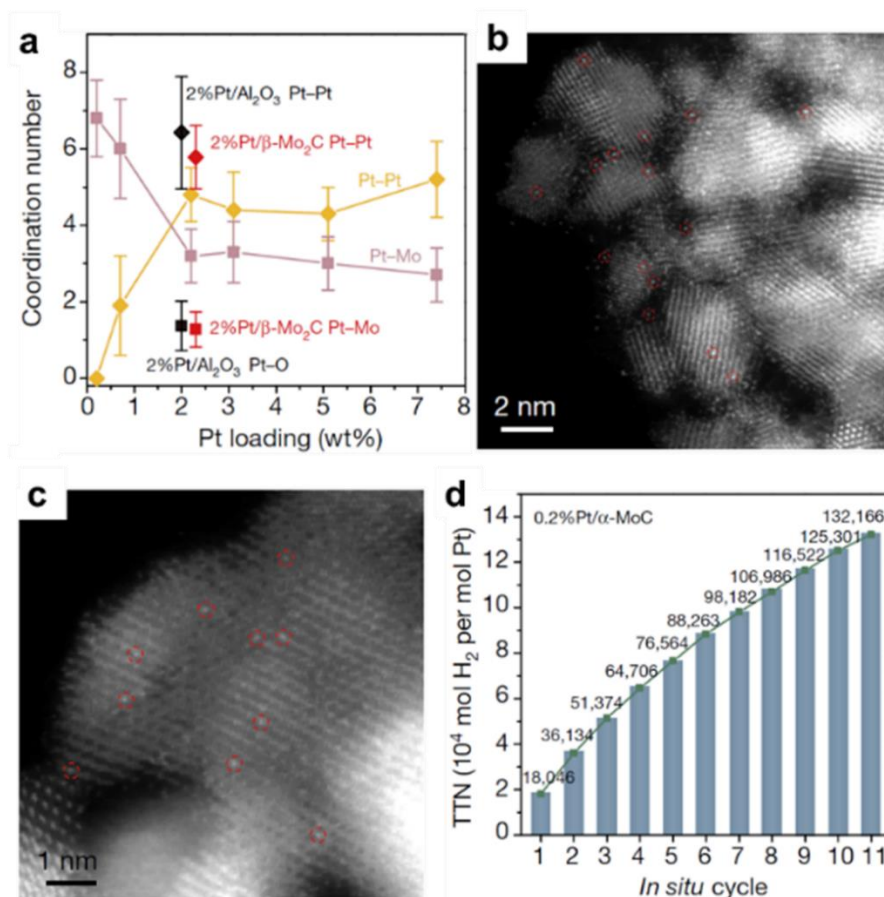
Figure 1.20. (a) Coordination number of Pt-Pt bonding and Pt-Mo bonding in different supported Pt catalysts. It is clearly shown in that, the Pt-Pt contribution in Pt/α-MoC catalysts will increase with the Pt loading. (b) High-resolution STEM image of Pt/α-MoC with 2.0 wt% of Pt. Singly dispersed Pt atoms can be observed as bright dots in this image. (c) High-resolution STEM image of Pt/α-MoC with 0.2 wt% of Pt. Singly dispersed Pt atoms can be observed as bright dots in this image. (d) Aqueous reforming of methanol for H_2 production on 0.2%Pt/α-MoC under practical conditions. Adapted with permission from ref **119**. Copyright 2017 Macmillan Publishers Limited, part of Springer Nature.

Reforming of methanol with water for production of H_2 is an attractive alternative to provide H_2 for polymer electrolyte membrane fuel cells. It has

been reported that, homogeneous Ru-based catalyst can catalyze the reforming of methanol into H_2 and CO_2 in the presence of a strong base, at low temperature (95 °C).[117] From a practical point of view, it will be more desirable to develop heterogeneous catalysts for reforming of methanol with H_2O for H_2 production.[118] Recently, Lin *et al.* have developed a new series of supported Pt catalysts on α-MoC as efficient heterogeneous catalysts for methanol reforming with water.[119] Only Pt species supported on α-MoC showed excellent activity and very low CO selectivity for methanol reforming with water. When compared with Pt species supported on other solid carriers (such as β-Mo_2C, Al_2O_3, TiO_2), the activities were much lower. The size of Pt species supported on α-MoC could be tuned by modulation of the Pt loading, which were quantified by EXAFS (see **Figure 1.20a**). Notably, singly dispersed Pt atoms on α-MoC were observed by high-resolution STEM (see **Figure 1.20b** and **Figure 1.20c**) in a series of Pt/α-MoC catalysts, even when the Pt loading was as high as 2 wt%. When the Pt loading decreased to 0.2 wt%, it was claimed that only Pt single atoms were observed and all the Pt atoms were bonded with α-MoC through strong interaction, according to DFT calculations. Those single Pt atoms dispersed on α-MoC showed the highest TOF and superior stability for methanol reforming reaction. The critical role of Pt single atoms was emphasized in this work while the catalytic properties of Pt clusters and Pt nanoparticles were not fully discussed. According to the EXAFS results, it was clearly shown that, Pt clusters and nanoparticles were the dominating species when the Pt loading was higher than 0.2 wt% and those Pt catalysts were also active for this reaction, even though the TOF values based on single Pt atoms were lower.
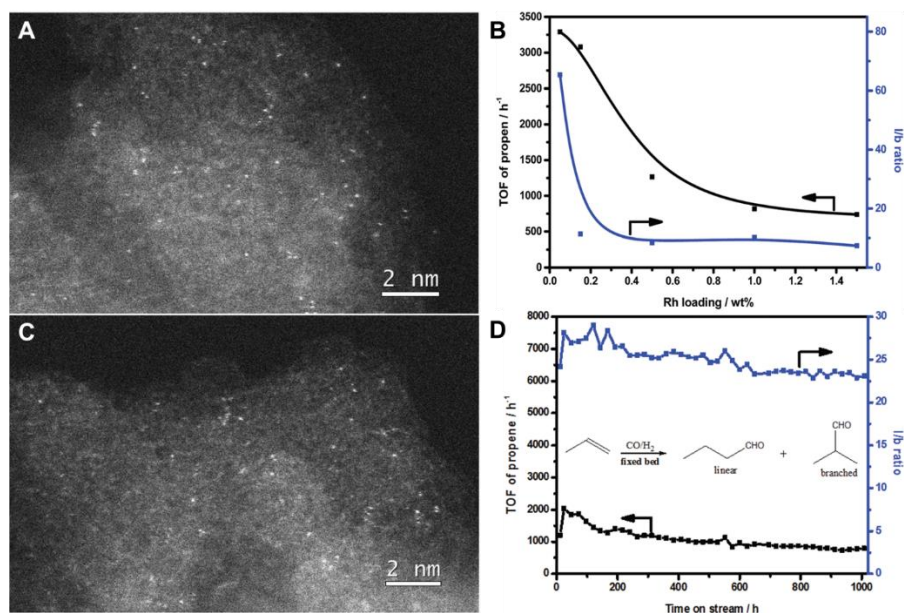
Figure 1.21. (A) High-resolution STEM image of the catalyst containing singly dispersed Rh atoms in porous organic co-polymers. (B) TOF values for hydroformylation of propene catalyzed by various Rh-biphephos&PPh3@co-polymers catalysts with different loading of Rh. The catalyst with the lowest Rh loading shows the highest TOF values and higher linear/branched ratio in the products. (C) High-resolution STEM image of the same catalyst after 1008 h of time-on-stream for propene hydroformylation, showing the presence of singly dispersed Rh atoms. (D) Long-term stability test of the Rh-biphephos&PPh3@co-polymers containing singly dispersed Rh atoms for hydroformylation of propene. Adapted with permission from ref **124**. Copyright 2016 The Royal Society of Chemistry.

1.4.6 Hydroformylation

Hydroformylation of olefins is an important industrial process for the production of aldehydes and alcohols. So far, the industrial hydroformylation reactions are performed under homogeneous conditions, using molecular Rh-based and Co-based complexes as catalysts.[120] In the last two decades, great efforts have been devoted to transform the conventional homogeneous into heterogeneous systems for convenient separation and recyclability of the

catalysts.[121,122] Generally, the active sites for hydroformylation are thought to be mononuclear metal centers. Therefore, it could be possible to achieve immobilized single-atom catalyst for heterogeneous hydroformylation reactions if the metal centers can be stabilized by the solid support and their reactivity is not suppressed. Recently, singly dispersed Rh atoms have been successfully anchored on porous organic polymer from the co-polymerization of vinyl functionalized phosphorous ligands, and these single-atom Rh catalysts showed excellent activity and reusability for hydroformylation of olefins.[123,124] As shown in **Figure 1.21**, singly dispersed Rh atoms in organic support containing vinyl biphephos ligands can be clearly observed by high-resolution STEM. These Rh atoms showed high TOFs in hydroformylation of propene and high selectivity to linear butaldehyde. Even after reaction for more than 1000 h, the fine dispersion of single Rh atoms was still preserved in the catalyst.

Other than organic polymers, inorganic solids can also serve as the supports for single Rh atoms for hydroformylation reactions. For instance, single Rh atoms supported ZnO nanowires showed comparable performances (in terms of turn-over numbers) like state-of-art $RhCl(PPh_3)_3$ complex for hydroformylation of styrene.[125] In another work, single Rh atoms supported on CoO also showed excellent TOFs for hydroformylation of propene.[126] It was also found that the distributions of aldehyde products were related with the size of Rh species. Single Rh atoms gave the highest selectivity towards linear butaldehyde (~94%) while Rh nanoparticles gave much more isobutyraldehyde, which might come from the different adsorption geometry of propene molecules on different Rh sites. Considering the influences of metal-support interaction, comprehensive studies on the support effects on Rh single-atom catalysts will bring more information and mechanistic insights for developing more efficient and selective heterogenous catalysts for hydroformylation reactions.

1.4.7 Photocatalytic reactions

In recent works, Yang *et al.* have prepared isolated Pt atoms and Pt clusters with different sizes through a ligand-assisted method, and their activity for photocatalytic H_2 evolution from methanol has been reported.[127,128] In their samples, Pt mainly existed as PtO, as determined by XPS. The TOF of Pt

species decreased when increasing the particle size. Pt single atoms showed the highest activity among the as-prepared catalysts, with about 30 times higher activity than Pt NPs (ca. 2 nm). In that work, only the chemical states of Pt in the pristine photocatalysts have been characterized by XPS. However, considering the transfer of photo-generated electrons to PtO sites, PtO species would probably be reduced. And if this occurs, it should also be considered.
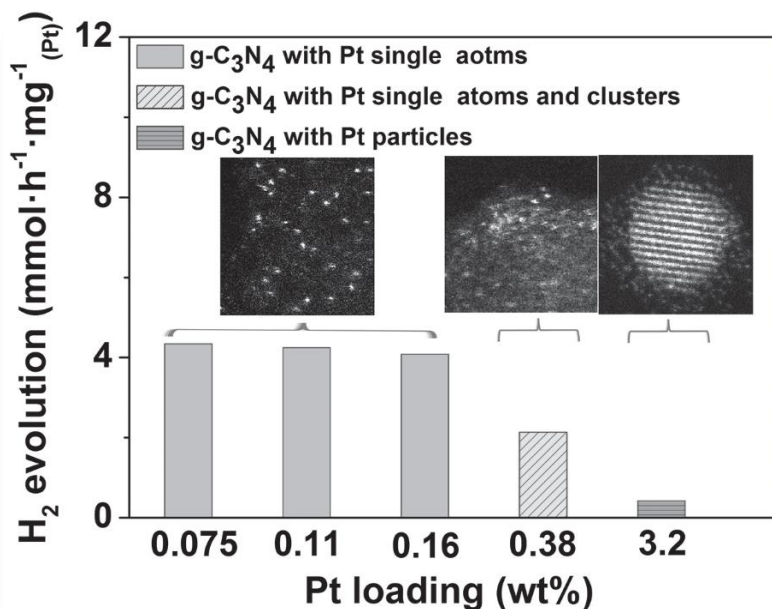
Figure 1.22. Photocatalytic hydrogen evolution rates from triethanolamine aqueous solution on various Pt/C$_3$N$_4$ catalysts with different loading of Pt. When the Pt loading is lower than 0.16 wt%, Pt mainly exist as singly dispersed atoms. When it increases to 0.38 wt%, Pt clusters will appear and Pt continues to grow into Pt nanoparticles in the Pt/C$_3$N$_4$ sample with 3.2 wt% of Pt. The H$_2$ evolution rates have been normalized to the mass of Pt co-catalyst in various catalysts. Adapted with permission from ref **129**. Copyright 2016 Wiley-VCH Verlag GmbH & Co. KGaA, Weinheim.

In another case, Pt single atoms deposited on C$_3$N$_4$ can catalyze the photocatalytic H$_2$ generation from triethanolamine aqueous solution.[129] As shown in **Figure 1.22**, Pt/C$_3$N$_4$ catalysts containing Pt single atoms show almost the same H$_2$ evolution rate normalized to Pt loading, when the Pt loading

varied from 0.075 wt% to 0.16 wt%. When the size of Pt species increases into cluster or even nanoparticle regime, the normalized H_2 evolution rate drops down with the particle size.

In a recent work, single-atom catalyst was reported as photocatalyst for CO_2 reduction using triethanolamine as electron donor under visible light irradiation.[130] Single-site Co species were incorporated to MOF-525 and stabilized by the porphyrin units. The introduction of Co showed much higher production rate of CO and CH_4 than the pristine MOF, although the production of CO and CH_4 is still quite low (less than 3 µmol after 6 h).

1.4.8 Single-atom sites in bimetallic particles

In the above examples, singly dispersed metal atoms were supported on solid supports (such as zeolites, metal oxides, polymers, etc.), and it has been usually proposed that those metal centers act as the active sites without synergistic effects from neighboring metal atoms. Actually, single-atom sites can also be generated in bimetallic particles. In that case, the electronic structures of single-atom sites can be affected by the neighboring metal atoms, which could lead into different catalytic behaviors compared with single-atom sites on non-metallic support.
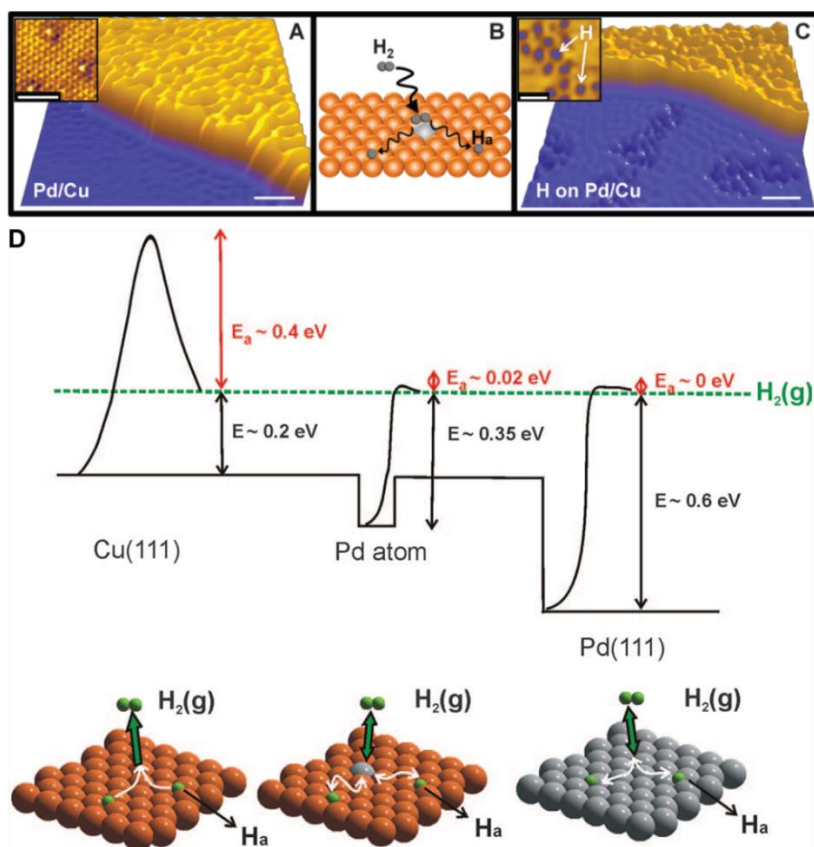
Figure 1.23. (A) STM image of single Pd atoms deposited on Cu(111) surface. (B) Schematic illustration of the activation of H_2 molecules on isolated Pd atoms and the subsequent H-spill over on Cu(111) surface. (C) STM image of the dissociated H on Pd/Cu(111) surface. (D) Activation energy of H2 on different types of surface. Adapted with permission from ref **131**. Copyright 2012 The American Association for the Advancement of Science.

Due to the weak interaction between H and Cu surface and suitable adsorption geometry of substrate molecules on Cu surface, Cu catalysts are selective catalyst for many hydrogenation reactions. However, due to the low intrinsic activity for H_2 activation, which is often a limiting step, Cu catalysts are not widely used for selective hydrogenation reactions. In 2012, Kyriakou *et al.* reported the application of an alloy structure containing single-atom sites for

selective hydrogenation reactions. As show in **Figure 1.23**, isolated Pd atoms deposited on Cu(111) surface can dissociate H_2 and those activated H species can spill over to Cu(111) surface.[131] By this strategy, the bottleneck for Cu-based hydrogenation catalysts can be overcome and due to the very low amount of Pd, the selectivity of Cu catalysts is not affected.[132] Therefore, Cu(111) surface modified with isolated Pd atoms show excellent selectivity for selective hydrogenation of alkynes. Actually, this concept has already been demonstrated in 2009 on supported Au catalysts, in which ppm level of Pt was added to Au/TiO_2 catalyst to improve the activity without affecting the high selectivity of Au catalysts.[133] Besides, this concept has also been proved by practical catalysts containing PdCu alloy nanoparticles with very low amount of Pd.[134] Lately, the concept of single-atom alloy structures has been extended to other combinations of metals and show promising performances for selective hydrogenation reactions. For instance, Pt-Cu alloys containing Pt single atoms show excellent activity and selectivity for hydrogenation of 1,3-butadiene to butenes.[135] Ag alloyed Pd single-atom catalysts are efficient catalysts for selective hydrogenation of acetylene to ethene in excess ethene.[136]
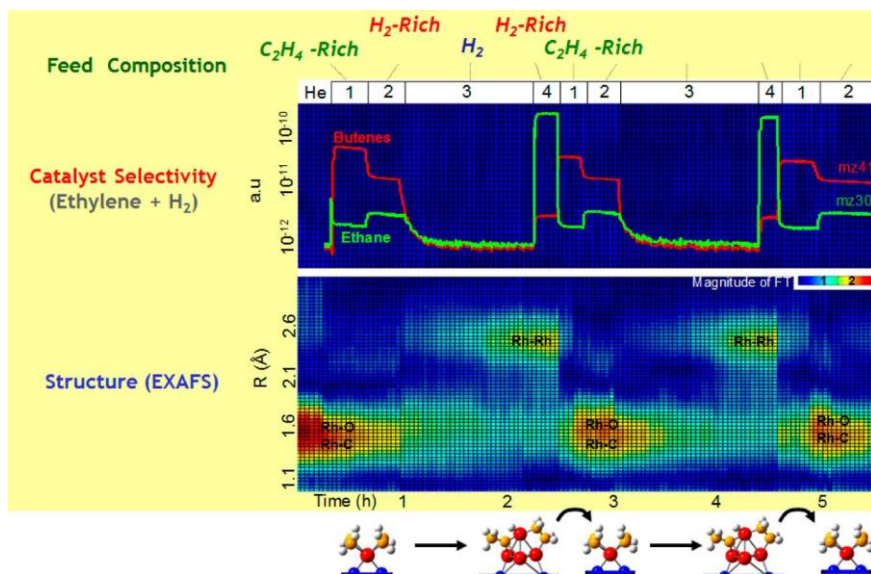
Figure 1.24. Evolution in selectivity of mononuclear $Rh(C_2H_4)_2$ complexes supported on HY zeolite with time on stream during the consecutively changed feed gases (ethylene and H_2). The coordination environment of Rh species is

followed by EXAFS spectroscopy. In the bottom panel, the horizontal axis and vertical axis represents time on stream and the Rh-backscatter distance, and the intensity of various contributions are represented by colors (change from red to yellow to green to blue shows a decrease in intensity of the contribution). Adapted with permission from ref **138**. Copyright 2011 American Chemical Society.

1.4.9 Evolution of single-atom catalysts under reaction conditions

One critical issue related with single-atom catalysts is their stability under reaction conditions. Considering the intrinsic instability of single-atom species, they have a strong tendency to agglomerate into clusters or nanoparticles, especially in reductive atmosphere, especially in the situation without strong protection from sintering.[137] Gates *et al.* have investigated the evolution of mononuclear Ir complexes supported on zeolites in H_2 atmosphere at room temperature. In the case of supported $Ir(C_2H_4)_2$/HY, the bonding between Ir and zeolite would be broken after the formation of iridium hydride species, leading to the formation of Ir clusters. Furthermore, they have also studied how mononuclear metal species transform into metal clusters during the hydrogenation reaction.[138] *In situ* EXAFS allows to correlate the catalyst selectivity with the structural information of supported Rh species, as shown in **Figure 1.24**. In C_2H_4-rich environment, butene was the major product and Rh mainly exists as mononuclear form. When these mononuclear Rh was treated with H_2, Rh_4 clusters appear and ethane turned to be the major product in H_2-rich environment. Interestingly, the dynamic transformation between mononuclear Rh and Rh_4 clusters can be modulated by the reaction atmosphere.
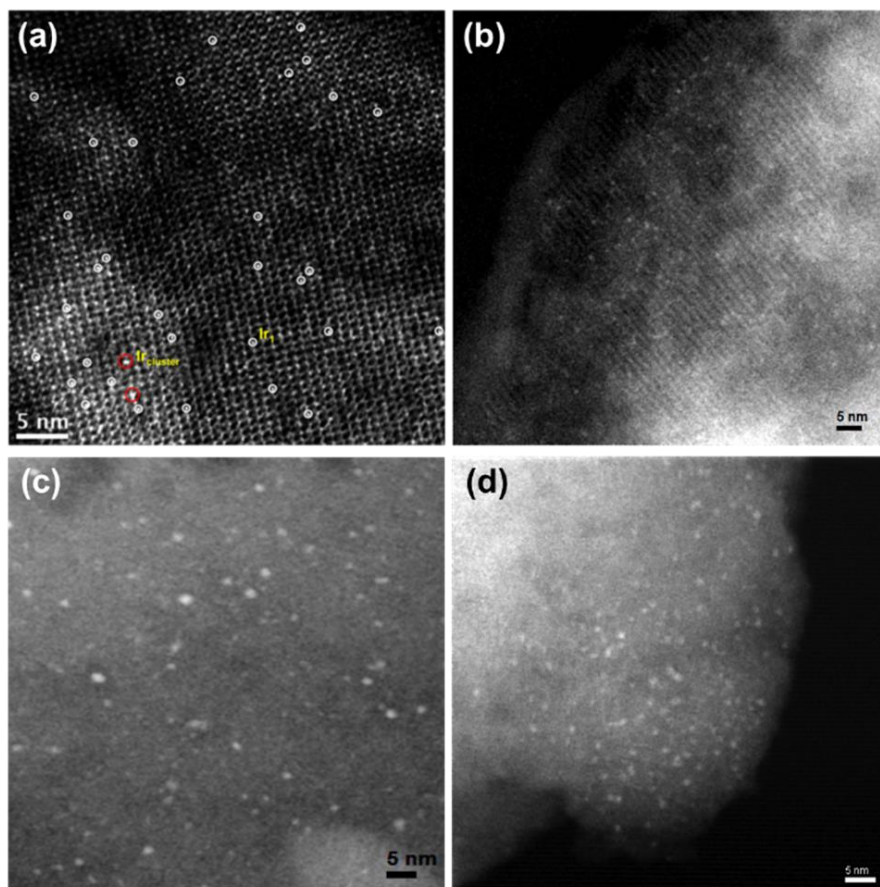
Figure 1.25. (a) High-resolution STEM images of the pristine Ir_1/Y catalyst, showing the presence of single Ir atoms with fine dispersion. (b) High-resolution STEM images of the Ir/Y catalyst after the first run of hydrogenation of cyclohexene, showing the presence of Ir clusters around 0.4 nm with 4-6 Ir atoms. (c) High-resolution STEM images of the Ir/Y catalyst after the second run of hydrogenation of cyclohexene, showing the presence of Ir clusters around 1 nm with ca. 40 Ir atoms. (d) High-resolution STEM images of the Ir/Y catalyst after the third run of hydrogenation of cyclohexene, showing the presence of Ir clusters around 1.3 nm with ca. 70 Ir atoms. Adapted with permission from ref **140**. Copyright 2015 American Chemical Society.

When the reaction is performed in liquid phase, the evolution of single-atom

49

catalysts will be more complicated than under gas-phase reaction conditions. In a typical example, Finke *et al.* have studied the stability of zeolite-supported mononuclear Ir complex under the reaction conditions for liquid-phase hydrogenation of cyclohexene at 22 °C.[139] According to the experimental results from kinetic, spectroscopic and electron microscopy characterizations, it was proven that those mononuclear Ir complex are stable at 22 °C, and the agglomeration of Ir single atoms into clusters or nanoparticles was not observed. However, when the reaction temperature increases for liquid-phase hydrogenation of cyclohexene, the situation changes.[140] The size of Ir species have been followed by both high-resolution STEM and EXAFS. As shown in **Figure 1.25**, three stages of evolution of mononuclear Ir species into Ir clusters (4-6 atom) and then to Ir nanoparticles (around 1 nm) were clearly observed during the three cycles of hydrogenation of cyclohexene. During the sequential sintering of Ir species, the activity for hydrogenation of cyclohexene was also decreasing.

In most of the abovementioned works on catalytic applications of single-atom catalysts, the evolution of single-atom metal species has not been intensively studied. In many cases, only the fresh catalyst has been well characterized. It has been demonstrated in nanoparticulate metal catalysts that dynamic structural transformation is quite common in heterogeneous catalytic reactions. Taking that point into consideration, it is required to study the stability of single-atom catalysts under reaction conditions by different types of characterization techniques.

1.4.10 Perspectives on single-atom catalysts

In the last few years, various single-atom catalysts have been prepared by different methods. For instance, singly dispersed Co in N-doped carbon can be generated using Co-complex or Co-containing metal-organic framework as precursor. Moreover, the morphologies of the resultant singly dispersed Co-N-C catalysts also show different morphologies. In those published works, Co-N-C catalysts from different methods have been tested for the same reaction (electrocatalytic oxygen reduction reaction). Spectroscopic and electron microscopic characterizations suggest that those Co-N-C catalysts show similar structures. However, although the reaction conditions maybe different in

different works, it is clear that the catalytic performance of different Co-N-C catalysts are different.[141-144] The differences between those Co-N-C catalysts are still unknown. Similar phenomenon has also been observed with Fe-N-C catalysts.[145-148]

It has been proposed that, single-atom catalysts are thought to be analogous to homogeneous coordination compounds. It has been well established that, the electronic structure of the metal center in coordination complex is strongly dependent on the ligand, which has significant influence on the catalytic properties. Therefore, it can be speculated that, the coordination environment of single atoms in heterogeneous catalysts can also influence their catalytic behavior. Therefore, the differences observed in recent published works on different Co-N-C catalysts may originate from their different coordination structure of the singly dispersed Co sites, which cannot be fully reflected by the current characterization results.

There is no doubt that, totally dispersed metals, and more specifically noble metals, is a way to minimize metal use, specially when they present high activity. These single metal atoms on organic and inorganic supports are very sensitive to electronic and geometric interactions with the atoms of the support. In some way, they can bridge homogeneous and heterogeneous catalysis, offering new perspectives for controlling activity and selectivity as well as for catalyzing less usual reactions.

Therefore, in order to have better understanding on the catalytic behavior of single-atom catalysts, it is necessary to correlate the catalytic behavior with the local coordination environment of the metal sites. Furthermore, it is also necessary to follow the evolution of the structures of single-site metal centers under reactions conditions. The geometric configuration of the metal site and its coordination environment may change during the catalytic cycles, in an analogous way to the catalytic cycle in homogeneous catalysis.

1.5 Catalytic applications of metal clusters

1.5.1 CO oxidation

CO oxidation is an excellent reaction test to discuss similarities and differences between single-atom and subnanometric clusters of different metals. Since much work on the reaction mechanism has been already carried out, it is of interest to use CO oxidation as a probe reaction to investigate how the size of metal species and the potential role of the support affect the activity. It should be considered that the electronic characteristics of metal species should be key to explain their catalytic behavior. We will now review the recent works on metal clusters for CO oxidation and will comment on the differences observed with single-atom metal catalysts.

CO oxidation on Au clusters

In 1999, Heiz *et al.* performed the first model study on size-selected metal nanoclusters for $^{13}CO+^{18}O_2$ reaction.[149] As shown in **Figure 1.26a**, ^{13}CO and $^{18}O_2$ were pumped into the reaction chamber at low temperature, and the reaction was monitored with a mass spectrometer. Notably, low activity for CO oxidation was observed for Au_n clusters with less than 10 atoms except Au_8. Moreover, two peaks in the temperature-programmed reaction (TPR) profiles of Au_8 and larger Au clusters were observed, suggesting that there may be two reaction pathways for CO oxidation at different temperature range. Later, Anderson *et al.* studied the activity of supported size-selected Au_n species (n=1, 2, 3 and 4) for CO oxidation. They observed that Au_1 and Au_2 were inert for this reaction and Au_3 is more active than Au_4. The authors claimed that the lack of activity of Au_1 and Au_2 may be related with the strong binding between Au and CO.[150] When the atomicity increased to 10~20, the CO oxidation activity of Au nanoclusters also increased, although in an odd-even oscillation way. As shown in **Figure 1.26b**, the reactivity of Au nanoclusters may change significantly by just changing one atomicity. Such variation pattern is similar to the size-dependent electronic structures of Au nanoclusters as discussed before in this review.[151] Notably, Au_8 clusters were found to be much more active than Au clusters with less than 8 atoms, implying that low-temperature CO oxidation may require multiple metal sites for the activation of CO and O_2.[152]

Furthermore, the role of the support on the catalytic behavior of Au clusters has been studied. It has been reported that Au_8 clusters deposited on a MgO(100) film, rich in oxygen defects, exhibited higher activity than those supported on defect-poor MgO(100) film. The reason for the enhanced activity of Au_8 clusters supported on defective MgO(100) could be related with the charge-transfer from MgO to Au clusters.[153] However, it should also be considered that, the electronic interaction between MgO and Au clusters could also affect the geometric structure of the Au clusters.[154] Indeed, if Au_{20} clusters were deposited on a MgO(100) film, the optimized geometric structure of Au_{20} cluster corresponded to a three-dimensional tetrahedron. However, when the support was two-layer MgO film on Mo(100), Au preferred to be in the form of two-dimensional Au island.
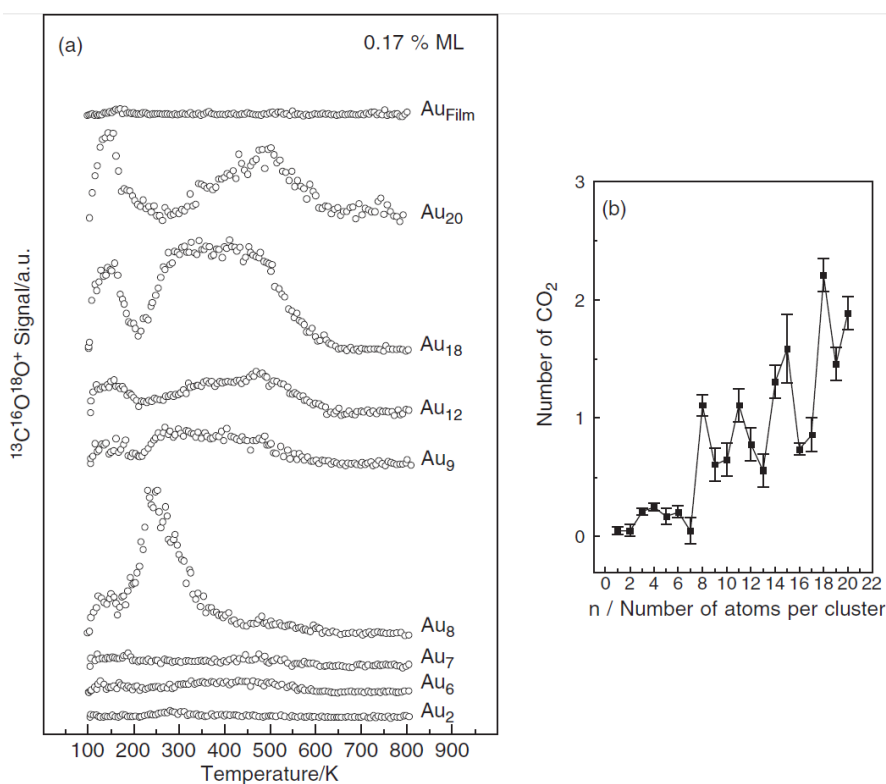
Figure 1.26. (a) Temperature-programmed reaction profiles for the CO oxidation on size-selected Au_n (n=2-20) clusters on defect-rich MgO(100)

surface. The model catalysts were saturated at 90 K with ^{13}CO and $^{18}O_2$ and the reaction product ($^{13}C^{18}O^{16}O$) was detected with a mass spectrometer, as a function of temperature. (b) The number of formed CO_2 molecule on each Au cluster with different atomicity. Adapted with permission from ref **149**. Copyright 1999 American Chemical Society.

In the abovementioned works, Au nanoclusters were generated by size-selected method and then deposited on support and used as model system. Actually, the catalytic behavior of Au nanoclusters prepared by conventional wet-chemistry methods, which is closer to practical heterogeneous catalysts, has also been investigated for CO oxidation. Gold catalysts supported on metal oxides (such as TiO_2, FeOx, Al_2O_3, etc.) have been prepared by impregnation or co-precipitation methods. The resultant catalysts usually contain various types of Au species (including singly dispersed Au atoms, subnanometric Au clusters and Au nanoparticles) and it becomes very difficult to measure those subnanometric Au species by conventional TEM due to the resolution limitation.[155] With the help of aberration-corrected STEM, it is possible to quantify the contribution of different types of Au species for CO oxidation. In 2008, Kiley and Hutchings reported the identification of active sites in Au/FeOx catalysts for CO oxidation.[156] By comparing the size of Au species present in two Au/FeOx samples (one active and the other catalytically inactive), the authors concluded that subnanometric Au clusters (around 0.5 nm) play a dominant role for the high activity in CO oxidation. Meanwhile, singly dispersed Au atoms and large Au nanoparticles (>5 nm) hardly contributed to the activity. In a recent work, these authors have performed a more systematic study on the contribution of different types of Au species in Au/FeOx catalyst.[157] By quantitatively analyzing the population of different types of Au species, they have concluded that both subnanometric Au clusters (~0.5 nm) and small Au nanoparticles (1-3 nm) are the active species with similar turn-over frequencies for CO oxidation, showing much higher TOF values than Au single atoms supported on FeOx.

CO oxidation on Pt-group metals clusters
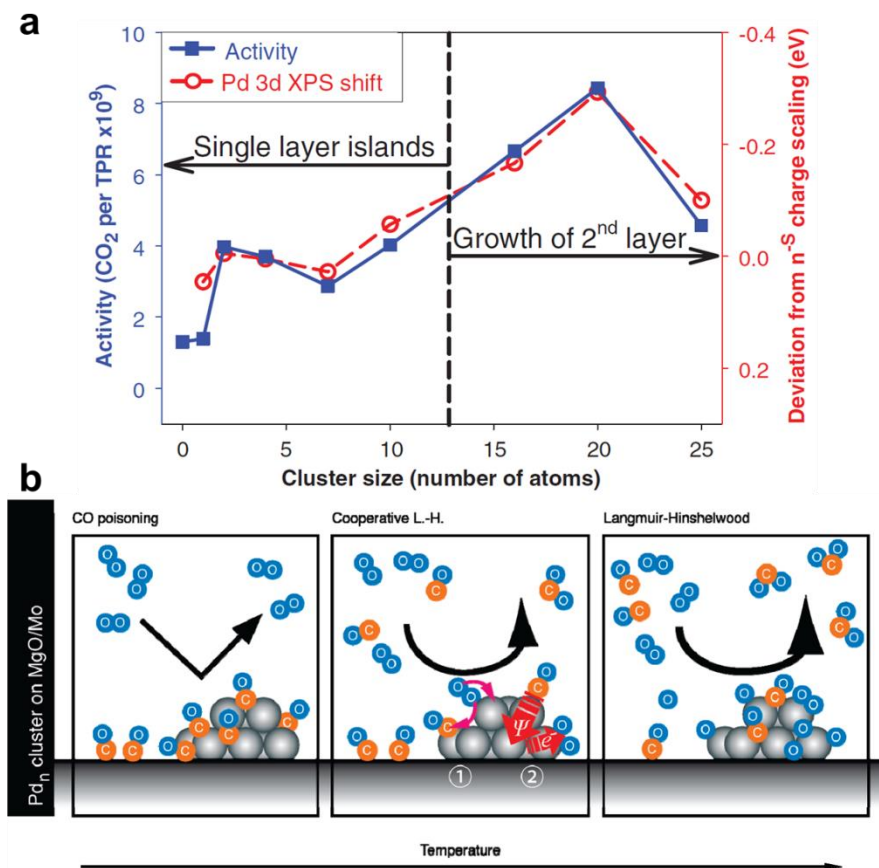
Figure 1.27. (a) Correlation between CO oxidation activity observed during temperature-programmed reaction (TPR) and the shifts of the Pd 3d binding energy observed by XPS. The XPS and TPR data for each type of Pd cluster were taken on the same sample. Adapted with permission from ref **213**. Copyright 2009 The American Association for the Advancement of Science. (b) Mechanism of CO oxidation on Pd clusters from low to high temperature. At low temperature, Pd clusters will be poisoned by CO and cannot catalyze the CO oxidation. When the temperature increases to ca. 300 K, part of the Pd clusters are exposed to O_2 molecules and become able to activate O_2 and catalyze $CO+O_2$ reaction. At ca. 400 K, Langmuir-Hinshelwood type reaction can be observed on Pd clusters for CO oxidation. Adapted with permission from ref **158**. Copyright 2010 American Chemical Society.

The catalytic properties of Pt-group metal clusters have also been studied for CO oxidation. Anderson *et al.* have prepared size-selected Pd_n clusters deposited on $TiO_2(110)$ as model catalysts, and attempted to correlated the catalytic activity with the electronic structures.[158] For doing that, the CO oxidation activity (determined by TPR) and the Pd 3d binding energy shifts relative to bulk Pd (measured by XPS), were plotted as a function of the atomicity of Pd_n clusters (**Figure 1.27a**). Obviously, these two plots showed a similar tendency when varying the cluster size. It could be seen there that CO oxidation activity increased substantially from Pd_2 to Pd_4, and then declined slowly when the cluster size increased to Pd_7. For larger clusters, activity increased gradually before dropping again for Pd_{25}. The good correlation between the Pd 3d binding energy shift and the catalytic activity suggests that electronic structures of metal clusters have significant influence on the catalytic properties. Indeed, it has been found that the catalytic properties of Pd clusters supported on alumina could be affected by the thickness of the alumina film and geometric structures of Pd_{20} clusters.[159] In this way, when the thickness of Re-doped alumina film was around 2 nm, the CO oxidation activity of Pd clusters was the lowest.

To investigate how the size of the Pd cluster affects the catalytic properties, Kunz *et al.* studied the catalytic behavior of three Pd clusters (Pd_8, Pd_{13} and Pd_{30}).[160] They found that these size-selected Pd clusters show temperature-dependent reaction mechanisms for $CO+O_2$ reaction. A schematic illustration of the proposed reaction mechanisms over Pd clusters is given in **Figure 1.27b**. When working in the low-temperature region, Pd clusters were poisoned by CO, and almost no CO_2 production was observed. When the temperature was increased to above 300 K, some of Pd atoms in Pd clusters were exposed to O_2, leading to activation of O_2 and oxidation of CO. When the temperature was further increased, a Langmuir-Hinshelwood (L-H) mechanism occurred, in which adsorbed CO exhibited a promoting instead of a blocking effect for oxygen dissociation. Finally, the activity results for CO oxidation at T>400 K showed that larger Pd clusters were active. Although no explanation for these results were given, it may occur that the CO poisoning effect was larger for small Pd clusters. If this is so, more Pd atoms could be exposed to O_2 in larger

Pd clusters, which could facilitate the CO oxidation. The above reaction mechanism is also supported by theoretical calculations.[161,162]

In the case of CeO_2-supported Pd catalysts, it has recently been reported that Pd nanoparticles can be transformed into Pd clusters after hydrothermal treatment. The amount of hydroxyl groups on CeO_2 increased significantly after hydrothermal treatment, which promoted the dispersion of Pd on CeO_2.[163] Those re-dispersed Pd clusters are highly active for CO oxidation, showing much higher activity than Pd single atoms supported on CeO_2.

The unique role of Pt-group metal clusters for CO oxidation has also been reflected in catalysts prepared by co-precipitation. Pt/FeOx (with ~2 wt% of Pt) containing Pt clusters and Pt single atoms show excellent activity for preferential oxidation of CO in the presence of rich H_2 at room temperature.[164] Although the TOF of Pt clusters (0.181 s^{-1}) is slightly lower than Pt singles (0.212 s^{-1}) under the same reaction conditions, the Pt loading of the Pt/FeOx with clusters is much higher than Pt/FeOx with single Pt atoms. Therefore, from a practical point of view, the Pt/FeOx containing Pt clusters are better catalysts for CO-PROX reaction than the Pt/FeOx catalyst with single atoms.

What we have learned up to now is that the electronic properties of the Pt group metals depend on the size and structure of the clusters, the interactions with the support and the atmosphere at which they are exposed. Obviously, all those factors will determine the final catalytic activity and selectivity of the metal catalyst. On those basis, we will now discuss the catalytic behavior of metal clusters for important catalytic applications, such as selective oxidation, selective hydrogenation, dehydrogenation, photocatalysis and electrocatalysis.

1.5.2 Oxidation of hydrocarbons

The oxidation of C-H bond is a promising green strategy to obtain functionalized products from abundant raw materials. For instance, direct oxidation of CH_4 to CH_3OH is a dream reaction for the valorization of natural gas. In nature, enzymes containing two-copper centers can catalyze this transformation at room temperature.[165,166] Inspired by nature, chemists try to mimic the active sites in natural enzymes and design heterogeneous catalysts for direct oxidation of CH_4 to CH_3OH. In the past decade, it has been reported that Cu-zeolite catalysts prepared by ion-exchange process can make the

selective transformation of CH_4 to CH_3OH through a cyclic process, as shown in **Figure 1.28a**.[167] In the case of Cu-exchanged ZSM-5, With the help of Raman spectroscopy and isotopic studies, it has been proposed that binuclear Cu species located in ZSM-5 are the active species for CH_4 oxidation to CH_3OH.[168] In a recent work, the generation and stabilization of trinuclear copper oxygen clusters at the pore mouth of 8-ring side pockets in mordenite was reported and these Cu_3 clusters showed activity and selectivity for oxidation of methane to CH_3OH.[169] Therefore, it can be seen that, there is still some debate on the nature of the active sites in Cu-exchanged zeolites. Indeed, in another report, it is proposed that Cu^{II}-O-Cu^{II} is the active site for methane oxidation to methanol.[170] Interestingly, when studying the Cu-zeolite catalysts by high-resolution TEM, it can be found that a large number of CuOx nanoparticles (1-3 nm) are also present in the active Cu-exchanged zeolite catalysts, implying that Cu species other than Cu clusters may also be active for oxidation of CH_4.[171,172] Moreover, it should also be considered that, the structures of the active Cu sites are also affected by the reaction conditions. Therefore, to clarify the role of Cu clusters for selective oxidation of methane, mechanistic studies based on catalysts with well-defined and stable metal species are required.[173] In a recent work, van Bokhoven *et al.* demonstrate an anaerobic approach for oxidation of methane to methanol using water as soft oxidant, giving very high selectivity (~97%) to methanol.[174] In that work, Cu-exchanged MOR zeolite was activated in He at 400 $^{\circ}$C and then reacted with CH_4 at 200 $^{\circ}$C, resulting the reduction of Cu(II) to Cu(I). Afterwards, the desorption of methanol and re-oxidation of Cu(I) to Cu(II) can be realized by introducing H_2O into the Cu-MOR zeolite. The above catalytic cycles have also been verified by in situ XANES and FT-IR. Although progress on the identification of the nature of the active sites has been achieved in the last decade, the catalytic performance of Cu-exchanged zeolite materials is still far below the requirements for practical application, and exploring new materials for oxidation of methane to methanol is an emerging challenge.
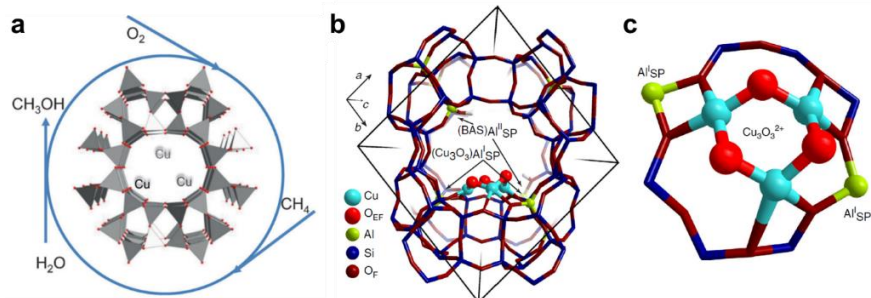
Figure 1.28. (a) Illustration of oxidation of CH_4 with Cu-exchanged zeolites through a cyclic process. Adapted with permission from ref **167**. Copyright 2016 Wiley-VCH Verlag GmbH & Co. KGaA, Weinheim. (b, c) Schematic illustration of Cu_3 clusters located in the side pockets of MOR zeolites. The $Cu_3(\mu\text{-}O)_3$ clusters are proposed to be the active sites for oxidation of CH_4. Adapted with permission from ref **169**. Copyright 2015 Macmillan Publishers Limited, part of Springer Nature.
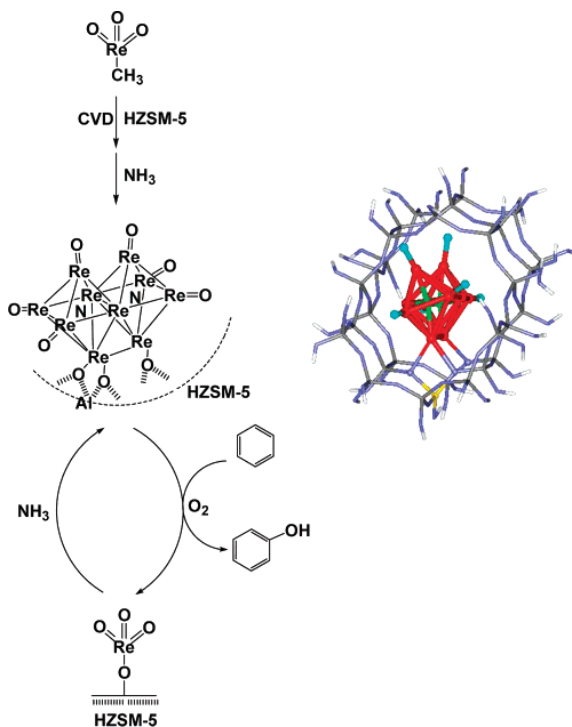
Figure 1.29. Generation of Re_{10} clusters in ZSM-5 by chemical vapor

deposition and the dynamic transformation of Re_{10} clusters and mononuclear Re species under reaction conditions. Adapted with permission from ref **175**. Copyright 2007 American Chemical Society.

The direct oxidation of C-H bond in benzene with O_2 for the production of phenol is another dream reaction for chemical industry. In 2006, Iwasawa *et al.* reported a Re/Zeolite catalyst prepared by chemical vapor deposition (CVD) of organometallic Re compound on ZSM-5 crystallites for direct oxidation of benzene to phenol with O_2 in presence of NH_3.[175] The catalyst could achieve 82.4-87.7% selectivity to phenol at 0.8-5.8% conversion of benzene under steady-state reaction. As described in **Figure 1.29**, EXAFS and XANES results reveal that Re_{10} clusters were the active sites under reaction conditions and they transformed into mononuclear Re under reaction conditions when there was no NH_3 in the feed gas. The presence of NH_3 is critical for the generation and stabilization of Re_{10} clusters in the pore channels of ZSM-5.[176]
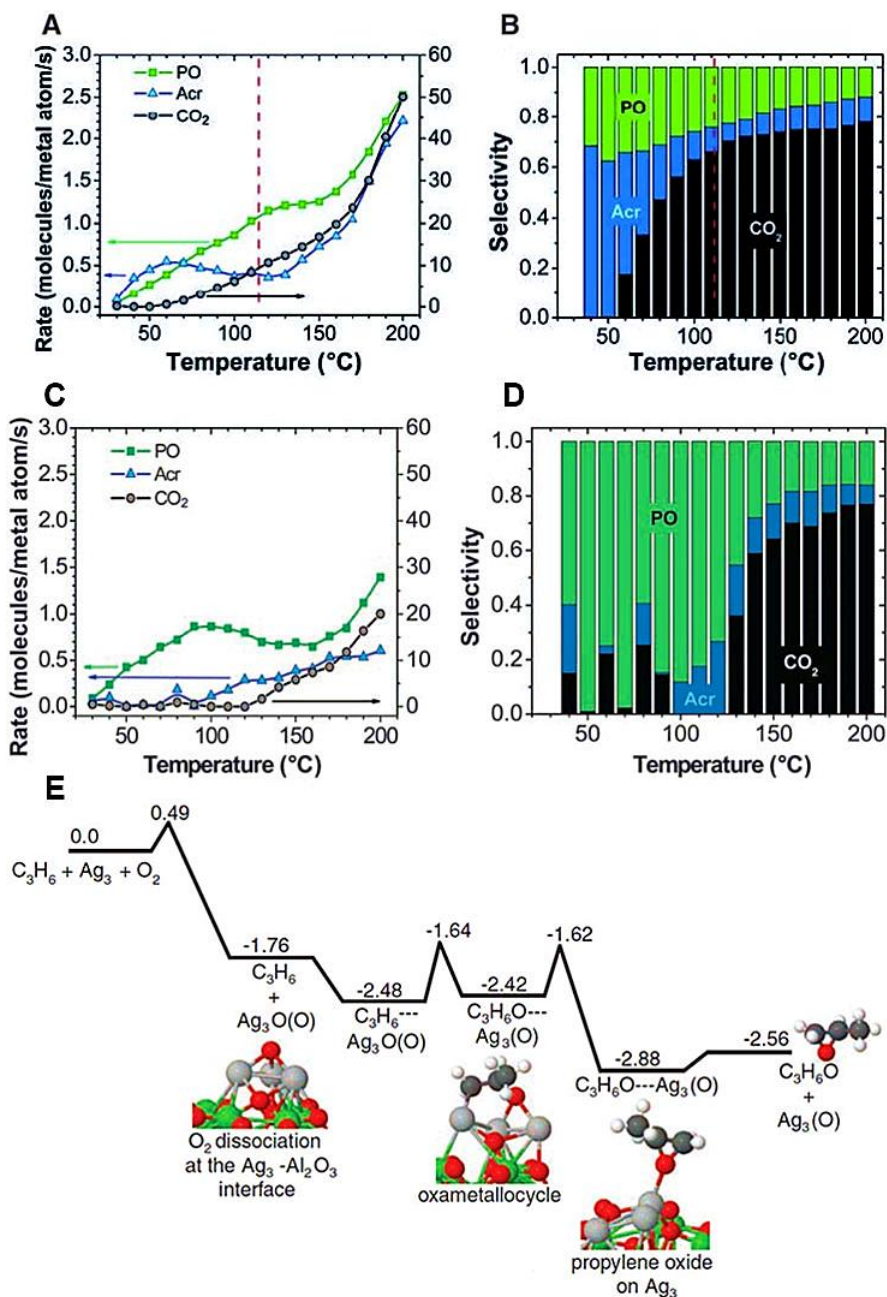
Figure 1.30. (A) Reaction rate of oxidation of propene to propene oxide (PO), acrolein (Acr) and CO_2 on Ag_3 clusters. (B) Selectivity towards different

products at different temperature on Ag_3 clusters supported on Al_2O_3. (C) Reaction rate of oxidation of propene to propene oxide (PO), acrolein (Acr) and CO_2 on Ag nanoparticles (~3.5 nm). (D) Selectivity towards different products at different temperature on Ag_3 clusters supported on Al_2O_3. (E) Reaction mechanism of oxidation of propene to propene oxide catalyzed by Ag_3 clusters based on DFT calculations. Adapted with permission from ref **177**. Copyright 2010 The American Association for the Advancement of Science.

Not only Au clusters, but subnanometric Ag clusters can also be active catalyst for epoxidation of propene. Vajda *et al.* showed that size-selected Ag_3 clusters deposited on Al_2O_3 were active and selective catalyst for epoxidation of propene at low temperature.[177] As shown in **Figure 1.30A** and **Figure 1.30B**, Ag_3 clusters exhibited good conversion of propene at low temperature (< 100 ºC). Notably, propene could be readily converted into propene oxide and acrolein at 60 ºC, which was remarkable compared with conventional Ag-based catalysts. From room temperature to 60 °C, the major product was acrolein. When the temperature was increased to between 70°C and 100°C, higher propene oxide/acrolein ratios could be achieved. However, selectivity to CO_2 also increased from 30% to 60%. DFT calculations (**Figure 1.30E**) suggest that O_2 molecules are activated at the Ag/Al_2O_3 interface through formation of Ag_3O structure. Alumina-supported Ag_3O cluster has a substantial net spin density (~0.6) on the Ag and O in the cluster. In contrast, there is no spin density present when atomic oxygen is adsorbed on an Ag(111) surface, assuming low oxygen coverage. This work indicates that the flexibility of metal clusters may account for their higher catalytic performance by adapting their configuration during molecular activation. Notably, those Ag_3 clusters were not stable at above 120 ºC, and they agglomerated into Ag nanoparticles of 2 to 3.5 nm, depending on the reaction temperature. The catalytic performance of those Ag nanoparticles has also been measured under the same conditions. As it can be seen in **Figure 1.30C** and **Figure 1.30D**, Ag nanoparticles (~3.5 nm, generated from the sintering of Ag_3 clusters) show similar turn-over frequency (based on surface Ag atoms) as Ag_3 clusters for the production of propene oxide, implying that size effects are not so significant in this system. Further investigation on size effects with different types of Ag species may provide more insights on nature

of the active species for epoxidation of propene.

1.5.3 Selective hydrogenation

It was said before that the electronic and geometric structures are strongly related with the size of the metal clusters and, consequently, it is not surprising that the catalytic properties of metal clusters also depend on the size. To this respect, Gates *et al.* have investigated the interactions between Ir species and H_2 to establish the size effects of metal clusters on hydrogenation of ethene.[178,179] A schematic illustration of different Ir species supported on MgO and Zeolite are shown in **Figure 1.51**. When mononuclear Ir complexes were supported on electron-withdrawing zeolite support, single Ir atoms could activate C_2H_4 and H_2 simultaneously. On the other hand, when the support was basic MgO, mononuclear Ir complexes were electron-rich and this situation was not favourable for the hydrogenation reaction. When Ir_4 clusters were loaded on MgO, activation of C_2H_4 and H_2 became easier, leading to higher TOF for ethene hydrogenation because the Ir_4 clusters could provide neighboring Ir sites for adsorption and activation of ethene and H_2. In contrast, for acid zeolite as support, Ir_4 clusters showed only minor improvement for the ethene hydrogenation reaction with respect to the mononuclear Ir complex, suggesting that the activation of ethene and H_2 on neighboring Ir sites is not the rate-determining step in zeolite-supported Ir catalysts.

The catalytic properties of supported Ir clusters can also be tuned through surface modification to introduce selective molecular recognition in the catalytic process. Thus, Ir_4 clusters were capped by calixarene-phosphine ligands, which blocked basal Ir sites in Ir_4 clusters and protect Ir_4 clusters from aggregation (see **Figure 1.31**). At the same time, the electronic and coordination environment of Ir_4 clusters were modulated. H-D exchange and ethene hydrogenation experiments provided evidence supporting that only the apical Ir were accessible for substrate molecules. Basal Ir sites were exposed after decarbonylation treatment. But they were not able to activate ethene molecules because of the blocking effect of calixarene-phosphine ligands as suggested by the simulation results.[180] This work demonstrates the possibility of controlling the catalytic properties of supported metal clusters in an accurate

way, which now is an emerging task for cluster catalysis.[181]
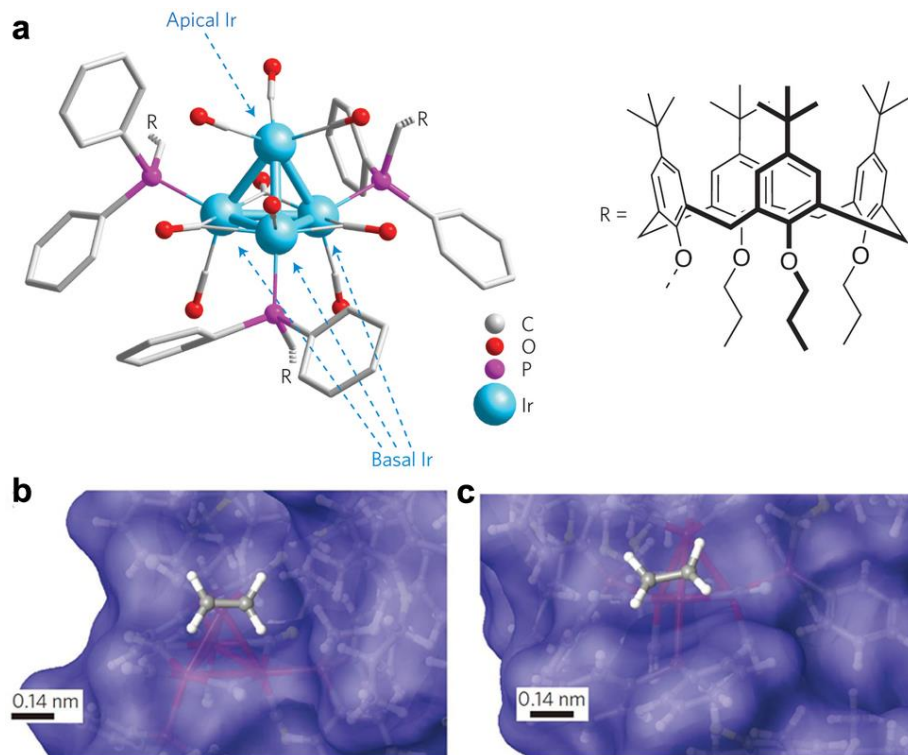
Figure 1.31. (a) Tetrahedral Ir$_4$ clusters stabilized by calixarene-phosphine ligands. Nine CO ligands are at first attached to the Ir$_4$ clusters. The CO ligands attached to the basal-plane Ir atoms can be removed with a thermal or gas-flowing treatment, creating 'CO vacancy' sites that can take up new CO molecules, but prevent ethylene adsorption. Alternatively, the CO ligands attached to the apical Ir atom can be removed by reactive decarbonylation, creating a CO vacancy site that can bind both CO and ethylene. (b, c) Molecular graphics: Lowest free-energy structures of ethylene bonded to apical (b) and basal-plane (c) Ir atoms, in the calixarene-phosphine capped Ir$_4$ cluster. Adapted with permission from ref **180**. Copyright 2014 Macmillan Publishers Limited, part of Springer Nature.
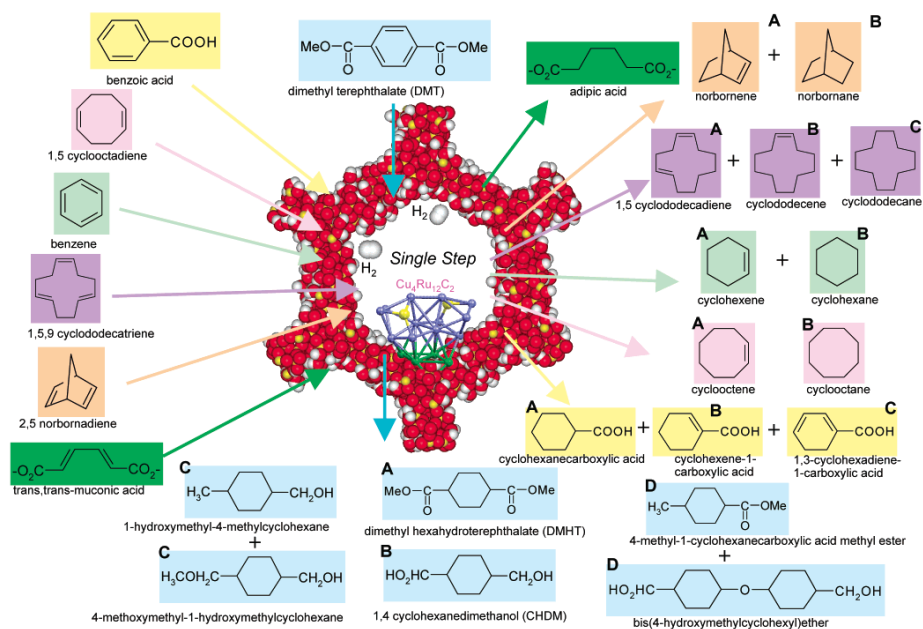
Figure 1.32. Single-step hydrogenation of some organic compounds using bimetallic cluster catalysts ($Cu_4Ru_{12}C_2$, in this case) supported on mesoporous solid carriers. Adapted with permission from ref **182**. Copyright 2003 American Chemical Society.

As we have discussed in the part of the generation of supported metal clusters, bimetallic clusters can be prepared in a controllable way through the thermal decomposition of bimetallic or trimetallic organometallic clusters. Thomas *et al.* have carried out systematic work on the catalytic properties of bimetallic and multimetallic clusters for selective hydrogenation reactions.[182] The composition of the bimetallic clusters and the reaction scopes are described in **Figure 1.32**. In those reactions, it is clearly demonstrated that the reactivity and selectivity of metal clusters are tunable by the chemical composition. For example, for the hydrogenation of benzoic acid, nearly 100% selectivity to hydrogenation of the aromatic ring was achieved with $Ru_{10}Pt_2$ clusters, giving cyclohexanecarboxylic acid as product, while the other Ru-based bimetallic clusters gave products of partial hydrogenation. More interestingly, when Ru_6Sn clusters were used as catalysts for hydrogenation of 1,5-cyclooctadiene,

only cyclooctene was obtained with 100% selectivity. While other Ru-based bimetallic clusters could give full hydrogenation product (cyclooctane) in some extent. These results demonstrate that the selectivity of metal clusters can be modulated by addition of a second metal component.

The catalytic performances of bimetallic clusters can be further tuned by adding a third metal.[183] Trimetallic Ru_5PtSn clusters were immobilized in mesoporous Davison silica (with a pore diameter of 3.8 nm) and used as catalyst for hydrogenation of dimethyl terephthalate (DMT). Compared with RuPt bimetallic clusters, the introduction of Sn can improve the activity and selectivity to desired products, simultaneously.[184]

1.5.4 Dehydrogenation reactions

The production of light alkenes from dehydrogenation of alkanes is an important route for chemical industry.[185] Currently, metal nanoparticles such as Pt supported on metal oxides are used in industrial plants for dehydrogenation of propane to propene. The dehydrogenation of alkanes is an endothermic process, which requires a large consumption of energy. Therefore, developing new stable and active catalyst for dehydrogenation reaction, specially if they are based on non-noble metals or they are coupled with other reactions or separation systems that allow to shift the dehydrogenation equilibrium, is a matter of much interest.

Vajda *et al.* deposited size-selected Pt clusters on anodized aluminium oxide (AAO, Anopore) membranes modified with Al_2O_3 and SnO and used this material for oxidative dehydrogenation of propane to propene.[186] The product distributions and a comparison of catalytic performance between Pt_{8-10} clusters and traditional catalysts (VOx/Al_2O_3 and Pt/monolith) are presented in **Figure 1.33**. Pt clusters (Pt_{8-10}) on various supports showed very high activity as well as high selectivity to propene, being 40-100 times more active for the oxidative dehydrogenation of propane than conventional Pt-based and V-based catalysts. According to DFT calculations, Pt atoms with unsaturated coordination sites in Pt_{8-10} clusters favor the dissociation of C-H bonds rather than C-C or C=C bonds. Therefore, lower amounts of CO_2 and CO were produced on subnanometric Pt clusters rather than on Pt nanoparticles.
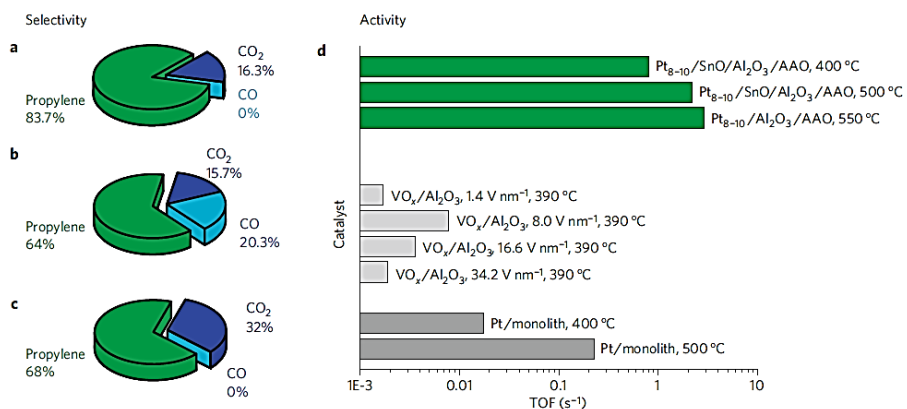
Figure 1.33. Catalytic performances of Pt-based and VOx/Al$_2$O$_3$ catalysts for oxidative dehydrogenation of propane to propene. (a-c) Selectivity to different products by the Pt$_{8-10}$ clusters deposited on various supports catalysts at different temperature: (a) Pt clusters on SnO/Al$_2$O$_3$ at 400 °C, (b) SnO/Al$_2$O$_3$ at 500 °C and (c) Al$_2$O$_3$ at 550 °C. (d) TOFs of propene produced on the Pt$_{8-10}$ catalysts (green) and conventional VOx/Al$_2$O$_3$ and Pt/monolith catalysts for oxidative dehydrogenation of propane to propene. The TOF values have already been normalized to single metal atoms in all catalysts. Adapted with permission from ref **186**. Copyright 2009 Macmillan Publishers Limited, part of Springer Nature.

In a recent work, Anderson *et al.* have studied the dehydrogenation of ethylene to acetylene on size-select Pt clusters (Pt$_4$, Pt$_7$ and Pt$_8$ clusters).[187] It was found that Pt$_7$ clusters showed the highest activity for ethylene dehydrogenation while Pt$_4$ and Pt$_8$ clusters showed similar activity. Experimental results and theoretical calculations indicate that the bonding of ethylene with Pt$_7$ clusters is stronger than that with Pt$_4$ and Pt$_8$ clusters. On the other hand, the higher affinity of Pt$_7$ clusters to ethylene molecules will lead to faster deactivation and agglomeration of Pt$_7$ clusters due to coke formation.

Non-noble metal clusters can also work for dehydrogenation reactions, and it has been found that Co clusters were active for the oxidative dehydrogenation of cyclohexene.[188] Co$_{27\pm4}$ clusters were deposited on various metal oxide supports (Al$_2$O$_3$, ZnO and TiO$_2$ and MgO) to study the influence of support on the catalytic performances. Co clusters supported on MgO showed the highest

initial reactivity to formation of benzene for the dehydrogenation of cyclohexane. The strong interaction between Co clusters and MgO may facilitate the dehydrogenation of cyclohexene. However, Co clusters supported on MgO deactivated with time on stream, due to the formation of a Co-Mg-O solid solution at high temperatures. After comparing four supports (Al_2O_3, ZnO, MgO and ultrananocrystalline diamond), the diamond support was found to be the best support for Co clusters during cyclohexane dehydrogenation.[189] It is proposed in that work that the different surface properties of various supports account for their different catalytic behavior.

So far, there are no reports on non-oxidative dehydrogenation of alkanes with subnanometric metal clusters, which is probably due to the low stability of subnanometric metal clusters at high temperature. In the absence of oxygen, subnanometric metal clusters may agglomerate into nanoparticles, which serve as the active sites for non-oxidative dehydrogenation of alkanes. It can be expected that, if subnanometric metal clusters can be stabilized on a suitable support under the dehydrogenation reaction conditions, higher activity may be achieved on those clusters.

1.5.5 deNOx reactions

Pt-group metal catalysts (including Pt, Pd and Rh) are the main active components of industrial three-way catalysts. Since the metal components mainly exist as nanoparticles, developing new catalysts with smaller metal crystalline size and higher activity as well as the introduction of non-noble metals to save the use of noble metals is an active research field. Heiz *et al.* have studied in an UHV system the catalytic properties of size-selected Pd_n clusters ($4 \leq n \leq 30$) deposited on MgO(100) for NO+CO, i.e. $2NO + 2CO \rightarrow N_2 + 2CO_2$, as a model reaction for deNOx application.[190] The temperature programed reaction (TPR) profiles of the reaction products $^{13}CO_2$ and $^{15}N_2$ as a function of cluster size are shown in **Figure 1.34**. In the case of Pd_4 clusters, almost no product was observed. When the atomicity increased from 5 to 30, the activity based on the production of CO_2 at 300 K also increased gradually with the particle size, except for a relative drop between Pd_{15} and Pd_{20}. Interestingly, the formation of $^{13}CO_2$ was readily observed at very low temperature (140 K) when the atomicity was larger than 20. For Pd_n ($n \leq 20$)

clusters, the NO+CO reaction could only occur at >300 K. It was proposed that adsorption and dissociation of NO can be the rate-determining step in this reaction. According to their results from FT-IR study, the authors have proposed two different reaction mechanisms for reaction temperature of 140 and 300 K, respectively. At higher temperature, NO can be dissociated to atomic N and O bonded to Pd clusters. CO can be oxidized to CO_2 by atomic oxygen. However, at low temperature, the oxidation of CO can only occur through the adsorbed molecular NO. For Pd clusters with atomicity below 20, NO adsorption is not favorable, this resulting in their low activity below 300 K.[191] The adsorption and dissociation of NO on Pd clusters with different sizes was also investigated by means of theoretical calculations.[192,193] Those works indicate that both the electronic and geometric structures of Pd clusters will affect the interaction between Pd and substrate molecules, which further affects the reaction pathway, especially at different temperature range.
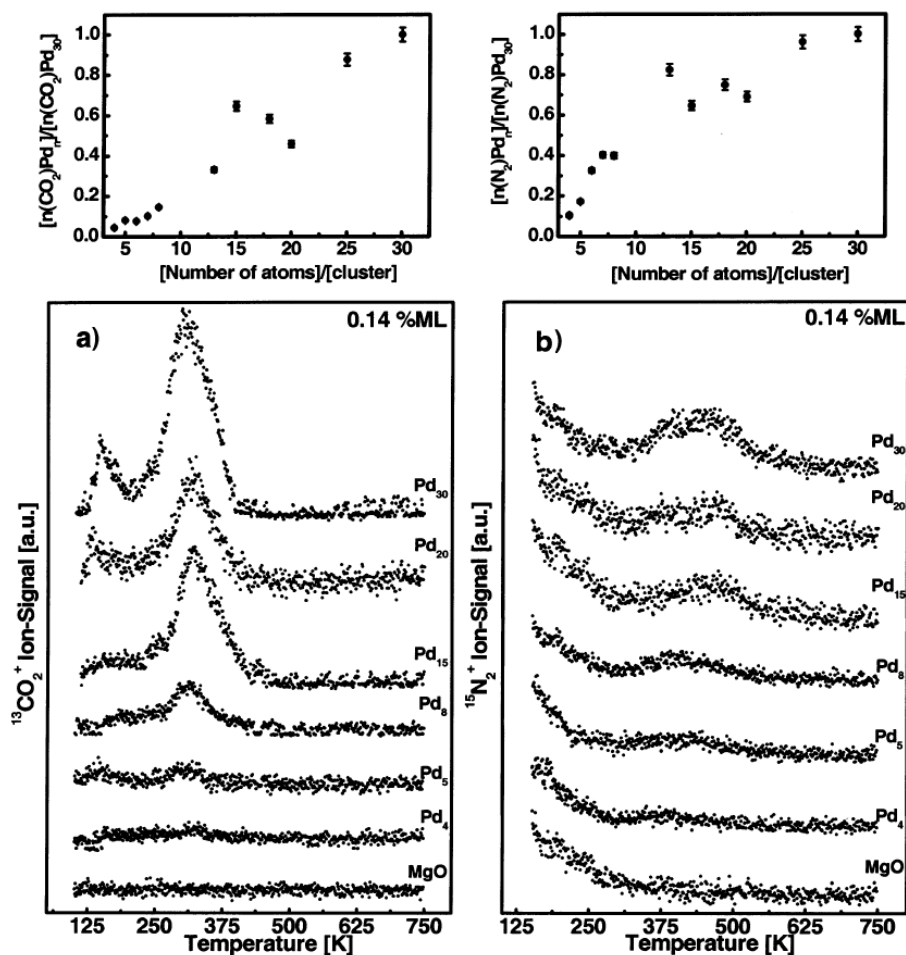
Figure 1.34. Temperature programed reaction (TPR) profiles of the reaction products $^{13}CO_2$ and $^{15}N_2$ as a function of cluster size. The Pd clusters were deposited on a clean MgO film and then were first exposed to ^{13}CO and then to ^{15}NO at 90 K. The activity of various Pd clusters for $^{13}CO_2$ and $^{15}N_2$ expressed as the number of product molecules formed per cluster and normalized to the reactivity of Pd_{30} are presented. Adapted with permission from ref **190**. Copyright 2004 American Chemical Society.
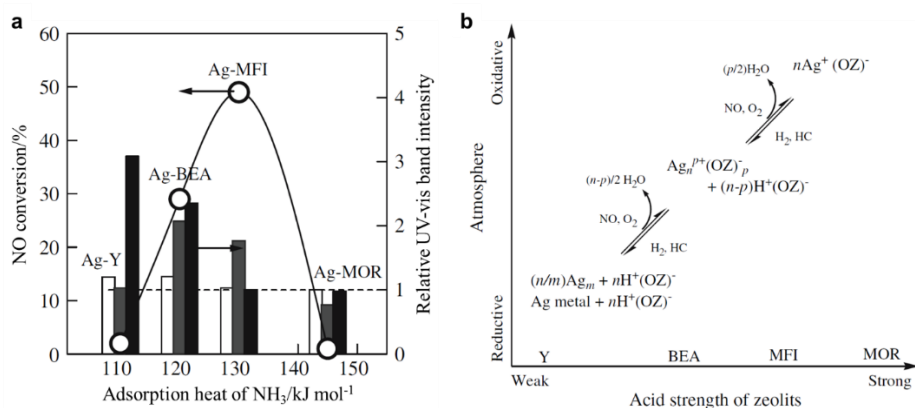
Figure 1.35. (a) Increment of NO conversion for C_3H_8-SCR with 0.5% H_2 at 573 K compared with the activity obtained in the absence of H_2 as a function of adsorption heat of NH_3 on H-form zeolites (open circles). The bars represent the intensity of UV-vis bands corresponding to different types of Ag species: 212 nm (Ag^+, white bar), 260 nm ($Ag_n^{\delta+}$ cluster, gray bar), and 312 nm (metallic Ag_m cluster, black bar) under C_3H_8-SCR with 0.5% H_2. Those intensity values have already been normalized to those bands obtained on the same catalyst under similar reaction conditions but in the absence of H_2. (b) Schematic diagram of the evolution of Ag species, depending on the acidity of zeolite support and the reaction atmosphere. (OZ) represents the zeolite ion-exchange site in this figure. Adapted with permission from ref **196**. Copyright 2005 Springer, Inc.

Ag-based catalysts also perform very well for selective catalytic reduction of NO by hydrocarbons (HC-SCR), and can serve as a substitute for expensive Pt-group catalysts.[194] Among different types of supported Ag catalysts, Ag/zeolite catalysts (usually prepared by ion-exchange process) show promising activity and stability for HC-SCR reaction.[195,196] As shown in **Figure 1.35a**, the addition of H_2 in the feed gas can significantly promote the NO conversion in C_3H_8-SCR reaction. The evolution of Ag species under reaction conditions was followed by EXAFS and UV-vis spectroscopy. In the case of Ag supported on zeolites with weaker acidity, Ag species tend to form metallic Ag nanoparticles under reaction conditions while tend to form cationic Ag species on zeolites with

stronger acidity. By correlating the activity with the contributions of different types of Ag species in various Ag/zeolite catalysts (see **Figure 1.35b**), it is proposed that positive charged Ag clusters (Ag_4^{2+} on average) are the active sites for HC-SCR reaction. Dynamic structural transformation of Ag species can occur when tuning the reaction conditions. By tuning the atmosphere (reductive or oxidative), the atomicity and chemical states of Ag species can be modulated, which will further affect the catalytic properties in HC-SCR reaction.

1.5.6 Photocatalytic reactions

In photocatalytic reactions such as water splitting and CO_2 reduction, metal nanoparticles are usually used as co-catalysts. Similarly, metal clusters can also work as co-catalysts. It has been well demonstrated that the size of metal co-catalysts has significant influences on the photocatalytic properties.[197,198] With suitable particle size, the promotion effect of metal species can be maximized for photocatalytic reactions.

Pt is widely used as co-catalyst in heterogeneous photocatalysts, especially for the photocatalytic water splitting to produce H_2. In some works, Pt clusters were prepared through a simple co-precipitation method for the study of size effects on the photocatalytic H_2 evolution reaction. However, the Pt clusters obtained by this method presented wide size distributions which are not ideal model catalysts for fundamental studies. To properly discuss the metal size effects, Berr *et al.* employed size-selected Pt nanoclusters with different sizes as co-catalysts on CdS nanorods for photocatalytic H_2 production.[199] As shown in **Figure 1.36a**, H_2 evolution efficiency below 1‰ h^{-1} was obtained for smaller clusters (Pt_8 and Pt_{22}), and this value increased to over 1‰ h^{-1} for Pt_{34}. After reaching a maximum H_2 production rate for Pt_{46} nanoclusters, the H_2 production rate dropped for Pt_{68}. Considering the reaction mechanism presented in **Figure 1.36b**, the catalytic efficiency was mainly associated with the higher charge separation efficiency between CdS and Pt nanoclusters, which is further related with the electronic structure of Pt nanoclusters. As it is known, the electronic structure (especially the position of lowest unoccupied molecular orbitals, LUMO) of metal clusters is strongly dependent on the atomicity of clusters. Therefore, by tuning the size, the charge transfer process between CdS and Pt

nanoclusters can be modulated, which would further affect the photocatalytic performance.[200] On the other hand, the reduction of protons to H_2 on Pt nanoclusters is also related with the electronic structure of Pt. The LUMO of Pt nanoclusters have to be higher than the H^+/H_2 redox potential. Therefore, Pt_{46} may have the suitable LUMO positions, which can facilitate the electron transfer from CdS to Pt_{46} nanoclusters and the subsequent reduction of H^+ to H_2.
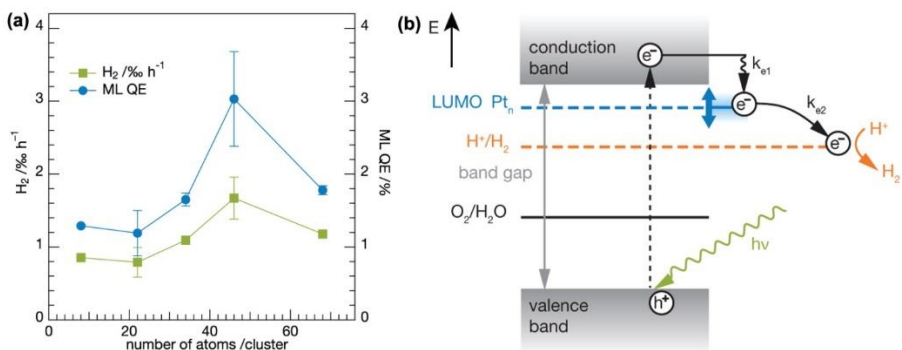
Figure 1.36. (a) Influences of Pt particle size on photocatalytic activity of the CdS nanorods with size-selected Pt clusters as co-catalysts. The average H_2 evolution rate as well as the quantum efficiency clearly changes with the size of Pt clusters. (b) Schematic illustration of the generation of electrons and holes in CdS after excitation by light. The photo-generated electrons will transfer to Pt clusters and then catalyze the reduction of protons for the evolution of H_2. Adapted with permission from ref **199**. Copyright 2012 American Chemical Society.

1.5.7 Catalysis with *in situ* formed metal clusters
In situ formed Pd clusters

It is common to find that, in many catalytic reactions, a reaction induction period can be observed and *in situ* evolution of the catalyst occurs during the catalytic processes. This means that the "real" catalyst is not the one initially added into the system. The *in situ* transformation of metal catalysts often occurs during liquid-phase organic reactions, as a consequence of the interactions between metal species, substrates and solvent in liquid-phase. For some metal-catalyzed reactions, metal clusters can be *in situ* formed from the precursors

(metal salts, transition metal complexes or metal NPs) and those metal clusters will work as the "real" catalysts. In the following section, we will discuss a number of reports showing the reactivity and mechanistic studies of the metal clusters formed during the reactions.

One typical example about the dynamic transformation of metal species under reaction conditions is the evolution of Pd species for C-C coupling reactions. For the classic C-C coupling reaction using Pd-based catalysts, it has been reported that catalytic reactions can be initiated by virtually any source of Pd (Pd salts, Pd complexes, Pd NPs, Pd colloids, etc.).[201-203] Spectroscopic and high-resolution TEM have confirmed that leaching and re-crystallization of Pd-based NPs occur under reaction conditions.[204-207] Subnanometric Pd species will leach from Pd NPs, resulting in the formation of Pd clusters, which can catalyze the C-C coupling reaction.[208] On the other hand, mononuclear Pd salts have also been found to aggregate to Pd clusters during the C-C coupling reactions.[209,210] These works infer that the real catalytic active species may be formed *in situ* during the reaction from different Pd sources. However, little is known about the nature of the *in situ* formed Pd species, including their size and their transformation pathway.

Recently, it has been presented that water-stabilized Pd_3 and Pd_4 clusters are excellent catalysts for C-C coupling reaction.[211] Nucleophilic molecules like water or amines can promote the formation of Pd clusters from Pd NPs and stabilize them. Those subnanometric Pd clusters show very high TOF and TON values for various C-C coupling reactions. When strongly bound ligands (like biaryl phosphines) are added to the reaction system, single Pd atoms can be coordinated by these ligands. These Pd complexes are highly active and can activate aryl chlorides that are considerably much less reactive than other aryl halides.[212] Thus, it seems that, the existing state of Pd species under C-C coupling reaction conditions is dependent on the coordination environment, but the nature of the species formed are still unrevealed.

Since it was indicated that Pd clusters could play an important role in liquid phase catalysis, Fu *et al.* prepared well-defined and highly stable

$[Pd_3Cl(PPh_2)_2(PPh_3)_3]^+[SbF_6]^-$ clusters (named as Pd_3Cl clusters) and these

Pd_3Cl clusters showed high activity for C-C coupling reaction while no

induction period was observed, being consistent with previous works from Corma group.[213] In that work, a new mechanism was proposed for the classic Suzuki-Miyaura reaction. In the classic mechanism, the oxidative addition of aryl halides on Pd(0) species is the initial step, followed by the transmetalation and reductive elimination. However, *in situ* EXAFS and mass spectroscopy led the authors to propose that the Pd_3Cl cluster first reacts with phenylboronic acid to generate the intermediate (Pd_3Ar). Based on the above works, plausible pathways of the Pd species transformation during the catalytic reaction have been proposed.[214,215]
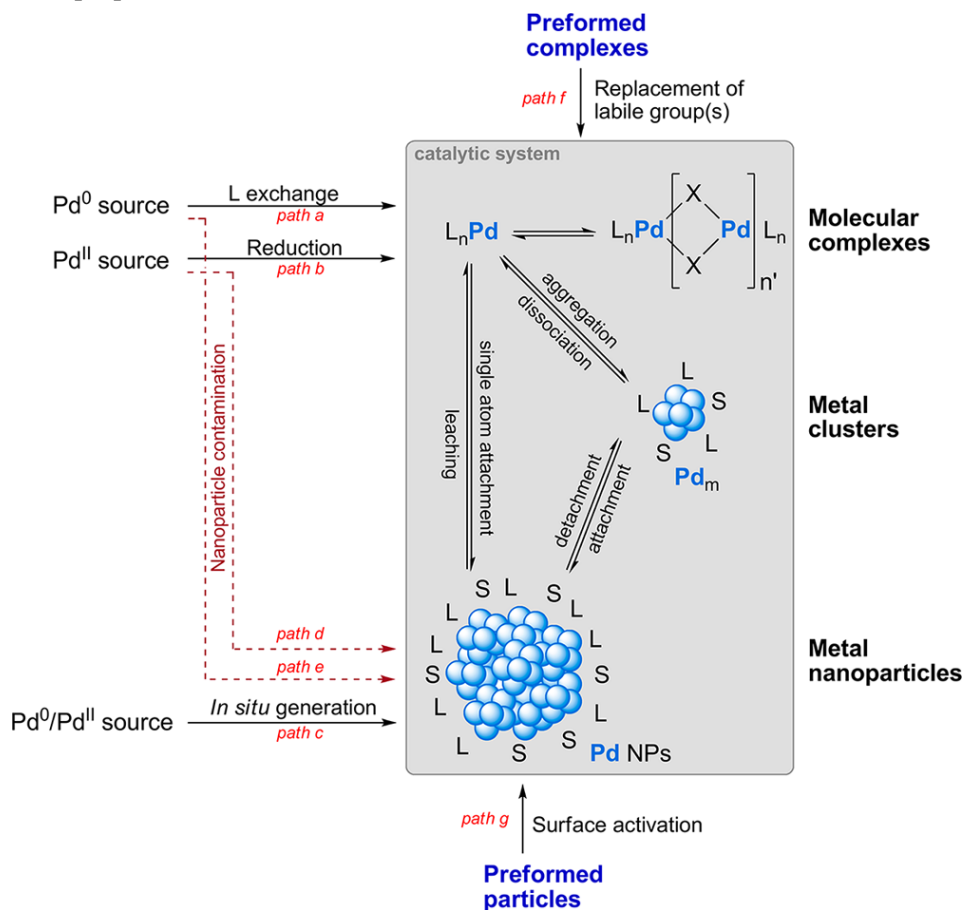
Figure 1.37. Plausible evolution of the Palladium species transformation under reaction conditions. (L, Ligand; S, Solvent; X, Heteroatom). Adapted with permission from ref **214**. Copyright 2013 American Chemical Society.

When using Pd complexes as precursors, they may decompose in some cases, and Pd atoms can aggregate together to form Pd_nL_m clusters with simultaneous replacement of ligands and reduction of metal ions. These Pd clusters can also contribute, and in some cases, be responsible for the final catalytic results. For reactions using Pd NPs as precursors, surface Pd atoms will detach to form Pd_nL_m clusters in the reaction solution through oxidative addition between Pd and the organic substrates. Probably, in the reaction environment, there is a dynamic transformation process between Pd complex (see **Figure 1.37**), Pd clusters and Pd NPs, depending on the concentration of the organic substrates and the products.

The *in situ* transformation of Pd species has also been found in various reactions.[216] For instance, Jiang *et al.* have reported the application of trinuclear Pd clusters for the conversion of CS_2 into CO_2 in the presence of HNO_3 at room temperature. The mononuclear Pd(II) complex firstly transformed into binuclear Pd complex, which further cleavage the C-S bond in the CS_2 molecules, leading to the formation of CO_2. As a consequence, a trinuclear Pd complex was formed, which could be further transformed into mononuclear pre-catalyst in the presence of an excess of HNO_3.

In situ **formed Au clusters**
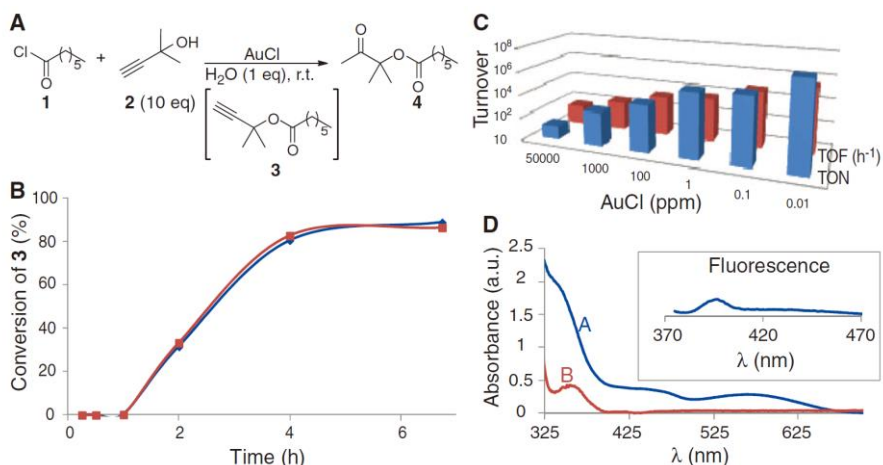
Figure 1.38. Ester-assisted hydration of alkyne by *in situ* formed Au clusters. (A) Scheme for the reaction. (B) Conversion for ester-assited hydration of alkyne promoted by AuCl (squares) and HAuCl₄ (diamonds) at 100 ppm, after correction with the blank experiment. (C) Turnover number (TON) and turnover frequency (TOF) for different amounts of AuCl, calculated as moles of product formed per mole of AuCl at final conversion (TON) and as the initial reaction rate after the induction time per mole of AuCl (TOF). (D) UV-vis spectra of the reaction mixture for the hydration of alkyne containing the Au active species along the induction time (curve A) and when the reaction proceeds (curve B) with the corresponding fluorescence spectrum (inset, irradiated at 349 nm). Adapted with permission from ref **217**. Copyright 2012 The American Association for the Advancement of Science.

As observed with Pd, we have found that the *in situ* formed Au clusters were the "real" active species for some Au-catalyzed reactions, such as ester-assisted hydration of alkyne and in the bromination reaction.[217] As shown in **Figure 1.38**, when mononuclear Au compounds (HAuCl₄ and AuCl) were used as the pre-catalyst, an induction period was observed. Fluorescence spectroscopy and MALDI-TOF prove that Au₃-Au₅ clusters were *in situ* formed under reaction

conditions and they were the catalytically active species for the ester-assisted hydration reaction. In the bromination reaction, similar phenomenon was observed. However, in this case, Au_7-Au_9 clusters were the catalytically relevant Au species for the bromination reaction, suggesting that different reactions may need Au clusters of different sizes. To confirm the size-dependent catalytic properties of Au clusters, dendrimer (Poly(amineamide-ethanol), PAMAM) encapsulated Au_5 and Au_8 clusters were prepared and tested for the hydration and bromination reactions. Au_5-PAMAM was able to catalyze the hydration reaction without induction period while Au_8-PAMAM shows poor activity for this reaction. In the case of bromination reaction, the situation was reversed. Au_8-PAMAM worked better than Au_5-PAMAM and both of them showed no induction period. It should be noted that dendrimer-encapsulated Au clusters showed much lower activity than *in situ* formed Au clusters, implying that *in situ* formed Au clusters have optimized structures and coordination environment for catalysis.

By a top-down approach, subnanometric Au clusters can be generated on solid support (such as Al_2O_3, TiO_2, ZnO, CeO_2 and carbon) after the treatment of supported Au nanoparticles with I_2 solution and those Au clusters are efficient catalyst for ester-assisted hydration of the alkyne.[218] Since it has also been observed that the *in situ* formation of Au clusters (Au_3-Au_6) play a key role in some other reactions, this may indicate that the transformation of mononuclear Au precursor into Au clusters can be a common phenomenon in Au-catalyzed organic reactions, including phenol synthesis from alkynylfurans rearrangement, *w*-bromination of phenylacetylene, bromination-hydration cascade reaction and Conia–ene reaction of alkyne.[219] The *in situ* formation process of Au clusters can be affected by the reaction environment. When a strong acid like HOTf (with a Bronsted acidity near to that of $HSbF_6$) was added to the reaction medium, the ester-assisted hydration of alkyne worked very fast without induction period. However, if basic ligands were added into the ester-assisted hydration of alkyne, the deactivation of Au clusters occured since Au clusters were strongly capped by these ligands.[220]
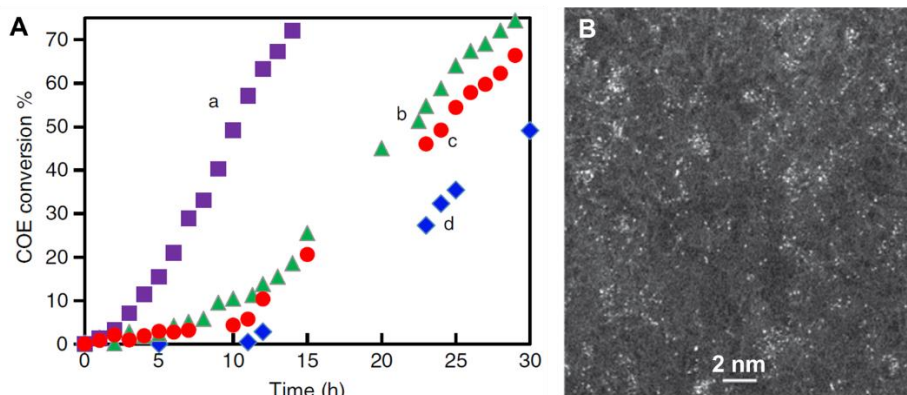
Figure 1.39. (A) Cyclooctene conversion with reaction time using different catalysts or without addition of Au catalyst. Au/SiO$_2$-A (a, square), 6 mg AuCl (b, triangle), 7mg AuCl$_3$ (c, circle), or no Au (d, diamond). (B) TEM images of filtrate solution from Au/SiO$_2$-A collected after conversion reached 18%. Au single atoms as well as subnanometric Au clusters are observed. Adapted with permission from ref **223**. Copyright 2017 Macmillan Publishers Limited, part of Springer Nature.

Direct oxidation of olefins to epoxides with O$_2$ is a very attractive and challenging reaction. Hutchings *et al.* have reported that Au nanoparticles supported on carbon can catalyze the epoxidation of olefins (such as cyclohexene, cis-cyclooctene, styrene) with O$_2$ in the presence of *t*-butyl hydroperoxide (TBHP) as initiator.[221] In a following work, Lambert *et al.* have demonstrated the application of Au$_{55}$ nanoparticles (~1.5 nm) as efficient catalyst for direct epoxidation of styrene to styrene oxide without initiator.[222] In that work, Au$_{55}$ nanoparticles could achieve such transformation while other Au nanoparticles with larger size (>3 nm) did not work. These results imply that the particle size of Au species should affect the epoxidation reaction. However, the catalytic mechanism was not fully revealed.

Also for epoxidation reaction, it has been recently reported that subnanometric Au clusters with less than 10 Au atoms are the active species for epoxidation of *cis*-cyclooctene with O$_2$.[223] As shown in **Figure 1.39**, both heterogeneous and homogeneous Au catalysts (including Au/SiO$_2$, AuCl and AuCl$_3$) could catalyze the epoxidation of cis-cyclooctene, with an induction

period in all cases, indicating that some transformation of Au species may occur under reaction conditions as we have discussed in abovementioned examples. Furthermore, hot filtration experiments showed that leaching of Au from supported Au/SiO$_2$ catalyst into the reaction solution occurred. After checking the filtrate solution by high-resolution STEM, it was found that subnanometric Au clusters were formed. In addition, spectroscopic characterizations (UV-vis and fluorescence spectroscopy) also confirmed the formation of Au clusters. Combining the above experimental results, it was concluded that in situ formed subnanometric Au clusters were the active species for epoxidation of cis-cyclooctene.

In situ formed metal clusters other than Pd and Au

Besides Pd and Au clusters, Fe and Cu clusters have also been detected in the reaction mixture when Fe and Cu salts are used for C-C coupling reactions.[224,225] Although there is still some debate on the true active species in coupling reactions for Cu and Fe, the formation of metal clusters or even metal NPs was confirmed by EXAFS. For the Fe-catalyzed C-C coupling reaction, Fe-Fe dimers were detected after the addition of one equivalent of PhMgCl. With two equivalents of PhMgCl, the coordination number of Fe increased to 5.1, indicating that Fe clusters with 13±2 atoms should be formed. This study indicates that there may be some common rules in metal-catalyzed C-C coupling reactions, namely the cluster-catalyzed mechanism. Recently, bi-nuclear compounds are used for C-C coupling reactions, which is also compatible with the cluster-catalyzed mechanism.[226,227]

Besides C-C coupling reactions, Cu-catalyzed C-heteroatom coupling reactions can also follow a cluster-involved mechanism.[228] An induction period was observed for the Goldberg reaction when 0.5 mol% Cu salts were used as the starting catalyst. Electrospray ionization mass spectrometry (ESI-MS) confirmed the presence of Cu clusters of 2−7 atoms in solution only when the coupling starts, but not during the induction time. Furthermore, Cu NPs were also prepared as pre-catalyst for the Goldberg reaction. An induction period was also observed and the *in-situ* formation of Cu clusters was also confirmed by UV-vis and fluorescence spectroscopy. A series of experiments were performed to identify the chemical nature of the active Cu clusters. Neutral Cu(0) clusters

were prepared by an electrochemical method and showed induction period in the C-N coupling reaction. In addition, Cu nanoparticles with surface Cu(II) species also showed induction period, indicating that the catalytically active clusters were neither Cu(0) or Cu(II) but in some form of deoxygenated Cu(I) species. To prove that hypothesis, deoxygenated Cu(I) clusters were prepared by a one-pot reduction-stabilization method within an oxygen-protective polymer. Meanwhile, no induction period was observed when the Cu clusters stabilized in polymer were used as the catalyst. Thus, deoxygenated Cu(I) clusters were proved to be the active species for the Goldberg reaction. Based on that point, the *in situ* formed Cu clusters were also used for other type of coupling reactions, like C-O, C-S and C-P coupling. Compared with the conventional Cu-diamine complexes, Cu clusters showed a better reactivity (lower amount of catalyst and higher TON) with different nucleophiles under optimized conditions, while Cu-diamine complexes can work at milder conditions and with a wider scope for more demanding reactions.
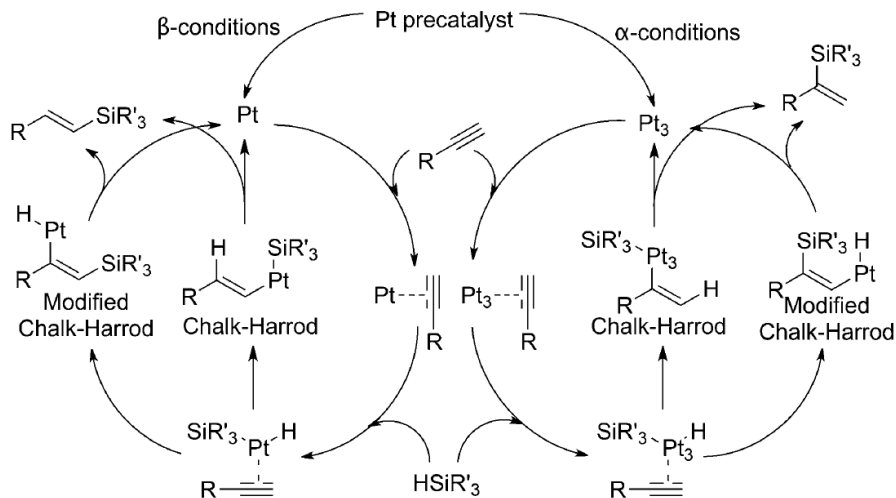
Figure 1.40. Possible pathways for the hydrosilylation of alkynes to obtain β-vinylsilanes (left) and α-vinylsilanes (right) through both Chalk-Harrod and modified Chalk-Harrod mechanism. Adapted with permission from ref **229**. Copyright 2017 Wiley-VCH Verlag GmbH & Co. KGaA, Weinheim.

The Pt-catalyzed hydrosilylation of alkynes is widely used for organic synthesis of vinylsilanes and their derivatives. It is well known that, only β-vinylsilanes (through an anti-Markovnikov addition mechanism) are obtained with simple Pt catalysts such as Kardstedt catalyst and H_2PtCl_6, whereas α-vinylsilanes (through a Markovnikov addition mechanism) can only be obtained in very low yield. Recently, it has been reported that, Pt_3 clusters can selectively catalyze the Markovnikov hydrosilylation of alkynes to α-vinylsilanes with very high turnover frequency (see **Figure 1.40**).[229] By following the evolution of Pt species by spectroscopic techniques, it was found that, simple Pt compounds or the Kardstedt's catalyst would transform into Pt_3 clusters under reaction conditions and those in situ formed Pt_3 clusters can afford a wide variety of new α-vinylsilanes with good yields. Compared with the classic catalytic mechanism on mononuclear Pt species for β-vinylsilanes, the selectivity of Pt_3 cluster is different, indicating the distinct behavior of metal clusters in organic reactions.

1.5.8 Perspectives on catalysis based on metal clusters

In the abovementioned works, it has been clearly demonstrated that, atomicity of metal clusters has significant influences on their catalytic behavior. However, the influence of geometric structure on catalytic properties of metal clusters are rarely studied. For metal clusters with a given atomicity, there should be several possible geometric configurations, which could have different catalytic reactivity under the same conditions. Furthermore, when metal clusters are supported on solid carriers, metal clusters with the same atomicity may have different geometric configuration if their local environment. Such variables make the situation of catalysis based on metal clusters more complicated than single-atom catalysis. Characterizations of the three-dimensional structure of supported metal clusters and tracking their dynamic structural evolution behavior should be key to establish the structure-activity relationship.

So far, the preparation of metal clusters with a few atoms in a controllable manner is still a challenge. When introducing organic ligands, well-defined metal clusters can be generated by wet-chemistry approach. However, the removal of those ligands will destroy the homogeneity of the as-prepared metal

clusters. Therefore, developing more robust synthetic methodologies will also be critical for understanding and improving the catalysis based on metal clusters.

1.6 Non-noble metal catalysts for heterogeneous catalysis
1.6.1 Non-noble metal catalysts for selective hydrogenation reactions
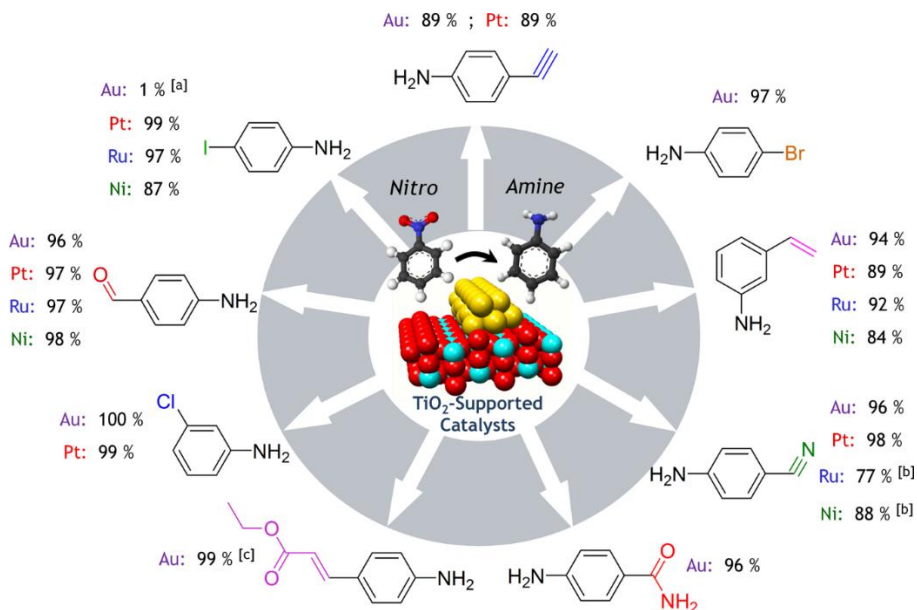
Figure 1.41. Scope of substituted anilines synthesized by hydrogenation of the corresponding nitro compounds with metal nanoparticles supported on TiO$_2$. Yields (%) are displayed. To achieve optimal performance Pt/TiO$_2$, Ru/TiO$_2$, and Ni/TiO$_2$ must be reduced in H$_2$ at 723 K before the reaction to promote a strong metal−support interaction. Low yield due to low catalytic activity. Loss of yield due to hydrolysis of the nitrile group.

Since the report of supported Au nanoparticles as chemoselective catalyst for hydrogenation of nitroarenes, the utilization of noble metal nanoparticles supported on various solid carriers (such as TiO$_2$, FeOx, CeO$_2$, carbon, hydrotalcite, zeolite, metal-organic frameworks etc.) has been intensively studied for various selective hydrogenation reactions, especially those related

with production of fine chemicals and the conversion of biomass to fuels and chemicals.[230-232] For instance, as shown in **Figure 1.41**, excellent yields to corresponding anilines can be obtained through the chemoselective hydrogenation of nitroarenes with different functional groups by supported nanoparticulate noble metal catalysts. Furthermore, by rational design of the combination of metal and the support, it is possible to perform cascade reactions with supported metal catalysts to obtain various chemicals starting from nitro compounds (see **Figure 1.42**). These works demonstrate the versatility of chemoselective hydrogenation reactions based on noble metal nanoparticles.
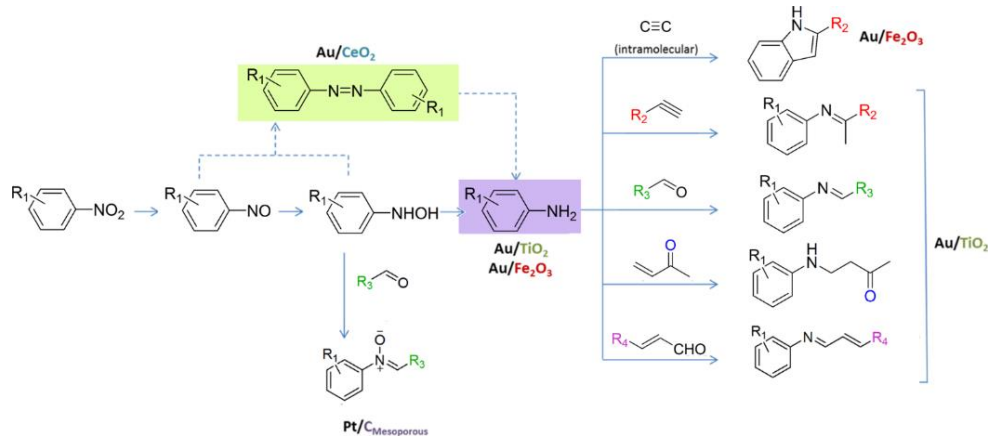
Figure 1.42. Diverse chemicals can be obtained from nitro compounds via single-step or cascade reactions through the chemoselective hydrogenation of nitro compounds by nanoparticulate noble metal catalysts.
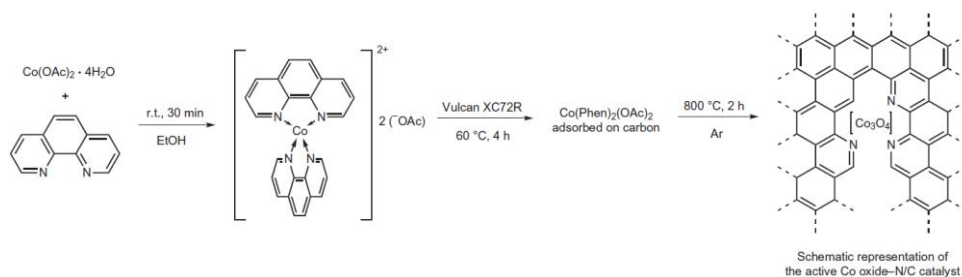
Figure 1.43. Schematic illustration of the preparation of Co nanoparticles encapsulated in N-doped carbon layers through pyrolysis of organometallic cobalt complexes (Co-phenanthroline coordination compound) in the presence of carbon black as the support.

In recent years, it is found that, non-noble metal nanoparticles can also serve as active and chemoselective catalysts for hydrogenation of nitroarenes. In 2012, Beller et al. reported the preparation of Co nanoparticles covered by N-doped carbon layers by pyrolysis of organometallic Co compounds (see **Figure 1.43**).[233] During the high-temperature pyrolysis process, the organic ligands will transform into N-doped carbon layers while the mononuclear Co precursor will agglomerate into nanoparticles. As shown in **Figure 1.44**, the size of Co nanoparticles are quite large (usually >20 nm) and the core of the nanoparticles are metallic while the surface are oxidized.
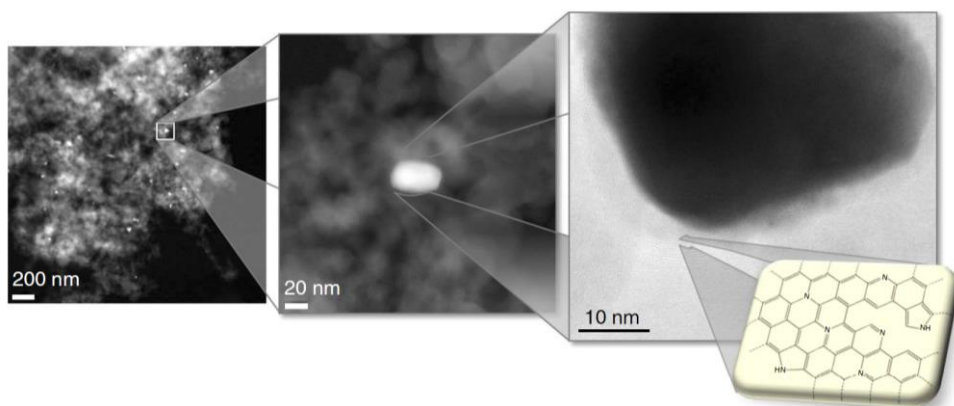
Figure 1.44. STEM and high-resolution TEM images of Co nanoparticles encapsulated by N-doped carbon layers.

Hydrogenation of nitrobenzene was chosen as a model reaction to test the catalytic properties of Co nanoparticles encapsulated by N-doped carbon layers. As shown in **Table 3**, the Co complex supported on carbon without pyrolysis treatment showed very low activity for hydrogenation of nitrobenzene. After high-temperature pyrolysis treatment, the activity was enhanced significantly. Moreover, the authors have also tested different N-containing ligands and it can be seen that the structure of the ligand has influence on the reactivity of the final pyrolyzed Co catalyst. It has also been shown in this work that, the encapsulated Co nanoparticles show excellent chemoselectivity for a wide scope of nitroarenes, including those compounds with unsaturated bonds, such as C=C, C=O and C≡N, showing that Co nanoparticles encapsulated by carbon

layers can be a promising candidate for substituting noble metal nanoparticles (see **Table 4**). In the following works, Beller et al. have applied this type of catalyst for various hydrogenation reactions, including hydrogenation of nitriles, ketones and quinolines.

Table 3. Hydrogenation of nitrobenzene with different Co-based catalysts.
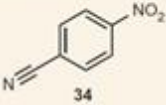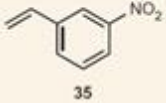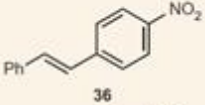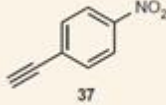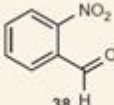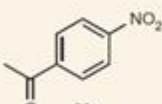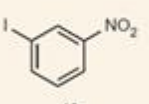
Entry	Catalyst	Conversion (%)*	Yield (%)*
1	Co/carbon	5	0[†]
2	L1/carbon	1	0[†]
3	Carbon[‡]	6	0[†]
4	Co-L1/carbon[§]	>99	95/99[ǁ]
5	Co-L2/carbon	8	5
6	Co-L3/carbon	26	19
7	Co-L4/carbon	<1	0
8	Co-L5/carbon	<1	0
9	Fe-L1/carbon	15	1[†]
10	Co-L1[¶]	4	0
11	Ni-L1[¶]	<1	0

L, ligand. Reaction conditions: 110 °C, 4 h, 0.5 mmol nitrobenzene, 1 mol% catalyst (3 wt% Co-L/C), 50 bar hydrogen, 2 ml THF, 100 ml H₂O.

*Determined by GC using n-hexadecane as an internal standard. †Reaction time 16 h. ‡Pyrolysed carbon. §Metal/ligand ratio 1:2. ‖Conducted in H_2O (3 ml). □Using Co and Ni complex as homogeneous catalyst.

Table 4. Scope study with the Co nanoparticles covered by N-doped carbon layers for selective hydrogenation of aromatics.

Entry	Substrate	Time (h)	Yield (%)*
1	34	4	83
2	35	6	91
3	36	6	96/97†
4	37	4	88‡
5	38	4	97
6	39	4	79
7	40	6	92/99†

Reaction conditions: 110 °C, 0.5 mmol nitroarene, 1 mol% catalyst (3 wt% Co-L1/C), 50 bar of H_2, 2 ml THF, 100 ml H_2O; .99% conversion observed in all cases. *Determined by GC using n-hexadecane as an internal standard. †

Isolated yield (5 mmol scale). ‡2 mol% cobalt catalyst.

By a similar procedure, Fe nanoparticles covered by N-doped carbon layers have also been prepared and can also be active and selective catalyst for hydrogenation of nitroarenes to corresponding anilines.[234] As shown in **Figure 1.45**, Fe nanoparticles show similar structures like Co nanoparticles although the average size is larger than that of Co. Notably, the reactivity of Fe nanoparticles are much lower than Co nanoparticles, which is not explained in that work.

Following the work from Beller and his co-workers, it has been reported in the literature that, several strategies can be used for preparation of non-noble metal encapsulated by thin carbon layers (Co, Fe, Ni etc.). For instance, using metal-organic framework as precursor, Co nanoparticles encapsulated in N-doped carbon structures can be obtained and those nanoparticles are also active for chemoselective hydrogenation of nitroarenes.[235-237] Besides, metal oxides or other solid carriers can also be employed as the support for those non-noble metal nanoparticles and a variety of N-containing ligands can also be used as the ligands to coordinate with the metal ions in the precursor. It seems that, all the catalysts reported in the literature show similar nanoscale structures. However, it is supposed that, there should be some differences between the materials prepared by different procedures, which are not discussed in the literature. As a result, for the same metal, different catalysts with different structures have been reported and that scattered information presented in the literature make it difficult to directly compare their catalytic performance.
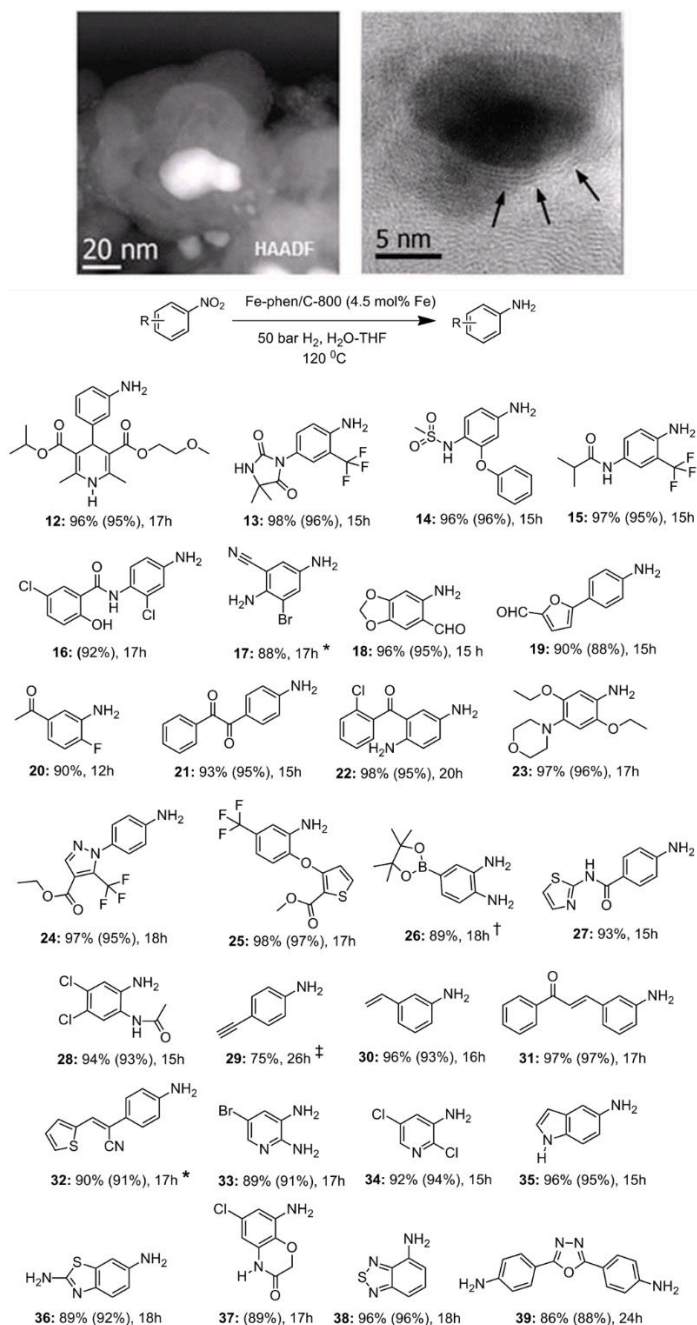
Figure 1.45. TEM image of Fe nanoparticles covered by N-doped carbon layers. The catalytic performance of those Fe nanoparticles for selective hydrogenation

of nitroarenes to corresponding anilines are also presented.
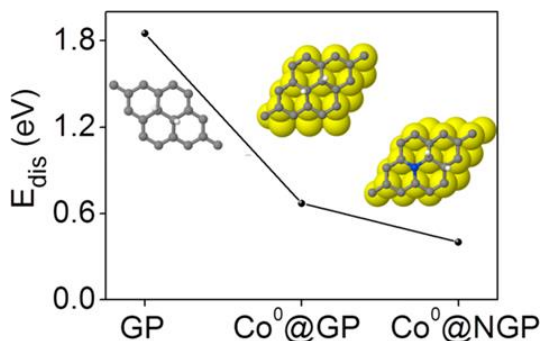
Figure 1.46. Dissociation energies of H_2 on different catalysts. Insets are the optimized dissociative structures. Color code: cobalt is yellow, carbon is gray, nitrogen is blue, and hydrogen is white.

However, the active sites for hydrogenation reactions in this type of catalyst is still not clear, especially the role of the carbon layers. Wang et al. observed the *in situ* transformation of CoOx to metallic Co during the selective hydrogenation of nitroarenes under 30 bar of H_2, although the catalyst was a mixture of CoOx and metallic Co.[238] In this work, it is claimed that the active sites for hydrogenation of nitroarenes can be on the surface of carbon layers. The energy for H_2 dissociation on N-doped graphene covering on Co nanoparticles is lowest (shown in **Figure 1.46**). In addition, in the previous works, N species that doped in the carbon layers are thought to be a key for achieving high reactivity for selective hydrogenation reactions.[239] However, looking into the literature, there is no suitable control experiments that can prove the indispensable role of N in the carbon layers. Therefore, the role of N still needs to be further clarified.
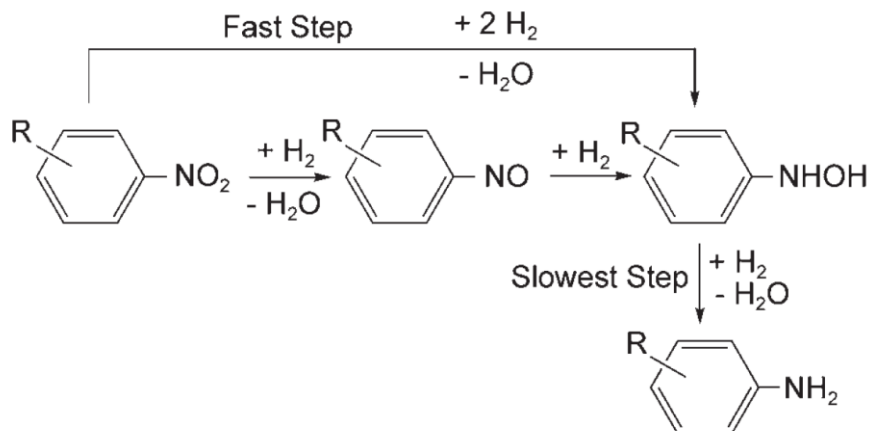
Figure 1.47. Proposed reaction pathway for the hydrogenation of aromatic nitro compounds to aniline derivatives in the presence of the Au/TiO$_2$ catalyst.

It has been demonstrated by kinetic and in situ IR spectroscopic studies that, the reaction pathway on supported gold nanoparticles is different to that reported on reported for Pt/CaCO$_3$ and Pt/C-H$_3$PO$_4$.[240] As shown in **Figure 1.47**, phenylhydroxylamine is formed as both a primary product (directly from nitrobenzene) and a secondary product (via hydrogenation of nitrosobenzene) at the Au-TiO$_2$ interfacial sites on the Au/TiO$_2$ catalyst. The accumulation of phenylhydroxylamine on the catalyst surface as observed by IR shows that the transformation of phenylhydroxylamine into aniline is the rate-determining step for the whole hydrogenation process. Furthermore, the fact that only very small amounts of azoxybenzene were observed in the solvent suggests strongly that the inhibition of the condensation of hydroxylamine and nitrosobenzene intermediates into azoxybenzene during the hydrogenation of nitroarenes on Au/TiO$_2$ catalysts is predominantly a result of the low concentration of nitrosobenzene present, together with the strong adsorption of nitrosobenzene and phenylhydroxylamine to the Au/TiO$_2$ active sites. Because of the strength of the adsorption, these compounds do not desorb from the catalyst/support surface and condensate to form azoxybenzene, but instead are hydrogenated to produce aniline. Regarding the selective hydrogenation of nitroarenes with substituting groups on Au-based catalyst, the preferential adsorption of –NO$_2$ group at the Au-support interface is thought to be the key to achieve high

chemoselectivity.[241] For non-selective catalysts, both $-NO_2$ groups and other unsaturated groups can be adsorbed on the metal surface, leading to the loss of selectivity.

Although a number of works have been published on the synthesis and catalytic applications of non-noble metal nanoparticles for chemoselective hydrogenation reactions, the reaction mechanism is still not clear. Whether the reaction pathway on non-noble metals is the same or it follows a different pathway is still unknown.

Nevertheless, the reactivity of these Co-based catalysts are still quite low compared to the noble metal catalysts, which leads to the use of the high pressure (usually ≥ 30 bar) when working with non-noble metal nanoparticles. From a practical point of view, in order to substitute noble metal catalysts, the catalytic performance of non-noble catalysts should be at least comparable to noble metal catalysts. Therefore, to synthesize non-noble metal catalysts with higher activity that allows to work under mild conditions and to reveal the active sites for chemoselective hydrogenation reactions are still necessary for better understanding the catalytic behavior of non-noble metal nanoparticles and to develop practical catalysts for selective hydrogenation reactions with comparable performance to noble metal catalysts.
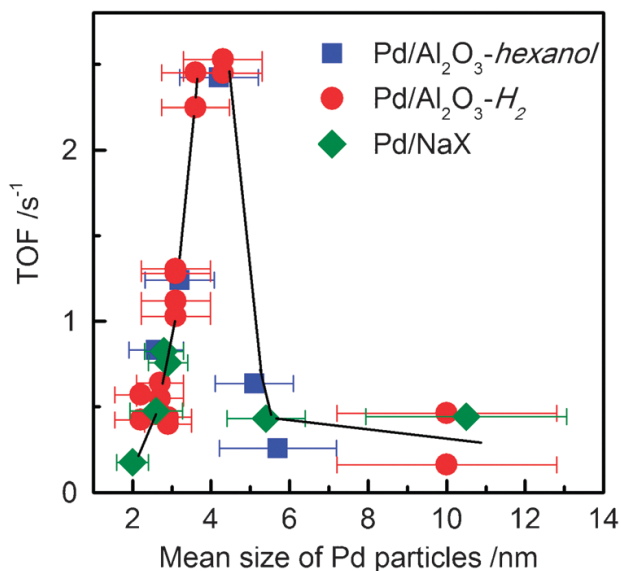
Figure 1.48. Dependence of turnover frequency on the mean size of Pd

nanoparticles for the selective oxidation of benzyl alcohol. The TOF values for oxidation of benzyl alcohol to benzyl aldehyde from three different supported Pd catalysts are presented. Adapted with permission from ref **245**. Copyright 2011 The Royal Society of Chemistry.

1.6.2 Non-noble metal catalysts for selective oxidation reactions

Selective oxidation is another important type of reaction that noble nanoparticles have been intensively studied. Herein, selective oxidation of alcohol will be taken as an example to show the structure-reactivity relationship before the introduction of using non-noble metal catalysts for selective oxidation reactions.

There are numerous works on the application of noble metal nanoparticles for selective oxidation of alcohols to aldehydes or ester. The particle size effect and the promotion effect from the support and synergistic effect of bimetallic nanoparticles have been intensively discussed.[242-244] Herein, we would like to emphasize the size effect of metal nanoparticles on their catalytic properties for oxidation of alcohols. As shown in **Figure 1.48**, Pd nanoparticles on three types of support showed the same variation on size-dependent activity for oxidation of benzyl alcohol. From a mechanistic point of view, during the oxidation of alcohol on metal surface, the alcohol molecule should be firstly adsorbed on the surface of metal nanoparticles, followed by activation of the O-H bond, resulting in formation of an alkoxide intermediate. Subsequently, β-H elimination occurs to give aldehyde or ketone as product. Finally, the surface of metal nanoparticles can be recovered when adsorbed H species are removed by O_2 to form water.[245] Taking into consideration that several elemental steps can affect the overall reaction rate and the sites for adsorption of alcohol, and that β-H elimination and activation of O_2 are different on Pd nanoparticles, it is speculated that a certain balance can be achieved on Pd nanoparticles around 4 nm, to give the highest activity for oxidation of benzyl alcohol.
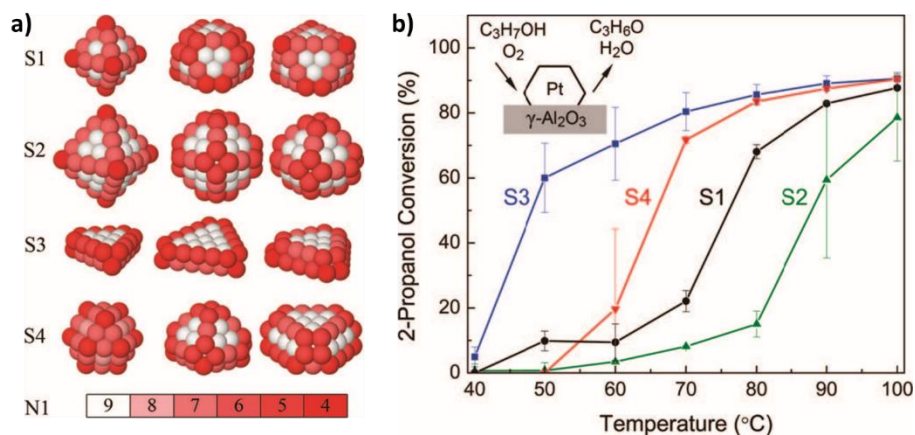
Figure 1.49. (a) Models of different Pt nanoparticles with similar particle size (~0.8 nm for S1 and ~1 nm for S2, S3, and S4) but different geometric shapes. The geometric shapes of different Pt/γ-Al$_2$O$_3$ samples (S1 to S4) were obtained based on the fitting of EXAFS data as well as with the TEM measurements. The geometric shapes that given the best fitting results are shown in the left column. The color coding indicates the different number of first nearest neighbors (N1) of surface atoms in each Pt nanoparticle. (b) Catalytic activity for oxidation of 2-propanol to acetone by Pt/γ-Al$_2$O$_3$ samples measured in a packed-bed mass flow reactor by mass spectrometry. Adapted with permission from ref **247**. Copyright 2010 American Chemical Society.

As we said before, not only the size of metal clusters and nanoparticles, but also the particle shape is an important impact on their catalytic properties, and such effects have been observed with Pt nanoparticles for alcohol oxidation reactions.[246] Cuenya *et al.* reported the influence of the shape on the reactivity of Pt particles (0.8~1 nm) supported on γ-Al$_2$O$_3$ for 2-propanol oxidation.[247] Four types of Pt nanoparticles with similar size and different shapes (illustrated in **Figure 1.49a**), according to EXAFS and STEM characterization respectively, were tested. These four supported Pt nanoparticles showed distinct activities for selective oxidation 2-propanol (as shown in **Figure 1.49b**), which implies that the shape of the cluster has a big impact on its catalytic properties. By correlating the coordination numbers of surface Pt atoms in four types of Pt clusters, they found that surface Pt atoms with lower coordination numbers

showed lower onset temperature, corresponding to the highest low-temperature activity. Among the four samples, the Pt nanoparticles with bilayer structure showed the highest activity for selective oxidation of 2-propanol. Furthermore, in the case of Pt nanoparticles with bilayer structure, the contact area between Pt and the Al_2O_3 support is larger, resulting in more perimetric Pt atoms. The interface effects between Pt and Al_2O_3 may also facilitate the oxidation reaction. Similar shape effect on catalytic properties of Pt nanoparticles has also been reflected for the selective oxidation of 2-butanol.[248] Pt nanoparticles with more edge and corner sites show higher selectivity to 2-butanone while Pt nanoparticles with less edge and corner sites show higher selectivity to combustion product (CO_2). Therefore, by tuning the geometric structure of metal nanoparticles, it is possible to modulate the selectivity during the selective oxidation of alcohols.

In 2013, Beller et al. reported the application of Co-based catalyst for selective oxidation of alcohol to esters.[249] It was claimed in this work that, CoOx nanoparticles covered by N-doped carbon are the active species for this esterification reaction. This type of catalyst has also been used for oxidation of 5-Hydroxymethylfurfural under base-free conditions.[250] Later, Zhang et al. reported the application of atomically dispersed Co-N-C catalyst for the oxidative coupling of primary and secondary alcohols to directly produce α,β-unsaturated ketones.[251] In this work, they have demonstrated that only atomically dispersed Co species in the N-doped carbon support are the active sites while Co or CoOx nanoparticles are not (see **Figure 1.50**). The Co-N-C catalyst after acid leaching treatment showed almost the same as the pristine one, which implies the innocent role of Co nanoparticles in the Co-N-C sample.

Not only Co, but also other atomically dispersed non-noble metals in N-doped carbon can also be used for oxidation of alcohols.[252] Xie et al. have compared the catalytic performance of Co-N-C, Cu-N-C, Cr-N-C Fe-N-C and Ni-N-C for oxidation of benzyl alcohol by O_2 in water and the catalytic results show that Cu-N-C and Co-N-C are active for benzyl alcohol oxidation while the other three samples show low activity. Kinetic and isotopic studies on Fe-N-C catalyst show that, the β-H elimination is the rate-limiting step for the oxidation of benzyl alcohol. They have also used those metal-N-C catalysts for oxidation of aliphatic alcohols (glycerol, ethanol and 1,6-hexanediol) and it has

been found that those metal-N-C catalysts show very low activity, indicating the low intrinsic reactivity of those non-noble metal-N-C species. In a recent work, Xie et al. have carried out further investigation on the active sites in Co-N-C and Cu-N-C catalysts for oxidation of alcohol.[253] By EXAFS and XANES, information on the chemical states and coordination environment of single-site Co species have been obtained. The mechanistic studies show that, Co(II) coordinated by N atoms are the active sites for oxidation of benzyl alcohol and those single-site Co species can be stable in H_2 up to 750 K. However, how these single-site Co(II) species activate O_2 and benzyl alcohol is still not clear.

Table 5. Esterification of benzyl alcohol with methanol by CoOx nanoparticles covered by N-doped carbon layers.
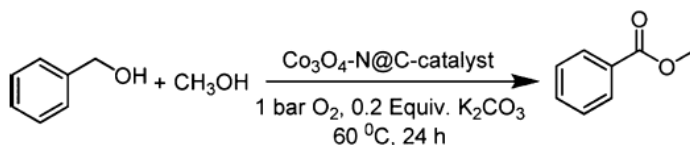
entry	carbon support	cobalt salt	L[f]	pyrolysis [°C, h, gas]	C[f] [%]	Y[f] [%]
1[a]	–	–	–	–	<2	<1
2[a]	–	$Co(OAc)_2 \cdot 4H_2O$	–	–	5	<1
3[a]	–	$Co(OAc)_2 \cdot 4H_2O$	L1	–	12	<1
4[b]	Vulcan XC72R	$Co(OAc)_2 \cdot 4H_2O$	–	–	7	2
5[b]	Vulcan XC72R	$Co(OAc)_2 \cdot 4H_2O$	L1	–	12	2
6[b]	Vulcan XC72R	$Co(OAc)_2 \cdot 4H_2O$	–	800, 2, Ar	20	12
7[b]	Vulcan XC 72R	$Co(OAc)_2 \cdot 4H_2O$	L1	800, 2, Ar	>99	97
8[b]	Vulcan XC72R	$Co(OAc)_2 \cdot 4H_2O$	L2	800, 2, Ar	80	74
9[b]	Vulcan XC72R	$Co(OAc)_2 \cdot 4H_2O$	L3	800, 2, Ar	68	60
10[b]	Vulcan XC72R	–	–	800, 2, Ar	<3	<1
11[b]	Vulcan XC72R	–	L1	800, 2, Ar	<4	<1
12[b]	Al_2O_3	$Co(OAc)_2 \cdot 4H_2O$	L1	800, 2, Ar	83	79
13[b]	TiO_2	$Co(OAc)_2 \cdot 4H_2O$	L1	800, 2, Ar	52	45
14[c]	Vulcan XC72R	$Co(OAc)_2 \cdot 4H_2O$	L1	800, 2, Ar	6	4
15[d]	Vulcan XC72R	$Co(OAc)_2 \cdot 4H_2O$	L1	800, 2, Ar	40	15
16[e]	Vulcan XC72R	$Co(OAc)_2 \cdot 4H_2O$	L1	800, 2, Ar	16	7

C=conversion, Y=yield. L=ligand. [a]Homogeneous catalysis conditions: 0.5 mmol benzyl alcohol, 4 mL CH_3OH, 0.0125 mmol $Co(OAc)_2 \cdot 4H_2O$, 0.025 mmol ligand, 0.1 mmol K_2CO_3. bHeterogeneous catalysis conditions: (3 wt % Co): 0.5 mmol benzyl alcohol, 4 mL CH_3OH, 0.1 mmol K_2CO_3, 25 mg catalyst (2.5 mol % Co). [c]Same as 'b' without base and O_2. [d]Same as 'b' without base. [e]Same as 'b' in the absence of O_2. [f]Determined by GC. In case of lower yields, benzaldehyde was detected as a minor product.
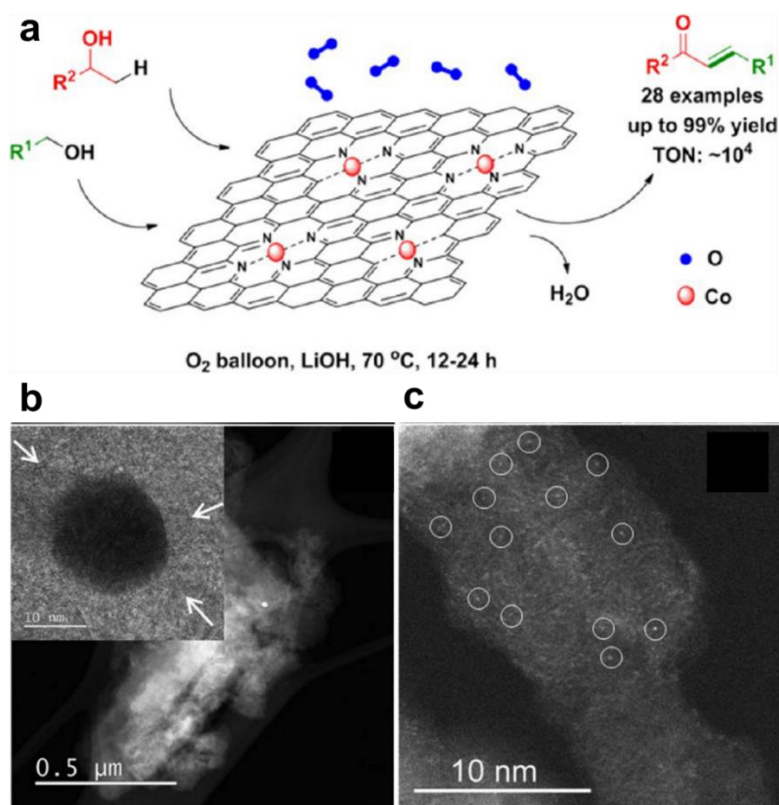
Figure 1.50. (a) Oxidative coupling of primary and secondary alcohols with Co-N-C catalyst towards the formation ofα,β-unsaturated ketones. (b) TEM images of Co-N-C catalysts. In this image, very few Co nanoparticles encapsulated in carbon layers can be seen. (c) High-resolution STEM image Co-N-C catalyst, showing the presence a large number of singly dispersed Co atoms in the carbon support.

Importantly, it should be noted that, in the abovementioned two works from the same group, the metal-N-C catalysts are prepared by different procedures. And in the *ChemSusChem* paper, Cu-N-C is more active than Co-N-C while in the *ACS Catalysis* paper, it is reversed, which implies that, the reactivity of metal-N-C catalyst is strongly related with the synthesis methodology. Although the characterization results based on high-resolution TEM and X-ray adsorption spectroscopy show that they share similar structures in the materials

in these two papers, their different catalytic properties indicate that there should be some other structural factors that are not fully considered when discussing the active sites for oxidation of benzyl alcohol.

Besides, some other selective oxidation reactions can also be achieved with the non-noble metal-N-C catalysts. For instance, Beller et al. have shown in the synthesis of nitriles with alcohol, ammonia and oxygen with Co-N-C catalyst.[254] Li et al. have demonstrated the construction of C=C bonds by oxidative coupling between alcohols and dimethyl sulfoxide (DMSO).[255] On the basis on the above discussions, it can be concluded that, non-noble metal-N-C catalysts have been shown to be active for some selective oxidation reactions. However, the active sites and how molecules are activated on those singly dispersed metal species are still not clear. Furthermore, the catalytic performance of those reported metal-N-C catalysts are much lower than noble metal catalysts. For practical applications, there is still plenty of room for improvement.
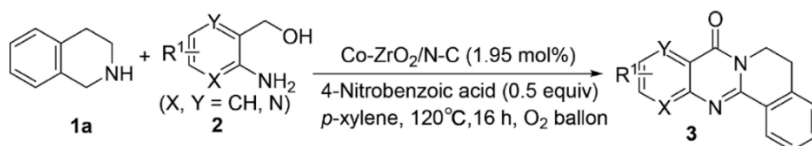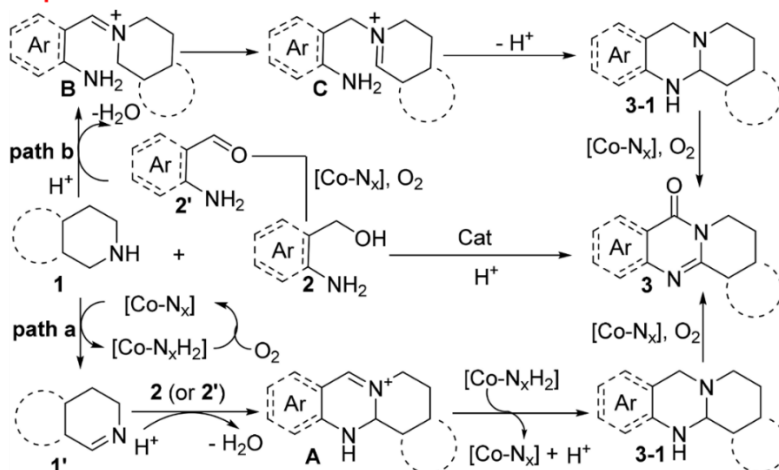
Figure 1.51. Oxidative functionalization of cyclic amines to quinazolinones with 2-aminoarylmethanols with Co-ZrO$_2$/N-C catalyst (atomically dispersed Co species dispersed on ZrO$_2$, surrounded by N-doped carbon).
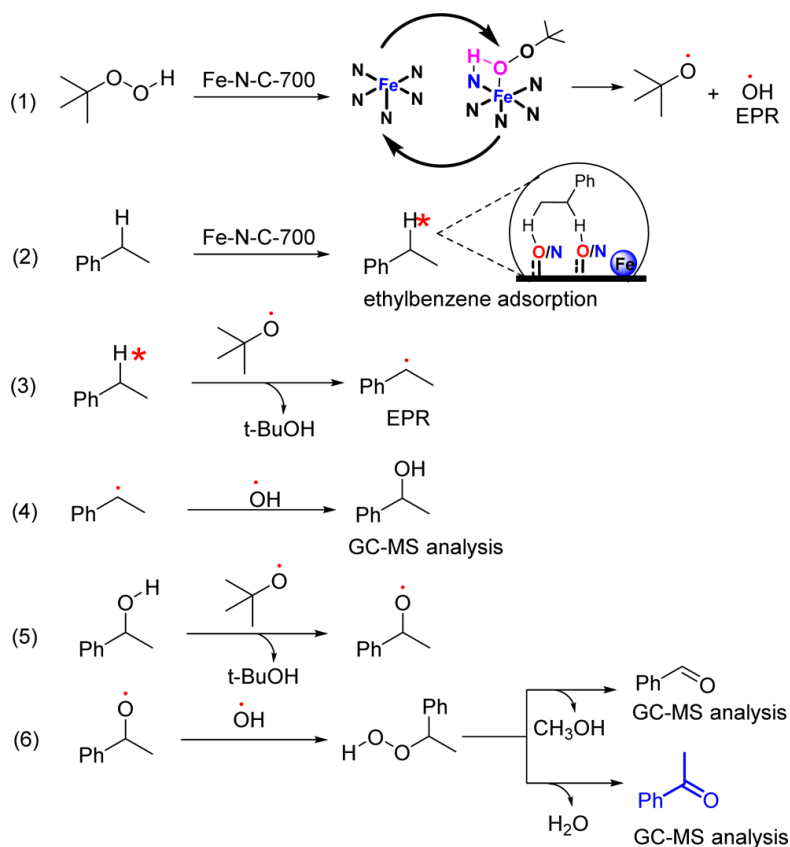
Figure 1.52. Proposed reaction mechanism of ethylbenzene oxidation on the Fe−N−C-700 catalyst.

A more complicated reaction has been achieved by using atomically dispersed Co-Nx species as catalysts. In a recent work, Xie et al. have prepared a Co-ZrO$_2$/N-C by introduction of inorganic Co salt together with N-containing ligands to a Zr-MOF (UiO-66-NH$_2$).[256] After pyrolysis at 800 °C, the metal-organic framework decomposed and formed the Co-ZrO$_2$/N-C sample. Structural characterizations show that, Co are highly dispersed on ZrO$_2$ and N-doped carbon. As shown in **Figure 1.51**, this composite material is able to catalyze the oxidative functionalization of cyclic amines to quinazolinones with 2-aminoarylmethanols to ring-fused quinazolinones. The proposed mechanism involves the oxidative dehydrogenation of -CH$_2$-OH to C=O, the condensation

between the amine groups and the subsequent hydrogenation and oxidative dehydrogenation steps.

Non-noble metal-N-C catalysts can also be used for oxidation reactions using peroxides as oxidant. For instance, Co-N-C catalyst was used as catalyst for epoxidation of alkenes using aqueous tert-butyl hydroperoxide (70%) was used as oxidant.[257] As shown in **Figure 1.52**, Liu et al. have shown the application of Fe-N-C catalyst for the oxidation of hydrocarbons to alcohols and ketones also with TBHP as oxidant.[258] From a mechanistic point of view, the role of atomically dispersed metal species may participate the activation of TBHP to generate active radicals, which initiate the oxidation of hydrocarbons.
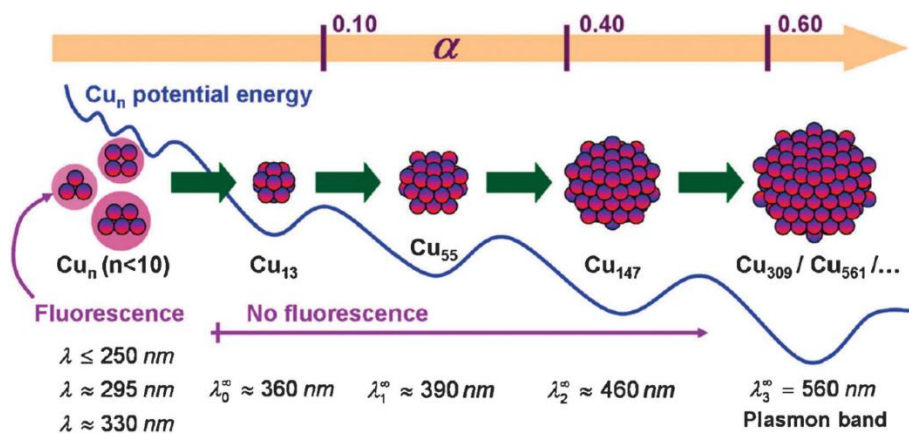
Figure 1.53. Schematic illustration of size-dependent optical properties of Cu clusters and nanoparticles. Estimated wavelengths of the plasmon band for Cu clusters or nanoparticles are shown at the bottom. Adapted with permission from reference **259**. Copyright 2009 American Chemical Society.

1.6.3 Metal nanoparticles for photocatalytic reactions

As shown above, the catalytic applications of non-noble metal catalysts for hydrogenation and oxidation reactions have been well studied. However, the applications of non-noble metal catalysts for photocatalytic reactions are rarely studied. In this part, we are going to summarize the previous works on photocatalysis based on metal nanoparticles. Although these works from the literature are mainly related with noble metals, they can provide the background

information on how light can change the catalytic behavior of metal catalysts.

For metal species, a very important character associated with the particle size is the size-dependent optical properties. For metal nanoparticles, it is well known that particle size and morphology has significant influence on their plasmonic properties. In the case of metal clusters as well as small nanoparticles (<2 nm), their optical adsorption behavior is also strongly related with the size. As shown in **Figure 1.53**, the UV-vis adsorption band will generally shift to lower wavelength when decreasing the particle size. In the case of subnanometric Cu clusters with less than 13 atoms, they can only absorb UV light (<400 nm) and show characteristic fluorescence emission depending on the atomicity.[259] Therefore, as a consequence of their different light absorption properties and electronic structures, metal clusters and nanoparticles show distinct photocatalytic properties. Basically, metal species may act as light sensitizer or co-catalyst in photocatalytic systems. In the case of co-catalysts, as discussed before, the charge transfer process between a semiconductor and a metal co-catalyst will vary with the particle size of the metal. Furthermore, the surface reaction kinetics will also be related with the particle size of the metal co-catalyst. This has already been demonstrated in some Pt/semiconductor photocatalysts.[260,261]
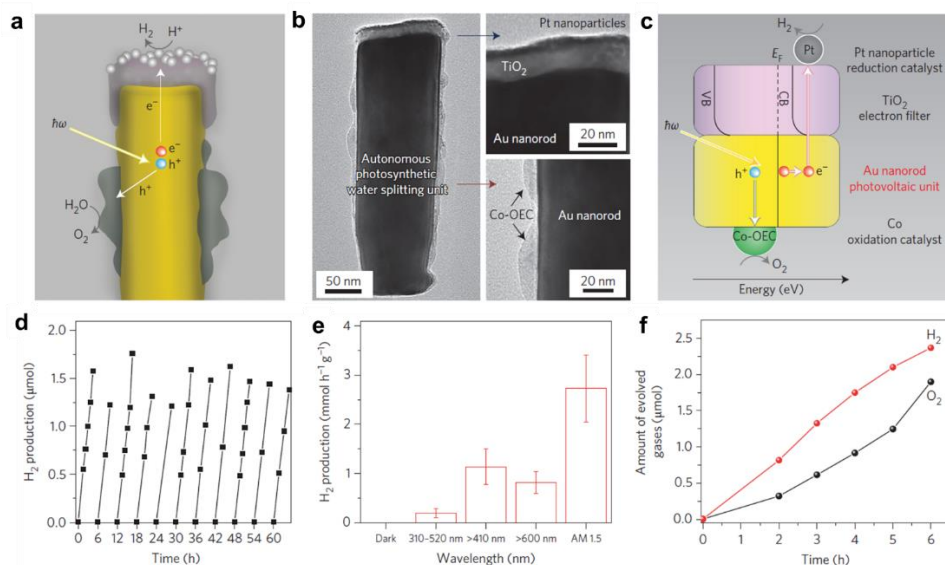
Figure 1.54. (a-c) Schematic illustrations and structural characterizations of plasmon-mediated overall water splitting on Au nanorods modified with co-catalysts. (d) Amount of H_2 produced on Au nanorods under visible light (>410 nm) irradiation. (e) H_2 production rate on Au nanorods under irradiation of light of different wavelength. (f) Measured O_2 and H_2 photoproducts as a function of time for a second device illuminated by 300 mW/cm^2 of white light (AM 1.5). Adapted with permission from reference **264**. Copyright 2013 Macmillan Publishers Limited, part of Springer Nature.
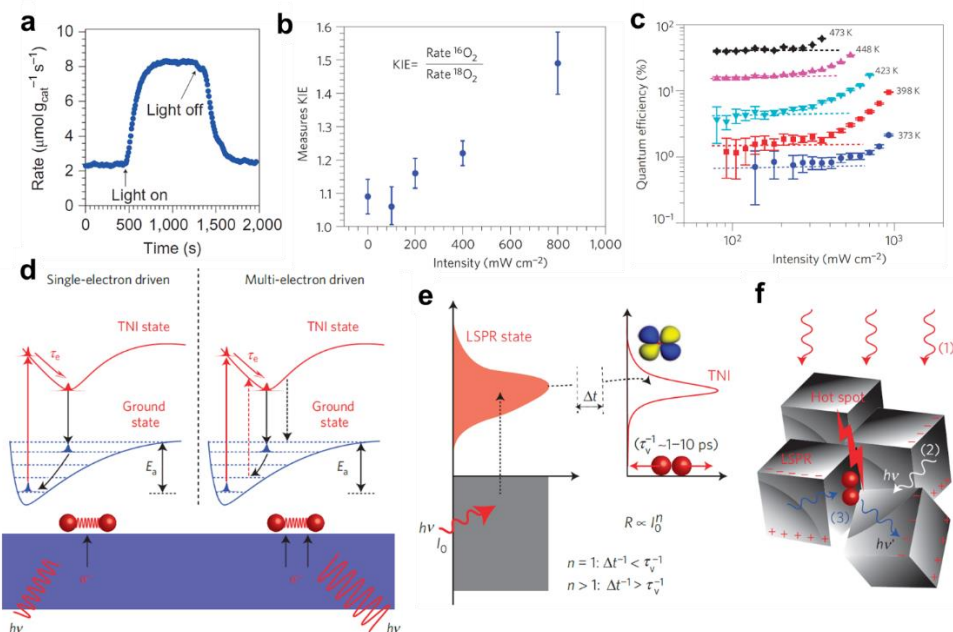
Figure 1.55. (a) Reaction rate for epoxidation of ethylene to ethylene oxide on Ag nanocubes with and without visible light irradiation at 450 K. (b) Isotopic studies on the influences of light intensity for epoxidation of ethylene on Ag nanocubes. (c) Influences of reaction temperature and light intensity on quantum efficiency for epoxidation of ethylene on plasmonic Ag nanocubes. (d) Schematic illustration of single-electron driven and multi-electron driven reactions on metal surface under light irradiation. (e) Schematic illustration on the plasmon-mediated electron transfer from Ag to O_2. When the rate of plasmon excitation, Δt^{-1}, is lower than the vibrational decay rate of O_2, τ_v^{-1}, the photocatalytic rate is linear with respect to the source intensity. On the other

hand, when $\Delta t^{-1} > \tau_v^{-1}$, the photocatalytic rate shifts to a super-linear dependence on source intensity. (f) Formation of a hot spot in a complex structure of Ag nanocubes for activation of O_2 under low-intensity visible light irradiation. Adapted with permission from reference **266** and reference **267**. Copyright 2011 and 2012 Macmillan Publishers Limited, part of Springer Nature, respectively.

In recent years, mononuclear metal complexes have been employed as photocatalyst for photoredox transformations by reacting with substrate molecules to generate radicals after being excited by visible light.[262,263] However, for supported single atoms, the above process seems not to be applicable anymore due to their different electronic structures. Then, in the following part, we would like to emphasize the different catalytic behaviors of metal nanoparticles and clusters when they are working as light absorbent without the involvement of semiconductor materials, and discuss how the particle size affects the metal-molecule interactions.

When metal clusters or nanoparticles are excited by light, electrons in the ground state will transfer to higher energy levels, which can further transfer to molecules or participate in surface reaction directly. For instance, it has been reported that, Au nanorods can serve as light sensitizer for adsorption of visible light (>410 nm) and produce photo-generated electrons and holes (see **Figure 1.54**). Subsequently, those photoelectrons and holes can transfer to co-catalysts for overall water splitting to H_2 and O_2, simultaneously.[264] Besides, it has also been reported that, photocatalytic conversion of CO_2 to HCOOH can be achieved on Au nanoparticles covered by reduced graphene oxide under visible-light irradiation through a plasmon-mediated mechanism.[265] So far, the efficiency of plasmon-based photocatalytic process is still much lower than that on traditional semiconductor-based photocatalysts, which is probably related with the short life time and low reactivity of photo-generated hot electrons.

On the other hand, photo-generated hot electrons can transfer to substrate molecules and favor the activation process. For instance, it has been demonstrated that under visible light irradiation, the activation of oxygen on Ag nanoparticles was promoted and thereof lead to higher catalytic reactivity for epoxidation of ethylene to ethylene oxide by O_2 (as shown in **Figure55a**).[266] Kinetic and isotopic studies show that, the reaction rate on Ag nanoparticles

under light irradiation exhibited a super-linear power law dependence on light intensity (rate~intensity^n, with $n>1$), even at much lower intensity than that required for super-linear behavior on extended metal surfaces (see **Figure 1.55b** and **Figure 1.55c**).[267] Nevertheless, the apparent quantum efficiency on plasmonic Ag nanoparticles for ethylene epoxidation increased when the light intensity and reaction temperature increased, which was also significantly different to the situation on traditional semiconductor photocatalysts. Considering that oxygen molecules are activated through the electron transferred from Ag nanoparticles, both single-electron and multi-electron transfer between Ag and O_2 may occur, which was dependent on the light intensity. According to the experimental results and theoretical calculations, it was proposed that when the light intensity was higher than the threshold (~300 mW/cm^2), multi-electron transfer between Ag and O_2 occured, leading to the super-linear power law dependence on light intensity (as shown in **Figure 1.55d** and **Figure 1.55e**). Nevertheless, according to simulation modeling, considering the intensity distribution of electric field intensity on Ag nanocubes, it seemed impossible to realize the super-linear law between reactivity and light intensity on monodispersed Ag nanocubes at relatively low light intensity used in this work (300~400 mW/cm^2). Therefore, it was speculated that, the enhanced electric field between composed Ag nanocubes could cause the experimental phenomenon, as described in **Figure 1.55f**. Therefore, it also implies that, by tuning the spatial assembly of plasmonic nanoparticles, their photocatalytic properties can be modulated.
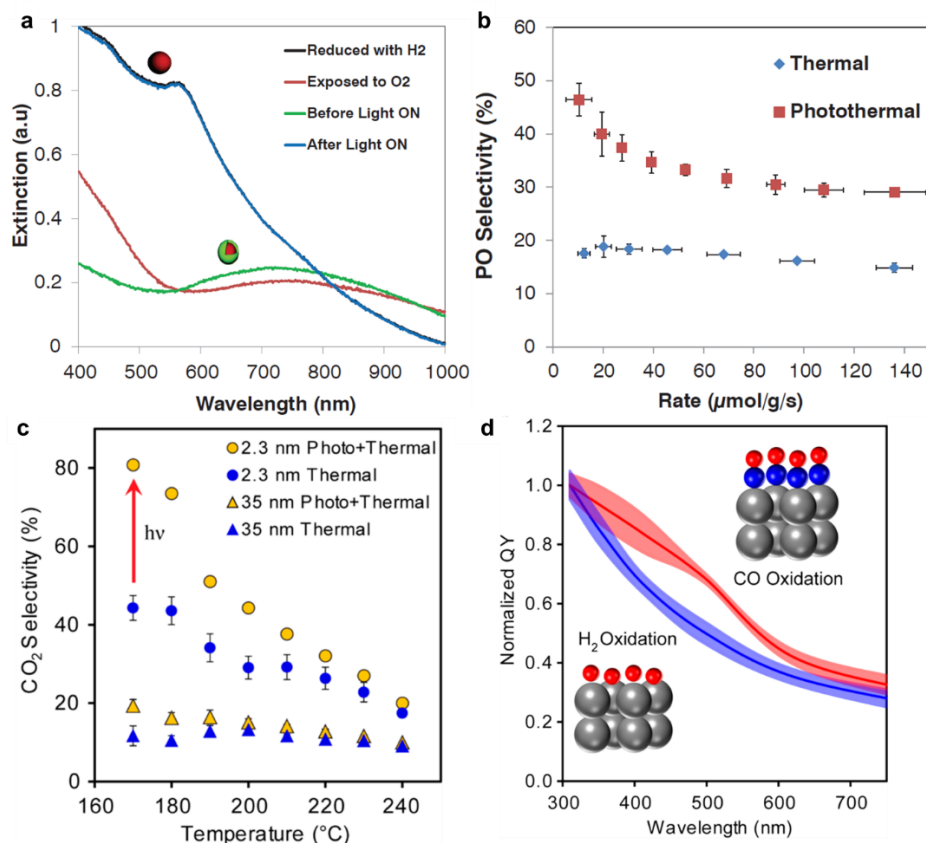
Figure 1.56. (a) UV-vis spectra of Cu nanoparticles under different conditions. (b) Selectivity to propene epoxide under photo-thermal and thermal conditions on Cu nanoparticles. (c) Influences of light irradiation on preferential oxidation of CO in rich H_2 on small and big Pt nanoparticles. (d) Normalized quantum yields for CO and H_2 oxidation driven by hot electrons after excitation of Pt states with a low intensity laser pulse obtained by theoretical calculations. The physical models of H_2 and CO adsorbed on Pt surface are also presented. The shaded regions represent variations in calculated quantum yield due to uncertainty in physical parameters used in the model. (a, b) Adapted with permission from references **268**. Copyright 2013 The American Association for the Advancement of Science. (c, d) Adapted with permission from references **269**. Copyright 2014 American Chemical Society.

The introduction of light-catalyst interaction can also change the chemoselectivity for heterogeneous catalytic processes. As shown in **Figure 1.56a** and **Figure 1.56b**, Linic *et al.* have also reported the influence of visible light irradiation on epoxidation of propene with Cu nanoparticles. Under visible-light irradiation, the partially oxidized Cu-CuOx nanoparticles will be reduced to metallic Cu and maintain stable under reaction conditions for epoxidation of propene. As a consequence, the selectivity to propene oxide is promoted compared with thermal catalytic process under the equal conditions since the selectivity to combustion product (CO_2) is much lower on metallic Cu nanoparticles.[268] When substrate molecules are absorbed on metal surface, electronic interaction between metal and the absorbent will occur. In a recent work, Christopher *et al.* have demonstrated the tuning of selectivity by controlling the metal-absorbent interaction with light. In their work, CO oxidation by O_2 in rich H_2 is chosen as the model reaction. As shown in **Figure 1.56c**, under photo-thermal conditions, the selectivity to CO oxidation is improved in a wide temperature range. Specifically, selectivity to CO oxidation by O_2 is increased from 44% to 81% on Pt nanoparticles (ca. 2.3 nm) supported on Al_2O_3 at 170 ℃. However, such enhancement is not observed on large Pt nanoparticles (ca. 35 nm).[269] When molecules are absorbed on metal surface, electronic interaction between metal and molecules will occur. The bonding between metal surface and substrate molecules can also be excited by incident light. Therefore, with the help of physical modeling and calculations, it is possible to obtained calculated quantum yields of photocatalytic reactions on metal surface. As shown in **Figure 1.56d**, the calculation results suggest that, the absorbed CO and H_2 show different response behavior to visible light. Therefore, when the catalyst is irradiated by light between 400-600 nm, the CO-Pt bonding will be preferentially activated, resulting in improved CO selectivity in CO-PROX reaction.

The modulation effects of light irradiation has also been reflected for hydrogenation reaction. Halas *et al.* have prepared Pd nanoparticles supported on plasmonic Al nanoparticles (e.g. antenna-reactor nanocomposites catalyst) for selective hydrogenation reactions. Under laser irradiation, hot electrons are generated on plasmonic Al nanoparticles and are transferred to Pd nanoparticles, which has been confirmed by ultra-fast spectroscopy. Subsequently, those light-

induced hot electrons can promote the H_2 activation process on Pd nanoparticles according to the results from H_2-D_2 exchange experiments. More interestingly, activity and chemoselectivity for hydrogenation of acetylene on Pd nanoparticles can also be modulated by the incident light irradiation. Under laser irradiation, the catalytic activity for acetylene hydrogenation is decreased and a C_2H_4/C_2H_6 ratio of ~37 can be achieved with an incident laser powder of ~14.3 W/cm^2. For comparison, the C_2H_4/C_2H_6 ratio in the products is only ~7 under thermal conditions without laser irradiation.[270]

Compared with the numerous reports on applications of plasmonic nanoparticles for photocatalytic reactions, the number of reports on photocatalytic applications of metal nanoparticles is much less. As shown before, most of the reports are on the role of metal clusters as co-catalysts of semiconductor materials, and their different catalytic behavior is probably related with different electronic structures between clusters and nanoparticles. Notably, there are only a few reports on the application of metal clusters without the presence of other semiconductor materials. It has been reported that, subnanometric Cu and Au clusters can serve as photocatalysts for degradation of organic dyes under visible light and their catalytic performance is dependent on their atomicity.[271,272] However, compared with those classic semiconductor photocatalysts, the efficiency of metal clusters is much lower and their stability is also a limitation.

Taking into consideration that metal clusters have been proved to be active species for various organic reactions, such as C-C and C-X (X=N, O, S, etc.) coupling reactions, there should be some influences of light irradiation on those catalytic processes. Indeed, there are some reports on light-promoted C-C coupling reactions with supported Pd catalysts.[273-275] With visible light irradiation, the reaction rates can be significantly enhanced. However, in those works, Pd mainly exist as nanoparticles, which seems not to be the real active species since Pd-leaching from nanoparticles into solution occurs under reaction conditions. Therefore, it is necessary to identify the mechanism that explains how visible light irradiation can promote Pd-catalyzed C-C coupling reactions. Electronic transfer between semiconductor support and Pd clusters may contribute the enhanced activity. On the other hand, as shown above, the

introduction of light irradiation may also change the chemoselectivity of metal clusters.

In summary, it has been shown in the literature that, light can have influence on the activity and selectivity of catalytic reactions on the surface of noble metal catalysts. It has been proposed that, the influence of light irradiation works by affecting the surface electronic structure of metal nanoparticles, which further affects the electronic interaction between reactant molecules and metal surface. As a consequence, the energy barrier for the activation of substrate molecules or reaction mechanism or reaction pathway can be modulated. However, it is still not clear that how the molecules interact with the metal surface and how the reactants are transformed to products through a series of elementary steps. Therefore, it is necessary to conduct in situ spectroscopic studies on the metal catalysts under photocatalytic conditions. Besides, the previous works on photocatalytic reactions are mainly on noble metal nanoparticles. It will also be highly interesting to study the influence of light irradiation on non-noble metal catalysts.

References

(1) Boudart, M. *J. Mol. Catal.* **1985,** *30*, 27-38.

(2) Ertl, G.; Knözinger, H.; Weitkamp, J. (Eds.), *Handbook of Heterogeneous Catalysis*, Wiley-VCH, 1997.

(3) Čejka, J.; Corma, A.; Zones, S. (Eds.) *Zeolites and Catalysis: Synthesis, Reactions and Applications*, Wiley-VCH, 2010.

(4) Somorjai, G. A.; Carrazza, J. *Ind. Eng. Chem. Fundamen.*, **1986,** *25*, 63-69.

(5) Che, M.; Bennett, C. O. *Adv. Catal.* **1989**, *36*, 55-172.

(6) Gates, B. C.; Guczi, L.; Knozinger, H. *Metal clusters in Catalysis*, *Studies Surf. Sci. Catal.*, Vol. 29, 1986, Elsevier.

(7) Yang, J. C.; Small, M. W.; Grieshaber, R. V.; Nuzzo, R. G. *Chem. Soc. Rev.* **2012,** *41*, 8179-8194.

(8) Roldan Cuenya, B.; Behafarid, F. *Surf. Sci. Rep.* **2015,** *70*, 135-187.

(9) Liu, L.; Corma, A. *Chem. Rev.* **2018**, doi: 10.1021/acs.chemrev.7b00776.

(10) Zhang, H.; Liu, G.; Shi, L.; Ye, J. *Adv. Energy Mater.* **2018**, *8*, 1701343.

(11) Wang, J.; Xu, F.; Jin, H.; Chen, Y.; Wang, Y. *Adv. Mater.* **2017**, *29*.

(12) He, L.; Weniger, F.; Neumann, H.; Beller, M. *Angew. Chem. Int. Ed.* **2016**,

55, 12582.

(13) Chaudhuri, P.; Verani, C. N.; Bill, E.; Bothe, E.; Weyhermüller, T.; Wieghardt, K. *J. Am. Chem. Soc.* **2001,** *123*, 2213-2223.

(14) Zaanen, J.; Sawatzky, G. A.; Allen, J. W. *Phys. Rev. Lett.* **1985,** *55*, 418-421.

(15) Taylor, K. J.; Pettiette - Hall, C. L.; Cheshnovsky, O.; Smalley, R. E. *J. Chem. Phys.* **1992,** *96*, 3319-3329.

(16) Boronat, M.; Leyva-Perez, A.; Corma, A. *Acc. Chem. Res.* **2014,** *47*, 834-844.

(17) Wang, J.; Wang, G.; Zhao, J. *Phys. Rev. B* **2002,** *66*, 035418.

(18) Buceta, D.; Piñeiro, Y.; Vázquez-Vázquez, C.; Rivas, J.; López-Quintela, M. *Catalysts* **2014,** *4*, 356-374.

(19) Kelly, K. L.; Coronado, E.; Zhao, L. L.; Schatz, G. C. *J. Phys. Chem. B* **2003,** *107*, 668-677.

(20) Fernández, E. M.; Soler, J. M.; Garzón, I. L.; Balbás, L. C. *Phys. Rev. B* **2004,** *70* 165403.

(21) Schauermann, S.; Hoffmann, J.; Johánek, V.; Hartmann, J.; Libuda, J.; Freund, H.-J. *Angew. Chem. Int. Ed.* **2002,** *41*, 2532-2535.

(22) Janssens, T. V. W.; Clausen, B. S.; Hvolbæk, B.; Falsig, H.; Christensen, C. H.; Bligaard, T.; Nørskov, J. K. *Top. Catal.* **2007,** *44*, 15-26.

(23) Wu, J.; Li, P.; Pan, Y. T.; Warren, S.; Yin, X.; Yang, H. *Chem. Soc. Rev.* **2012,** *41*, 8066-8074.

(24) Tauster, S. J. *Acc. Chem. Res.* **2002,** *20*, 389-394.

(25) Sasahara, A.; Pang, C. L.; Onishi, H. *J. Phys. Chem. B* **2006,** *110*, 13453-13457.

(26) Novotny, Z.; Argentero, G.; Wang, Z.; Schmid, M.; Diebold, U.; Parkinson, G. S. *Phys. Rev. Lett.* **2012,** *108*, 216103.

(27) Gong, X. Q.; Selloni, A.; Dulub, O.; Jacobson, P.; Diebold, U. *J. Am. Chem. Soc.* **2008,** *130*, 370-381.

(28) Campbell, C. T.; Parker, S. C.; Starr, D. E. *Science* **2002,** *298*, 811-814.

(29) Campbell, C. T. *Acc. Chem. Res.* **2013,** *46*, 1712-1719.

(30) Farmer, J. A.; Campbell, C. T. *Science* **2010,** *329*, 933-936.

(31) Hansen, T. W.; Delariva, A. T.; Challa, S. R.; Datye, A. K. *Acc. Chem. Res.* **2013**, *46*, 1720-1730.

(32) Simonsen, S. B.; Chorkendorff, I.; Dahl, S.; Skoglundh, M.; Sehested, J.; Helveg, S. *J. Am. Chem. Soc.* **2010,** *132*, 7968-7975.

(33) Simonsen, S. B.; Chorkendorff, I.; Dahl, S.; Skoglundh, M.; Sehested, J.; Helveg, S. *J. Catal.* **2011,** *281*, 147-155.

(34) Wettergren, K.; Schweinberger, F. F.; Deiana, D.; Ridge, C. J.; Crampton, A. S.; Rotzer, M. D.; Hansen, T. W.; Zhdanov, V. P.; Heiz, U.; Langhammer, C. *Nano Lett.* **2014,** *14*, 5803-5809.

(35) Kang, J. H.; Menard, L. D.; Nuzzo, R. G.; Frenkel, A. I. *J. Am. Chem. Soc.* **2006,** *128*, 12068-12069.

(36) Sanchez, S. I.; Menard, L. D.; Bram, A.; Kang, J. H.; Small, M. W.; Nuzzo, R. G.; Frenkel, A. I. *J. Am. Chem. Soc.* **2009,** *131*, 7040-7054.

(37) Vayssilov, G. N.; Lykhach, Y.; Migani, A.; Staudt, T.; Petrova, G. P.; Tsud, N.; Skala, T.; Bruix, A.; Illas, F.; Prince, K. C.; et al. *Nat. Mater.* **2011,** *10*, 310-315.

(38) Nilius, N.; Ganduglia-Pirovano, M. V.; Brazdova, V.; Kulawik, M.; Sauer, J.; Freund, H. J. *Phy. Rev. Lett.* **2008,** *100*, 096802.

(39) Lin, X.; Nilius, N.; Freund, H. J.; Walter, M.; Frondelius, P.; Honkala, K.; Hakkinen, H. *Phy. Rev. Lett.* **2009,** *102*, 206801.

(40) Lykhach, Y.; Kozlov, S. M.; Skala, T.; Tovt, A.; Stetsovych, V.; Tsud, N.; Dvorak, F.; Johanek, V.; Neitzel, A.; Myslivecek, J.; et al. *Nat. Mater.* **2016,** *15*, 284-288.

(41) Bamwenda, G. R.; Tsubota, S.; Nakamura, T.; Haruta, M. *Catal. Lett.* **1997,** *44*, 83-87.

(42) Serna, P.; Corma, A. *ACS Catal.* **2015,** *5*, 7114-7121.

(43) Sun, B.; Vorontsov, A. V.; Smirniotis, P. G. *Langmuir* **2003,** *19*, 3151-3156.

(44) Sterrer, M.; Risse, T.; Martinez Pozzoni, U.; Giordano, L.; Heyde, M.; Rust, H. P.; Pacchioni, G.; Freund, H. J. *Phys. Rev. Lett.* **2007,** *98*, 096107.

(45) Pacchioni, G.; Giordano, L.; Baistrocchi, M. *Phys. Rev. Lett.* **2005,** *94*, 226104.

(46) Giordano, L.; Pacchioni, G.; Goniakowski, J.; Nilius, N.; Rienks, E. D.; Freund, H. J. *Phy. Rev. Lett.* **2008,** *101*, 026102.

(47) Schneider, W. D.; Heyde, M.; Freund, H. J. *Chem. Eur. J.* **2018**, DOI:10.1002/chem.201703169.

(48) Yin, C.; Zheng, F.; Lee, S.; Guo, J.; Wang, W. C.; Kwon, G.; Vajda, V.;

Wang, H. H.; Lee, B.; DeBartolo, J.; et al. *J. Phys. Chem. A* **2014,** *118*, 8477-8484.

(49) Ferguson, G. A.; Yin, C.; Kwon, G.; Tyo, E. C.; Lee, S.; Greeley, J. P.; Zapol, P.; Lee, B.; Seifert, S.; Winans, R. E.; et al. *J. Phys. Chem. C* **2012,** *116*, 24027-24034.

(50) Haller, G. L.; Resasco, D. E. *Adv. Catal.* **1989,** *36*, 173-235.

(51) Fu, Q.; Wagner, T. *Surf. Sci. Rep.* **2007,** *62*, 431-498.

(52) Kitano, M.; Inoue, Y.; Yamazaki, Y.; Hayashi, F.; Kanbara, S.; Matsuishi, S.; Yokoyama, T.; Kim, S. W.; Hara, M.; Hosono, H. *Nat. Chem.* **2012,** *4*, 934-940.

(53) Kanbara, S.; Kitano, M.; Inoue, Y.; Yokoyama, T.; Hara, M.; Hosono, H. *J. Am. Chem. Soc.* **2015,** *137*, 14517-14524.

(54) Zhang, Z.; Yates, J. T., Jr. *Chem. Rev.* **2012,** *112*, 5520-5551.

(55) Subramanian, V.; Wolf, E. E.; Kamat, P. V. *J. Am. Chem. Soc.* **2004,** *126*, 4943-4950.

(56) Lee, J., Shim, H. S., Lee, M., Song, J. K.; Lee, D. *J. Phys. Chem. Lett.* **2011**, *2*, 2840-2845.

(57) Sitja, G.; Le Moal, S.; Marsault, M.; Hamm, G.; Leroy, F.; Henry, C. R. *Nano Lett.* **2013,** *13*, 1977-1982.

(58) Yudanov, I. V.; Genest, A.; Schauermann, S.; Freund, H. J.; Rosch, N. *Nano Lett.* **2012,** *12*, 2134-2139.

(59) Meier, D. C.; Goodman, D. W. *J. Am. Chem. Soc.* **2004,** *126*, 1892-1899.

(60) Lei, Y.; Zhao, H.; Rivas, R. D.; Lee, S.; Liu, B.; Lu, J.; Stach, E.; Winans, R. E.; Chapman, K. W.; Greeley, J. P.; et al. *J. Am. Chem. Soc.* **2014,** *136*, 9320-9326.

(61) Newton, M. A.; Belver-Coldeira, C.; Martinez-Arias, A.; Fernandez-Garcia, M. *Nat. Mater.* **2007,** *6*, 528-532.

(62) Nagai, Y.; Dohmae, K.; Ikeda, Y.; Takagi, N.; Tanabe, T.; Hara, N.; Guilera, G.; Pascarelli, S.; Newton, M. A.; Kuno, O.; et al. *Angew. Chem. Int. Ed.* **2008,** *47*, 9303-9306.

(63) Moliner, M.; Gabay, J. E.; Kliewer, C. E.; Carr, R. T.; Guzman, J.; Casty, G. L.; Serna, P.; Corma, A. *J. Am. Chem. Soc.* **2016,** *138*, 15743-15750.

(64) Sá, J.; Taylor, S. F. R.; Daly, H.; Goguet, A.; Tiruvalam, R.; He, Q.; Kiely, C. J.; Hutchings, G. J.; Hardacre, C. *ACS Catal.* **2012,** *2*, 552-560.

(65) Kim, D.; Becknell, N.; Yu, Y.; Yang, P. *Nano Lett.* **2017,** *17*, 2732-2737.

(66) Duan, X.; Tian, X.; Ke, J.; Yin, Y.; Zheng, J.; Chen, J.; Cao, Z.; Xie, Z.; Yuan, Y. *Chem. Sci.* **2016,** *7*, 3181-3187.

(67) Morgan, K.; Goguet, A.; Hardacre, C. *ACS Catal.* **2015,** *5*, 3430-3445.

(68) Haruta, M. *Catal. Today* **1997**, *36*, 153-166.

(69) Qiao, B.; Liang, J.-X.; Wang, A.; Xu, C.-Q.; Li, J.; Zhang, T.; Liu, J. J. *Nano Res.* **2015**, *8*, 2913-2924.

(70) Qiao, B.; Liang, J.-X.; Wang, A.; Liu, J.; Zhang, T., *Chinese J. Catal.* **2016**, *37*, 1580-1586.

(71) Qiao, B.; Liu, J.; Wang, Y.-G.; Lin, Q.; Liu, X.; Wang, A.; Li, J.; Zhang, T.; Liu, J., *ACS Catal.* **2015**, *5*, 6249-6254.

(72) Qiao, B.; Wang, A.; Yang, X.; Allard, L. F.; Jiang, Z.; Cui, Y.; Liu, J.; Li, J.; Zhang, T., *Nat. Chem.* **2011**, *3*, 634-641.

(73) Moses-DeBusk, M.; Yoon, M.; Allard, L. F.; Mullins, D. R.; Wu, Z.; Yang, X.; Veith, G.; Stocks, G. M.; Narula, C. K., *J. Am. Chem. Soc.* **2013**, *135*, 12634-12645.

(74) DeRita, L.; Dai, S.; Lopez-Zepeda, K.; Pham, N.; Graham, G. W.; Pan, X.; Christopher, P. *J. Am. Chem. Soc.* **2017,** *139*, 14150-14165.

(75) [Kistler, J. D.; Chotigkrai, N.; Xu, P.; Enderle, B.; Praserthdam, P.; Chen, C. Y.; Browning, N. D.; Gates, B. C. *Angew. Chem. Int. Ed.* **2014**, *53*, 8904-8907.

(76) [Costello, C. K.; Yang, J. H.; Law, H. Y.; Wang, Y.; Lin, J. N.; Marks, L. D.; Kung, M. C.; Kung, H. H., *Appl. Catal. A: Gen.* **2003**, *243*, 15-24.

(77) Saavedra, J.; Whittaker, T.; Chen, Z.; Pursell, C. J.; Rioux, R. M.; Chandler, B. D., *Nat. Chem.* **2016**, *8*, 584-589.

(78) Wang, C.; Gu, X.-K.; Yan, H.; Lin, Y.; Li, J.; Liu, D.; Li, W.-X.; Lu, J., *ACS Catal.* **2017**, *7*, 887-891.

(79) Jones, J.; Xiong, H.; DeLaRiva, A. T.; Peterson, E. J.; Pham, H.; Challa, S. R.; Qi, G.; Oh, S.; Wiebenga, M. H.; Pereira Hernandez, X. I.; Wang, Y.; Datye, A. K., *Science* **2016**, *353*, 150-154.

(80) Zhang, Z.; Zhu, Y.; Asakura, H.; Zhang, B.; Zhang, J.; Zhou, M.; Han, Y.; Tanaka, T.; Wang, A.; Zhang, T.; et al. *Nat. Commun.* **2017,** *8*, 16100.

(81) Fu, Q.; Saltsburg, H.; Flytzani-Stephanopoulos, M., *Science* **2003**, *301*, 935-938.

(82) Zhai, Y.; Pierre, D.; Si, R.; Deng, W.; Ferrin, P.; Nilekar, A. U.; Peng, G.; Herron, J. A.; Bell, D. C.; Saltsburg, H.; Mavrikakis, M.; Flytzani-Stephanopoulos, M., *Science* **2010**, *329*, 1633-1636.

(83) Yang, M.; Li, S.; Wang, Y.; Herron, J. A.; Xu, Y.; Allard, L. F.; Lee, S.; Huang, J.; Mavrikakis, M.; Flytzani-Stephanopoulos, M., *Science* **2014**, *346*, 1498-1501.

(84) Yang, M.; Liu, J.; Lee, S.; Zugic, B.; Huang, J.; Allard, L. F.; Flytzani-Stephanopoulos, M., *J. Am. Chem. Soc.* **2015**, *137*, 3470-3473.

(85) Flytzani-Stephanopoulos, M. *Acc. Chem. Res.* **2014,** *47*, 783-792.

(86) Lin, J.; Wang, A.; Qiao, B.; Liu, X.; Yang, X.; Wang, X.; Liang, J.; Li, J.; Liu, J.; Zhang, T., *J. Am. Chem. Soc.* **2013**, *135*, 15314-15317.

(87) Guan, H.; Lin, J.; Qiao, B.; Miao, S.; Wang, A.-Q.; Wang, X.; Zhang, T. *AIChE J.* **2017**, *63*, 2081-2088.

(88) Zhang, S.; Shan, J. J.; Zhu, Y.; Frenkel, A. I.; Patolla, A.; Huang, W.; Yoon, S. J.; Wang, L.; Yoshida, H.; Takeda, S.; Tao, F. F., *J. Am. Chem. Soc.* **2013**, *135*, 8283-8293.

(89) Gai, P. L.; Yoshida, K.; Ward, M. R.; Walsh, M.; Baker, R. T.; van de Water, L.; Watson, M. J.; Boyes, E. D., *Catal. Sci. Technol.* **2016**, *6*, 2214-2227.

(90) Carter, J. H.; Liu, X.; He, Q.; Althahban, S.; Nowicka, E.; Freakley, S. J.; Niu, L.; Morgan, D. J.; Li, Y.; Niemantsverdriet, J. W. H.; et al. *Angew. Chem. Int. Ed.* **2017**, *56*, 16037-16041.

(91) Davis, S. E.; Ide, M. S.; Davis, R. J. *Green Chem.* **2013,** *15*, 17-45.

(92) Abad, A.; Concepcion, P.; Corma, A.; Garcia, H. *Angew. Chem. Int. Ed.* **2005,** *44*, 4066-4069.

(93) Hackett, S. F.; Brydson, R. M.; Gass, M. H.; Harvey, I.; Newman, A. D.; Wilson, K.; Lee, A. F., *Angew. Chem. Int. Ed.* **2007**, *46*, 8593-8596.

(94) Abad, A.; Almela, C.; Corma, A.; Garcia, H. *Chem. Commun.* **2006**, 3178-3180.

(95) Jagadeesh, R. V.; Junge, H.; Pohl, M. M.; Radnik, J.; Bruckner, A.; Beller, M., *J. Am. Chem. Soc.* **2013**, *135*, 10776-10782.

(96) Jagadeesh, R. V.; Junge, H.; Beller, M., *Nat. Commun.* **2014**, *5*, 4123.

(97) Zhang, L.; Wang, A.; Wang, W.; Huang, Y.; Liu, X.; Miao, S.; Liu, J.; Zhang, T., *ACS Catal.* **2015**, *5*, 6563-6572.

(98) Xie, J.; Yin, K.; Serov, A.; Artyushkova, K.; Pham, H. N.; Sang, X.; Unocic,

R. R.; Atanassov, P.; Datye, A. K.; Davis, R. J., *ChemSusChem* **2017**, *10*, 359-362.

(99) Wei, H.; Liu, X.; Wang, A.; Zhang, L.; Qiao, B.; Yang, X.; Huang, Y.; Miao, S.; Liu, J.; Zhang, T. *Nat. Commun.* **2014,** *5*, 5634.

(100)   Zhang, B.; Asakura, H.; Zhang, J.; Zhang, J.; De, S.; Yan, N. *Angew. Chem. Int. Ed.* **2016,** *55*, 8319-8323.

(101)   Yan, H.; Cheng, H.; Yi, H.; Lin, Y.; Yao, T.; Wang, C.; Li, J.; Wei, S.; Lu, J. *J. Am. Chem. Soc.* **2015,** *137*, 10484-10487.

(102)   Vile, G.; Albani, D.; Nachtegaal, M.; Chen, Z.; Dontsova, D.; Antonietti, M.; Lopez, N.; Perez-Ramirez, J. *Angew. Chem. Int. Ed.* **2015,** *54*, 11265-11269.

(103)   Rossell, M. D.; Caparrós, F. J.; Angurell, I.; Muller, G.; Llorca, J.; Seco, M.; Rossell, O. *Catal. Sci. Technol.* **2016,** *6*, 4081-4085.

(104)   Westerhaus, F. A.; Jagadeesh, R. V.; Wienhofer, G.; Pohl, M. M.; Radnik, J.; Surkus, A. E.; Rabeah, J.; Junge, K.; Junge, H.; Nielsen, M.; et al. *Nat. Chem.* **2013,** *5*, 537-543.

(105)   Liu, L.; Concepción, P.; Corma, A. *J. Catal.* **2016**, *340*, 1-9.

(106)   Liu, L.; Gao, F.; Concepción, P.; Corma, A. *J. Catal.* **2017**, *350*, 218-225.

(107)   Liu, W.; Zhang, L.; Yan, W.; Liu, X.; Yang, X.; Miao, S.; Wang, W.; Wang, A.; Zhang, T. *Chem. Sci.* **2016**, *7*, 5758-5764.

(108)   Combita, D.; Concepción, P.; Corma, A. *J. Catal.* **2014,** *311*, 339-349.

(109)   Liu, X.; Li, H. Q.; Ye, S.; Liu, Y. M.; He, H. Y.; Cao, Y. *Angew. Chem. Int. Ed.* **2014,** *53*, 7624-7628.

(110)   Sun, X.; Olivos-Suarez, A. I.; Osadchii, D.; Romero, M. J. V.; Kapteijn, F.; Gascon, J. *J. Catal.* **2018,** *357*, 20-28.

(111)   Ji, P.; Manna, K.; Lin, Z.; Urban, A.; Greene, F. X.; Lan, G.; Lin, W. *J. Am. Chem. Soc.* **2016,** *138*, 12234-12242.

(112)   Li, Z.; Schweitzer, N. M.; League, A. B.; Bernales, V.; Peters, A. W.; Getsoian, A. B.; Wang, T. C.; Miller, J. T.; Vjunov, A.; Fulton, J. L.; et al. *J. Am. Chem. Soc.* **2016,** *138*, 1977-1982.

(113)   Cohen, S. M.; Zhang, Z.; Boissonnault, J. A. *Inorg. Chem.* **2016,** *55*, 7281-7290.

(114)   Spivey, J. J.; Hutchings, G. *Chem. Soc. Rev.* **2014**, *43*, 792-803.

(115)   Guo, X.; Fang, G.; Li, G.; Ma, H.; Fan, H.; Yu, L.; Ma, C.; Wu, X.; Deng, D.; Wei, M.; et al. *Science* **2014,** *344*, 616-619.

(116)   Sakbodin, M.; Wu, Y.; Oh, S. C.; Wachsman, E. D.; Liu, D. *Angew. Chem. Int. Ed.* **2016,** *55*, 16149-16152.

(117)   Nielsen, M.; Alberico, E.; Baumann, W.; Drexler, H. J.; Junge, H.; Gladiali, S.; Beller, M. *Nature* **2013,** *495*, 85-89.

(118)   Shabaker, J. *J. Catal.* **2003,** *215*, 344-352.

(119)   Lin, L.; Zhou, W.; Gao, R.; Yao, S.; Zhang, X.; Xu, W.; Zheng, S.; Jiang, Z.; Yu, Q.; Li, Y. W.; et al. *Nature* **2017,** *544*, 80-83.

(120)   Franke, R.; Selent, D.; Borner, A. *Chem. Rev.* **2012,** *112*, 5675-5732.

(121)   Horvath, I. T.; Rabai, J. *Science* **1994,** *266*, 72-75.

(122)   Nowotny, M.; Maschmeyer, T.; Johnson, B. F.; Lahuerta, P.; Thomas, J. M.; Davies, J. E. *Angew. Chem. Int. Ed.* **2001,** *40*, 955-958.

(123)   Sun, Q.; Dai, Z.; Liu, X.; Sheng, N.; Deng, F.; Meng, X.; Xiao, F. S. *J. Am. Chem. Soc.* **2015,** *137*, 5204-5209.

(124)   Li, C.; Yan, L.; Lu, L.; Xiong, K.; Wang, W.; Jiang, M.; Liu, J.; Song, X.; Zhan, Z.; Jiang, Z.; Ding, Y. *Green Chem.* **2016,** *18*, 2995-3005.

(125)   Lang, R.; Li, T.; Matsumura, D.; Miao, S.; Ren, Y.; Cui, Y. T.; Tan, Y.; Qiao, B.; Li, L.; Wang, A.; et al. *Angew. Chem. Int. Ed.* **2016,** *55*, 16054-16058.

(126)   Wang, L.; Zhang, W.; Wang, S.; Gao, Z.; Luo, Z.; Wang, X.; Zeng, R.; Li, A.; Li, H.; Wang, M.; et al. *Nat. Commun.* **2016,** *7*, 14036.

(127)   Li, Y. H.; Xing, J.; Yang, X. H.; Yang, H. G. *Chem. Eur. J.* **2014,** *20*, 12377-12380.

(128)   Xing, J.; Chen, J. F.; Li, Y. H.; Yuan, W. T.; Zhou, Y.; Zheng, L. R.; Wang, H. F.; Hu, P.; Wang, Y.; Zhao, H. J.; et al. *Chem. Eur. J.* **2014,** *20*, 2138-2144.

(129)   Li, X.; Bi, W.; Zhang, L.; Tao, S.; Chu, W.; Zhang, Q.; Luo, Y.; Wu, C.; Xie, Y. *Adv. Mater.* **2016,** *28*, 2427-2431.

(130)   Zhang, H.; Wei, J.; Dong, J.; Liu, G.; Shi, L.; An, P.; Zhao, G.; Kong, J.; Wang, X.; Meng, X.; et al. *Angew. Chem. Int. Ed.* **2016,** *55*, 14310-14314.

(131)   Kyriakou, G.; Boucher, M. B.; Jewell, A. D.; Lewis, E. A.; Lawton, T. J.; Baber, A. E.; Tierney, H. L.; Flytzani-Stephanopoulos, M.; Sykes, E. C. *Science* **2012,** *335*, 1209-1212.

(132)   Lucci, F. R.; Marcinkowski, M. D.; Lawton, T. J.; Sykes, E. C. H. *J. Phys. Chem. C* **2015**, *119*, 24351-24357.

(133)   Serna, P.; Concepción, P.; Corma, A. *J. Catal.* **2009,** *265*, 19-25.

(134)   Boucher, M. B.; Zugic, B.; Cladaras, G.; Kammert, J.; Marcinkowski, M. D.; Lawton, T. J.; Sykes, E. C.; Flytzani-Stephanopoulos, M. *Phys. Chem. Chem. Phys.* **2013,** *15*, 12187-12196.

(135)   Lucci, F. R.; Liu, J.; Marcinkowski, M. D.; Yang, M.; Allard, L. F.; Flytzani-Stephanopoulos, M.; Sykes, E. C. *Nat. Commun.* **2015**, *6*, 8550.

(136)   Pei, G. X.; Liu, X. Y.; Wang, A.; Lee, A. F.; Isaacs, M. A.; Li, L.; Pan, X.; Yang, X.; Wang, X.; Tai, Z.; et al. *ACS Catal.* **2015**, *5*, 3717-3725.

(137)   Lu, J.; Aydin, C.; Browning, N. D.; Gates, B. C. *J. Am. Chem. Soc.* **2012**, *134*, 5022-5025.

(138)   Serna, P.; Gates, B. C. *J. Am. Chem. Soc.* **2011**, *133*, 4714-4717.

(139)   Bayram, E.; Lu, J.; Aydin, C.; Uzun, A.; Browning, N. D.; Gates, B. C.; Finke, R. G. *ACS Catal.* **2012,** *2*, 1947-1957.

(140)   Bayram, E.; Lu, J.; Aydin, C.; Browning, N. D.; Özkar, S.; Finney, E.; Gates, B. C.; Finke, R. G. *ACS Catal.* **2015**, *5*, 3514-3527.

(141)   Han, Y.; Wang, Y.-G.; Chen, W.; Xu, R.; Zheng, L. R.; Zhang, J.; Luo, J.; Shen, R.-A.; Zhu, Y.; Cheong, W.-C.; et al. *J. Am. Chem. Soc.* **2017**, *139*, 17269-17272.

(142)   Yin, P.; Yao, T.; Wu, Y.; Zheng, L.; Lin, Y.; Liu, W.; Ju, H.; Zhu, J.; Hong, X.; Deng, Z.; et al. *Angew. Chem. Int. Ed.* **2016,** *55*, 10800-10805.

(143)   Cheng, Q.; Yang, L.; Zou, L.; Zou, Z.; Chen, C.; Hu, Z.; Yang, H. *ACS Catal.* **2017,** *7*, 6864-6871.

(144)   Zheng, Y.; Jiao, Y.; Zhu, Y.; Cai, Q.; Vasileff, A.; Li, L. H.; Han, Y.; Chen, Y.; Qiao, S. Z. *J. Am. Chem. Soc.* **2017,** *139*, 3336-3339.

(145)   Chen, Y.; Ji, S.; Wang, Y.; Dong, J.; Chen, W.; Li, Z.; Shen, R.; Zheng, L.; Zhuang, Z.; Wang, D.; et al. *Angew. Chem. Int. Ed.* **2017,** *56*, 6937-6941.

(146)   Chung, H. T.; Cullen, D. A.; Higgins, D.; Sneed, B. T.; Holby, E. F.; More, K. L.; Zelenay, P. *Science* **2017**, *357*, 479-484.

(147)   Zhu, C.; Fu, S.; Song, J.; Shi, Q.; Su, D.; Engelhard, M. H.; Li, X.; Xiao, D.; Li, D.; Estevez, L.; et al. *Small* **2017**, *13* (15) 1603407.

(148)   Zhang, Z.; Gao, X.; Dou, M.; Ji, J.; Wang, F. *Small* **2017,** *13* (22) 1604290.

(149)   Sanchez, A.; Abbet, S.; Heiz, U.; Schneider, W. D.; Häkkinen, H.; Barnett, R. N.; Landman, U. *J. Phys. Chem. A* **1999,** *103*, 9573-9578.

(150)   Lee, S.; Fan, C.; Wu, T.; Anderson, S. L. *J. Am. Chem. Soc.* **2004,** *126*, 5682-5683.

(151)   Arenz, M.; Landman, U.; Heiz, U. *ChemPhysChem* **2006,** *7*, 1871-1879.

(152)   Landman, U.; Yoon, B.; Zhang, C.; Heiz, U.; Arenz, M. *Top. Catal.* **2007,** *44*, 145-158.

(153)   Yoon, B.; Hakkinen, H.; Landman, U.; Worz, A. S.; Antonietti, J. M.; Abbet, S.; Judai, K.; Heiz, U. *Science* **2005,** *307*, 403-407.

(154)   Harding, C.; Habibpour, V.; Kunz, S.; Farnbacher, A. N.; Heiz, U.; Yoon, B.; Landman, U. *J. Am. Chem. Soc.* **2009,** *131*, 538-548.

(155)   Ohyama, J.; Esaki, A.; Koketsu, T.; Yamamoto, Y.; Arai, S.; Satsuma, A. *J. Catal.* **2016,** *335*, 24-35.

(156)   Herzing, A. A.; Kiely, C. J.; Carley, A. F.; Landon, P.; Hutchings, G. J., *Science* **2008**, *321*, 1331-1335.

(157)   He, Q.; Freakley, S. J.; Edwards, J. K.; Carley, A. F.; Borisevich, A. Y.; Mineo, Y.; Haruta, M.; Hutchings, G. J.; Kiely, C. J. *Nat. Commun.* **2016**, *7*, 12905.

(158)   Kaden, W. E.; Wu, T.; Kunkel, W. A.; Anderson, S. L. *Science* **2009,** *326*, 826-829.

(159)   Kane, M. D.; Roberts, F. S.; Anderson, S. L. *J. Phys. Chem. C* **2015,** *119*, 1359-1375.

(160)   Kunz, S.; Schweinberger, F. F.; Habibpour, V.; Röttgen, M.; Harding, C.; Arenz, M.; Heiz, U. *J. Phys. Chem. C* **2010,** *114*, 1651-1654.

(161)   Yoon, B.; Landman, U.; Habibpour, V.; Harding, C.; Kunz, S.; Heiz, U.; Moseler, M.; Walter, M. *J. Phys. Chem. C* **2012,** *116*, 9594-9607.

(162)   Moseler, M.; Walter, M.; Yoon, B.; Landman, U.; Habibpour, V.; Harding, C.; Kunz, S.; Heiz, U. *J. Am. Chem. Soc.* **2012,** *134*, 7690-7699.

(163)   Jeong, H.; Bae, J.; Han, J. W.; Lee, H. *ACS Catal.* **2017,** *7*, 7097-7105.

(164)   Qiao, B.; Wang, A.; Li, L.; Lin, Q.; Wei, H.; Liu, J.; Zhang, T., *ACS Catal.* **2014**, *4*, 2113-2117.

(165)   Sirajuddin, S.; Rosenzweig, A. C., *Biochemistry* **2015**, *54*, 2283-2294.

(166)   Himes, R. A.; Barnese, K.; Karlin, K. D., *Angew. Chem. Int. Ed.* **2010**,

49, 6714-6716.

(167)   Tomkins, P.; Ranocchiari, M.; van Bokhoven, J. A. *Acc. Chem. Res.* **2017**, 50, 418-425.

(168)   Woertink, J. S.; Smeets, P. J.; Groothaert, M. H.; Vance, M. A.; Sels, B. F.; Schoonheydt, R. A.; Solomon, E. I., *Proc. Natl. Acad. Sci. USA* 2009, 106, 18908-18913.

(169)   Grundner, S.; Markovits, M. A.; Li, G.; Tromp, M.; Pidko, E. A.; Hensen, E. J.; Jentys, A.; Sanchez-Sanchez, M.; Lercher, J. A., *Nat. Commun.* 2015, 6, 7546.

(170)   Haack, P.; Limberg, C. *Angew. Chem. Int. Ed.* **2014**, *53*, 4282-4293.

(171)   Tomkins, P.; Mansouri, A.; Bozbag, S. E.; Krumeich, F.; Park, M. B.; Alayon, E. M.; Ranocchiari, M.; van Bokhoven, J. A., *Angew. Chem. Int. Ed.* **2016**, *55*, 5467-5471.

(172)   Narsimhan, K.; Iyoki, K.; Dinh, K.; Roman-Leshkov, Y., *ACS Central Sci.* **2016**, *2*, 424-429.

(173)   Alayon, E. M. C.; Nachtegaal, M.; Bodi, A.; van Bokhoven, J. A., *ACS Catal.* **2014**, *4*, 16-22.

(174)   Sushkevich, V. L.; Palagin, D.; Ranocchiari, M.; van Bokhoven, J. A. *Science* **2017**, *356*, 523-527.

(175)   Bal, R.; Tada, M.; Sasaki, T.; Iwasawa, Y., *Angew. Chem. Int. Ed.* **2006**, *45*, 448-452.

(176)   Tada, M.; Bal, R.; Sasaki, T.; Uemura, Y.; Inada, Y.; Tanaka, S.; Nomura, M.; Iwasawa, Y., *J. Phys. Chem. C* **2007**, *111*, 10095-10104.

(177)   Lei, Y.; Mehmood, F.; Lee, S.; Greeley, J.; Lee, B.; Seifert, S.; Winans, R. E.; Elam, J. W.; Meyer, R. J.; Redfern, P. C.; et al. *Science* **2010**, *328*, 224-228.

(178)   Argo, A. M.; Odzak, J. F.; Lai, F. S.; Gates, B. C. *Nature* **2002,** *415*, 623-626.

(179)   Lu, J.; Serna, P.; Aydin, C.; Browning, N. D.; Gates, B. C. *J. Am. Chem. Soc.* **2011,** *133*, 16186-16195.

(180)   Okrut, A.; Runnebaum, R. C.; Ouyang, X.; Lu, J.; Aydin, C.; Hwang, S. J.; Zhang, S.; Olatunji-Ojo, O. A.; Durkin, K. A.; Dixon, D. A.; et al. *Nat. Nanotechnol.* **2014,** *9*, 459-465.

(181)   Corma, A. *Nat. Nanotechnol.* **2014,** *9*, 412-413.

(182)   Thomas, J. M.; Johnson, B. F.; Raja, R.; Sankar, G.; Midgley, P. A. *Acc. Chem. Res.* **2003,** *36*, 20-30.

(183)   Hungria, A. B.; Raja, R.; Adams, R. D.; Captain, B.; Thomas, J. M.; Midgley, P. A.; Golovko, V.; Johnson, B. F. *Angew. Chem. Int. Ed.* **2006,** *45*, 4782-4785.

(184)   Raja, R.; Khimyak, T.; Thomas, J. M.; Hermans, S.; Johnson, B. F. G. *Angew. Chem. Int. Ed.* **2001,** *40*, 4638-4642.

(185)   Sattler, J. J.; Ruiz-Martinez, J.; Santillan-Jimenez, E.; Weckhuysen, B. M. *Chem. Rev.* **2014**, *114*, 10613-10653.

(186)   Vajda, S.; Pellin, M. J.; Greeley, J. P.; Marshall, C. L.; Curtiss, L. A.; Ballentine, G. A.; Elam, J. W.; Catillon-Mucherie, S.; Redfern, P. C.; Mehmood, F.; et al. *Nat. Mater.* **2009,** *8*, 213-216.

(187)   Baxter, E. T.; Ha, M.-A.; Cass, A. C.; Alexandrova, A. N.; Anderson, S. L. *ACS Catal.* **2017**, *7*, 3322-3335.

(188)   Lee, S.; Di Vece, M.; Lee, B.; Seifert, S.; Winans, R. E.; Vajda, S. *Phys. Chem. Chem. Phys.* **2012,** *14*, 9336-9342.

(189)   Lee, S.; Di Vece, M.; Lee, B.; Seifert, S.; Winans, R. E.; Vajda, S. *ChemCatChem* **2012,** *4*, 1632-1637.

(190)   Judai, K.; Abbet, S.; Worz, A. S.; Heiz, U.; Henry, C. R. *J. Am. Chem. Soc.* **2004,** *126*, 2732-2737.

(191)   Worz, A. S.; Judai, K.; Abbet, S.; Heiz, U. *J. Am. Chem. Soc.* **2003,** *125*, 7964-7970.

(192)   Ahmed, F.; Nagumo, R.; Miura, R.; Suzuki, A.; Tsuboi, H.; Hatakeyama, N.; Takaba, H.; Miyamoto, A. *J. Phys. Chem. C* **2011,** *115*, 24123-24132.

(193)   Liu, X.; Tian, D.; Ren, S.; Meng, C. *J. Phys. Chem. C* **2015,** *119*, 12941-12948.

(194)   Shimizu, K.-i.; Satsuma, A.; Hattori, T. *Appl. Catal. B: Environ.* **2000,** *25*, 239-247.

(195)   Shibata, J. *J. Catal.* **2004,** *222*, 368-376.

(196)   Satsuma, A.; Shibata, J.; Shimizu, K.-i.; Hattori, T. *Catal. Surveys Asia* **2005,** *9*, 75-85.

(197)   Murdoch, M.; Waterhouse, G. I.; Nadeem, M. A.; Metson, J. B.; Keane, M. A.; Howe, R. F.; Llorca, J.; Idriss, H. *Nat. Chem.* **2011,** *3*, 489-

492.

(198)   Wang, W. N.; An, W. J.; Ramalingam, B.; Mukherjee, S.; Niedzwiedzki, D. M.; Gangopadhyay, S.; Biswas, P. *J. Am. Chem. Soc.* **2012,** *134*, 11276-11281.

(199)   Berr, M. J.; Schweinberger, F. F.; Doblinger, M.; Sanwald, K. E.; Wolff, C.; Breimeier, J.; Crampton, A. S.; Ridge, C. J.; Tschurl, M.; Heiz, U.; et al. *Nano Lett.* **2012,** *12*, 5903-5906.

(200)   Schweinberger, F. F.; Berr, M. J.; Doblinger, M.; Wolff, C.; Sanwald, K. E.; Crampton, A. S.; Ridge, C. J.; Jackel, F.; Feldmann, J.; Tschurl, M.; et al. *J. Am. Chem. Soc.* **2013,** *135*, 13262-13265.

(201)   Yin, L.; Liebscher, J. *Chem. Rev.* **2007,** *107*, 133-173.

(202)   Molnar, A. *Chem. Rev.* **2011,** *111*, 2251-2320.

(203)   Fihri, A.; Bouhrara, M.; Nekoueishahraki, B.; Basset, J. M.; Polshettiwar, V. *Chem. Soc. Rev.* **2011,** *40*, 5181-5203.

(204)   Fang, P. P.; Jutand, A.; Tian, Z. Q.; Amatore, C. *Angew. Chem. Int. Ed.* **2011,** *50*, 12184-12188.

(205)   Niu, Z.; Peng, Q.; Zhuang, Z.; He, W.; Li, Y. *Chem. Eur. J.* **2012,** *18*, 9813-9817.

(206)   Phan, N. T. S.; Van Der Sluys, M.; Jones, C. W. *Adv. Synth. Catal.* **2006,** *348*, 609-679.

(207)   Briggs, B. D.; Bedford, N. M.; Seifert, S.; Koerner, H.; Ramezani-Dakhel, H.; Heinz, H.; Naik, R. R.; Frenkel, A. I.; Knecht, M. R. *Chem. Sci.* **2015,** *6*, 6413-6419.

(208)   Thathagar, M. B.; ten Elshof, J. E.; Rothenberg, G. *Angew. Chem. Int. Ed.* **2006,** *45*, 2886-2890.

(209)   de Vries, A. H.; Mulders, J. M.; Mommers, J. H.; Henderickx, H. J.; de Vries, J. G. *Org. Lett.* **2003,** *5*, 3285-3288.

(210)   de Vries, J. G. *Dalton Trans.* **2006**, 421-429.

(211)   Leyva-Perez, A.; Oliver-Meseguer, J.; Rubio-Marques, P.; Corma, A. *Angew. Chem. Int. Ed.* **2013,** *52*, 11554-11559.

(212)   Bruno, N. C.; Tudge, M. T.; Buchwald, S. L. *Chem. Sci.* **2013,** *4*, 916-920.

(213)   Fu, F.; Xiang, J.; Cheng, H.; Cheng, L.; Chong, H.; Wang, S.; Li, P.; Wei, S.; Zhu, M.; Li, Y. *ACS Catal.* **2017,** *7*, 1860-1867.

(214)   Kashin, A. S.; Ananikov, V. P. *J. Org. Chem.* **2013,** *78*, 11117-11125.

(215)   Ananikov, V. P.; Beletskaya, I. P. *Organometallics* **2012,** *31*, 1595-1604.

(216)   Jiang, X. F.; Huang, H.; Chai, Y. F.; Lohr, T. L.; Yu, S. Y.; Lai, W.; Pan, Y. J.; Delferro, M.; Marks, T. J. *Nat. Chem.* **2017,** *9*, 188-193.

(217)   Oliver-Meseguer, J.; Cabrero-Antonino, J. R.; Dominguez, I.; Leyva-Perez, A; Corma, A. *Science* 2012, **338**, 1452-1455.

(218)   Oliver-Meseguer, J.; Dominguez, I.; Gavara, R.; Domenech-Carbo, A.; Gonzalez-Calbet, J. M.; Leyva-Perez, A.; Corma, A. *Chem. Commun.* **2017,** *53*, 1116-1119.

(219)   Oliver-Meseguer, J.; Leyva-Pérez, A.; Corma, A. *ChemCatChem* **2013,** *5*, 3509-3515.

(220)   Oliver-Meseguer, J.; Leyva-Perez, A.; Al-Resayes, S. I.; Corma, A. *Chem. Commun.* **2013,** *49*, 7782-7784.

(221)   Hughes, M. D.; Xu, Y. J.; Jenkins, P.; McMorn, P.; Landon, P.; Enache, D. I.; Carley, A. F.; Attard, G. A.; Hutchings, G. J.; King, F.; et al. *Nature* **2005,** *437*, 1132-1135.

(222)   Turner, M.; Golovko, V. B.; Vaughan, O. P.; Abdulkin, P.; Berenguer-Murcia, A.; Tikhov, M. S.; Johnson, B. F.; Lambert, R. M. *Nature* **2008,** *454*, 981-983.

(223)   Qian, L.; Wang, Z.; Beletskiy, E. V.; Liu, J.; Dos Santos, H. J.; Li, T.; Rangel, M. D.; Kung, M. C.; Kung, H. H. *Nat. Commun.* **2017,** *8*, 14881.

(224)   He, C.; Zhang, G.; Ke, J.; Zhang, H.; Miller, J. T.; Kropf, A. J.; Lei, A. *J. Am. Chem. Soc.* **2013,** *135*, 488-493.

(225)   Schoch, R.; Desens, W.; Werner, T.; Bauer, M. *Chem. Eur. J.* **2013,** *19*, 15816-15821.

(226)   Das, R. K.; Saha, B.; Rahaman, S. M.; Bera, J. K. *Chem. Eur. J.* **2010,** *16*, 14459-14468.

(227)   Sarkar, M.; Doucet, H.; Bera, J. K. *Chem. Commun.* **2013,** *49*, 9764-9766.

(228)   Oliver-Meseguer, J.; Liu, L.; Garcia-Garcia, S.; Canos-Gimenez, C.; Dominguez, I.; Gavara, R.; Domenech-Carbo, A.; Concepcion, P.; Leyva-Perez, A.; Corma, A. *J. Am. Chem. Soc.* **2015,** *137*, 3894-3900.

(229)   Rivero-Crespo, M. A.; Leyva-Perez, A.; Corma, A. *Chem. Eur. J.*

2017, *23*, 1702-1708.

(230)   Corma, A.; Serna, P. *Science* **2006**, 313, 332-334.

(231)   Serna, P.; Corma, A. *ACS Catal.* **2015,** *5*, 7114-7121.

(232)   Corma, A.; Garcia, H. *Chem. Soc. Rev.* **2008,** *37*, 2096-2126.

(233)   Westerhaus, F. A.; Jagadeesh, R. V.; Wienhofer, G.; Pohl, M. M.; Radnik, J.; Surkus, A. E.; Rabeah, J.; Junge, K.; Junge, H.; Nielsen, M.; Bruckner, A.; Beller, M. *Nat. Chem.* **2013**, *5*, 537.

(234)   Jagadeesh, R. V.; Surkus, A. E.; Junge, H.; Pohl, M. M.; Radnik, J.; Rabeah, J.; Huan, H.; Schunemann, V.; Bruckner, A.; Beller, M. *Science* **2013**, *342*, 1073.

(235)   Schwob, T.; Kempe, R. *Angew. Chem. Int. Ed.* **2016**, *55*, 15175.

(236)   Wang, X.; Li, Y. *J. Mol. Catal. A: Chem.* **2016**, *420*, 56.

(237)   Zhang, F.; Zhao, C.; Chen, S.; Li, H.; Yang, H.; Zhang, X.-M. *J. Catal.* **2017**, *348*, 212.

(238)   Wei, Z.; Wang, J.; Mao, S.; Su, D.; Jin, H.; Wang, Y.; Xu, F.; Li, H.; Wang, Y. *ACS Catal.* **2015**, *5*, 4783.

(239)   Formenti, D.; Ferretti, F.; Topf, C.; Surkus, A.-E.; Pohl, M.-M.; Radnik, J.; Schneider, M.; Junge, K.; Beller, M.; Ragaini, F. *J. Catal.* **2017**, *351*, 79.

(240)   Corma, A.; Concepcion, P.; Serna, P. *Angew. Chem. Int. Ed.* **2007**, *46*, 7266.

(241)   Boronat, M.; Concepcion, P.; Corma, A.; Gonzalez, S.; Illas, F.; Serna, P. *J. Am. Chem. Soc.* **2007**, *129*, 16230.

(242)   Vinod, C. P.; Wilson, K.; Lee, A. F. *J. Chem. Technol. Biotechnol.* **2011,** *86*, 161-171.

(243)   Zhang, Q.; Deng, W.; Wang, Y. *Chem. Commun.* **2011,** *47*, 9275-9292.

(244)   Mallat, T.; Baiker, A. *Chem. Rev.* **2004,** *104*, 3037-3058.

(245)   Abad, A.; Corma, A.; Garcia, H. *Chem. Eur. J.* **2008,** *14*, 212-222.

(246)   Roldan Cuenya, B. *Acc. Chem. Res.* **2013,** *46*, 1682-1691.

(247)   Mostafa, S.; Behafarid, F.; Croy, J. R.; Ono, L. K.; Li, L.; Yang, J. C.; Frenkel, A. I.; Cuenya, B. R. *J. Am. Chem. Soc.* **2010,** *132*, 15714-15719.

(248)   Mistry, H.; Behafarid, F.; Zhou, E.; Ono, L. K.; Zhang, L.; Roldan Cuenya, B. *ACS Catal.* **2014,** *4*, 109-115.

(249)   Jagadeesh, R. V.; Junge, H.; Pohl, M. M.; Radnik, J.; Bruckner, A.;

Beller, M. *J. Am. Chem. Soc.* **2013**, *135*, 10776.

(250)   Sun, Y.; Ma, H.; Jia, X.; Ma, J.; Luo, Y.; Gao, J.; Xu, J. *ChemCatChem* **2016**, *8*, 2907.

(251)   Zhang, L.; Wang, A.; Wang, W.; Huang, Y.; Liu, X.; Miao, S.; Liu, J.; Zhang, T. *ACS Catalysis* **2015**, *5*, 6563.

(252)   Xie, J.; Yin, K.; Serov, A.; Artyushkova, K.; Pham, H. N.; Sang, X.; Unocic, R. R.; Atanassov, P.; Datye, A. K.; Davis, R. J. *ChemSusChem* **2017**, *10*, 359.

(253)   Xie, J.; Kammert, J. D.; Kaylor, N.; Zheng, J. W.; Choi, E.; Pham, H. N.; Sang, X.; Stavitski, E.; Attenkofer, K.; Unocic, R. R.; Datye, A. K.; Davis, R. J. *ACS Catal.* **2018**, 3875.

(254)   Jagadeesh, R. V.; Junge, H.; Beller, M. *Nat. Commun.* **2014**, *5*, 4123.

(255)   Li, J.; Liu, G.; Shi, L.; Xing, Q.; Li, F. *Green Chem.* **2017**, *19*, 5782.

(256)   Xie, F.; Chen, Q.-H.; Xie, R.; Jiang, H.-F.; Zhang, M. *ACS Catal.* **2018**, 8, 5869-5874.

(257)   Banerjee, D.; Jagadeesh, R. V.; Junge, K.; Pohl, M. M.; Radnik, J.; Bruckner, A.; Beller, M. *Angew. Chem. Int. Ed.* **2014**, *53*, 4359.

(258)   Liu, W.; Zhang, L.; Liu, X.; Liu, X.; Yang, X.; Miao, S.; Wang, W.; Wang, A.; Zhang, T. *J. Am. Chem. Soc.* **2017**, *139*, 10790.

(259)   Vazquez-Vazquez, C.; Banobre-Lopez, M.; Mitra, A.; Lopez-Quintela, M. A.; Rivas, J. *Langmuir* **2009**, *25*, 8208-8216.

(260)   Murdoch, M.; Waterhouse, G. I.; Nadeem, M. A.; Metson, J. B.; Keane, M. A.; Howe, R. F.; Llorca, J.; Idriss, H. *Nat. Chem.* **2011**, *3*, 489-492.

(261)   Ben-Shahar, Y.; Scotognella, F.; Kriegel, I.; Moretti, L.; Cerullo, G.; Rabani, E.; Banin, U. *Nat. Commun.* **2016**, *7*, 10413.

(262)   Prier, C. K.; Rankic, D. A.; MacMillan, D. W. *Chem. Rev.* **2013**, *113*, 5322-5363.

(263)   Narayanam, J. M.; Stephenson, C. R. *Chem. Soc. Rev.* **2011**, *40*, 102-113.

(264)   Mubeen, S.; Lee, J.; Singh, N.; Kramer, S.; Stucky, G. D.; Moskovits, M. *Nat. Nanotechnol.* **2013**, *8*, 247-251.

(265)   Kumar, D.; Lee, A.; Lee, T.; Lim, M.; Lim, D. K. *Nano Lett.* **2016**, *16*, 1760-1767.

(266)   Christopher, P., Xin, H. & Linic, S. *Nat. Chem.* **2011**, *3*, 467-472.

(267)   Christopher, P.; Xin, H.; Marimuthu, A.; Linic, S. *Nat. Mater.* **2012**, *11*, 1044-1050.

(268)   Marimuthu, A.; Zhang, J.; Linic, S. *Science* **2013**, *339*, 1590-1593.

(269)   Kale, M. J.; Avanesian, T.; Xin, H.; Yan, J.; Christopher, P. *Nano Lett.* **2014,** *14*, 5405-5412.

(270)   Swearer, D. F.; Zhao, H.; Zhou, L.; Zhang, C.; Robatjazi, H.; Martirez, J. M.; Krauter, C. M.; Yazdi, S.; McClain, M. J.; Ringe, E.et al. *Proc. Natl. Acad. Sci. USA* **2016**, *113*, 8916-8920.

(271)   Vilar-Vidal, N.; Rey, J. R.; Lopez Quintela, M. A. *Small* **2014**, *10*, 3632-3636.

(272)   Zhou, S.; Duan, Y.; Wang, F.; Wang, C. *Nanoscale* **2017**, *9*, 4981-4988.

(273)   Wang, Z. J.; Ghasimi, S.; Landfester, K.; Zhang, K. A. I. *Chem. Mater.* **2015,** *27*, 1921-1924.

(274)   Jiao, Z.; Zhai, Z.; Guo, X.; Guo, X.-Y. *J. Phys. Chem. C* **2015,** *119*, 3238-3243.

(275)   Zhang, S.; Chang, C.; Huang, Z.; Ma, Y.; Gao, W.; Li, J.; Qu, Y. *ACS Catal.* **2015,** *5*, 6481-6488.

Chapter 2

Objectives

As mentioned in the Introduction part of this thesis, the particle size of metal catalysts has significant influences on the electronic and geometric structures of heterogeneous metal catalysts, which further influences their catalytic properties. In this thesis, the works presented in the following chapters will be related with the heterogeneous metal catalysts including single atoms, clusters and nanoparticles supported on various solid carriers. The whole thesis can be divided into three parts, covering from synthesis, characterization to catalytic studies of single atoms, clusters and nanoparticles.

In the first part of this thesis (**Chapter 3** and **Chapter 4**), it will be shown that how the metal species (single atoms, clusters and nanoparticles) evolve under reaction conditions and the identification of the active species by following their structural evolution during catalytic processes. In **Chapter 3**, it will be shown that, mononuclear Cu complex will undergo in situ structural transformation under the reaction conditions for oxidative coupling of terminal alkynes. By following the evolution of the homogeneous Cu species in solution, it has been found that small CuOx nanoparticles (~2 nm) are the active species for the oxidative coupling of alkynes. Furthermore, we have performed comparative studies between subnanometric Cu species, small CuOx nanoparticles and large CuOx nanoparticles for activation of O_2, alkyne molecules and propose the size-dependent reaction mechanism for Cu-catalyzed oxidative coupling of alkynes. In **Chapter 4**, a comparative study on supported Pt single atoms, clusters and nanoparticles will be presented. A series supported Pt catalysts on different supports (Al_2O_3, TiO_2 and CeO_2) are prepared containing different types of Pt species. These catalysts have been used for selective hydrogenation, CO oxidation, oxidation of alcohol and photocatalytic H_2 evolution reactions. By kinetic studies and electron microscopy characterizations, the reactivity of different types of Pt species have been compared. It will be shown that, Pt clusters and nanoparticles are more active than Pt single atoms and more importantly, the sintering of Pt single atoms to clusters or nanoparticles under reaction conditions should be paid special attention when studying their catalytic behavior. These works demonstrate that, it is challenging to stabilize subnanometric metal species (single atoms and clusters) under high-temperature oxidation-reduction conditions, especially on inorganic solid carriers. Therefore, it is vital to

develop new synthesis methodologies to stabilize those subnanometric metal species and use them for practical catalytic reactions.

In the second part (**Chapter 5 to Chapter 7**), a new strategy for encapsulation of subnanometric metal species (single atoms and clusters) into MWW zeolite will be presented in **Chapter 5**. Firstly, taking Pt as an example, it will be shown the incorporation of Pt single atoms and clusters into the supercages and cavities of pure-silica MCM-22 zeolite by the transformation of a two-dimensional to three-dimensional zeolite. These subnanometric Pt species show size-selective catalytic behavior for hydrogenation of light olefins (propene and isobutene), which further confirms their location in the MCM-22 zeolite. After high-temperature oxidation-reduction treatment at 650 ^{o}C, the size of Pt particles confined in MCM-22 crystallites only slightly increases to 1-2 nm, showing excellent stability against sintering under harsh conditions. Then, using the Pt@MCM-22 material as a model catalyst, the evolution of subnanometric Pt species under reaction conditions has been studied by in situ TEM, which will be shown in **Chapter 6**. The in situ TEM studies will show how the subnanometric Pt species are very sensitive to the gas atmosphere and show dynamic structural transformation under various reaction conditions. Our results demonstrate that, when studying the catalytic properties of subnanometric metal species (single atoms and clusters), *in situ* or *operando* characterization is necessary when one tries to identify the active species for specific reaction. The developed methodology can also be applied for the encapsulation of other subnanometric metal catalysts in MCM-22 zeolite. In **Chapter 7**, it will be shown the preparation of Au@MCM-22 materials containing Au nanoclusters and their application for selective oxidation of cyclohexane to KA-oil. Those Au nanoclusters are much more active than nanoparticulate Au species for this radical-type oxidation reaction.

In the third part of the thesis (**Chapter 8** to **Chapter 11**), the works related with synthesis and catalytic applications of non-noble metal nanoparticles will be presented. Starting with Co@C nanoparticles (**Chapter 8**), the preparation of Co nanoparticles stabilized by thin carbon layers and the structural and spectroscopic characterizations of Co@C nanoparticles. Catalytic studies on this Co@C catalyst have revealed the active sites for chemoselective hydrogenation of nitroarenes and the role of carbon layers is found to be the

protection of metallic Co from deep oxidation by air. Following the work on Co@C, a new method for the preparation of bimetallic non-noble metal catalysts has been developed to further improve the activity of Co nanoparticles. As can be seen in **Chapter 9**, the introduction of Ni into Co@C nanoparticles leads to the formation of CoNi alloyed nanoparticles covered by thin carbon layers and these bimetallic CoNi nanoparticles show much activity than Co nanoparticles for chemoselective hydrogenation of nitroarenes and the high selectivity is also preserved, indicating the advantages of bimetallic non-noble metal catalysts.

In the literature, the reaction mechanism on non-noble metal nanoparticles (Co, Fe, etc.) for chemoselective hydrogenation of nitroarenes are barely discussed. In **Chapter 10**, it will be shown that, a new reaction pathway has been discovered on Ni@C nanoparticles, which is different to that found with conventional noble metal catalysts (Au, Pt, Ru, etc.). By combining DFT calculations and experimental studies, it has been found that the oxophylic character of Ni strongly facilitates the rupture of the N-O bonds in nitrobenzene, yielding nitrosobenzene as primary reaction intermediate. Following the discovery of the new reaction pathway on Ni nanoparticles, a bifunctional catalyst has been proposed for chemoselective hydrogenation of nitroarenes to condensation products (azoxy and azo compounds) instead of the formation of anilines. Following that discovery, direct hydrogenation of nitrobenzene to azoxybenzene and then to azobenzene can be achieved with the combination of Ni@C nanoparticles and CeO_2. Nitrosobenzene is formed as the primary product and then transfer to CeO_2, on which the further hydrogenation of nitrosobenzene to phenylhydroxylamine and condensation between nitrosobenzene and phenylhydroxylamine occurs. The Ni@C+CeO_2 catalyst enables the direct conversion of nitroarenes to azoxy compound with high chemoselectivity under mild conditions, which surpasses the performance of the state-of-art Au/CeO_2 catalyst.

In **Chapter 11**, the hydrogenation of CO_2 into hydrocarbons promoted by the action of sunlight has been studied on Co nanoparticles covered by thin carbon layers. In particular, nearly 100% selectivity to hydrocarbons is obtained with increased selectivities towards C2+ hydrocarbons and alcohols (mainly ethanol) when using nanostructured materials comprising metallic cobalt nanoparticles,

carbon layers, and sodium as promoter (Na-Co@C). The reaction mechanism for photoassisted CO_2 hydrogenation on the Co-based catalysts was investigated by near ambient-pressure X-ray photoelectron (AP-XPS) and *in situ* Raman spectroscopies, which provided information on the role of light and Na promoter in the modulation of product distribution for CO_2 hydrogenation. Spectroscopic studies suggested that surface CO_2 dissociation to CO, the stabilization of CO adsorbed on the surface of Na-Co@C catalyst and the easy desorption of reaction products is a key step for photothermal CO_2 hydrogenation to ethanol and C2+ hydrocarbons.

In the last part of this thesis (**Chapter 12**), perspectives for my PhD work will be given, based on the results obtained presented in this thesis and some ideas for the future directions on understanding, designing and applications of heterogeneous metal catalysts. Specifically, the catalytic behavior of different types of metal species (from single atoms to nanoclusters and nanoparticles) will be discussed.

This chapter is reused from the following publication:

Facile synthesis of surface-clean monodispersed CuOx nanoparticles and their catalytic properties for oxidative coupling of alkynes, **L. Liu**, T. Matsushita, P. Concepción, A. Leyva-Pérez and A. Corma, *ACS Catalysis*, 2016, 6, 2211-2221.

Chapter 3

Facile Synthesis of Surface-Clean Monodispersed CuO$_x$

Nanoparticles and Their Catalytic Properties for

Oxidative Coupling of Alkynes
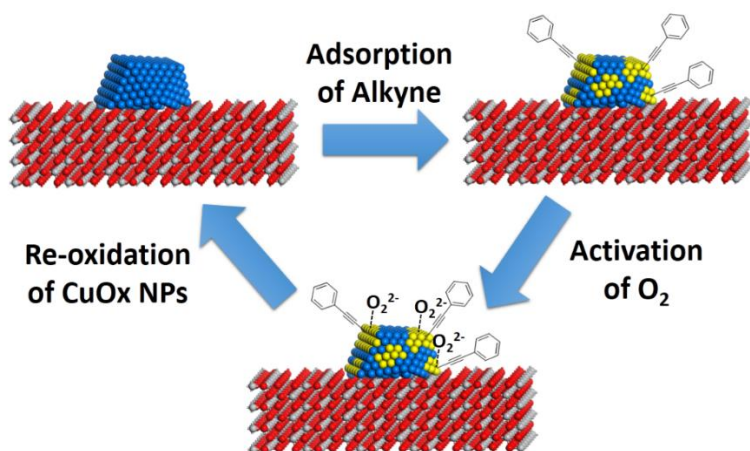
Abstract

We show a facile method to prepare surface-clean monodispersed small and stable CuOx nanoparticles with controllable average sizes from below 1 nm up to ~5 nm without using bulk capping agent. Structural and surface characterizations show that the chemical states of CuOx nanoparticles and their interactions with O_2 are dependent on the particle size. To show their relevance to catalysis, the well-defined monodispersed CuOx nanoparticles have been used for oxidative coupling of alkynes. While the generally used CuCl catalysts presents a reaction induction period and agglomerate into CuOx nanoparticles during the reaction, the induction period disappears when monodispersed CuOx nanoparticles (~2 nm) were used as catalyst. Supported CuOx nanoparticles on TiO_2 behave in the same way as monodispersed CuOx nanoparticles. Kinetic, spectroscopic and isotopic studies show that O_2 activation is the rate-controlling step and the nature of the oxygen species formed on supported CuOx nanoparticles are dependent on the size of CuOx and determine the catalytic properties for oxidative coupling of alkynes.

1. Introduction

CuO_x (Cu_2O and CuO) are important semiconductors that present wide applications in catalysis, gas sensing and photocatalysis. There is much work on controllable synthesis of Cu_2O and CuO nanostructures and their applications in energy conversion, gas sensing and catalysis.[1,2] However, most CuO_x nanomaterials prepared in the literatures are larger than 5 nm with low surface areas. Since the catalytic properties of nanoparticles (NPs) are obviously related with their size, developing methodologies for synthesis of small CuO_x NPs with diameter below 3 nm can be of much importance for catalytic applications.

In 2005, Yin et al. presented a method for the synthesis of uniform monodispersed Cu_2O nanocrystals with sizes between 2 and 10 nm,[3] in where oleic acid was used as capping agent and showed a negative effect on catalytic properties of Cu_2O NPs. Meanwhile, high-temperature calcination (> 200 ºC) is usually required to remove the ligands with long carbon chains.[4] Others have also prepared CuOx NPs but strongly interacting capping agents were also needed.[5] So far, the preparation of small "surface clean" CuO_x NPs

without bulky capping agent still remains a challenge.

Copper compounds (like CuCl, CuCl$_2$, Cu(acac)$_2$ et al.) are widely used in organic synthesis as catalysts for oxidation reactions.[6,7] There are many mechanistic studies on the role of Cu for oxidation reactions, and most of those works have been performed on the basis that mononuclear Cu or, in some cases, double Cu centers stabilized by ligands are thought to be active centers.[8,9] Although there are some reports on the application of Cu NPs for aerobic oxidation reaction, the relationships between Cu compounds and Cu NPs are still not clear. In a recent work, we have seen that the Cu salts used initially as the catalyst for C-N coupling reactions are not necessarily the active species, but they agglomerate during the reaction to form Cu clusters with a few atoms.[10] This can be particularly relevant for oxidation reactions in where O$_2$ activation may require Cu species with a certain number of Cu atoms. In the case of organic reactions that take place at low temperature, O$_2$ dissociation or, in a more general way, O$_2$ activation can become the rate-controlling step. To achieve the activation of the organic compounds and O$_2$ simultaneously on isolated Cu cations seems like a difficult task, and in natural Cu-containing enzymes, binuclear Cu centers are thought to be the active sites for activation of O$_2$.[11,12] In the case of Cu NPs, the activation of O$_2$ could be easier on small Cu NPs and the size as well as redox properties of Cu NPs, will be a key issue for establishing structure-activity relationships for Cu-catalyzed oxidation reactions.[13]

In the present work, we will show a facile method to prepare monodispersed small CuOx NPs with controllable average sizes from below 1 nm up to ~5 nm. By kinetic experiments, we will show how the size of the CuOx NPs controls the adsorption and activation of organic reactants and O$_2$, as well as their facility to go into redox cycles. To show their relevance to catalysis, we have used these well-defined monodispersed CuOx NPs for oxidative coupling of alkynes. Then, by comparing with CuCl (the widely used catalyst for oxidative coupling of alkynes), it has been proved that a reaction induction period exists when CuCl is used as the starting catalyst. We have found that CuCl will evolve and agglomerate during the reaction. On the other hand, the reaction induction period disappears when monodispersed CuOx NPs (~2 nm) were used as catalyst. After identifying the important role

of CuOx NPs in oxidative coupling of alkynes, supported CuOx NPs on TiO_2 were prepared as heterogeneous catalysts. The $CuOx/TiO_2$ catalysts show, the same particle size effects, the with well-defined isolated nanoparticles. By means of kinetic, spectroscopic and isotopic studies, it has been found that O_2 activation is the rate-controlling step and the nature of the oxygen species formed on supported CuOx NPs are dependent on the size of CuOx NPs.

2. Experiments

2.1 Synthesis of monodispersed CuOx NPs and supported CuOx NPs.

The CuOx NPs with different sizes were prepared as following. CuCl powder was added into 20 mL dimethylsulfoxide (DMSO). The suspension was heated to 90 °C under stirring. The CuCl powder became dissolved into DMSO when the suspension was kept at 90 °C for 20 minutes, leading to formation of a homogeneous solution and the size of CuOx NPs was modulated through the amount of CuCl in the solution. Samples will be labeled as CuOx-xx with xx corresponding to the average particle size determined from TEM images.

Supported CuOx NPs were prepared by a wet impregnation method. 2 g TiO_2 nanopowder (from Aldrich, 21 nm average particle size), 30 mL H_2O and the desired $Cu(CH_3COO)_2$ were mixed at room temperature and kept under stirring at room temperature for 1 h. Then water is evaporated by heating in an oil bath at 120 °C. Finally, CuO_x/TiO_2 samples were obtained after calcination in N_2 at 450 °C for 2 h.

Cu clusters with 8-16 atoms were prepared by an electrochemical method according to reference.[14]

2.2 Characterizations

The sizes of copper particles on supports were analyzed by TEM microscopy. Samples for electron microscopy studies were prepared by dropping the suspension of CuOx NPs directly onto holey-carbon coated Nickel grids. Studies have been performed in a JEOL 2100F microscope operating at 200 kV both in transmission (TEM) and scanning-transmission modes (STEM). STEM images were obtained using a High Angle Annular Dark Field detector (HAADF), which allows Z-contrast imaging.

X-ray photoelectron spectra of the catalysts were carried out with a SPECS spectrometer equipped with a Phoibos 150MCD multichannel analyzer using MgKα (1253.6 eV) irradiation. The spectra were recorded at -175ºC and with an X-ray power of 50 mW in order to avoid photo-reduction of the copper species. The residual pressure in the analytical chamber was maintained below 10^{-9} mbar during data acquisition. For spectra acquisition, a drop of the monodispersed CuOx NP solution was deposited onto a Molibdenum sample holder and dried under N_2 atmosphere inside the load lock of the XPS spectrometer. On the other hand, supported CuOx NP were prepared for analysis by depositing the powder onto a molybdenum sample holder. The binding energies of Cu 2p were corrected for surface charging by referencing them to the energy of C1s peak of adventitious carbon, set at 284.5 eV. Peak intensities have been calculated after nonlinear Shirley-type background subtraction and corrected by the transmission function of the spectrometer. The CasaXPS software has been used for spectra deconvolution.

Raman spectra were obtained with an "in via Reflex" Renishaw spectrometer, equipped with an Olympus microscope. The exciting wavelength was 785 nm from a Renishaw HPNIR laser with a power of ca. 15 mW on the sample. A micro quartz reactor located in a furnace has been used for the in situ Raman studies. The furnance is provided with a small hole in order to allow focalization on the sample with the laser spot. The reactor was positioned below the microscope objective, using a x50 long working distance objective (WD=10.6 nm). For the in situ studies the sample (10mgr) has been in situ activated in N_2 flow for 1h at 25 ºC. Then the sample has been exposed to a phenylacetylene + O_2 flow at 90 ºC for 1h. Afterwards the temperature was decrease to 25 ºC, and the gas flow switch to only O_2. Temperature was increased from 25º to 60º and 90 ºC, collecting several spectra at each temperature.

FTIR spectra have been collected with a Nexus spectrometer from Thermo equipped with a DTGS detector (4 cm^{-1} resolution, 32 scans).The samples were pressed into self-supported pellets (ca. 10mg cm^{-2}) and activated in vacuum (10^{-4} mbar) for 1h at 25 ºC prior to the IR studies. In the phenylacetylene adsorption studies, deuterated phenylacetylene (Ph-C≡C-D) was adsorbed at 25ºC at increasing dosing from 0.5 to 6.5 mbar, followed by

further increasing the temperature to 60 and 90 ºC. Spectra were acquired at each temperature and after each dose. After 90 ºC, the sample was evacuated and the temperature lowered to 25 ºC where 35 mbar CO was adsorbed for surface titration experiments. After CO evacuation the sample was exposed to 30 mbar O_2 at 90 ºC for 45min, followed by evacuation and further decreasing temperature to 25 ºC were 35 mbar CO was again re-adsorbed for surface titration. In the in situ IR studies 6.5 mbar phenylacetylene was coadsorbed with 30 mbar O_2 at 25ºC and kept for 45 min at that temperature. Afterwards the temperature was raised to 90 ºC for 45 min followed by sample evacuation at 10^{-4} mbar.

^{18}O Isotopic exchange of surface oxygen species followed by H_2 titration, were carried out in a quarzt flow reactor coupled to a quadrupole mass spectrometer (Omnistar, Balzers) for on-line monitoring of the exit gas composition. In each experiment, 100 mg of sample diluted in SiC (1:1 ratio), has been activated in N_2 flow for 1 h at 25 ºC. In the TPR of the $^{18}O_2$ oxidized samples, the sample, after activation, was exposed to a 20% $^{18}O_2$ in Ar flow for 1 h at 90 ºC, followed by decreasing the temperature to 40 ºC in an Ar flow and kept at that temperature for 20 min. Afterwards the gas feed was switch to 10% H_2 in Ar, and the temperature raised to 450 ºC, with a heating rate of 2 ºC/min. In the TPR of the phenylacetylene+$^{18}O_2$ experiments the sample, after activation, was exposed to a phenylacetylen+$^{18}O_2$ flow at 90 ºC for 1h, followed by decreasing the temperature to 40 ºC in an Ar flow and kept at that temperature for 20 min. Afterwards the gas feed was switch to 10% H_2 in Ar, and the temperature raised to 450 ºC, with a heating rate of 2 ºC/min.

Powder X-ray diffraction (XRD) was performed with a HTPhilips X'Pert MPD diffractometer equipped with a PW3050 goniometer using CuKα radiation and a multisampling handler.

Sample compositions of the DMSO solution of CuOx NPs were measured after acid-digestion by ICP-OES on a Varian 715-ES instrument.

The redox properties of copper particles on supports are evaluated by Temperature-programmed reduction (TPR). Micromeritics AutoChem 2910 catalyst characterization system with a thermal conductivity detector (TCD) was used. Prior to each experiment, about 100 mg of sample was pretreated at room temperature in flowing He (10 mL/min) for 20 min. The sample was

treated by heating from 25 °C to 600 °C at a rate of 5 °C min^{-1} in a flow of 10 vol.% H_2 in Ar. The total gas flow rate was 50 mL/min^{-1}.

Fluorescence spectra were obtained with a LP S-220B (Photon Technology International) equipped with 75 W Xe lamp.

2.3 Oxidative homo-coupling of alkynes.
2.3.1 Oxidative homo-coupling of alkynes by monodispersed CuOx NPs

110 μL of alkyne (phenylacetylene) and 50 μL nitrobenzene (as internal standard) and a given amount of copper catalyst (Cu amount ranges from 0.5 mol% to 10.0 mol%) were added to 2 ml of solvent (DMSO) in 10 mL round-bottom test tube with stirrer. The reaction flask was introduced in a preheated silicon oil bath at 90 °C and stirred at around 1000 rpm under oxygen atmosphere (1 bar). Gas chromatography (Bruker with FID detector) was used for quantitative analysis of substrate and product.

2.3.2 Oxidative homo-coupling of alkynes by supported CuOx NPs

55 μL of alkyne (phenylacetylene) and 50 μL nitrobenzene (as internal standard) and supported copper catalyst (Cu amount ranges from 1.0 mol% to 8.0 mol%) were added to 2 ml of solvent (Toluene) in 10 mL round-bottom test tube with stirrer. The reaction flask was introduced in a preheated silicon oil bath at 90 °C and stirred at around 1000 rpm under oxygen atmosphere (1 bar). Gas chromatography (Bruker with FID detector) was used for quantitative analysis of substrate and product.

2.3.3 Oxidative hetero-coupling of alkynes by supported CuOx NPs

0.5 mmol alkyne A, 0.25 mmol alkyne B and 40 μL dodecane (as internal standard) and supported copper catalyst (CuOx/TiO$_2$-2.5%, 100 mg) were added to 2 ml of solvent (Toluene) in 10 mL round-bottom test tube with stirrer. The reaction flask was introduced in a preheated silicon oil bath at 100 °C and stirred at 1000 rpm under oxygen atmosphere (5 bar). Gas chromatography (Bruker with FID detector) was used for quantitative analysis of substrate and product.

Figure 3.1. (a-d) STEM images of small CuOx NPs with different sizes, a) CuOx-NC, b) CuOx-1.8, c) CuOx-2.2 and d) CuOx-2.5. (e-h) size distributions of small CuOx NPs with different sizes, e) CuOx-NC, f) CuOx-1.8, g) CuOx-2.2 and h) CuOx-2.5.
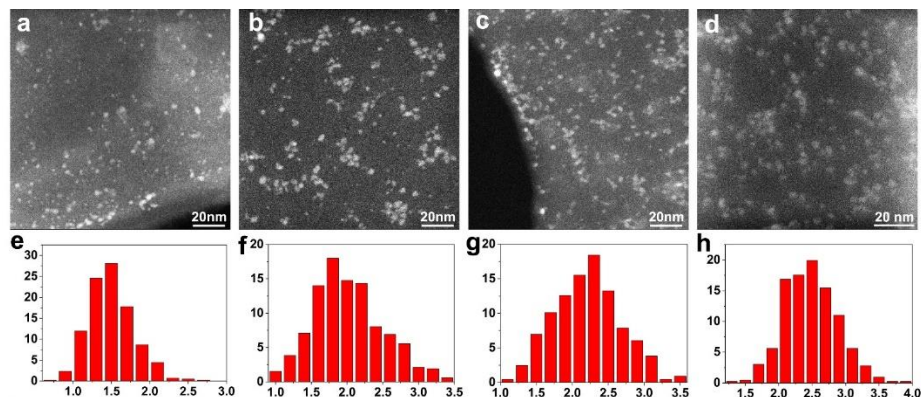
3. Results and Discussions

3.1 Synthesis and characterizations of monodispersed CuOx nanoparticles

Monodispersed CuOx NPs could be easily synthesized by a thermal decomposition of CuCl in DMSO. CuCl powder is not soluble in DMSO at room temperature. However, after heating the suspension at 90 °C for 20~30 min, a transparent solution was obtained. The formation of CuOx NPs should be a result of the thermal decomposition of CuCl in DMSO in air. If CuCl-DMSO mixture is heated in N_2 atmosphere, only small amount of CuCl can be dissolved in DMSO, suggesting that O_2 participate in the thermal decomposition process. When the concentration of Cu is as low as 0.08 mg/mL, CuOx NPs (denoted in this case as CuOx-NC) with sizes below 2 nm can be seen in the STEM images. According to the STEM images, the average size of those small CuOx NPs is about 1.5 nm. However, it should be noticed that a large number of Cu clusters with size below 1 nm appear to exist but, due to the limitation of our STEM, they cannot be seen clearly. Indeed, photoemission studies show the presence of Cu clusters with 10-20 atoms (see the following discussion). So, the ~1.5 nm average size given is certainly an over estimation of the average particle size. Increasing the concentration of

Cu species leads to increasing the size of CuOx NPs. Then by controlling the concentration of Cu, CuOx NPs with different sizes and narrow size distributions can be obtained ranging from clusters (< 1 nm) up to ~5 nm, as shown in Figure 3.1 and **Figure 3.2**.
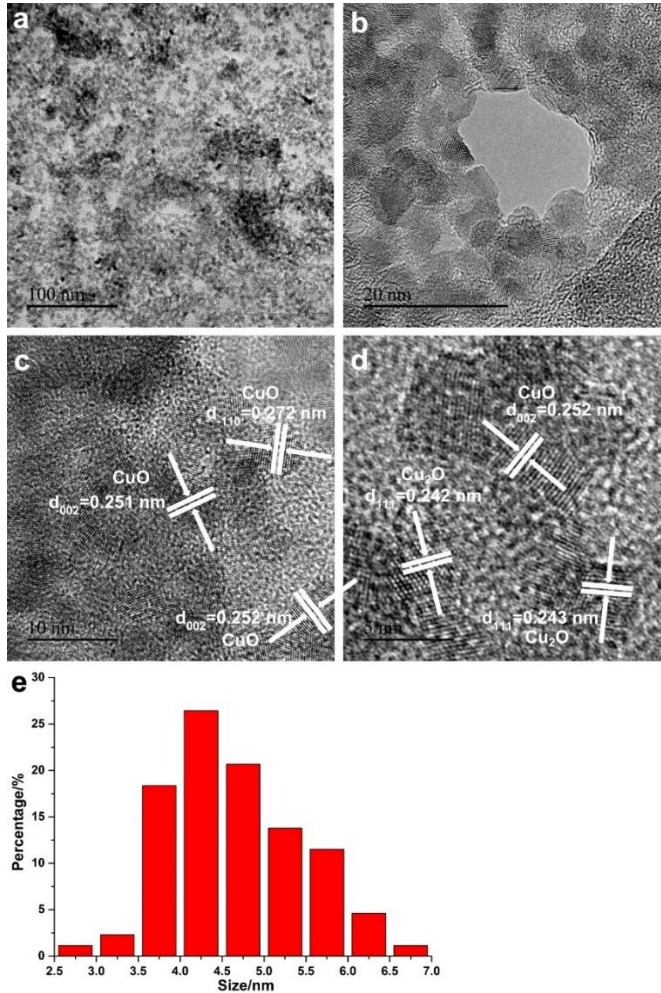
Figure 3.2. TEM images and size distributions of CuOx-4.5 sample.

In a deeper structural characterization, the crystal lattice information of the CuOx NPs was acquired with high-resolution TEM. As shown in **Figure 3.3**, lattice fringes corresponding to Cu_2O and CuO can be seen in the NPs of those four samples (From CuOx-NC to CuOx-2.5), suggesting that they

should consist of both Cu(I) and Cu(II).[15,16] The elemental mapping results (shown in **Figure 3.4**) also confirm that those nanoparticles consist of both Cu and O. Small amount of Cl (< 10% of Cl in the CuCl precursor) can also be detected by EDX, which can be the residual Cl in DMSO or Cl absorbed by CuOx NPs. However, in the HRTEM images of CuOx NPs with larger size (CuOx-4.5), most of the particles show lattice fringes of CuO (**Figure 3.2**). Based on these HRTEM images, it is implied that the chemical states of Cu species may be different in different samples, depending on the particle size of CuOx.
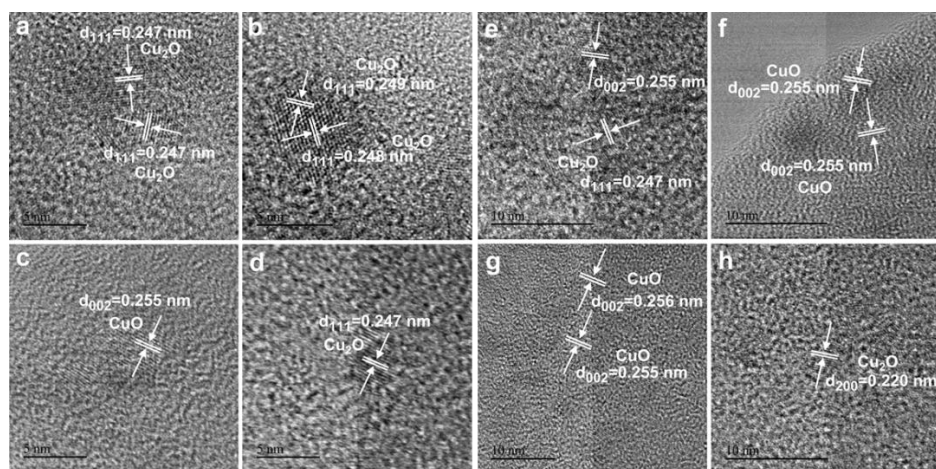
Figure 3.3. HRTEM images of CuOx particles with different sizes. CuOx-NC (a, b), CuOx-1.8 (c, d), CuOx-2.2 (e, f) and CuOx-2.5 (g, h).
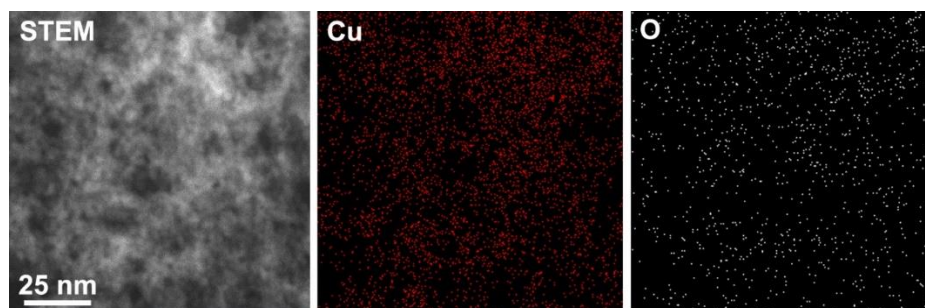
Figure 3.4. Elemental mapping of CuOx-2.2 sample, indicating that the nanoparticles consist both Cu and O.
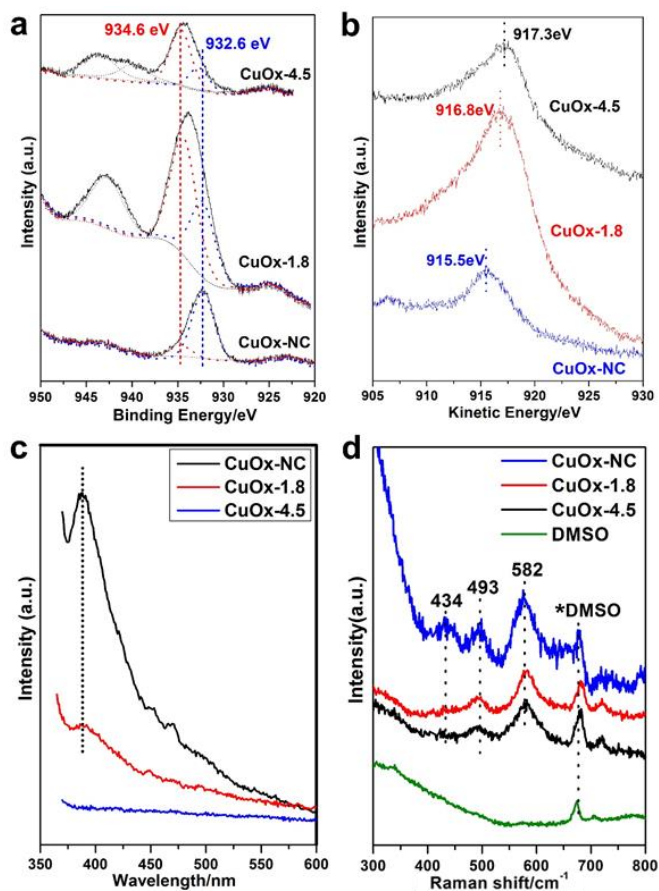
Figure 3.5. Spectroscopic characterizations of monodispersed CuO$_x$ NPs of different sizes. Cu 2p 3/2 XPS peak (a), CuL3VV Auger line (b), fluorescence spectra at 350 nm excitation (c) and Raman spectra (d).

Table 1. Fitting results of XPS spectra of CuOx-4.5, CuOx-2.2 and CuOx-NC. a) Cu(II)/Cu(I) atomic ratio determined from XPS peak decovolution b) Satellite to main peak area ratio.

Sample	Cu(II) **(934.6eV)**/Cu(I) **(932.6eV)**[a]	s/m[b]
CuOx-NC	0.16	0
CuOx-1.8	2.8	0.35
CuOx-4.5	5	0.66

The Cu 2p3/2 X-ray photo-electron spectra (XPS) and Cu L3VV Auger spectra of the above samples are shown in **Figure 3.5a** and **Figure 3.5b** respectively. Two components at binding energy (BE) of 934.6eV and 932.6eV are observed in all samples but in different proportion. The higher BE of 934.6eV is due to Cu^{2+}, while the lower BE of 932.6eV can be related either to Cu(I) or metallic Cu^{0}.[17] However, Assignation to Cu^{0} can be excluded according to the peak position and band shape of the auger Cu L3VV peak. Following the above assignment, it can be seen that from the values given in **Table 1**, the relative amount of Cu(II) to Cu(I) increases when increasing particle size (from clusters to 5 nm), which fits with the increase in the shake-up satellite intensity. Moreover, the Cu L3VV peak position agrees with a higher contribution of Cu(II) in sample CuOx-4.5 (Cu L3VV of 917.8 eV) and higher contribution of Cu(I) in sample CuOx-1.8 (Cu L3VV of 916.8 eV)[18], while an anomalous Cu L3VV KE value is observed on sample CuOx-NC (915.5eV). Similar behavior, due to a small particle size effect, has already been observed by others.[19]

The existence of Cu clusters in CuOx-NC sample is also confirmed by fluorescence spectroscopy. As shown in **Figure 3.5c**, a strong emission peak can be found around 390 nm, which corresponds to Cu clusters with 10~20 atoms.[14] The fluorescence intensity decreases dramatically when the particle size increases to 1.8 nm, due to the high sensitivity of fluorescence with particle size. For CuOx-4.5 sample, almost no emission signal can be observed under those conditions. Accordingly with the characterization results observed up to now, it is possible to say that CuOx NPs with controllable and very narrow size distribution, ranging from clusters to ~ 5 nm NPs, can be easily obtained by decomposing CuCl in DMSO, and the size of CuOx NPs can be tuned by changing the Cu concentration. Moreover, we can also say that the chemical state of Cu in the CuOx NPs changes with the particle size, increasing the Cu(II) to Cu(I) ratio when increasing the size of CuOx NPs. In order to identify the textural structure of CuOx nanoparticles, we have employed Raman spectra to measure the monodispersed CuOx nanoparticles. The Raman spectra of the three CuOx samples are shown in **Figure 3.5d**. The typical vibration mode of CuCl is around 200 cm^{-1}, which cannot be observed in the three samples.[20] Bulk CuO shows normally three Raman peaks at 295,

342, 628cm^{-1}, while in our case, peaks at 434, 493 and 582cm^{-1} are observed, associated to other Cu-O-Cu stretching modes less intense in bulk CuO.[21,22] This, in fact goes in line with the different surface properties of nanoparticles versus bulk samples.

3.2 Catalytic properties of monodispersed CuOx NPs
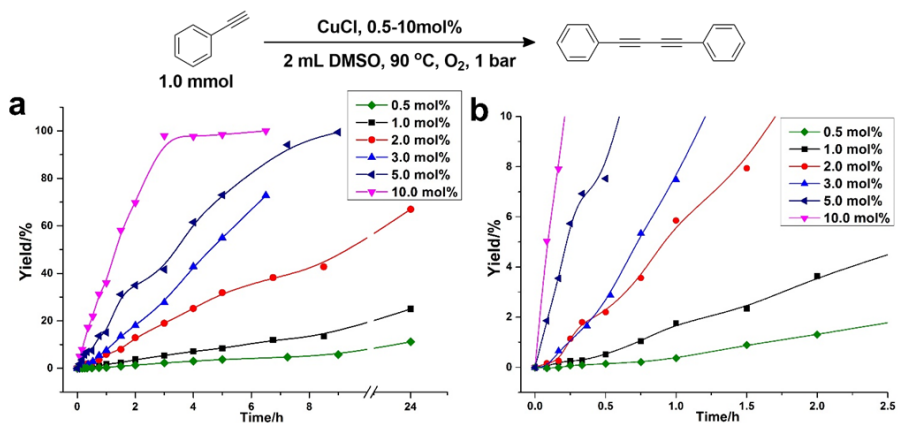
Figure 3.6. The kinetic curves of Cu-catalyzed homo-coupling of phenylacetylene using different amounts of CuCl as catalysts are shown in (a) and (b).
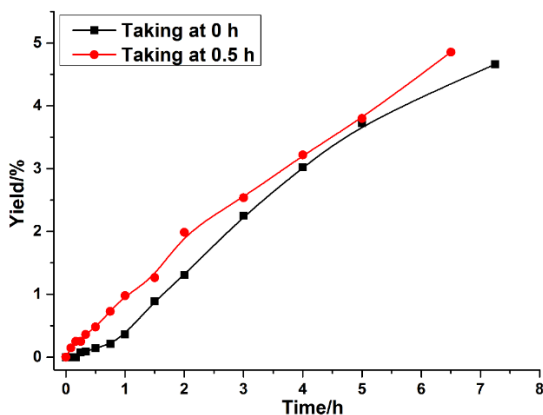
Figure 3.7. Kinetic study of Cu species which are in-situ formed during the homo-coupling reaction catalyzed by 10.0 mol% of CuCl. As indicated in the figure, 0.5mol% of Cu species are taken from the reaction mixture and added into a new reactor with solvent and reactant.
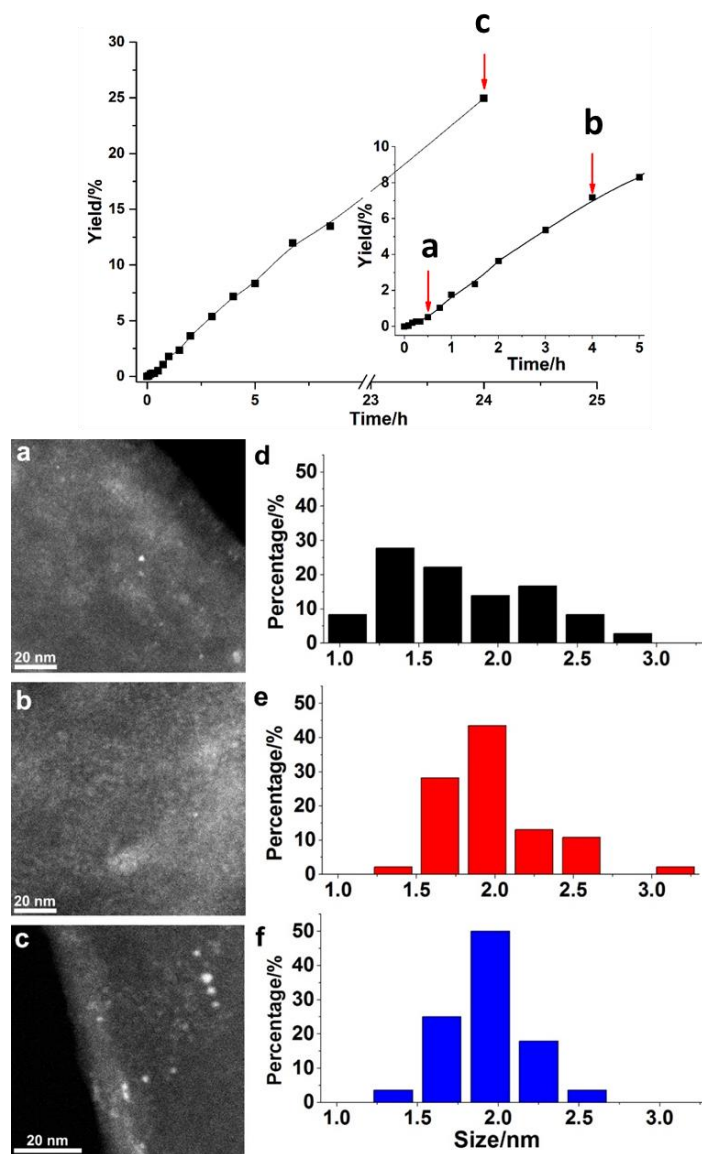
Figure 3.8. Evolution of Cu species during the homo-coupling of alkyne. The reaction mixture were taken at different reaction time. (a) 0.5 h, (b) 4 h and (c) 24 h. The size distribution of CuOx NPs are shown in (d), (e) and (f), respectively.

Cu compounds are widely used as superior catalysts for the oxidative homo-coupling of alkynes. Cu salts in pyridine media or in alcohol media can give high conversion for oxidative coupling of alkynes.[23,24] It is not infrequent to find in the literatures that the reaction mechanism is thought to involve the mononuclear Cu-alkyne complex. However, since Cu species can evolve during the reaction, one has to investigate the dynamic evolution of Cu species in the catalytic process to determine which are the catalytically active species. Therefore, we have used CuCl as the starting catalyst for performing the homo-coupling of phenylacetylene. Different amounts of CuCl were used as catalyst and the evolution of the reactants and catalyst were followed with time. As shown in **Figure 3.6a** and **Figure 3.6b**, it can be seen that when the amount of CuCl was below 5 mol%, the reaction goes through an induction period. During that time, conversion was not observed in the first 10-20 min. Furthermore, the induction period decreases when increasing the amount of CuCl. These kinetic results indicate that the initial CuCl may not be the real active catalyst, and some in situ transformation of CuCl may occur during reaction that give rise to the catalytically active Cu species.

In order to identify the evolution process of CuCl during the homo-coupling of the alkyne, the following experiment was carried out. A reaction mixture was prepared in one reactor with 10 mol% CuCl and phenylacetylene. An aliquot of the reaction mixture was taken at different reaction times and introduced into a second reactor in where only the phenylacetylene was present. The amount of Cu in the second reactor was kept as 0.5 mol%. It should be remembered that when the oxidative coupling of phenylacetylene was catalyzed by 0.5 mol% of CuCl, an induction period of about 1 h was observed (see **Figure 3.6**). As shown in **Figure 3.7**, an induction period was observed in the second reaction when the aliquot from the first reactor was taken at time zero with the still no evolved original CuCl. However, if the aliquot of the reaction mixture was taken from the first reactor after 0.5 h, and it was added into the second reactor, the reactor started immediately without induction period (see **Figure 3.7**). The above experiment shows that, whatever the Cu active species for the oxidative coupling of alkynes are, they are not the CuCl but are formed in situ during the reaction. Therefore, we follow the evolution of the Cu species by taking samples at

different reaction times. We choose the homo-coupling reaction catalyzed by 1.0 mol% of CuCl and the Cu species in solution were analyzed by with STEM. STEM results (see **Figure 3.8**) show that the reaction starts when nanoparticles with size between 1 and 3 nm are present. Elemental mapping and high-resolution TEM images (see **Figure 3.9**) confirm that those nanoparticles should be CuOx NPs with lattice fringes corresponding to Cu_2O. The results imply that, the in situ transformation of CuCl into CuOx NPs may play an important role in the oxidative coupling of alkynes.
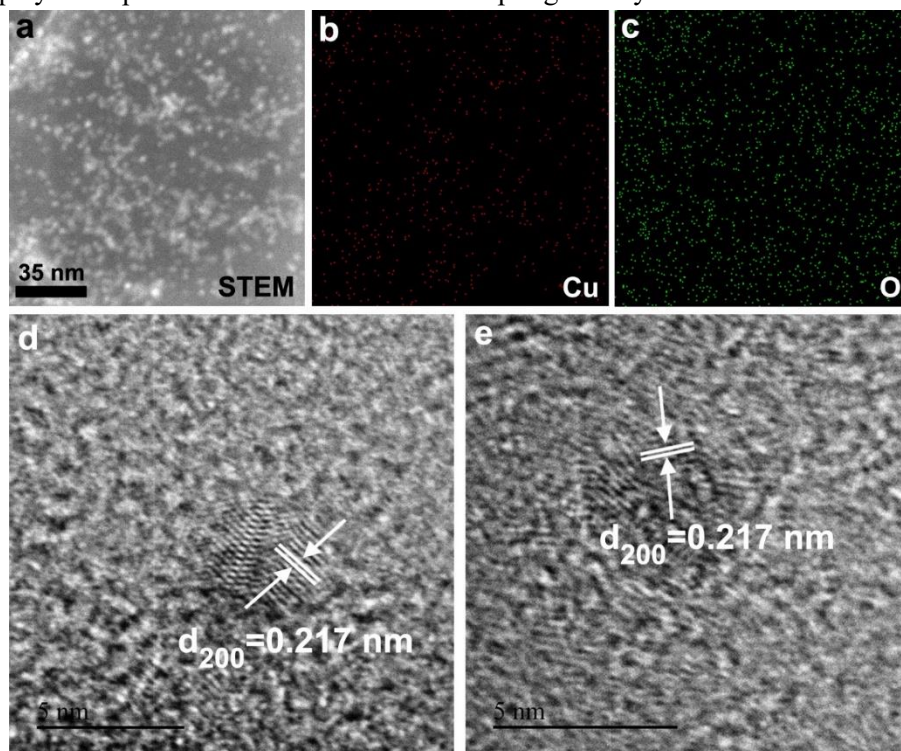
Figure 3.9. (a-c) STEM image and the corresponding elemental mapping of Cu and O in CuOx NPs that in situ formed during the CuCl-catalyzed oxidative coupling of phenylacetylene after reaction for 24 h. (d, e) High-resolution TEM images of CuOx NPs, corresponding to the (200) facets of Cu_2O.
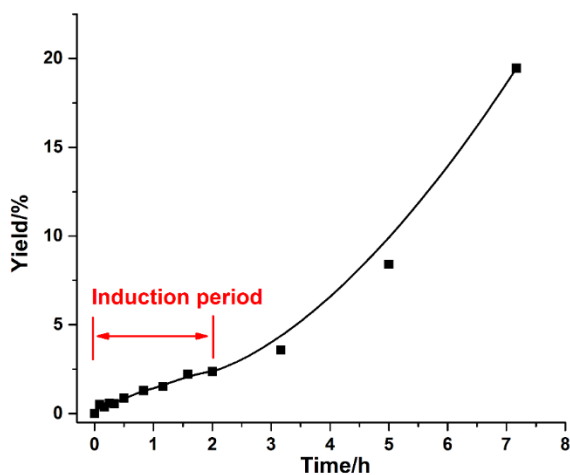
Figure 3.10. Kinetic curves of $Cu(Ac)_2$-catalyzed homo-coupling of phenylacetlyene. The amount of $Cu(Ac)_2$ is 5.0 mol%. The other reaction condition is the same with CuCl.
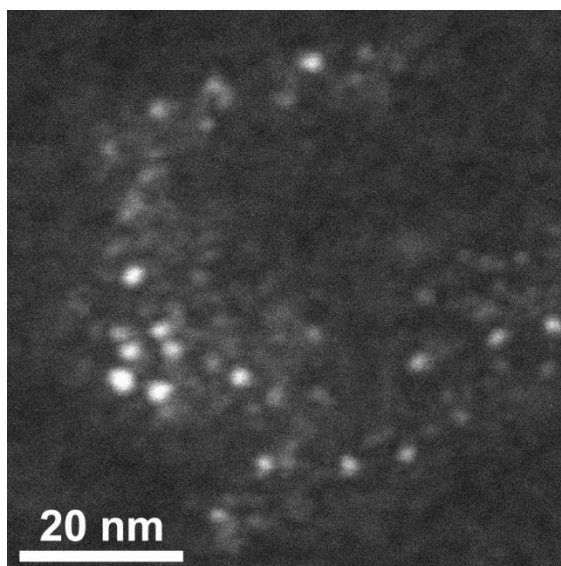
Figure 3.11. STEM image of the CuOx nanoparticles which are in-situ formed in the $Cu(Ac)_2$-catalyzed homo-coupling of phenylacetlyene. The sample is taken after the induction period (time=2 h).
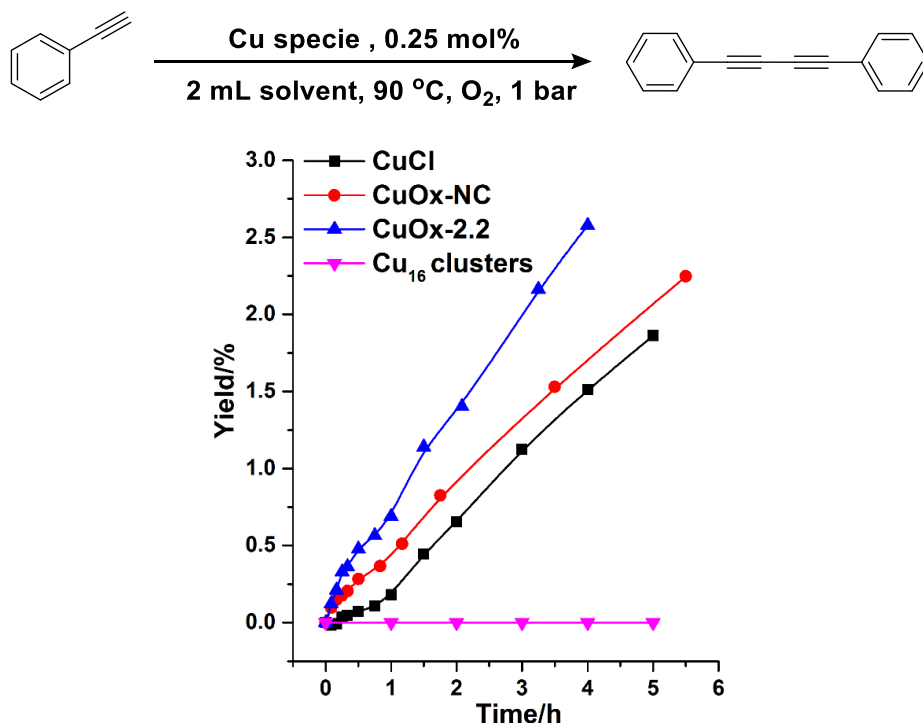
Figure 3.12. Comparison of the kinetic results in the oxidative homo-coupling of phenylacetlyene catalyzed by different kinds of Cu species.

Similar phenomenon of the in situ transformation of Cu species during the oxidative coupling of alkynes have also been observed when other starting Cu compounds were used as the starting catalysts. For example, when 5.0 mol% of $Cu(Ac)_2$ was used as catalyst, an induction period of about 3 h occurs (see **Figure 3.10**) and small CuOx NPs can also be observed with STEM after the induction period, as shown in **Figure 3.11**. For different Cu compounds, the induction period may be different, but when the reaction takes off, the in situ formed CuOX NPs show similar average sizes of ~2 nm. This common point implies that small CuOx NPs may play an important role in the oxidative homo-coupling of alkynes. Therefore, since CuOx NPs of controllable sizes can now be prepared, we performed the reaction using the separately prepared monodispersed CuOx NPs described before. Moreover, we have also used Cu clusters with 8-16 atoms prepared by electrochemical method (see

experimental section) and their catalytic property was measured. Results given in **Figure 3.12** clearly show that metal clusters give no activity for the oxidative homo-coupling of phenylacetylene. Moreover, the monodispersed CuOx samples (CuOx-NC and CuOx-2.2) are not only active but also give no induction period. Nevertheless, CuOx-2.2 show higher activity than CuOx-NC. Then, considering the presence of both small clusters and NPs in the CuOx-NC sample, we can speculate that only CuOx NPs are responsive for the catalytic activity.
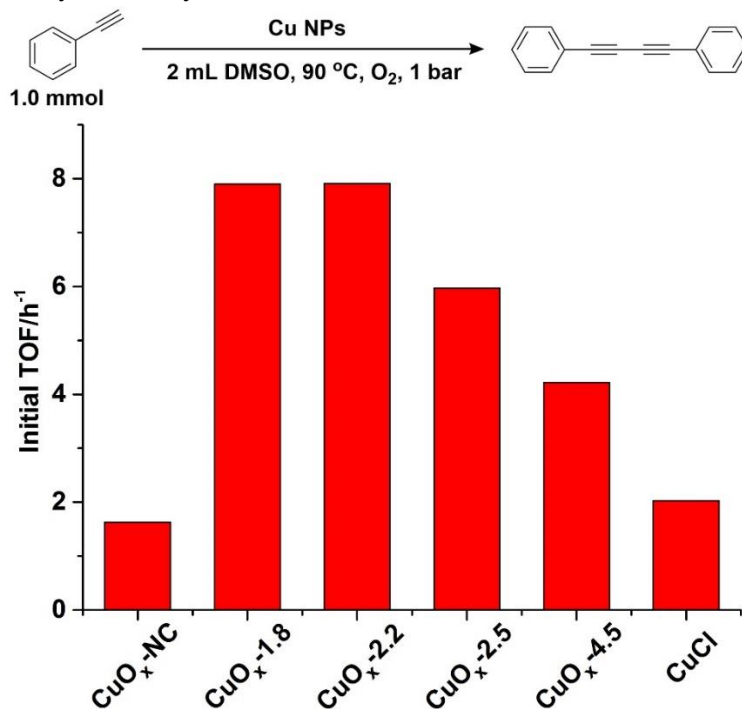
Figure 3.13. Kinetic studies of small CuOx NPs for homo-coupling of phenylacetylene. The initial TOF values of different CuOx NPs are calculated based on considering all the Cu species used in the reaction.

The catalytic properties of the other CuO_x NPs with different sizes have also been tested, and the results given in **Figure 3.13** show a maximum activity for CuOx NPs around ~2 nm. Moreover, when the initial reaction rate is plotted versus the amount of CuOx-2.2 NPs added as catalyst (shown in **Figure 3.14a** and **Figure 3.14b**), a linear relationship is observed, indicating that the CuOx NPs are the active species for the oxidative coupling of

phenylacetylene. The morphology of the CuOx-2.2 NPs was again checked after the homo-coupling reaction (after reaction time of 4 h) and the size distribution is very similar to the fresh sample (see **Figure 3.14c** and **Figure 3.14d**). It should be remarked here that, the CuOx NPs with larger size (CuOx-4.5) show a short but visible induction period (about 10 min) for the homo-coupling of phenylacetylene (see **Figure 3.15**). STEM and HRTEM images of CuOx-4.5 NPs after the homo-coupling reaction indicate that they have been transformed into CuOx NPs of around 2 nm during the reaction (see **Figure 3.16**). These results are again in line with the conclusion that CuOx NPs of ~2 nm are the active species for the reaction.
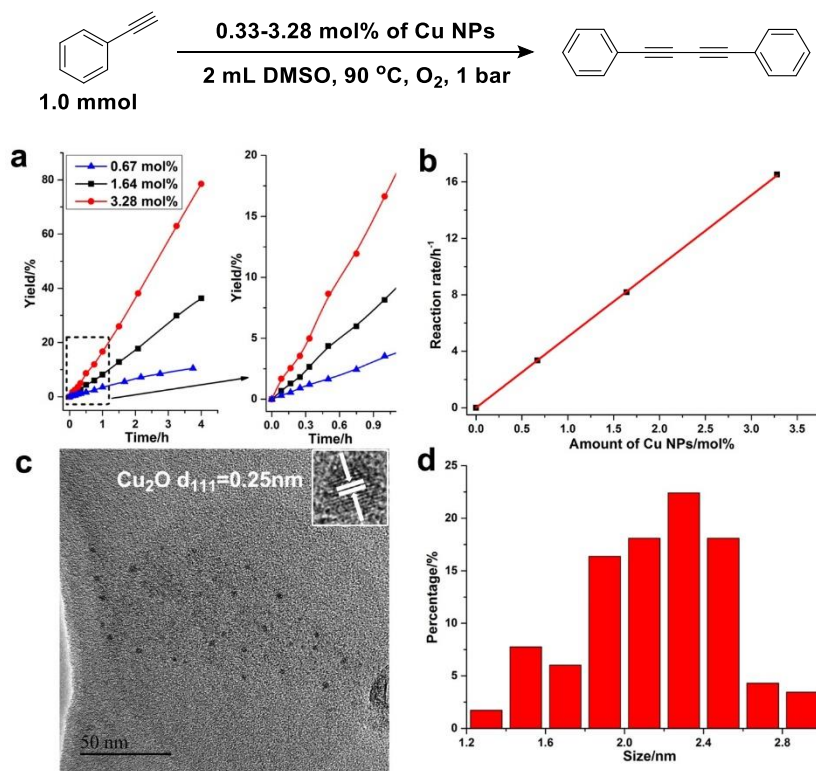
Figure 3.14. (a) Kinetic studies of CuOx-2.2 sample for homo-coupling reaction with different amounts of CuOx-2.2 nanoparticles. (b) Plot of the initial reaction rate with the amount of CuOx NPs used for the reaction. (c) TEM images of CuOx-2.2 after the homo-coupling reaction. (d) Size distribution of CuOx-2.2 NPs after the homo-coupling reaction.
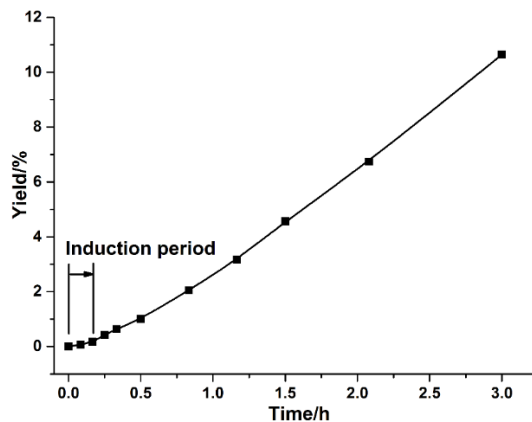
Figure 3.15. Kinetic studies of CuOx-4.5 NPs in the homo-coupling of phenylacetylene. Short induction period (about 10 min) can be observed.
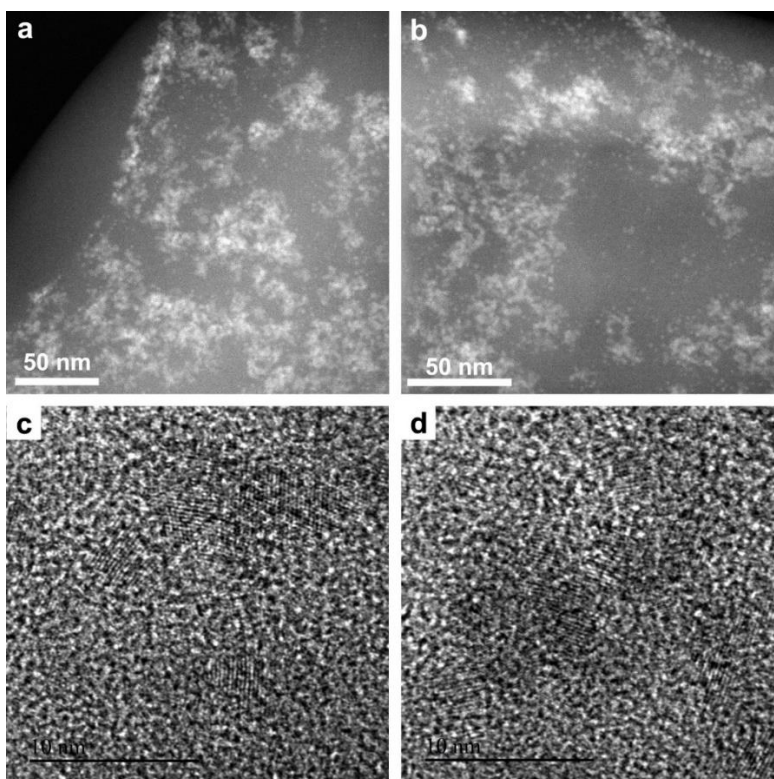
Figure 3.16. STEM and HRTEM images of CuOx-4.5 NPs after the homo-coupling reaction. Big CuOx nanoparticles (4.5 nm) will transform into

smaller CuOx nanoparticles (around 2 nm) after the second run of homo-coupling reaction.
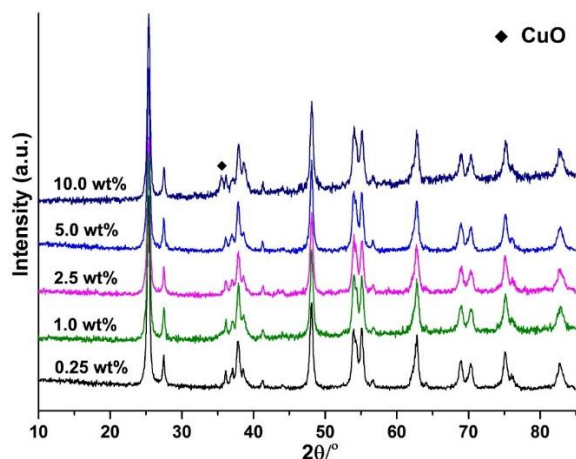
Figure 3.17. XRD patterns of CuOx/TiO$_2$ samples with different loading amount of CuOx.
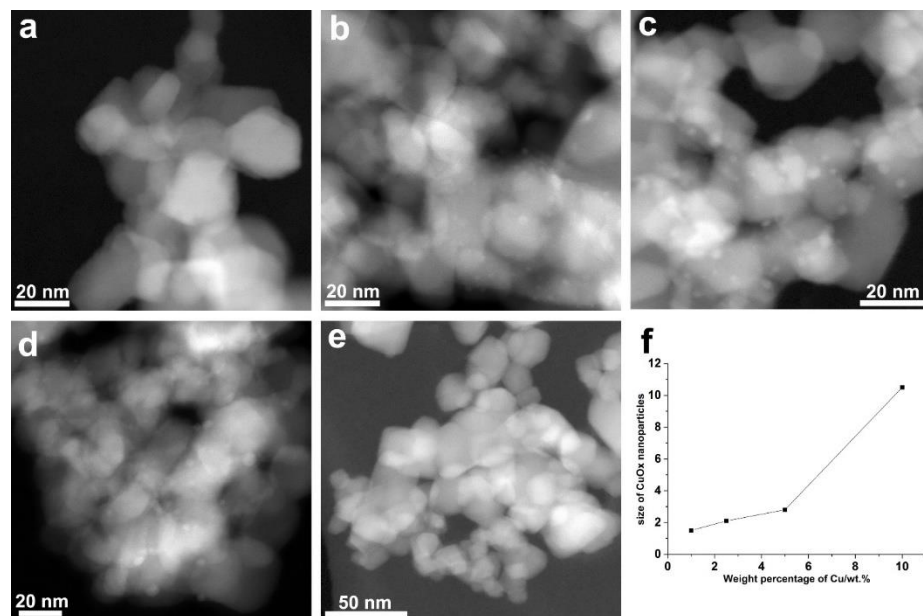
Figure 3.18. STEM images of CuOx/TiO$_2$ samples with different sizes and the corresponding average sizes of CuOx nanoparticles. For CuOx/TiO$_2$-0.25wt%

sample, the CuOx species are highly dispersed on TiO_2, which cannot be seen by our STEM.

CuO_x/TiO_2-0.25wt.%
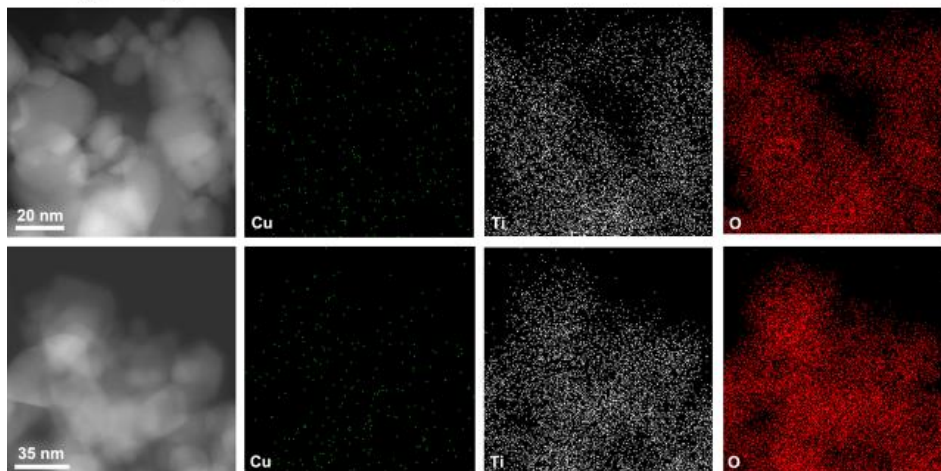
Figure 3.19. Elemental mapping of CuOx/TiO$_2$-0.25%.

CuO_x/TiO_2-1.0wt.%
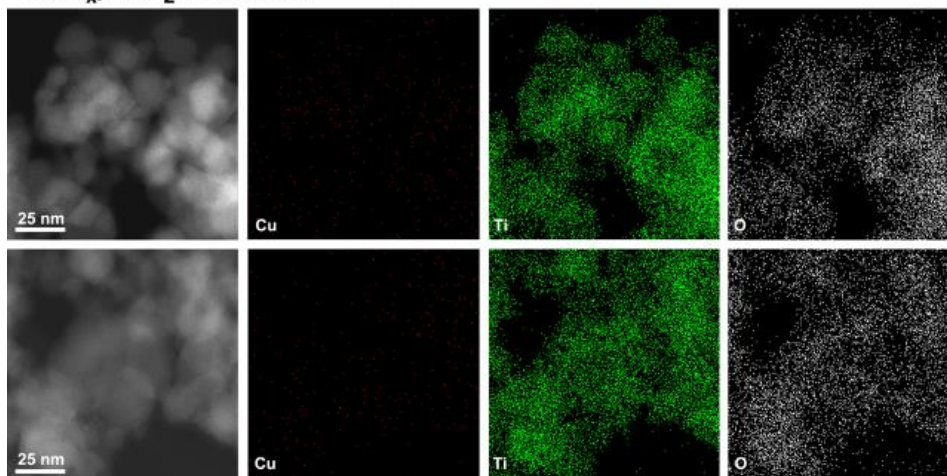
Figure 3.20. Elemental mapping of CuOx/TiO$_2$-1.0%.

CuO$_x$/TiO$_2$-2.5wt.%
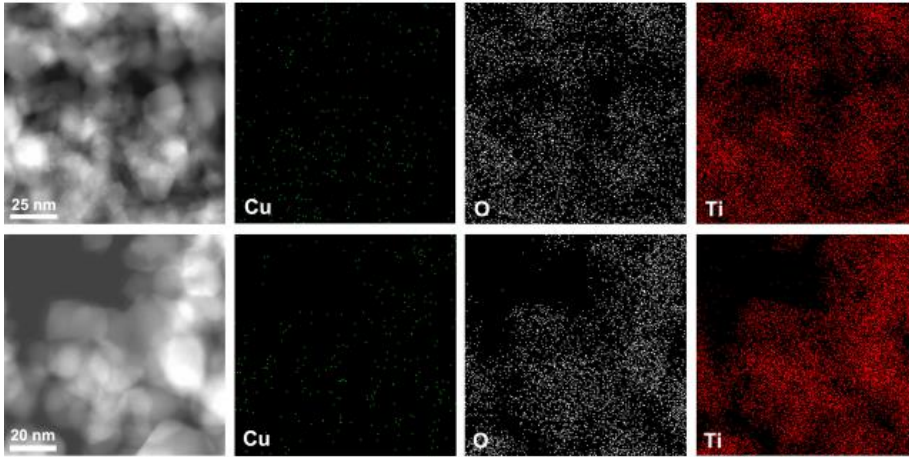
Figure 3.21. Elemental mapping of CuOx/TiO$_2$-2.5%.

CuO$_x$/TiO$_2$-5.0wt.%
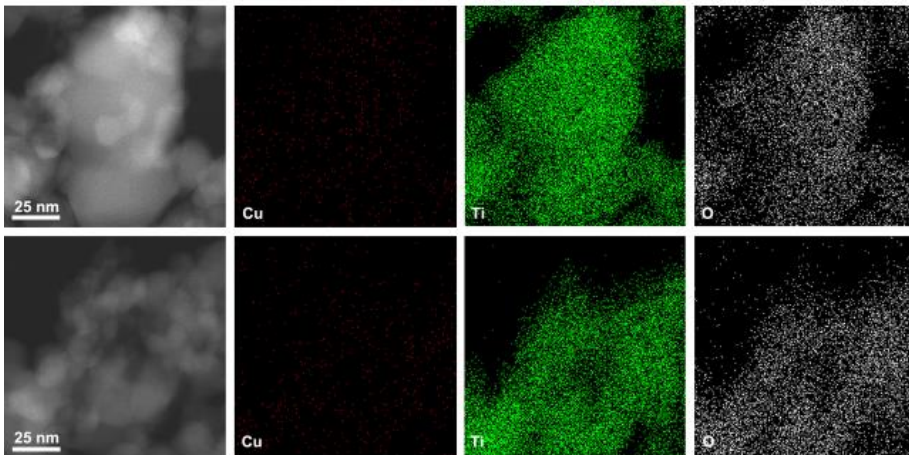
Figure 3.22. Elemental mapping of CuOx/TiO$_2$-5.0%.

CuOx/TiO₂-10wt.%
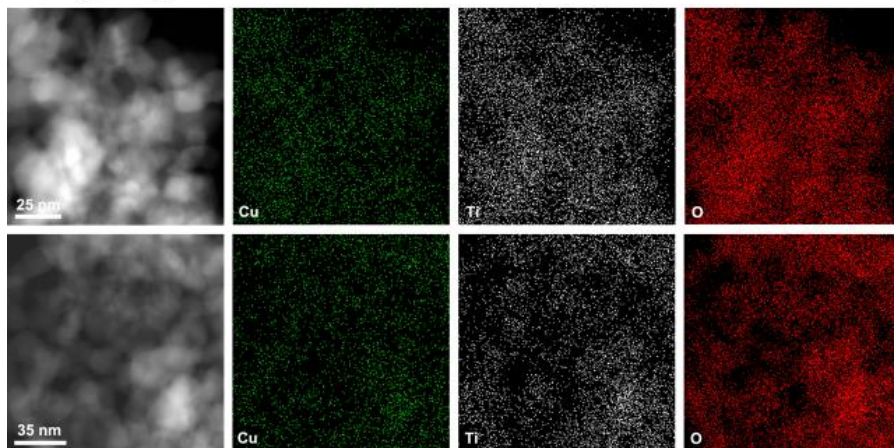
Figure 3.23. Elemental mapping of CuOx/TiO₂-10%.
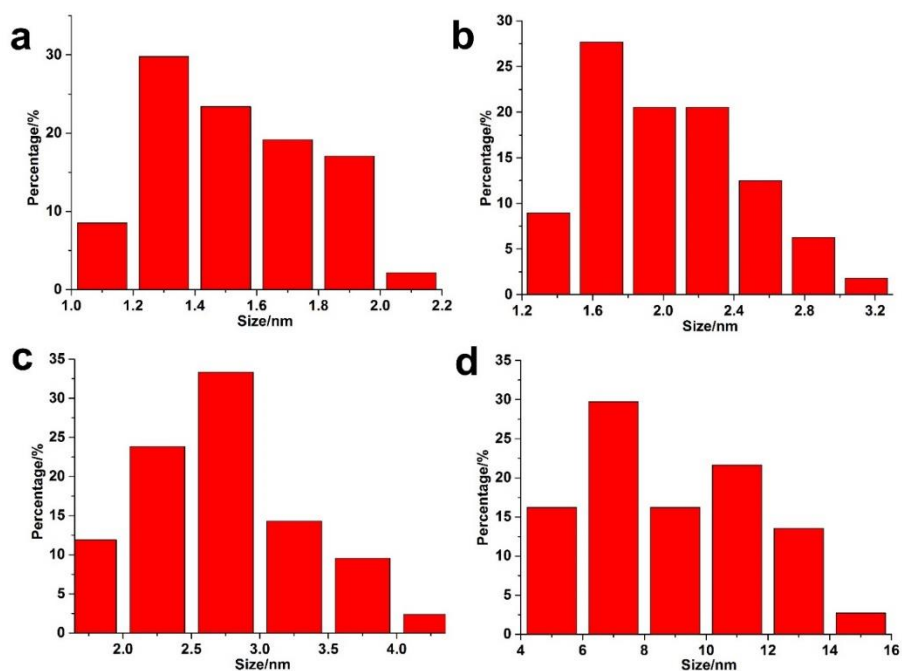
Figure 3.24. Size distributions of CuOx nanoparticles supported on TiO₂. (a) CuOx/TiO₂-1.0%, (b) CuOx/TiO₂-2.5%, (c) CuOx/TiO₂-5.0% and (d) CuOx/TiO₂-10%.
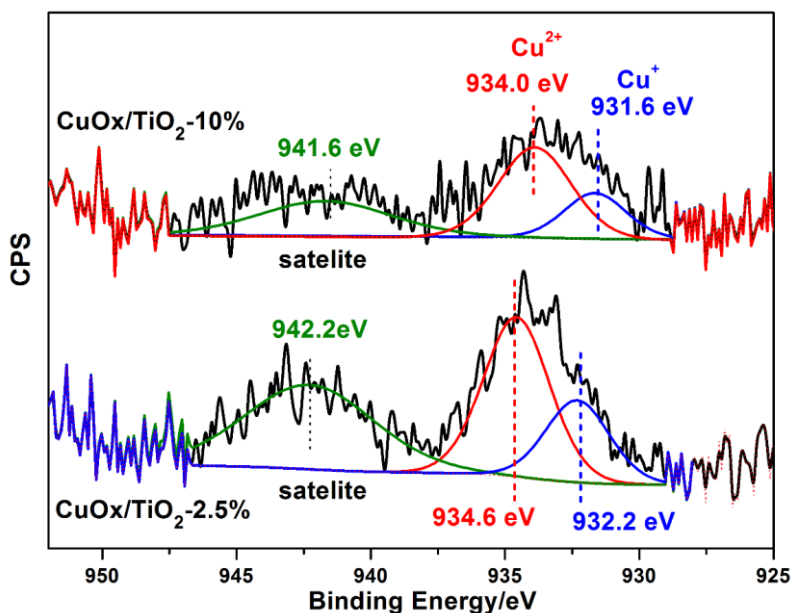
Figure 3.25. XPS of Cu 2p region of CuOx/TiO$_2$-2.5% and CuOx/TiO$_2$-10%. The Cu^{2+}/Cu$^+$ ratio in CuOx/TiO$_2$-2.5 and CuOx/TiO$_2$-10% is 2.4 and 2.0, respectively.
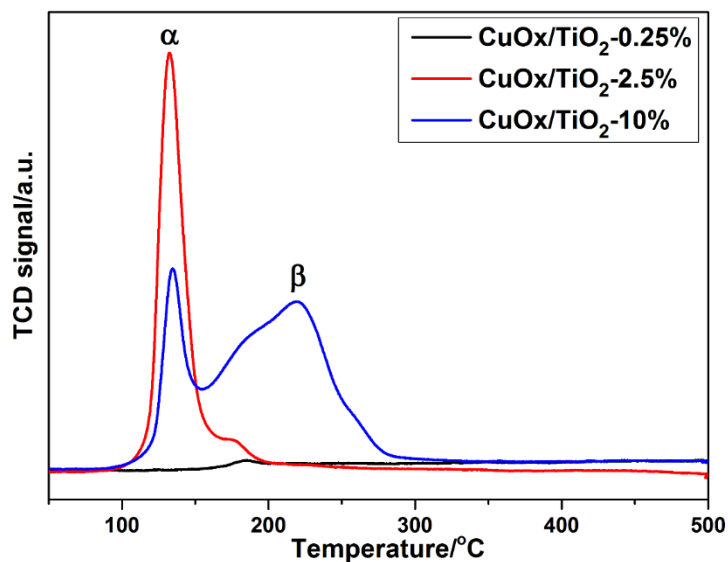
Figure 3.26. TPR profiles of CuOx/TiO$_2$-0.25%, CuOx/TiO$_2$-2.5% and CuOx/TiO$_2$-10%.

3.3 Preparation and characterizations of supported CuOx NPs

From the work on isolated CuOx NPs, we have learnt that oxidative coupling of phenylacetylene is better catalyzed by CuOx NPs of ~2 nm. Thus, before studying why this occurs, we thought on the possibility to extend the knowledge acquired to prepare active supported Cu catalyst for the above reaction, by generating the adequate CuOx NPs on a support, to prepare an optimized and recyclable solid catalyst. Herein, a series of CuOx/TiO$_2$ samples (denoted as CuOx/TiO$_2$-x%, where x is the loading weight percentage of Cu) were prepared through an impregnation method (see experimental section). Their XRD patterns are shown in **Figure 3.17**. Only diffraction peaks of anatase TiO$_2$ and rutile TiO$_2$ can be seen when the loading amount of Cu is lower than 5.0 %. For CuOx/TiO$_2$ samples with 10.0 wt% of Cu, diffraction peaks corresponding to CuO can be observed, indicating the formation of big CuO NPs in this sample. As shown in **Figure 3.18**, the sizes of the different CuOx NPs supported on TiO$_2$ were also investigated by STEM. According to the STEM images, their sizes range from below 1 nm to ca. 10 nm. The elemental mapping results (shown in **Figure 3.19** to **Figure 3.23)** also confirm the uniform dispersion of CuOx NPs on TiO$_2$ support. The size distributions of CuOx NPs are also presented in **Figure 3.24**, indicating that the size of CuOx NPs increases when increasing the loading of CuOx on TiO$_2$.

The chemical states of Cu species in (CuOx/TiO$_2$-2.5% and CuOx/TiO$_2$-10%) were measured by XPS. From **Figure 3.25**, it can be deduced that both Cu$^+$ and Cu^{2+} are present in the two samples. Moreover, CuOx/TiO$_2$-10% has a higher ratio of Cu^{2+}/Cu$^+$ than CuOx/TiO$_2$-2.5. The reducibility of CuOx NPs with different sizes was also measured by temperature-programmed reduction (TPR). As shown in **Figure 3.26**, for CuOx/TiO$_2$-0.25% the H$_2$ consumption is very low compared to CuOx/TiO$_2$-2.5% and to CuOx/TiO$_2$-10% with lager particle sizes, implying the low redox reactivity of the subnanometric CuOx species in CuOx/TiO$_2$-0.25%.[13] For CuOx/TiO$_2$-2.5%, a big sharp peak (**α** peak) can be observed in the TPR profile, which is associated to the reduction of small CuOx NPs of around 2 nm. In the case of CuOx/TiO$_2$-10%, two reduction peaks (**α** and **β** peak) can be observed, which can be ascribed to small CuOx

NPs and big CuOx NPs, respectively.[25] Considering that the H_2 consumption corresponding to the **β** peak is much larger than that for the **α** peak, it could be deduced that most CuOx NPs in CuOx/TiO$_2$-10% are big CuOx NPs, which is consistent with the STEM characterization.
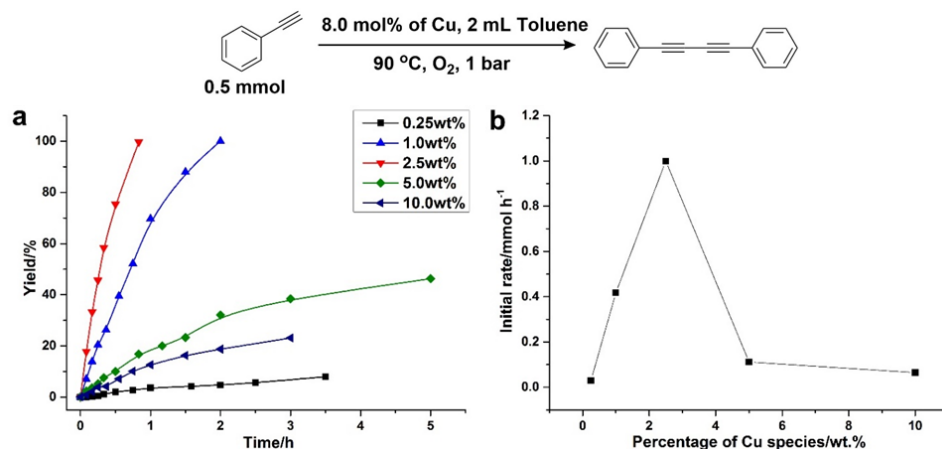
Figure 3.27. Kinetic studies of CuOx/TiO$_2$ samples with different sizes of CuOx NPs in the homo-coupling reaction.
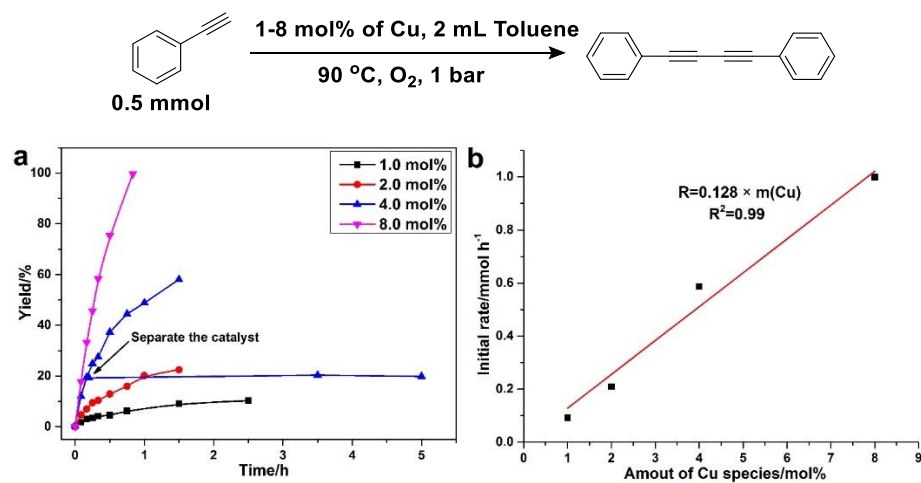
Figure 3.28. Kinetic studies of CuOx/TiO$_2$-2.5wt% sample in the homo-coupling reaction with different amount of catalyst.
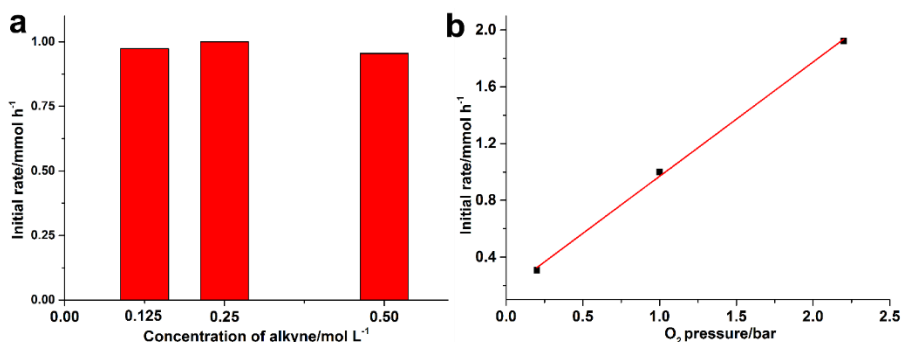
Figure 3.29. The initial reaction rate of oxidative coupling of phenylacetylene catalyzed by CuOx/TiO$_2$-2.5 (8 mol%) under different reaction conditions. (a) Different concentration of alkyne and (b) different O$_2$ pressure.
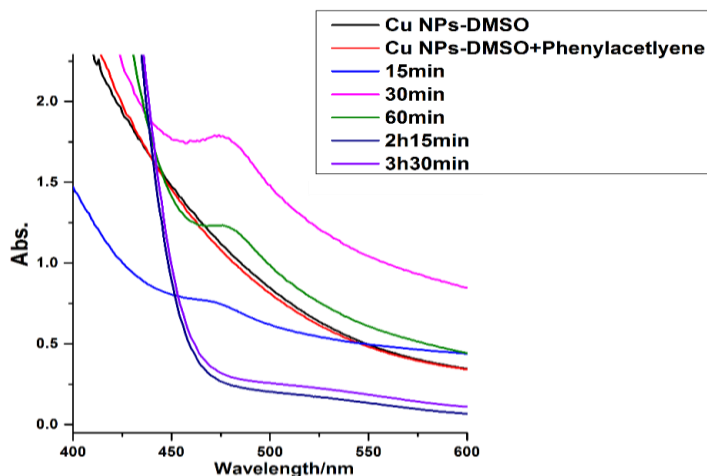
Figure 3.30. Following the homo-coupling reaction catalyzed by CuOx nanoparticles (CuOx-2.2) with UV-vis spectra. The amount of CuOx nanoparticles is 5 mol.%. The other reaction conditions are the same as those described in the main text.

3.4 Catalytic properties of supported CuOx NPs

The activities of CuOx/TiO$_2$ samples in the homo-coupling of phenylacetylene were measured under the experimental conditions described in the experimental section. As shown in **Figure 3.27a**, no induction period was observed and the activity of CuOx/TiO$_2$ samples is related with the sizes

of the CuOx NPs formed on TiO_2. CuOx/TiO_2-2.5% sample with CuOx NPs around 2 nm gives the best activity compared with smaller or larger CuOx NPs (see **Figure 3.27b**), and the reaction can be finished in 40 min when CuOx/TiO_2-2.5% is used as catalyst.

Combining the results on monodispersed and supported CuOx NPs, we can propose that the suitable size of CuOx NPs in CuOx/TiO_2-2.5% should be the reason accounting for its high activity. Furthermore, the size-dependent catalytic properties of CuOx NPs follow a similar trend on both monodispersed and supported NPs.

The activity CuOx/TiO_2-2.5% sample was also tested for homo-coupling of phenylacetylene using different amounts of Cu as the catalyst. As presented in **Figure 3.28a**, the reaction will boost once the catalyst is added into the reaction mixture, indicating that CuOx/TiO_2-2.5% sample can catalyze the reaction directly. When the catalyst is separated from the reaction mixture, the formation of the coupling product stops, indicating that the active Cu species are those supported on TiO_2 and the process is heterogeneous. The linear relationship between the initial reaction rate and amount of Cu species (shown in **Figure 3.28b**) also confirms that small CuOx NPs supported on TiO_2 are the active species for the oxidative coupling of alkynes.

As discussed previously, Cu clusters seem not to be active for the oxidative coupling of phenylacetylene. Theoretical calculations have shown that the activation energy of O_2 on Cu clusters is quite high,[13] which may explain the very low activity of Cu clusters. In the CuOx/TiO_2-0.25% catalyst, Cu exists as subnanometric species dispersed on TiO_2, namely supported Cu clusters. As can be seen in **Figure 3.27a**, CuOx/TiO_2-0.25% sample shows negligible activity and, in any case, the activity per Cu atom is much lower than that for CuOx/TiO_2-2.5% with CuOx NPs around 2 nm. On the other hand, when the size of CuOx NPs in CuOx/TiO_2 sample is larger than 5 nm, the activity drops dramatically, indicating that only CuOx NPs around 2 nm are active. It should be taken into account that, due to the stabilization effect of TiO_2 support and, specially, to the use of toluene instead of DMSO as solvent, large CuOx NPs ($\geq$ 5 nm) cannot undergo in situ transformation into smaller NPs during the oxidative coupling reaction, what results in their low activity. At this point, it has become clear that regardless how the CuOx NPs are obtained, a maximum

activity for the oxidative coupling of phenylacetylene occurs with CuOx NPs of ~2 nm. Thus, now we will attempt to explain the size-dependent activity of CuOx NPs for the oxidative coupling of alkynes.
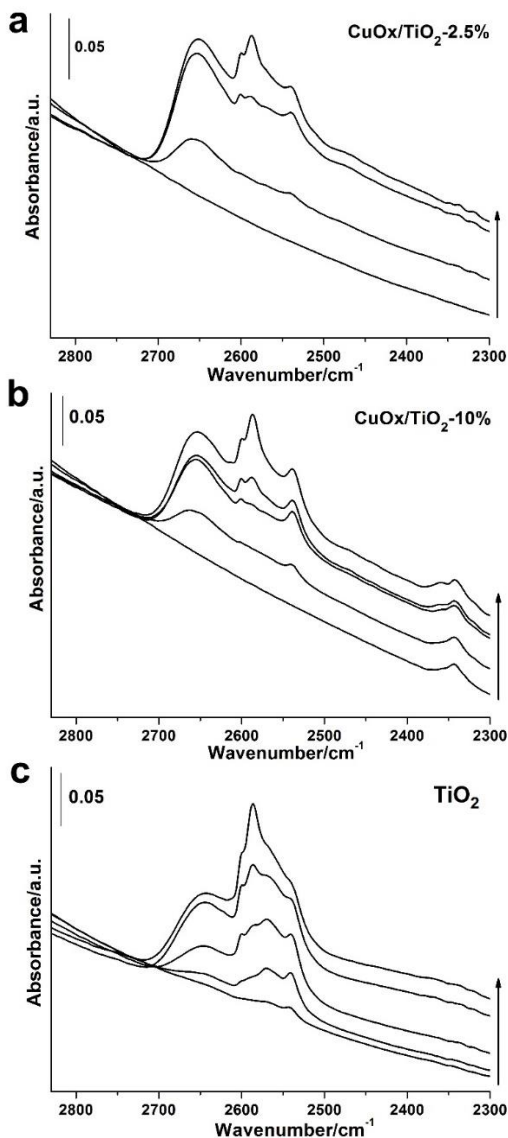
Figure 3.31. IR spectra of -OD formation on CuO_X/TiO_2 -2.5% (a), CuO_X/TiO_2-10% (b) and TiO_2 (c) samples after phenylacetlyene adsorption at 25ºC. In each figure, several spectrum were collected under different pressure

of phenylacetlyene.
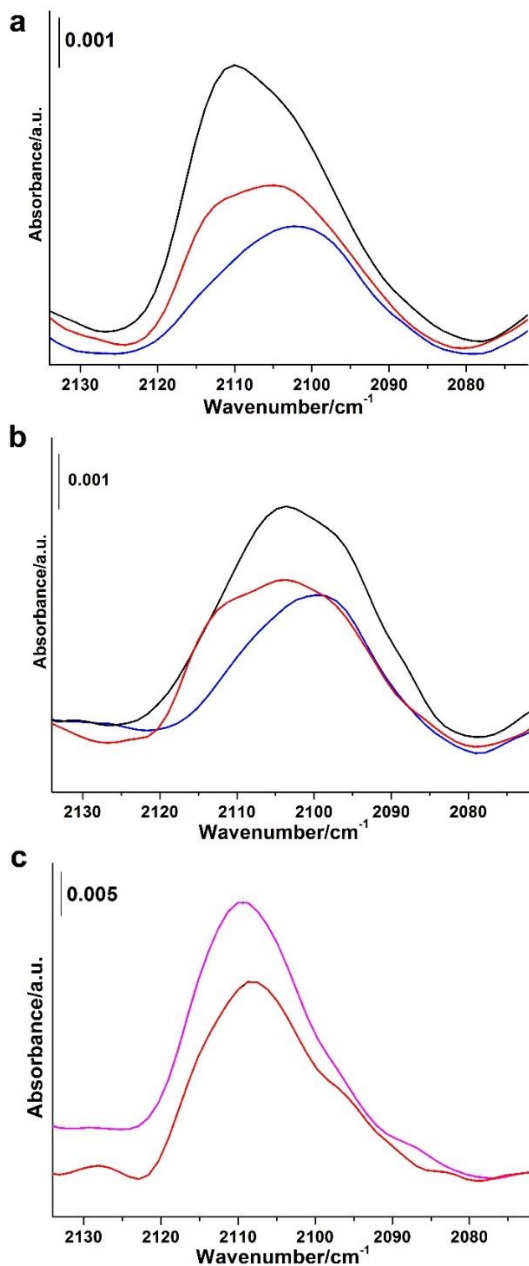
Figure 3.32. IR spectra in the C≡C stretching frequency IR region after phenylacetlyene adsorption at 25 ºC on CuO$_X$/TiO$_2$-2.5% (a), CuO$_X$/TiO$_2$-10%

(b) and TiO$_2$ (c) samples. In each figure, several spectrum were collected under different pressure of phenylacetlyene. The $-C\equiv C-$ stretching peaks locate at 2095$-$2110 cm^{-1}.
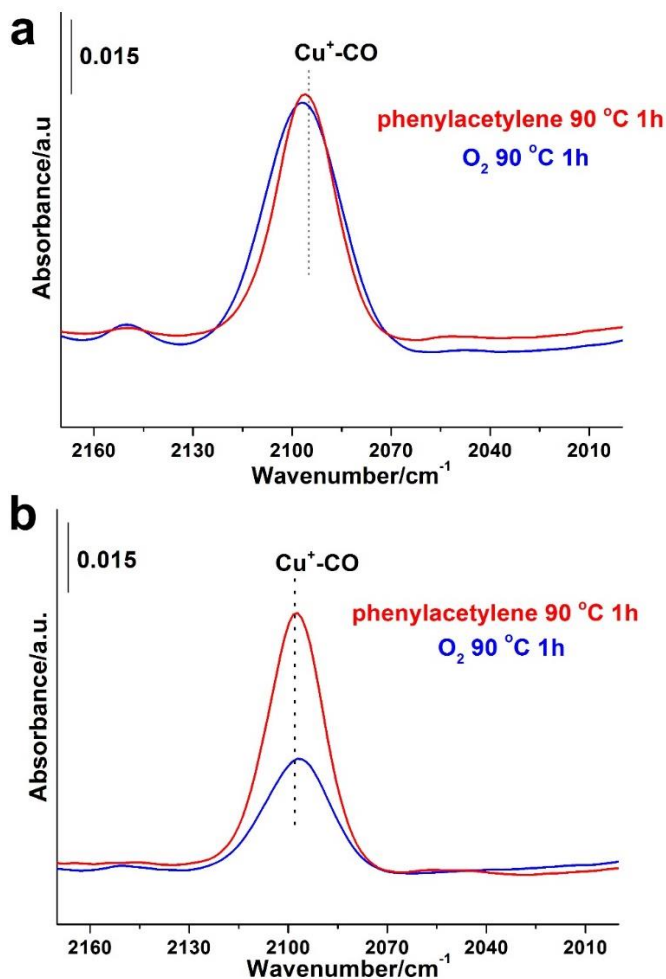
Figure 3.33. IR spectra of CO adsorption at 25 ºC on the CuO$_X$/TiO$_2$-2.5% (a) and CuO$_X$/TiO$_2$-10% (b) samples after phenylacetlyene adsorption at 90 ºC 1h and after subsequent introduction of O$_2$ at 90 ºC and 1h.
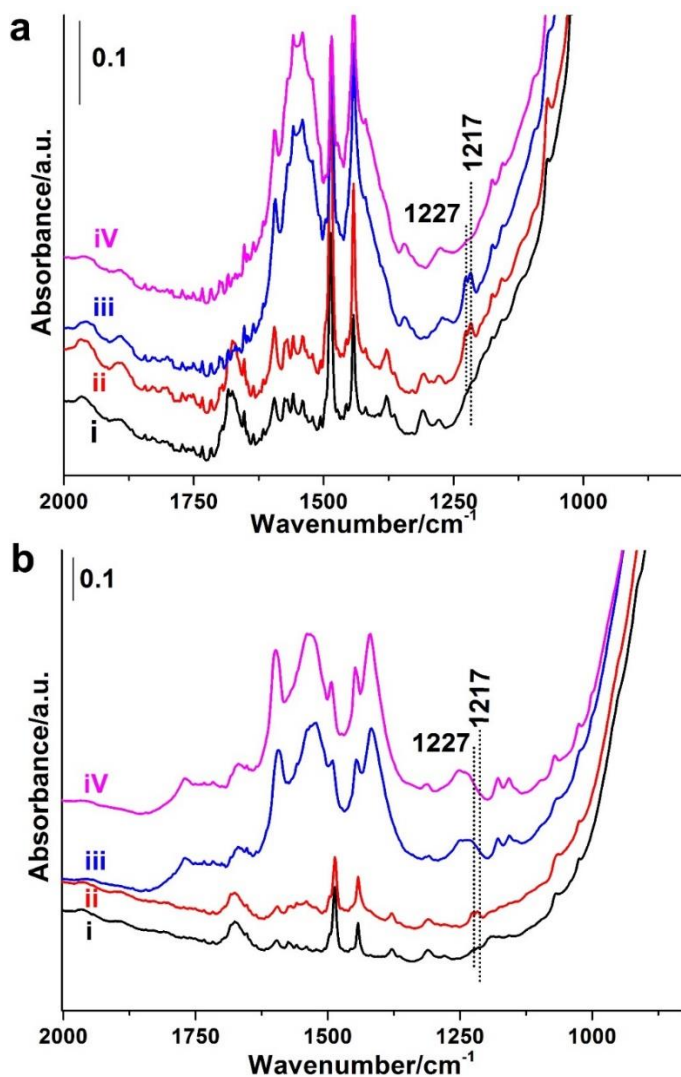
Figure 3.34. (a) In situ IR spectra on the CuO_X/TiO_2-2.5% sample in the presence of phenylacetlyene (6.5 mbar) (i) and after O_2 (30 mbar) co-adsorption at 25 ºC (ii), 90ºC (iii) and after evacuation at 10-2 mbar and 25 ºC (iv). (b) In situ IR spectra on the CuO_X/TiO_2-10% sample in the presence of phenylacetlyene (6.5 mbar) (i) and after O_2 (30 mbar) co-adsorption at 25 ºC (ii), 90 ºC (iii) and after evacuation at 10^{-2} mbar and 25 ºC (iv).

3.5 Kinetic and in situ spectroscopic studies

The global process for oxidative coupling of alkynes can be decomposed into the following elementary steps: activation of the C-H bond in the alkyne group, coupling reaction, O_2 activation and reaction of the adsorbed H with the activated O_2.[26] To find which one is the reaction controlling step, CuOx/TiO$_2$-2.5% was used as catalysts and the initial rate of the reaction was measured by keeping the O_2 pressure (1 bar) constant and changing the initial concentration of phenylacetylene. Results in **Figure 3.29** indicate that under these reaction conditions, the rate of the reaction does not depend on the concentration of alkyne, indicating that neither the phenylacetylene activation nor the homo-coupling can be the rate-controlling step. On the other hand, the initial rate of the reaction clearly increases when increasing the oxygen pressure while keeping the concentration of phenylacetylene constant. From the kinetic results, one should then conclude that the controlling step during the oxidative coupling of alkynes corresponds to O_2 activation, or to the reaction between activated O_2 and the abstracted hydrogen.

With respect to the molecular interaction of the reactants with the catalyst, the surface interaction of phenylacetylene was clearly seen from the UV-vis spectra of the alkyne adsorbed on the monodispersed CuOx NPs (see **Figure 3.30**). When phenylacetylene is interacted with CuOx NPs at room temperature, no obvious change occurs in the UV-vis spectra. However, when the system is heated to the reaction temperature (90 °C), a new peak at ~475 nm is observed that can be associated to the formation of C≡C-Cu bond, suggesting that the adsorption and dissociation of the C-H bond of phenylacetylene on the CuOx NPs has occurred.[27] After one hour, when the phenylacetylene has been consumed, the peak at ~475 nm disappears.

Alkyne activation on supported CuOx NPs has also been studied by in situ IR spectroscopy. When deuterated phenylacetylene is adsorbed on TiO$_2$, CuOx/TiO$_2$-2.5% (active sample) and CuOx/TiO$_2$-10% (non-active sample), a band corresponding to O-D bond has been identified in all samples at room temperature (see **Figure 3.31**). It was not possible to identify whether the -OD groups come from the TiO$_2$ support or from the CuO$_X$ NP, due to the fact that a fast isotopic scrambling with the -OH groups of the support can also occur. On the other hand, the formation of C≡C-Cu bond at the surface is consistent with

the presence of a rather asymmetric C≡C IR bond in both CuOx/TiO$_2$ samples (see **Figure 3.32**) when compared with that formed on pure TiO$_2$. The asymmetric vibration mode of C≡C bond in IR spectra can be due to the interaction of the Ph-C≡C-* adduct with surface copper sites on both CuOx/TiO$_2$-2.5% and CuOx/TiO$_2$-10%.[28] According to the data from UV-vis and IR spectra, C≡C-H activation really occur on the surface of the CuOx nanoparticles.

XPS results of CuOx/TiO$_2$-2.5% and CuOx/TiO$_2$-10% presented before showed that the chemical states of Cu species in the two samples are different, which may be a reason for their different catalytic activity. To further investigate the nature of the surface Cu species on CuOx/TiO$_2$-2.5% and CuOx/TiO$_2$-10% in the presence of phenylacetylene and O$_2$, CO has been used as probe molecule for in situ IR spectroscopy. Indeed, CO is very sensitive to Cu(I) species while Cu(II) cannot be detected by CO even at low temperature.[29,30] As depicted in **Figure 3.33**, Cu(I) has been observed on both samples after the adsorption of phenylacetylene at 90 °C for 1 hour due to the surface reduction reaction. After O$_2$ addition at 90 °C, interestingly, the amount of Cu(I) remains stable on the CuOx/TiO$_2$-2.5% sample while the amount of Cu(I) clearly decreases on CuOx/TiO$_2$-10% sample as a result of re-oxidation of Cu(I) into Cu(II) by O$_2$. In other words, these results indicate that the type of interaction between O$_2$ and the CuOx NPs and the nature of the active oxygen species are different in the two samples. Therefore, since the rate-controlling step in the oxidative coupling of alkynes is O$_2$ activation, the observed size effects of CuOx NPs on the catalytic properties for oxidative coupling of alkynes should be related to their influence on the activation of O$_2$.

3.6 Relation between particle size of CuOx and O$_2$ activation
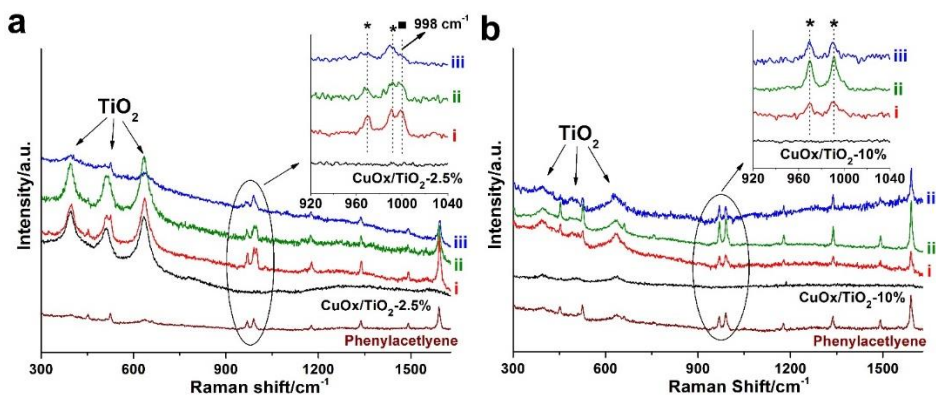
Figure 3.35. In situ Raman spectra of CuOx/TiO$_2$-2.5% (a) and CuOx/TiO$_2$-10% (b) in O$_2$ atmosphere after pre-treatments in reactant mixture of phenylacetylene and O$_2$. In (a) and (b), spectra were obtained at different temperature. (i) 25 ºC, (ii) 60 ºC and (iii) 90 ºC. For comparison, the fresh CuOx/TiO$_2$ samples and phenylacetylene adsorbed on CuOx/TiO$_2$ are also presented.

To further identify the nature of surface species generated under reaction conditions, in situ Raman and in situ IR studies have been performed on both CuOx/TiO$_2$-2.5% and CuOx/TiO$_2$-10% samples. **Figure 3.35a** shows the in situ Raman spectra acquired on the active CuOx/TiO$_2$-2.5% sample in the presence of phenylacetylene and O$_2$ at different reaction temperatures. A Raman band at 998 cm^{-1}, ascribed to peroxo species, is clearly detected at 25 ºC, 60 ºC and at the reaction temperature used in the catalytic studies (90 ºC).[31] No peroxo species have been detected on pure TiO$_2$. Notice that a decrease in the intensity of the 998 cm^{-1} band at 90 ºC occurs, which could be due to thermal desorption or to dissociation into atomic oxygen, and regeneration of surface lattice oxygen species. Moreover, peroxo species (IR active vibration mode at 1227 and 1217 cm^{-1}) have also been detected by in situ IR studies performed at different reaction temperatures (**Figure 3.34a**).[32] These results indicate that peroxo species can be formed on the surface of CuOx/TiO$_2$-2.5 sample. In opposite, on the much less active CuOx/TiO$_2$-10%

sample, peroxo species have not been observed during the in situ Raman studies (**Figure 3.35b**), and peroxo species (1227 and 1217 cm^{-1}) are detected by IR spectroscopy only at 25 ºC and disappear after increasing temperatures to 60 ºC (**Figure 3.34b**). Based on these data, it can be speculated that oxygen as peroxo species is preferentially stabilized on the CuO_X/TiO_2-2.5% sample. In contrast, the peroxo species and less favorable on $CuOx/TiO_2$-10% at the reaction temperature. Considering the high reactivity of peroxo species in selective oxidation reaction, the formation of peroxo species could be the reason accounting for the higher activity of $CuOx/TiO_2$-2.5%.[33]
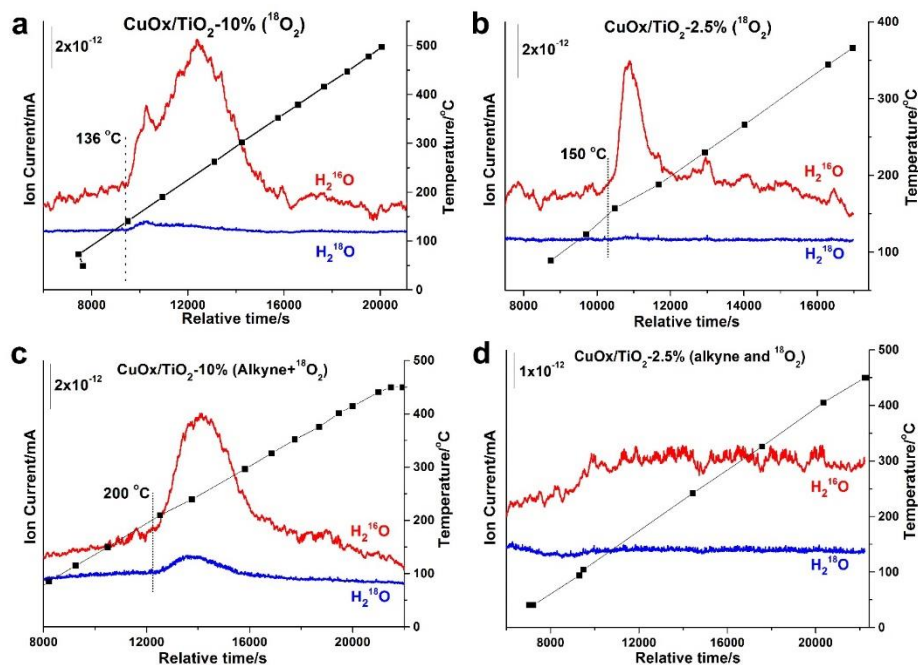
Figure 3.36. TPR profile on $^{18}O_2$ oxidized CuO_X/TiO_2-10% and CuO_X/TiO_2-2.5% samples (a, b), and after in situ reaction in the presence of phenylacetlyene and $^{18}O_2$ (c, d).

It has been presented in the literature that oxygen activation can also be performed with the help of surface lattice defects.[34] Since we cannot observe surface adsorbed active oxygen species on $CuOx/TiO_2$-10%, the activation of O_2 on $CuOx/TiO_2$-10% may be performed through the re-oxidation of Cu(I) species on big CuOx NPs as observed in the IR spectra (see **Figure 3.33**). In

order to distinguish whether the different reactivity is associated to peroxo species or lattice oxygen species, $^{18}O_2$ has been used for the in situ spectroscopic studies. By analyzing the composition of water ($H_2^{16}O$ or $H_2^{18}O$) formed after reaction by H_2 titration of the catalyst (TPR), it could be distinguished whether the O in the water comes from the $^{18}O_2$ feed or from the lattice oxygen of $CuOx/TiO_2$ catalyst (the corresponding TPR profile are shown in **Figure 3.36**). For comparison, the fresh $CuOx/TiO_2$-2.5% and $CuOx/TiO_2$-10% were oxidized by $^{18}O_2$ at 90 ºC and then reduced by H_2. The TPR profile of the $^{18}O_2$ oxidized $CuOx/TiO_2$-10% sample shows both $H_2^{16}O$ and $H_2^{18}O$ formation with an onset temperature of 136 ºC in both cases. $H_2^{16}O$ formation takes place in a very broad temperature range of 136-355 ºC, corresponding to lattice oxygen species of different reactivity. A small amount of $H_2^{18}O$ is formed, indicating the oxygen exchange between $^{18}O2$ and the CuOx NPs in $CuOx/TiO_2$-10% (see **Figure 3.36a**). In opposite the TPR profile of the $^{18}O_2$ oxidized $CuOx/TiO_2$-2.5% sample, shows only one peak corresponding to $H_2^{16}O$ with an onset temperature of 150 ºC, corresponding to lattice oxygen species. Interestingly $H_2^{18}O$ is not detected in this sample, indicating that no oxygen exchange between the O_2 and the CuOx lattice takes place on $CuOx/TiO_2$-2.5% (**Figure 3.36b**).

When the two samples have been exposed to a mixture of phenylacetylene and $^{18}O_2$ at reaction conditions (90 ºC, 1h), different TPR profiles have been observed in both cases. On the $CuOx/TiO_2$-2.5% sample, neither $H_2^{16}O$ nor $H_2^{18}O$ are detected (see **Figure 3.36d**). It means, the surface has been reduced under reaction conditions, but it is not re-oxidized by $^{18}O_2$. With $CuOx/TiO_2$-10% sample, both $H_2^{16}O$ and $H_2^{18}O$ are observed with an onset temperature of 203 ºC (**Figure 3.36c**), which indicates the surface has been partially reduced and re-oxidized by $^{18}O_2$ under reaction conditions.

From the above presented results combined with the in situ Raman and IR studies, we speculate that oxygen is activated by CuOx NPs in the $CuOx/TiO_2$-2.5% sample as peroxo species on the catalyst surface. Meanwhile, in the case of $CuOx/TiO_2$-10% sample, O_2 dissociation occurs, transforming into lattice oxygen species. This hypothesis would also be supported by the IR results where the catalysts surface has been titrated, using CO as probe molecule, after phenylacetylene adsorption at 90 ºC and after subsequent O_2

insertion at the same temperature (see **Figure 3.33**).

Thus we can conclude that the different reactivity observed between the CuOx/TiO$_2$-2.5% and CuOx/TiO$_2$-10% samples is related to a different nature of the oxygen species on the catalyst surface. Stabilization of molecular oxygen as peroxo species or further dissociation into atomic oxygen and generation of lattice oxygen species is strongly related to the different particle size of CuOx NP in both samples. On CuOx NPs around 2 nm, O$_2$ molecules are activated to form peroxo species, which is more active than surface lattice oxygen formed on big CuOx NPs in CuOx/TiO$_2$-10%.[35,36] As a consequence, CuOx/TiO$_2$-2.5% with ~2 nm particle size shows much higher activity than CuOx/TiO$_2$-10% with ~10 nm particle size in the oxidative coupling of alkynes. Notice that this is the case regardless that monodispersed isolated CuOx NPs or supported NPs are used as catalysts.

3.7 Proposed reaction mechanism
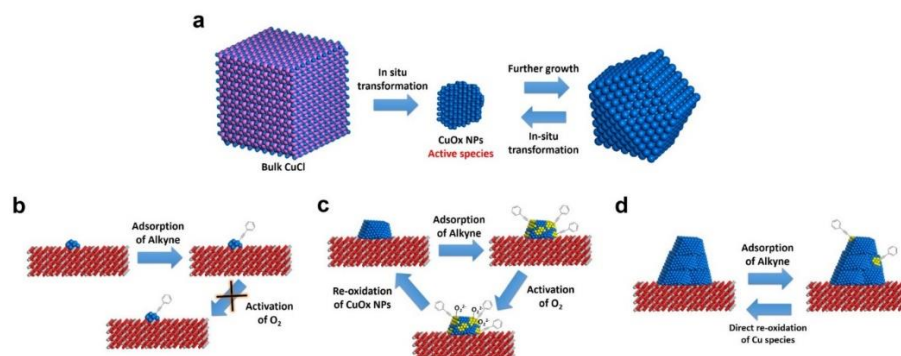
Figure 3.37. (a) Schematic illustration of the dynamic transformation of monodispersed Cu species. Size-dependent catalytic mechanism of supported CuOx NPs, (b) CuOx/TiO$_2$-0.25%, (c) CuOx/TiO$_2$-2.5% and (d) CuOx/TiO$_2$-10%.

Based on the above results and discussions, a proposed reaction mechanism for CuOx NPs with different sizes is shown in **Figure 3.37**. For monodispersed Cu species (see **Figure 3.37a**), small CuOx NPs around 2 nm are formed from the in situ transformation of bulk CuCl, as a result of which an induction period can be observed. These in situ formed small CuOx NPs

are the active species for the oxidative coupling of alkynes when DMSO was chosen as solvent. When a large amount of CuCl is used as the catalyst, small CuOx NPs will further grow into big CuOx NPs around 5 nm, which can transform back with time to small CuOx NPs in the oxidative coupling of alkynes. In the case of supported CuOx NPs (see **Figure 3.37b** to **Figure 3.37d**), the activity will also be dependent on the size of CuOx NPs, being the dynamic transformation between different sizes of CuOx NPs restricted under the reaction condition used here. For Cu clusters supported on TiO_2, according to theoretical calculation, O_2 activation is not favorable, resulting in their very low activity. When the size of CuOx NPs increases to around 2 nm, O_2 can be activated into active peroxo species on the surface of $CuOx/TiO_2$-2.5%, which can serve as the active intermediate for the oxidative coupling of alkynes. However, a further increase in the size of CuOx NPs will change the nature of the oxygen species formed. O_2 will form lattice oxygen species after activation by large CuOx NPs, which is less active for the oxidative coupling reaction.
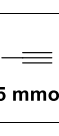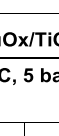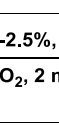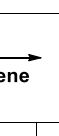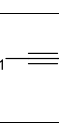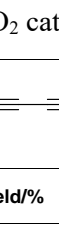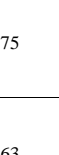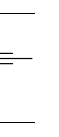
3.8 Synthesis of unsymmetric 1,3-diynes with CuOx/TiO$_2$ catalyst

Compared with oxidative homo-coupling of alkynes, the coupling reaction between two different alkyne molecules is more difficult due to their different reactivity. The yield of unsymmetric 1,3-diynes is much lower than the oxidative homo-coupling of alkynes as a result of the competitive reaction pathways between homo-coupling and hetero-coupling reactions.[37] Therefore, in some cases, only trace amount of 1,3-diynes can be obtained when Cu-based catalyst is used, even though one alkyne substrate is in a large excess (the molar ratio of two alkynes is 5.).[38,39] Since the CuOx NPs supported TiO_2 in the $CuOx/TiO_2$-2.5% sample can catalyze the oxidative coupling of alkynes directly, the oxidative hetero-coupling of different alkynes could be processed smoothly with higher yield of unsymmetric 1,3-diynes. The catalytic results in the synthesis of unsymmetric 1,3-diynes with $CuOx/TiO_2$ catalyst are shown in **Table 2**. It should be noted that, in this work, the molar ratio of two alkynes is 2. And higher temperature and O_2 pressure is used to accelerate the hetero-coupling between different alkynes. As can be seen in **Table 2**, unsymmetric 1,3-diynes can be obtained with

moderate to good yield, ranging from 61% to 92%. The coupling between phenylacetylene and hexyne can be realized with 61% yield although the amount of phenylacetylene is only twice that of hexyne. It should be noticed that only trace amount of the unsymmetric coupling product was obtained in previous work (but five times excess of hexyne).[40] These results suggest that supported small CuOx NPs can work as efficient catalyst for synthesis of unsymmetric 1,3-diynes.

Table 2. Synthesis of unsymmetric 1,3-diynes with CuOx/TiO$_2$ catalyst[a]

Entry	R$_1$ ═	R$_2$ ═	Yield/%
1			74
2			75
3			63
4			32
5			38
6			65
7			51

[a] 40 μL dodecane was added as internal standard and the reaction time was 8 h.

The yield is calculated based on $R_2 \!\!-\!\!\!\equiv$.

4. Conclusions

In this work, a facile method for synthesis of monodispersed small CuOx NPs has been presented. Through kinetic analysis and following the dynamic transformation of Cu species, small CuOx NPs around 2 nm are proved to be the active species in Cu-catalyzed oxidative coupling of alkynes. Furthermore, the size-dependent catalytic properties of supported CuOx NPs on TiO_2 was also studied. Similar activity trend is obtained on supported CuOx NPs and monodispersed CuOx NPs. By spectroscopic characterizations, it has been clarified that the nature of the active oxygen species are dependent on the size of CuOx NPs. Active peroxo species are preferentially formed on small CuOx NPs (~2 nm) while O_2 prefers to form lattice oxygen species after dissociation on large CuOx NPs (~10 nm). Therefore, the catalytic properties in oxidative coupling of alkynes are greatly dependent on the size of CuOx. Finally, monodispersed CuOx NPs are able to catalyze the unsymmetric coupling of alkynes.

References

(1) Kuo, C.-H.; Huang, M. H. *Nano Today* **2010**, *5*, 106-116.

(2) Zhang, Q.; Zhang, K.; Xu, D.; Yang, G.; Huang, H.; Nie, F.; Liu, C.; Yang, S. *Prog. Mater. Sci.* **2014**, *60*, 208-337.

(3) Yin, M.; Wu, C. K.; Lou, Y.; Burda, C.; Koberstein, J. T.; Zhu, Y.; O'Brien, S. *J. Am. Chem. Soc.* **2005**, *127*, 9506-9511.

(4) Hua, Q.; Cao, T.; Gu, X. K.; Lu, J.; Jiang, Z.; Pan, X.; Luo, L.; Li, W. X.; Huang, W. *Angew. Chem. Int. Ed.* **2014**, *53*, 4856-4861.

(5) Liu, Y.; Shi, J.; Peng, Q.; Li, Y. *Chem. Eur. J.* **2013**, *19*, 4319-4326.

(6) Allen, S. E.; Walvoord, R. R.; Padilla-Salinas, R.; Kozlowski, M. C. *Chem. Rev.* **2013**, *113*, 6234-6458.

(7) Wendlandt, A. E.; Suess, A. M.; Stahl, S. S. *Angew. Chem. Int. Ed.* **2011**, *50*, 11062-11087.

(8) Haack, P.; Limberg, C. *Angew. Chem. Int. Ed.* **2014**, *53*, 4282-4293.

(9) Zhang, G.; Yi, H.; Zhang, G.; Deng, Y.; Bai, R.; Zhang, H.; Miller, J. T.;

Kropf, A. J.; Bunel, E. E.; Lei, A. *J. Am. Chem. Soc.* **2014**, *136*, 924-926.

(10) Oliver-Messeguer, J.; Liu, L.; Garcia-Garcia, S.; Canos-Gimenez, C.; Dominguez, I.; Gavara, R.; Domenech-Carbo, A.; Concepcion, P.; Leyva-Perez, A.; Corma, A. *J. Am. Chem. Soc.* **2015**, *137*, 3894-3900.

(11) Chen, P.; Solomon, E. I. *Proc. Natl. Acad. Sci. USA* **2004**, *101*, 13105-13110.

(12) Solomon, E. I.; Chen, P.; Metz, M.; Lee, S.-K.; Palmer, A. E. *Angew. Chem. Int. Ed.* **2001**, *40*, 4570-4590.

(13) Fernández, E.; Boronat, M.; Corma, A. *J. Phys. Chem. C* **2015**, *119*, 19832-19846.

(14) Vilar-Vidal, N.; Rivas, J.; López-Quintela, M. A. *ACS Catal.* **2012**, *2*, 1693-1697.

(15) Zou, W.; Liu, L.; Zhang, L.; Li, L.; Cao, Y.; Wang, X.; Tang, C.; Gao, F.; Dong, L. *Appl. Catal. A: Gen.* **2015**, *505*, 334-343.

(16) Bao, H.; Zhang, W.; Hua, Q.; Jiang, Z.; Yang, J.; Huang, W. *Angew. Chem. Int. Ed.* **2011**, *50*, 12294-12298.

(17) B. R. Strohmeier, D. E. Leyden, R. S. Field, D. M. Hercules, J. Catal., 94, 1985, 514-530.

(18) Grünert, W.; Hayes, N.W.; Joyner, R.W.; Shpiro, E.S.; Rafiq, M.; Siddiqui, H.; Baeva, G. *J. Phys. Chem.*, **1994**, *98*, 10832-10846.

(19) Vilar-Vidal, N.; Blanco, M. C.; López-Quintela, M. A.; Rivas, J.; Serra, C. *J. Phys. Chem. C*, **2010**, *114*, 15924-15930.

(20) Göbel, A.; Ruf, T.; Cardona, M.; Lin, C. T. *Phys. B: Conden. Matter.* **1996**, *219-220*, 511-513.

(21) Xu, J. F.; Ji, W.; Shen, Z. X.; Li, W. S.; Tang, S. H.; Ye, X. R.; Jia, D. Z.; Xin, X. Q. *J. Raman Spectrosc. 30*, **1999**, 413-415.

(22) Kliche, G.; Popovic, Z. V. *Phys. Rew. B.*, *42*, **1990**, 10060-10066.

(23) Adimurthy, S., Malakar, C. C., Beifuss, U. *J. Org. Chem.*, **2009**, *74*, 5648-5651.

(24) Oishi, T., Katayama, T., Yamaguchi, K., Mizuno, N. *Chem. Eur. J.*, **2009**, *15*, 7539-7542.

(25) Chary, K. V.; Sagar, G. V.; Naresh, D.; Seela, K. K.; Sridhar, B. *J. Phys. Chem. B* **2005**, *109*, 9437-9444.

(26) Fomina, L.; Vazquez, B.; Tkatchouk, E.; Fomine, S. *Tetrahedron* **2002**,

58, 6741-6747.

(27)   Sagadevan, A.; Ragupathi, A.; Lin, C.-C.; Hwu, J. R.; Hwang, K. C. *Green Chem.* **2015**, *17*, 1113-1119.

(28)   Maity, P.; Takano, S.; Yamazoe, S.; Wakabayashi, T.; Tsukuda, T. *J. Am. Chem. Soc.* **2013**, *135*, 9450-9457.

(29)   Hadjiivanov, K. I.; Kantcheva, M. M.; Klissurski, D. G. *J. Chem. Soc., Faraday Trans.*, **1996**, *92*, 4595-4600.

(30)   Kannan, S.; Venkov, T.; Hadjiivanov, K.; Knözinger, H. *Langmuir*, **2004**, *20*, 730-736.

(31)   Guzman, J.; Carrettin, S.; Corma, A. *J. Am. Chem. Soc.* **2005**, *127*, 3286-3287.

(32)   Root, D. E.; Mahroof-Tahir, M.; Karlin, K. D.; Solomon, E. I. *Inorg. Chem.* **1998**, *37*, 4838-4848.

(33)   *Metal-Oxo and Metal-Peroxo Species in Catalytic Oxidations*; Meunier, B., Ed.; Springer: Berlin Heidelberg, 2000; p 179-211.

(34)   Palmer, M. S.; Neurock, M.; Olken, M. M. *J. Am. Chem. Soc.* **2002**, *124*, 8452-8461.

(35)   Wu, Z.; Li, M.; Howe, J.; Meyer, H. M., III; Overbury, S. H. *Langmuir* **2010**, *26*, 16595-16605.

(36)   Huang, M.; Fabris, S. *Phys. Rev. B* **2007**, *75*, 081404.

(37)   Peng, H.; Xi, Y.; Ronaghi, N.; Dong, B.; Akhmedov, N. G.; Shi, X. *J. Am. Chem. Soc.* **2014**, *136*, 13174-13177.

(38)   Yin, W.; He, C.; Chen, M.; Zhang, H.; Lei, A. *Org. Lett.* **2009**, *11*, 709-712.

(39)   Siemsen, P.; Livingston, R. C.; Diederich, F. *Angew. Chem. Int. Ed.* **2000**, *39*, 2632-2657.

(40)   Wang, D.; Li, J.; Li, N.; Gao, T.; Hou, S.; Chen, B. *Green Chem.* **2010**, *12*, 45-48.

Chapter 4

Comparative study on the catalytic behavior of supported single Pt atoms, clusters and nanoparticles
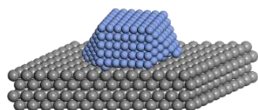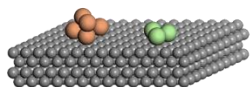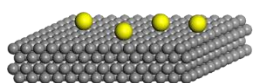
Hydrogenation of $-NO_2$

Hydrogenation of $C=C$

CO oxidation

Oxidation of alcohol

Photocatalysis

1. Introduction

Heterogeneous Single-atom catalysts have attracted tremendous attention in the field of catalysis in recent years and it has been shown in some reactions that single-atom catalysts show superior catalytic performance than the conventional nanoparticulate catalysts.[1] The recent progress made in this direction has gained more knowledge for understanding catalysis at atomic level.[2] By decreasing the size of metal catalysts down to atomically species, the utilization efficiency of metal can be maximized and more importantly, unique catalytic behavior may appear associated with those atomically dispersed metal catalysts.[3]

However, there are still some arguments on the role of single atoms and their intrinsic activity in the catalytic processes. For instance, Pt single atoms supported on Al_2O_3, FeOx, TiO_2 and CeO_2 are reported to be more active than Pt nanoparticles for CO oxidation, while in some other works, Pt atoms supported on zeolites or metal oxides are claimed to be less active than Pt nanoparticles.[4-7] Similar issues have also been reported with single-atom Au catalysts for CO oxidation. Singly dispersed Au atoms have been reported as efficient catalyst for CO oxidation,[8,9] while in some other works it has been shown that Au nanoclusters and nanoparticles supported on CeO_2 are much more active than singly dispersed Au atoms.[10,11] Nevertheless, singly dispersed Pt and Pd atoms on various supports have been reported as active catalysts for hydrogenation of nitroarenes, olefins and ketones, photocatalytic H_2 evolution reactions.[12-15] However, there is also some work showing that single Pd atoms supported on FeO_x show no activity in hydrogenation of alkenes while Pd clusters and nanoparticles on the same support are active.[16]

In most of the previous works, the catalytic performance of single atoms is usually compared with nanoparticulate catalysts, without the involvement of metal clusters. As a transition state between single atoms and nanoparticles, metal clusters show distinct electronic and geometric structures compared to the other two entities.[17-19] It has been shown in some examples that, only subnanometric metal clusters can catalyze some reactions while neither their single-atom nor nanoparticulate counterparts are active.[20-22] Therefore, it is necessary to study the size effect on catalysis with direct comparison of the catalytic performance of single atoms, clusters and nanoparticles for a global

understanding on the size-reactivity relationships.

Besides, in some of the previous works, single-atom catalysts and the nanoparticulate counterpart are prepared by different methodologies, which may bring uncertain factors into the studies for the comparison of their catalytic properties, especially when considering the complexity of heterogeneous metal catalysts.[23,24] Therefore, for a fair comparative study, the model catalysts should be better prepared in the same method and the particle size of metal species is controlled by the synthesis parameters. Nevertheless, it has been observed in several systems that, atomically dispersed metal species can occur dynamic structural transformation under reaction conditions.[25] Therefore, when studying the catalytic behavior of single-atom catalysts, it is necessary to follow the evolution of Pt species under reaction conditions. Taking into account of the well-established metal-support interaction for nanoparticulate metal catalysts, the metal-support interaction for single-atom catalysts should also be paid attention when comparing their reactivity with metal clusters and nanoparticles.

In this work, we have prepared a series of supported Pt catalysts by the same method with different particle size and post-treatments, ranging from singly dispersed atoms to clusters to nanoparticles on different supports (TiO$_2$, Al$_2$O$_3$ and CeO$_2$), as model catalysts with high comparability. Their catalytic performance for selective hydrogenation and CO oxidation have been tested and it is found that, Pt clusters and nanoparticles show obviously higher activity than Pt single atoms. Furthermore, we have observed the structural transformation of single Pt atoms under reaction conditions also depends on the support, making the situation for evaluating the catalytic properties of different metal entities (single atoms, clusters and nanoparticles) more complicated.

2. Experiments
2.1 Synthesis of different types of Pt species on various supports

TiO$_2$ (nanopowder, from Aldrich), Al$_2$O$_3$ (nanopowder, from NanoActive Corp.) and nanosized CeO$_2$ were used as the support to prepare supported Pt catalysts, by conventional wet impregnation.

2 g of solid support was dispersed in 50 mL aqueous solution of H$_2$PtCl$_6$ (containing certain amount of Pt, determined by the loading of Pt in the final catalyst) under rigorous stirring. After 2 h of stirring at room temperature, water

was removed by rotavapor. The obtained solid was dried at 60 oC over night and then calcined in flow air at 450 oC for 3 h, resulting the formation of singly dispersed Pt atoms on Al_2O_3, TiO_2 and CeO_2. Supported Pt catalysts with clusters and nanoparticles were prepared by reducing the single-atom Pt catalysts at different temperature by H2, as indicated later in the results and discussion section.

2.2 Characterization on the Pt catalysts

Samples for electron microscopy studies were prepared by dropping the suspension of the powder catalyst using ethanol as the solvent directly onto holey-carbon coated Cu grids. The measurements were performed in a JEOL 2100F microscope operating at 200 kV both in transmission (TEM) and scanning-transmission modes (STEM). STEM images were obtained using a High Angle Annular Dark Field detector (HAADF), which allows Z-contrast imaging. High-resolution STEM measurement was performed on FET Titan low-base microscope at 300 kV equipped with a Cs probe corrector, a monochromator and an ultrabright X-FEG electron source. The convergence angle was 25 mrad and the inner and outer angles for HAADF imaging were 70 and 200 mrad, respectively.

2.3 Catalytic studies on the Pt catalysts
2.3.1　Hydrogenation of 3-nitrostyrene

The hydrogenation of 3-nitrostyrene was performed in batch reactor. A certain amount of solid catalyst (10 mg or 20 mg), 0.5 mmol of 3-nitrostyrene, 50 µL of dodecane as internal standard, 2 mL of toluene as solvent was placed in the batch reactor. Then the reactor was purged with H_2 for several times. The reaction was performed at 40 or 50 ºC with 3 bar of H_2. 50 µL of reaction mixture was taken out of the reactor at different reaction time and analyzed by GC with FID detector.

2.3.2　Hydrogenation of styrene

The hydrogenation of styrene was performed in batch reactor. A certain amount of solid Pt/Al_2O_3 catalyst (10 mg), 1.0 mmol of styrene, 50 µL of hexadodecane as internal standard, 2 mL of toluene as solvent was placed in the batch reactor. Then the reactor was purged with H_2 for several times. The reaction was

performed at 50 $^{\circ}$C with 3 bar of H$_2$. 50 µL of reaction mixture was taken out of the reactor at different reaction time and analyzed by GC with FID detector.

2.3.3   Oxidation of benzyl alcohol

The oxidation of CO was performed in a fix-bed reactor. 120 mg of solid catalyst was used for each test. The feed gas was 2% of CO and 1% of O$_2$ in He. The total flow was 85 mL/min. The product was analyzed by gas chromatograph with thermal conductivity detector.

2.3.4   Oxidation of benzyl alcohol

The oxidation of benzyl alcohol was performed in batch reactor. A certain amount of solid Pt/CeO$_2$ catalyst (50 mg), 1.0 mmol of styrene, 2 mL of toluene as solvent was placed in the batch reactor. Then the reactor was purged with O$_2$ for several times. The reaction was performed at 80 $^{\circ}$C with 7 bar of O$_2$. 50 µL of reaction mixture was taken out of the reactor at different reaction time and analyzed by GC with FID detector.

2.3.5   Photocatalytic H$_2$ evolution with Pt/TiO$_2$ catalysts

The photocatalyst powder (25 mg) was dispersed in a water/ethanol mixture (1:1 v/v, 25 mL) by sonication for 15 min. The resulting suspension was then transferred to a quartz cell (volume $\approx$ 50 mL, equipped with a gas inlet valve, a gas outlet valve and a pressure gauge) and purged with argon (5 mL/min for 10 min). Finally, the cell was pressurized with argon (1.5 bar) and tightly closed. The suspension was stirred at 500 rpm and irradiated with a medium pressure Hg lamp (125 W, irradiation intensity$\approx$ 1.5 kW/m^2).

3. Results and Discussions

3.1 Selective hydrogenation of 3-nitrostyrene with Pt single atoms, clusters and nanoparticles

Firstly, we have prepared a series of Pt/TiO$_2$ catalysts by conventional wetness impregnation (see experimental section for details) and the size of Pt species supported on TiO$_2$ can be controlled by the Pt loading and the treatments in the preparation procedure. As shown in **Figure 4.1a**, Pt single atoms supported on TiO$_2$ (named as 0.2%Pt/TiO$_2$-SA with 0.2 wt% of Pt) can be directly observed by high-resolution scanning electron microscopy. After reduction by H$_2$, those singly dispersed Pt atoms agglomerated into Pt nanoparticles (see **Figure 4.1f**). In order to obtain subnanometric Pt clusters on

TiO$_2$, the loading of Pt has to be decreased to ca. 0.03 wt%, and then Pt clusters of ca. 0.5-1.0 nm can be formed on TiO$_2$ (see **Figure 4.1d**). More images of the Pt/TiO$_2$ samples with different sizes of Pt species are presented in **Figure 4.2** to **Figure 4.4**. These STEM images suggest that Pt clusters and nanoparticles with fine dispersion and narrow size distributions can be generated on TiO$_2$. Therefore, we can use these Pt/TiO$_2$ catalysts as model catalyst to study the size effect on the catalytic properties.
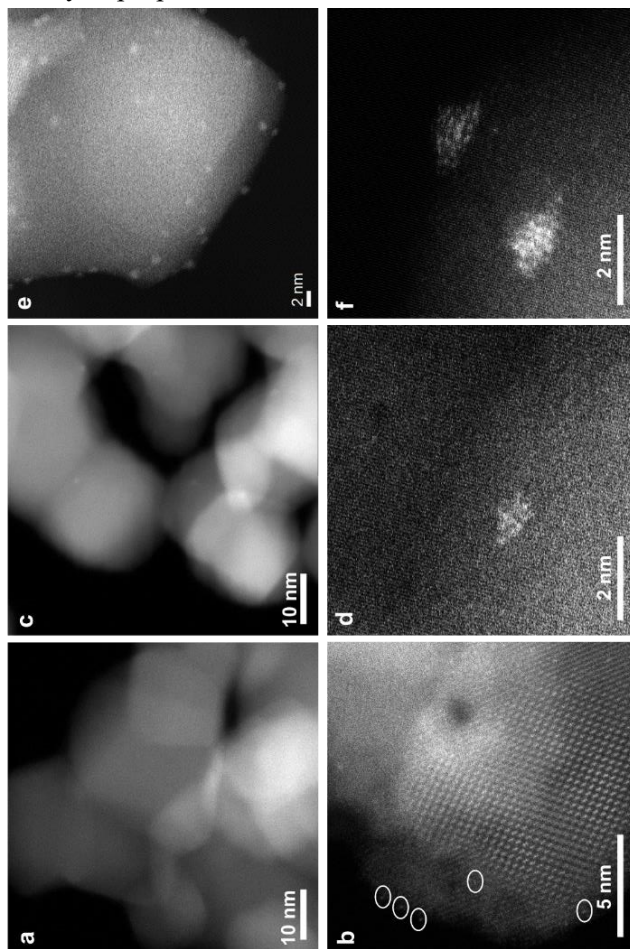
Figure 4.1. Characterization of Pt/TiO$_2$ catalysts with single atoms, clusters and nanoparticles. (a, b) 0.2%Pt/TiO$_2$-SA sample containing singly dispersed Pt atoms. (c, d) 0.03%Pt/TiO$_2$-450H$_2$ sample containing subnanometric Pt clusters. (e, f) 0.2%Pt/TiO$_2$-450H$_2$ sample containing Pt nanoparticles.
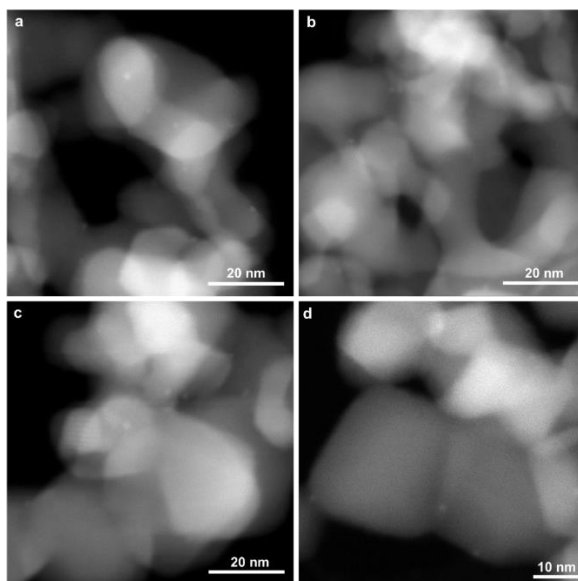
Figure 4.2. STEM images of 0.03%Pt/TiO$_2$-450H$_2$, showing the presence of Pt clusters supported on TiO$_2$.
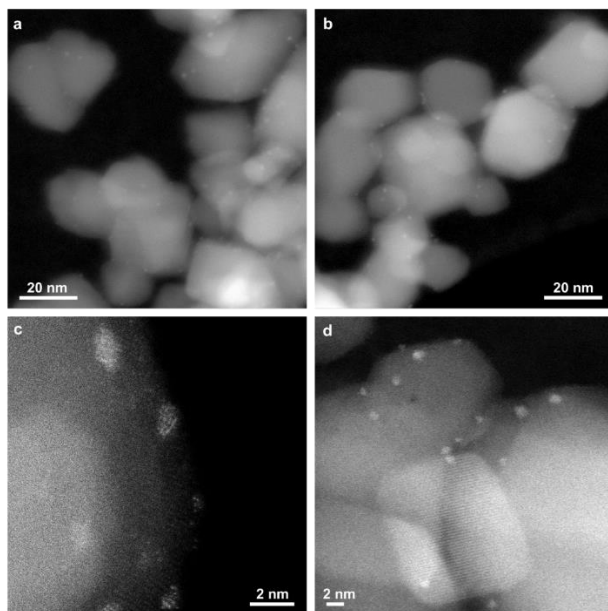
Figure 4.3. STEM images of 0.2%Pt/TiO$_2$-450H$_2$, showing the presence of Pt nanoparticles supported on TiO$_2$.
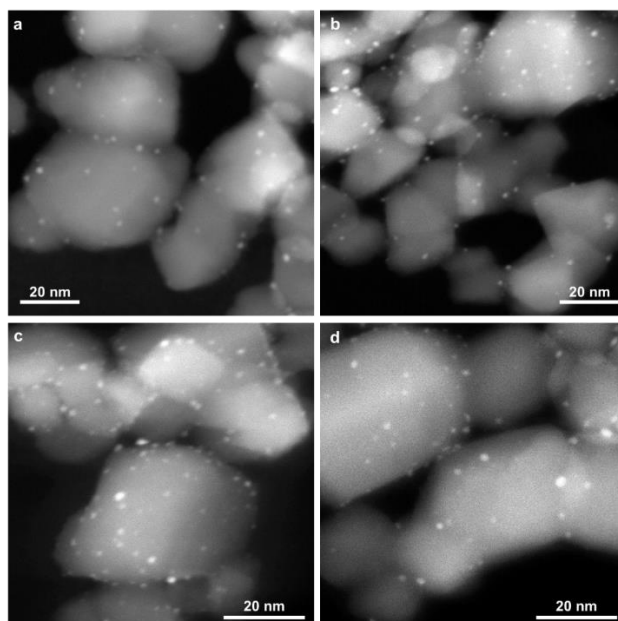
Figure 4.4. STEM images of 0.5%Pt/TiO$_2$-450H$_2$, showing the presence of Pt nanoparticles supported on TiO$_2$.
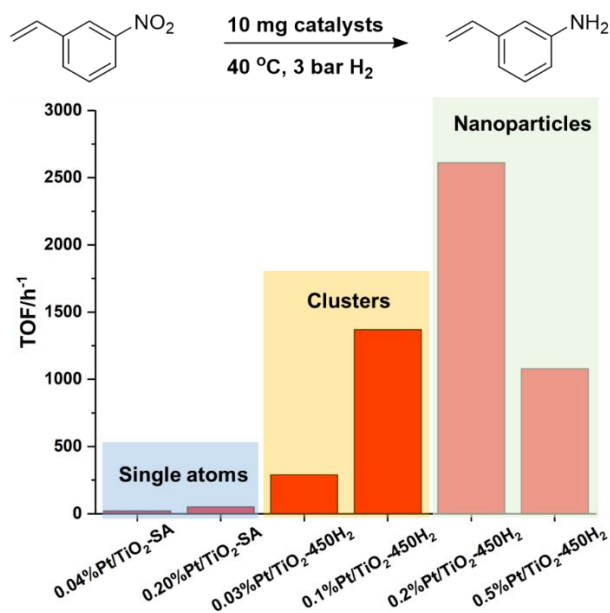
Figure 4.5. Catalytic performance of different Pt species supported on TiO$_2$ for hydrogenation of 3-nitrostyrene. Reaction conditions: 0.5 mmol 3-

nitrostyrene, 2 mL toluene as solvent, 10 mg of solid catalyst, 40 °C and 3 bar of H_2. High selectivity to 3-aminostyrene has been achieved for all the Pt/TiO$_2$ samples containing Pt clusters and nanoparticles.

The hydrogenation of 3-nitrostyrene was chosen as the model reaction to study the catalytic performance of different types of Pt species. As shown in **Figure 4.5**, the Pt single atoms show negligible activity. In the case of Pt/TiO$_2$ catalysts containing subnanometric clusters (the 0.03%Pt/TiO$_2$-450H$_2$ and 0.1%Pt/TiO$_2$-450H$_2$ sample), the activity is significantly higher than Pt single atoms. Further increasing the Pt particle size to ~1 nm will result in a highly active catalyst for chemoselective hydrogenation of 3-nitrostyrene to 3-aminostyrene, with a TOF of ~2600 h^{-1}, which is higher than the best Pt catalysts reported in the literature at the same temperature and H_2 pressure up to now. Pt/FeOx containing atomically dispersed Pt atoms on FeOx showed a TOF of ~1500 h^{-1} and Pt single atoms embedded in Ni nanoparticles showed a TOF of ~1800 h^{-1}.[26] Moreover, further increasing the size of Pt nanoparticles to ~1.5 nm (the 0.5%Pt/TiO$_2$-450H$_2$ sample) leads to the drop of activity, suggesting that Pt nanoparticles of ~1 nm are the most active species for the hydrogenation of 3-nitrostyrene under our conditions. These results indicate that, by the same preparation method, Pt nanoparticles can show much higher activity than single atoms and clusters for selective hydrogenation reaction.
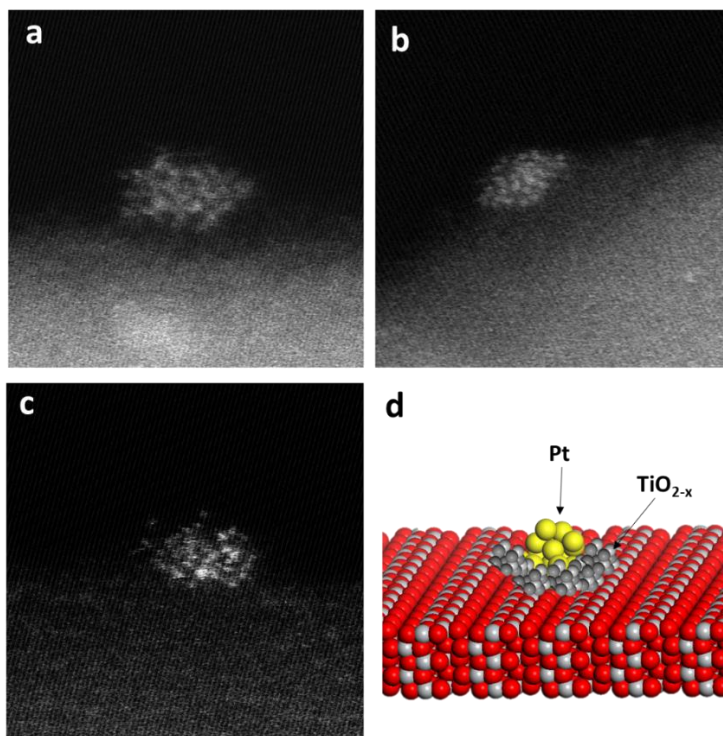
Figure 4.6. Atomic structure of small Pt nanoparticles supported on TiO₂. The size of these Pt nanoparticles is ~1 nm. According to the EELS results, Pt nanoparticles are surrounded by TiO_2 layer, with only several atoms exposed on the surface.

In our previous work, it has been proposed that, Pt nanoparticles partially covered by TiO_{2-x} are the active sites for chemoselective hydrogenation of nitroarenes in Pt/TiO_2 catalysts.[27] Herein, with the help of high-resolution STEM imaging and EELS mapping, we are able to give information on the structure of those small Pt particles (~1 nm) at atomic level. As displayed in **Figure 4.6**, Pt nanoparticles show semi-spherical shapes supported on TiO_2. The EELS mapping results indicate that Pt nanoparticles are surrounded by TiO_2 layers and the exposed surface area for each Pt nanoparticle is less than 1×1 nm. In other words, due to the strong metal-support interaction between Pt and TiO_2, only a few Pt atoms are exposed to the reactants, which are the active sites for chemoselective hydrogenation of nitroarenes.
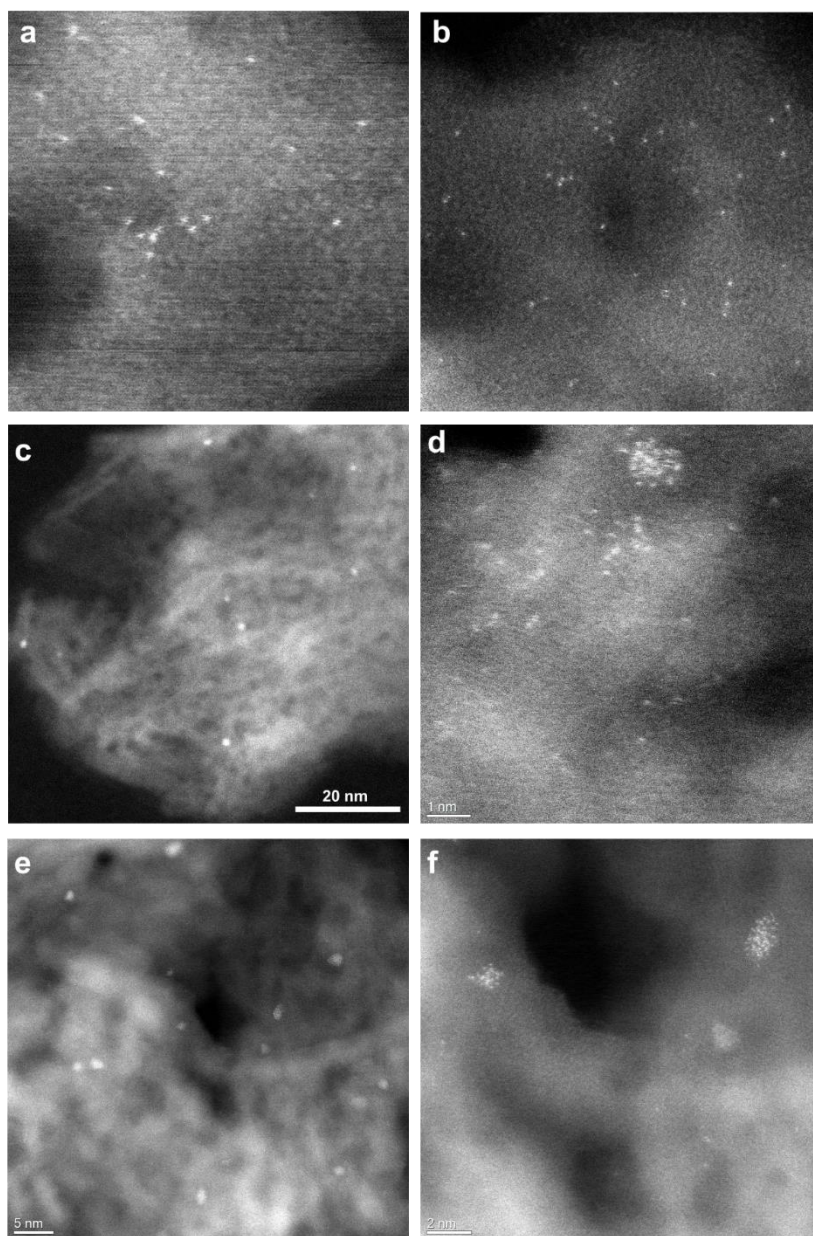
Figure 4.7. Pt/Al$_2$O$_3$ samples with different types of Pt species. High-resolution STEM images of Pt/Al$_2$O$_3$-SA (a, b) containing only singly dispersed Pt atoms, Pt/Al$_2$O$_3$-200H$_2$ (c, d) containing a mixture of both singly Pt atoms and Pt nanoclusters and Pt/Al$_2$O$_3$-400H$_2$ (e, f) containing mainly Pt

nanoparticles and a few singly dispersed Pt atoms.

In addition, we have also prepared a series of Pt/Al_2O_3 samples containing different sizes of Pt species from single atoms to clusters and nanoparticles. Firstly, a Pt/Al_2O_3-SA sample containing Pt single atoms was prepared by impregnation according to the literature.[28] As shown in **Figure 4.7a-b**, only singly dispersed Pt atoms can be observed in the high-resolution STME images of Pt/Al_2O_3-SA sample. After reduction by H_2 at 200 °C, some of the single Pt atoms agglomerate into Pt clusters while there are still some single Pt atoms preserved in the Pt/Al_2O_3-200H_2 sample. When raising the reduction temperature to 300 °C (**Figure 4.7c-d**) and 450 °C (**Figure 4.7e-f**), the fraction of single Pt atoms in the reduced Pt/Al_2O_3 decreases and only very few Pt atoms can still be found in the Pt/Al_2O_3-400H_2 sample. Therefore, the percentage of Pt single atoms can be modulated by the reduction temperature and this series of Pt/Al_2O_3 samples can be model catalysts for the direct comparison between single Pt atoms, clusters and nanoparticles.
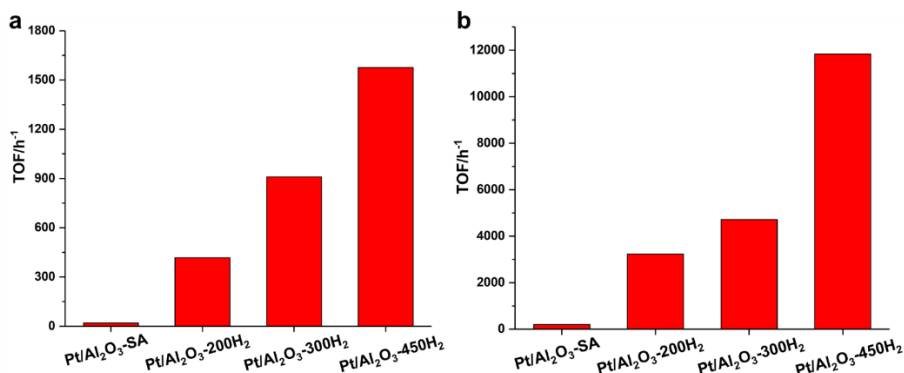
Figure 4.8. Catalytic performance of Pt/Al_2O_3 catalysts for hydrogenation reactions. (a) Hydrogenation of 3-nitrostyrene with various Pt/Al_2O_3 catalysts. Reaction conditions: 0.5 mmol 3-nitrostyrene, 2 mL toluene as solvent, 20 mg of solid catalyst, 50 °C and 3 bar of H_2. (b) Hydrogenation of styrene with various Pt/Al_2O_3 catalysts. Reaction conditions: 1.0 mmol styrene, 2 mL toluene as solvent, 10 mg of solid catalyst, 50 °C and 3 bar of H_2.

Firstly, we have tested the catalytic performance of Pt/Al_2O_3 catalysts for hydrogenation of 3-nitrostyrene. As shown in **Figure 4.8a**, similar to the

situation of Pt/TiO$_2$ catalysts, Pt/Al$_2$O$_3$-SA sample shows negligible activity for hydrogenation of 3-nitrostyrene. In the case of reduced Pt/Al$_2$O$_3$ samples, considerable conversion of 3-nitrostyrene can be observed and the reactivity increases with the reduction temperature, which corresponds to higher percentage of Pt nanoparticles in the Pt/Al$_2$O$_3$ catalyst. Although the Pt/Al$_2$O$_3$ catalysts are not chemoselective for 3-aminostyrene, the tendency of the activity for hydrogenation of 3-nitrostyrene is similar to Pt/TiO$_2$ catalysts, indicating that Pt clusters and nanoparticles show more superior reactivity than Pt single atoms.

Since it has been reported in the literature that singly dispersed Pt atoms can be used for hydrogenation of C=C bonds, we have also tested the reactivity of Pt/Al$_2$O$_3$ catalysts for hydrogenation of styrene. As can be seen in **Figure 4.8b**, singly dispersed Pt atoms also show negligible activity towards hydrogenation of C=C bonds. The reduced Pt/Al$_2$O$_3$ catalysts show much higher activity and the activity increases with the percentage of Pt nanoparticles in the catalyst, indicating that Pt nanoparticles are more active than single Pt atoms and clusters for the hydrogenation of C=C bonds.

From a mechanistic point of view, the hydrogenation of -NO$_2$ and C=C may follow different reaction mechanism on metal catalysts.[29,30] It has been reported that, hydrogenation of C=C on nanoparticulate Pt catalysts are structure-insensitive reaction while hydrogenation of -NO$_2$ are structure-sensitive reaction. Nevertheless, our experimental results show that, Pt nanoparticles are more active than Pt clusters and single Pt atoms in these hydrogenation reactions. Specially, our results indicate that, singly dispersed Pt atoms supported on TiO$_2$ and Al$_2$O$_3$ show much lower activity for the hydrogenation of -NO$_2$ and C=C groups.
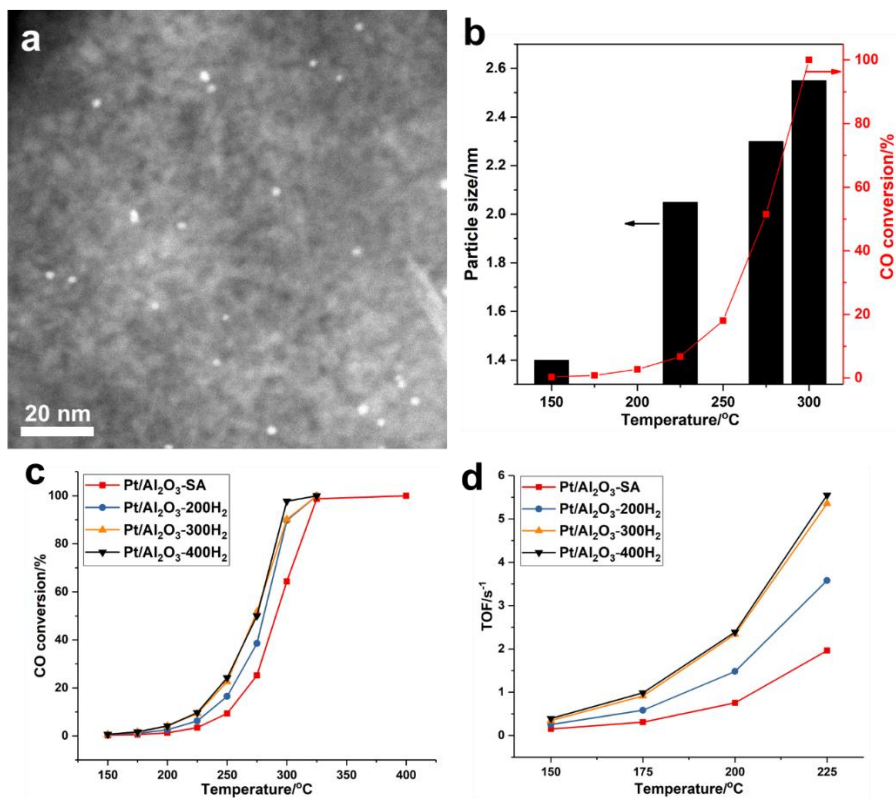
Figure 4.9. Size effect of Pt species supported on Al_2O_3 for CO oxidation. (a) The catalytic result of 0.2%Pt/Al_2O_3-SA sample for CO oxidation and the evolution of Pt single atoms to Pt nanoparticles under CO oxidation reaction conditions. (b) The average particle size of 0.2%Pt/Al_2O_3 sample after reduction by H_2 at different temperature. The higher reduction temperature will result in formation of larger Pt nanoparticles. (c) Comparison of the catalytic performance of Pt/Al_2O_3 catalysts with different size, ranging from single atoms to clusters to nanoparticles. (d) Turnover frequency values of different Pt/Al_2O_3 catalysts in low-temperature range (150-225 ^oC) for CO oxidation reaction.

3.2 CO oxidation reaction with Pt single atoms, clusters and nanoparticles

CO oxidation is another important model reaction to study the structure-reactivity correlations of supported metal catalysts. It has been reported in the

literature that, Pt single atoms support on Al_2O_3 are active for CO oxidation. In this work, we have tested the catalytic activity of Pt single atoms supported on Al_2O_3 and followed the evolution of Pt single atoms during the CO oxidation reaction. As shown in **Figure 4.9**, it is found that Pt single atoms agglomerate into small nanoparticles under reaction conditions. As displayed in **Figure 4.10** to **Figure 4.13**, the size of the *in situ* formed Pt nanoparticles also increase with the reduction temperature (from 200 to 400 ^oC), indicating that Pt species occur dynamic structural transformation under CO oxidation conditions. In order to compare the reactivity of Pt single atoms, clusters and nanoparticles, we have also tested the Pt/Al_2O_3 catalysts containing different types of Pt species for CO oxidation. As shown in **Figure 4.9c**, both Pt clusters and Pt nanoparticles show significantly higher TOFs (normalized to the amount of Pt atoms in the catalyst) than Pt single atoms. Pt/Al_2O_3-$300H_2$ and Pt/Al_2O_3-$400H_2$ samples show similar activity while Pt/Al_2O_3-$200H_2$ show intermediate activity between these two samples. It should be mentioned that, the TOF values shown in **Figure 4.9d** are calculated based on all the Pt species in the catalyst. If we calculate the TOF based on surface exposed atoms, then Pt clusters and nanoparticles may show even higher TOF values while Pt atoms will maintain the same.

Based on the catalytic results shown in **Figure 4.9** and combining the size distribution of Pt species in various Pt/Al_2O_3 samples, it can be concluded that, the Pt/Al_2O_3 sample with a higher fraction of single Pt atoms shows a lower activity for CO oxidation, implying that Pt nanoparticles and clusters are more active than Pt single atoms for CO oxidation reaction when they are supported on Al_2O_3.
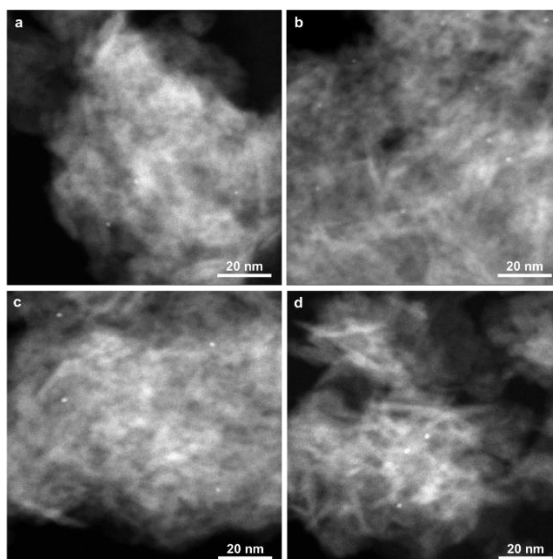
Figure 4.10. STEM images of Pt/Al₂O₃-SA sample after CO oxidation at 150 ºC. A few small Pt nanoparticles can be observed in the used catalyst.
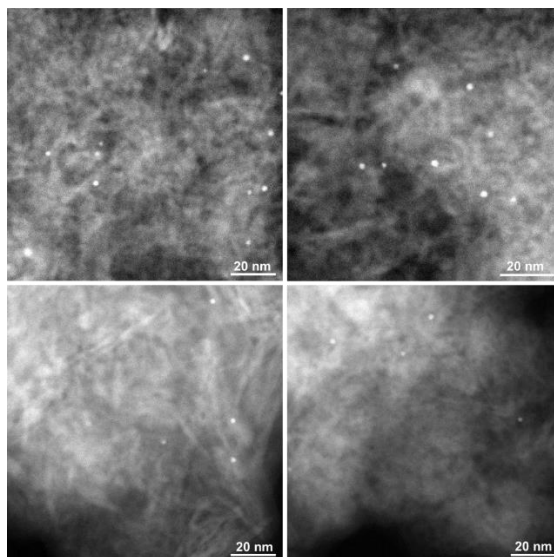
Figure 4.11. STEM images of Pt/Al₂O₃-SA sample after CO oxidation at 225 ºC. Pt nanoparticles can be observed in the used catalyst, due to the agglomeration of highly dispersed Pt atoms.
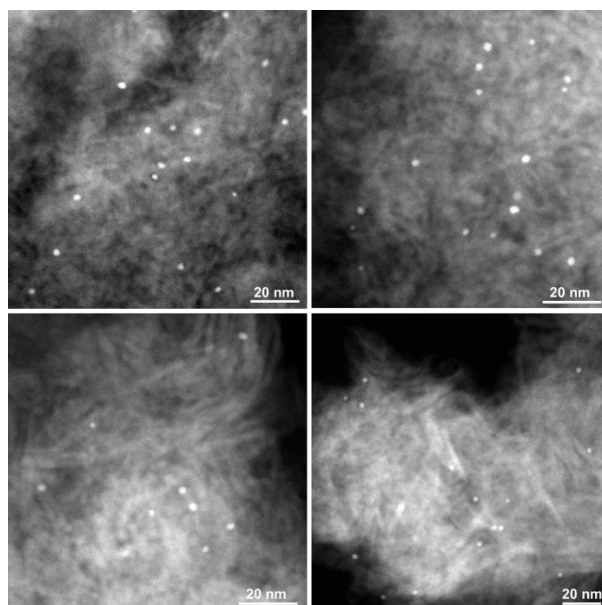
Figure 4.12. STEM images of Pt/Al$_2$O$_3$-SA sample after CO oxidation at 275 ^{o}C. Pt nanoparticles can be observed in the used catalyst, due to the agglomeration of highly dispersed Pt atoms.
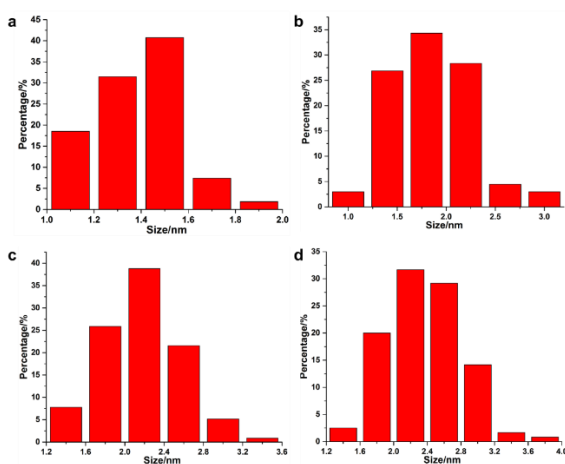
Figure 4.13. Size distributions of Pt nanoparticles observed in Pt/Al$_2$O$_3$-SA sample after CO oxidation reaction at different temperature. (a) 150 ^{o}C, (b) 225 ^{o}C, (c) 275 ^{o}C and (d) 300 ^{o}C.
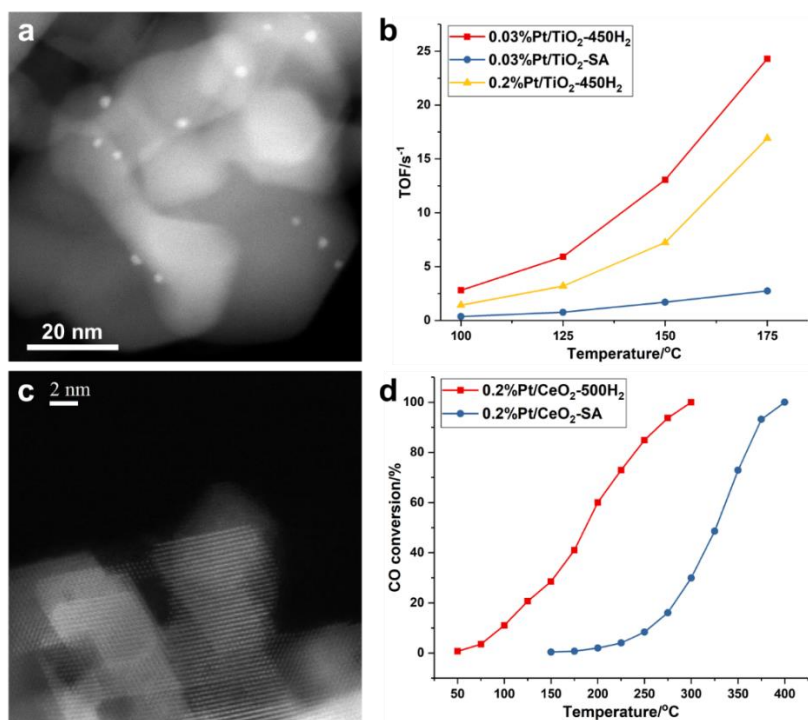
Figure 4.14. Size effect of Pt species supported on TiO_2 and CeO_2 for CO oxidation. (a) STEM image of Pt/TiO_2-SA catalyst after the CO oxidation reaction, showing the transformation of singly dispersed Pt atoms into Pt nanoparticles under reaction conditions. (b) Comparison of the activity of Pt single atoms, clusters and nanoparticles for low-temperature CO oxidation. (c) STEM image of Pt/CeO_2-SA catalyst after the CO oxidation reaction. Pt nanoparticles are not found in the used catalyst. (d) Comparison of the activity of Pt single atoms and nanoparticles for low-temperature CO oxidation.

Nevertheless, we have also studied the catalytic behavior of Pt single atoms supported on TiO_2 for CO oxidation. In the case of Pt/TiO_2-SA, a similar agglomeration behavior from single atoms to nanoparticles is observed during the CO oxidation test (see **Figure 4.14a**). Then, we have compared the activity of Pt clusters and nanoparticles with single Pt atoms. As shown in **Figure 4.14b**, Pt clusters show the highest TOF value, followed by Pt nanoparticles. Similar to the case of Pt/Al_2O_3, Pt single atoms supported on TiO_2 exhibit the lowest

TOF. It should be pointed out that, the variation tendency of CO oxidation activity versus Pt particle size is different on Al_2O_3 and TiO_2, implying that, the reactivity of different types of metal entities may depend on the support. In the case of Pt/CeO_2 containing single Pt atoms (Pt/CeO_2-SA), the activity is quite low, which is in line with the reported work.[31] After the CO oxidation test, the agglomeration of Pt atoms into clusters or nanoparticles are not observed (see **Figure 4.14c**), implying that Pt atoms are stabilized by CeO_2 under reaction conditions, which is different to the situation for Pt atoms supported on Al_2O_3 and TiO_2, suggesting that the evolution behavior of Pt single atoms also depends on the interaction between Pt and the support. Afterwards, as done before, $0.2\%Pt/CeO_2$-SA sample was reduced by H_2 at 500 ºC to generate Pt nanoparticles on CeO_2. As shown in **Figure 4.14d**, the $0.2\%Pt/CeO_2$-500H_2 sample exhibit much higher activity than $0.2\%Pt/CeO_2$-SA. The above results suggest that, for low-temperature CO oxidation reaction, Pt clusters and nanoparticles are more active than Pt single atoms on Al_2O_3, TiO_2 and CeO_2. Furthermore, the reactivity of Pt clusters and nanoparticles and the evolution behavior is strongly relevant to the support, implying the importance of considering the role of the support when discussing the catalytic behavior of heterogeneous single-atom catalysts.

3.3 Oxidation of alcohol with Pt single atoms, clusters and nanoparticles

In the above two examples, H_2 activation and O_2 activation has been considered to be the rate-limiting step. In the case of oxidation of alcohols, both the activation of O_2 and the -CHx-OH group on metal surface are key steps to convert alcohols to aldehydes. It has been reported in the literature that, singly dispersed Pd atoms are more efficient catalysts for oxidation of alcohols than corresponding metal clusters and nanoparticles.[32,33]

Herein, we have studied the catalytic performance of Pt single atoms (Pt/CeO_2-SA), clusters (Pt/CeO_2-200H_2) and nanoparticles (Pt/CeO_2-500H_2) supported on CeO_2 for oxidation of benzylalcohol to benzylaldehyde. As can be seen in **Figure 4.15**, $0.2Pt/CeO_2$-SA sample show the lowest initial activity while the other two samples containing Pt clusters and nanoparticles are more active than the Pt single atoms.
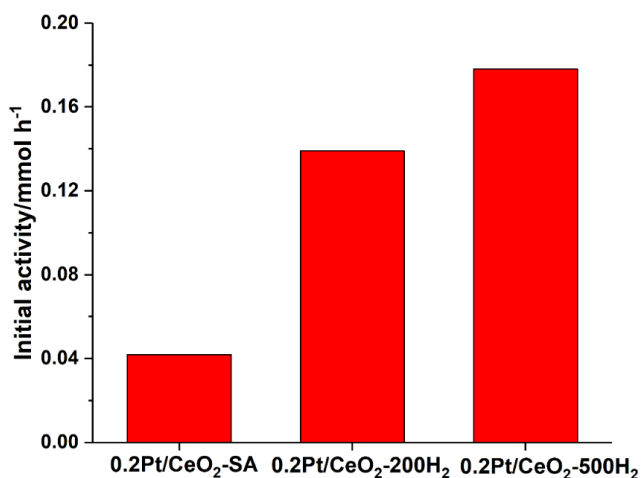
Figure 4.15. Initial reactivity for oxidation of benzyl alcohol to benzyl aldehyde by Pt/CeO$_2$. Three Pt/CeO$_2$ catalysts containing Pt single atoms (0.2Pt/CeO$_2$-SA), Pt clusters (0.2Pt/CeO$_2$-200H$_2$) and Pt nanoparticles (0.2Pt/CeO$_2$-500H$_2$) were tested under the same conditions: 50 mg Pt/CeO$_2$ as solid catalyst, 1 mmol benzyl alcohol, 80 °C, 7 bar of O$_2$ and 2 mL toluene as solvent.
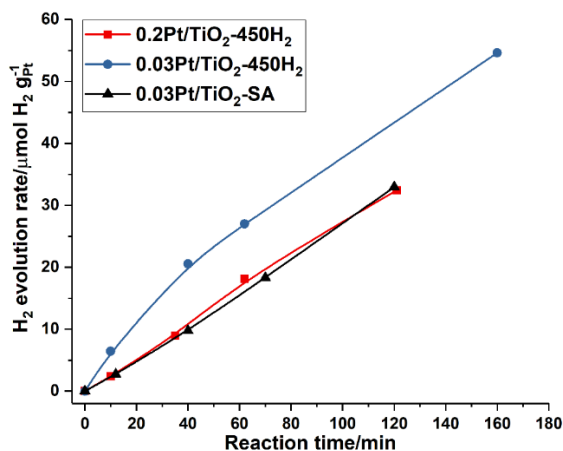
Figure 4.16. Catalytic performance of Pt single atoms, clusters and nanoparticles supported on TiO$_2$ for photocatalytic H$_2$ evolution under solar light. Same amount of solid Pt/TiO$_2$ catalysts was used as the catalyst and the H$_2$ evolution rate was normalized to the Pt mass in different catalysts.
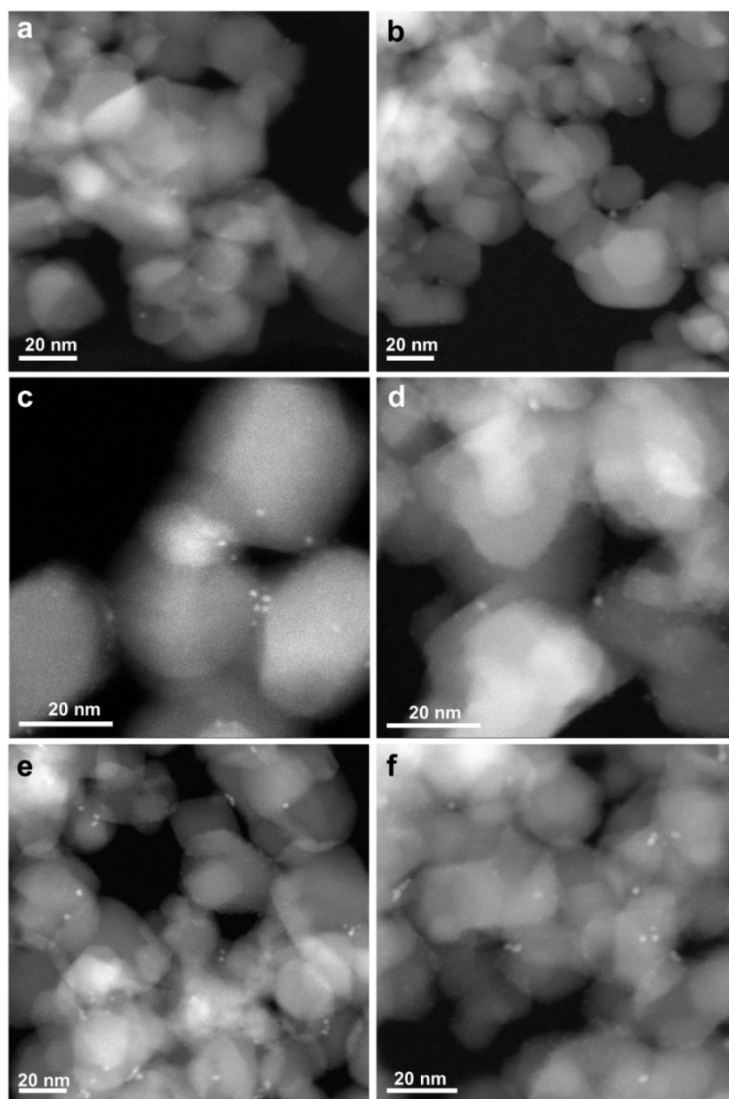
Figure 4.17. STEM images of various Pt/TiO$_2$ catalysts after photocatalytic H$_2$ evolution reaction. Pt clusters and nanoparticles are formed in the Pt/TiO$_2$-SA sample after photocatalytic H$_2$ evolution reaction. In the other two cases, the size of Pt clusters and nanoparticles also slightly increases, indicating the instability of Pt species under the photocatalytic reaction conditions.

3.4 Photocatalytic H$_2$ evolution with Pt single atoms, clusters and

nanoparticles

In the above examples, conventional heterogeneous catalysis involving activation of small molecules are employed to study the catalytic behavior of different types of Pt species. Pt is also widely used for photocatalysis, in which, Pt is usually thought to serve as the co-catalyst. The photo-generated electrons in the semiconductors will transfer to Pt sites, which catalyze the half reaction between protons and electrons to form H_2.[34] It has been reported in the literature that, the size of Pt co-catalysts has significant influence on the photocatalytic reactivity due to their size-dependent electronic structures.[35,36] Recently, it has been reported that, single-site based metal catalysts can also be used for photocatalysis.[37,38] In the following example, we have compared three Pt/TiO_2 catalysts with different sizes of Pt species for photocatalytic H_2 evolution from ethanol-H_2O mixture under sunlight.

As shown in **Figure 4.16**, all the three Pt/TiO_2 catalysts are active for photocatalytic H_2 evolution reaction and $0.03Pt/TiO_2$-$450H_2$ sample containing Pt clusters shows the highest activity while the other two samples show similar activity. The three used Pt/TiO_2 catalysts after photocatalytic reaction have also been measured by STEM. As presented in **Figure 4.17**, a large number of Pt nanoparticles and some Pt clusters can be found in the $0.03Pt/TiO_2$-SA sample, implying the sintering of singly dispersed Pt atoms under the photocatalytic reaction conditions. In the case of the other two samples, slight sintering is also observed, implying the instability of Pt species during the photocatalytic process under sunlight. Based on the above results, it can be concluded that, Pt clusters and nanoparticles show higher activity when working as co-catalyst for photocatalytic H_2 evolution reaction. And singly dispersed Pt atoms on TiO_2 are not stable under the photocatalytic conditions and their sintering behavior may be associated with the surface reaction (oxidation of ethanol by photo-generated holes and the reduction of H^+ to H_2 by photo-generated electrons) under solar light irradiation.

4. Conclusions

In summary, we have carried out a comparative study on the catalytic behavior of supported single Pt atoms, clusters and nanoparticles on solid carriers for hydrogenation, oxidation and photocatalytic reactions. The catalytic

results presented in this work show that, Pt clusters and nanoparticles can work as more efficient catalytic than singly dispersed Pt atoms when prepared by a similar procedure and tested under the same conditions. Furthermore, it has been observed in some reactions that, singly dispersed Pt atoms can agglomerate into Pt clusters and nanoparticles under reaction conditions and such behavior is also related with the support. Our work demonstrates that, when studying the catalytic properties of single-atom catalysts, in order to show the uniqueness of singly dispersed metal species, it is important to prepare comparable catalysts containing corresponding metal clusters or nanoparticles as reference catalysts. Nevertheless, the stability of the singly dispersed metal species under reaction conditions is also a critical issue that should be carefully considered.

References

(1) Yang, X. F.; Wang, A.; Qiao, B.; Li, J.; Liu, J.; Zhang, T. *Acc. Chem. Res.* **2013**, *46*, 1740.

(2) Flytzani-Stephanopoulos, M.; Gates, B. C. *Ann. Rev. Chem. Biomol. Eng.* **2012**, *3*, 545.

(3) Gates, B. C.; Flytzani-Stephanopoulos, M.; Dixon, D. A.; Katz, A. *Catal. Sci. Technol.* **2017**, *7*, 4259.

(4) Qiao, B.; Wang, A.; Yang, X.; Allard, L. F.; Jiang, Z.; Cui, Y.; Liu, J.; Li, J.; Zhang, T. *Nat. Chem.* **2011**, *3*, 634.

(5) DeRita, L.; Dai, S.; Lopez-Zepeda, K.; Pham, N.; Graham, G. W.; Pan, X.; Christopher, P. *J. Am. Chem. Soc.* **2017**, *139*, 14150.

(6) Jones, J.; Xiong, H.; DeLaRiva, A. T.; Peterson, E. J.; Pham, H.; Challa, S. R.; Qi, G.; Oh, S.; Wiebenga, M. H.; Pereira Hernandez, X. I.; Wang, Y.; Datye, A. K. *Science* **2016**, *353*, 150.

(7) Ding, K.; Gulec, A.; Johnson, A. M.; Schweitzer, N. M.; Stucky, G. D.; Marks, L. D.; Stair, P. C. *Science* **2015**, *350*, 189.

(8) Qiao, B.; Liu, J.; Wang, Y.-G.; Lin, Q.; Liu, X.; Wang, A.; Li, J.; Zhang, T.; Liu, J., *ACS Catal.* **2015**, *5*, 6249-6254.

(9) Qiao, B.; Liang, J.-X.; Wang, A.; Xu, C.-Q.; Li, J.; Zhang, T.; Liu, J. J. *Nano Res.* **2015**, *8*, 2913.

(10) Wang, J.; Tan, H.; Yu, S.; Zhou, K. *ACS Catalysis* **2015**, *5*, 2873.

(11) Guo, L. W.; Du, P. P.; Fu, X. P.; Ma, C.; Zeng, J.; Si, R.; Huang, Y. Y.; Jia, C. J.; Zhang, Y. W.; Yan, C. H. *Nat. Commun.* **2016,** *7*, 13481.

(12) Wei, H.; Liu, X.; Wang, A.; Zhang, L.; Qiao, B.; Yang, X.; Huang, Y.; Miao, S.; Liu, J.; Zhang, T. *Nat. Commun.* **2014,** *5*, 5634.

(13) Zhang, B.; Asakura, H.; Zhang, J.; Zhang, J.; De, S.; Yan, N. *Angew. Chem. Int. Ed.* **2016,** *55*, 8319-8323.

(14) Vile, G.; Albani, D.; Nachtegaal, M.; Chen, Z.; Dontsova, D.; Antonietti, M.; Lopez, N.; Perez-Ramirez, J. *Angew. Chem. Int. Ed.* **2015,** *54*, 11265-11269.

(15) Liu, P.; Zhao, Y.; Qin, R.; Mo, S.; Chen, G.; Gu, L.; Chevrier, D. M.; Zhang, P.; Guo, Q.; Zang, D.; Wu, B.; Fu, G.; Zheng, N. *Science* **2016**, *352*, 797.

(16) Rossell, M. D.; Caparrós, F. J.; Angurell, I.; Muller, G.; Llorca, J.; Seco, M.; Rossell, O. *Catal. Sci. Technol.* **2016,** *6*, 4081-4085.

(17) Vajda, S.; White, M. G. *ACS Catal.* **2015**, *5*, 7152.

(18) Boronat, M.; Leyva-Perez, A.; Corma, A. *Acc. Chem. Res.* **2014**, *47*, 834.

(19) Liu, L.; Corma, A. *Chem. Rev.* **2018**, *118*, 4981-5079.

(20) Corma, A.; Concepcion, P.; Boronat, M.; Sabater, M. J.; Navas, J.; Yacaman, M. J.; Larios, E.; Posadas, A.; Lopez-Quintela, M. A.; Buceta, D.; Mendoza, E.; Guilera, G.; Mayoral, A. *Nat. Chem.* **2013**, *5*, 775.

(21) Oliver-Meseguer, J.; Liu, L.; Garcia-Garcia, S.; Canos-Gimenez, C.; Dominguez, I.; Gavara, R.; Domenech-Carbo, A.; Concepcion, P.; Leyva-Perez, A.; Corma, A. *J. Am. Chem. Soc.* **2015**, *137*, 3894.

(22) Gates, B. C. *Chem. Rev.* **1995**, *95*, 511.

(23) Hoffman, A. S.; Debefve, L. M.; Zhang, S.; Perez-Aguilar, J. E.; Conley, E. T.; Justl, K. R.; Arslan, I.; Dixon, D. A.; Gates, B. C. *ACS Catal.* **2018**, *8*, 3489.

(24) He, Q.; Freakley, S. J.; Edwards, J. K.; Carley, A. F.; Borisevich, A. Y.; Mineo, Y.; Haruta, M.; Hutchings, G. J.; Kiely, C. J. *Nat. Commun.* **2016**, *7*, 12905.

(25) Liu, L.; Zakharov, D. N.; Arenal, R.; Concepcion, P.; Stach, E. A.; Corma, A. *Nat. Commun.* **2018**, *9*, 574.

(26) Peng, Y.; Geng, Z.; Zhao, S.; Wang, L.; Li, H.; Wang, X.; Zheng, X.; Zhu, J.; Li, Z.; Si, R.; Zeng, J. *Nano letters* **2018**, doi: 10.1021/acs.nanolett.8b01059.

(27) Corma, A.; Serna, P.; Concepcion, P.; Calvino, J. J. *J. Am. Chem. Soc.* **2008**, *130*, 8748.

(28) Moses-DeBusk, M.; Yoon, M.; Allard, L. F.; Mullins, D. R.; Wu, Z.; Yang, X.; Veith, G.; Stocks, G. M.; Narula, C. K. *J. Am. Chem. Soc.* **2013**, *135*, 12634.

(29) Song, H.; Rioux, R. M.; Hoefelmeyer, J. D.; Komor, R.; Niesz, K.; Grass, M.; Yang, P.; Somorjai, G. A. *J. Am. Chem. Soc.* **2006,** *128*, 3027-3037.

(30) Claus, P.; Brückner, A.; Mohr, C.; Hofmeister, H. *J. Am. Chem. Soc.* **2000**, *122*, 11430.

(31) Jones, J.; Xiong, H.; DeLaRiva, A. T.; Peterson, E. J.; Pham, H.; Challa, S. R.; Qi, G.; Oh, S.; Wiebenga, M. H.; Pereira Hernandez, X. I.; Wang, Y.; Datye, A. K. *Science* **2016**, *353*, 150.

(32) Hackett, S. F.; Brydson, R. M.; Gass, M. H.; Harvey, I.; Newman, A. D.; Wilson, K.; Lee, A. F. *Angew. Chem. Int. Ed.* **2007**, *46*, 8593.

(33) Xin, P.; Li, J.; Xiong, Y.; Wu, X.; Dong, J.; Chen, W.; Wang, Y.; Gu, L.; Luo, J.; Rong, H.; Chen, C.; Peng, Q.; Wang, D.; Li, Y. *Angew. Chem. Int. Ed.* **2018**, *57*, 4642.

(34) Yang, J.; Wang, D.; Han, H.; Li, C. *Acc. Chem. Res.* **2013**, *46*, 1900.

(35) Berr, M. J.; Schweinberger, F. F.; Doblinger, M.; Sanwald, K. E.; Wolff, C.; Breimeier, J.; Crampton, A. S.; Ridge, C. J.; Tschurl, M.; Heiz, U.; et al. *Nano Lett.* **2012**, *12*, 5903-5906.

(36) Schweinberger, F. F.; Berr, M. J.; Doblinger, M.; Wolff, C.; Sanwald, K. E.; Crampton, A. S.; Ridge, C. J.; Jackel, F.; Feldmann, J.; Tschurl, M.; et al. *J. Am. Chem. Soc.* **2013**, *135*, 13262-13265.

(37) Xing, J.; Chen, J. F.; Li, Y. H.; Yuan, W. T.; Zhou, Y.; Zheng, L. R.; Wang, H. F.; Hu, P.; Wang, Y.; Zhao, H. J.; Wang, Y.; Yang, H. G. *Chem. Eur. J.* **2014**, *20*, 2138.

(38) Li, X.; Bi, W.; Zhang, L.; Tao, S.; Chu, W.; Zhang, Q.; Luo, Y.; Wu, C.; Xie, Y. *Adv. Mater.* **2016,** *28*, 2427-2431.

This chapter is reused from the following publication:

Generation of subnanometric platinum with high stability during transformation of a 2D zeolite into 3D. **L. Liu**, U. Díaz, R. Arenal, G. Agostini, P. Concepción and A. Corma, *Nature Materials*, 2017, 16, 132-138.

Chapter 5

Generation of subnanometric platinum with high stability during transformation of two-dimensional into three-dimensional zeolite
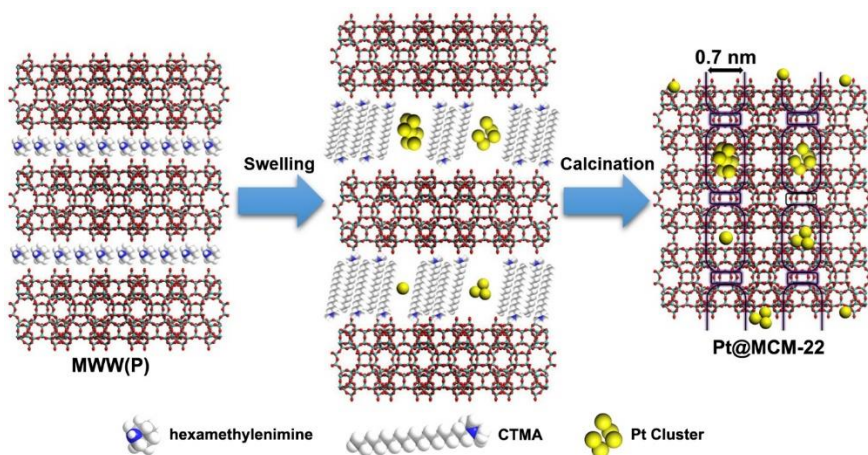
Abstract

The applications of single atoms and clusters for heterogeneous catalysis have attracted much attention due to the special catalytic properties of single atoms and clusters. However, the generation of stable single atoms and clusters on a solid support is still challenging. Herein, we report a new strategy for the generation of single Pt atoms and Pt clusters with exceptional high thermal stability in purely siliceous MCM-22 during the transformation of a two-dimensional into a three-dimensional zeolite. Those subnanometric Pt species are still stabilized by MCM-22 after treatment in air at 540 °C. Furthermore, Pt species confined in the internal cavities show size-selective catalytic properties in the hydrogenation of alkenes. High-temperature oxidation-reduction treatments result in the growth of encapsulated Pt species to small nanoparticles between 1~2 nm. The stability and catalytic activity of encapsulated Pt species is also reflected in the dehydrogenation of propane to propylene.

1. Introduction

The unique catalytic properties of metal cluster catalysts have attracted, great attention because of their distinct behavior compared with metal nanoparticles (NPs) and mononuclear metal compounds.[1,2] However, the stability of metal clusters can be a limitation for their applications in heterogeneous catalysis at higher temperatures, and loading atomic dispersed metal species on solid supports can be a method to improve their stability.[3,4] To this respect, because of their high thermal stability and confinement effects, zeolite materials appear as promising supports for preparing supported metal clusters.[5] By conventional methods (such as wet impregnation and ion exchange), the location of metal species cannot always be controlled and metal NPs will usually be formed after the post-treatment. Moreover, during the reaction or during some harsh thermal treatments, active species on the external surface can aggregate to form large NPs (>5 nm), resulting in a decrease of catalytic activity.[6-9]

Recently, Iglesia *et al.* have developed a method to encapsulate small metal NPs into microporous cavities during the synthesis of different zeolitic materials. Different types of metal NPs with size between 1~2 nm are encapsulated into zeolites such as Sodalite (SOD), Analcime (ANA) and Gismondine (GIS).[10,11] This method has been used, so far, for the synthesis of

Al-containing zeolites and the metal nanoparticles encapsulated in those zeolites are resistant to sintering.[12] Nevertheless, in some cases, the introduction of Al into the zeolites may restrict the reaction scope of these materials because of the acidity associated to the presence of Al sites. Gates *et al.* have prepared single metal atoms and metal clusters (below 1 nm) confined in zeolites and performed excellent detailed characterizations on the location and atomic structure of these metal species.[13,14] In this case, metal clusters with identified atomicity can be anchored into the pores of pure-silica zeolites, and the stability of metal clusters obtained by thermal decomposition of the metal precursor (e.g. organometallic compounds) could be an issue. In some cases, they may agglomerate even at room temperature under ambient environment. Therefore, developing a facile and sustainable method for incorporating metal clusters in high-silica zeolites with high thermal stability is still a challenge.

In this work, we present a new strategy for preparation of zeolite-confined subnanometric Pt species (single Pt atoms and Pt clusters) catalysts with high stability during transformation of two-dimensional (2D) into three-dimensional (3D) zeolite. As the starting material, we choose a pure siliceous layered precursor of MCM-22 (MWW-type zeolite)[15] with the idea that during the condensation of the layered zeolite precursor, the hemi-cages (cups) and cages with internal dimensions of ~0.7 and ~0.7×1.8 nm, respectively, would entrap the subnanometric Pt species. The resultant material will be named as Pt@MCM-22. In this way, Pt individual atoms and Pt clusters will be incorporated into the cups and cages of MCM-22 zeolite. It will be shown that subnanometric Pt species in the cavities can differentiate reactants by size and show exceptional high thermal stability and better catalytic activity.
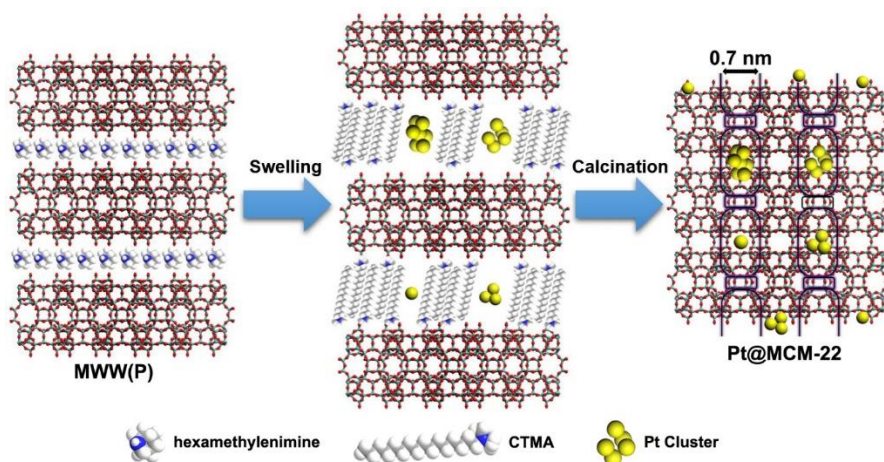
Figure 5.1. Schematic illustration of the preparation of Pt@MCM-22.
During the swelling process of layered MWW zeolitic precursors (MWW(P)),
solution containing subnanometric Pt species are added. MWW layers are
expanded by the surfactant (hexadecyltrimethylammonium, CTMA$^+$OH$^-$) and
subnanometric Pt species are also incorporated into the internal channels
between individual MWW layers. Removing the organic agents will lead to the
formation of 3D Pt@MCM-22, in which subnanometric Pt species are confined
in the external cups on the surface or encapsulated in the supercages of MCM-
22.

2.1 Structural characterizations

The preparation process of Pt@MCM-22 is schematized in **Figure 5.1**. In
order to incorporate subnanometric Pt species into MCM-22, purely siliceous
MWW precursor (namely ITQ-1) was firstly synthesized.[16] Subnanometric Pt
species were prepared using dimethylformamide (DMF) as weak reduction and
capping agent.[17,18] The fluorescence emission spectrum and picture of the DMF
solution containing subnanometric Pt species are shown in **Figure 5.2**. The
incorporation of subnanometric Pt species was carried out during the swelling
process of lamellar zeolitic precursor (MWW(P)), which can be followed by X-
ray diffraction (see **Figure 5.3**). After the swelling process, subnanometric Pt
species as well as the surfactant molecules were located between the layers.
Then, the organic surfactant was removed by calcination in air at 540 ºC,

leading to formation of Pt atoms and clusters encapsulated by the supercages of 3D MCM-22, giving the final Pt@MCM-22 sample (the loading amount of Pt is 0.11 wt%, measured by ICP). Besides, Pt species could also be confined in the cups located at the external surface of MWW crystallites.

The structures of as-prepared Pt@MCM-22 were characterized by transmission electron microscopy (TEM) and high-resolution STEM imaging with high-angle annular dark field detector (HAADF-HRSTEM imaging). As shown in **Figure 5.5a**, only MCM-22 crystallites can be seen in the TEM image. The hexagonal structure of MCM-22 is preserved after the incorporation of Pt species, as confirmed by the fast Fourier transformation (FFT) and XRD patterns (**Figure 5.4**). In STEM images (**Figure 5.5b**), the 12 member-ring (MR) sub-units of the external cups in MCM-22 with diameter ca. 0.7 nm can be clearly seen from the view of *c*-axis. Indeed, this imaging technique is chemical sensitive because it provides Z (atomic number)-contrast between heavy Pt atoms (bright features) and MCM-22 zeolite composed by light atoms.[19] The contrast for single Pt atoms have been analyzed based on the intensity profiles, as shown in **Figure 5.5e** and **Figure 5.5f**. The good dispersion of subnanometric Pt species is confirmed in additional STEM images (see **Figure 5.6**). Furthermore, Pt clusters and individual Pt atoms with fine dispersion can be distinguished clearly in HAADF-HRSTEM images (**Figure 5.5c** and **Figure 5.5d**). More intensity profiles of different types of Pt species can be found in supplementary information (see **Figure 5.7** and **Figure 5.8**).[20] It is worth mentioning that the intensity differences of the bright dots displayed in the HRSTEM-HAADF images maybe due to the focus conditions of the electron beam on the Pt atoms/clusters (or equivalently to the location of these atoms within the zeolite crystallites). For instance, **Figure 5.5e** (area #2) and **Figure 5.7** (area #3) clearly illustrate how the intensity of the dots corresponding to two neighboring atoms is slightly different, indicating their different location in the MCM-22 crystallites. In order to better understand these findings, we have carried out HRSTEM-HAADF image simulations (see **Figure 5.9**). The simulation results confirm the interpretation of experimental HRSTEM images, which correspond to individual Pt atoms and Pt clusters incorporated in MCM-22. Even though it is difficult to obtain the exact location of Pt species, some important information can still be obtained based on the HRSTEM images. As

shown in **Figure 5.10** and **Figure 5.11**, Pt single atoms and small clusters appear to be confined in the cups and at the connecting walls between the cups, while some Pt clusters could also be encapsulated in the supercages in MCM-22 (as illustrated in **Figure 5.5g**). Meantime, there are also some atomically dispersed Pt species anchored on the framework of MCM-22. Since the internal dimensions of the supercages is 0.7×1.8 nm, 10-13 Pt atoms can be contained, considering their three-dimensional structures (a schematic illustration of Pt_5 cluster confined in supercages of MCM-22 is shown in **Figure 5.5h**).[21] We could only find a few big Pt clusters (ca. 0.7-1.0 nm), which can fill up the supercages of MCM-22. However, there are few Pt particles larger than 2 nm which were observed in the sample.
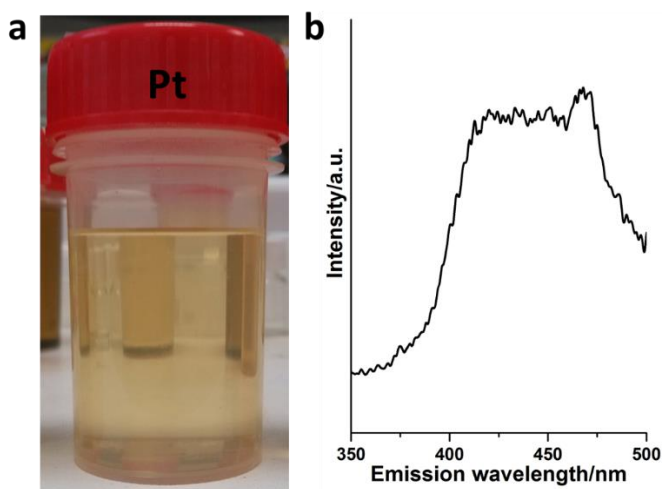
Figure 5.2. a, A picture of Pt-DMF solution containing subnanometric Pt species. **b**, Fluorescence emission spectrum of Pt-DMF solution. Excitation wavelength: 260 nm.
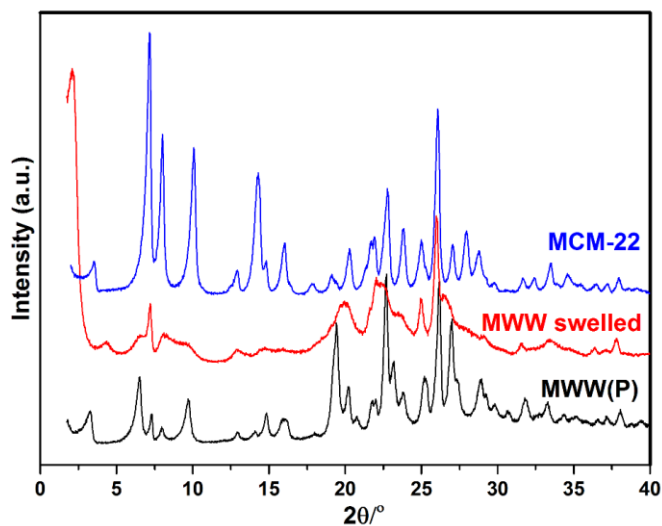
Figure 5.3. XRD Patterns of MWW(P), swelled MWW and MCM-22 obtained from the swelled MWW after calcination.
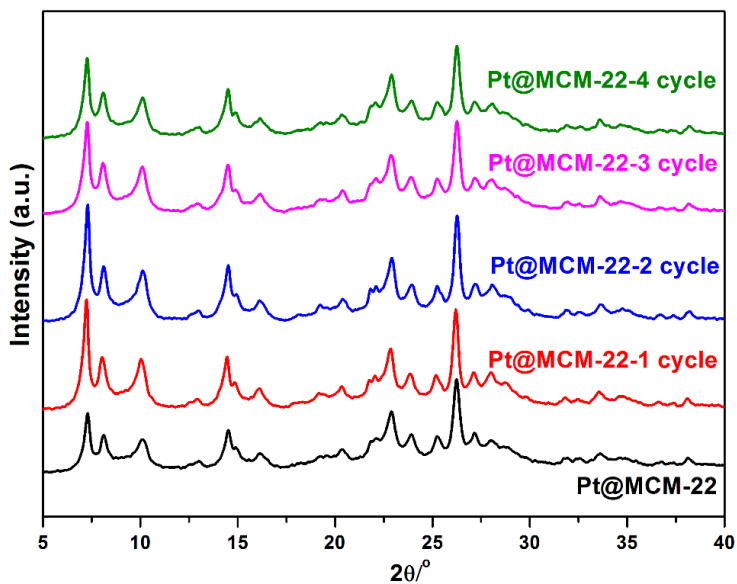
Figure 5.4. XRD patterns of fresh Pt@MCM-22 sample and samples after different cycles of oxidation-reduction treatments at 650 °C. The crystal structure of MCM-22 zeolite is preserved after the high-temperature treatments.
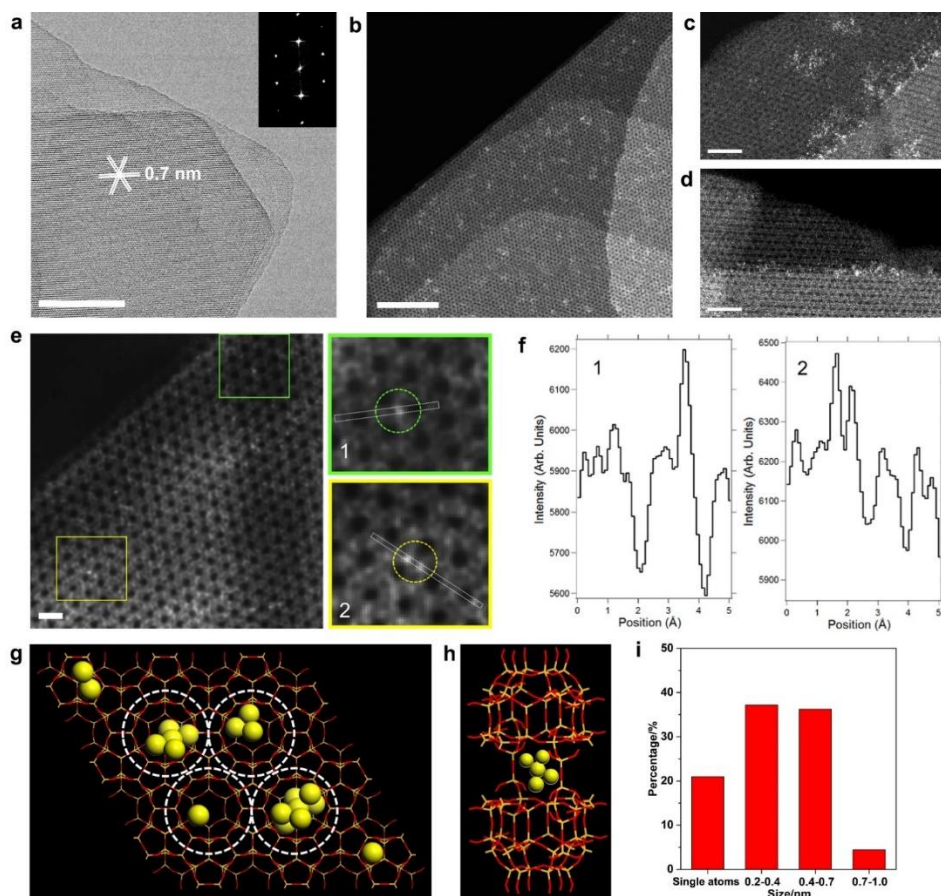
Figure 5.5. Atomic structures of Pt@MCM-22. a, TEM image of Pt@MCM-22. The insert is the corresponding FFT diffractogram of the TEM image. Scale bar, 50 nm. **b**, HAADF-STEM image of Pt@MCM-22. Scale bar, 20 nm. **c** and **d**, Atomic structures of Pt clusters confined in MCM-22. Scale bar, 5 nm. **e**, HAADF-HRSTEM image of Pt@MCM-22, where two zooms have been done in the square regions (marked in green (#1) and yellow (#2)). In these two areas, several single atoms have been highlighted. Scale bar, 2 nm. **f**. Corresponding intensity profiles obtained on the two zoomed areas. **g**, Schematic illustration of Pt@MCM-22 in a "top-down" view along the *c* axis. Pt clusters and individual Pt atoms are located in the surface cups, cavities and 12-MR supercages. **h**, Schematic illustration of Pt_5 cluster in supercages of MCM-22.

i, Size distribution of subnanometric Pt species in Pt@MCM-22 sample.
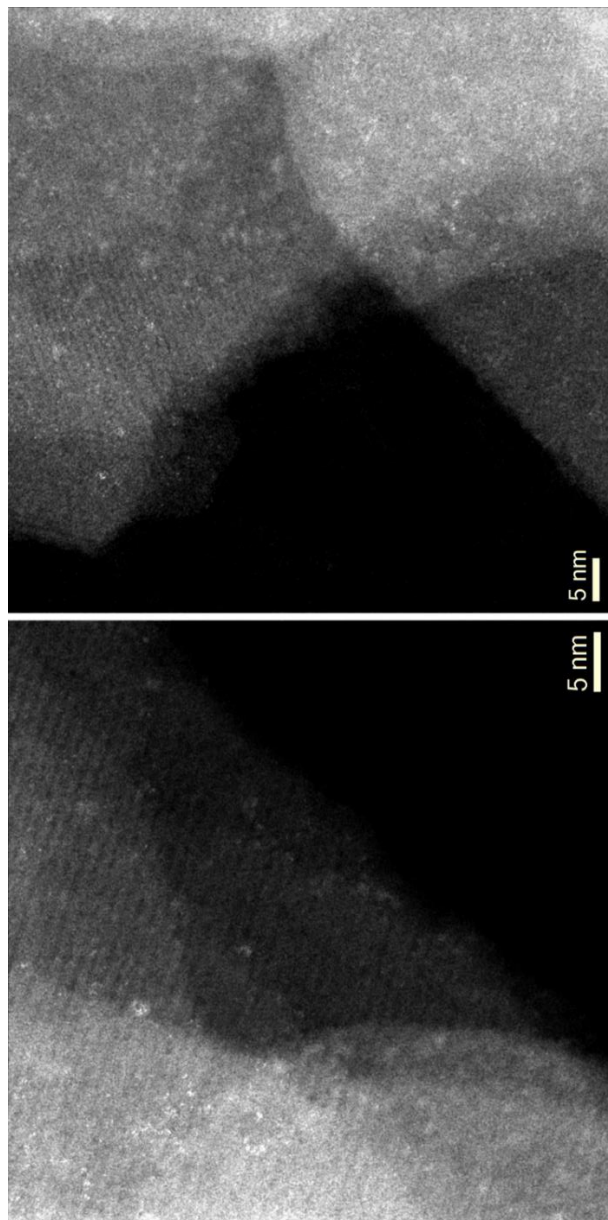
Figure 5.6. Enlarged STEM images of Pt@MCM-22. The bright points correspond to Pt species. The fine dispersion of subnanometric Pt species can be seen clearly.
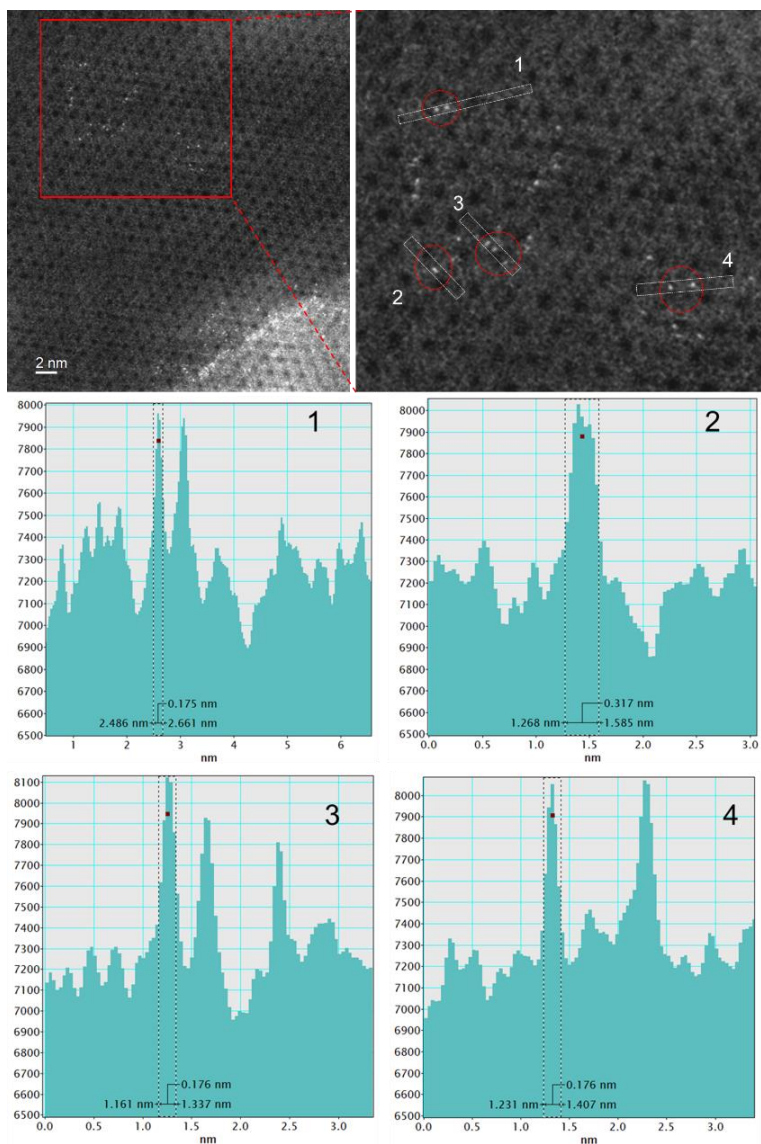
Figure 5.7. HAADF-HRSTEM micrograph, where a zoom has been done (red marked area). Several single and two superposed/neighboring atoms (see example labelled as #2) have been highlighted and different intensity profiles have been obtained on them (see graphs #1 to #4). The different brightness of two neighboring atoms can be caused by their different heights in c direction.
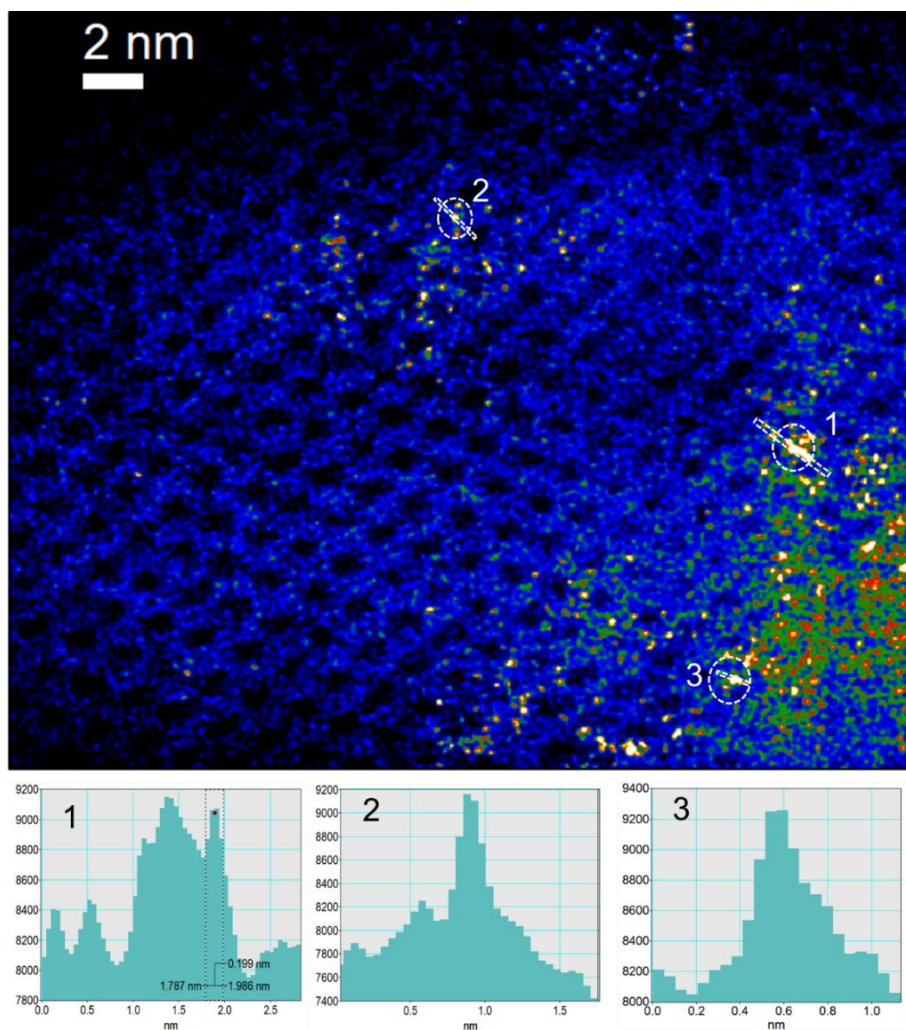
Figure 5.8. HAADF-HRSTEM images of Pt@MCM-22, where three zooms have been done. Individual Pt atoms and Pt clusters have been highlighted and their intensity profiles have been obtained on them (see graphs #1 to #3). In particular, #1 corresponds to a cluster of five Pt atoms, #2 to a single Pt atom and #3 to three Pt atoms, respectively. According to the simulation results, some very bright spots may correspond to a linear Pt chain (several Pt atoms along c direction) in the MCM-22 crystallite.
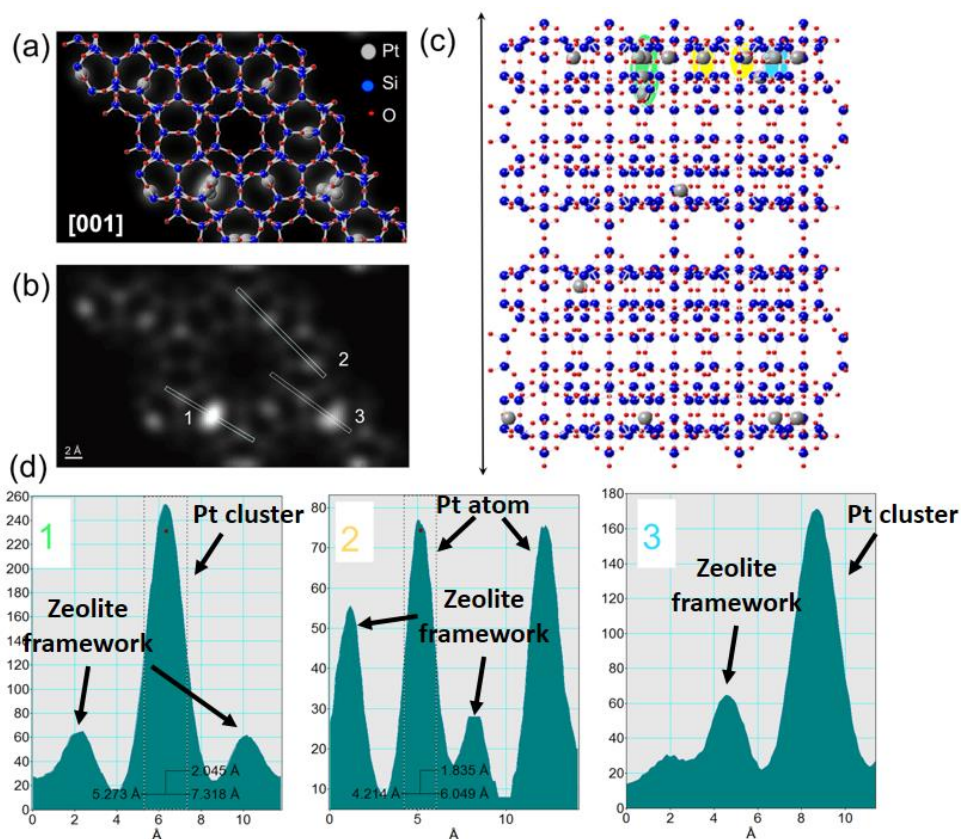
Figure 5.9. Simulation of STEM images of Pt species in MCM-22 zeolite.
(a) Ball and stick model of the original MCM-22 zeolite where Pt species
(single atoms and clusters) are incorporated. This illustration is viewed from
[001] direction. The simulated HRSTEM–HAADF image is superposed to this
model. However, for sake of clarity, this simulated HRSTEM–HAADF image
is also displayed in (b). (c) Ball and stick model of the same structure depicted
in (a) and (b), viewed from the [010] direction. (d) Intensity profiles obtained
at different locations (marked in green, yellow and blue, respectively)
corresponding to: (area 1#) a Pt_4 cluster, with a linear chain of three Pt atoms
along the "*c*" direction; (area 2#) two single Pt atoms; (area 3#) a Pt_4 cluster, 2
of them at almost the same X and Y coordinates.
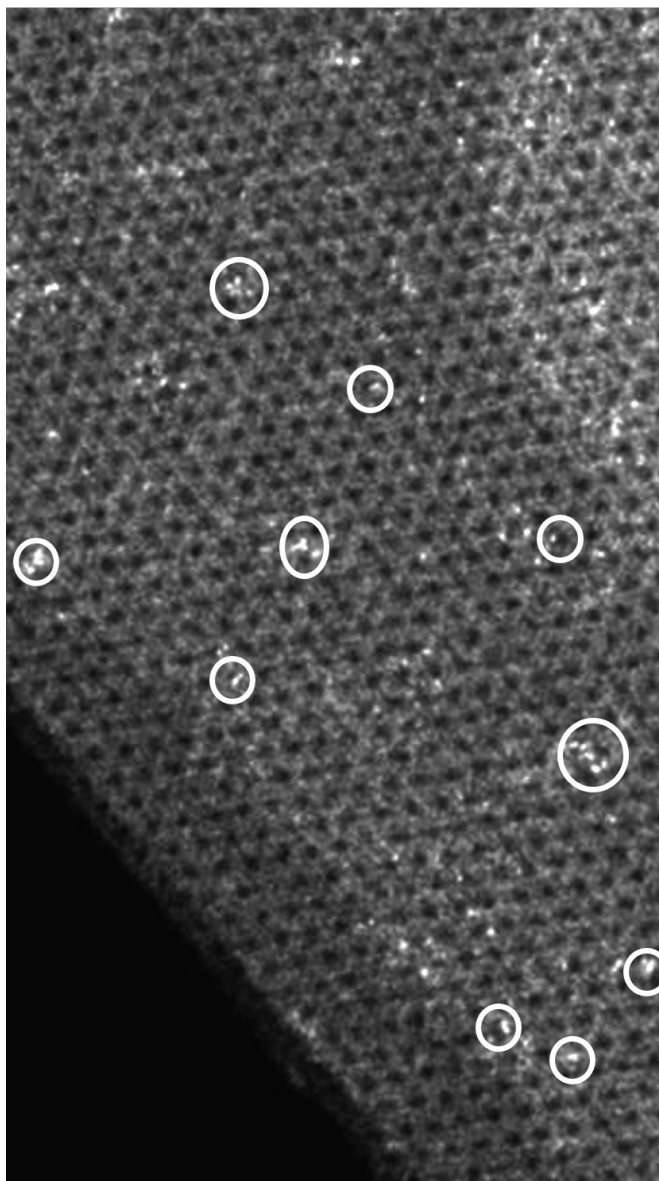
Figure 5.10. High-resolution STEM image of Pt@MCM-22. Pt single atoms and Pt clusters as well as the 12-member ring of MCM-22 can be seen clearly. The white circles indicate some typical subnanometric Pt species located in the cavities or supercages of MCM-22. In this image, we can also observe some Pt single atoms and clusters located on the framework of MCM-22.
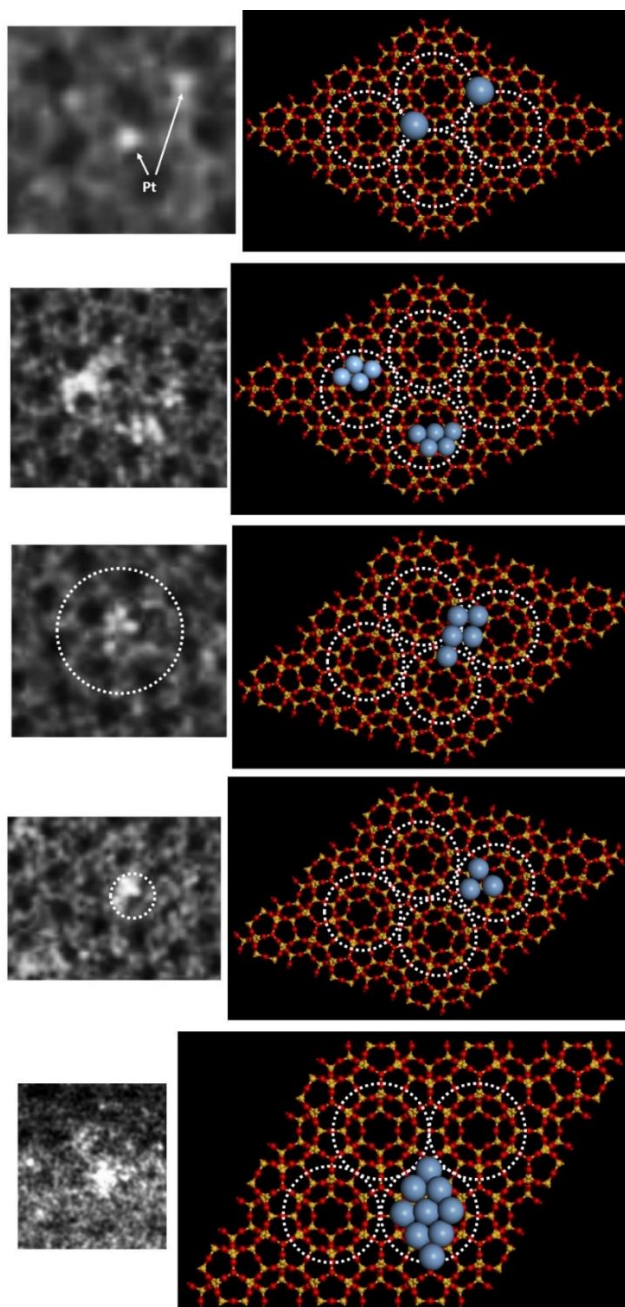
Figure 5.11. Schematic illustration of the location of Pt species in MCM-22.
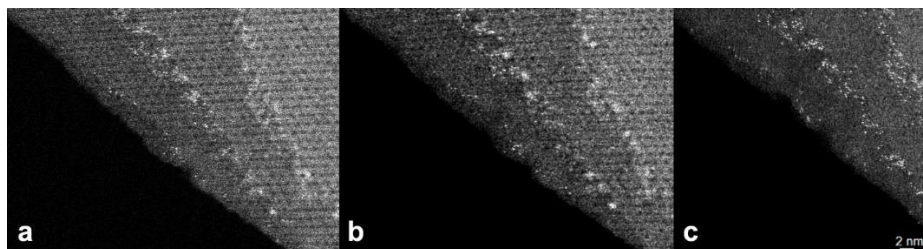
Figure 5.12. HAADF-HRSTEM images of Pt@MCM-22 acquired consecutively. The electron beam damage in the MCM-22 structure is clearly visible between (b) and (c). The destruction of the crystalline structure of MCM-22 and consequent mass loss, allow to better resolve the Pt atoms/clusters due to the change of focus conditions in (c).

Due to the beam sensitivity of zeolites, the location of the atoms/clusters cannot be investigated by focal-series studies.[22,23] However, the fact that we are performing these HRSTEM-HAADF studies in an aberration-corrected microscope offers the possibility to have access to the third dimension by varying the depth of focus. As can be seen in **Figure 5.12**, even if the structure of MCM-22 is destroyed (including mass loss) by electron beam, Pt species still remain at the same position or just move only a few angstroms, indicating that these Pt atoms/clusters are probably embedded/anchored in the internal space of zeolite crystallites. Nevertheless, information about the location of Pt species can be deduced according to the molecular sieving effect of MCM-22, which will be discussed in the following catalytic activity section.

The particle size distribution of subnanometric Pt species shown in **Figure 5.5i** has been obtained by counting more than 300 particles. And a size distribution ranging from single atoms to Pt clusters nearly to 1 nm, with a majority for Pt clusters between 0.2-0.7 nm, can be seen there. It has been reported that subnanometric metal species (single atoms and clusters) are unstable above 250 °C.[24-26] However, if one considers that the preparation procedure of Pt@MCM-22 includes a high-temperature process (540 °C for 4 h) for removal of organic template, it appears that subnanometric Pt species in Pt@MCM-22 show excellent thermal stability in air.
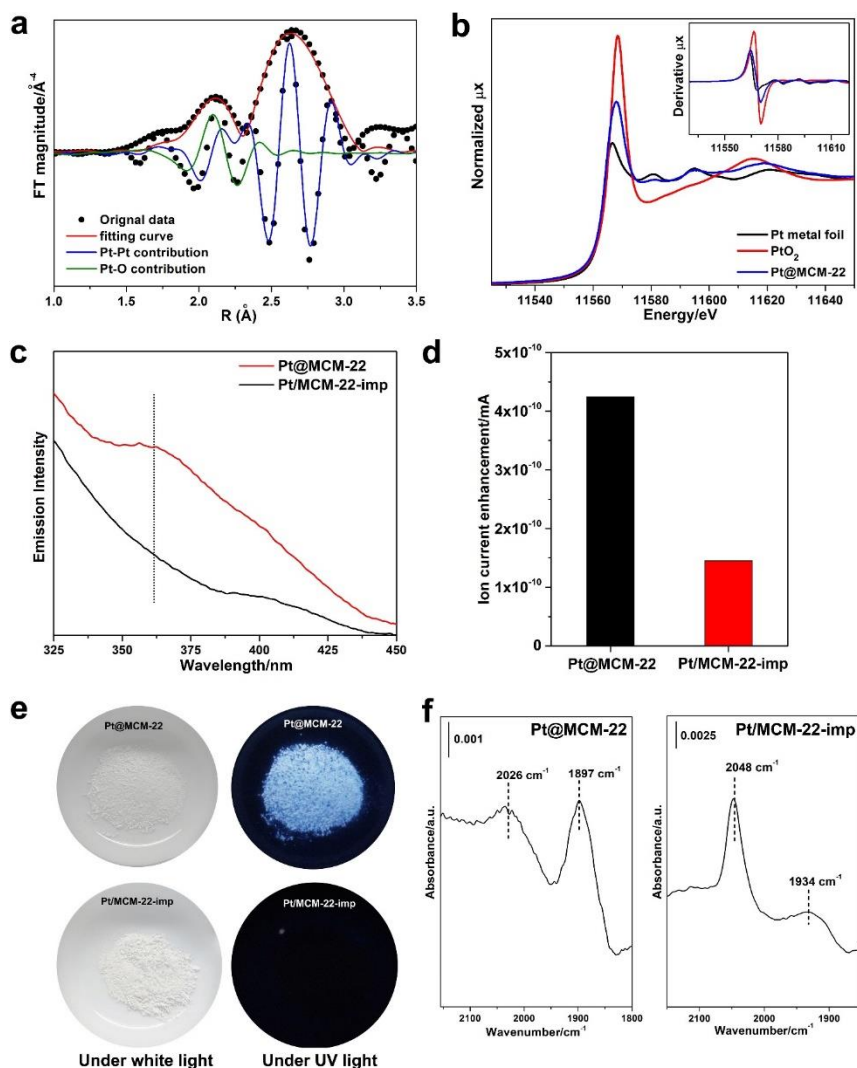
Figure 5.13. Characterizations of Pt@MCM-22 and Pt/MCM-22-imp. a, Fourier transform of k^3-weighted EXAFS spectrum of the Pt@MCM-22 sample (not phase-corrected). The fitting curves for Pt-O and Pt-Pt contribution are also presented. **b**, XANES spectrum of Pt@MCM-22 as well as the first-order derivative spectrum. **c**, Fluorescence emission spectra excited at 260 nm. **d**, Enhancement of the mass signal of HD in H_2-D_2 exchange experiments on Pt@MCM-22 and Pt/MCM-22-imp at room temperature. **e**, photographs of Pt@MCM-22 and Pt/MCM-22-imp under white light and UV light. **f**, IR

spectra of CO adsorption on Pt@MCM-22 and Pt/MCM-22-imp.

Table 1 Result of the fit performed on **Pt@MCM-22** EXAFS spectrum

	CN	σ^2	**R**	**E$_0$**
Path		Å^{-2}	Å	eV
Pt-O	2.1±0.6	0.004	2.506±0.017	2.9
Pt-Pt	4.7±0.5	0.005	2.765±0.004	

$S_0^2 = 0.85$ fixed from the value extracted from the fit of the Pt foil, E_0 and ss^2 fixed from Pt foil; $\Delta k = (3.6–14.3)$ Å^{-1} and $\Delta R = (1.4–3.5)$ Å

Spectroscopic characterization of samples

Pt@MCM-22 sample has been measured by X-ray adsorption spectroscopy (XAS) to study the local environment of Pt and to estimate the coordination numbers of Pt species. The Fourier transform of extended X-ray absorption fine structure (EXAFS) spectra of Pt@MCM-22 and the Pt and PtO$_2$ reference are shown in **Figure 5.13a** and **Figure 5.14**. Considering the first shell, Pt@MCM-22 spectrum is dominated by a peak centered around 2.65 Å with a smaller contribution at 2.08 Å (both distances not phase corrected). Comparing with reference samples, the stronger contribution can be assigned to Pt-Pt bonds in Pt clusters. The assignation of weaker peak is too long to be ascribed to Pt-O bonds from PtO$_2$ (1.65 Å, see **Figure 5.14**), but according to literature data it is compatible with Pt-O bonds between Pt and the zeolite frameworks.[27] The presence of Pt-O bonds in Pt@MCM-22 sample has also been confirmed by the X-ray absorption near edge structure (XANES) spectrum of Pt@MCM-22. As it can be seen in **Figure 5.13b**, the curve shape of Pt@MCM-22 sample looks like Pt(0) (first derivative and oscillations around 11580 and 11595 eV) but white line intensity is higher, indicating the presence of Pt-O bonds.[25] Based on the fitting results of the EXAFS spectrum (see **Table 1**), the coordination number of Pt in Pt@MCM-22 is ca. 4.7, that would correspond to Pt clusters with size less than 0.7 nm (i.e. with less than 13 atoms), assuming that Pt clusters show cubo-octahedral shape.[28,29] Even though the atomicity of Pt species obtained based on EXAFS data is slightly larger than that obtained based on HRSTEM images, the average size is still in the cluster size range (below 0.7 nm), which is in line with the results obtained from electron

microscopy and our synthesis principle.
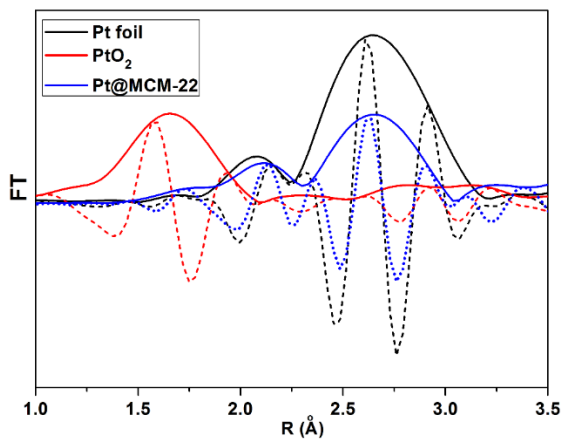
Figure 5.14. |FT| spectrum of Pt@MCM-22. Pt foil and PtO_2 reference spectra are also presented for comparison.
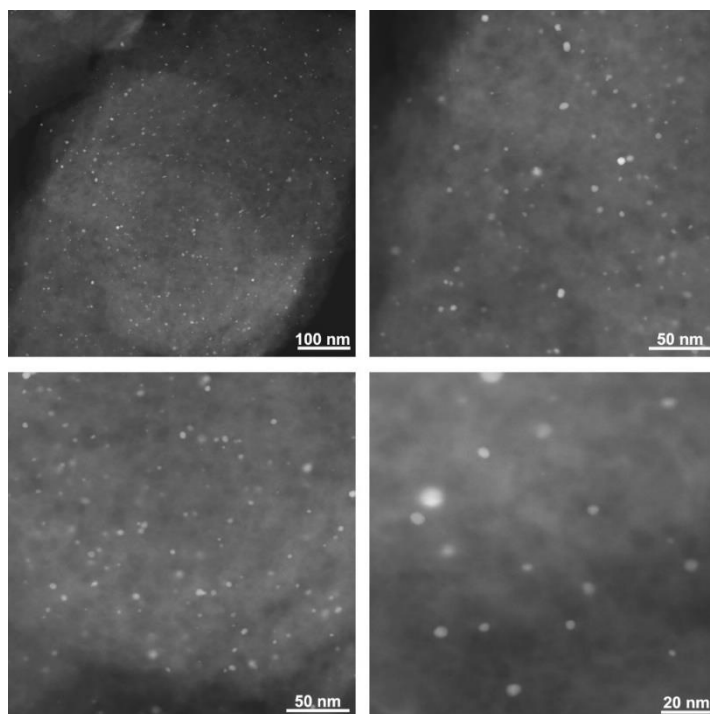
Figure 5.15. STEM images of Pt/MCM-22-imp prepared from conventional

impregnation method.

As it is well known, the optical properties of metal clusters and metal NPs are very different due to their distinct electronic structures. For comparison, we have prepared a Pt/MCM-22-imp sample with 0.2 wt% of Pt by a conventional impregnation method (see **Methods**). As shown in **Figure 5.S15**, Pt NPs with size of 1~5 nm are formed on MCM-22. The fluorescence emission spectra under excitation at 260 nm (see **Figure 5.13c**) show that Pt@MCM-22 with Pt clusters present a clear emission peak around 360 nm which can be associated to Pt clusters with less than 10 atoms.[31,32] In contrast, no fluorescence emission signal can be observed in Pt/MCM-22-imp. The fluorescence emission of Pt clusters can also be seen from the pictures of the two samples under white light and UV light, respectively. As shown in **Figure 5.13e**, strong fluorescent light emission can be observed in Pt@MCM-22 sample under UV light.

To compare the different properties of subnanometric Pt species in Pt@MCM-22 and Pt NPs in Pt/MCM-22-imp on H_2 activation, H_2-D_2 exchange experiments were carried out.[33] Notice that H_2 can diffuse through the 10-MR window that communicate the supercages in where a portion of Pt species are encapsulated. The results given in **Figure 5.13d** show that the formation rate of HD over Pt@MCM-22 is much higher than over Pt/MCM-22-imp, indicating that subnanometric Pt species in Pt@MCM-22 are more active on the H_2 activation than Pt NPs in Pt/MCM-22-imp, which is in agreement with literature.[34]

In order to investigate the chemical states of Pt species in Pt@MCM-22 and Pt/MCM-22-imp, CO was used as probe molecule for IR spectroscopy. As shown in **Figure 5.13f**, two CO adsorption bands can be observed, which can be ascribed to CO interacting in lineal and bridge configuration, respectively. The reported CO frequency for Pt species in Pt@MCM-22 are lower than those observed for CO adsorbed in atop positions of Pt nanoparticles supported on MCM-22 and some conventional oxide carriers,[35,36] which indicates a higher electron donor capacity of the subnanometric Pt species. It was suggested that zeolite matrix can act as electron donor increasing electron density of encapsulated Pt clusters.[37] On the other hand, small metal cluster may bear a higher electron charge due to their higher unsaturation degree, while specific supports could modify net electronic charge of the clusters.[38]
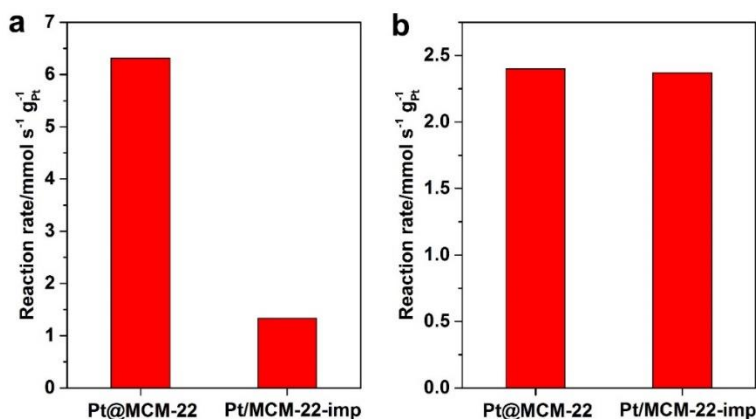
Figure 5.16. Reaction rates of Pt@MCM-22 and Pt/MCM-22-imp in hydrogenation of light olefins. (a) Hydrogenation of propylene and (b) hydrogenation of isobutene. The reaction rates are normalized based on the amount of Pt species in both catalysts.

Catalytic activity

As it has been presented above, incorporation of Pt in expanded layered precursor of MCM-22 leads to isolated Pt atoms and Pt clusters on the cups located at external surface and also probably in the internal space of MCM-22. On the other hand, in the case of Pt/MCM-22-imp sample prepared by impregnation method, most of Pt NPs (1~5 nm) should be only located at the external surface. To test the catalytic properties and to bring more information on the location of Pt species in Pt@MCM-22 sample, we have chosen hydrogenation of alkenes with different molecular sizes as probe reactions. Firstly, the hydrogenation of propylene, which can diffuse through 10-MR windows and reach the supercavities with subnanometric Pt species, was performed in fixed-bed reactor. Results in **Figure 5.16a** show a higher activity of Pt@MCM-22 than Pt/MCM-22-imp. Notice that the reaction rate of Pt species is about five times higher for Pt@MCM-22. This difference of activity between Pt@MCM-22 and Pt/MCM-22-imp has also been observed before for the H_2-D_2 exchange experiment. The results would confirm the accessibility of propylene to all Pt species regardless of their location within the zeolite. However, as we said before, Pt species can also be encapsulated within 0.7×

1.8 nm supercavities of MCM-22, which are only accessible through the 10-MR windows. As shown in **Figure 5.16b**, the reaction rates for hydrogenation of isobutene of Pt/MCM-22-imp is similar to that of Pt@MCM-22, which is contrary to the activity difference for the propylene hydrogenation. Indeed, due to the molecular sieving effect of 10-MR windows in MCM-22, isobutene is only accessible to Pt species located at the external cups on the surface of MCM-22 while it should not be accessible to Pt atoms and clusters encapsulated in the cavities inside MCM-22. Therefore, by combining STEM characterization and the catalytic results on hydrogenation of propylene and isobutene, one can speculate that a large part of Pt species are located within the supercavities of MCM-22 in the Pt@MCM-22 sample.
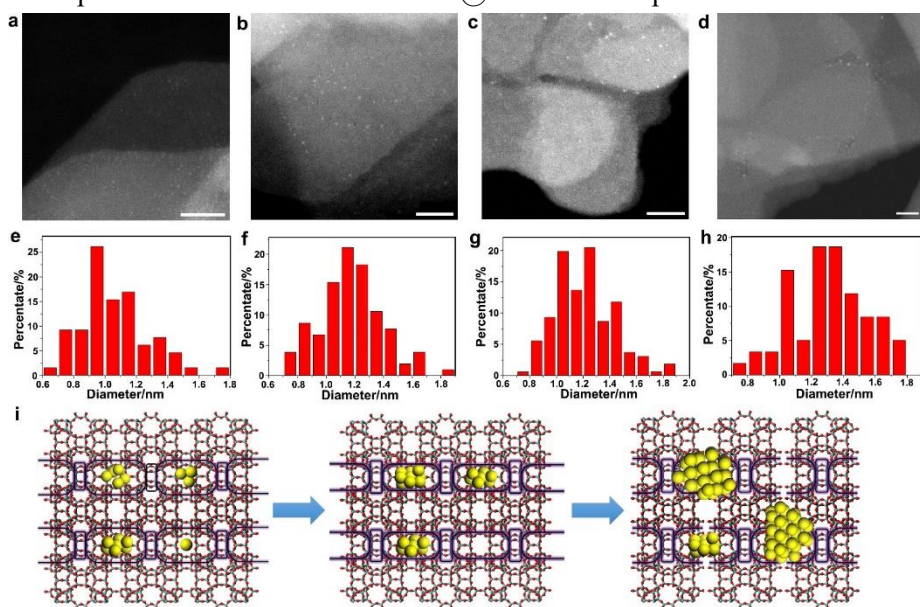
Figure 5.17. Pt@MCM-22 after high-temperature oxidation-reduction treatments. STEM images of Pt@MCM-22 after different cycles of oxidation-reduction treatments at 650 °C. **a**, Pt@MCM-22-1cycle. **b**, Pt-@MCM-22-2cycles. **c**, Pt-@MCM-22-3cycles. **d**, Pt@MCC-22-4cycles. Scale bar in **a-d**, 20 nm. Size distributions of small Pt nanoparticles encapsulated in Pt@MCM-22 after different cycles of oxidation-reduction treatments at 650 °C. **e**, Pt@MCM-22-1cycle. **f**, Pt-@MCM-22-2cycles. **g**, Pt-@MCM-2 2-3cycles. **h**, Pt@MCC-22-4cycles. **i**, Schematic illustration of the evolution of Pt individual

atoms and Pt clusters encapsulated in MCM-22 during the high-temperature oxidation-reduction treatments.

High-temperature stability of Pt@MCM-22

The exceptional stability of the subnanometric Pt species in Pt@MCM-22 have been demonstrated by performing oxidation-reduction treatments at 650 $^{\circ}$C. Under such harsh conditions, small Pt NPs with size of ~1 nm can be found in Pt@MCM-22 after one cycle of oxidation-reduction treatment at 650 $^{\circ}$C (see **Figure 5.17a** and **Figure 5.18**). Those individual Pt atoms and small Pt clusters with a few atoms located in the internal space of MCM-22 crystallite have mostly aggregate to larger Pt clusters or small Pt NPs (1~2 nm). As for Pt clusters with more than 5 atoms, they should be more stable because they are captured by the cups and supercages of MCM-22. Checking by STEM, we have observed some Pt clusters below 1 nm while few Pt individual atoms can be found on in the Pt@MCM-22-1cycle sample (as shown in **Figure 5.19**). With more cycles of oxidation-reduction treatments, Pt clusters will continue to grow larger, as presented in **Figure 5.17b** to **Figure 5.17d** (more STEM images can be found from **Figure 5.20** to **Figure 5.22**). Nevertheless, their size distributions **(Figure 5.17f** to **Figure 5.17h**) show that most of the small Pt NPs are still below 2 nm, indicating the high stability of encapsulated Pt species in MCM-22 crystallites during the very extreme oxidation-reduction treatments at 650 $^{\circ}$C. In the case of Pt/MCM-22-imp, oxidation-reduction treatments at 650 $^{\circ}$C lead to continuous growth of Pt NPs (images are presented from **Figure 5.S23** to **Figure 5.S26** and the size distributions of Pt NPs are shown in **Figure 5.S27.**). In the Pt/MCM-22-imp-4cycles sample (**Figure 5.S26**), some Pt NPs as large as 30~50 nm are observed. However, it is important to take into account that, due to the lower melting and boiling point of Pt nanoclusters, subnanometric Pt species can be mobile during the high-temperature treatments, especially for those Pt species located on the external surface.[39-41] Thus, after four oxidation-reduction cycles at 650 $^{\circ}$C, only ~30% of the initial Pt (measured by ICP) will be remaining in the Pt@MCM-22 sample. Despite that, the stability against agglomeration of Pt species encapsulated in MCM-22 are still much better than the Pt/MCM-22-imp materials prepared through conventional impregnation methods.
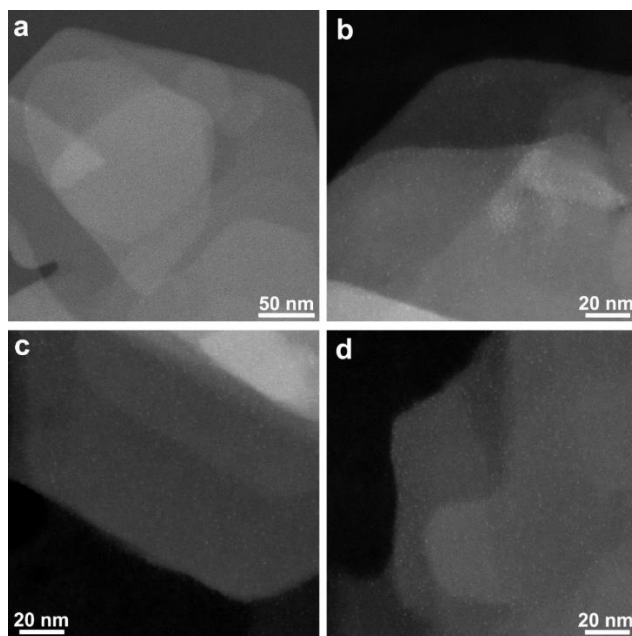
Figure 5.18. Some enlarged typical STEM images of Pt@MCM-22-1cycle sample.
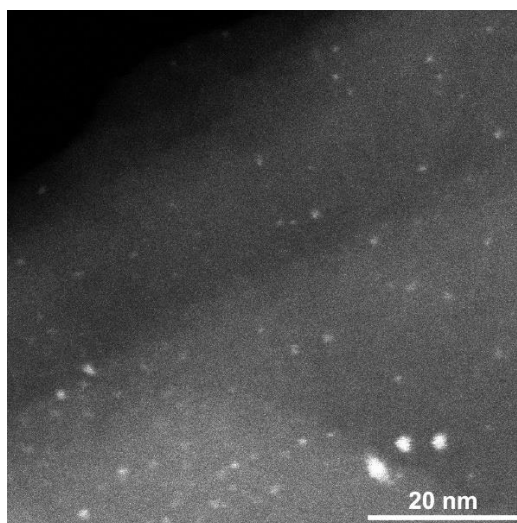
Figure 5.19. STEM image of Pt@MCM-22-1cycle sample. Pt clusters around 0.5 nm as well as some small Pt nanoparticles between 1-2 nm can been seen.
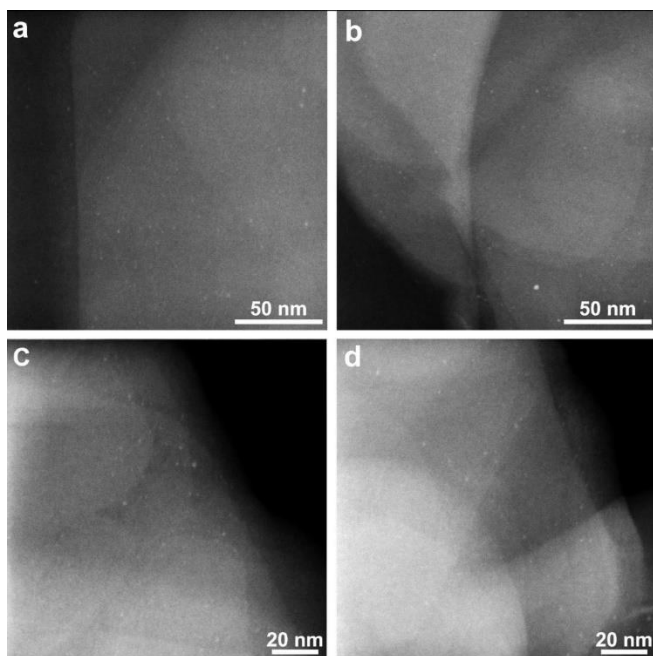
Figure 5.20. Some enlarged typical STEM images of Pt@MCM-22-2cycles.
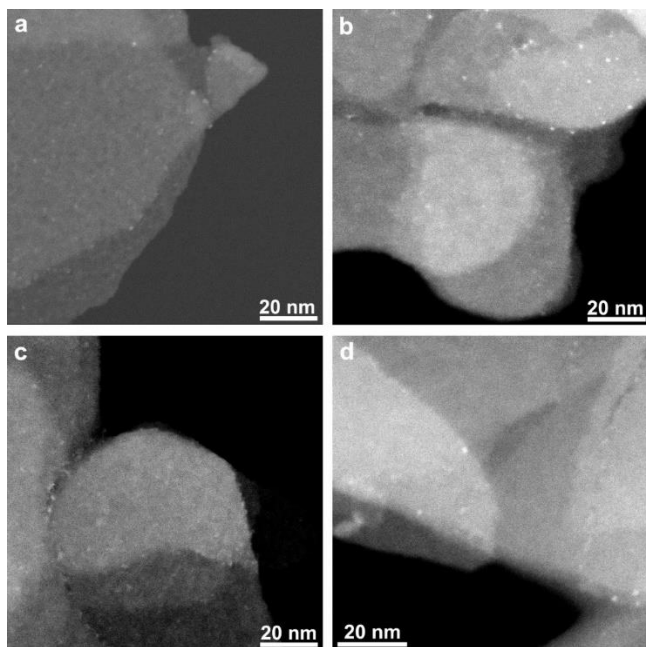
Figure 5.21. Some enlarged typical STEM images of Pt@MCM-22-3cycles.
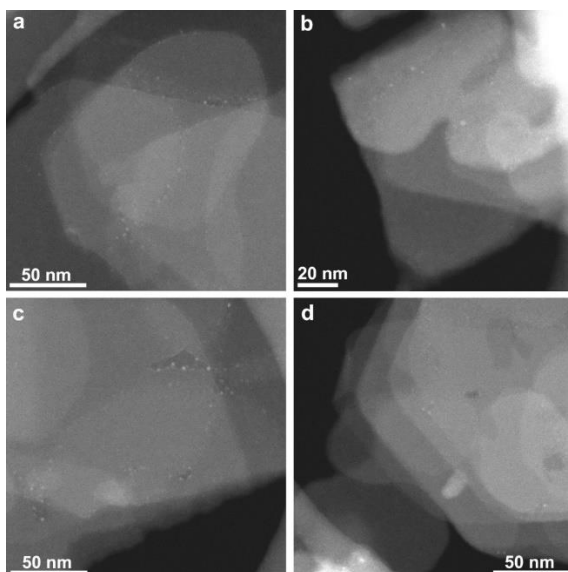
Figure 5.22. Some enlarged typical STEM images of Pt@MCM-22-4cycles.
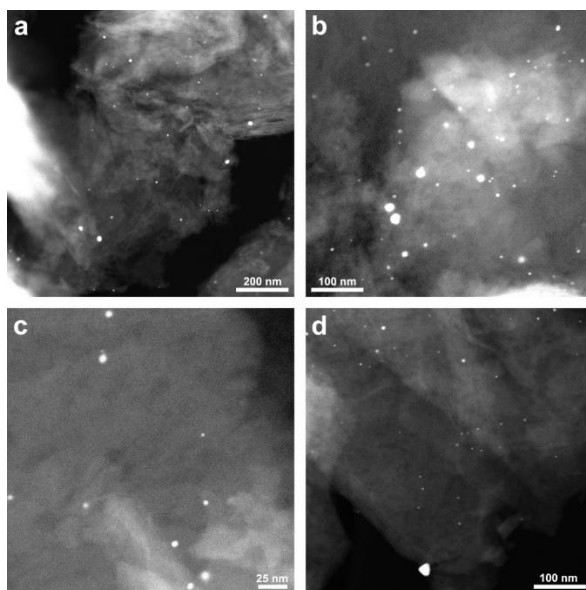
Figure 5.23. STEM images of Pt/MCM-22-imp prepared from conventional impregnation method after one oxidation-reduction cycle at 650 °C. This sample is named as Pt/MCM-22-imp-1cycle.
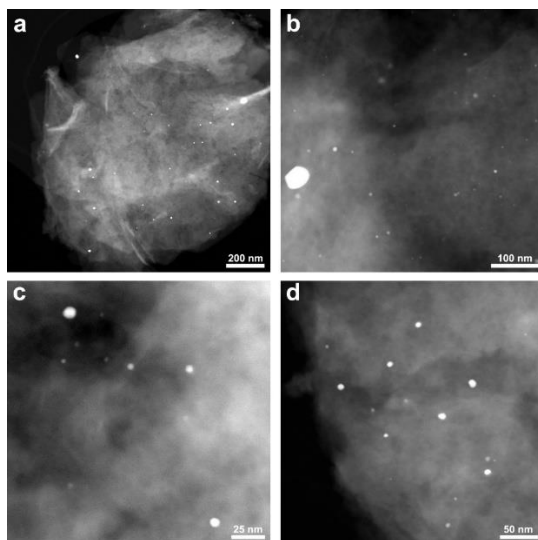
Figure 5.24. STEM images of Pt/MCM-22-imp prepared from conventional impregnation method after two oxidation-reduction cycle at 650 $^{\circ}$C. This sample is named as Pt/MCM-22-imp-2cycles.
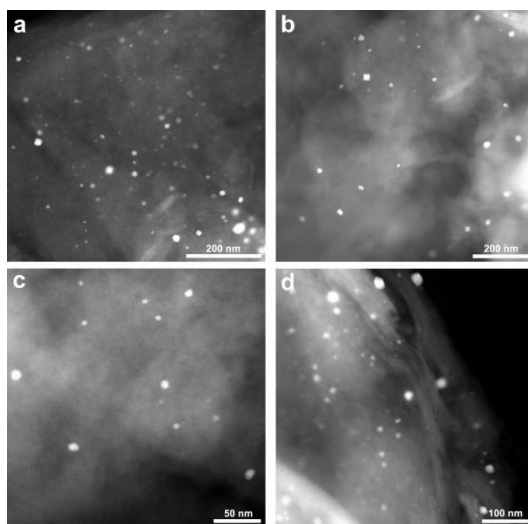
Figure 5.25. STEM images of Pt/MCM-22-imp prepared from conventional impregnation method after three oxidation-reduction cycle at 650 $^{\circ}$C. This sample is named as Pt/MCM-22-imp-3cycles.
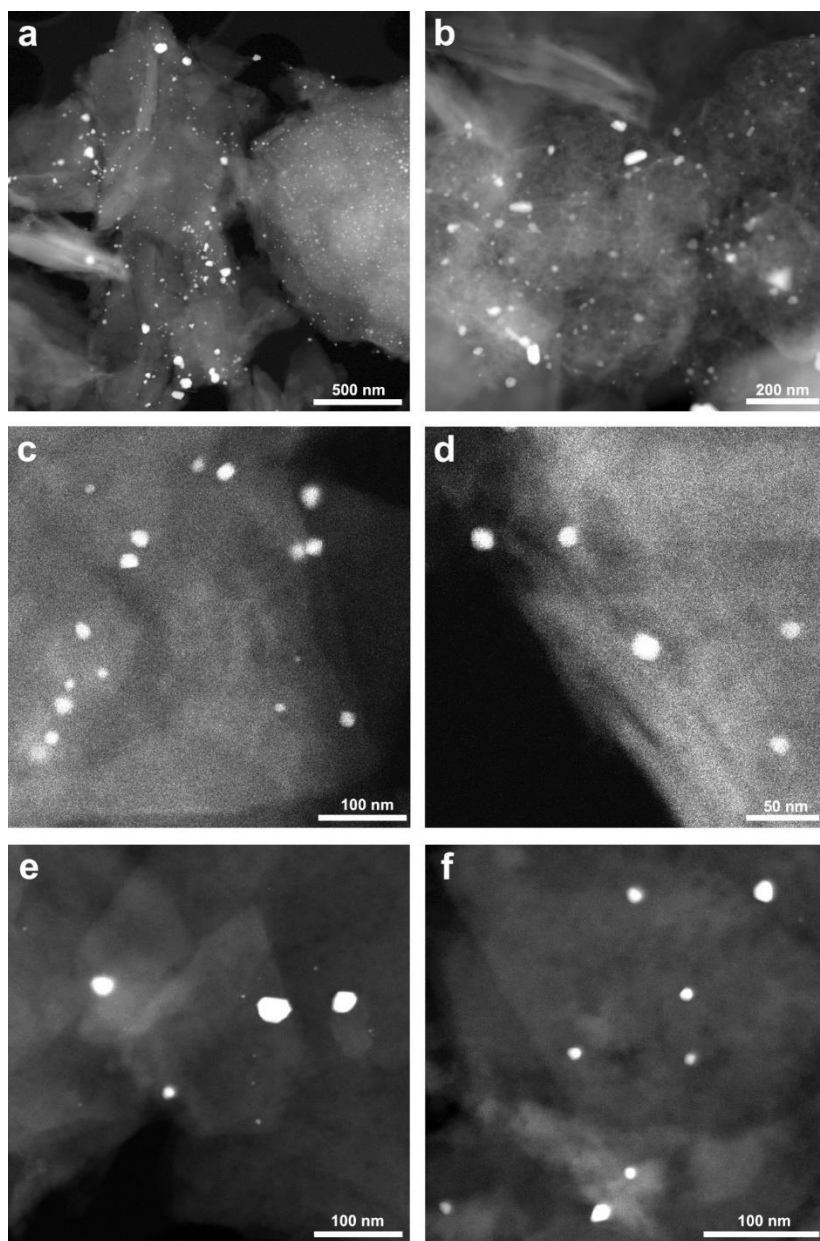
Figure 5.26. STEM images of Pt/MCM-22-imp prepared from conventional impregnation method after four oxidation-reduction cycle at 650 °C. This sample is named as Pt/MCM-22-imp-4cycles.
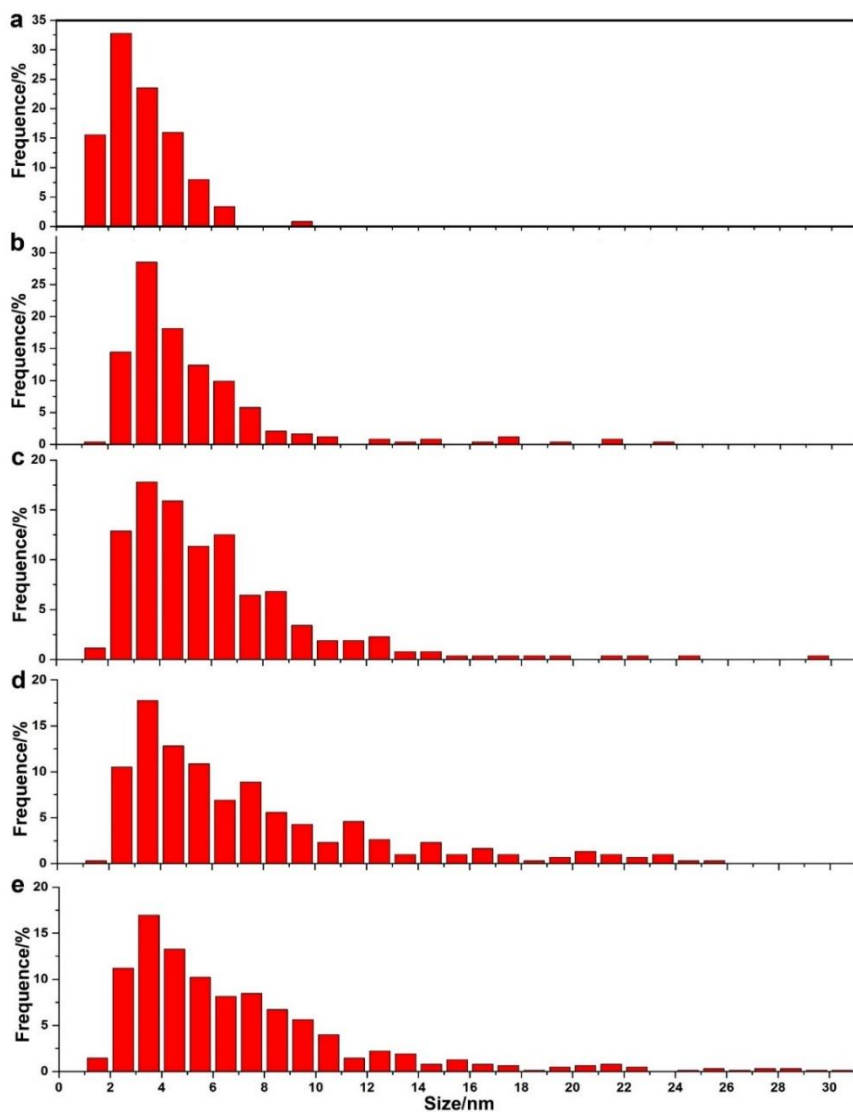
Figure 5.27. Size distribution of Pt nanoparticles in Pt/MCM-22-Imp samples and samples after different cycles of oxidation-reduction treatments at 650 ºC. a, Fresh Pt/MCM-22-Imp, **b**, Pt/MCM-22-imp-1cycle, **c**, Pt/MCM-22-imp-2cycles, **d**, Pt/MCM-22-imp-3cycles and **e**, Pt/MCM-22-imp-4cycles.
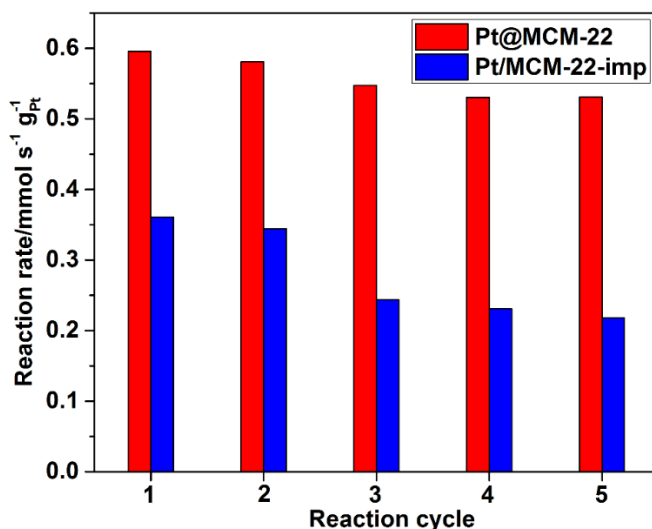
Figure 5.28. Stability tests of Pt@MCM-22 and Pt/MCM-22-imp in five cycles of dehydrogenation of propane to propylene. The reaction works at 550 °C. The reaction rates were measured when the conversion of propane is lower than 10% and the values have been normalized to the amount of Pt in the catalysts.
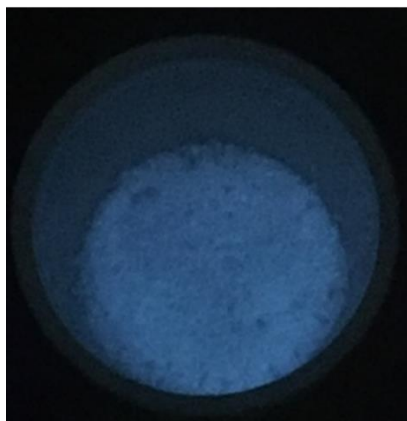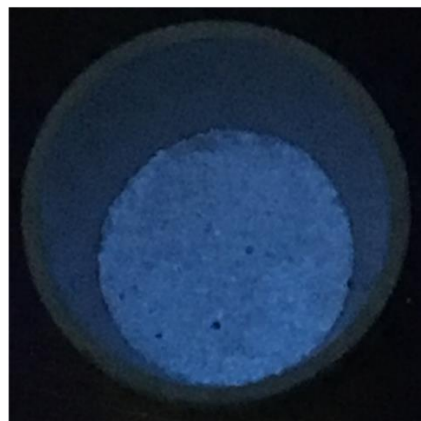
Figure 5.29. Photograph of Pt@MCM-22 samples after two cycles and five cycles of oxidation-reduction treatments in dehydrogenation of propane at 550 °C. The two samples show fluorescence emission under UV light.
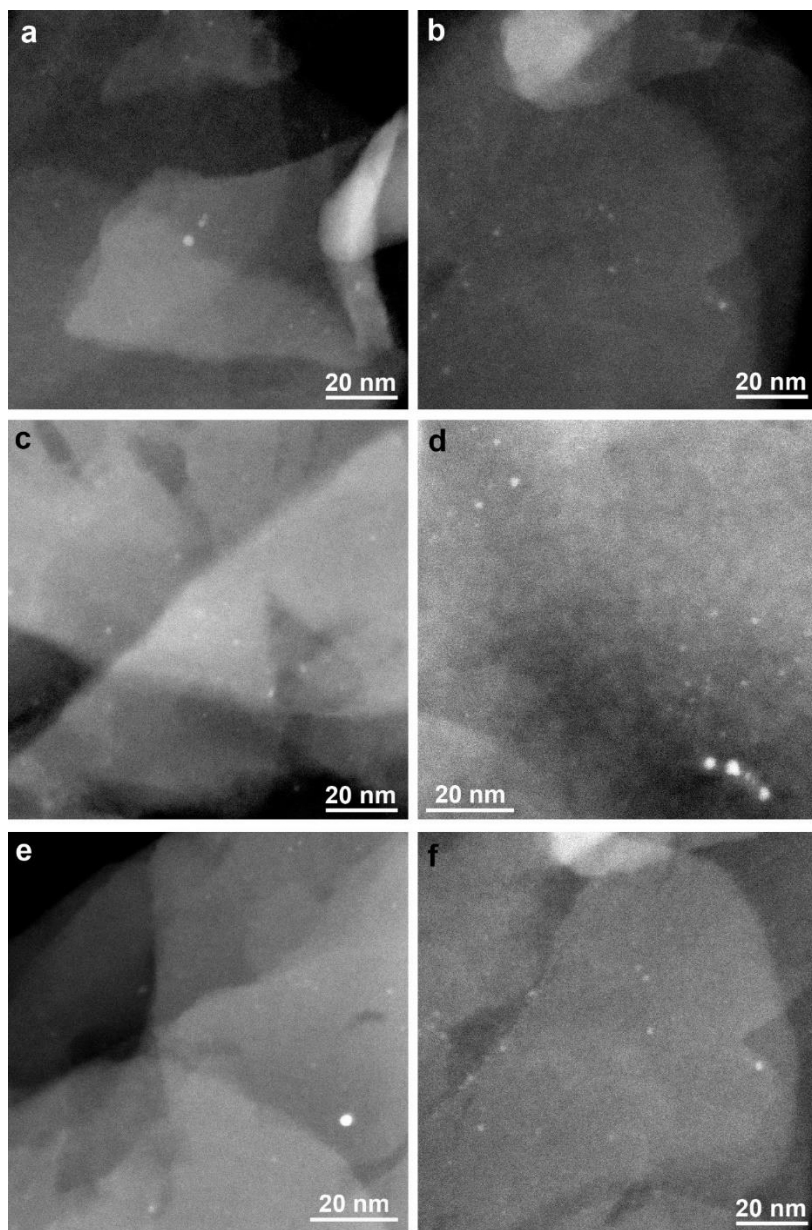
Figure 5.30. STEM images of Pt@MCM-22 sample after two cycles of oxidation-reduction treatments in propane dehydrogenation reaction at 550 ºC.
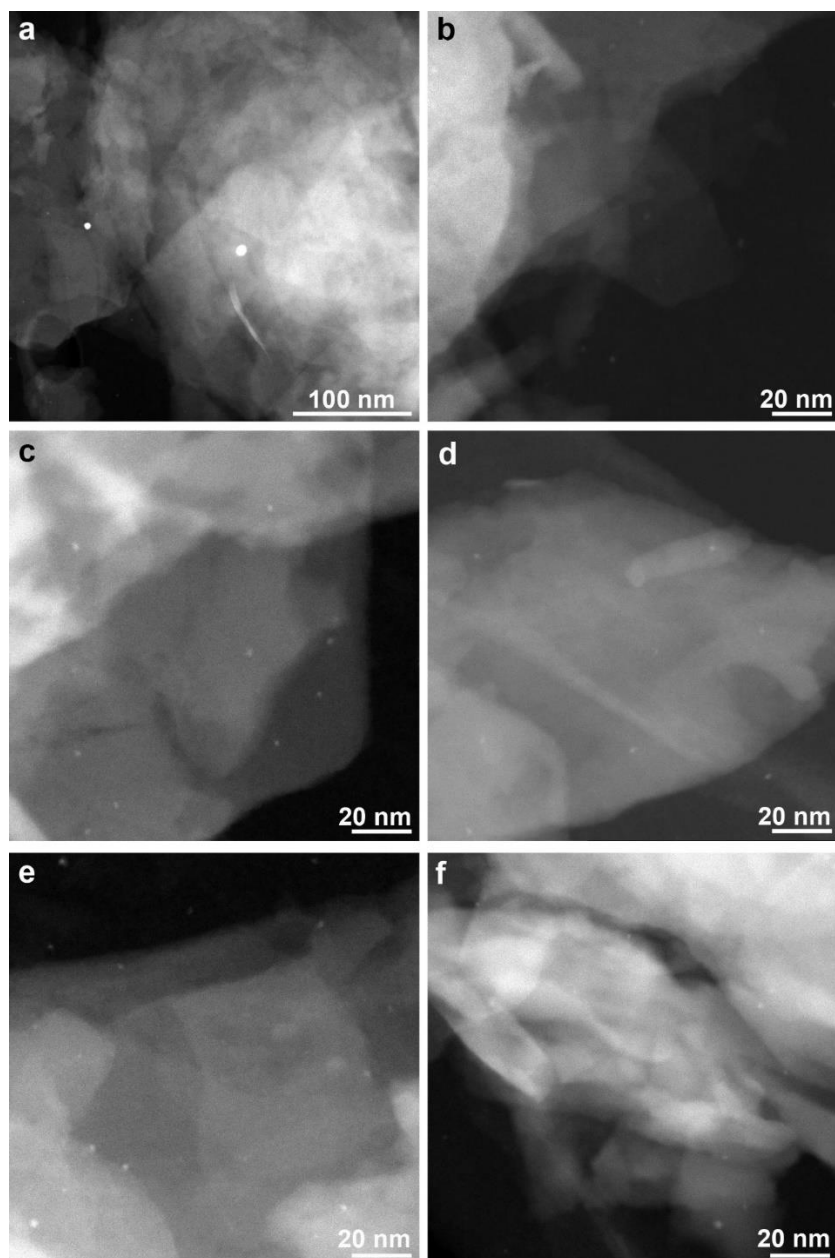
Figure 5.31. STEM images of Pt@MCM-22 sample after five cycles of oxidation-reduction treatments in propane dehydrogenation reaction at 550 ºC.

Taking into account the higher stability of Pt@MCM-22, we also decide to

test its catalytic activity for dehydrogenation of propane. Indeed, dehydrogenation of short alkane molecules is of much interest to activate alkanes and catalytic processes require frequent reaction-regeneration cycles at high temperature.[42] As can be seen in **Figure 5.28**, Pt@MCM-22 exhibits higher activity than Pt/MCM-22-imp at 550 °C. Moreover, after five reaction-regeneration cycles at 550 °C during the catalytic dehydrogenation of propane, Pt@MCM-22 sample retains ~90% of its initial activity while Pt/MCM-22-imp has lost more than 40% of the initial activity. It should be remarked that no significant loss of Pt in Pt@MCM-22 sample is observed by ICP after five cycles of propane dehydrogenation reaction. Then, Pt@MCM-22 sample after two and five oxidation-reduction cycles at 550 °C has also been studied by STEM. As shown in **Figure 5.30** and **Figure 5.31**, particle sizes of most of the Pt species slightly increase and still remain below 2 nm. Strong fluorescence emission under UV light can also be observed on those two samples (see **Figure 5.29**), indicating the presence of Pt clusters even after treatments at 550 °C. This is in agreement with the higher thermal stability of the Pt@MCM-22 sample.

Conclusions

We have presented a new strategy to prepare subnanometric Pt catalysts in 3D MCM-22 zeolite with exceptional high stability, starting from a 2D MWW-type precursors. Pt single atoms and clusters are stable after calcination in air at 540 °C and under reaction conditions. This new method provides a possibility for the generation of highly stable subnanometric metal catalysts for high-temperature catalytic reactions in pure siliceous zeolites.

Methods

Synthesis of the solution containing Pt clusters. Subnanometric Pt species are prepared by a dimethylformamide (DMF) reduction method. 20 mg Pt(acac)$_2$ (Platinum(II) acetylacetonate) are dissolved in 40 mL DMF. Then the solution is heated at 140 °C for 16 h.

Synthesis of ITQ-1 and Swelled ITQ-1. ITQ-1 zeolite (IZA code MWW) is the pure silica analog of MCM-22. It can be synthesized using trimethyladamantammonium (TMAda$^+$) as structure directing agent in absence

of alkali cations, but reproducibility problems appeared. If hexamethyleneimine (HMI) is added as second SDA, the reproducibility of the synthesis, as well as the quality of the materials obtained, are greatly improved. The use of TMAda$^+$, HMI and sodium cations allows a fast and highly reproducible synthesis of pure silica ITQ-1.

An example of the procedure for the synthesis of ITQ-1 using TMAda$^+$, HMI and Na$^+$ cations is as follows: 0.95 g of NaCl are dissolved in 50.70 g of a solution 0.42 M of N,N,N-trimethyl-1-adamantanamonium hydroxide, previously diluted with 21.33 g of water. Then, 2.62 g of hexamethyleneimine are added to this solution, followed by 4.88 g of silica (Aerosil 200, Degussa) under continuous stirring. This reaction mixture is heated in a PTFE lined stainless steel autoclave at 150 °C rotated at 60 rpm for 5 days. After filtering, the white solid obtained is washed until pH was less than 9.

In order to prepare the swelled purely siliceous ITQ-1 with subnanometric Pt species, 2 g of the lamellar precursor was dispersed in 8 g of H$_2$O milliQ, and 40 g of a cetyltrimethylammonium hydroxide solution (25 wt.%, 50% exchanged Br$^-$/OH$^-$) and 12 g of a solution of tetrapropylammonium hydroxide (40 wt.%, 30% exchanged Br$^-$/OH$^-$) were added together with 40 mL of Pt-DMF solution, being the final pH around 12.5. The resultant mixture was heated at 52 ^{o}C, stirring vigorously, for 16 hours in order to facilitate the swelling of the layers of the precursor material. At this point, the solid was recovered by centrifugation and washed with distilled water, being dried at 60 ^{o}C for 12 hours.

Synthesis of Pt@MCM-22. Pt@MCM-22 can be obtained through the calcination of the Pt@Swelled MWW(P) composite. The calcination process is performed as following. 1) Rising temperature from room temperature to 540 ^{o}C with a ramp rate of 2 ^{o}C/min in N$_2$ atmosphere. The total time in N$_2$ atmosphere is about 4.5 h. 2) Switching the atmosphere to air and keep at 540 ^{o}C for 4 h. 3) Cooling from 540 ^{o}C to room temperature in air atmosphere. The obtained sample is denoted as Pt@MCM-22.

Stability test of Pt@MCM-22 samples. In order to test the thermal stability of the subnanometric Pt species, a high-temperature oxidation-reduction cyclic treatment was used. Fresh Pt@MCM-22 sample is firstly sent to reduction treatment at 650 ^{o}C in O$_2$ (temperature ramp rate is 2 ^{o}C/min and maintain at

650 °C for 2 h). After reduction treatment, the sample is calcined at 650 °C in H_2 (temperature ramp rate is 2 °C/min and maintain at 650 °C for 2 h). The above reduction and oxidation treatment is considered as one cycle and the sample after one-cycle treatment is called Pt@MCM-22-1cycle. In a similar way, Pt@MCM-22-1cycle can be further treated in consecutive oxidation-reduction cycles.

Preparation of Pt/MCM-22-imp through impregnation method. In order to compare with the Pt@MCM-22 materials, Pt/MCM-22-imp sample was prepared through conventional wet-impregnation method. MCM-22 (prepared through the calcination of ITQ-1) is used as the support. DMF solution containing subnanometric Pt species are used as the precursor for Pt nanoparticles. In a typical preparation of Pt/MCM-22-imp with 0.2 wt.% of Pt, 2.2 g MCM-22 (pure silica) was firstly dispersed in 25 mL of H_2O and 35 mL of Pt-DMF solution. The suspension was kept stirring at room temperature for 30 min and then sent to a silicone oil bath at 120 °C to remove the solvent. After removing the solvent, the solid was dried in air at 100 °C for 16 h. At last, Pt/MCM-22-imp can be obtained after reduction in H_2 at 450 °C (temperature ramp rate is 5 °C/min) for 3 h.

We have also tried to use incipient wetness impregnation (IWI) method to prepare supported Pt nanoparticles on MCM-22. However, the dispersion of Pt obtained by the IWI method does not give better dispersion of Pt species on MCM-22.

Characterizations

Samples for electron microscopy studies were prepared by dropping the suspension of Pt@MCM-22 or other materials using ethanol as the solvent directly onto holey-carbon coated Cu grids. The measurements were performed using a JEOL 2100F microscope operating at 200 kV both in transmission (TEM) and scanning-transmission modes (STEM). STEM images were obtained using a High Angle Annular Dark Field detector (HAADF), which allows Z-contrast imaging. The current density is 0.9 pA/cm^2 when working on JEOL 2100F. High-resolution STEM (HRSTEM) imaging, using the HAADF detector, was performed using a FEI Titan Low-Base microscope operated at

300 kV and equipped with a Cs probe corrector (CESCOR from CEOS GmbH), a monochromator and an ultra-bright X-FEG electron source. The convergence angle was 25 mrad and the inner and outer angles for HAADF imaging were 70 and 200 mrad, respectively. The typical probe current was set to 2 pA and the total dose on the sample varied between ~ 0.2-3 C/cm^2 under the HRSTEM imaging conditions, which corresponds to low-dose conditions.[43] Multi-slice HRSTEM-HAADF image simulations have been carried out using QSTEM software,[44] with the experimental settings of the FEI Titan Low Base as inputs. For this purpose, the thermal diffuse scattering parameter was fixed at 30 for a temperature of 300 K.

Hydrogen/deuterium (H_2-D_2) exchange experiments were carried out in a flow reactor at room temperature (25 ^{o}C). The formation rate of HD species can be measured by the enhancement of the mass signal intensity (ion current). The feed gas consisted of 4 mL/min H_2, 4 mL/min D_2 and 18 mL/min argon, and the total weight of catalyst was 115 mg. The sample has been diluted with 230 mg of SiC. Reaction products (H_2, HD and D_2) were analysed with a mass spectrometer (Omnistar, Balzers). The m/z mass used are 2 for H_2, 4 for D_2 and 3 for HD. The sample was in situ reduced at 200 ^{o}C for 2 h with a temperature-rising rate of 10 ^{o}C/min from room temperature to 200 ^{o}C. Then the temperature was decreased to 25 ^{o}C and, once stabilized, the H_2 feed was changed to the reactant gas composition. The temperature was maintained at 25 ^{o}C for about 60 minutes.

Powder X-ray diffraction (XRD) was performed with a HTPhilips X'Pert MPD diffractometer equipped with a PW3050 goniometer using Cu Kα radiation and a multisampling handler.

XAS measurements were carried out on the BM23 beamline at ESRF facility (Grenoble, France). Fluorescence XAS spectra at the Pt L_3-edge (11.564 keV) were collected with a 13-element Ge detector on self-supported pellet at room temperature, Pt reference foil was collected for energy calibration. The beam energy were selected by double-crystal Si(111) monochromator, third harmonic rejection was performed by Rh coated mirror with an angle of -4 mrad.[45] EXAFS signal were extracted and analyzed by IFEFFIT package.[46]

Measurement of catalytic performance of Pt@MCM-22 and Pt/MCM-22-imp.

Hydrogenation of propylene was performed in a flow fix-bed continuous reactor. 30 mg Pt@MCM-22 diluted with 2 g SiC (the grain size of SiC used in this work is between 0.4 to 0.6 mm) powder was loaded in a quartz tube reactor. The reaction was performed at room temperature with a flow of 2 mL/min of propylene, 6 mL/min of H_2 and 32.7 mL of Ar. Products were analyzed with a Bruker on-line GC with FID detector. The conversion of C_3H_6 was kept below 15 % to calculate the reaction rates.

Hydrogenation of isobutene was performed in a flow fix-bed continuous reactor. 30 mg Pt@MCM-22 diluted with 2 g SiC powder was loaded in a quartz tube reactor. The reaction was performed at room temperature with a flow of 1.5 mL/min of isobutene, 4.5 mL/min of H_2 and 24 mL of Ar. Products were analyzed by Bruker on-line GC with FID detector. The conversion of isobutene was kept below 15 % when calculating reaction rates.

Dehydrogenation of propane was performed in a fix-bed reactor. A cylindrical quartz tube was loaded with 1.10 g of Pt@MCM-22 catalyst material (In the case of Pt/MCM-22-imp, the amount of catalyst was 0.60 g). Catalyst was diluted with SiC to keep the total volume of solid constant (3 cm^3). Before the reaction, the sample was reduced by H_2 at 550 $^{\circ}$C. The reaction was run at 550 $^{\circ}$C with a flow of 30 mL/min of propane and 3 mL/min of N_2 for 15 min, followed by a regeneration step at 550 $^{\circ}$C with a flow of air for 30 min. The reaction stream was analyzed by an on-line Varian GC, which was equipped with a flame ionization detector (FID) and a thermal conductivity detector (TCD). Conversion of C_3H_8 was kept below 10 % to calculate the initial reaction rate.

References

(1) Boronat, M.; Leyva-Perez, A.; Corma, A. *Acc. Chem. Res.* **2014,** *47*, 834-844.

(2) Flytzani-Stephanopoulos, M.; Gates, B. C. Atomically dispersed supported metal catalysts. *Ann. Rev. Chem. Biomol. Eng.***2012,** *3*, 545-574.

(3) Gates, B. C. *Chem. Rev.***1995,** *95*, 511-522.

(4) Corma, A.; Concepcion, P.; Boronat, M.; Sabater, M. J.; Navas, J.; Yacaman,

M. J.; Larios, E.; Posadas, A.; Lopez-Quintela, M. A.; Buceta, D.et al. *Nat. Chem.* **2013, 5**, 775-781.

(5) Yang, M.; Li, S.; Wang, Y.; Herron, J. A.; Xu, Y.; Allard, L. F.; Lee, S.; Huang, J.; Mavrikakis, M.; Flytzani-Stephanopoulos, M. *Science* **2014, 346**, 1498-1501.

(6) Rivallan, M.; Seguin, E.; Thomas, S.; Lepage, M.; Takagi, N.; Hirata, H.; Thibault-Starzyk, F. *Angew. Chem. Int. Ed.* **2010, 49**, 785-789.

(7) Zecevic, J.; van der Eerden, A. M.; Friedrich, H.; de Jongh, P. E.; de Jong, K. P. *ACS Nano* **2013, 7**, 3698-3705.

(8) Philippaerts, A.; Paulussen, S.; Breesch, A.; Turner, S.; Lebedev, O. I.; Van Tendeloo, G.; Sels, B.; Jacobs, P. *Angew. Chem. Int. Ed.* **2011, 50**, 3947-3949.

(9) Kim, J.; Kim, W.; Seo, Y.; Kim, J.-C.; Ryoo, R. *J. Catal.* **2013, 301**, 187-197.

(10) Goel, S.; Wu, Z.; Zones, S. I.; Iglesia, E. *J. Am. Chem. Soc.* **2012, 134**, 17688-17695.

(11) Choi, M.; Wu, Z.; Iglesia, E. *J. Am. Chem. Soc.* **2010, 132**, 9129-9137.

(12) Choi, M.; Yook, S.; Kim, H. *ChemCatChem* **2015, 7**, 1048-1057.

(13) Kulkarni, A.; Lobo-Lapidus, R. J.; Gates, B. C. *Chem. Commun.* **2010, 46**, 5997-6015.

(14) Guzman, J.; Gates, B. C. *Dalton Trans.* **2003**, 3303.

(15) Leonowicz, M. E.; Lawton, J. A.; Lawton, S. L.; Rubin, M. K. *Science* **1994, 264**, 1910-1913.

(16) Camblor, M. A.; Corell, C.; Corma, A.; Díaz-Cabañas, M.-J.; Nicolopoulos, S.; González-Calbet, J. M.; Vallet-Regí, M. *Chem. Mater.* **1996, 8**, 2415-2417.

(17) Hyotanishi, M.; Isomura, Y.; Yamamoto, H.; Kawasaki, H.; Obora, Y. *Chem. Commun.* **2011, 47**, 5750-5752.

(18) Duchesne, P. N.; Zhang, P. *Nanoscale* **2012, 4**, 4199-4205.

(19) Lu, J.; Aydin, C.; Browning, N. D.; Gates, B. C. *Angew. Chem. Int. Ed.* **2012, 51**, 5842-5846.

(20) *Advanced Transmission Electron Microscopy: Applications to Nanomaterials*, Eds. Francis, L.; Mayoral, A.; Arenal, R. **2015**, Springer.

(21) Jena, P.; S. N. Khanna, S. N.; Rao, B. K. *Physics and Chemistry of Finite*

Systems: From Clusters to Crystals, **1992**, Springer Netherlands.

(22) Yamasaki, J.; Mori, M.; Hirata, A.; Hirotsu, Y.; Tanaka, N. *Ultramicroscopy* **2015,** *151*, 224-231.

(23) Yang, M. L.; Zhu, Y. A.; Fan, C.; Sui, Z. J.; Chen, D.; Zhou, X. G. *Phys. Chem. Chem. Phys.* **2011,** *13*, 3257-3267.

(24) Aydin, C.; Lu, J.; Browning, N. D.; Gates, B. C. *Angew. Chem. Int. Ed.* **2012,** *51*, 5929-5934.

(25) Wei, H.; Liu, X.; Wang, A.; Zhang, L.; Qiao, B.; Yang, X.; Huang, Y.; Miao, S.; Liu, J.; Zhang, T. *Nat. Commun.* **2014,** *5*, 5634.

(26) Addou, R.; Senftle, T. P.; O'Connor, N.; Janik, M. J.; van Duin, A. C.; Batzill, M. *ACS Nano* **2014,** *8*, 6321-6333.

(27) Jung, U.; Elsen, A.; Li, Y.; Smith, J. G.; Small, M. W.; Stach, E. A.; Frenkel, A. I.; Nuzzo, R. G. *ACS Catal.* **2015,** *5*, 1539-1551.

(28) Agostini, G.; Piovano, A.; Bertinetti, L.; Pellegrini, R.; Leofanti, G.; Groppo, E.; Lamberti, C. *J. Phys. Chem. C* **2014,** *118*, 4085-4094.

(29) Alexeev, O.; Gates, B. C. *Top. Catal.* **2000,** *10*, 273-293.

(30) Fornasini, P.; Grisenti, R. *J. Synchrotron Rad.* **2015,** *22*, 1242-1257.

(31) Chakraborty, I.; Bhuin, R. G.; Bhat, S.; Pradeep, T. *Nanoscale* **2014,** *6*, 8561-8564.

(32) Zheng, J.; Nicovich, P. R.; Dickson, R. M. *Ann. Rev. Phys. Chem.* **2007,** *58*, 409-431.

(33) Okrut, A.; Runnebaum, R. C.; Ouyang, X.; Lu, J.; Aydin, C.; Hwang, S. J.; Zhang, S.; Olatunji-Ojo, O. A.; Durkin, K. A.; Dixon, D. A.et al. *Nat. Nanotechnol.* **2014,** *9*, 459-465.

(34) Zhou, C.; Wu, J.; Nie, A.; Forrey, R. C.; Tachibana, A.; Cheng, H. *J. Phys. Chem. C* **2007,** *111*, 12773-12778.

(35) De La Cruz, C.; Sheppard, N. *Spectr. Acta A: Mol. Spectr.* **1994,** *50*, 271-285.

(36) Klünker, C.; Balden, M.; Lehwald, S.; Daum, W. *Surf. Sci.* **1996**, *360*, 104-111.

(37) Stakheev, A. Y.; Shpiro, E. S.; Jaeger, N. I.; Schulz-Ekloff, G. *Catal. Lett.* **1995,** *32*, 147-158.

(38) Heiz, U.; Sanchez, A.; Abbet, S.; Schneider, W. D. *J. Am. Chem. Soc.* **1999,** *121*, 3214-3217.

(39) Levitas, V. I.; Samani, K. *Nat. Commun.* **2011,** *2*, 284.

(40) Jiang, H.; Moon, K.-s.; Dong, H.; Hua, F.; Wong, C. P. *Chem. Phys. Lett.* **2006,** *429*, 492-496.

(41) Nanda, K. K.; Kruis, F. E.; Fissan, H. *Phys. Rev. Lett.* **2002,** *89*, 256103.

(42) Vajda, S.; Pellin, M. J.; Greeley, J. P.; Marshall, C. L.; Curtiss, L. A.; Ballentine, G. A.; Elam, J. W.; Catillon-Mucherie, S.; Redfern, P. C.; Mehmood, F. et al. *Nat. Mater.* **2009,** *8*, 213-216.

(43) Ortalan, V.; Uzun, A.; Gates, B. C.; Browning, N. D. *Nat. Nanotechnol.* **2010,** *5*, 843-847.

(44) Koch, C. *PhD Thesis*, 2002, Arizona State University.

(45) Mathon, O.; Beteva, A.; Borrel, J.; Bugnazet, D.; Gatla, S.; Hino, R.; Kantor, I.; Mairs, T.; Munoz, M.; Pasternak, S. et al. *J. Synchrotron Rad.* **2015,** *22*, 1548-1554.

(46) Newville, M. *J. Synchrotron Rad.* **2001,** *8*, 322-324.

This chapter is reused from the following publication:

Evolution and stabilization of subnanometric metal species in confined space by in situ TEM, **L. Liu**, D.N. Zakharov, R. Arenal, P. Concepcion, E.A. Stach and A. Corma, ***Nature Communications***, 2018, 9, 574.

Rights and permissions

Chapter 6

Evolution and stabilization of subnanometric metal species in confined space by *in situ* TEM
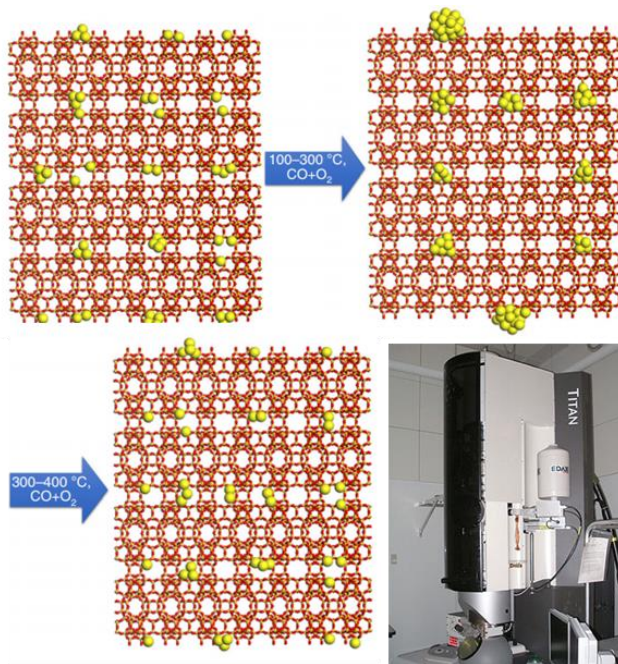
Abstract

Understanding the behavior and dynamic structural transformation of subnanometric metal species under reaction conditions will be helpful for understanding catalytic phenomena and for developing more efficient and stable catalysts based on single atoms and clusters. In this work, the evolution and stabilization of subnanometric Pt species confined in MCM-22 zeolite has been studied by *in situ* transmission electron microscopy (TEM). By correlating the results from *in situ* TEM studies and the results obtained in a continuous fix-bed reactor, it has been possible to delimitate the factors that control the dynamic agglomeration and redispersion behavior of metal species under reaction conditions. The dynamic reversible transformation between atomically dispersed Pt species and clusters/nanoparticles during CO oxidation at different temperatures has been elucidated. It has also been confirmed that subnanometric Pt clusters can be stabilized in MCM-22 crystallites during NO reduction with CO and H_2.

Introduction

Subnanometric metal catalysts (including single-atom metal species and metal clusters) have attracted great attention in material science in general and more specifically in the heterogeneous catalysis community, due to their unique properties and behaviors compared with conventional nanoparticulate catalysts.[1,2] While it is already possible to prepare supported single atoms and metal clusters of a few atoms, stabilization of subnanometric metal catalysts under reaction conditions is a key issue and can limit the practical applications of cluster catalysts for industrial processes.[3] Subnanometric metal species can be stabilized on solid supports and their catalytic properties can be tuned by metal-support interaction.[4,5] However, under reaction conditions, the agglomeration of subnanometric metal species into nanoparticles are still difficult to avoid even when they are supported on solid carriers.[6-8]

It has been presented that it is possible to generate well-defined single atoms or metal clusters in zeolites crystallites by introduction of mononuclear or multinuclear organometallic compounds into zeolites.[9] However, these subnanometric metal species are usually not stable under reaction conditions,

and even under mild conditions (for instance, hydrogenation of cyclohexene at ca. 70 °C), mononuclear Ir species will migrate and stepwise agglomerate into Ir clusters and nanoparticles with reaction time.[10]   Therefore, the factors that affect the stability of subnanometric species confined in zeolites need to be addressed for practical catalytic applications.

Recently, we reported a new strategy to directly generate subnanometric Pt species (Pt single atoms and clusters) in the supercages and internal cavities of MCM-22 zeolite.[11] It was found that, when Pt loading was kept ca. 0.1 wt% or lower, Pt species can show exceptional stability under consecutive oxidation-reduction treatments at high temperature (>550 °C). Since lower loadings can be a limitation for some practical applications, it is then necessary to improve the loading of Pt in MCM-22 while preserving the dispersion and stability of the subnanometric Pt species.

The fast development of *in situ* transmission electron microscopy (TEM) techniques in recent years has enabled researchers to study the dynamic structural evolution of nanoparticles under different atmospheres.[12] In this way, the dynamic changes in the shape of metal nanoparticles,[13] oscillatory behaviour of metal nanoparticles,[14] reconstruction of bimetallic catalysts[15] and the interaction between metal surface and substrate molecules have already been visualized by *in situ* TEM.[16] However, in previous reports, the working catalysts are usually large nanoparticles (>5 nm), which are far from most interesting subnanometric particles. Indeed, owing to limitations associated with the instrument resolution and the stability of materials under electron beam, it is quite difficult to follow the dynamic structural evolution of subnanometric metal species under reaction conditions, especially at high temperature (>600 °C).[17]

To directly observe and obtain more detailed information on the evolution process of subnanometric metal species under redox and reaction conditions, we report herein an *in situ* TEM study with Pt@MCM-22 catalyst with well-defined metal species confined in the zeolite structure. Thanks to the unique structure of Pt@MCM-22 catalyst, it has been possible to have direct observations on the dynamic structural transformation of subnanometric Pt species under oxidation-reduction treatments and during $CO+O_2$, $NO+CO$ and $NO+H_2$ reactions. Then, by correlating the results from *in situ* TEM studies and

the results obtained in a continuous fix-bed reactor, the factors that control the dynamic agglomeration and redispersion process and the stability of subnanometric metal clusters under reaction conditions at high temperature have been delimitated. With a better understanding on those processes, we have been able to prepare Pt@MCM-22 catalyst with three times higher loading of Pt (ca. 0.3 wt%) within the subnanometric regime. It has also been confirmed that subnanometric Pt clusters can be stabilized by this particular zeolite structure at very high temperature (>800 $^\circ$C) during NO reduction with CO and H$_2$.
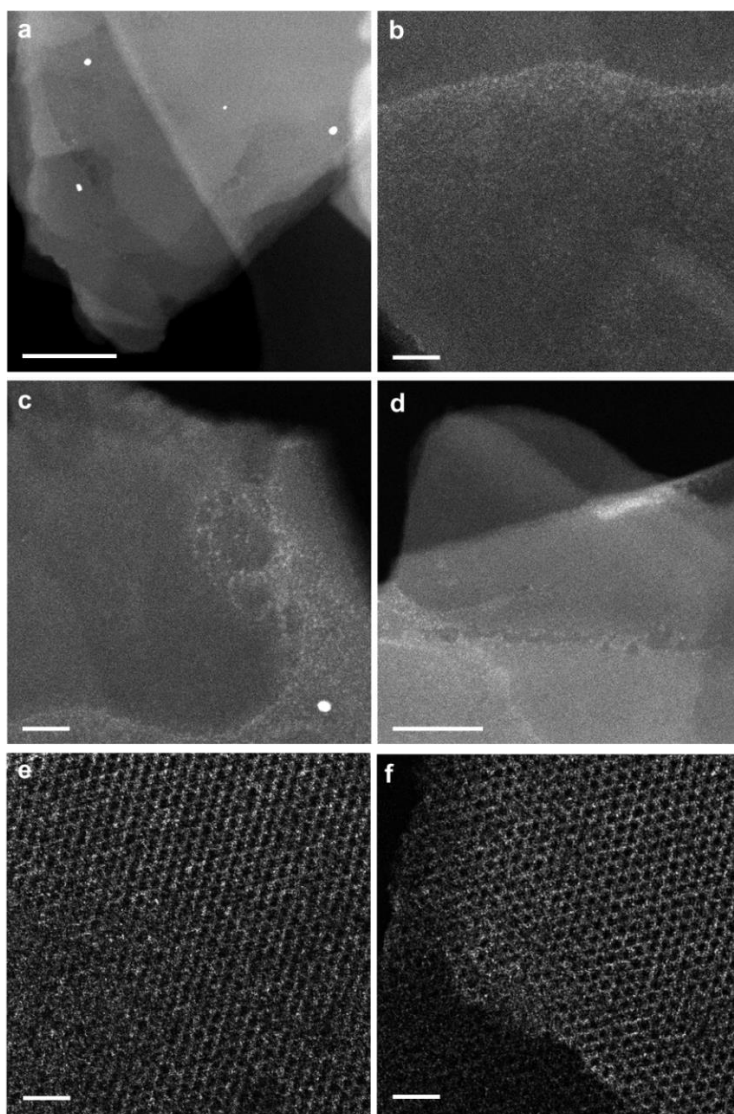
Figure 6.1. Morphological characterization of 0.17%Pt@MCM-22 sample after calcination in air at 550 ºC. (a-d) STEM images of the 0.17%Pt@MCM-22 sample, showing the presence of subnanometric Pt clusters and a few Pt nanoparticles on the surface of MCM-22 zeolite. (e, f) High-resolution STEM images of 0.17%Pt@MCM-22 sample. As shown in these images, Pt single atoms as well as the pore structures of MCM-22 zeolite can be observed. Scale bar: (a) 100 nm, (b, c) 20 nm, (d) 50 nm and (e, f) 5 nm.
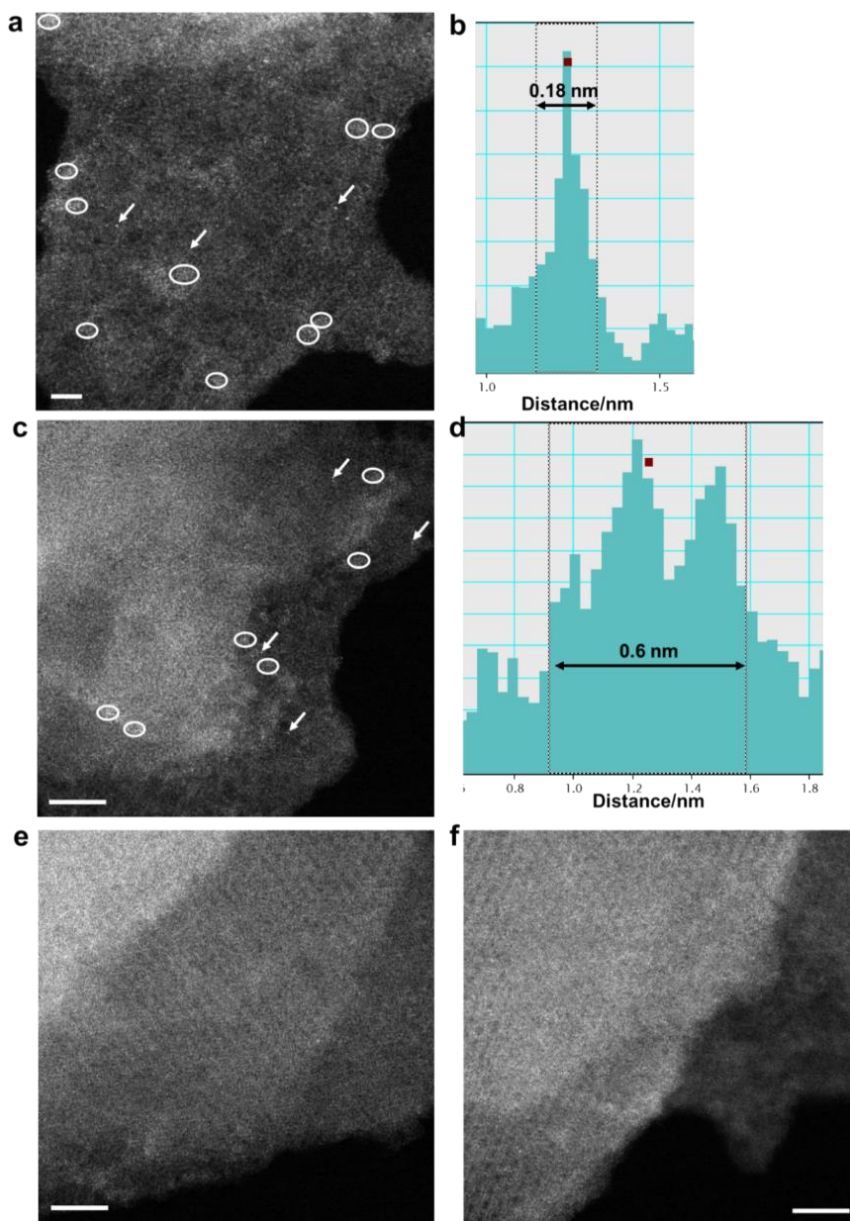
Figure 6.2. Identification of Pt single atoms and clusters in the 0.17%Pt@MCM-22 sample. As shown in (a), both Pt atoms (bright dots) and clusters (aggregates of several Pt atoms) can be seen. The intensity of a single Pt atom is displayed in (b). (c) Pt atoms and clusters in another area of the

0.17%Pt@MCM-22 sample. The intensity of a Pt cluster (~0.6 nm) is displayed in (d). (e, f) Two more representative STEM image of the 0.17%Pt@MCM-22 sample, showing the pore structure of MCM-22 and presence of subnanometric Pt species. Scale bar: (a) 2 nm, (c, e, f) 5 nm.

Structural evolution of Pt species under redox conditions

A purely siliceous Pt@MCM-22 sample with 0.17wt% Pt was synthesized following a modification of our previously reported preparation method (see **Methods** for experimental details).[11] After the calcination in air at 550 °C, the 0.17%Pt@MCM-22 sample is mainly consisted of highly dispersed Pt species in MCM-22 zeolite crystallites. As shown in **Figure 6.1**, Pt species cannot be observed in many areas due to the low contrast of atomically dispersed Pt species. Meanwhile in some other areas, subnanometric Pt clusters, as well as very few Pt nanoparticles, can still be observed. With the help of High-resolution scanning transmission electron microscopy (HRSTEM), Pt single atoms as well as subnanometric Pt clusters in the0.17%Pt@MCM-22 sample can be observed (see **Figure 6.1** and **Figure 6.2**). Thus, the pristine 0.17%Pt@MCM-22 sample contains a mixture of Pt single atoms and clusters, as well as very few Pt nanoparticles. Then, the 0.17%Pt@MCM-22 sample was studied by environmental TEM (FEI Titan 80-300 ETEM) under high angle annular dark field-scanning transmission electron microscopy (HAADF-STEM) imaging model. It should be pointed out that, to minimize the effects of beam irradiation on the sample, very low dose of electron beam was used for HAADF-STEM imaging during *in situ* TEM studies (see **Methods** for experimental details).
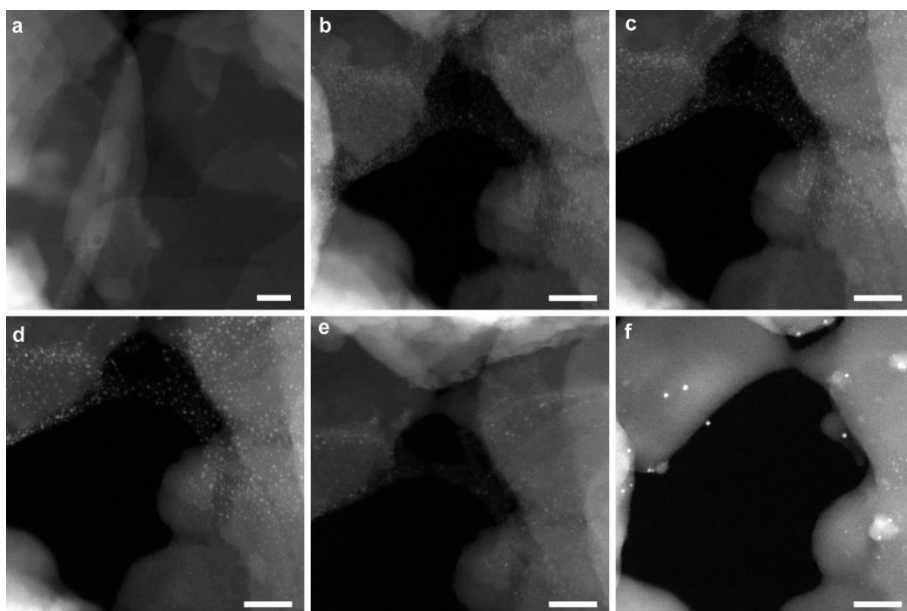
Figure 6.3. Structural evolution of 0.17%Pt@MCM-22 sample under redox conditions. (a) 350 °C in H_2 for 15 min (0.1 torr), (b) 550 °C in H_2 (0.1 torr) for 15 min, (c) 700 °C in H_2 (0.1 torr) for 15 min, (d) 800 °C in H_2 (0.1 torr) for 10 min, (e) 500 °C in O_2 (0.1 torr) for 15 min, (f) 700 °C in O_2 (0.1 torr) for 15 min. Scale bar in all the images in this figure: 20 nm.

It has been demonstrated by *in situ* spectroscopic techniques that, during redox catalytic processes, metal catalysts will undergo dynamic structural transformations, which is often related with the redox properties of the metal catalysts.[18,19] Therefore, before studying the evolution behavior of subnanometric Pt species under reactions that involve oxidative and reductive reactants, the structural transformation of the metal catalyst under reduction-oxidation (H_2-O_2) conditions has been studied. To show the evolution of atomically dispersed Pt species, we have chosen an area showing only the presence of a few Pt clusters without Pt nanoparticles to perform the *in situ* TEM experiments. When the sample was exposed to H_2 (0.1 torr) at 350 °C, a few Pt clusters (below 0.5 nm) started to appear (see **Figure 6.3a**). When the temperature was increased to 550 °C and 700 °C in H_2 atmosphere, more subnanometric Pt species (below 0.8 nm) appeared and the average size

increased (see **Figure 6.3b** and **Figure 6.3c**). The size of subnanometric Pt clusters continued to increase up to 0.8-1 nm when the temperature was increased to 800 °C (see **Figure 6.3d**). Notably, the size of most of the Pt species remained below 1 nm even after reduction in H_2 at such high temperature, indicating the exceptional stability of Pt clusters encapsulated in the MCM-22 zeolite framework. This is even more exceptional if one takes into account that this is a purely siliceous zeolite.
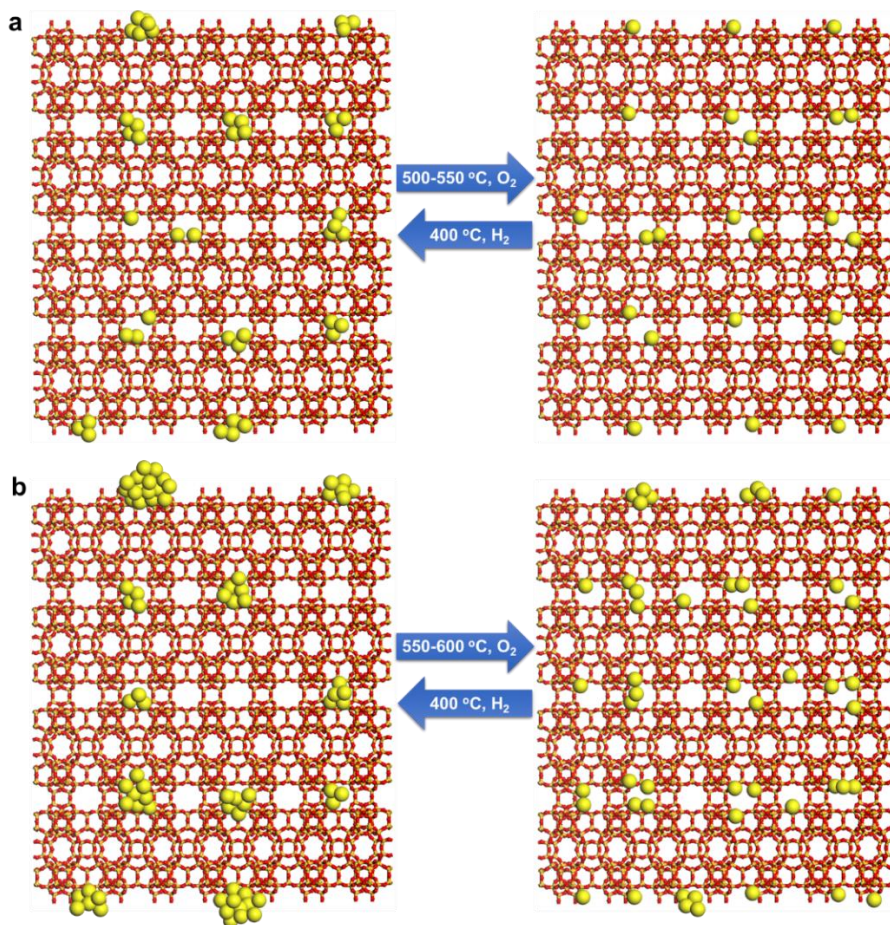
Figure 6.4. Schematic illustration of structural evolution of Pt@MCM-22 material under redox conditions. (a) In the case of Pt@MCM-22 material with low Pt loading (≤ 0.1 wt%), Pt mainly exist in internal space of MCM-22 crystallites, as shown in our previous work.[11] Therefore, the redispersion of Pt

can be achieved under relatively mild conditions. Subnanometric Pt clusters and small Pt nanoparticles (1-2 nm) are formed in subsequent reduction treatment by H_2. (b) In the case of Pt@MCM-22 material with higher loading (>0.15 wt%), some of the Pt species will form Pt nanoparticles and locate on the external surface of MCM-22, which need treatments at higher temperature as driving force to achieve the redispersion. Subsequent reduction treatment by H_2 will cause the agglomeration of Pt species on the surface, giving Pt nanoparticles (>2 nm).
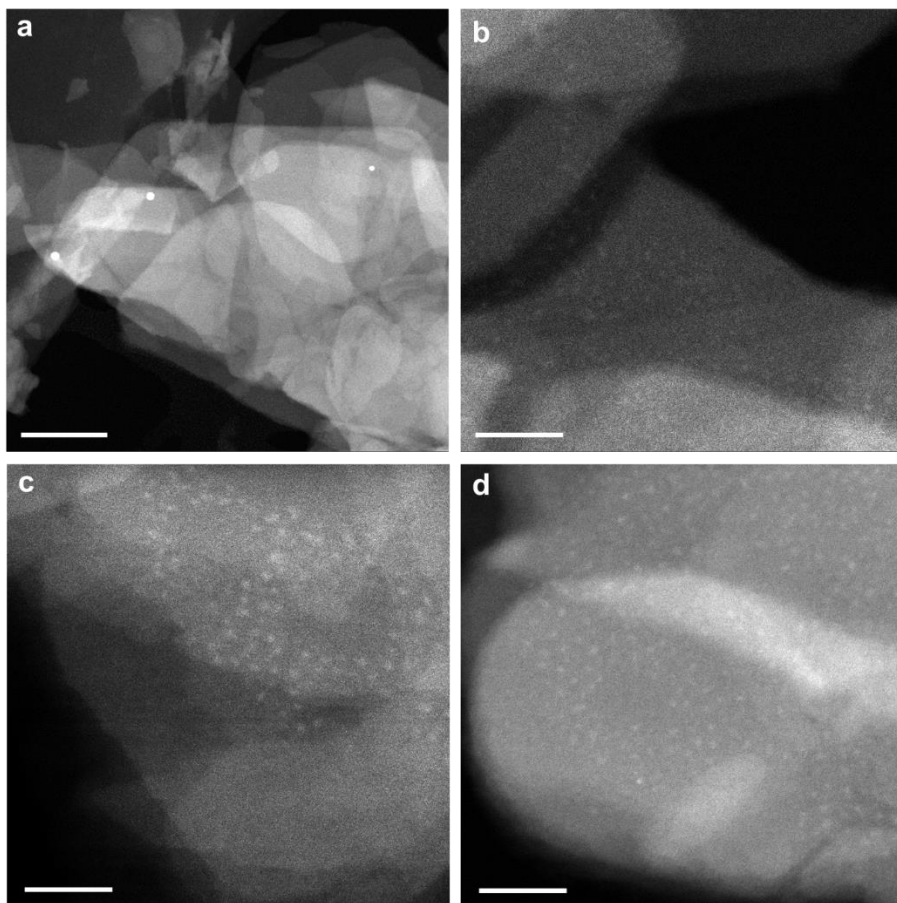
Figure 6.5. Morphological characterization of 0.17%Pt@MCM-22-200H_2. As shown in these images, Pt clusters can be observed in the sample after reduction by H_2 at 200 °C. Scale bar: (a) 100 nm, (b-d) 20 nm.
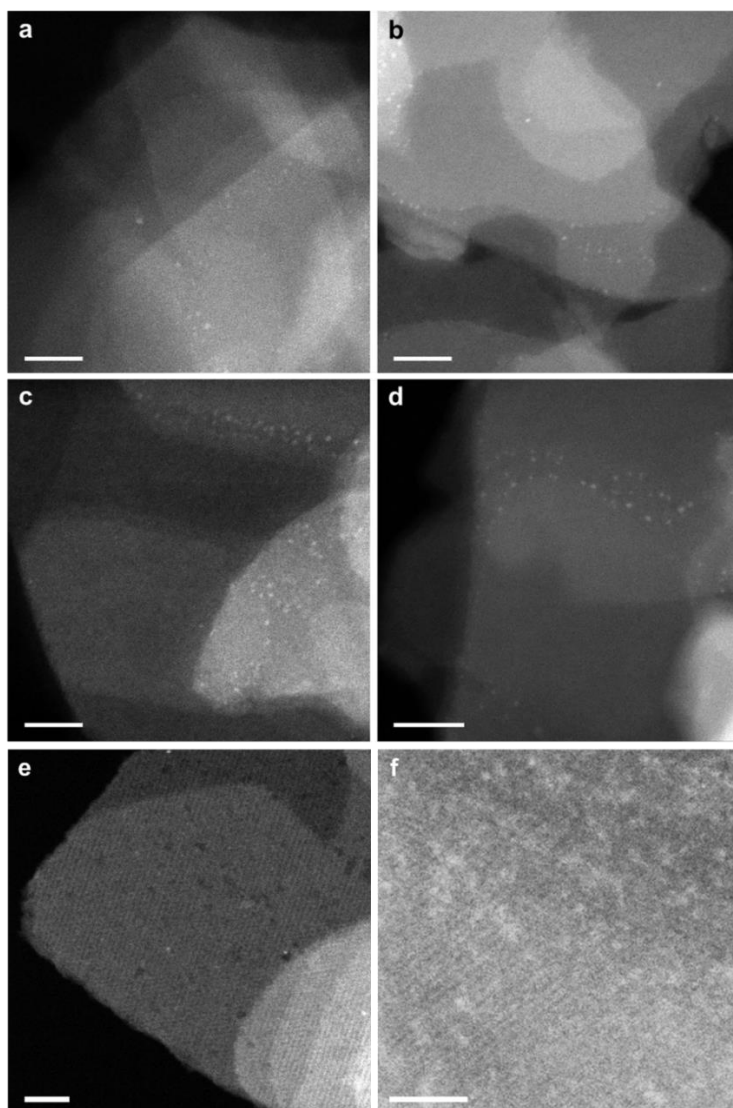
Figure 6.6. Morphological characterization of 0.17%Pt@MCM-22-300H$_2$ sample. (a-d) As shown in these images, part of the highly dispersed Pt species agglomerate into Pt clusters. The size of Pt clusters increases compared with the 0.17%Pt@MCM-22-200H$_2$ sample shown in **Figure 6.5**. In (e, f), the pore structures of MCM-22 can be observed. Moreover, the presence of subnanometric Pt species in this sample is also confirmed in these high-resolution STEM images. Scale bar: (a-d) 20 nm, (e, f) 10 nm.
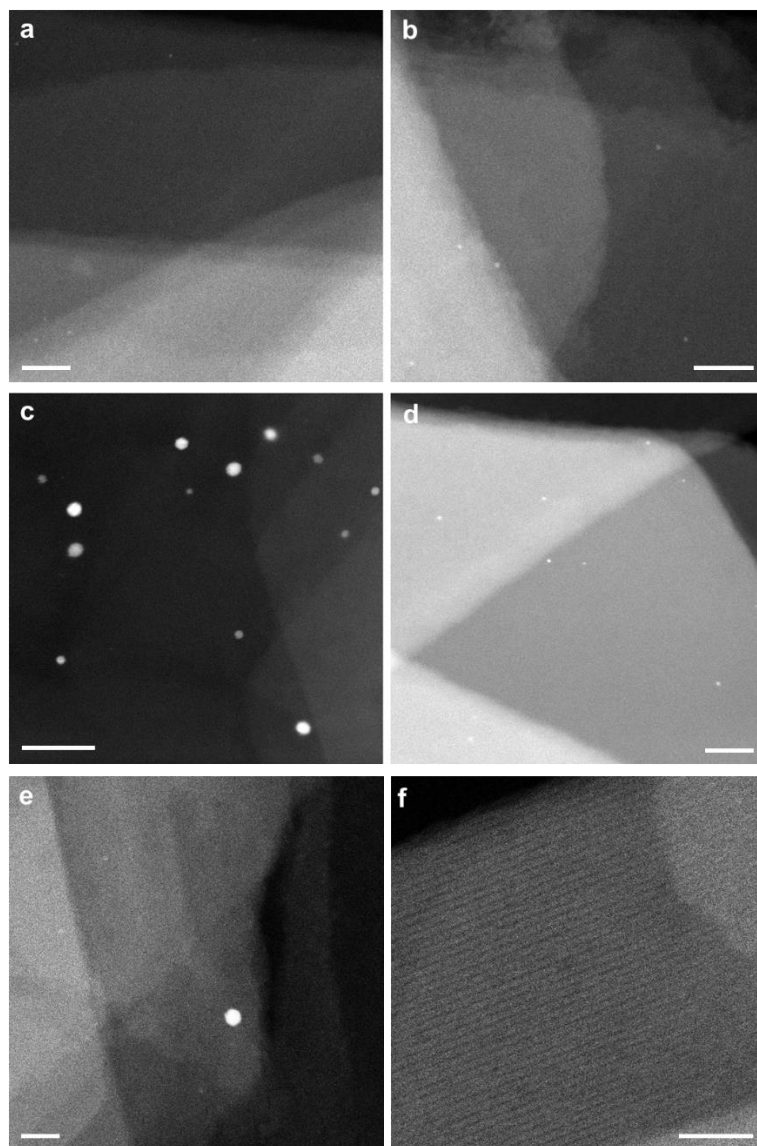
Figure 6.7. Morphological characterization of 0.17%Pt@MCM-22-400H$_2$ sample. (a-d) Pt clusters as well as some Pt nanoparticles around 1 nm can be observed in this sample. Besides, Pt nanoparticles from the agglomeration of Pt species on the surface of MCM-22 crystallites can be observed. (e, f) Pt single atoms are not observed in the high-resolution STEM images. Scale bar: (a, b, d) 20 nm, (c) 50 nm, (e, f) 10 nm.
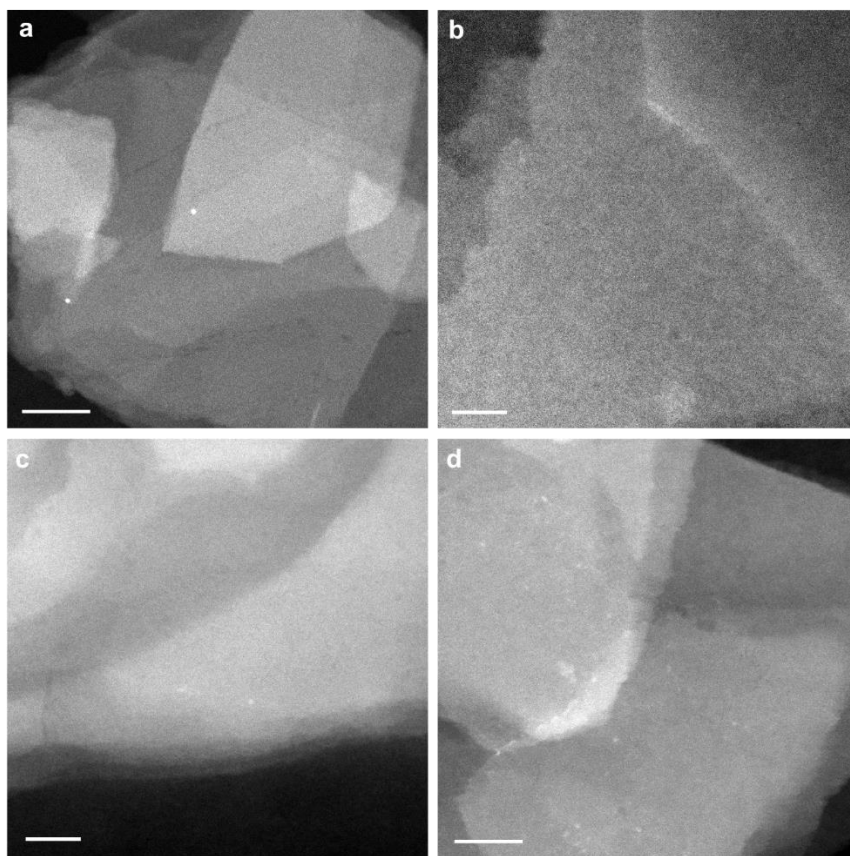
Figure 6.8. Morphological characterization of 0.17%Pt@MCM-22 sample after reduction by H_2 at 400 ºC and another calcination treatment in air at 550 ºC. It is clearly shown in the images (a-d) that, most of the small Pt nanoparticles in the sample were redispersed into Pt clusters and highly dispersed Pt species. Scale bar: (a) 50 nm, (b-d) 20 nm.

After the reduction treatment, H_2 was switched to O_2 to study the behavior of Pt clusters under oxidative atmosphere. As it can be seen in **Figure 6.3e**, Pt clusters start to redisperse after exposure to O_2 at 550 ºC, which has also been observed by *in situ* extended X-ray absorption fine structure spectroscopy (EXAFS) in our recent work.[20] It can be clearly seen that the number and the size of Pt species decreased after the gas was switched from H_2 to O_2. Therefore, the redispersion behavior of Pt species in O_2 is valid. Taking a careful look and comparing the images recorded in O_2 atmosphere, it can be seen that small Pt

clusters (below 0.7 nm) located in the MCM-22 crystallites seems easier to become redispersed, than those larger Pt clusters or small nanoparticles (~1 nm) located on the external surface of MCM-22. When the temperature increases to 700 $^{\circ}$C in O_2, most of the Pt clusters disappear and only several small Pt nanoparticles (~1 nm) remain in this area (see **Figure 6.3f**). It should be mentioned that, it seems that the MCM-22 zeolite was also damaged by the beam irradiation at high temperature. Those Pt nanoparticles may come from the sintering of Pt species located on the external surface of MCM-22 zeolite after long-time exposure to the electron beam at high temperature.

Nevertheless, all these direct observations were performed by *in situ* TEM. Considering the pressure gap between *in situ* TEM studies and more realistic catalytic reaction conditions, we have also performed *ex situ* TEM studies on the sample subjected to the above described oxidation-reduction treatments at atmospheric pressure. Then, when the size distributions of the Pt species were studied by TEM, it was found that highly dispersed Pt species agglomerated into clusters (<0.5 nm) after reduction with H_2 at 200 $^{\circ}$C (see **Figure 6.5**). Increasing the reduction temperature to 300 $^{\circ}$C results in formation of slightly larger Pt clusters (ca. 0.5-1.0 nm), but the average size still remains in the subnanometric range (See **Figure 6.6**). Further increase of the temperature to 400 $^{\circ}$C leads to formation of some Pt nanoparticles on the external surface of MCM-22 crystallites (see **Figure 6.7**). Notably, Pt single atoms are not observed in after reduction by H_2 at 400 $^{\circ}$C. Afterwards, the redispersion of Pt nanoparticles in the reduced Pt@MCM-22 sample (by H_2 at 400 $^{\circ}$C) can be achieved by another calcination in air at 550 $^{\circ}$C (see **Figure 6.8**), indicating a reversible sintering and redispersion behavior of subnanometric Pt species during oxidation-reduction treatments.

It should be mentioned that, in our previous work, we have also tested the stability of subnanometric Pt species during consecutive oxidation-reduction treatments, and it was found that, when the loading of Pt in Pt@MCM-22 material was ca. 0.1 wt% or lower, a large percentage of Pt species were located in the internal space of MCM-22 crystallite.[11] In that case, subnanometric Pt species and small Pt nanoparticles (~1 nm) can be stabilized by the zeolite structure.

Combining the results obtained from the *in situ* and *ex situ* TEM studies, the

factors related with the dynamic agglomeration-redispersion behaviors are illustrated in **Figure 6.4**. When the loading of Pt in purely siliceous MCM-22 zeolite is low (below 0.1 wt%), subnanometric Pt species can disintegrate into atomically dispersed Pt in O_2 under relatively mild conditions. Furthermore, since most of the Pt species are located in the internal space of MCM-22 crystallites, they are protected by the zeolite framework from agglomeration into nanoparticles during reductive treatments. However, when the loading amount increase to >0.15 wt%, a part of the subnanometric Pt species will be located on the external surface or subsurface of MCM-22 crystallites. Therefore, in afterward reduction treatment with H_2 at relatively high temperature (>400 $^{\circ}$C), Pt species located on the external surface of subsurface will agglomerate into Pt nanoparticles (>2 nm), as observed in **Figure 6.7**, while those Pt species located in the internal space of MCM-22 crystallites will only grow into clusters or very small nanoparticles as a consequence of the confinement in the zeolite structure.
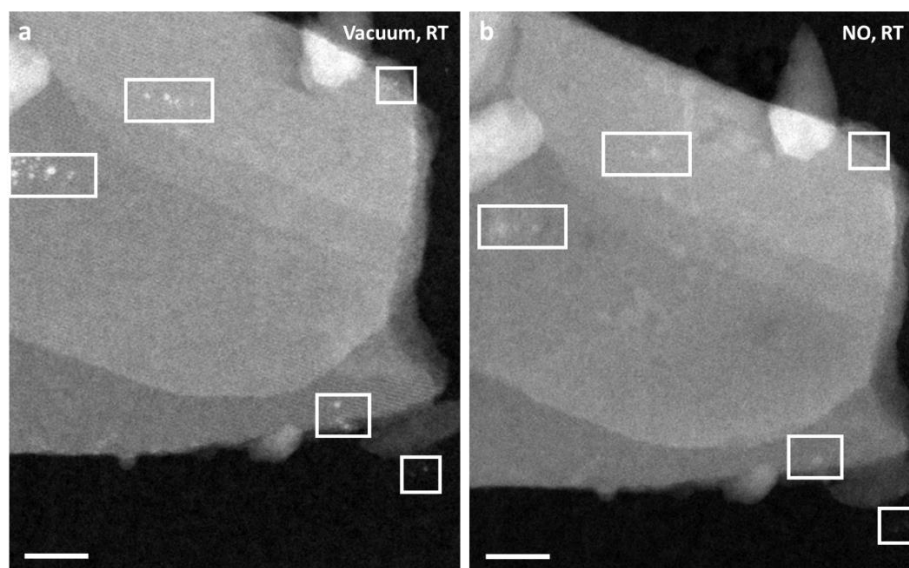
Figure 6.9. Evolution of Pt clusters in the presence of NO at room temperature. (a) In vacuum, Pt clusters around 0.8 nm are visible. (b) After introduction of NO (0.1 torr) and being kept in NO (0.1 torr) for 10 min, Pt clusters react with NO and show morphological transformation, corresponding to redispersion of Pt clusters into highly dispersed Pt species. In (a), both Pt

clusters and nanoparticles are present. After treatment with NO at room temperature (b), Pt clusters (<1 nm) disappear and Pt nanoparticles (>1 nm) can still be observed, although the geometric shape of those Pt nanoparticles already change. Scale bar: (a, b) 20 nm.
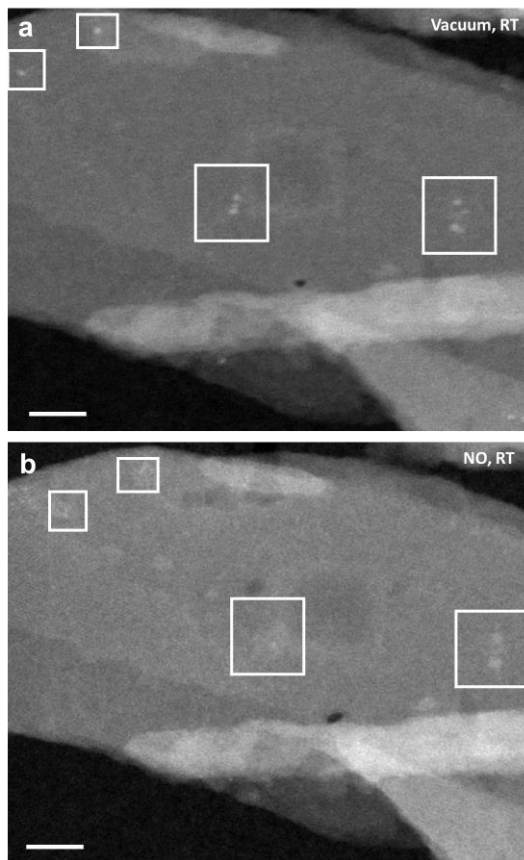
Figure 6.10. Evolution of Pt clusters in the presence of NO at room temperature. (a) STEM image of Pt particles in vacuum at room temperature. (b) STEM image of the same area after NO treatment at room temperature. The structural transformation of the Pt species is indicated by white rectangular. In (a), both Pt clusters and nanoparticles are present. After treatment with NO at room temperature (b), Pt clusters (<1 nm) disappear and Pt nanoparticles (>1 nm) can still be observed, although the geometric shape of those Pt nanoparticles already change. Scale bar: (a, b) 20 nm.
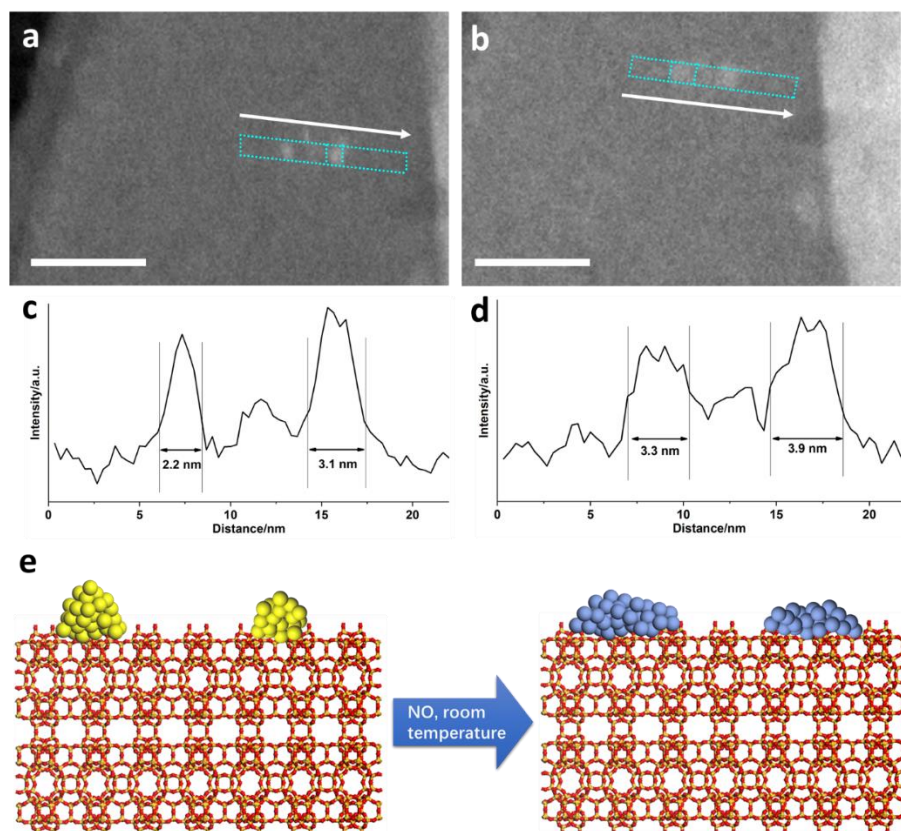
Figure 6.11. Structural transformation of Pt particles in NO. (a) STEM image of two Pt particles in vacuum. (b) STEM image of the same area after NO treatment at room temperature. (c) Intensity profile of the two Pt particles and their particle sizes. (d) Intensity profile of the two Pt particles and their particle sizes after NO treatment at room temperature. (e) Schematic illustration of structural transformation of Pt particles during the NO treatment at room temperature. Pt particles are oxidized by NO and the diameter of the particle also increases after the NO treatment. Scale bar: (a, b) 20 nm.
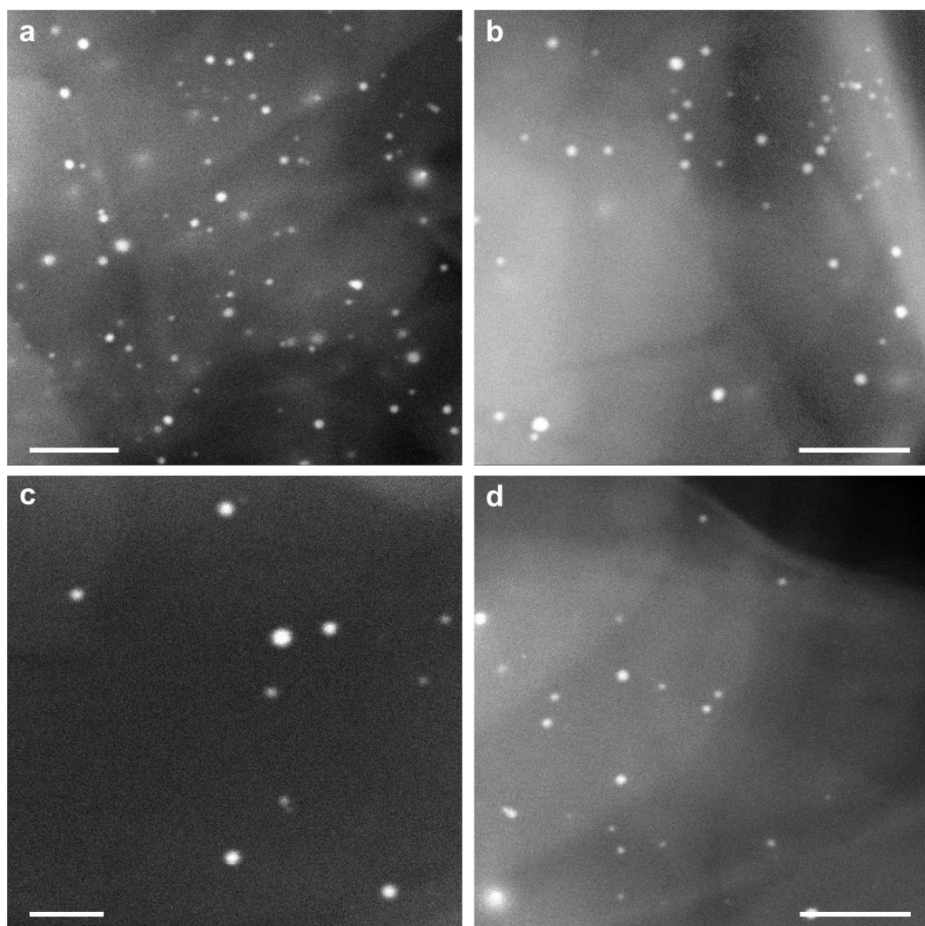
Figure 6.12. Morphological characterization of as-prepared 0.3%Pt@MCM-22 sample. As shown in the images (a-d), a large fraction of Pt nanoparticles is present in this sample, especially on the external surface of MCM-22 zeolite. Scale bar: (a, b, d) 50 nm, (c) 20 nm.
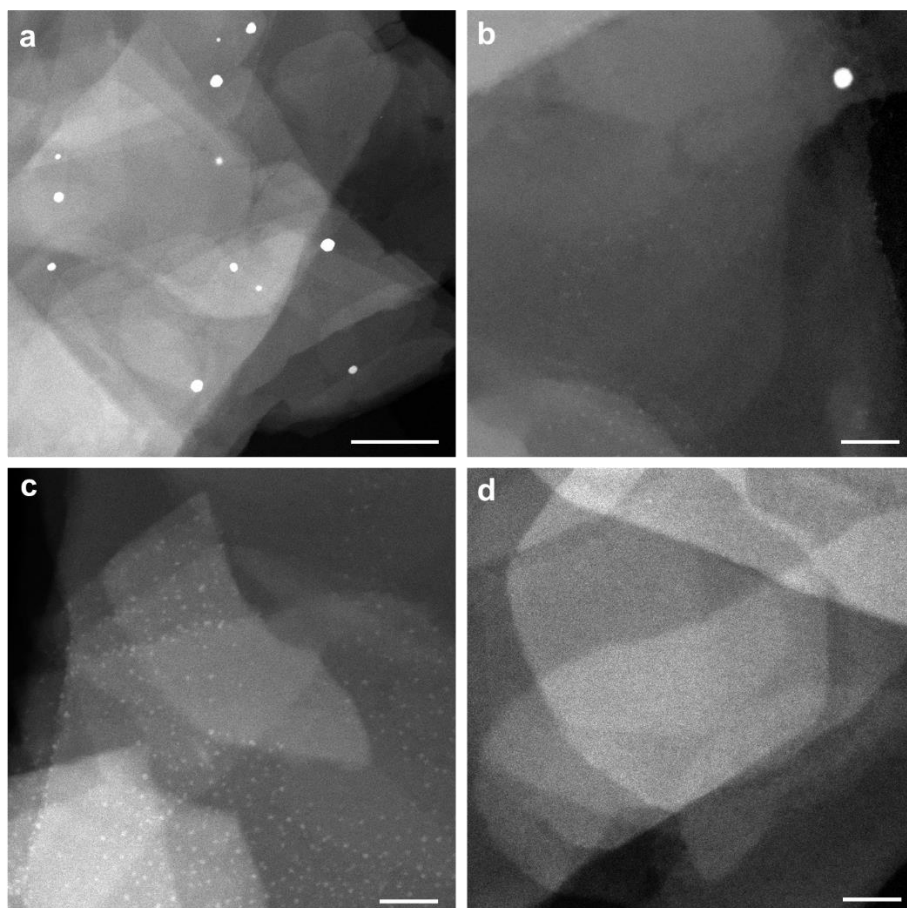
Figure 6.13. Morphological characterization of 0.3%Pt@MCM-22 sample after calcination in NO at 200 ºC. (a) After NO treatment at 200 ºC, it can be observed that, the number of the Pt nanoparticles decreases compared with the pristine 0.3%Pt@MCM-22 sample. (b-d) The STEM images show the presence of smaller Pt nanoparticles (1~2 nm) and subnanometric Pt clusters in this sample. Nevertheless, some Pt nanoparticles can still be observed on the surface of MCM-22 zeolite, suggesting only part of the Pt nanoparticles are redispersed during the NO treatment at 200 ºC. Scale bar: (a) 100 nm, (b-d) 20 nm.
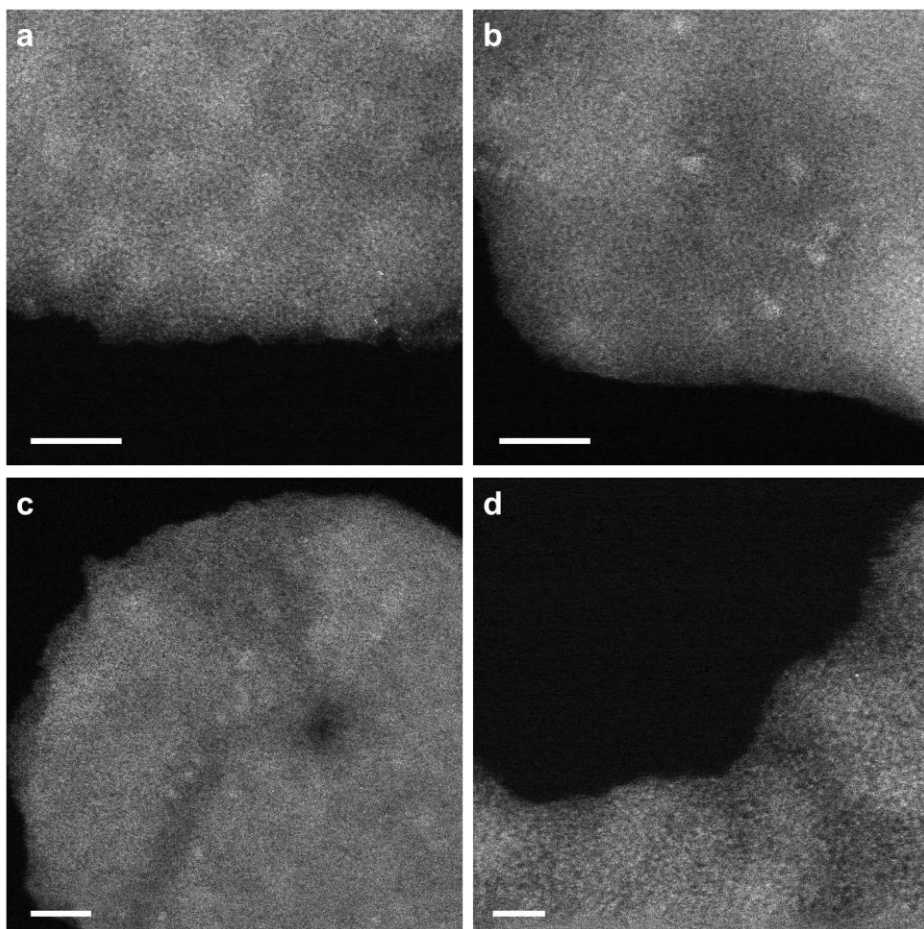
Figure 6.14. High-resolution STEM images of 0.3%Pt@MCM-22 sample after calcination in NO at 200 ºC. In these images (a-d), the presence of Pt clusters and singly dispersed Pt atoms can be clearly seen. These subnanometric Pt species should come from the redispersion of Pt nanoparticles in the pristine sample after NO treatment at 200 ºC. Scale bar: (a-c) 5 nm, (d) 2 nm.
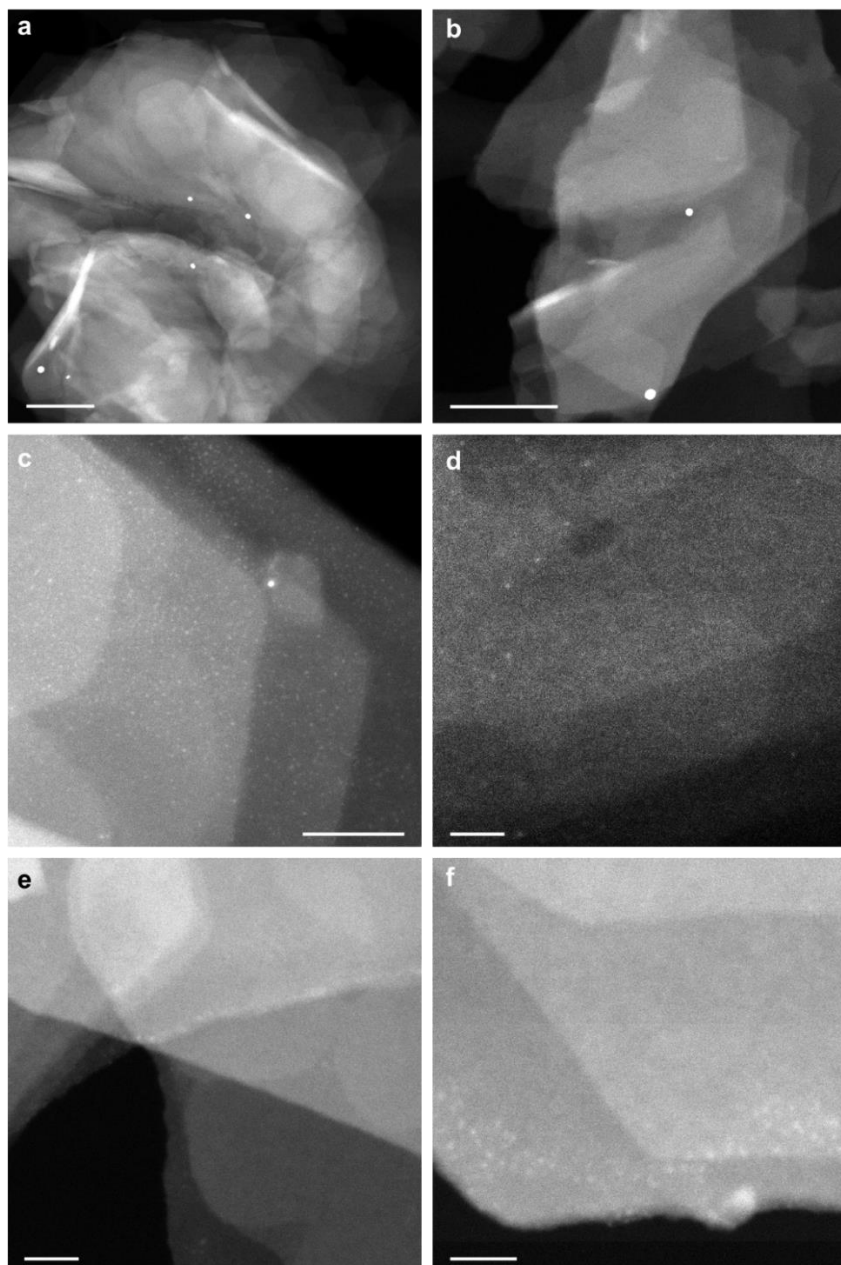
Figure 6.15. Morphological characterization of 0.3%Pt@MCM-22 sample after calcination in NO at 300 ºC. (a, b) As shown in these images, the number of Pt nanoparticles decrease significantly after NO treatment at 300 ºC

compared to the sample after NO treatment at 200 ºC (shown in **Figure 6.14**). (c-d) Most of the Pt nanoparticles are re-dispersed, forming highly dispersed Pt species and subnanometric Pt clusters. Scale bar: (a, b) 200 nm, (c) 50 nm, (d-f) 20 nm.
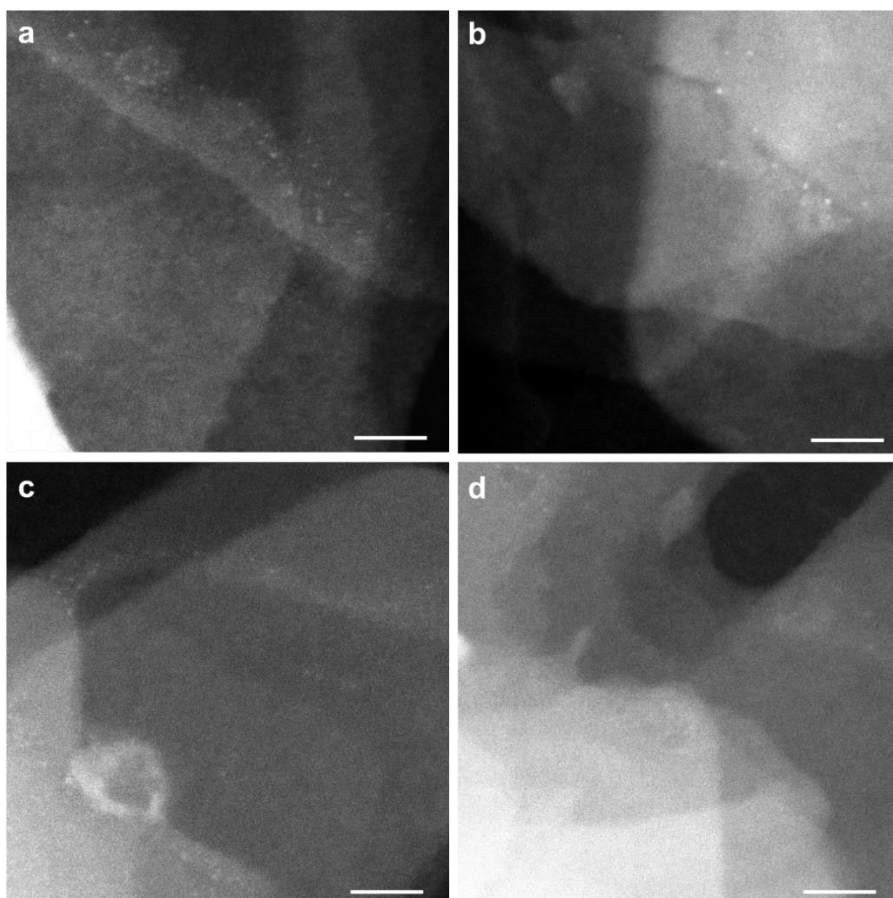
Figure 6.16. Morphological characterization of 0.3%Pt@MCM-22 sample after calcination in NO at 300 ºC and subsequent reduction by H$_2$ at 200 ºC. (a-d) As shown in the above STEM images, the size of Pt species are still remaining small (<2 nm) after the H$_2$ reduction treatment, suggesting the stability of the redispersed Pt species after NO treatment. Scale bar: (a-d) 20 nm.

Since two of the reactions that will be investigated later by *in situ* TEM

involve reduction of NO by CO or H_2, we will also study the morphological transformation of Pt species in NO atmosphere with *in situ* TEM. As it can be seen in **Figure 6.9** and **Figure 6.10**, after exposure to NO (0.1 torr) at room temperature, the contrast of Pt species decreased while the size increased after NO treatment. For smaller Pt species (below 1 nm), they disappear in the STEM image after the NO treatment, indicating redispersion of Pt species. Furthermore, we have also measured the size of Pt particles after NO treatment. As presented in **Figure 6.11**, the size of Pt particles increases slightly after NO treatment according to the contrast profiles, implying the possible structural transformation of Pt particles.[13] However, as we have seen previously in O_2 atmosphere under the same conditions, Pt clusters will remain unchanged, indicating that NO is much more efficient than O_2 for the redispersion of Pt species. The redispersion of Pt particles in NO is probably related with the NO dissociation on Pt species, leading to the oxidative disintegration of Pt clusters and nanoparticles.[21,22]

According to the above results, we have made some modifications on the preparation of Pt@MCM-22 to achieve high Pt loading with still good dispersion of subnanometric Pt species. Then, a 0.3%Pt@MCM-22 sample was prepared, and Pt nanoparticles can be seen on the surface of MCM-22 zeolite crystallites as a consequence of higher Pt loading (see **Figure 6.12**). At this point, treatment with NO was carried out with the aim to promote the redispersion of Pt nanoparticles into subnanometric Pt species. As shown in **Figure 6.13**, subnanometric Pt clusters were observed with this 0.3%Pt@MCM-22 sample after oxidative treatment with NO at 200 ºC. The high-resolution STEM image of the sample after NO treatment at 200 ºC clearly demonstrate the presence of Pt clusters and single Pt atoms (see **Figure 6.14**). However, a small amount of Pt nanoparticles was still present after NO treatment at 200 ºC (see **Figure 6.13a**). Further increasing the temperature to 300 ºC results in better redispersion of Pt nanoparticles in the sample (see **Figure 6.15**). It appears then that NO can also redisperse the Pt nanoparticles on the external surface of the MCM-22 crystallites. This is an important observation since it indicates that the rejuvenation of industrial catalysts containing metal nanoparticles should be better achieved by introducing NO during the treatment. More interestingly, a reduction treatment with H_2 at 200

°C on the NO-induced redispersed Pt@MCM-22 sample would cause the sintering of highly dispersed Pt species into Pt clusters as well as a small fraction of nanoparticles (see **Figure 6.16**). Notably, most of the Pt species are present as subnanometric Pt clusters in the reduced sample, suggesting that the NO treatment not only disintegrates the Pt nanoparticles into highly dispersed Pt species, but also led to the migration of Pt species within MCM-22 crystallites. Notice that, high-temperature calcination at 650 °C in air was necessary to fully achieve redispersion of Pt species with the 0.3%Pt@MCM-22 sample. It appears therefore that treating Pt-zeolite catalysts, or even Pt on other supports, with NO can be an effective way to achieve redispersion of Pt nanoparticles at relatively lower temperature compared with treatment with O_2, especially for those samples containing a higher loading of Pt species.
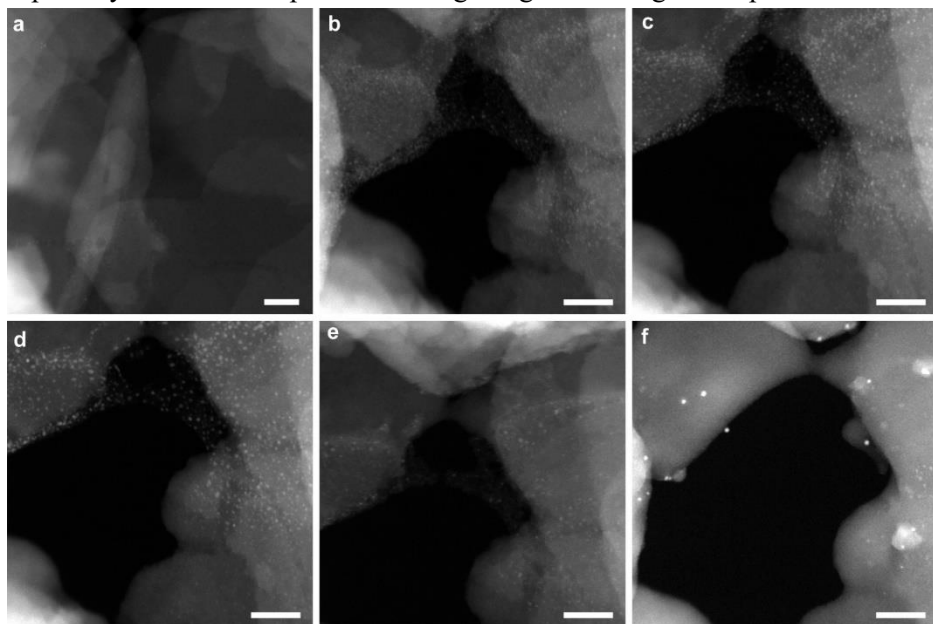
Figure 6.17. Structural evolution of 0.17%Pt@MCM-22-300H₂ sample under CO+O₂ reaction conditions. During the in situ TEM experiments, the sample was treated in mixture of CO (0.2 torr) and O_2 (0.1 torr) for 15 min at different reaction temperature, respectively. In order to avoid the carbon deposition of CO by the electron beam, the TEM chamber was evacuated to remove CO gas after exposure of the sample to CO+O_2 gases. (a) room temperature, (b) 100 °C, (c) 150 °C, (d) 200 °C, (e) 300 °C, (f) 400 °C. Scale bar

in all the images in this figure: 10 nm.
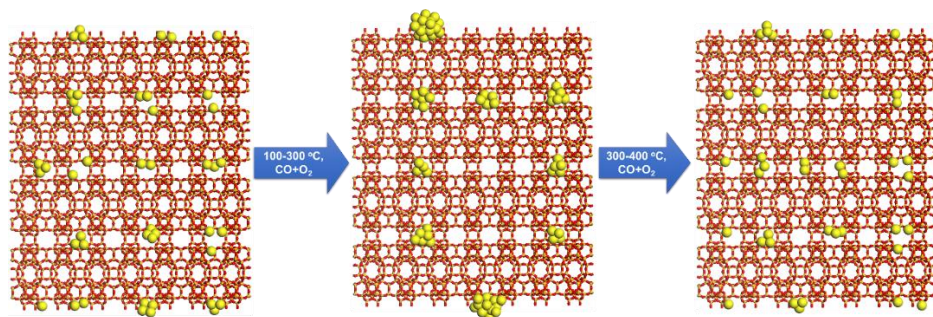
Figure 6.18. Schematic illustration of structural evolution of 0.17%Pt@MCM-22-300H$_2$ sample. At 100-200 °C, highly dispersed Pt species will agglomerate into Pt clusters or even small nanoparticles. When the reaction temperature continues to increase to higher temperature (300-400 °C), Pt nanoparticles will disintegrate and form highly dispersed Pt species and Pt clusters.

Structural evolution of Pt under CO+O$_2$ conditions

Up to now, we have studied the dynamics of the Pt nanoparticles and subnanometric species when performing *in situ* and *ex situ* treatments with H$_2$, O$_2$ or NO. Now, we will firstly study the stability and the evolution of subnanometric Pt species with the 0.17%Pt@MCM-22-300H$_2$ sample during CO oxidation with O$_2$ by *in situ* TEM. As presented in **Figure 6.17**, highly dispersed Pt species evolved into Pt clusters when the reaction temperature for CO oxidation was increased to 100-150 °C. The agglomeration of highly dispersed Pt species should be caused by the interaction between Pt and CO.[23] Those subnanometric Pt clusters and small Pt nanoparticles (1-2 nm) remained stable when reaction temperature was increased up to 300 °C. More STEM images of the other areas of 0.17%Pt@MCM-22-300H$_2$ sample under CO+O$_2$ reaction conditions are shown in **Figure 6.19**. The results obtained imply that atomically dispersed Pt species can undergo in situ structural transformation under reaction conditions and the MCM-22 zeolite, even in its purely siliceous form, can stabilized subnanometric Pt clusters from sintering further into Pt nanoparticles. Surprisingly, when the reaction temperature for CO+O$_2$ reaction was increased to as high as 400 °C, Pt clusters almost remained unchanged while the Pt nanoparticles disintegrated into Pt clusters (as illustrated in **Figure**

6.18). Since subnanometric Pt clusters remain unchanged, the possibility that the disintegration is caused by the redispersion of Pt nanoparticles at high temperature due to the presence of O_2 under reaction conditions can be ruled out.

In a recent theoretical study, Wang *et al.* have employed density functional theory (DFT)-based *ab initio* molecular dynamics (AIMD) simulations of Au/CeO_2 catalysts under CO oxidation conditions.[24] Their work shows that single-atom Au species can be generated from Au clusters or nanoparticles as a result of interaction between Au and CO at the $Au-CeO_2$ interface. Experimental work has also been reported on the dynamic transformation of Pt clusters or nanoparticles in CO atmosphere by spectroscopic techniques. The Pt_{13} clusters confined in NaY zeolite would disintegrate into $Pt_2(CO)_m$ carbonyl clusters when exposed to CO.[25] According to previous experimental and theoretical work and the results presented in this work, we speculate that the disintegration of Pt nanoparticles under $CO+O_2$ reaction conditions is caused by the interaction between Pt and the CO molecules.[26] The presence of O_2 also contributes the stabilization of highly dispersed Pt species at high temperature. To the best of our knowledge, this is the first direct observation of the reversible transformation between atomically dispersed Pt species, clusters and nanoparticles under reaction conditions.
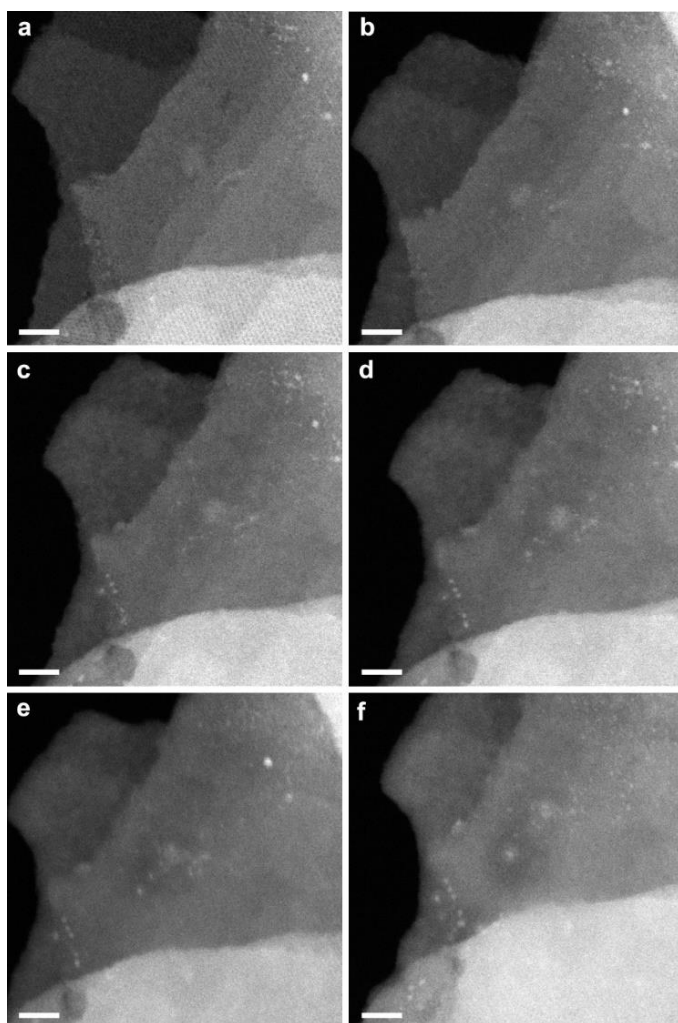
Figure 6.19. Structural evolution of 0.17%Pt@MCM-22-300H$_2$ catalyst under CO+O$_2$ reaction conditions at different reaction temperature measured by *in situ* TEM. During the *in situ* TEM experiments, the sample was treated in mixture of CO (0.2 torr) and O$_2$ (0.1 torr) for 15 min at different reaction temperature, respectively. In order to avoid the carbon deposition of CO by the electron beam, the TEM chamber was evacuated to remove CO gas after exposure of the sample to CO+O$_2$ gases at each temperature. (a) room temperature, (b) 100 ^{o}C, (c) 150 ^{o}C, (d) 200 ^{o}C, (e) 300 ^{o}C, (f) 400 ^{o}C. Scale bar: (a-f) 10 nm.
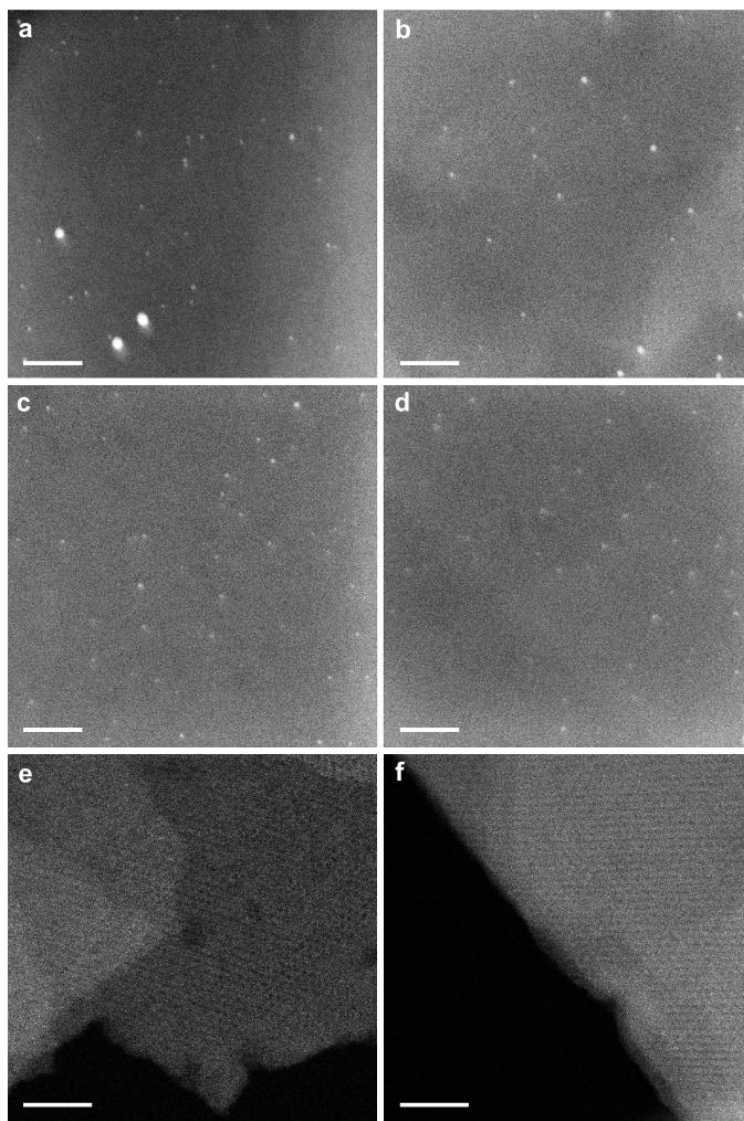
Figure 6.20. STEM images of 0.17Pt@MCM-22 sample after CO+O$_2$ reaction at 300 ºC. Before the reaction, the pristine catalyst mainly contains highly dispersed Pt species, as shown in **Supplementary Figure 6.2**. (a-d) After the CO+O$_2$ reaction, Pt clusters and nanoparticles can be seen in the used catalyst. (e, f) The pore structures of MCM-22 can be seen In the high-resolution STEM images. Scale bar: (a-d) 20 nm, (e, f) 10 nm.
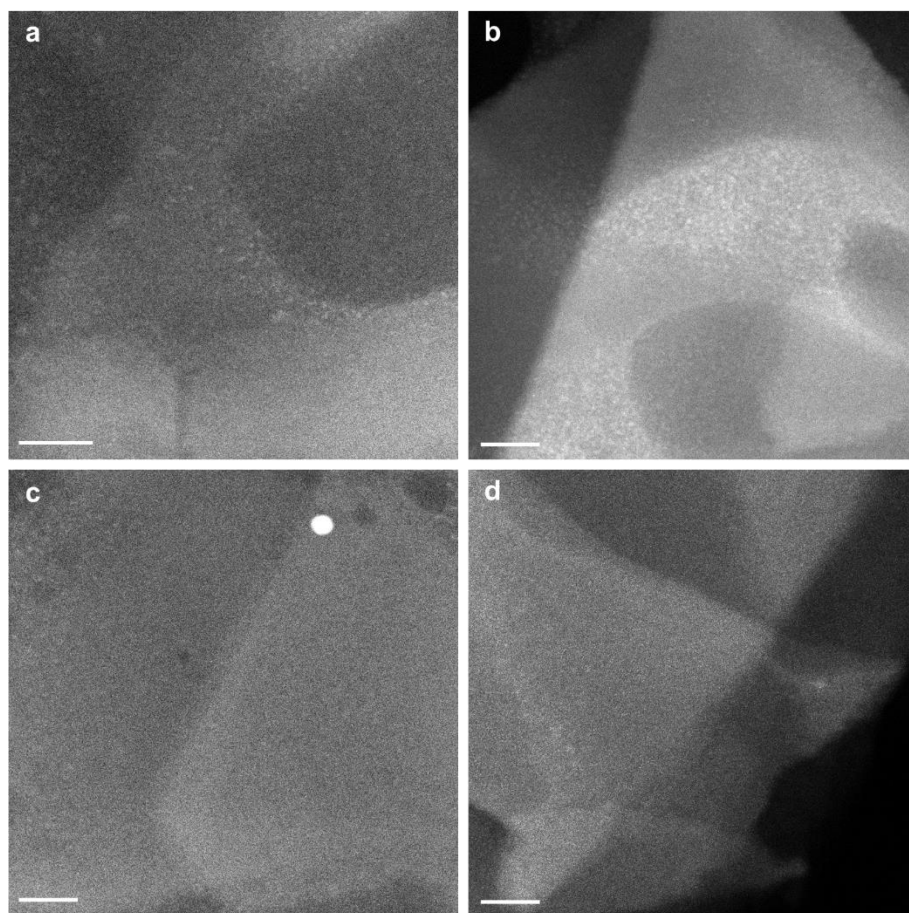
Figure 6.21. STEM images of 0.17Pt@MCM-22 sample after CO+O$_2$ reaction at 400 ºC. Before the reaction, the pristine catalyst mainly contains highly dispersed Pt species, as shown in **Supplementary Figure 6.2**. After the CO+O$_2$ reaction at 300 ºC, Pt clusters and nanoparticles can be seen in the used catalyst. Afterwards, as shown in this Figure 6.(a-d), the reaction temperature is further elevated to 400 ºC and Pt nanoparticles become redispersed after the high-temperature treatment under CO+O$_2$ reaction conditions. Pt species mainly exist as clusters. A few Pt nanoparticles can be observed. Scale bar: (a-d) 20 nm.
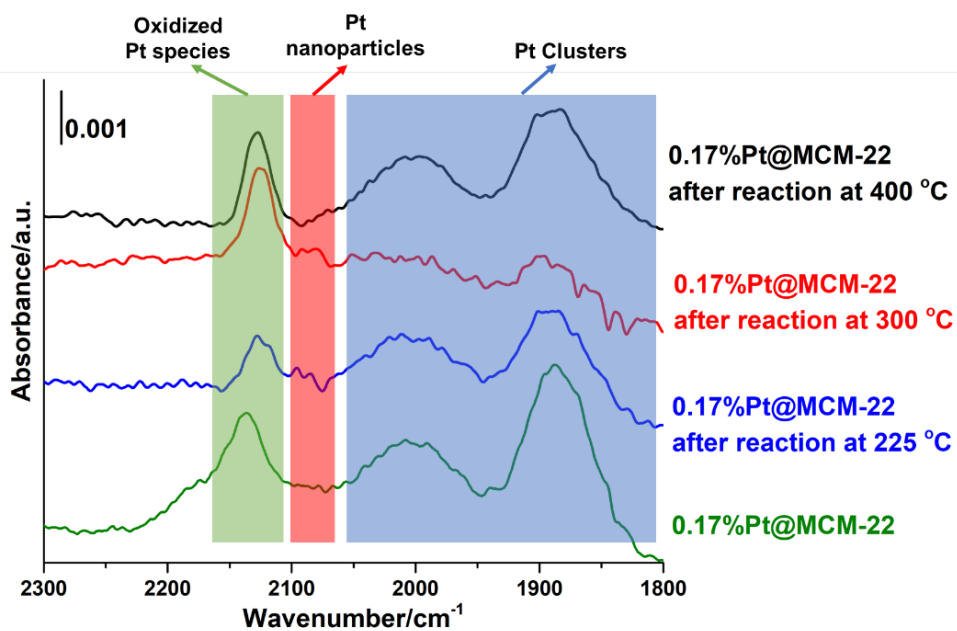
Figure 6.22. *In situ* CO-IR spectra of fresh 0.17%Pt@MCM-22 sample and the sample after CO+O_2 reaction at different temperature.
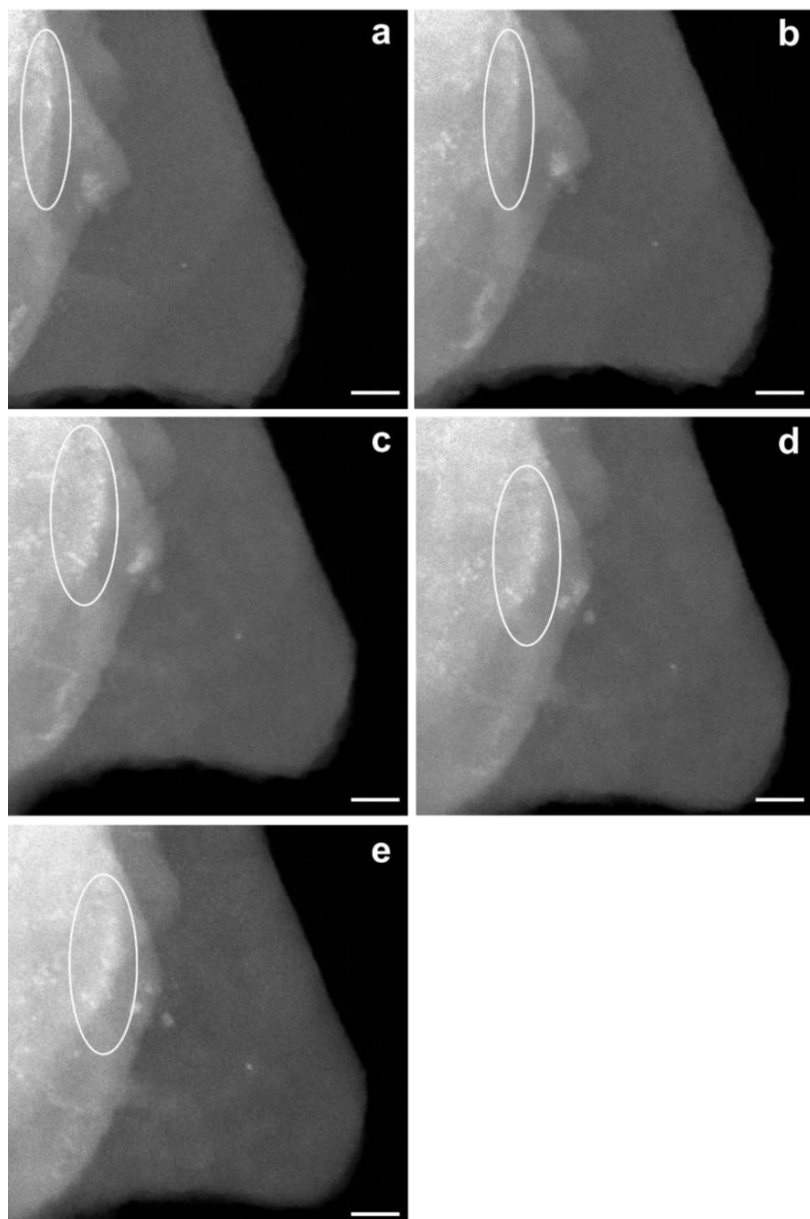
Figure 6.23. Evolution of Pt species in 0.17%Pt@MCM-22-300H₂ sample under water-gas shift (WGS) reaction conditions measured by *in situ* TEM. During the *in situ* TEM experiments, the sample was treated in mixture of CO (0.1 torr) and H_2O (0.2 torr) for 15 min at different reaction temperature,

respectively. In order to avoid the carbon deposition of CO by the electron beam, the TEM chamber was evacuated to remove CO gas after exposure of the sample to CO+H_2O gases at each temperature. (a) room temperature, (b) 100 ºC, (c) 200 ºC, (d) 300 ºC and (e) 400 ºC. Scale bar in all the images in this figure: 10 nm. As indicated by the white circle, the agglomeration of highly dispersed Pt species into Pt clusters can be observed during the elevation of temperature. And those Pt clusters remain stable up to 400 ºC without redispersion. Scale bar in all the images in this figure: 10 nm.
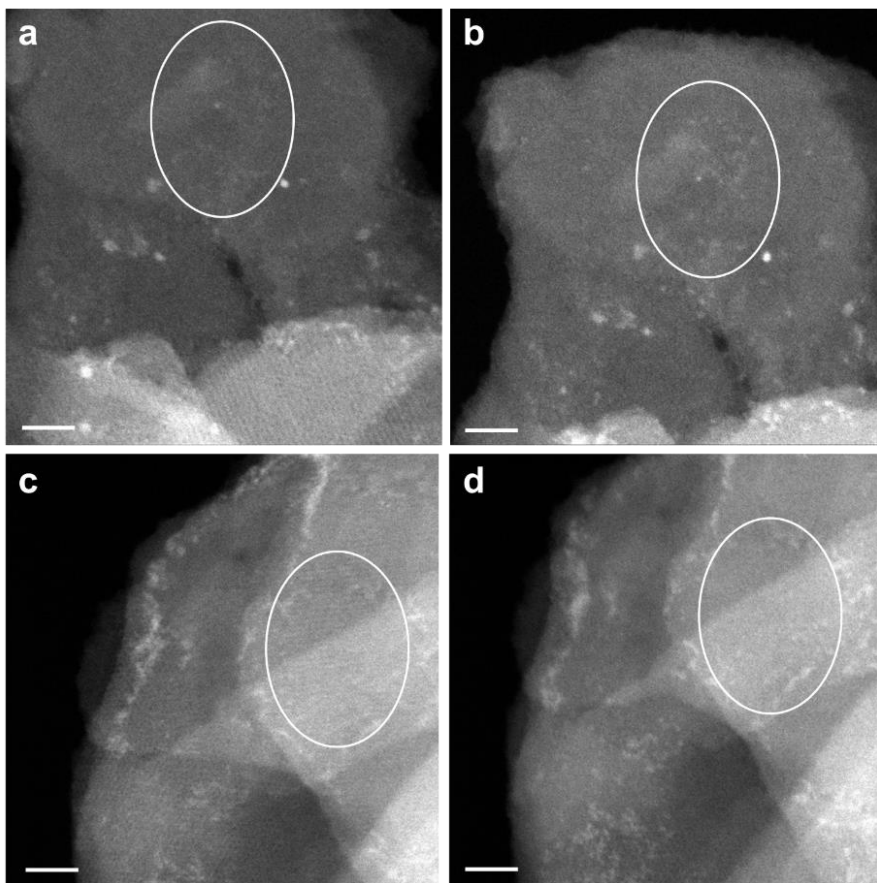
Figure 6.24. Evolution of Pt species in 0.17%Pt@MCM-22-300H$_2$ sample under water-gas shift (WGS) reaction conditions measured by *in situ* TEM in two different areas. (a, c) STEM image obtained at room temperature and (b, d) STEM images obtained at 100 ºC. During the *in situ* TEM experiments,

the sample was treated in mixture of CO (0.1 torr) and H_2O (0.2 torr) for 15 min at different reaction temperature, respectively. In order to avoid the carbon deposition of CO by the electron beam, the TEM chamber was evacuated to remove CO gas after exposure of the sample to $CO+H_2O$ gases at each temperature. The agglomeration of highly dispersed Pt species into Pt clusters are indicated by white circles. Scale bar in all the images in this figure: 10 nm.

Then, to correlate the information presented above on the structural transformation of Pt species obtained during the *in situ* TEM studies, we have also conducted the catalytic studies on the 0.17wt%Pt@MCM-22 sample for CO oxidation in a fix-bed reactor. To demonstrate the transformation of highly dispersed Pt species under CO oxidation conditions, the 0.17%Pt@MCM-22 sample was firstly calcined in air at 550 °C to achieve the redispersion of Pt into highly dispersed Pt species in MCM-22. Therefore, in the starting catalyst, Pt species mainly exist as highly dispersed species. After performing the $CO+O_2$ reaction at 300 °C and achieving 100% conversion, the catalyst was studied by *ex situ* STEM. As shown in **Figure 6.20**, a large number of Pt clusters as well as a small fraction of Pt nanoparticles appear in the used catalyst, indicating the transformation of singly dispersed Pt species into Pt clusters and nanoparticles under reaction conditions, which is consistent with the results obtained with the *in situ* TEM experiments. After following the evolution of the Pt species and catalytic activity by *in situ* and *ex situ* STEM, we can elaborate the active sites of Pt catalysts for CO oxidation.

Furthermore, as mentioned before when discussing our *in situ* TEM results for CO oxidation, redispersion of Pt nanoparticles at high temperature in $CO+O_2$ atmosphere was observed. To confirm that phenomenon in a practical system, the 0.17%Pt@MCM-22-300H$_2$ sample has also been tested under $CO+O_2$ reaction conditions at 400 °C (full conversion of CO was achieved at 400 °C) to check the structural evolution of Pt species at high temperature. As it can be seen in **Figure 6.21**, the number of Pt nanoparticles decreased in the used catalyst, indicating the redispersion of Pt under $CO+O_2$ reaction conditions at 400 °C.

In recent years, there are some reports on the applications of supported single-atom Pt catalysts for CO oxidation reaction. For instance, Narula *et al*.

claimed that Pt single atoms supported on Al_2O_3 could serve as the active sites for CO oxidation.[27] Besides, in a recent paper, Lu *et al.* have prepared a Pt/CeO_2 sample containing Pt single atoms by atomic layer deposition and the catalyst was used for CO oxidation.[28] It should be noted that, only fresh catalysts were characterized in those works while the evolution of the catalysts under reaction conditions were not followed. Based on these results shown above, it seems that for Pt supported on MCM-22, Pt clusters and nanoparticles are the active species for CO oxidation at 200-300 ^oC, while highly dispersed Pt species (single atoms and clusters) may serve as the active sites at high temperature (~400 ^oC).[29] This phenomenon also indicates that, treating the Pt catalysts under $CO+O_2$ atmosphere at high temperature can be an alternative route for the transformation of Pt nanoparticles into highly dispersed Pt species. And this strategy may also be applicable to other group VIII metal catalysts.

Nevertheless, we have also followed the evolution of Pt species by *in situ* IR spectroscopy for $CO+O_2$ under flow conditions, and CO was used as probe molecules to study the chemical states and atomicity of Pt species after $CO+O_2$ reaction at different temperature.[30-32] As shown in **Figure 6.22**, both oxidized Pt species as well as Pt clusters were observed in the CO adsorption spectrum for the starting 0.17%Pt@MCM-22 sample and those Pt species remain almost unchanged after $CO+O_2$ reaction at 225 ^oC. When the temperature was increased to 300 ^oC, the amount of subnanometric Pt clusters decreased and they were transformed into oxidized Pt species, which should be caused by the sintering of Pt clusters to small Pt nanoparticles as observed by TEM. Interestingly, those agglomerated Pt nanoparticles will disintegrate into Pt clusters again after reaction at 400 ^oC.

Combining our results and reported works, it can be concluded that the evolution of singly dispersed metal species under reaction conditions is a critical issue when studying the catalytic properties of single-atom catalysts.[33] Special attention should be paid to the structural evolution of metal species under reaction conditions. Nevertheless, the state (particle size and chemical states) of metal species may also be dependent on the reaction conditions (atmosphere and temperature). Therefore, the possibility that different reaction mechanism and different types of active species may exist under various reaction conditions has to be considered.
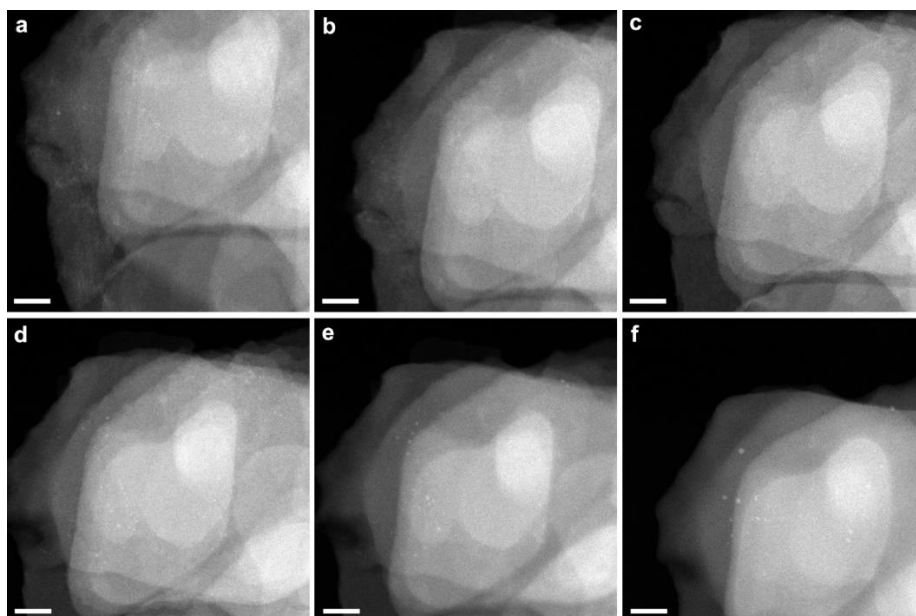
Figure 6.25. High-temperature stability test of 0.17%Pt@MCM-22-300H₂ sample under CO+NO reaction conditions. During the in situ TEM experiments, the sample was treated in mixture of CO (0.1 torr) and NO (0.1 torr) for 15 min at different reaction temperature, respectively. In order to avoid the carbon deposition of CO by the electron beam, the TEM chamber was evacuated to remove CO gas after exposure of the sample to CO+NO gases. (a) 200 °C, (b) 400 °C, (c) 600 °C, (d) 800 °C, (e) 1000 °C, (f) 1200 °C. Scale bar in all the images in this figure: 20 nm.

Evolution of Pt under water-gas shift conditions

The evolution of Pt species under water-gas shift (WGS) reaction condition has also been studied by *in situ* TEM. As shown in **Figure 6.23** and **Figure 6.24**, the transformation of highly dispersed Pt species into Pt clusters was observed when the temperature was increased to 100 °C. Further increase of reaction temperature to 200, 300 and 400 °C results in further growth of Pt clusters. However, as a result of the confinement effect of MCM-22 zeolite, the Pt clusters are prevented from agglomeration into large Pt nanoparticles. Notably, Pt clusters or small Pt nanoparticles remained stable at 400 °C, and the redispersion of Pt nanoparticles was not observed. This is different to the

dynamic behavior of subnanometric Pt species under CO oxidation reaction conditions, in where redispersion of Pt nanoparticles into Pt clusters and atoms occurs at 400 ºC. As discussed before, the agglomeration-redispersion behavior of Pt species is strongly related with the atmosphere.
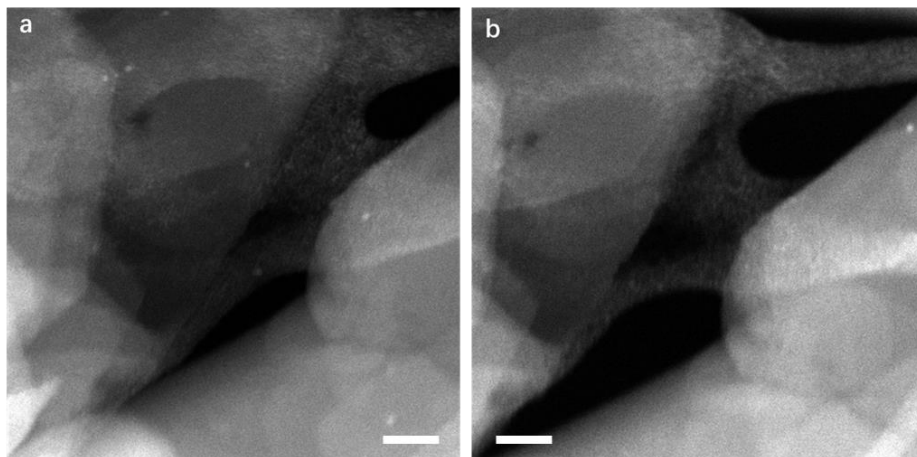
Figure 6.26. Evolution of Pt clusters from 200 ºC to 400 ºC in NO+CO atmosphere. As shown in the STEM image, Pt clusters were observed at 200 ºC (a) and they disappeared when the temperature was increased to 400 ºC (b). Scale bar: (a, b) 20 nm.
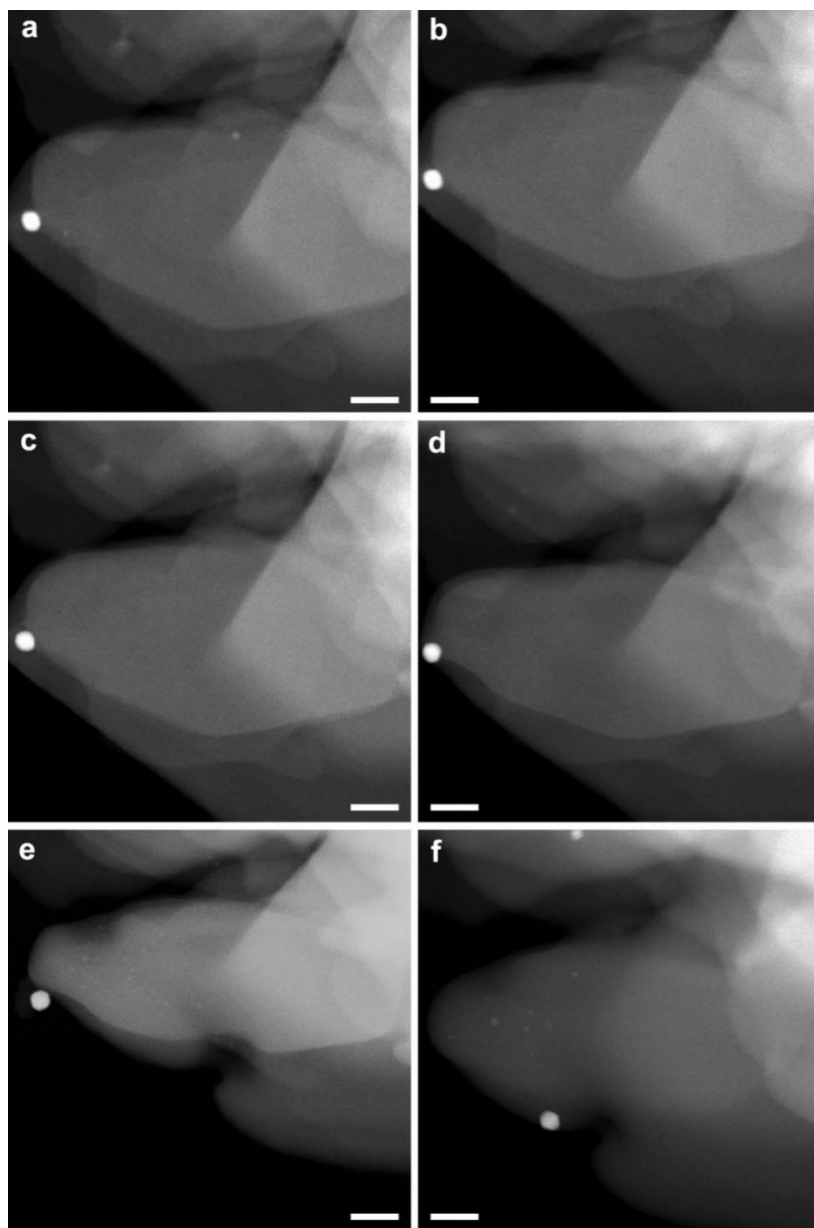
Figure 6.27. High-temperature stability test of 0.17%Pt@MCM-22-300H$_2$ catalyst under NO+CO reaction conditions measured by *in situ* TEM. During the in situ TEM experiments, the sample was treated in mixture of CO (0.1 torr) and NO (0.1 torr) for 15 min at different reaction temperature,

respectively. In order to avoid the carbon deposition of CO by the electron beam, the TEM chamber was evacuated to remove CO gas after exposure of the sample to CO+NO gases at each temperature. (a) 200 ℃, (b) 400 ℃, (c) 600 ℃, (d) 800 ℃, (e) 1000 ℃, (f) 1200 ℃. Scale bar in all the images in this figure: 20 nm.
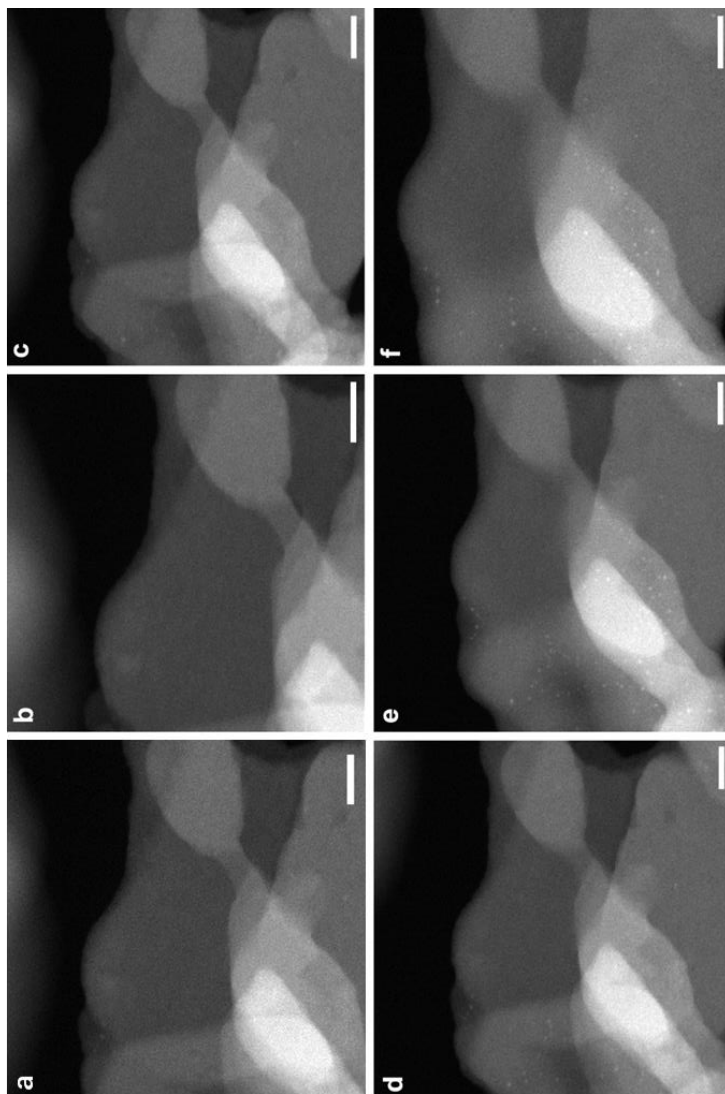
Figure 6.28. High-temperature stability test of 0.17%Pt@MCM-22-300H₂ sample under NO+H₂ reaction conditions. During the in situ TEM

experiments, the sample was treated in mixture of H_2 (0.1 torr) and NO (0.1 torr) for 15 min at different reaction temperature, respectively. The above images were recorded in the presence of NO+H_2 gases at different temperature. (a) 200 ºC, (b) 400 ºC, (c) 600 ºC, (d) 800 ºC, (e) 1000 ºC, (f) 1200 ºC. Scale bar in all the images in this figure: 20 nm.
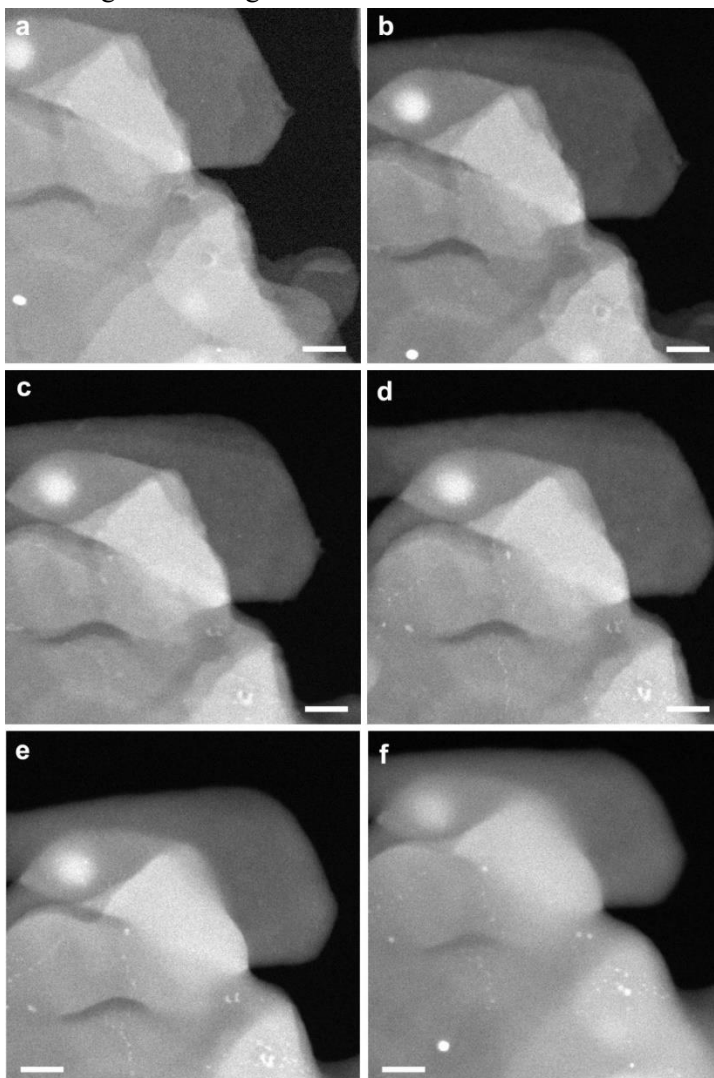
Figure 6.29. High-temperature stability test of 0.17%Pt@MCM-22-300H₂ catalyst under H₂+NO reaction conditions measured by *in situ* TEM. During the in situ TEM experiments, the sample was treated in mixture of H_2

(0.1 torr) and NO (0.1 torr) for 15 min at different reaction temperature, respectively. The above images were recorded in the presence of NO+H_2 gases at different temperature. (a) 200 ℃, (b) 400 ℃, (c) 600 ℃, (d) 800 ℃, (e) 1000 ℃, (f) 1200 ℃. Scale bar in all the images in this figure: 20 nm.
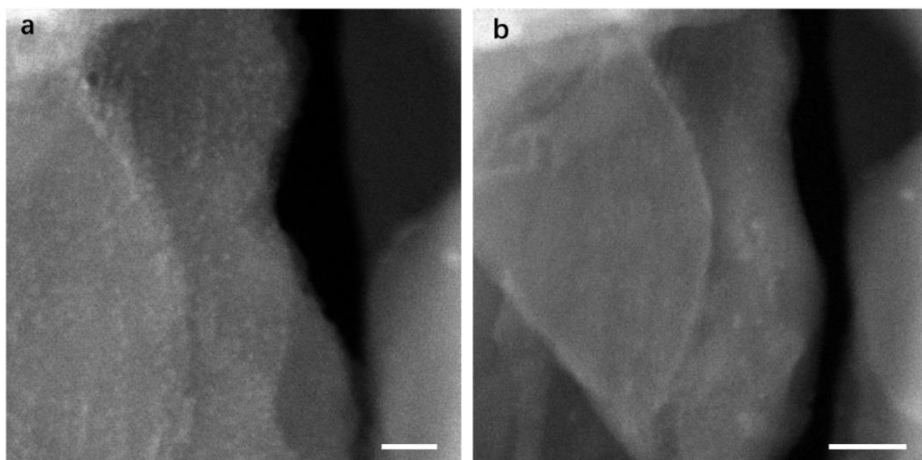
Figure 6.30. Evolution of Pt clusters from room temperature to 200 ℃ in NO+H_2 atmosphere. As shown in the STEM image, Pt clusters were observed at room temperature (a) and most of them disappeared when the temperature was increased to 200 ℃ (b). Scale bar: (a) 10 nm, (b) 20 nm.

Evolution of Pt under selective reduction of NO by CO or H_2

In this section, selective reduction of NO by CO or H_2 has been chosen as model reaction for studying the behavior of the subnanometric Pt species in the Pt@MCM-22-300H_2 sample under the reaction conditions of elimination of NOx in exhaust gases.[34-37] As shown in **Figure 6.25a**, subnanometric Pt species were observed at 200 ℃ in the presence of CO+NO. Interestingly, it appeared that when the temperature was increased from room temperature to 400 ℃ (see **Figure 6.25b**), the contrast of subnanometric Pt species decreased, implying some structural transformation. Considering our abovementioned results for the dynamic agglomeration-redispersion behaviors of Pt species, it can be speculated that Pt clusters become redispersed at 200-400 ℃ in CO+NO atmosphere. Similar phenomenon has also been observed in another area of the sample, as shown in **Figure 6.26**. When the temperature was increased to 800

°C, subnanometric Pt clusters with higher contrast appeared again. Further increase of the temperature to 1000 or even 1200 °C results in the growth of the particle size of Pt clusters. Notably, most of the Pt species are still below 1 nm with a small fraction of Pt nanoparticles (~1 nm), indicating the excellent stability of Pt nanoclusters at high temperature when encapsulated in MCM-22 zeolite. More STEM images of the other areas of 0.17%Pt@MCM-22-300H$_2$ sample under CO+NO reaction conditions are shown in **Figure 6.27**, showing similar tendency during the process from 200 °C to 1200 °C under reaction conditions.

The stability of subnanometric Pt species during the reaction of NO with H$_2$ has also been investigated by *in situ* TEM. As shown in **Figure 6.28**, the behavior of Pt species shows a similar evolution pattern to that observed during the NO+CO reaction. More STEM images of the other areas under NO+H$_2$ reaction conditions are shown in **Figure 6.29**. Interestingly, when the temperature was increased from room temperature to 200 °C, redispersion of Pt clusters to atomically dispersed Pt species was observed (see **Figure 6.30**), which is similar to the situation for NO+CO reaction when increasing the reaction temperature. Furthermore, at 400-600 °C, Pt mainly existed as subnanometric or atomically dispersed Pt species, with low contrast in STEM images. When the temperature was increased to 800 °C, Pt clusters as well as a small fraction of Pt nanoparticles (~1 nm) appeared, corresponding to structural transformation at this temperature. The evolution of Pt species in MCM-22 from room temperature to high temperature is summarized in **Figure 6.31**.
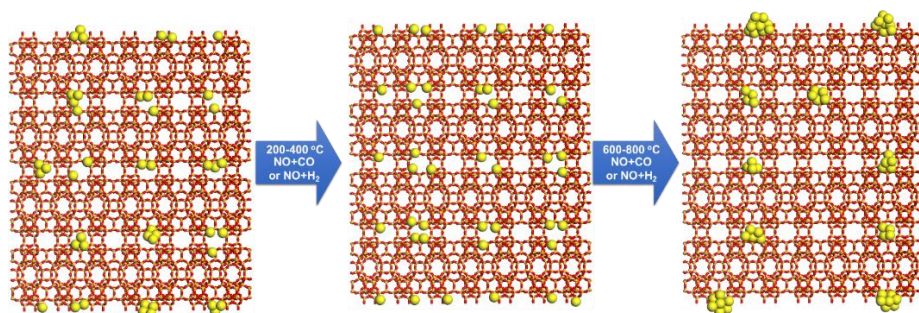
Figure 6.31. Schematic illustration of structural evolution of Pt species in 0.17%Pt@MCM-22-300H$_2$ sample under CO+NO and NO+H$_2$ conditions. At 200-400 °C, Pt clusters will disintegrate and form highly dispersed Pt species.

At higher temperature (600-800 ºC), highly dispersed Pt species agglomerate into Pt clusters or even small Pt nanoparticles (1-2 nm). Due to the protection effect from MCM-22 framework, Pt clusters and small nanoparticles (1-2 nm) can be stabilized at such high temperature.
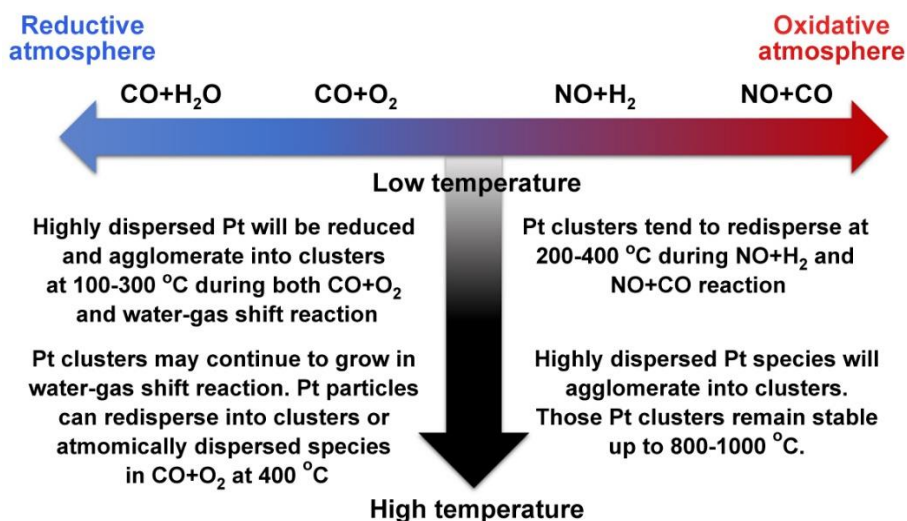
Figure 6.32. Comparison of the dynamic evolution of subnanometric Pt species under different reaction atmosphere from low temperature to high temperature. The evolution of subnanometric Pt species is related with the reactants and reaction temperature.

Based on the above results obtained from *in situ* TEM studies, we can have a summary on the evolution of subnanometric Pt species under different reaction conditions, as presented in **Figure 6.32**. Under reductive atmosphere ($CO+O_2$ and $CO+H_2O$), atomically dispersed Pt species will agglomerate into Pt clusters (at 100-300 ºC). However, in an oxidative atmosphere ($NO+H_2$ and $NO+CO$), subnanometric Pt clusters will disintegrate into atomically dispersed Pt species at relative lower temperature (200-400 ºC). At higher temperature, the behavior of Pt species is also strongly related with the atmosphere.

In summary, the dynamic structural transformation of encapsulated subnanometric Pt species in zeolites (including atomically dispersed Pt and Pt clusters) has been studied with *in situ* TEM under oxidation-reduction and

reaction conditions. Comparing with conventional Pt nanoparticles, the behaviors of subnanometric Pt species is much more sensitive to the presence of reactants. Dynamic and reversible transformation between single atoms, clusters and nanoparticles has been observed under $CO+O_2$ reaction conditions at different temperature. Furthermore, their local coordination environment (in this work, this factor corresponds to the location of Pt species in the zeolite crystallites) also affects the behaviors of Pt species. By tuning the size and spatial distribution of Pt species in MCM-22, subnanometric Pt clusters can be stabilized under reaction conditions, even at very high temperature (>800 ^{o}C).

Nevertheless, considering our results shown in this work obtained under different conditions, it can be a general phenomenon that subnanometric metal species will undergo dynamic structural evolution under reaction conditions.[38,39] For the same reaction, the states of metal species are dependent on the temperature and atmosphere. Therefore, when studying the catalytic properties of subnanometric metal species (single atoms and clusters), *in situ* or *operando* characterization is necessary when one tries to identify the active species for specific reaction. Finally, by studying the evolution patterns of subnanometric metal species under reaction conditions, it can also help us to develop new methodologies (using different pretreatment conditions) for preparation of metal catalysts containing subnanometric metal species for catalytic applications.

Methods
Preparation of 0.17%Pt@MCM-22 sample.

The 0.17%Pt@MCM-22 sample was prepared according to our previous work, with minor modifications. Firstly, subnanometric Pt species were prepared by reduction of Pt precursor with N,N-dimethylformamide (DMF). 110 mg H_2PtCl_6 was dissolved in 120 mL DMF and then the solution was heated at 140 ^{o}C for 6 h. After being heated at 140 ^{o}C for 6 h, a yellow solution was obtained.

In order to prepare the swelled purely siliceous ITQ-1 with ultra-small Pt nanoparticles, 0.75 g of the lamellar precursor were dispersed in 3.0 g of H_2O milliQ, and 15.0 g of a cetyltrimethylammonium hidroxide solution (50 wt.%,

50% exchanged Br⁻/OH⁻) and 4.5 g of a solution of tetrapropylammonium hidroxide (40 wt.%, 50% exchanged Br⁻/OH⁻) were added together with 15 mL of the DMF solution containing Pt species. The resultant mixture was heated at 52 °C under stirring vigorously for 16 hours in order to facilitate the swelling of the layers of the precursor material. At this point, the solid was recovered by centrifugation and washed with distilled water. Finally, the solid product was dried in an oven at 60 °C. Afterwards, the swelled sample containing subnanometric Pt species was calcined in air to remove the organic templates and surfactants at 550 °C in air for 4 h with a ramp rate of 2 °C/min from room temperature to 550 °C. After removing the organic templates and surfactants, the solid sample was calcined again at 550 °C in air for 4 h with a ramp rate of 2 °C/min from room temperature to 550 °C, resulting in the formation of 0.17%Pt@MCM-22 sample. The loading of Pt was measured by inductively coupled plasma.

0.17%Pt@MCM-22-300H$_2$ was prepared by reducing 0.17%Pt@MCM-22 sample with H$_2$ at 300 °C for 30 min with a ramp rate of 5 °C/min from room temperature to 300 °C.

NO gas (4% of NO in N$_2$) was used to oxidize the Pt species in Pt@MCM-22 sample to achieve redispersion of Pt nanoparticles in the Pt@MCM-22 with 0.3 wt% of Pt.

Characterizations

Samples for *ex situ* electron microscopy studies were prepared by dropping the suspension of Pt@MCM-22 or other materials using ethanol as the solvent directly onto holey-carbon coated Cu grids. The measurements were performed in a JEOL 2100F microscope operating at 200 kV both in transmission (TEM) and scanning-transmission modes (STEM). STEM images were obtained using a High Angle Annular Dark Field detector (HAADF), which allows Z-contrast imaging. High-resolution STEM measurement was performed on FET Titan low-base microscope at 300 kV equipped with a Cs probe corrector, a monochromator and an ultrabright X-FEG electron source. The convergence angle was 25 mrad and the inner and outer angles for HAADF imaging were 70 and 200 mrad, respectively. The typical probe current was set to 2 pA under the HR-STEM imaging conditions. Control experiments have been performed and

it was found that, under our experimental conditions, the subnanometric Pt species remain stable under the electron beam in the first several acquisitions.

In situ electron microscopy experiments were performed using a Titan 80-300 Environmental Transmission Electron Microscope at the Centre for Functional Nanomaterials, Brookhaven National Laboratory. The reaction conditions and experimental procedures were presented in the figure captions for different reactions. The *in situ* TEM experiments were performed at 300 kV. The beam current is 0.418 nA and the dose rate is 176 e A^{-2} s^{-1}. The convergence angle, the inner angle and the outer angle is 10, 25 and 51mrad, respectively. TEM chips from DENS solution with through holes were used in all the in situ TEM experiments.

In situ infrared (IR) experiments. IR spectra were recorded with a Bruker spectrometer, Vertex 70, using a DTGS detector and acquiring at 4 cm^{-1} resolution. An IR cell allowing in situ treatments in controlled atmospheres and temperatures from 25 ºC to 500 ºC was connected to a vacuum system with gas dosing facility. For IR studies, the samples were pressed into self-supported wafers and treated at 150 ºC in vacuum (10^{-4} mbar) for 1 h. Afterwards the sample has been exposed to a flow of 1.6 mL/min of CO and 0.8 mL/min of O_2 (CO/O_2 = 2/1 molar ratio) for 1h and at different temperatures, 225 ºC, 300 ºC and 400 ºC. Each temperature corresponded to an independent experiment. After being kept at the corresponding temperature, the sample was cooled down to room temperature, and then evacuated at 10^{-4} mbar and followed by CO dosing at increasing pressure (0.4-2.5 mbar). IR spectra were recorded after each dosage. An additional CO adsorption experiment of the fresh catalyst was done on the Pt@MCM-22 sample without being exposed to CO+O_2 reaction.

Catalytic measurement. The CO oxidation was performed in a fix-bed reactor. 120 mg of solid catalyst was used for each test. The feed gas was 2% of CO and 1% of O_2 in He. The total flow was 85 mL/min. The product was analyzed by gas chromatograph with thermal conductivity detector.

References
(1) Yang, X. F.; Wang, A.; Qiao, B.; Li, J.; Liu, J.; Zhang, T. *Acc. Chem. Res.* **2013,** *46*, 1740-1748.

(2) Boronat, M.; Leyva-Perez, A.; Corma, A. *Acc. Chem. Res.* **2014,** *47*, 834-844.

(3) Flytzani-Stephanopoulos, M.; Gates, B. C. *Ann. Rev. Chem. Biomol. Eng.* **2012,** *3*, 545-574.

(4) Lu, J.; Serna, P.; Aydin, C.; Browning, N. D.; Gates, B. C. *J. Am. Chem. Soc.* **2011,** *133*, 16186-16195..

(5) Jones, J.; Xiong, H.; DeLaRiva, A. T.; Peterson, E. J.; Pham, H.; Challa, S. R.; Qi, G.; Oh, S.; Wiebenga, M. H.; Pereira Hernandez, X. I.et al. *Science* **2016,** *353*, 150-154.

(6) Corma, A.; Concepcion, P.; Boronat, M.; Sabater, M. J.; Navas, J.; Yacaman, M. J.; Larios, E.; Posadas, A.; Lopez-Quintela, M. A.; Buceta, D.et al. *Nat. Chem.* **2013,** *5*, 775-781.

(7) Aydin, C.; Lu, J.; Browning, N. D.; Gates, B. C. *Angew. Chem. Int. Ed.* **2012,** *51*, 5929-5934.

(8) Xiong, H.; Lin, S.; Goetze, J.; Pletcher, P.; Guo, H.; Kovarik, L.; Artyushkova, K.; Weckhuysen, B. M.; Datye, A. K. *Angew. Chem. Int. Ed.* **2017,** *56*, 8986-8991.

(9) Serna, P.; Gates, B. C. *Acc. Chem. Res.* **2014,** *47*, 2612-2620.

(10) Bayram, E.; Lu, J.; Aydin, C.; Browning, N. D.; Özkar, S.; Finney, E.; Gates, B. C.; Finke, R. G. *ACS Catal.* **2015,** *5*, 3514-3527.

(11) Liu, L.; Diaz, U.; Arenal, R.; Agostini, G.; Concepcion, P.; Corma, A. *Nat. Mater.* **2017,** *16*, 132-138.

(12) Tao, F. F.; Crozier, P. A. *Chem. Rev.* **2016,** *116*, 3487-3539.

(13) Hansen, P. L.; Wagner, J. B.; Helveg, S.; Rostrup-Nielsen, J. R.; Clausen, B. S.; Topsoe, H. *Science* **2002,** *295*, 2053-2055.

(14) Vendelbo, S. B.; Elkjaer, C. F.; Falsig, H.; Puspitasari, I.; Dona, P.; Mele, L.; Morana, B.; Nelissen, B. J.; van Rijn, R.; Creemer, J. F.et al. *Nat. Mater.* **2014,** *13*, 884-890.

(15) Zugic, B.; Wang, L.; Heine, C.; Zakharov, D. N.; Lechner, B. A. J.; Stach, E. A.; Biener, J.; Salmeron, M.; Madix, R. J.; Friend, C. M. *Nat. Mater.* **2017,** *16*, 558-564.

(16) Yoshida, H.; Kuwauchi, Y.; Jinschek, J. R.; Sun, K.; Tanaka, S.; Kohyama, M.; Shimada, S.; Haruta, M.; Takeda, S. *Science* **2012,** *335*, 317-319.

(17) Li, Y.; Zakharov, D.; Zhao, S.; Tappero, R.; Jung, U.; Elsen, A.; Baumann,

P.; Nuzzo, R. G.; Stach, E. A.; Frenkel, A. I. *Nat. Commun.* **2015,** *6*, 7583.

(18) Schlogl, R. *Angew. Chem. Int. Ed.* **2015,** *54*, 3465-3520.

(19) Topsøe, H. *J. Catal.* **2003,** *216*, 155-164.

(20) Moliner, M.; Gabay, J. E.; Kliewer, C. E.; Carr, R. T.; Guzman, J.; Casty, G. L.; Serna, P.; Corma, A. *J. Am. Chem. Soc.* **2016,** *138*, 15743-15750.

(21) Ge, Q.; Neurock, M. *J. Am. Chem. Soc.* **2004,** *126*, 1551-1559.

(22) Zhu, J. F.; Kinne, M.; Fuhrmann, T.; Denecke, R.; Steinrück, H. P. *Surf. Sci.* **2003,** *529*, 384-396.

(23) Bliem, R.; van der Hoeven, J. E.; Hulva, J.; Pavelec, J.; Gamba, O.; de Jongh, P. E.; Schmid, M.; Blaha, P.; Diebold, U.; Parkinson, G. S. *Proc. Natl. Acad. Sci. USA* **2016,** *113*, 8921-8926.

(24) Wang, Y. G.; Mei, D.; Glezakou, V. A.; Li, J.; Rousseau, R. *Nat. Commun.* **2015,** *6*, 6511.

(25) Akdogan, Y.; Anantharaman, S.; Liu, X.; Lahiri, G. K.; Bertagnolli, H.; Roduner, E. *J. Phys. Chem. C* **2009,** *113*, 2352-2359.

(26) Newton, M. A. *Chem. Soc. Rev.* **2008,** *37*, 2644-2657.

(27) Moses-DeBusk, M.; Yoon, M.; Allard, L. F.; Mullins, D. R.; Wu, Z.; Yang, X.; Veith, G.; Stocks, G. M.; Narula, C. K. *J. Am. Chem. Soc.* **2013,** *135*, 12634-12645.

(28) Wang, C.; Gu, X.-K.; Yan, H.; Lin, Y.; Li, J.; Liu, D.; Li, W.-X.; Lu, J. *ACS Catal.* **2017,** *7*, 887-891.

(29) Yu, X.; Wang, Y.; Kim, A.; Kim, Y. K. *Chem. Phys. Lett.* **2017,** *685*, 282-287.

(30) Ding, K.; Gulec, A.; Johnson, A. M.; Schweitzer, N. M.; Stucky, G. D.; Marks, L. D.; Stair, P. C. *Science* **2015,** *350*, 189-192.

(31) De La Cruz, C.; Sheppard, N. *Spectr. Acta A: Mol. Spectr.* **1994,** *50*, 271-285.

(32) Stakheev, A. Y.; Shpiro, E. S.; Jaeger, N. I.; Schulz-Ekloff, G. *Catal. Lett.* **1995,** *32* (1-2), 147-158.

(33) Heiz, U.; Sanchez, A.; Abbet, S.; Schneider, W. D. *J. Am. Chem. Soc.* **1999,** *121*, 3214-3217.

(34) Bera, P.; Patil, K. C.; Jayaram, V.; Subbanna, G. N.; Hegde, M. S. *J. Catal.* **2000,** *196*, 293-301.

(35) Burch, R.; Breen, J. P.; Meunier, F. C. *Appl. Catal. B: Environ.* **2002,** *39*,

283-303.

(36) Paredis, K.; Ono, L. K.; Behafarid, F.; Zhang, Z.; Yang, J. C.; Frenkel, A. I.; Cuenya, B. R. *J. Am. Chem. Soc.* **2011,** *133*, 13455-13464.

(37) Lira, E.; Merte, L. R.; Behafarid, F.; Ono, L. K.; Zhang, L.; Roldan Cuenya, B. *ACS Catal.* **2014,** *4*, 1875-1884.

(38) Schlogl, R. *Angew. Chem. Int. Ed.* **2015**, *54*, 3465-3520.

(39) Ye, R.; Hurlburt, T. J.; Sabyrov, K.; Alayoglu, S.; Somorjai, G. A. *Proc. Natl. Acad. Sci. USA* **2016**, *113*, 5159-5166.

Chapter 7

Generation of Gold Nanoclusters Encapsulated in MCM-22 Zeolite for Aerobic Oxidation of Cyclohexane
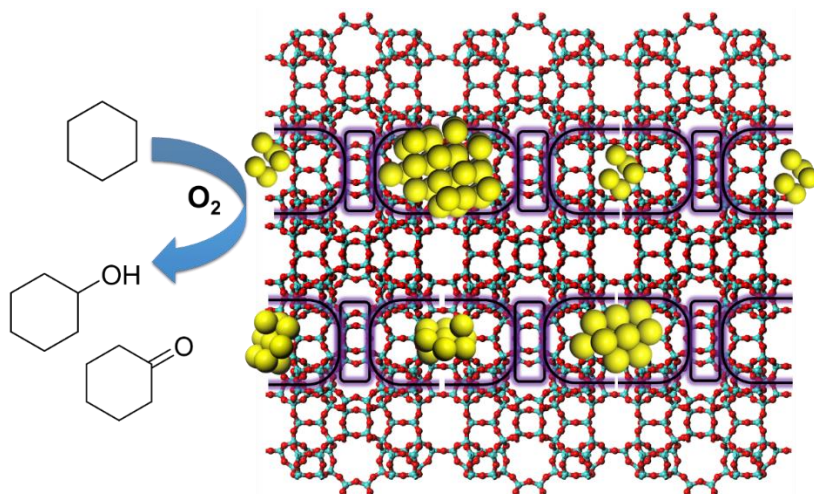
Abstract

In this work, we will report the generation of Au clusters in purely siliceous MCM-22 zeolite. High-resolution and spectroscopic characterizations have confirmed the presence of subnanometric Au clusters in MCM-22. We have tested the catalytic properties of these Au clusters for selective oxidation of cyclohexane to cyclohexanol and cyclohexanone (KA-oil). It will be shown that, the Au clusters encapsulated in MCM-22 zeolite are highly active and selective for oxidation of cyclohexane to KA-oil, which is superior to Au nanoparticles on the same support. These results suggest that, Au clusters are highly active for the activation of oxygen to produce radical species.

1. Introduction

Gold catalysts have been intensively studied in recent years and they have shown unique and remarkable catalytic performances in many reactions, including selective hydrogenation, selective oxidation, organic transformations, electrocatalysis and photocatalysis.[1-4] As well known, the catalytic behavior of Au catalysts is strongly related with the particle size. Small Au particles (<2 nm) have been shown to be much more active than larger Au particles in many reactions.[5] Nevertheless, when the size of Au decrease to subnanometric regime, the catalytic properties of Au clusters are quite distinct to Au nanoparticles due to the size-dependent electronic structures of Au species.[6] In our recent works, it has been demonstrated in some reactions that, only Au clusters with a few atoms are active while neither single Au atoms nor Au nanoparticles are active.[7,8] However, due to their low stability and strong tendency for agglomeration, naked subnanometric Au clusters with open surface sites has been barely reported.[9,10] Using organometallic Au complexes as precursor, Au clusters can be generated in zeolites.[11] However, the high price and toxicity of organometallic compounds as well as the low stability of resultant supported metal clusters at high temperature (>500 °C) are also drawbacks of this strategy.

Considering the low thermal stability of Au particles, the encapsulation of Au species in zeolites should be a promising approach to enhance their stability.[12] The well-defined pore structures of zeolites can provide effective protection for Au species under reaction conditions and achieve size-selective catalytic properties in some cases. During the past several years, encapsulation

of Au into zeolite crystallites have been achieved by several methods. Au nanoparticles (2-3 nm) can be encapsulated in Silicalite-1 with intraparticle voids and mesopores through a simple impregnation method.[13] Recently, Iglesia and his co-workers report a method to generate small Au nanoparticles (1~2 nm) in Al-containing zeolites with high thermal stability and resistance to poison molecules in catalytic reactions.[14]

In our recent work, subnanometric Pt single atoms and Pt clusters are encapsulated in MCM-22 through a 2D to 3D transformation process. Those subnanometric Pt species show excellent stability even at high temperature (as high as 550 °C).[15] In this work, by transformation of two-dimensional zeolite into three-dimensional zeolite, naked subnanometric Au clusters can also be generated in purely siliceous MCM-22.

As shown in **Figure 7.1**, the Au@MCM-22 sample is prepared through a similar procedure as we have reported in our recent work. Au clusters dispersed in DMF are prepared firstly as the metal precursor. Subsequently, the Au clusters are incorporated between the MWW layers in ITQ-1 during a swelling process. After removal of the organics in the swelled material, Au species can be encapsulated by the MCM-22 zeolite, leading to the formation of Au@MCM-22-S. However, the Au loading in the Au@MCM-22-S sample is only 0.025 wt.%. In order to improve the Au loading in the final Au@MCM-22 material, 1-octanethiol is added to the swelling mixture (see **Figure 7.1b**), since the Au-S bonding may help the incorporation of Au species into the MWW layers. As a result, a Au@MCM-22-L sample was obtained, with Au loading of 0.11 wt%. In principle, the introduction of 1-octanethiol can also be applied to incorporation of other metals into MCM-22 by our strategy, leading to higher metal loading and maintaining good metal dispersion in the zeolite at the same time.

2. Experimental Section
2.1 Synthesis of Au@MCM-22-S and Au@MCM-22-L

The Au@MCM-22 sample was prepared according to our previous work, with some modifications. Firstly, subnanometric Au clusters were prepared by reduction of $HAuCl_4$ with N,N-dimethylformamide (DMF). 0.3 mL of 0.5 mol/L HAuCl4 solution was dissolved in 200 mL DMF and then the solution

was heated at 140 °C for 48 h. After being kept at 48 h, a yellow solution was obtained and the solution was cooled to room temperature and excess DMF was removed by rotary evaporator, until the volume of the DMF solution is ca. 15 mL.

2.2 Preparation of Au@MCM-22-S

In order to prepare the swelled purely siliceous ITQ-1 with subnanometric Au species, 1.0 g of the lamellar precursor were dispersed in 12.0 g of H_2O milliQ, and 20.0 g of a cetyltrimethylammonium hidroxide solution (50 wt.%, 50% exchanged Br$^-$/OH$^-$) and 6.0 g of a solution of tetrapropylammonium hidroxide (40 wt.%, 50% exchanged Br$^-$/OH$^-$) were added together with 15 mL of the DMF solution containing Au species. The resultant mixture was heated at 52 °C under stirring vigorously for 16 hours in order to facilitate the swelling of the layers of the precursor material. At this point, the solid was recovered by centrifugation and washed with distilled water. Finally, the solid product was dried in an oven at 60 °C. Afterwards, the swelled sample containing subnanometric Au species was calcined in air to remove the organic templates and surfactants. The calcination process was performed as following: 1) increasing the temperature from room temperature to 550 °C with a rate of 2 °C/min in N_2 atmosphere. The total time in N_2 atmosphere is about 4.5 h. 2) switching the atmosphere to air and keeping the temperature at 550 °C for 4 h. 3) Cooling down from 550 °C to room temperature in air.

2.3 Preparation of Au@MCM-22-L

In order to prepare the swelled purely siliceous ITQ-1 with subnanometric Au species, 1.0 g of the lamellar precursor were dispersed in 12.0 g of H_2O milliQ, and 20.0 g of a cetyltrimethylammonium hidroxide solution (50 wt.%, 50% exchanged Br$^-$/OH$^-$) and 6.0 g of a solution of tetrapropylammonium hidroxide (40 wt.%, 50% exchanged Br$^-$/OH$^-$) and 1.0 mL of 1-octanethiol were added together with 15 mL of the DMF solution containing Au species. The resultant mixture was heated at 52 °C under stirring vigorously for 16 hours in order to facilitate the swelling of the layers of the precursor material. At this point, the solid was recovered by centrifugation and washed with distilled water. Finally, the solid product was dried in an oven at 60 °C. Afterwards, the swelled

sample containing subnanometric Au species was calcined in air to remove the organic templates and surfactants. The calcination process was performed as following: 1) increasing the temperature from room temperature to 550 °C with a rate of 2 °C/min in N_2 atmosphere. The total time in N_2 atmosphere is about 4.5 h. 2) switching the atmosphere to air and keeping the temperature at 550 °C for 4 h. 3) Cooling down from 550 °C to room temperature in air.

2.4 Preparation of Au/MCM-22-imp

The Au/MCM-22-imp with 0.1 wt.% of Au was prepared by conventional wetness impregnation. Pure-silica MCM-22 was dispersed in 50 mL distilled water. A certain amount of $HAuCl_4$ solution (calculated based on the final Au loading in the Au/MCM-22-imp sample.

2.4 Characterizations

High-resolution STEM images were obtained using a High Angle Annular Dark Field detector (HAADF), which allows Z-contrast imaging. The powder sample was dispersed in ethanol and then dropped on Cu grid. The high-resolution STEM measurement was performed on FET Titan low-base microscope at 300 kV equipped with a Cs probe corrector, a monochromator and an ultrabright X-FEG electron source. The convergence angle was 25 mrad and the inner and outer angles for HAADF imaging were 70 and 200 mrad, respectively. The typical probe current was set to 2 pA under the HR-STEM imaging conditions.

X-ray absorption near-edge structure (XANES) and Extended X-Ray Absorption Fine Structure (EXAFS) at Au L_3-edge (11919 eV) and Pd K-edge (24350 eV) were carried out on BM23 at European Synchrotron Radiation Facility (ESRF). A double crystal monochromator equipped with a pair of Si (111) crystals was used. Si and Pt mirrors with an angle of 2 mrad were used to reject the harmonics, for Au and Pd, respectively. Data was collected in fluorescence mode using a Si drift detector. The samples were prepared as self-supported pellets and measured at room temperature. A corresponding metallic foil reference was collected simultaneously for energy calibration. EXAFS oscillations were extracted using Athena code and analysed using Arthemis software. The range used to transform the EXAFS oscillations ($k^2 \chi(k)$) was Δk

$= (3-11)$ Å^{-1} and the fits were performed in the interval $\Delta R = (1.7-3.3)$ Å. The local environment of the Au atoms was determined using the phase shift and amplitude functions for Au-Au calculated for gold foil. The photoelectron energy origin correction (ΔE_0), the passive electron amplitude reduction factor (S_0^2) were found for the Au standard and used as fixed parameters to fit the samples. For each contribution a coordination number (N_i) and a distance (R_i) were fitted independently while the mean square relative displacement (σ_i^2) were set to be the same for both samples.

Powder X-ray diffraction (XRD) was performed with a HTPhilips X'Pert MPD diffractometer equipped with a PW3050 goniometer using Cu Kα radiation and a multisampling handler.

2.5 Catalytic measurements for aerobic oxidation of cyclohexane

The aerobic oxidation of cyclohexane was carried out in batch reactor. 2 mL of cyclohexane (1.6 g) and 25 mg solid catalyst was mixed and the reactor was flashed with O_2 several times. The reaction was performed at 150 °C with 10 bar of O_2. 50 μL of liquid mixture was taken out of the reactor and mixed with 1 mL of acetone at different reaction time. 100 uL of triphenylphosphine solution (10 wt%) and 7.3 mg of dodecane as internal standard was then added to the acetone solution with agitation of 5 min. The reaction products were analyzed by Varian GC (CP3800) with HP-5 column with a length of 30 m and diameter of 0.25 mm. The injector temperature was 250 °C and detector temperature was 300 °C. Helium was used as carrier gas with a flow of 2 mL/min and a split ratior of 40. 1.0 μL of liquid was injected into the column.

In order to quantify the yield of adipic acid, esterification reaction with methanol was carried out to transform adipic acid into dimethyl adipate. 50 uL of the reaction mixture was mixed with 200 mg of 10% of boron trifluoride-methanol solution (~1.3 M, from Fluka) and kepted at 80 °C for 1.5 h. After the esterification reaction, 0.8 g of H_2O and 2.0 g of CH_2Cl_2 was added to the mixture. After extraction, the organic layer was injected to the GC for analysis.
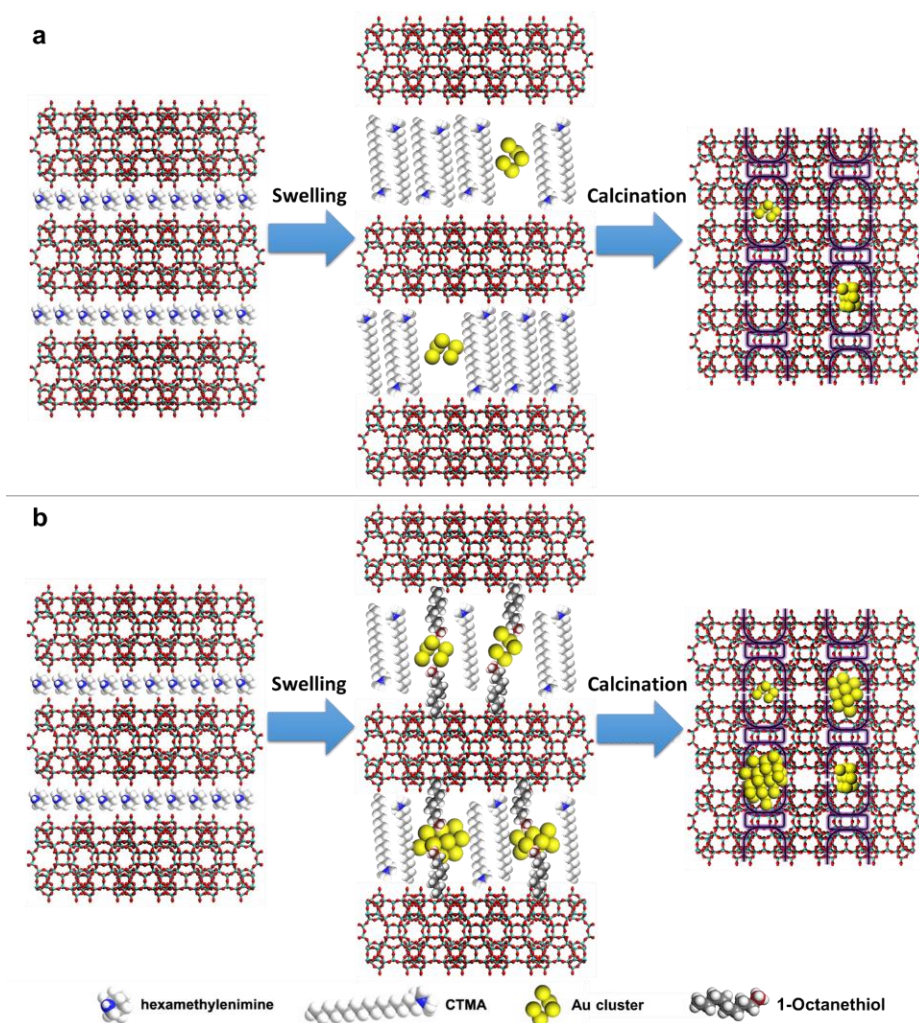
Figure 7.1. Schematic illustration of incorporation of Au nanoclusters into zeolite through the transformation of 2D zeolite into 3D structure (MCM-22). (a) The incorporation of Au clusters in MCM-22 by swelling of the ITQ-1 with surfactant and DMF solution containing Au clusters. (b) The incorporation of Au clusters in MCM-22 by swelling of the ITQ-1 with surfactant, 1-octanethiol and DMF solution containing Au clusters.
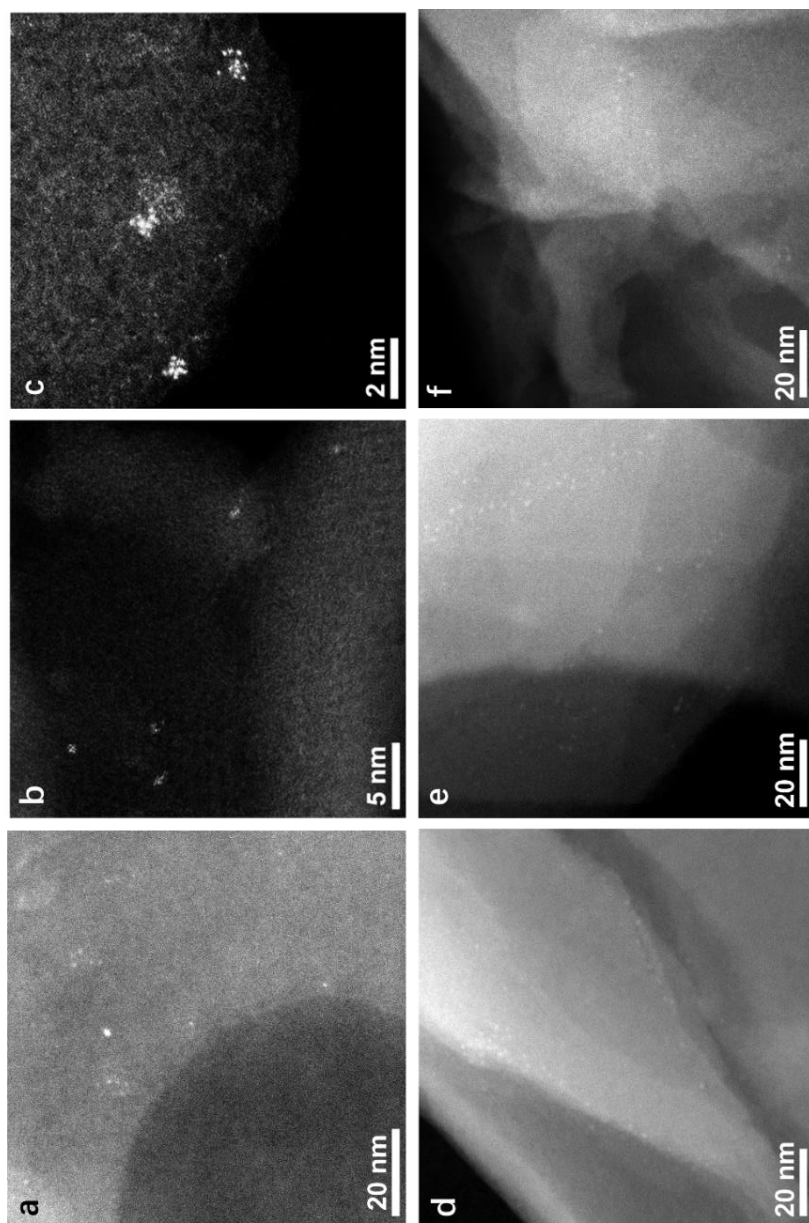
Figure 7.2. Electron microscopy characterizations on Au@MCM-22 samples. (a) STEM image of Au@MCM-22-S sample. (c, d) STEM image of Au@MCM-22-L sample. (d-f) STEM image of Au@MCM-22-S sample, showing the presence of both subnanometric Au clusters and Au nanoclusters

around 1 nm.

3. Results and Discussions

Firstly, the Au species in Au@MCM-22-S and Au@MCM-22-L samples have been characterized by electron microscopy. In the low-magnification STEM image of Au@MCM-22-L (see **Figure 7.2a**), Au nanoclusters with particle size ranging from 0.5 nm to 1 nm can be seen in STEM image, together with a few small Au nanoparticles of 1-2 nm. The atomic structure of subnanometric Au clusters can be revealed by high-resolution STEM images (see **Figure 7.2b** and **Figure 7.2c**). As it can be seen, Au nanoclusters with less than 15 atoms are located in the supercages or surface "cups" of MCM-22. More high-resolution STEM images of various subnanometric Au species are shown in **Figure 7.3**, including single Au atom and Au clusters with less than 10 atoms. Considering the size of supercages in MCM-22, the maximum size of Au clusters is below 1 nm, corresponding to Au clusters with less than 15 atoms. In the case of Au@MCM-22-L, Au nanoclusters around 1 nm with higher amount can also be observed in the STEM images (see Figure 7.1d-Figure 7.1f). The particle size of Au species in the Au@MCM-22-L sample is slightly larger than the Au@MCM-22-S sample.
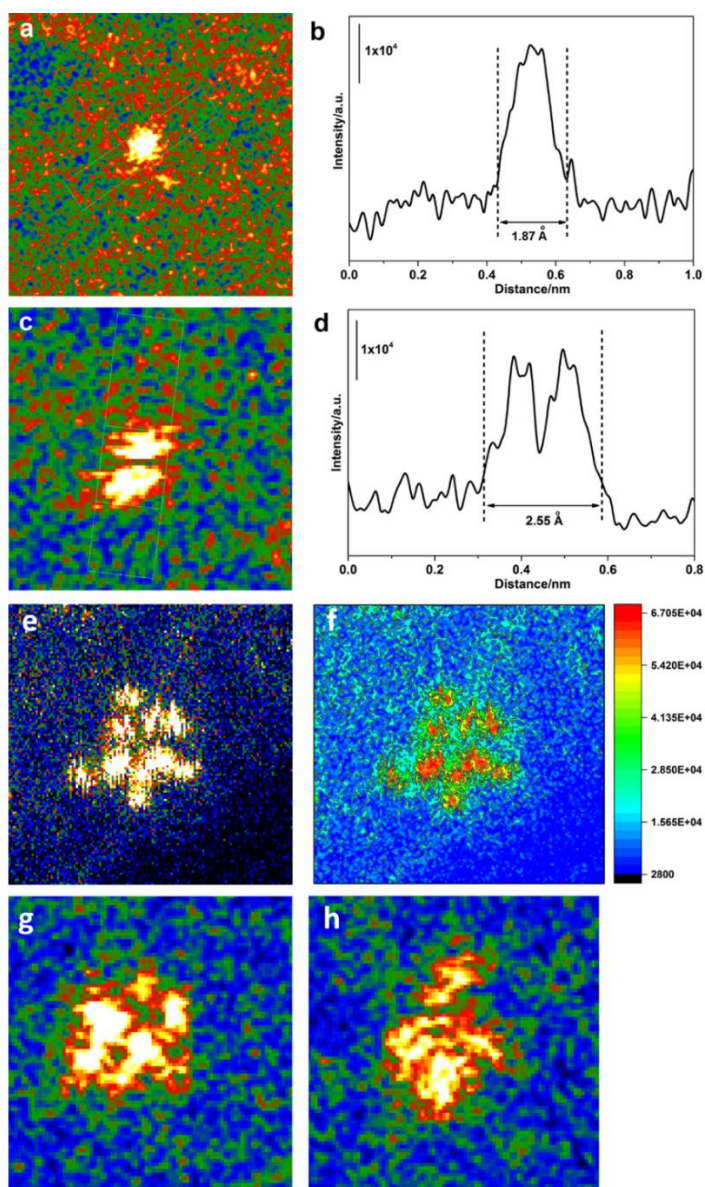
Figure 7.3. High-resolution STEM images of Au@MCM-22-S sample. (a, b) STEM image of a single Au atom and the corresponding contrast profile of the Au atom. (c, d) STEM image of Au_2 cluster and the corresponding contrast profile. (e, f) STEM image of Au_{12} cluster and the corresponding contrast profile. (g) STEM image of Au_7 cluster. (h) STEM image of Au_9 cluster.
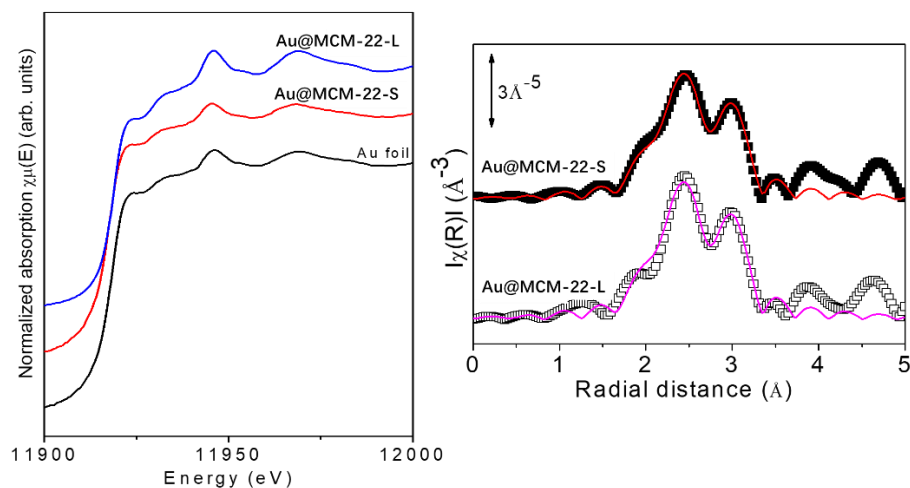
Figure 7.4. (a) XANES spectra of Au@MCM-22-L and Au@MCM-22-S samples and the Au foil reference. (b) Fourier transform of k^2-weighted EXAFS spectra and the fitting curves for Au@MCM-22-L and Au@MCM-22-S samples.

Table 1. Fitting results of the EXAFS spectra for Au@MCM-22-L and Au@MCM-22-S samples. $S^2_0 = 0.8$ and $E_0 = 5$, found for the Au foil and kept for the sample.

Sample	CN_{Au-Au}	σ^2 (Å^{-2})	R (Å)	CN_{ref}	R_{ref} (Å)
Au@MCM-22-L	7.7 ± 0.6	0.008±0.001	2.853±0.003	12	2.88470
Au@MCM-22-S	7.0 ± 0.6		2.855±0.004		

To gain more information on the structures of Au clusters in Au@MCM-22 samples, various spectroscopic characterization tools are used to study them. The coordination environmental and average size of Au species in the AuCL@MCM-22 sample is measured by X-ray absorption spectroscopy (XAS). The chemical states of Au species in Au@MCM-22-S and Au@MCM-22-L samples are measured by X-ray absorption near edge structure (XANES). As displayed in **Figure 7.4a**, both Au@MCM-22-S and Au@MCM-22-L show similar XANES spectrum to the reference metallic Au, indicating that Au nanoclusters exist as metallic state in the MCM-22 zeolite. Furthermore, the

coordination environment of Au species has also been studied by extended X-ray absorption fine structure (EXAFS). As can be seen in **Figure 7.4b**, the fitting results of the EXAFS spectra are shown in **Table 1**. The Au-Au coordination number in Au@MCM-22-S and Au@MCM-22-L is 7.0 and 7.9, respectively. Thus, the average size of Au species in Au@MCM-22-S is ~1 nm and the Au@MCM-22-L is ~1.2 nm, which is consistent with the electron microscopy images in **Figure 7.2**. Combining the results from electron microscopy and XAS, it can be deduced that, the both Au@MCM-22-L and Au@MCM-22-S are consisted by a mixture of subnanometric Au clusters and small Au nanoparticles (1-2 nm). Furthermore, the percentage of subnanometric Au clusters in the Au@MCM-22-S sample is higher than the Au@MCM-22-L according to the EXAFS fitting results.
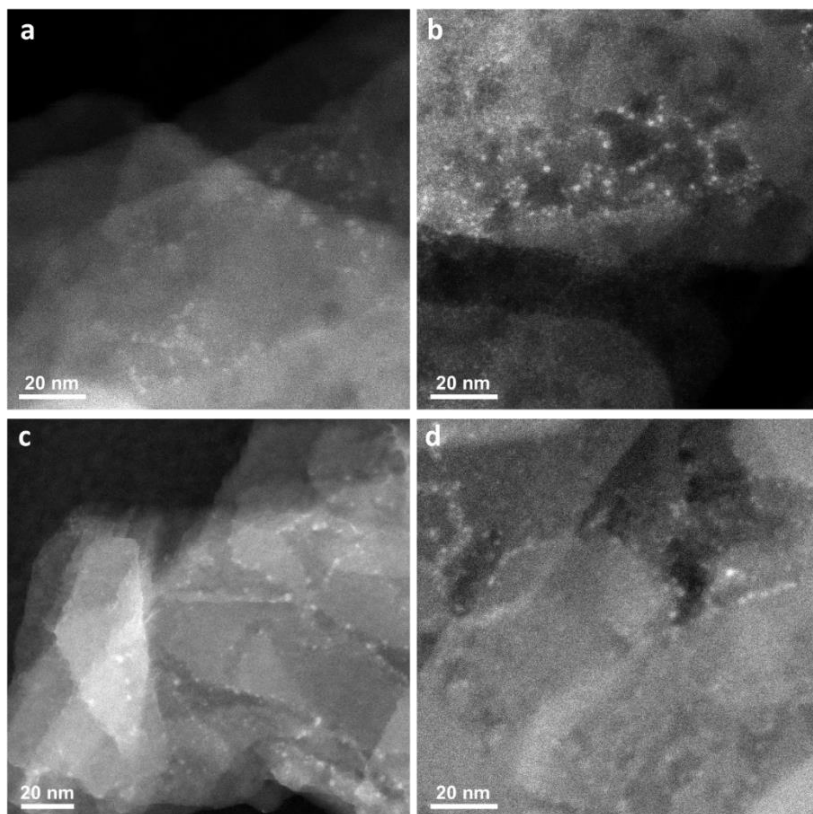
Figure 7.5. STEM images of AuNP/MCM-22 sample prepared by deposition-precipitation method. The size of Au nanoparticles is between 1-2 nm.

For comparison, a sample consisting of Au nanoparticles supported on MCM-22 (containing 0.1 wt.% of Au, denoted as AuNP/MCM-22) is also prepared by deposition-precipitation method (see supplementary for experimental details). As shown in **Figure 7.5**, the particle size of Au nanoparticles in AuNP/MCM-22 ranges from 1.5 to 2.5 nm. It is well known that, the electronic structures of metal clusters and nanoparticles are usually associated with their optical properties. As shown in **Figure 7.6**, The typical surface plasmon resonance of Au nanoparticles can be observed in the UV-vis spectrum of AuNP/MCM-22 sample at ~530 nm. In the case of Au@MCM-22 samples containing Au nanoclusters, we can observed the absorption peaks of at ~615 and ~670 nm in the Au@MCM-22 samples, corresponding to the absorption between the HOMO and LUMO of Au clusters with different sizes.[16] Based on the above structural and spectroscopic characterizations, it is confirmed that Au nanoclusters have been generated and stabilized in MCM-22.
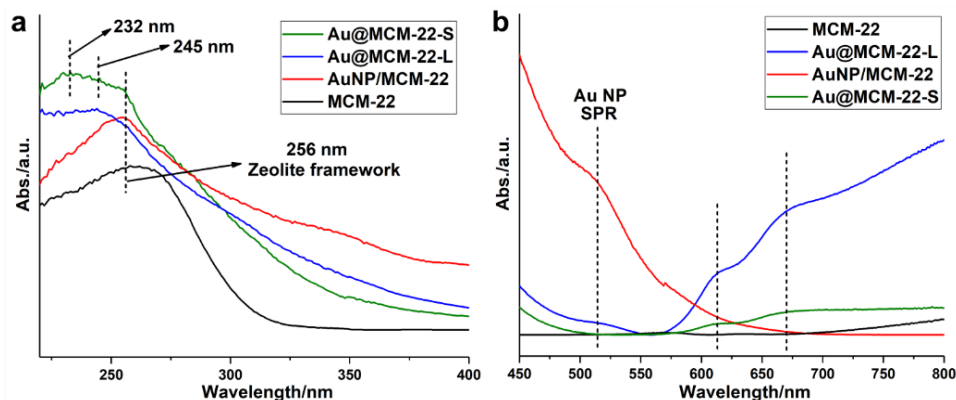
Figure 7.6. UV-vis spectra of MCM-22, AuNP/MCM-22 and two Au@MCM-22 samples containing Au nanoclusters.
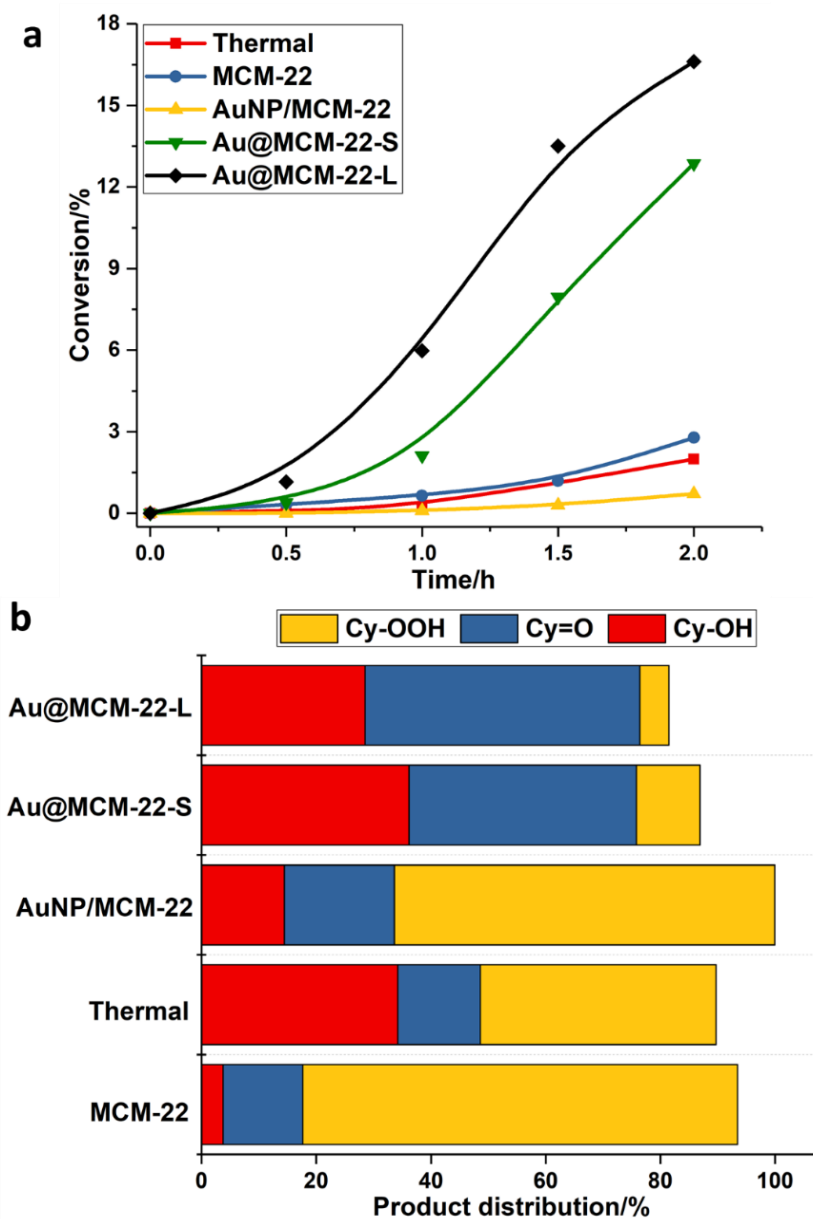
Figure 7.7. Catalytic performance of AuNP/MCM-22 and Au@MCM-22 catalysts for aerobic oxidation of cyclohexane. Reaction conditions: 2 mL cyclohexane, 25 mg solid catalyst, 150 °C, 10 bar of O_2. The "Thermal" test was carried out under the same conditions in the absence of catalyst.
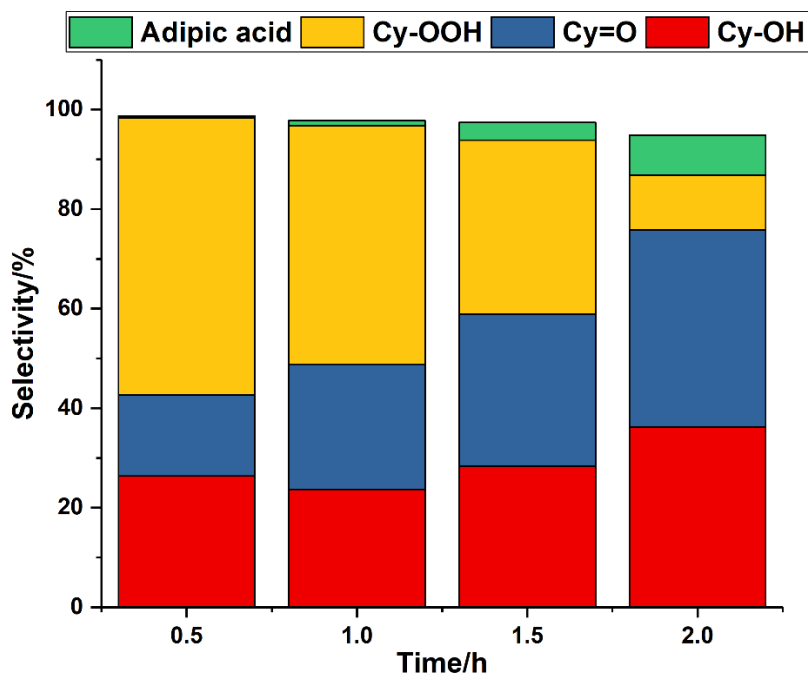
Figure 7.8. Distributions of products in the oxidation of cyclohexane by Au@MCM-22-S sample. Reaction conditions: 2 mL cyclohexane, 25 mg solid catalyst, 150 °C, 10 bar of O_2. The "Thermal" test was carried out under the same conditions in the absence of catalyst.

To test the catalytic properties of Au clusters, the oxidation of cyclohexane to cyclohexanol and cyclohexanone (KA-oil) is employed as a model reaction. It has been established in the literature that, auto-oxidation of cyclohexane is a radical-chain reaction.[17] Moreover, it has also been proposed that, supported Au nanoparticles are actually inert in the oxidation of cyclohexane.[18] Recently, it has been demonstrated recently by our group that, Au clusters are efficient catalyst for activation of O_2 and production of radical oxygen species.[7,8] Therefore, it is supposed that, Au clusters stabilized in MCM-22 zeolite may serve as active species for the initiation of autocatalytic oxidation of cyclohexane to KA-oil.
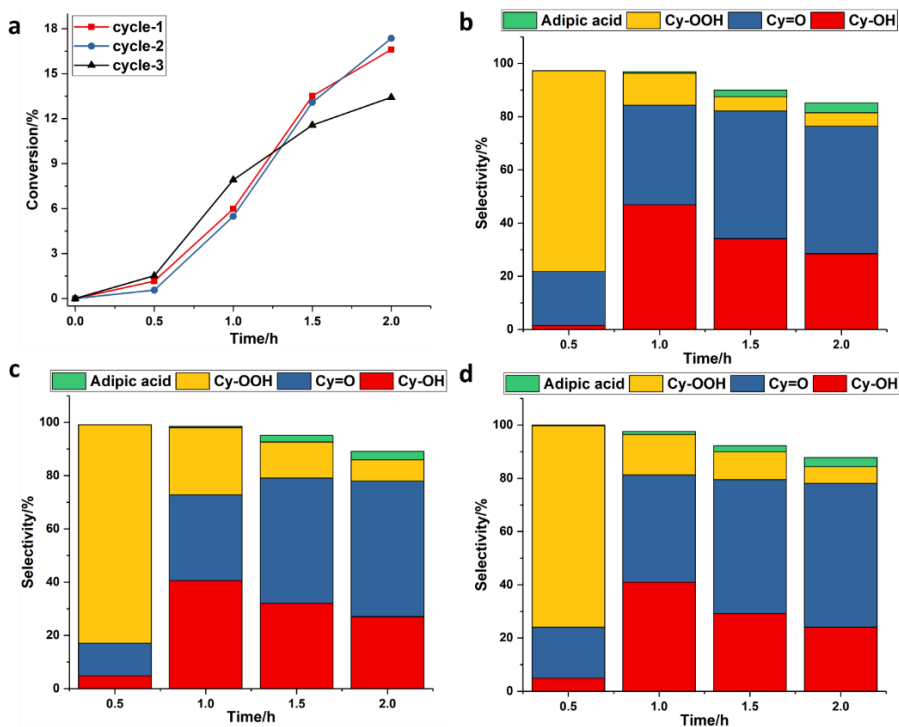
Figure 7.9. Recycle tests of Au@MCM-22-L sample for oxidation of cyclohexane. (a) Conversion of cyclohexane and the corresponding distributions of products in three cycles: (b) first cycle, (c) second cycle and (d) third cycle. Reaction conditions: 2 mL cyclohexane, 25 mg solid catalyst, 150 °C, 10 bar of O_2. The "Thermal" test was carried out under the same conditions in the absence of catalyst. After each test, the solid catalyst was recycled by filtration and then washed with acetone, before being used for another catalytic test.
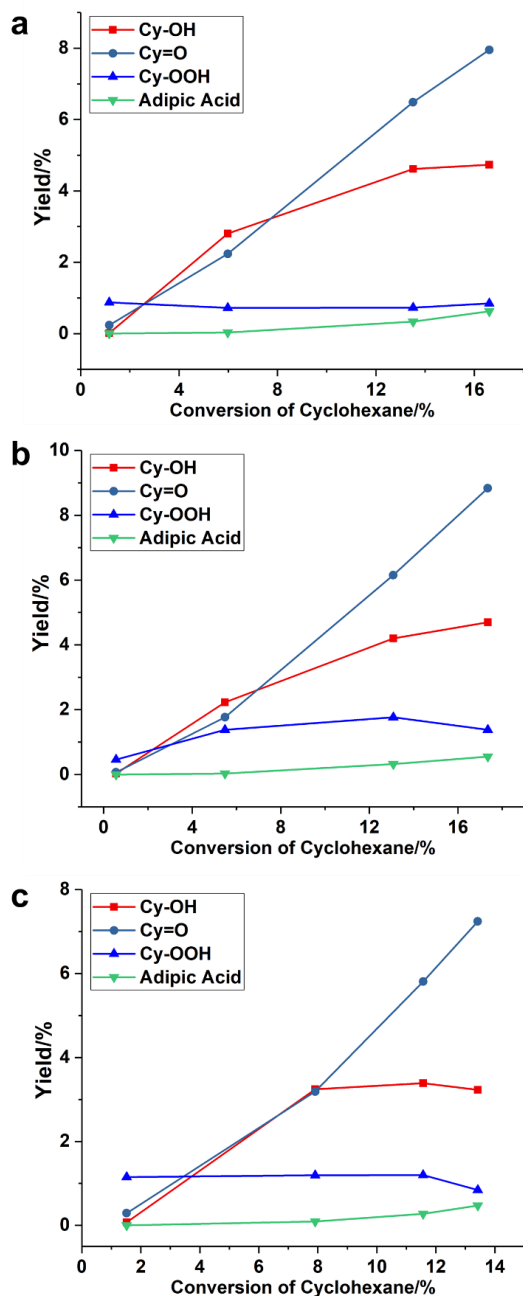
Figure 7.10. Yields of various products at different conversion of cyclohexane when using Au@MCM-22-L as the catalyst. (a) first cycle, (b)

second cycle and (c) third cycle. Reaction conditions: 2 mL cyclohexane, 25 mg solid catalyst, 150 ºC, 10 bar of O$_2$. After each test, the solid catalyst was recycled by filtration and then washed with acetone, before being used for another catalytic test.
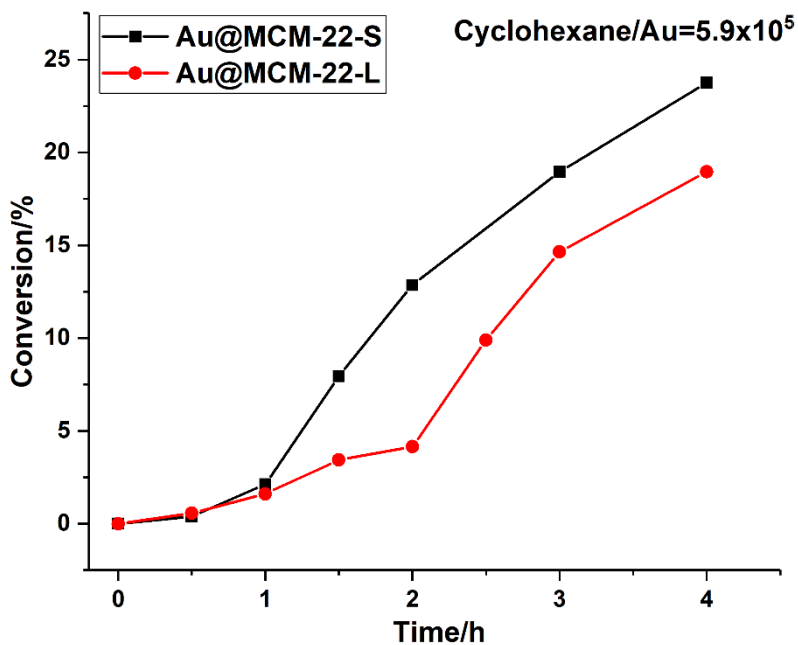
Figure 7.11. Catalytic test of Au@MCM-22-S and Au@MCM-22-L using the same amount of Au. The molar ratio of cyclohexane/Au was kept the same for both tests. Reaction conditions: 2 mL cyclohexane, 150 ºC, 10 bar of O$_2$. The "Thermal" test was carried out under the same conditions in the absence of catalyst.
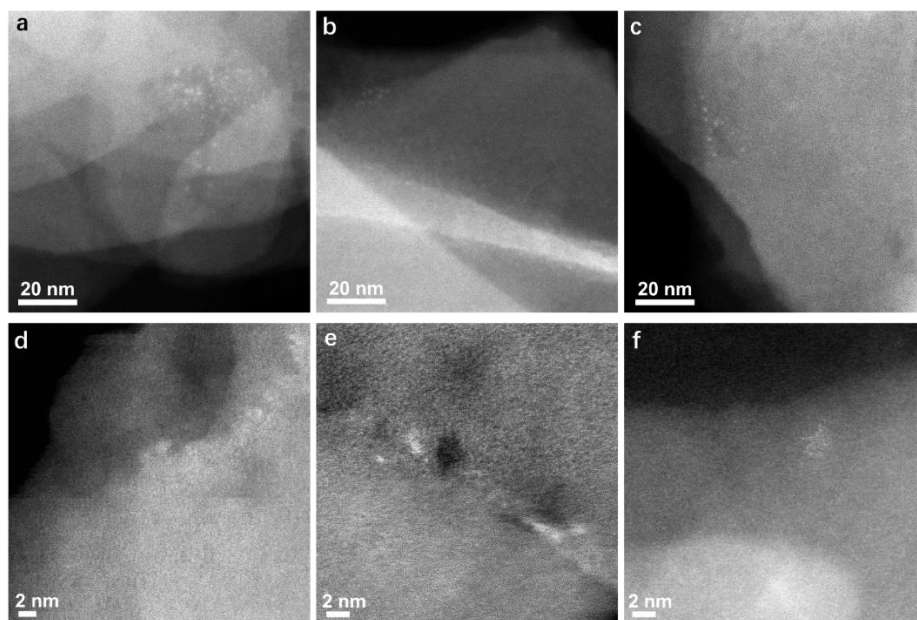
Figure 7.12. STEM images of Au@MCM-22-L sample after three consecutive cycles of oxidation of cyclohexane. Au clusters with size of ~1 nm can be seen in these images.

In this work, the oxidation of cyclohexane was performed in a batch reactor without the addition of radical initiator. As presented in **Figure 7.7a**, all the samples show an induction period in the oxidation of cyclohexane, corresponding to the *in situ* generation of radicals under reaction condition since no external initiator is added. The control experiments without solid catalyst (Thermal) and the MCM-22 support show low conversion of cyclohexane after 2 h, and the major product is cyclohexyl hydroperoxide (see **Figure 7.7b**). Furthermore, the conversion of cyclohexane with AuNP/MCM-22 catalyst is even lower than MCM-22 at the starting stage, indicating the inert role of Au nanoparticles for this process, which is consistent with the previous works.[18]

Remarkably, both Au@MCM-22-S and Au@MCM-22-L show short induction period (~0.5 h) in the oxidation of cyclohexane, indicating the higher activity for generation of radicals. As we can see in **Figure 7.7a**, high

conversion of cyclohexane (>12%) can be achieved with Au@MCM-22-S and Au@MCM-22-L after 2 hours and the selectivity to KA-oil and cyclohexyl hydroperoxide on both Au@MCM-22 samples are similar (see **Figure 7.7b**). The evolution of the product distribution with the reaction time is similar on both Au@MCM-22 catalysts (see **Figure 7.8** to **Figure 7.10**). It should be noted that, when using the same amount of solid catalyst (25 mg), Au@MCM-22-L shows higher yields of products at the same reaction time. However, if the amount of Au species is kept the same for the two catalysts, then Au@MCM-22-S shows better performance for oxidation of cyclohexane to KA-oil (see **Figure 7.11**). Considering the higher percentage of subnanometric Au clusters in the Au@MCM-22-S sample, these results imply that the Au clusters with low atomicity may be the active species instead of the ones larger than 1 nm.

The oxidation of cyclohexane has been proved to be initiated by the formation of cyclohexyl hydroperoxide radicals and subsequently cleavage homolytic cleavage of cyclohexyl hydroperoxide to form free radicals. Therefore, the role of catalyst for this reaction can be related to accelerating the generation of hydroperoxide radicals.[19] And it has been observed in different systems that, the activation mechanism of O_2 on metal particles is related with the particle size. In the case of Au nanoparticles, O_2 is activated into atomic oxygen species at >80 °C. While in the case of Au clusters, O_2 can be activated and transformed into radical-type species on Au clusters.[8,20] The different catalytic behavior of Au nanoclusters and nanoparticles for aerobic oxidation of cyclohexane may be related with the size-dependent O_2 activation mechanism on Au species.

We have also study the stability of Au clusters for the oxidation of KA-oil. As shown in **Figure 7.9**, the catalyst show good recyclability during three consecutive tests. The conversion and yields of different products are similar among the three tests. As presented in **Figure 7.12**, the presence of Au nanoclusters in the used catalyst is confirmed by electron microscopy images and the agglomeration of Au species into Au nanoparticles are not observed, suggesting the good stability of Au nanoclusters encapsulated in MCM-22.

4. Conclusions

In summary, we have reported the synthesis of Au@MCM-22 materials containing subnanometric Au clusters in MCM-22 zeolite by incorporating Au species during the transformation of a 2D zeolite into 3D structure. Those highly stable Au clusters can serve as active species for the aerobic oxidation of cyclohexane into cyclohexanol and cyclohexanone without the presence of radical initiator.

References

(1) P. Claus, *Appl. Catal. A: Gen.* **2005**, *291*, 222-229.

(2) T. Takei, T. Akita, I. Nakamura, T. Fujitani, M. Okumura, K. Okazaki, J. Huang, T. Ishida, M. Haruta, *Adv. Catal.* **2012**, *55*, 1-126.

(3) A. S. Hashmi, G. J. Hutchings, *Angew. Chem. Int. Ed.* **2006**, *45*, 7896-7936.

(4) A. Corma, H. Garcia, *Chem. Soc. Rev.* **2008**, *37*, 2096-2126.

(5) M. Valden, X. Lai, D. W. Goodman, *Science* **1998**, *281*, 1647-1650.

(6) J. Oliver-Meseguer, J. R. Cabrero-Antonino, I. Dominguez, A. Leyva-Perez, A. Corma, *Science* **2012**, *338*, 1452-1455.

(7) A. Corma, P. Concepcion, M. Boronat, M. J. Sabater, J. Navas, M. J. Yacaman, E. Larios, A. Posadas, M. A. Lopez-Quintela, D. Buceta, E. Mendoza, G. Guilera, A. Mayoral, *Nat. Chem.* **2013**, *5*, 775-781.

(8) M. Boronat, A. Leyva-Perez, A. Corma, *Acc. Chem. Res.* **2014**, *47*, 834-844.

(9) S. Yamazoe, K. Koyasu, T. Tsukuda, *Acc. Chem. Res.* **2014**, *47*, 816-824.

(10) R. Jin, C. Zeng, M. Zhou, Y. Chen, *Chem. Rev.* **2016**, *116*, 10346-10413.

(11) J. C. Fierro-Gonzalez, Y. Hao, B. C. Gates, *J. Phys. Chem. C* **2007**, *111*, 6645-6651.

(12) M. T. Bore, H. N. Pham, E. E. Switzer, T. L. Ward, A. Fukuoka, A. K. Datye, *J. Phys. Chem. B* **2005**, *109*, 2873-2880.

(13) J. Mielby, J. O. Abildstrom, F. Wang, T. Kasama, C. Weidenthaler, S. Kegnaes, *Angew. Chem. Int. Ed.* **2014**, *53*, 12513-12516.

(14) T. Otto, S. I. Zones, E. Iglesia, *J. Catal.* **2016**, *339*, 195-208.

(15) L. Liu, U. Diaz, R. Arenal, G. Agostini, P. Concepcion, A. Corma, *Nat. Mater.* **2017**, *16*, 132-138.

(16) M. Zhu, C. M. Aikens, F. J. Hollander, G. C. Schatz and R. Jin, *J. Am.*

Chem. Soc., 2008, 130, 5883-5885.

(17) I. Hermans, 2015. Liquid Phase Aerobic Oxidation Catalysis-Industrial Applications and Academic Perspectives (Ed. S Stahl, P Alsters).

(18) B. P. C. Hereijgers, B. M. Weckhuysen, *J. Catal.* **2010**, *270*, 16-25.

(19) I. Hermans, P. A. Jacobs and J. Peeters, *Chem. Eur. J.*, 2006, 12, 4229-4240.

(20) L. Qian, Z. Wang, E. V. Beletskiy, J. Liu, H. J. Dos Santos, T. Li, M. D. Rangel, M. C. Kung and H. H. Kung, *Nat. Commun.*, 2017, 8, 14881.

This chapter is reused from the following publication:

Non-noble metal catalysts for hydrogenation: A facile method for preparing Co nanoparticles covered with thin layered carbon, **L. Liu**, F. Gao, P. Conception and A. Corma, *Journal of Catalysis*, 2016, 340, 1-9.

Chapter 8

Non-noble metal catalysts for hydrogenation: a facile method for preparing Co nanoparticles covered by thin layered carbon

Selective and less active

Non-selective

Active and Selective

Chapter 8
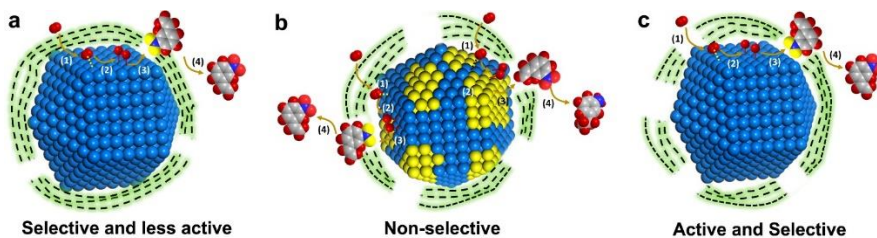
Abstract

Metallic cobalt nanoparticles with surface CoOx patches covered by thin layered carbon (named as Co@C), have been directly synthesized by thermal decomposition of Co-EDTA complex. Raman spectra and HRTEM images suggest that discontinuities can be found in the disordered layered carbon. XPS shows that the CoOx patches in the Co@C nanoparticles can reduced to metallic Co by H_2 under reaction conditions (7 bar at 120 ºC), and H_2-D_2 exchange experiments show that the reduced metallic Co nanoparticles covered by carbon layers can dissociate H_2. The Co@C nanoparticles show excellent activity and selectivity during chemoselective hydrogenation of nitroarenes for a wide scope of substrates under mild reaction conditions. Based on the results from DRIFTS adsorption experiments, we propose that metallic Co in the Co@C nanoparticles is the active phase. The role of the carbon layers is to protect the Co from over-oxidation by air, leading to the chemoselective hydrogenation of nitroarenes.

1. Introduction

The chemoselective hydrogenation of nitroarenes is an important hydrogenation reaction for production of fine and bulk chemicals with wide industrial and pharmaceutical applications.[1] Noble metals such as Au, Pt, Ru, Pd, Ir have been proved to be active components for hydrogenation of nitroarenes.[2,3] By controlling the metal-support interaction and particle size, the chemoselective hydrogenation of nitroarenes can be carried out with high chemoselectivity.[4,5] However, considering the high price and limited availability of noble metals, it is of interests to develop non-noble metal catalysts for chemoselective hydrogenation reactions.

In the last years, non-noble metal catalysts have attracted much attention due to their comparable properties with noble metal catalysts in photocatalysis, electrocatalysis, and in homogeneous and heterogeneous catalysis.[6-9] Recently, the applications of CoO_x@N-doped carbon and Fe_2O_3@N-doped carbon materials for chemoselective hydrogenation of nitroarenes has been reported.[10,11] In their works, the catalysts work under high-pressure conditions (50 bar of H_2), and the authors claimed that metal oxide nanoparticles covered by carbon layers were thought to be the active species for the chemoselective

hydrogenation and hydrogenation-transfer reaction. In a recent paper, Wang et al. observed the *in situ* transformation of CoOx to metallic Co during the selective hydrogenation of nitroarenes under 30 bar of H_2, although the catalyst was a mixture of CoOx and metallic Co.[12] As substitutes for noble metal catalysts, the non-noble metal catalysts should work under similar conditions like Pt (3-6 bar of H_2) and Au (9-15 bar of H_2) catalysts. However, the reported catalysts are working under much higher H_2 pressure than noble metal catalysts.

And from the above reports, it's still not clear whether metallic Co or CoOx is the active phase for the selective hydrogenation reaction. Moreover, if one considers that *in situ* dynamic transformation of metal species can occur under reaction conditions, the real active species in the hydrogenation reaction may not be the starting materials. Furthermore, the role of the layered carbon materials in the catalytic mechanism during the catalytic hydrogenation reaction has not been clarified. In some works, the carbon layers can protect metal NPs. For example, Ding et al. prepared supported Ni NPs embedded in carbon nitride layers for hydrogenation of nitrobenzene under strong acid condition.[13] The carbon layers may also block the accessibility of substrates to the metal NPs. In some previous works,[10-12] it was proposed that the hydrogenation reactions occur on the surface of carbon layers. However, considering the impermeability of graphene, H_2 cannot diffuse directly through perfect graphene layers making even more difficult to unravel the role of carbon layers in hydrogenation reactions.[14,15]

In the first part of this work, by following the thermal decomposition of a Co-EDTA complex, we prepare monodispersed Co nanoparticles with a thin carbon shell (Co@C). Compared with conventional method for monodispersed Co nanoparticles, organic ligands are not required here to stabilize the Co nanoparticles. The resultant material can catalyze the chemoselective hydrogenation of nitroarenes under mild reaction conditions similar to Au catalysts (7-10 bars of H_2) with high activity and selectivity (> 93%). In the second part of this work, with the help of *in situ* spectroscopic characterizations, we will show that the selective adsorption of reactants occurs on the surface of cobalt nanoparticles. Metallic Co, instead of CoOx, is the active phase for hydrogenation reaction and the role of the carbon layers is to protect the metallic Co NPs from over-oxidation.

2. Experiments

Preparation of Co@C NPs. The Co@C NPs were prepared through the reduction of Co-EDTA complex by H_2. The Co-EDTA complex were prepared through a hydrothermal process. First, 6.98 g $Co(NO_3)_2$, 4.47 g Na_2EDTA and 0.96 g NaOH are dissolved in 20 mL H_2O. Then, 10 mL methanol was added to the mixed aqueous solution temperature under stirring at room temperature. After the formation of a homogeneous solution, 23 mL of the purple solution was transferred into a 35 mL stainless steel autoclave followed by static hydrothermal processing at 200 °C for 24 h. After cooling to room temperature, the generated precipitates were filtered and washed with deionized water and acetone several times followed by drying at 100 °C in air for 16 h. The obtained complex was denoted as Co-EDTA. Then, Co@C NPs were prepared by reduction of Co-EDTA in H_2 (50 mL/min) at 450 °C for 2 h with a ramp rate of 10 °C/min from room temperature to 450 °C. After the H_2 reduction process at 450 °C, the sample was cooled down to room temperature in H_2 atmosphere. Then the black solid product was stored in a glass vail in ambient environment. The ICP analysis shows that the amount of cobalt in the Co@C NPs is ≥ 95 wt%. The Co@C-250Air and Co@C-450Air were prepared through the calcination of Co@C sample in air (50 mL/min) at 250 and 450 °C for 2 h with a ramp rate of 5 °C/min, respectively.

Catalytic studies. The chemoselective hydrogenation of nitroarenes was performed in batch reactors. The reactant, internal standard (dodecane), solvent (toluene or THF), powder catalyst as well as a magnetic bar were added into the batch reactor. After the reactor was sealed, air was purged by flushing two times with 10 bar of hydrogen. Then the autoclave was pressurized with H_2 to the corresponding pressure. The stirring speed is kept at 800 rpm and the size of the catalyst powder is below 0.02 mm to avoid either external or internal diffusion limitation. Finally, the batch reactor was heated to the target temperature. For the kinetic studies, 50 μL of the mixture was taken out for GC analysis at different reaction time. For the scope studies, 100 μL of the mixture was taken out for GC analysis. The products were also analyzed by GC-MS.

Characterization techniques. Samples for electron microscopy studies were prepared by dropping the suspension of Co@C NPs using CH_2Cl_2 as the solvent directly onto holey-carbon coated Nickel grids. All the measurements were performed in a JEOL 2100F microscope operating at 200 kV both in transmission (TEM) and scanning-transmission modes (STEM). STEM images were obtained using a High Angle Annular Dark Field detector (HAADF), which allows Z-contrast imaging.

Field-emission scanning electron microscopy (FESEM) measurement is performed with a ZEISS Ultra 55 FESEM. The solid powder sample was adsorbed on conductive carbon tape.

X-ray photoelectron spectra of the catalysts were recorded with a SPECS spectrometer equipped with a Phoibos 150MCD-9 multichannel analyzer using non-monochromatic MgKα (1253.6 eV) irradiation. Spectra were recorded using analyser pass energy of 30 eV, an X-ray power of 100W and under an operating pressure of 10^{-9} mbar. The fresh Co@C NPs sample was reduced by H_2 (7 bar) at 120 ºC for 60min in a high pressure catalytic cell connected, under ultra-high vacuum, to the XPS analyze chamber. Peak intensities have been calculated after nonlinear Shirley-type background subtraction and corrected by the transmission function of the spectrometer. During data processing of the XPS spectra, binding energy (BE) values were referenced to C1s peak (284.5 eV). CasaXPS software has been used for spectra treatment.[16]

Raman spectra were recorded at ambient temperature with a 785 nm HPNIR excitation laser on a Renishaw Raman Spectrometer ("Reflex") equipped with an Olympus microscope and a CCD detector. The laser power on the sample was 15mW and a total of 20 acquisitions were taken for each spectra.

Hydrogen /deuterium (H/D) exchange experiments were carried out in a flow reactor at 25 and 80 ºC. The feed gas consisted of 4 mL/min H_2, 4 mL/min D_2 and 18 mL/min argon, and the total weight of catalyst was 180 mg. Reaction products (H_2, HD and D_2) were analysed with a mass spectrometer (Omnistar, Balzers). The Co@C sample has been *in situ* reduced at 450 ºC for 2 h with a ramp rate of 10 ºC/min from room temperature to 450 ºC. Then the temperature was decreased to 25 ºC and, once stabilized, the H_2 feed was change to the reactant gas composition. The temperature was increased to 80 ºC and maintained at 80 ºC for 1 h.

DRIFT spectra were recorded at room temperature with a Nexus 8700 FTIR spectrometer using a DTGS detector and acquiring at 4 cm^{-1} resolution. Prior to the adsorption experiments, the ex situ reduced samples was *in situ* reduced at 120 ºC in H$_2$ atmosphere for 2 h. After activation the sample was evacuated at 10^{-2} mbar and nitrobenzene and/or styrene adsorbed until sample saturation followed by evacuation (10^{-2} mbar) in order to remove physisorbed species. A commercial DRIFT cell (SPECAC) has been used. Spectra were acquired in Kubelka-Munk units.

Powder X-ray diffraction (XRD) was performed in a HTPhilips X'Pert MPD diffractometer equipped with a PW3050 goniometer using Cu Kα radiation and a multisampling handler.

3. Results and discussions

3.1 Catalyst preparation and characterization

The Co@C NPs were prepared by thermal decomposition of Co-EDTA complex in H$_2$ atmosphere at 450 ºC. The morphological characterization of Co-EDTA complex can be found in supporting information (see **Figure 8.1**). The morphology of Co@C NPs was characterized by FESEM and TEM. As it is shown in **Figure 8.2** and **Figure 8.3a**, the Co@C material is formed by monodispersed metal NPs ranging from ca. 20 nm to ca. 150 nm. Those Co NPs are covered by carbon layers with thickness ranging from ca. 1 nm to ca. 10 nm (**Figure 8.3b**). From the HRTEM images (**Figure 8.3c** and **Figure 8.3d**), the lattice fringe of metallic Co can be seen.[17] A further look to the surface structures of the Co NPs allows to observe the crystal lattice fringes of Co$_3$O$_4$, as shown in **Figure 8.S3**.[18] Therefore, one can assume, in a first approximation, that the Co NP can be formed by a core-shell structure with metal Co at the core and CoOx as the shell. In order to know the chemical composition of the Co@C sample, STEM-HADDF elemental mapping was performed and the results are displayed in **Figure 8.3g** to **3j**. They confirm that Co NPs are covered by carbon layers. Meanwhile, oxygen can also be found in the sample, that may come from surface CoOx and/or from the oxygenated groups in carbon layers. Contrast profiles of the carbon layers over Co NPs were also obtained, as presented in **Figure 8.3e** and **Figure 8.3f**. It can be seen there that the distance between the carbon layers is 0.34-0.37 nm, which corresponds to the distance

between graphene layers. The thickness of most carbon layers are between 1 nm and 5 nm, with several layers of graphene.[19] A schematic illustration about the structure of Co@C NP is shown in **Figure 8.3k**, indicating that the particle contains metallic Co as the core as well as some CoOx patches on the surface and carbon layers surrounding.
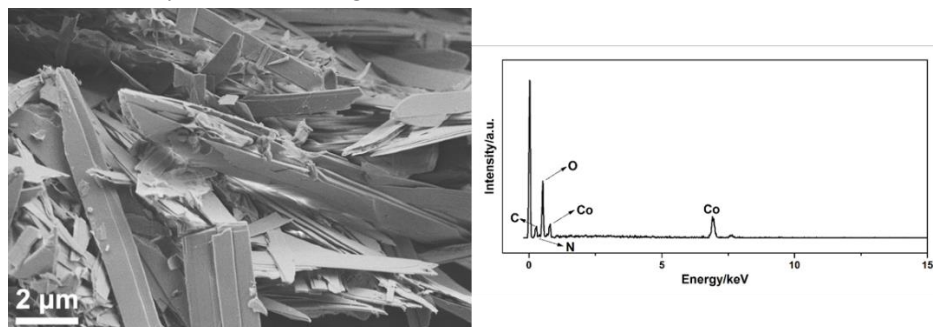
Figure 8.1. Field-emission scanning electron microscopy (FESEM) image of Co-EDTA complex and the corresponding EDS spectrum. C, N, O and Co can be found in the Co-EDTA complex.
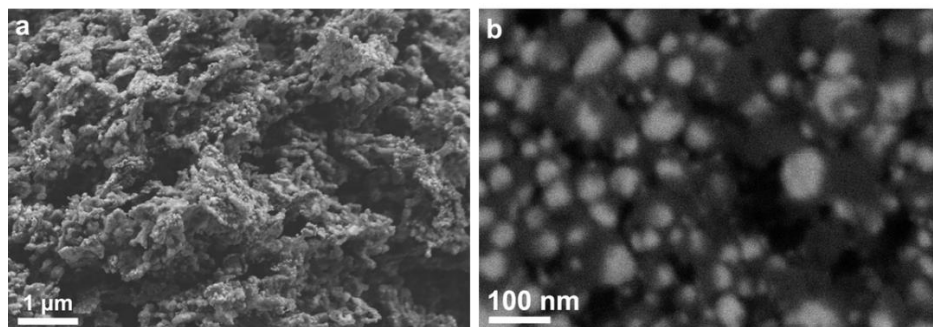
Figure 8.2. Field-emission scanning electron microscopy (FESEM) images of Co@C NPs obtained by SE2 detector (a) and ESB detector (b). In **Figure 8.S2a**, Co NPs are surrounded by foam-like carbon and those Co NPs with particle size ranging from 20 to 100 nm can be seen in **Figure 8.S2b**.
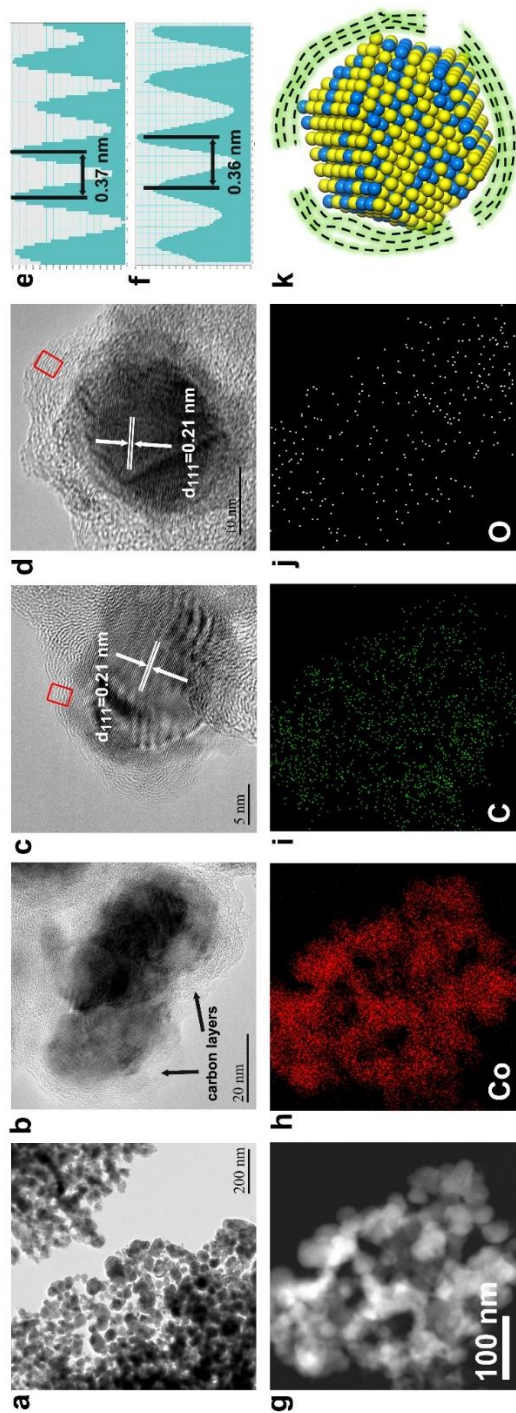
Figure 8.3. Morphological characterizations of Co@C NPs. (a, b) Low-magnification TEM image of Co@C. The size of Co NPs ranges from ca. 20 to ca. 150 nm. Monodispersed Co NPs are separated by carbon layers, as show in (b). (c, d) HRTEM images of Co NPs covered by carbon layers. (e, f) Profile of the carbon layers in selected areas in c and d, respectively. The distance between two carbon layers is about 0.36-0.37 nm. (g) STEM-HADDF image of Co@C NPs. (h-j) Elemental mapping of Co, C and O. (k) Schematic illustration of the structure of Co@C NPs. Blue balls stand for metallic Co and yellow balls stands for CoOx. The surface of Co NP is mainly made of CoOx while the core is metallic Co. The green circle surrounding the particle is the carbon layers with cracks.
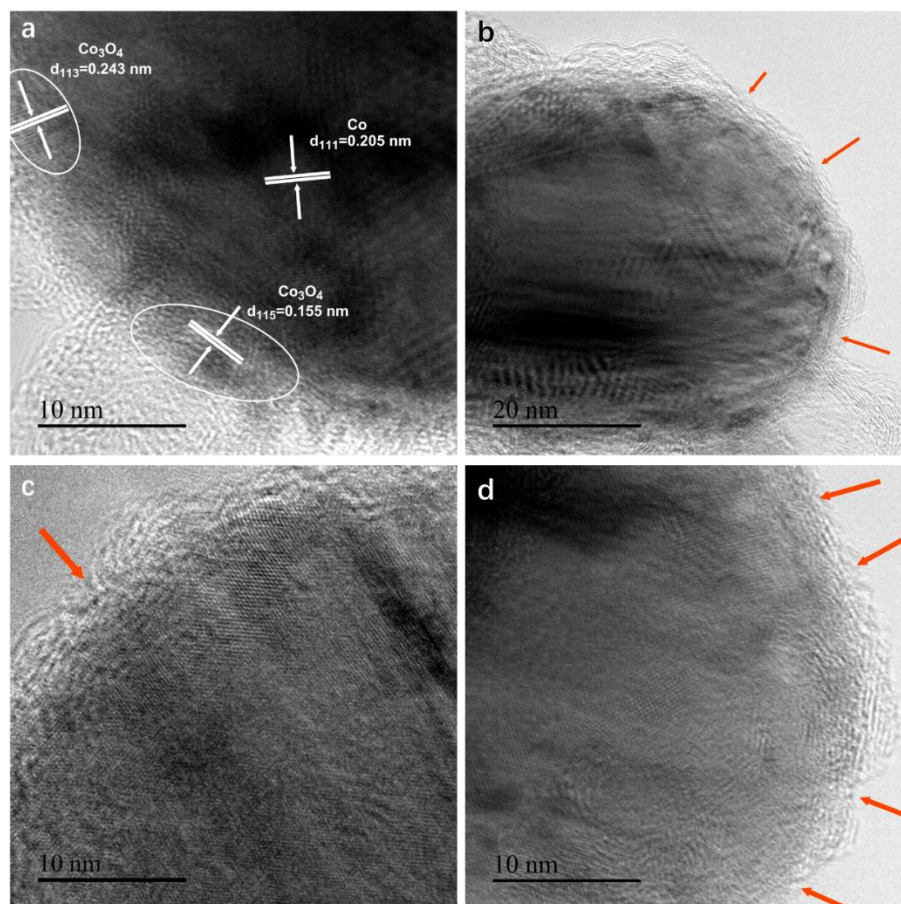
Figure 8.4. (a) HRTEM image of surface structures of Co NP covered by thin carbon layers. The lattice of Co_3O_4 can be observed on the outer surface layer of Co@C NP. (b-d) HRTEM image of a single Co NP covered by thin carbon layers with cracks indicated by red arrows.

From the HRTEM images (**Figure 8.4**), it can also be seen that the thin carbon layers over Co NPs are not closed and some cracks can be found, implying that reactant molecules can have access to the Co NPs through the carbon layers. This can explain why the Co@C NPs could be partially oxidized by air in ambient condition after the preparation procedure. In a recent work of Bao and his co-workers, they have prepared a sample with CoNi alloy NPs totally encapsulated by several layers of graphene.[20] Those CoNi NPs are not

soluble in a strong acid environment due to the protection effect of the carbon layers. However, in our case, Co NPs covered by cracked carbon layers can be almost totally dissolved in aqueous H_2SO_4 (photographs of the dissolving process can be seen in **Figure 8.5**), suggesting that Co@C NPs are not totally covered by carbon layers.
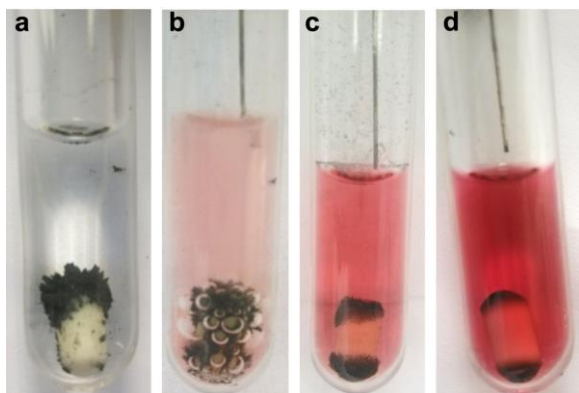
Figure 8.5. Photographs of the dissolution process of Co@C NPs in aqueous H_2SO_4 (2 mol/L) at 80 ^{o}C for 2 h.

In general, due to the instability of metallic Co NPs, their preparation for heterogeneous catalytic application still remains a challenge. So far, metallic Co NPs are usually prepared through wet-chemistry method.[21-23] In those methods, Co NPs are capped by organic ligands to protect them from agglomeration and oxidation by air, but, at the same time, these long-chain organic ligands decrease the activity of Co NPs. Furthermore, Co NPs prepared from wet-chemistry methods are usually not stable in ambient conditions due to the oxidation of Co by air. In contrast, with the protection effect of carbon layers, the Co NPs prepared by our method can be stored under ambient conditions for over one month without obvious morphological changes. Only the oxidation of Co NPs at the surface occurs and CoOx patches are formed that can be easily reduced by H_2 to metallic Co. Compared with previous reported pyrolysis methods (calcination at 800 ^{o}C), well-defined Co@C NPs with carbon layers can be directly synthesized at relatively lower temperature. These air-stable Co@C NPs with CoOx patches can be prepared in large scale (several grams) in a facile way.
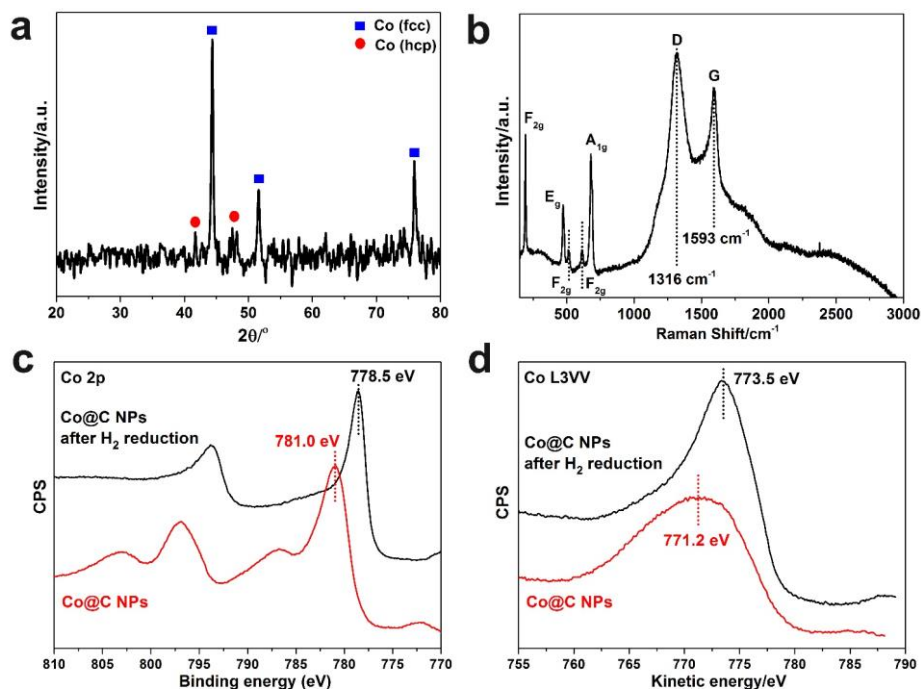
Figure 8.6. Structure characterizations of Co@C NPs. (a) XRD pattern of fresh Co@C NPs, (b) Raman spectrum of Co@C NPs, XPS spectra of Co 2p region (c) and Co L3VV Auger spectra (d) of the fresh Co@C NPs and the sample after *ex situ* reduction by 7 bar of H$_2$ at 120 °C.

The bulk and surface properties of the Co@C NPs were also investigated. The XRD pattern of Co@C NPs is shown in **Figure 8.6**. Only the X-ray diffraction patterns of metallic Co can be observed with no X-ray diffraction peaks corresponding to other species, although the formation of CoOx patches could be observed by HRTEM. The fact that CoOx is not detected by XRD should be due to the low amount of CoOx patches in the Co@C sample. In the case of metallic Co, besides the cubic Co phase (PDF code: 96-900-8467), a small amount of hexagonal Co phase (PDF code: 96-900-8493) can also be observed in the XRD pattern. For metallic Co, the hexagonal-closed packed (*hcp*) phase is more stable at lower temperature than the face-centered cubic (*fcc*) phase.[24] Since the Co-EDTA complex was decomposed and reduced at 450

^{o}C, it is not surprising to see that both phases can exist.[25]

The surface structures of Co@C NPs as well as the carbon layers were also studied by Raman spectroscopy. As it is indicated in **Figure 8.6b**, vibration modes of Co_3O_4 (F_{2g}, E_g and A_{1g}) can be observed.[26] Besides, the typical Raman signals of layered carbon, bands at 1318 cm^{-1} and 1595 cm^{-1}, can be observed, which are corresponding to **D** and **G** band, respectively.[27] No peak related to **2D** band is detected between 2500 and 2800 cm^{-1}. The intensity ratio of G band (I_G) to D band (I_D) is ca. 0.8, suggesting that there is a large percentage of disorder in the structured carbon in Co@C NPs.[28] Combing these results and those from HRTEM images, it can be speculated that the degree of graphitization is relatively low in the carbon layers around Co NPs. Therefore, based on the structural characterizations, we can propose that Co@C NPs have core-shell structures with metallic Co as the core, CoOx on the surface of Co crystallites and thin layered carbon as the shell.
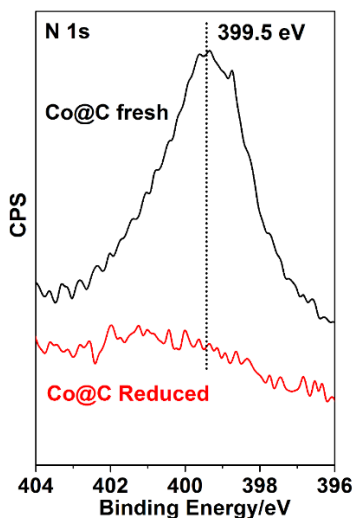
Figure 8.7. XPS of N 1s region in the fresh Co@C sample and the sample after ex-situ reduction in H_2 (7 bar) at 120 ^{o}C.

X-Ray photoelectron spectroscopy (XPS) was employed to study the chemical state of Co in the as-prepared Co@C NPs. The Co@C NPs were reduced by H_2 at 7 bar and 120 ^{o}C (That condition will also be used in the hydrogenation reaction.) within a pre-reactor integrated to the apparatus and the

sample is maintained isolated from any external contact during all the process. The XPS spectra of Co 2p region and Auger spectra of Co L3VV are shown in **Figure 8.6c** and **Figure 8.6d**, respectively. In the as-prepared Co@C sample, only CoO_x can be observed, which can be ascribed to the CoOx patches on the surface of Co NPs.[29] After H_2 reduction treatment (7 bar of H_2 at 120 °C), the CoOx is totally transformed into metallic Co, as confirmed by both Co 2p XPS and Co L3VV Auger spectra. In the fresh as-prepared catalyst, N is presented in the sample, as shown by elemental mapping (see **Figure 8.7**). However, after the *ex situ* reduction treatment, no N can be found in the sample by XPS, indicating that there is practically no N species in the working catalyst.

With the characterization results presented up to now, we can say that during preparation of Co@C NPs, Co NPs of 20-150 nm were generated which are formed by a metallic Co core with CoOx on the surface that are surrounded by disordered carbon layers. Moreover, under reduction conditions, that are the same used for performing the catalytic test, the CoOx patches can be totally reduced to metallic Co.
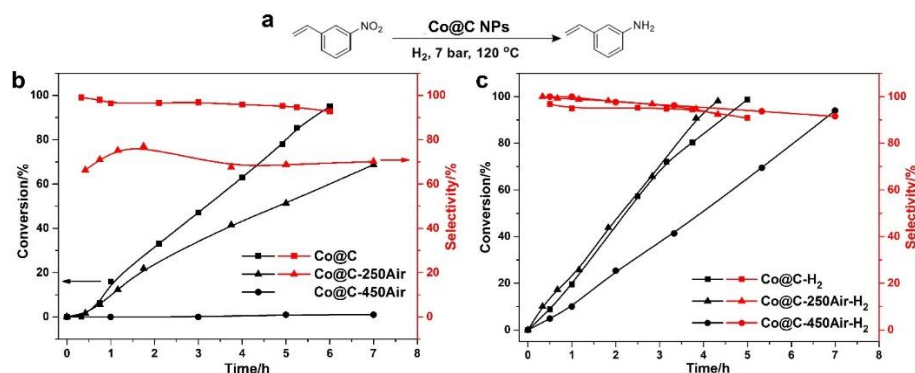
Figure 8.8. (a) Reaction scheme of the chemoselective hydrogenation of 3-nitrostyrene. Reaction conditions: 0.5 mmol 3-nitrostyrene, 30 mg Co@C NPs as the catalyst, 2 mL toluene as solvent, 30 μL dodecane as the internal standard. (b) Catalytic performances of Co@C, Co@C-250Air and Co@C-450Air in chemoselective hydrogenation of 3-nitrostyrene to 3-aminostyrene. The black legends and red legends correspond to conversion and selectivity, respectively. (c) Catalytic performances of Co@C-H_2, Co@C-250Air-H_2 and Co@C-450Air-H_2 in chemoselective hydrogenation of 3-nitrostyrene to 3-

aminostyrene. The black legends and red legends correspond to conversion and selectivity, respectively.
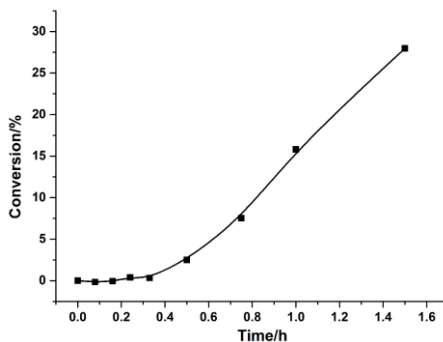
Figure 8.9. The kinetic curve of chemoselective hydrogenation of 3-Nitrostyrene catalyzed by Co@C NPs. The reaction conditions is the same as we described in the experimental section. As it can be seen, an induction period about 0.4 h can be observed as a result of the in-situ activation of Co@C NPs under reaction conditions.

3.2 Catalytic results

At this point, the chemoselective hydrogenation of 3-nitrostyrene was chosen as the model reaction to study the catalytic properties of Co@C NPs and to see if the non-noble metal cobalt nanoparticles can behave as a chemoselective catalyst. For testing this, the same reaction conditions that showed chemoselective hydrogenation when using noble metal catalysts, i.e. 120 $^{\circ}$C and 7 bar of H_2 were selected.[4,5] Notice that these are much milder conditions than those reported for the hydrogenation of 3-nitrostyrene with Co- and Fe-based catalysts.[10,11] The reaction conditions and catalytic results are given in **Figure 8.8**. Ii can be seen there that fresh Co@C NPs are active and selective catalyst for the hydrogenation of 3-nitrostyrene. When the conversion of 3-nitrostyrene is 95%, the selectivity to 3-aminostyrene is 93% which is comparable to the values obtained with noble metal catalysts.[4,5] The initial TOF calculated based on surface Co atoms is ca. 8.2 h^{-1} according to the particle size distribution of Co@C NPs. Notably, a reaction induction period of about 20-30 min can be observed in the kinetic curve (**Figure 8.9**) when starting with the fresh catalyst that contains a core of metallic cobalt and a shell of CoOx.

According with XPS results, this induction period could be caused by the time required for the reduction of surface CoOx to metallic Co under the reaction conditions. As presented in **Figure 8.10**, the morphology and particle size distribution after the reduction under reaction conditions is similar to the fresh Co@C sample, suggesting that no structural changes or agglomeration has occurred. HRTEM images of the used sample also confirm that metallic Co NPs are still surrounded by carbon layers. Therefore, the above morphological characterization indicates that the nanoscale structures of the Co@C NPs sample is stable under reaction condition.
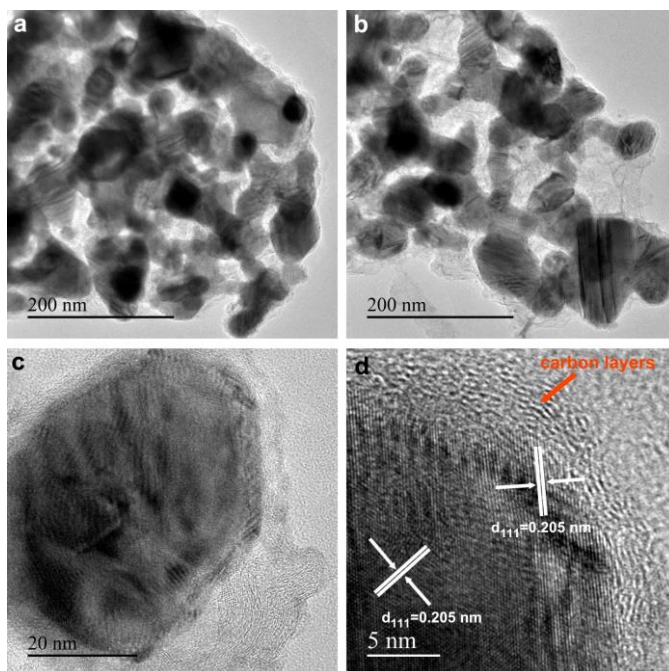
Figure 8.10. TEM and HRTEM images of Co@C NPs after the hydrogenation of 3-nitrostyrene.

In a recent work, Zhang et al. have demonstrated that atomically dispersed Co species in the carbon matrix can serve as the active sites for oxidation reactions.[30] Herein, in order to exclude the role of atomically dispersed Co species in the hydrogenation reaction, we have also measured the residual solid after the acid leaching treatment (as shown in **Figure 8.5**). No activity can be observed in the hydrogenation of 3-nitrostyrene, suggesting that the metallic

Co NPs should be the active sites for hydrogenation reactions.

Figure 8.11. Photograph of the batch reactor after the hydrogenation of 3-Nitrostyrene. The Co@C NPs are absorbed by the magnetic bar, as a result of which, the catalyst separation is very simple.

Table 8.1. The catalytic performances of recycled Co@C NPs in hydrogenation of 3-nitrostyrene. The reaction condition is the same with the description in the main text. 0.5 mmol of 3-nitrostyrene, 2 mL toluene, 30 μL of dodecane as internal standard, 120 $^{\circ}$C and 7 bar of H_2.

Run	Reaction time	Conversion	Selectivity
1	6 h	95%	93%
2	6.5 h	93%	92%
3	7.5 h	95%	94%
4	7.5 h	94%	93%
5	7.5 h	92%	92%

The recyclability of Co@C NPs in hydrogenation of 3-nitrostyrene was also tested. Since metallic Co NPs are paramagnetic, the separation of the solid catalyst from the liquid was very facile with the help of a magnetic bar[31,32] (see **Figure 8.11**). After washing several times with toluene, the catalyst can be reused without further treatments, and the Co@C catalyst shows good activity and selectivity for 5 recycles (see **Table 8.1**).

3.3 Role of the carbon layers in the catalyst

At this point, we know that the reduced Co@C NPs are active and chemoselective for reduction of substituted nitroarenes into corresponding anilines under mild reaction conditions. To investigate if the carbon layers play an intrinsic role for the chemoselective hydrogenation reaction, calcination of the Co NPs at 250 and 450 °C in air was performed to remove the carbon layers on the nanoparticles. The samples after calcination in air are denoted as Co@C-250Air and Co@C-450Air, respectively. From the Raman spectra (**Figure 8.12**), we can find that in Co@C-250Air, bands at 1318 and 1595 cm^{-1} are still visible indicating that part of the carbon layers are still preserved. In Co@C-450Air, the above Raman bands are already very small suggesting that almost all the carbon layers have already been removed. As shown in **Figure 8.8b**, it is possible to see that activity and selectivity drops when Co@C-250Air is used, while Co@C-450Air shows no activity in the hydrogenation reaction. The product distribution in the hydrogenation of 3-nitrostyrene with a Co@C-250Air sample as the catalyst is shown in **Figure 8.13**. To explain these changes, TEM is used to clarify the structural transformation occurring with Co@C NPs after calcination in air. As shown in **Figure 8.14**, metallic Co NPs crack into smaller CoOx NPs after the calcination in air at 250 °C, which has also been observed in other works.[33] The crystal lattice fringes of CoOx NPs can be observed in the HRTEM images, though, there are still some metallic Co NPs in the Co@C-250Air sample. Some carbon layers can still be found on Co-CoOx and CoOx NPs in Co@C-250Air, as was confirmed by Raman spectra. It should be noted that part of the carbon layers were burn during the calcination in air, resulting in the formation of naked Co and CoOx NPs.
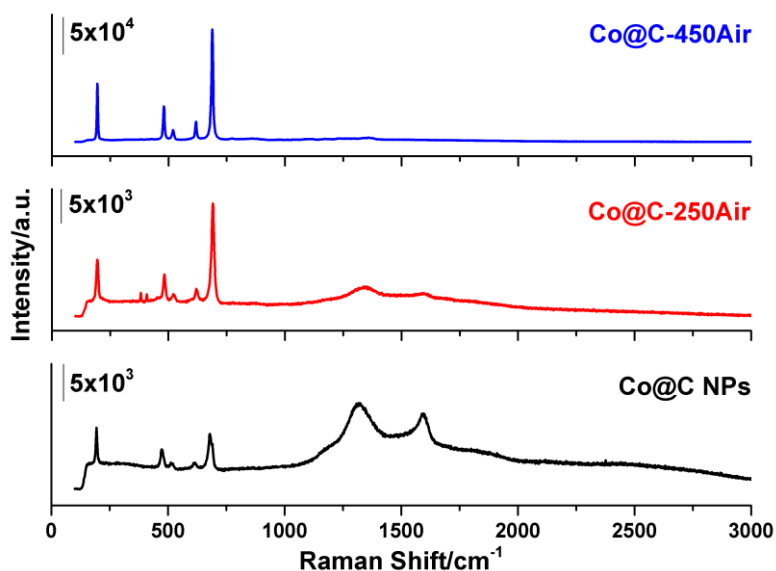
Figure 8.12. Raman sepctra of Co@C NPs, Co@C-250Air and Co@C-450Air. The ratio of the peak intensity between CoOx and carbon are quite different in these samples. After calcination in air at 250 °C, the intensity of D band and G band decrease a lot while the peaks corresponding to CoOx increase. When the calcination temperature increases to 450 °C, only peaks corresponding to CoOx can be observed.
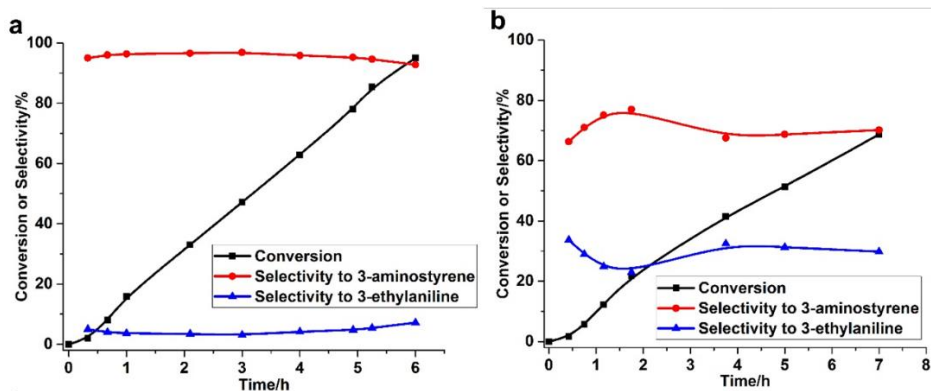
Figure 8.13. Distributions of the products in the hydrogenation of 3-nitrostyrene catalyzed by Co@C (a) and Co@C-250Air (b).
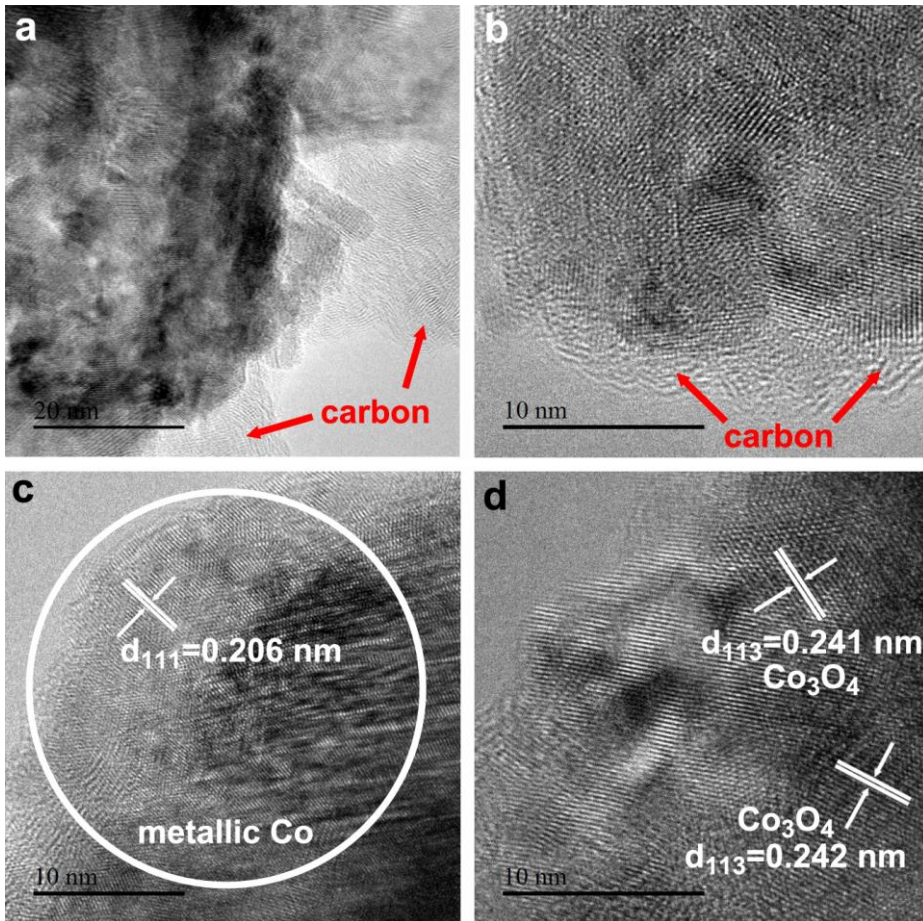
Figure 8.14. TEM and HRTEM images of Co@C-250Air. Both metallic Co and Co_3O_4 can be found in this sample.
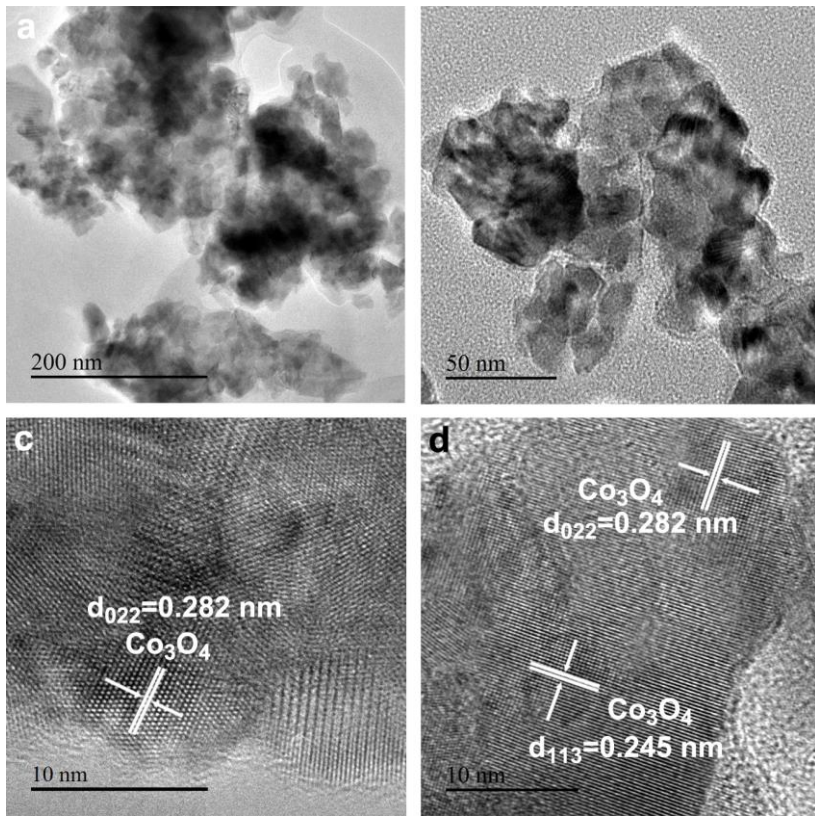
Figure 8.15. TEM and HRTEM images of Co@C-450Air. Only Co_3O_4 can be found in this sample.
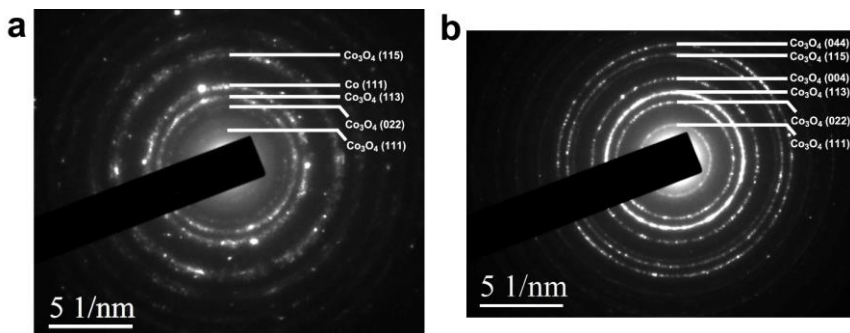
Figure 8.16. Selected-area electron diffraction (SAED) patterns of Co@C-250Air and Co@C-450Air.

In the Co@C-450Air sample (shown in **Figure 8.15**), Co NPs are totally converted into Co_3O_4 NPs. The phase composition of the samples after calcination in air can also be measured by selective area electron diffraction (SAED). As can be seen in **Figure 8.16**, metallic Co NPs transform into a mixture of Co and Co_3O_4 when calcined at 250 ℃, and to pure Co_3O_4 when calcination was performed at 450 ℃. Considering the significant decrease of activity observed when the Co@C sample was calcined at 250 ℃ and even more when temperature was 450 ℃, it can be deduced that CoOx or Co_3O_4 cannot be the catalytically active phase.

Co@C, Co@C-250Air and Co@C-450Air NPs were reduced in the batch reactor under higher temperature and H_2 pressure (200 ℃, 10 bar of H_2) before the hydrogenation reaction to reduce the CoOx species into metallic Co. After the reduction pre-treatment, 3-nitrostyrene was added and the hydrogenation reaction was performed at 7 bar of H_2 and 120 ℃. As presented in **Figure 8.8c**, the Co@C-H_2 gives a similar kinetic curve as the pristine Co@C except for the disappearance of the induction period due to the reduction pre-treatment. However, the situation changes a lot in the case of Co@C-250Air and Co@C-450Air. The Co@C-250Air-H_2 sample shows higher activity than pristine Co@C NPs and very good selectivity. This would indicate that the metallic Co NPs formed after reduction of Co@C-250Air should be responsible for the high activity and selectivity in hydrogenation reaction observed with Co@C-250Air-H_2. What's more, the reduction pre-treatment also has a significant effect on Co@C-450Air. After H_2 reduction, the Co@C-450Air-H_2 sample shows moderate activity and high selectivity, which further indicates that the chemoselective hydrogenation of 3-nitrostyrene is related with metallic Co and the role of carbon layers in Co@C NPs is mainly to protect Co NPs from over-oxidation by air.
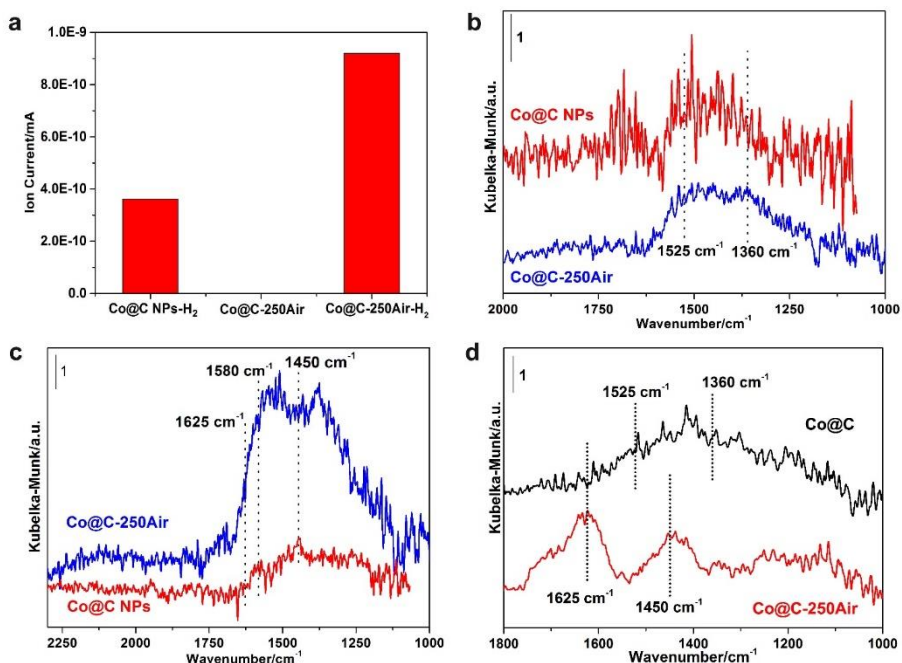
Figure 8.17. H_2-D_2 exchange and DRIFTS adsorption experiments. (a) Enhancement of the ion current in mass signal of HD during the H_2-D_2 exchange experiment over Co@C-H_2, Co@C-250Air and Co@C-250Air-H_2 NPs at 80 °C. (b) DRIFTS of adsorbed nitrobenzene, (c) DRIFTS of adsorbed styrene and (d) DRIFTS of co-adsorbed nitrobenzene and styrene on Co@C NPs and Co@C-250Air sample.

3.4 *In situ* adsorption spectroscopy study.

In order to explain the activity and high selectivity of Co@C NPs, H_2-D_2 exchange and the adsorption of substrates on Co@C NPs followed by diffuse reflectance infrared Fourier transform spectroscopy (DRIFTS) were carried out. The H_2-D_2 exchange rates on Co NPs and Co@C-250Air (with and without H_2 pre-reduction) are shown in **Figure 8.17a**. H_2-D_2 exchange can be observed on Co@C NPs. Interestingly, as displayed in **Figure 8.18**, a large amount of H_2 was released from Co NPs when the atmosphere was changed from H_2 to Ar after the *in situ* reduction process. The H_2 released should come from the H_2 adsorbed by Co NPs.[34,35] It appears then that H_2 diffuses through the potential cracks present in carbon layers and it is activated on the surface of Co NPs. In

the case of Co@C-250Air, no H_2-D_2 exchange can be observed when the sample is not pre-reduced. After H_2 pre-treatment, the H_2-D_2 exchange rate is higher on Co@C-250Air-H_2 than on Co@C suggesting that more Co sites are exposed after the removal of carbon layers and reduction of CoOx. The H_2-D_2 exchange experiments further confirm that metallic Co are the active sites for H_2 activation and carbon layers are not playing a direct role on the catalytic process.

We have found in previous work that the way that the reactant is adsorbed on metal catalysts can determine the chemoselectivity during hydrogenation of substituted nitroaromatics.[36] Then, in order to explain different catalytic behavior of Co@C NPs and Co@C-250Air samples for chemoselective hydrogenation of 3-nitrostyrene, we have performed *in situ* IR adsorption experiments by DRIFTS with nitrobenzene and styrene as probe molecules. For comparison, the IR spectra of nitrobenzene and styrene on KBr substrate have also been measured (see **Figure 8.19**). The adsorption spectra of the probe molecules on Co@C and Co@C-250Air are shown in **Figure 8.20**. The IR adsorption spectra of nitrobenzene on Co@C and Co@C-250Air samples show wide IR bands between 1600 cm^{-1} to 1250 cm^{-1} in both samples (see **Figure 8.17b**). The vibration bands of -NO_2 groups can be observed at ca. 1525 cm^{-1} and 1360 cm^{-1}.[37,38] The intensity of the IR bands is similar on both samples suggesting that the adsorption spectra of Co@C and Co@C-250Air for nitrobenzene are similar. On the other hand, the adsorption spectra of styrene on Co@C and Co@C-250Air (**Figure 8.17c**) are significantly different. Indeed, as can be seen in **Figure 8.17c**, the IR band corresponding to the aromatic ring can be observed between 1580 cm^{-1} and 1450 cm^{-1}, with the vibration mode of C=C bond at ca. 1625 cm^{-1}.[39] Co@C-250Air shows much stronger adsorption of styrene than Co@C sample, indicating that the adsorption of styrene on CoOx NPs will be enhanced when metallic Co NPs are oxidized. We have also studied the co-adsorption of nitrobenzene and styrene on Co@C and Co@C-250Air by DRIFTS. As can be seen in **Figure 8.17d**, only the adsorption of nitrobenzene can be observed on Co@C, while a strong adsorption of styrene on Co@C-250Air occurs. In the case of Co@C-450Air, only the adsorption of styrene can be observed after the evacuation (see **Figure 8.21**). Therefore, based on the IR adsorption results, we can conclude that the chemical states of

Co have significant influences on the adsorption properties of substrate molecules in Co@C NPs. For metallic Co NPs, only $-NO_2$ groups will be preferentially adsorbed. In contrast, when the Co NPs are partially oxidized, the C=C instead of $-NO_2$ groups will be preferentially adsorbed. The selective adsorption observed in above experiments can explain the differences for the chemoselective hydrogenation of 3-nitrostyrene on metallic and partially oxidized cobalt nanoparticles.
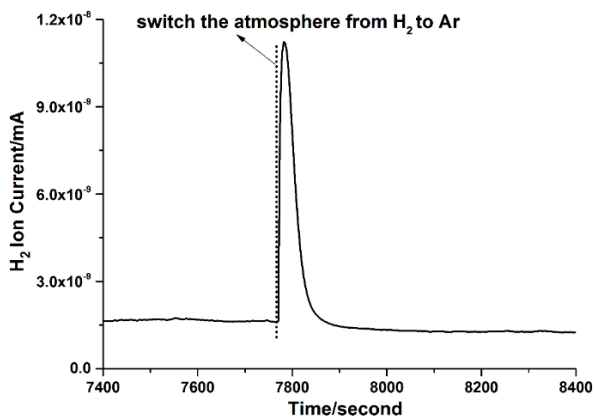
Figure 8.18. Mass signal of H_2 ion current after switching the atmosphere from H_2 to Ar. The sample was firstly treated by H_2 for reduction before the H-D exchange experiment. When the gas was switched from H_2 to Ar, the H_2 adsorbed on Co NPs would be released due to the decrease of H_2 pressure. Therefore, after changing the gas, a sudden release of H_2 from the sample can be observed in the mass spectra.
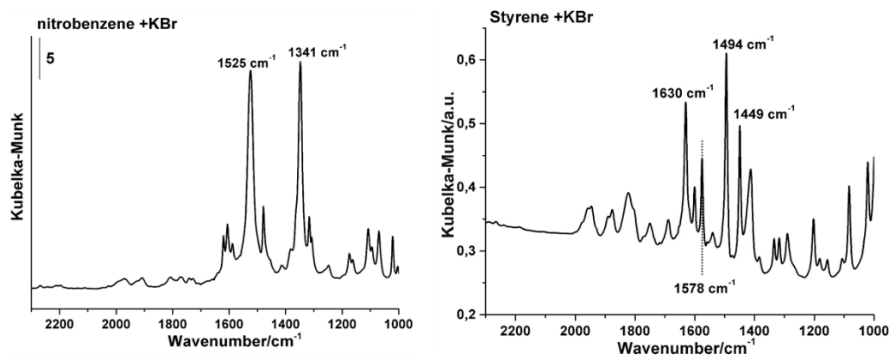
Figure 8.19. IR spectra of nitrobenzene (up) and styrene (down) on KBr.
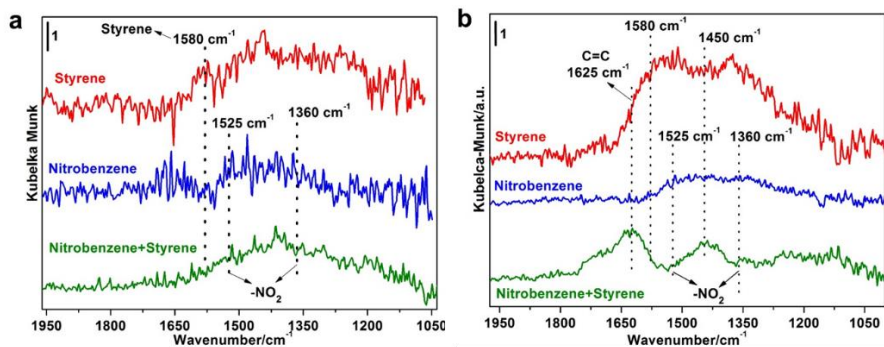
Figure 8.20. DRIFTS adsorption of nitrobenzene, styrene and co-adsorption of nitrobenzene and styrene on Co@C NPs (a) and Co@C-250Air (b).
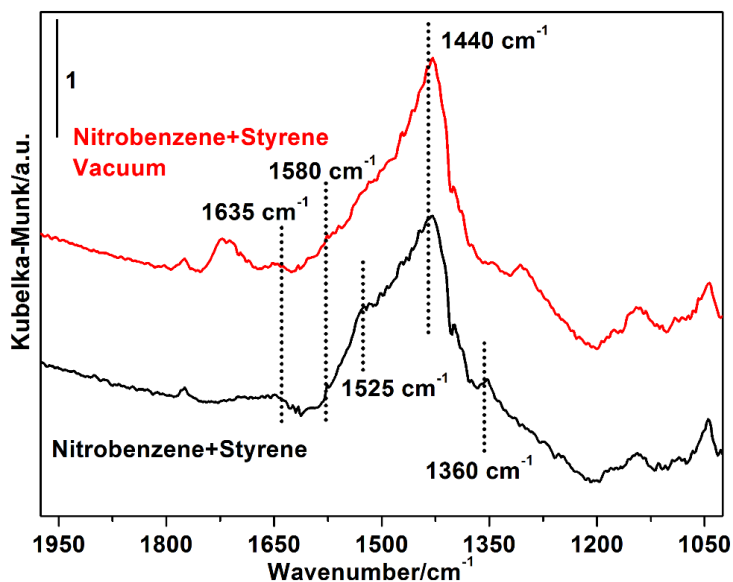
Figure 8.21. DRIFTS co-adsorption of nitrobenzene and styrene on Co@C-450Air. Both spectrum collected after the adsorption (black line) and spectrum collected after evacuation (blue line) are presented.

3.5 Catalytic mechanism
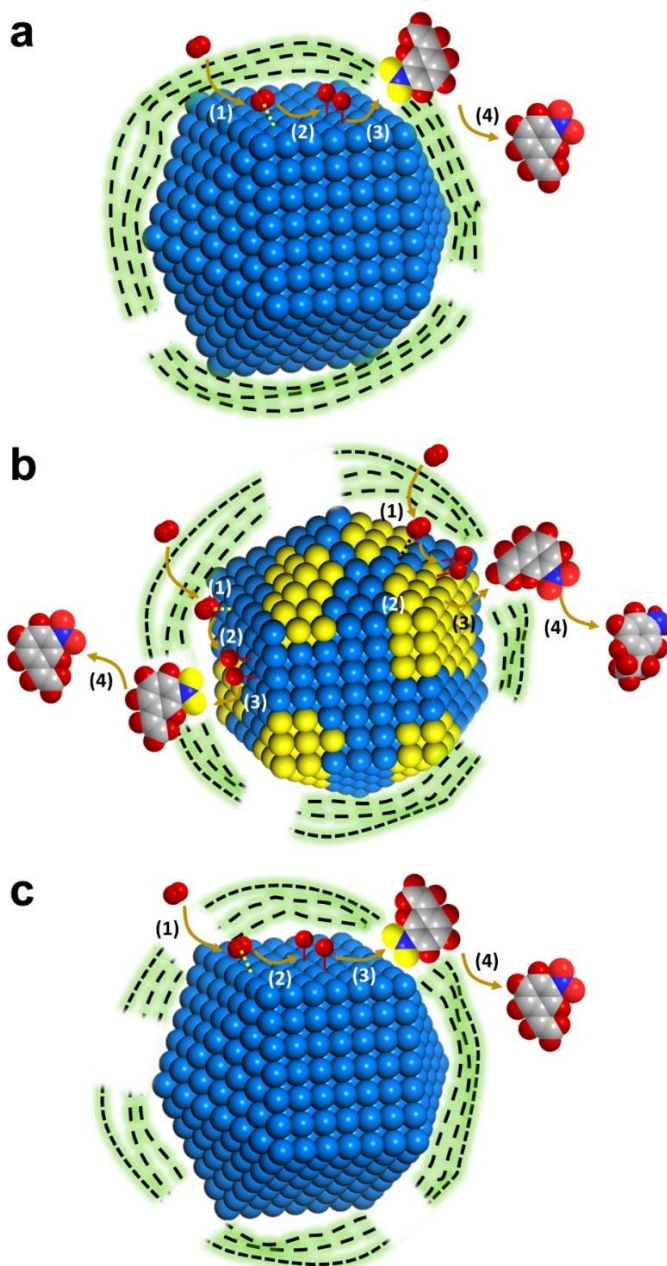
Figure 8.22. Proposed reaction pathways of hydrogenation of 3-nitrostyrene on Co@C NPs with coverage of carbon layers (a) and defective coverage of carbon

layers (b). In schematic illustration **(a)**, the chemoselective hydrogenation of – NO_2 groups can be divided into the following steps: the diffusion of H_2 from the gas phase up to the surface of metallic Co NPs (1), activation of H_2 (2), adsorption of the nitro aromatic (3), H-transfer from Co NPs to $-NO_2$ groups (4) for selective hydrogenation of $-NO_2$ groups. The scheme presented in **(b)**, sample with Co_3O_4 patches after removal part of carbon layers, hydrogenation of $-NO_2$ and $=C$ groups can be divided into following steps, including the diffuse of H_2 to the surface of metallic Co NPs (1), activation of H_2 (2), hydrogen transfer (3) and hydrogenation of both $-NO_2$ and $C=C$ groups (4). In schematic illustration **(c)**, for the *in situ* reduced sample after removal part of carbon layers, the chemoselective hydrogenation of $-NO_2$ groups can be divided into several steps, including the diffuse of H_2 to the surface of metallic Co NPs (1), activation of H_2 (2), H-transfer from Co NPs to $-NO_2$ groups (3) and selective hydrogenation of $-NO_2$ groups (4).

It appears then that unless Co nanoparticles are reduced to metallic nanoparticles, their activity and selectivity will be relatively low. In the case that partial (surface) oxidation occurs not only the hydrogenation activity is low, but also it will favor adsorption of styrene versus nitrobenzene, which can further favor the loss of chemoselectivity during the hydrogenation of 3-nitrostryrene.

Based on the above catalytic results and spectroscopic characterizations, we propose a reaction mechanism of chemoselective hydrogenation of 3-nitrostyrene on Co@C NPs covered by disordered carbon layers. Three cases with different oxidation state of Co and coverage of carbon layers are considered. As shown in **Figure 8.22**, the first step in the hydrogenation reaction catalyzed by both Co@C and Co@C-250Air is the diffusion of H_2 to the surface of Co NPs under the cover of carbon layers. Then H_2 will be activated by Co NPs and form active H species. The third step will be different for Co@C and Co@C-250Air due to their different adsorption properties to the substrate molecules. In the case of Co@C (**Figure 8.22a**), 3-nitrostyrene will be adsorbed on metallic Co preferentially through the $-NO_2$ groups, which will be reduced by the active H species formed on Co NPs. The adsorption of $C=C$ bond on Co@C sample is relatively weak. However, in the case of Co@C-
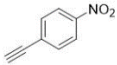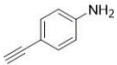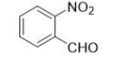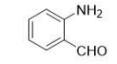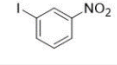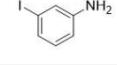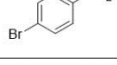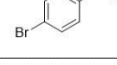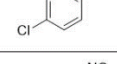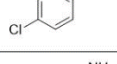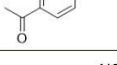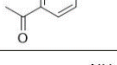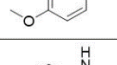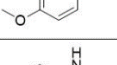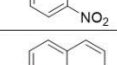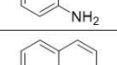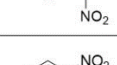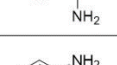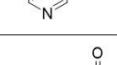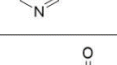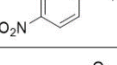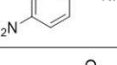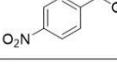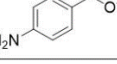
250Air (**Figure 8.22b**), both C=C and –NO$_2$ group can have direct access to the surface of Co NPs. As a consequence, both –NO$_2$ and C=C groups can be hydrogenated by H$_2$, resulting in lower selectivity. When Co@C-250Air is reduced by H$_2$ before the catalytic test (**Figure 8.22c**), more metallic Co sites will selectively absorb –NO$_2$ group instead of C=C bond, leading to high activity and selectivity.

3.6 Scope of the catalyst

The scope of Co@C NPs in hydrogenation of substituted nitroarenes was investigated by reacting substituted nitrobenzene with halogens, amides, ester groups. In all cases, activity and chemoselectivity were high when working under mild reaction condition (**Table 8.2**). Selective hydrogenation of –NO$_2$ groups can be performed in the presence of groups such as olefins, alkynes and carbonyl under much lower H$_2$ pressure (7-10 bar) compared with previous reports (30-50 bar).[10-12] As it can be seen in **Table 8.2**, all the substrates can be selectively transformed with over 93% selectivity. Most of the entries show over 90% yield in the case of both electron-deficient and electron-rich substituents. Co@C NPs are also active and selective for nitroarenes with easily reducible moieties including alkyne, amide, ester, ketone and halogens. In previous work, the yields of heteroaromatic amines are not very high (from 53% to 75%). With Co@C NPs, we can get much higher yield of heteroaromatic amines (Entry 9 and 10 in **Table 8.2**). Thus, Co@C NPs are superior catalysts for chemoselective hydrogenation of nitroarenes under mild conditions.

Table 8.2. Scope of the hydrogenation of nitroarenes catalyzed by Co@C NPs. Reaction condition: Co@C NPs is 30 mg. 0.5 mmol nitroarenes, 30 μL dodecane as the internal standard, 2 mL toluene as the solvent. †100 mg Co@C NPs as the catalyst. ‡2 mL THF as the solvent.

Entry	Substrate	Product	Time (h)	H$_2$ pressure (bar)	Temp. (°C)	Con.	Sel.
1			6	7	120	93%	95%
2†			12	10	100	95%	95%
3			5	10	140	99%	97%
4			10	10	140	95%	99%
5			8	10	140	99%	97%
6			12	10	140	99%	95%
7			10	8	120	99%	99%
8			10	8	120	91%	93%
9			15	10	140	98%	95%
10			15	10	140	99%	95%
11‡			10	10	140	97%	99%
12			10	10	140	97%	99%

4. Conclusions

In this work, we present a strategy for the synthesis of Co@C NPs. Metallic Co NPs are covered by thin carbon layers with small cracks. H_2 can diffuse through the cracks in the thin carbon layers and be activated at room temperature. The existence of carbon layers can protect the Co NPs from over-oxidation by air. This type of material shows good activity and selectivity for hydrogenation of nitroarenes with wide scope and good tolerance. They can also give high yields of heteroaromatic amines. The adsorption properties of substrate molecules will be affected by the chemical state of Co. Combing with *in situ* IR adsorption experiments and results from electron microscopy, a reaction mechanism is proposed in where the important role of metallic cobalt and the negative role of CoOx for the selective hydrogenation reaction is shown. And non-direct involvement of the carbon in the reaction is also proposed. The role of carbon layers is as protection of the Co NPs from getting deeply oxidized. This work provides new insights to design non-noble metal catalysts for heterogeneous catalytic applications.

References

(1) Blaser, H.-U.; Siegrist, U.; Steiner, H. *Aromatic Nitro Compounds: Fine Chemicals Through Heterogeneous Catalysis* (Wiley-VCH, Weinheim, Germany, 2001).

(2) Corma, A.; Serna, P. *Science* **2006**, *313*, 332.

(3) Blaser, H.-U.; Steiner, H.; Studer, M. *ChemCatChem* **2009**, *1*, 210.

(4) Corma, A.; Serna, P.; Concepcion, P.; Calvino, J. J. *J. Am. Chem. Soc.* **2008**, *130*, 8748.

(5) Serna, P.; Boronat, M.; Corma, A. *Top. Catal.* **2011**, *54*, 439.

(6) Ran, J.; Zhang, J.; Yu, J.; Jaroniec, M.; Qiao, S. Z. *Chem. Soc. Rev.* **2014**, *43*, 7787.

(7) Byon, H. R.; Suntivich, J.; Shao-Horn, Y. *Chem. Mater.* **2011**, *23*, 3421.

(8) Jagadeesh, R. V.; Junge, H.; Beller, M. *Nat. Comm.* **2014**, *5*, 4123.

(9) Su, B.; Cao, Z. C.; Shi, Z. J. *Acc. Chem. Res.* **2015**, *48*, 886.

(10) Westerhaus, F. A.; Jagadeesh, R. V.; Wienhofer, G.; Pohl, M. M.; Radnik, J.; Surkus, A. E.; Rabeah, J.; Junge, K.; Junge, H.; Nielsen, M.; Bruckner, A.; Beller, M. *Nat. Chem.* **2013**, *5*, 537.

(11)   Jagadeesh, R. V.; Surkus, A. E.; Junge, H.; Pohl, M. M.; Radnik, J.; Rabeah, J.; Huan, H.; Schunemann, V.; Bruckner, A.; Beller, M. *Science* **2013**, *342*, 1073.

(12)   Wei, Z.; Wang, J.; Mao, S.; Su, D.; Jin, H.; Wang, Y.; Xu, F.; Li, H.; Wang, Y. *ACS Catal.* **2015,** *5*, 4783-4789.

(13)   Fu, T.; Wang, M.; Cai, W.; Cui, Y.; Gao, F.; Peng, L.; Chen, W.; Ding, W. *ACS Catal.* **2014**, *4*, 2536.

(14)   Berry, V. *Carbon* **2013**, *62*, 1.

(15)   Bunch, J. S.; Verbridge, S. S.; Alden, J. S.; van der Zande, A. M.; Parpia, J. M.; Craighead, H. G.; McEuen, P. L. *Nano Lett.* **2008**, *8*, 2458.

(16)   N. Fairley, CasaXPS Version 2.3.14, Casa Software Ltd, **2008**.

(17)   Zhong, W.; Liu, H.; Bai, C.; Liao, S.; Li, Y. *ACS Catal.* **2015,** *5*, 1850-1856.

(18)   Ward, M. R.; Boyes, E. D.; Gai, P. L. *ChemCatChem* **2013**, *5*, 2655.

(19)   Qiu, L.; Liu, J. Z.; Chang, S. L.; Wu, Y.; Li, D. *Nat. Comm.* **2012**, *3*, 1241.

(20)   Deng, J.; Ren, P.; Deng, D.; Bao, X. *Angew. Chem. Int. Ed.* **2015,** *54*, 2100-2104.

(21)   Sun, S.; Murray, C. B. *J. Appl. Phys.* **1999**, *85*, 4325.

(22)   Guo, S.; Zhang, S.; Wu, L.; Sun, S. *Angew. Chem. Int. Ed.* **2012**, *51*, 11770.

(23)   Lu, Y.; Lu, X.; Mayers, B. T.; Herricks, T.; Xia, Y. *J. Solid State Chem.* **2008**, *181*, 1530.

(24)   Zhao, X. Q.; Veintemillas-Verdaguer, S.; Bomati-Miguel, O.; Morales, M. P.; Xu, H. B. *Phys. Rev. B* **2005**, *71*.

(25)   de la Peña O'Shea, V. c. A.; de la Piscina, P. R. r.; Homs, N.; Aromí, G.; Fierro, J. L. G. *Chem. Mater.* **2009**, *21*, 5637.

(26)   Hadjiev, V. G.; Iliev, M. N.; Vergilov, I. V. *J. Phys. C: Solid State Phys.* **1988**, *21*, L199.

(27)   Ferrari, A. C.; Robertson, J. *Phil. Trans. R. Soc. A* **2004**, *362*, 2477.

(28)   Wang, Y.; Alsmeyer, D. C.; McCreery, R. L. *Chem. Mater.* **1990**, *2*, 557.

(29)   Iablokov, V.; Beaumont, S. K.; Alayoglu, S.; Pushkarev, V. V.; Specht, C.; Gao, J.; Alivisatos, A. P.; Kruse, N.; Somorjai, G. A. *Nano Lett.* **2012**, *12*, 3091.

(30)   Zhang, L.; Wang, A.; Wang, W.; Huang, Y.; Liu, X.; Miao, S.; Liu, J.;

Zhang, T. *ACS Catal.* **2015,** *5*, 6563-6572.

(31)   Wang, D.; Astruc, D. *Chem. Rev.* **2014**, *114*, 6949.

(32)   Gawande, M. B.; Branco, P. S.; Varma, R. S. *Chem. Soc. Rev.* **2013**, *42*, 3371.

(33)   Wang, H.; Chen, C.; Zhang, Y.; Peng, L.; Ma, S.; Yang, T.; Guo, H.; Zhang, Z.; Su, D. S.; Zhang, J. *Nat. Comm.* **2015**, *6*, 7181.

(34)   Bartholomew, C. H.; Reuel, R. C. *Ind. Eng. Chem. Prod. Res. Dev.* **1985**, *24*, 56.

(35)   Yates, I. C.; Satterfield, C. N. *Energy Fuels* **1991**, *5*, 168.

(36)   Boronat, M.; Concepcion, P.; Corma, A.; Gonzalez, S.; Illas, F.; Serna, P. *J. Am. Chem. Soc.* **2007**, *129*, 16230.

(37)   Ahmad, I.; Dines, T. J.; Rochester, C. H.; Anderson, J. A. *J. Chem. Soc., Faraday Trans.* **1996**, *92*, 3225.

(38)   Koutstaal, C. A.; Angevaare, P. A. J. M.; Grootendorst, E. J.; Ponec, V. *J. Catal.* **1993**, *141*, 82.

(39)   Bachiller-Baeza, B.; Anderson, J. A. *J. Catal.* **2002**, *212*, 231.

This chapter is reused from the following publication:

A new strategy to transform mono and bimetallic non-noble metal nanoparticles into highly active and chemoselective hydrogenation catalysts, **L. Liu**, F. Gao, P. Concepcion and A. Corma, *Journal of Catalysis*, 2017, 350, 218-225.

Chapter 9

Transforming mono and bimetallic non-noble metal nanoparticles into highly active and chemoselective hydrogenation catalysts
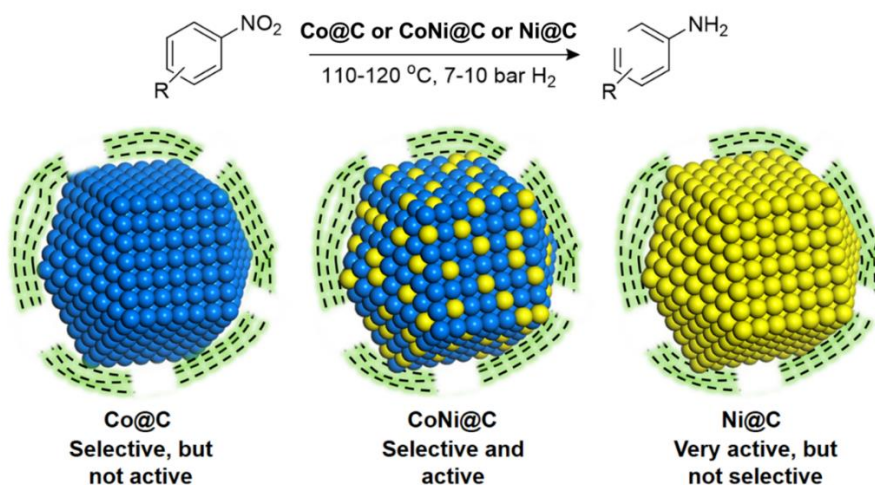
Abstract

A new strategy to transform non-noble metal oxide nanoparticles (NPs) into highly active and selective metallic NPs as hydrogenation catalysts by a simple carbon coating process based on hydrothermal treatment with glucose is presented. During the carbon coating process, metal oxide NPs will be reduced to metallic NPs and covered by thin carbon layers, resulting in formation of Metal@C NPs. Through this method, monometallic Co@C has been prepared, which show excellent activity and selectivity for chemoselectivity hydrogenation of substituted nitroarenes to corresponding anilines under mild conditions. Kinetic, isotopic and spectroscopic studies indicate that hydrogen dissociation-addition is the controlling step in chemoselective hydrogenation reaction with Co@C NPs. Stabilization and the reaction rate of metallic Co is improved by preparing bimetallic CoNi@C catalyst, leading to almost five-fold improved activity. Our preparation method enables to synthesize non-noble bimetallic CoNi@C nanoparticles with nearly one-order magnitude higher activity than any Co-based non-noble metal catalysts prepared by other methods, without necessity to involve the promoting role of metal-N interactions. At last, we also show the application of of Co@C NPs for hydrogenation of levulinic acid to γ-valerolactone.

1. Introduction

Substituting noble metal (NM) catalyst by non-noble metal (NNM) catalyst not only presents economic advantages but also represents a promising approach for a more sustainable chemistry.[1] Non-noble metal nanoparticles (NPs) have been utilized as efficient catalyst for electrocatalysis, photocatalysis and heterogeneous catalysis.[2-4] Nevertheless, in most of the results presented up to now, the catalytic performances achieved by the alternative NNM are still lower than those of NM catalysts.

With the aim to improve activity and selectivity of NNM, several catalyst synthesis methodologies have been presented and for preparing and stabilizing the transition metal NPs, they have to be protected by some capping ligands or solid support. In the last decade, the preparation of transition metal NPs by wet-chemistry method has been well established, and it has been shown that organic ligands can stabilize transition metal NPs.[5,6] However, the productivity of this

method is usually low and these metal NPs are not stable enough in air. In addition, expensive organic ligands are required in some cases. Bimetallic NPs can also be prepared by wet-chemistry method through the thermal decomposition of metal precursors in solvent,[7] though in some cases, it is difficult to obtain alloyed bimetallic nanoparticles due to their different nucleation dynamics in solution.[8,9] Thermal decomposition of metal complex or metal-organic framework (MOF) materials is another preparation procedure leading to metal NPs covered by carbon layers.[10,11] Unfortunately, it will be difficult to prepare bimetallic or multi-metallic NPs by the thermal decomposition procedure.

In this work, we will present a general strategy to transform easily transition metal oxide NPs into mono and bimetallic NPs with well-defined nanostructures. The synthesis methodology presented here uses glucose as a green carbon source and employs a hydrothermal treatment to obtain mono and bimetallic catalysts coated by thin carbon layers. The resultant materials are protected by the carbon layers from deep oxidation by air. The catalyst preparation strategy is illustrated here by Co@C and CoNi@C samples. The obtained materials show much higher catalytic activity for chemoselective hydrogenation of substitute nitroarenes into corresponding substituted anilines than previously reported non-noble metal catalysts.

In has to be pointed out that in previous works, it has been proposed that preparation of NNM catalysts by decomposition of organometallic precursors with nitrogen-containing ligands yields highly active catalysts for the abovementioned reaction. It was claimed that a metal-nitrogen interaction was established in the final catalyst and metal-nitrogen interaction was thought to be a key factor to explain the high catalytic activity.[12,13] In this work, we will present that our preparation strategy does not require organometallic compound as metal source, neither requires to introduction metal-nitrogen interaction to achieve mono and bimetallic NNM catalysts with higher activities.

2. Experiments

Synthesis of Co_3O_4 NPs as precursor for Co@C NPs. Co_3O_4 NPs were prepared by following a reported procedure.[14] 4.94 g of $Co(Ac)_2$ was dissolved

in 100 mL of glycol under stirring at 160 $^{\circ}$C. 4.24 g of Na_2CO_3 was dissolved in 160 mL of distilled water. When $Co(Ac)_2$ was totally dissolved in glycol and a purple solution was formed, Na_2CO_3 aqueous was added into the $Co(Ac)_2$ glycol solution drop by drop. It took about 1.5 h to 2 h to finish the process. After adding Na_2CO_3 aqueous, the suspension was aged for one additional hour before cooling down. Purple solid product would be obtained after filtration of the suspension and washed with water and acetone. After drying in oven at 60 $^{\circ}$C for 16 h, the solid product was sent to calcination in static air at 450 $^{\circ}$C for 3 h with a ramp rate of 1 $^{\circ}$C/min from room temperature to 450 $^{\circ}$C.

Synthesis of Co@C NPs through carbon coating process. 360 mg of glucose was dissolved in 20 mL distilled water. Then 0.5 g of Co_3O_4 NPs was dispersed in the glucose aqueous under ultrasonic treatment. The black suspension was transferred into autoclave and kept at 175 $^{\circ}$C for 18 h. After cooling down to room temperature, the solid product was washed by water and acetone and dried in oven at 60 $^{\circ}$C, resulting the formation of two-dimensional $Co(OH)_2$/C composites. Co@C NPs could be obtained by annealing the $Co(OH)_2$/C composites in N_2 at 600 $^{\circ}$C for 2 h with a ramp rate of 10 $^{\circ}$C/min from room temperature to 600 $^{\circ}$C. After keeping at 600 $^{\circ}$C for 2 h, the sample was cooled down in N_2 flow to room temperature and stored in glass vail in the ambient environment.

Synthesis of Ni-Co_3O_4 NPs as precursor for bimetallic NPs. The preparation of Ni-Co_3O_4 NPs was similar to Co_3O_4 NPs with some modifications of the amount of inorganic metal salts. 4.94 g of $Co(Ac)_2$ and 2.5 g of $Ni(Ac)_2 \cdot 4H_2O$ was dissolved in 100 mL of glycol under stirring at 160 $^{\circ}$C. 5.0 g of Na_2CO_3 was dissolved in 160 mL of distilled water. When $Co(Ac)_2$ and $Ni(Ac)_2$ were totally dissolved in glycol and form red solution, Na_2CO_3 aqueous was added into the $Co(Ac)_2$ glycol solution drop by drop. It took about 1.5 h to 2 h to finish the process. After adding Na_2CO_3 aqueous, the suspension was aged for one additional hour before cooling down. Solid product would be obtained after filtration of the suspension and washed with water and acetone. After drying in oven at 60 $^{\circ}$C for 16 h, the solid product was sent to calcination in static air at 450 $^{\circ}$C for 3 h with a ramp rate of 1 $^{\circ}$C/min from room temperature to 450 $^{\circ}$C.

Synthesis of bimetallic CoNi@C NPs through carbon coating process. For the preparation of bimetallic CoNi@C NPs, we followed a similar procedure to the one described for monometallic Co@C NPs. 0.5 g of Ni-doped Co_3O_4 (Ni-Co_3O_4) NPs was used as the precursor. The other experimental procedures were the same.

Synthesis of Ni@C through carbon coating process.

5.0 g of $Ni(Ac)_2 \cdot 4H_2O$ was dissolved in 100 mL glycol under stirring at 160 °C. 5.0 g of Na_2CO_3 was dissolved in 160 mL of distilled water. When $Ni(Ac)_2$ was totally dissolved in glycol and a green solution was formed, Na_2CO_3 aqueous was added into the $Ni(Ac)_2$ glycol solution drop by drop. It took about 1.5 h to 2 h to finish the process. After adding Na_2CO_3 aqueous, the suspension was aged for one additional hour before cooling down. Green solid product would be obtained after filtration of the suspension and washed with water and acetone. After drying in oven at 60 °C for 16 h, collect the solid and use as the precursor for Ni@C NPs. The preparation of Ni@C NPs was similar to monometallic Co@C NPs using 0.5 g green solid from the precipitation of $Ni(Ac)_2$ as the precursor. The other experimental procedures were the same.

Preparation of Co@C nanoparticles from the thermal decomposition of metal-organic framework (MOF) precursor.

Herein, two types of Co-containing MOF materials were prepared using different linkers. One linker is trimesic acid with nitrogen and the other is 2-methylimidazole with nitrogen. Co-BTC MOF was prepared using trimesic acid as linker. In a typical synthesis, 1.05 g of trimesic acid and 2.91 g of cobalt nitrate hexahydrate was dissolved in a mixed solvent (20 mL DMF + 20 mL H_2O + 20 mL ethanol) under stirring at room temperature. When all the solid precursor was dissolved, the mixture was transferred to an autoclave and kept at 100 °C for 18 h. After the hydrothermal reaction, the solid purple product was washed and dried at 60 °C. The Co@C-BTC sample was obtained by thermal decomposition of Co-BTC-MOF in Ar at 600 °C.

In a typical synthesis of ZIF-67, cobalt nitrate hexahydrate (0.9 g) was dissolved in 6 mL of deionized water, and 2-methylimidazole (11.0 g) was dissolved in 40 mL of deionized water. The two solutions were mixed and kept

stirring for 24 h at room temperature. The resulting purple precipitates were collected by centrifugation and filtration, washed with water and methanol subsequently for 3 times, and finally dried under vacuum at 60 °C for 24 h. The Co@C-ZIF sample was obtained by thermal decomposition of ZIF-67 in N_2 at 600 °C.

Preparation of Co@C/C catalyst.

The supported Co@C/C catalyst was prepared according to literature. [10] Cobalt(II) acetate tetrahydrate (127 mg) and 1,10-phenanthroline (184 mg) (Co:phenanthroline=1:2 molar ratio) were dissolved in ethanol (50 mL) at room temperature. Then, carbon powder (690 mg) (VULCAN® XC72R, Cabot Corporation) was added and the whole mixture was refluxed for 4 hours. The mixed suspension was cooled to room temperature and the solvent was removed by evaporation. The solid sample obtained was dried at 60 °C for 12 hours. The oven was heated to 800 °C with a ramp rate of 25 °C/min and held at 800 °C for 2 hours under Ar atmosphere. After that, the sample was cooled down to room temperature.

2.2 Characterizations

Powder X-ray diffraction (XRD) was performed with a HTPhilips X'Pert MPD diffractometer equipped with a PW3050 goniometer using Cu Kα radiation and a multisampling handler.

Samples for electron microscopy studies were prepared by dropping the suspension of solid sample using CH_2Cl_2 as the solvent directly onto holey-carbon coated copper grids. All the measurements were performed in a JEOL 2100F microscope operating at 200 kV both in transmission (TEM) and scanning-transmission modes (STEM). STEM images were obtained using a High Angle Annular Dark Field detector (HAADF), which allows Z-contrast imaging.

Raman spectra were recorded at ambient temperature with a 785 nm HPNIR excitation laser on a Renishaw Raman Spectrometer ("Reflex") equipped with an Olympus microscope and a CCD detector. The laser power on the sample was 15mW and a total of 20 acquisitions were taken for each spectrum.

X-ray photoelectron spectra (XPS) of the catalysts were recorded with a

SPECS spectrometer equipped with a Phoibos 150MCD-9 multichannel analyzer using non-monochromatic MgKα (1253.6 eV) irradiation. Spectra were recorded using analyser pass energy of 30 eV, an X-ray power of 100W and under an operating pressure of 10^{-9} mbar. Peak intensities have been calculated after nonlinear Shirley-type background subtraction and corrected by the transmission function of the spectrometer. During data processing of the XPS spectra, binding energy (BE) values were referenced to C1s peak (284.5 eV). CasaXPS software has been used for spectra treatment. The H_2 pre-treatment on the NNM@C samples was performed in a reaction cell connected to XPS analysis chamber. After the H_2 reduction treatment, the samples were transferred into the XPS analysis chamber without contact with air.

H_2-D_2 exchange experiments were carried out in a flow reactor. The feed gas consisted of 4 mL/min H_2, 4 mL/min D_2 and 18 mL/min argon, and the total weight of catalyst was ca. 40 mg. Reaction products (H_2, HD and D_2) were analysed with a mass spectrometer (Omnistar, Balzers). For the samples that need to be reduced before the H_2-D_2 exchange experiments, they were *in situ* reduced at 120 ºC for 2 h with a temperature-rising rate of 10 ºC/min from room temperature to 120 ºC. Then the temperature was decreased to 25 ºC and, once stabilized, the H_2 feed was change to the reactant gas composition.

The redox properties of NNM@C NPs are evaluated by Temperature-programmed reduction (TPR). Micromeritics AutoChem 2910 catalyst characterization system with a thermal conductivity detector (TCD) was used. Prior to each experiment, about 40 mg of sample was pretreated at room temperature in flowing He (10 mL/min) for 20 min. The sample was treated by heating from 25 °C to 600 °C at a rate of 5 °C min^{-1} in a flow of 10 vol.% H_2 in Ar. The total gas flow rate was 50 mL/min^{-1}.

2.3 Catalytic tests
2.3.1 Hydrogenation of nitroarenes

The chemoselective hydrogenation of nitroarenes was performed in batch reactors. The reactant, internal standard (dodecane), solvent (toluene or THF), powder catalyst as well as a magnetic bar were added into the batch reactor. After the reactor was sealed, air was purged by flushing two times with 10 bar of hydrogen. Then the autoclave was pressurized with H_2 to the corresponding

pressure. The stirring speed is kept at 1100 rpm and the size of the catalyst powder is below 0.05 mm to avoid either external or internal diffusion limitation. Finally, the batch reactor was heated to the target temperature. For the kinetic studies, 50 µL of the mixture was taken out for GC analysis at different reaction time. For the scope studies, 100 µL of the mixture was taken out for GC analysis. The products were also analyzed by GC-MS.

2.3.2 Hydrogenation of levulinic acid to γ-valerolactone

The chemoselective hydrogenation of levulinic acid was performed in batch reactors. 1 mmol of levulinic acid, internal standard (dodecane), solvent (toluene), and powder catalyst as well as a magnetic bar were added into the batch reactor. After the reactor was sealed, air was purged by flushing two times with 10 bar of hydrogen. Then the autoclave was pressurized with H_2 to the corresponding pressure. The stirring speed is kept at 1100 rpm and the size of the catalyst powder is below 0.05 mm to avoid either external or internal diffusion limitation. Finally, the batch reactor was heated to the target temperature. The products were also analyzed by GC and GC-MS.
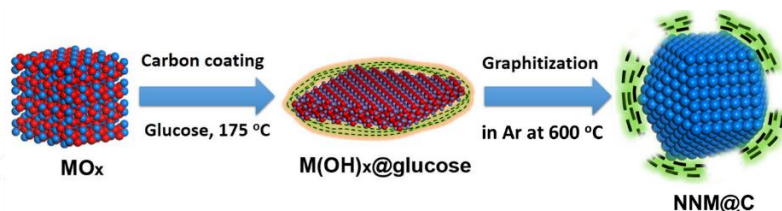
Figure 9.1. Schematic illustration of the transformation of metal oxide NPs (MOx) into metallic transition NPs covered by thin carbon layers (NNM@C) through a facile carbon-coating and graphitization process.

3. Results and discussions
3.1 Preparation of transition metal NPs

Metal oxide nanoparticles can easily be achieved by a precipitation-calcination procedure (see experimental section for details) and their transformation into non-noble metallic NPs covered by carbon layers (NNM@C) is described in **Figure 9.1**. The carbon source was coated on the metal oxide NPs by a hydrothermal treatment with aqueous glucose. After

graphitization treatment at 600 ^{o}C, the organic layers coated on the metal oxide NPs decomposed and condensed into thin carbon layers. Simultaneously, metal oxide NPs were reduced by the carbon, forming metallic NPs covered by thin carbon layers. More specifically, Co@C NPs were prepared starting from Co_3O_4 NPs with high surface areas (with a BET surface area of 110 m^2/g measured by N_2 isotherms). Preparation procedure of the Co_3O_4 NPs is given in the experimental section. The morphological characterization of Co_3O_4 nanoparticles is shown in **Figure 9.2**. When Co_3O_4 nanoparticles were dispersed in a solution of glucose in water and treated under hydrothermal condition at 175 ^{o}C, they transformed into ultrathin $Co(OH)_2$ nanosheets (see **Figure 9.3** and **Figure 9.4**). During the hydrothermal process, glucose was coated on the $Co(OH)_2$ nanosheets, resulting in formation of $Co(OH)_2$/glucose nanocomposites, as confirmed by elemental mapping (see **Figure 9.S4**). A subsequent thermal treatment in inert atmosphere at 600 ^{o}C led to the graphitization of carbon and the reduction of Co_3O_4 into metallic Co by carbon, resulting in the formation of Co@C NPs.
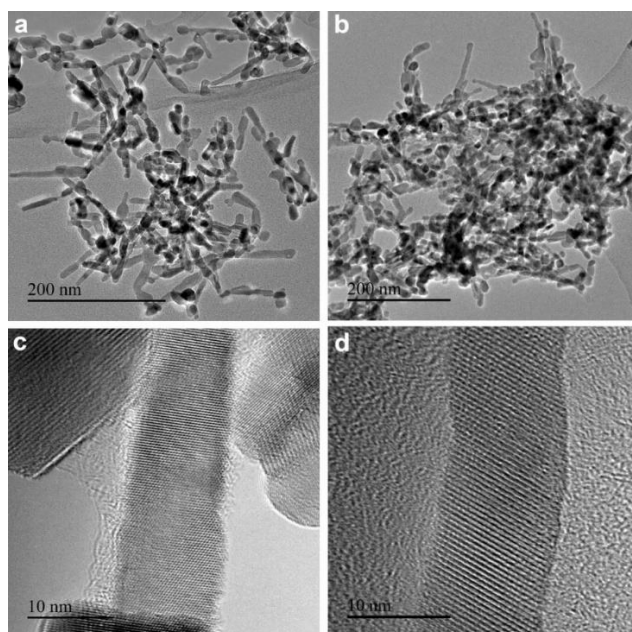
Figure 9.2. TEM images of Co_3O_4 nanoparticles.
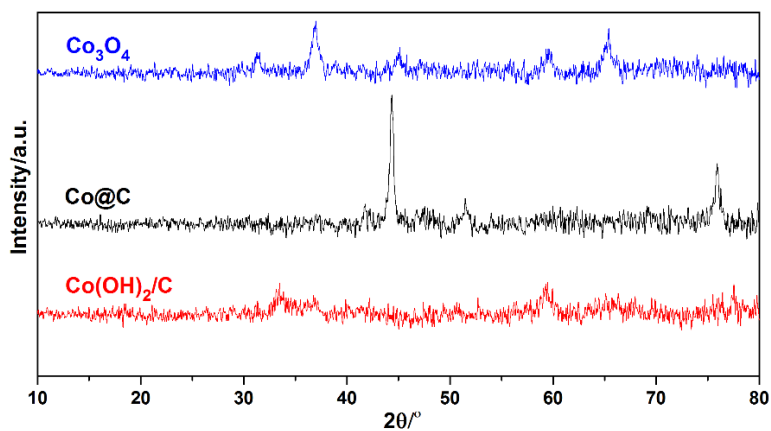
Figure 9.3. XRD patterns of Co_3O_4, $Co(OH)_2$/C nanosheets and Co@C NPs.
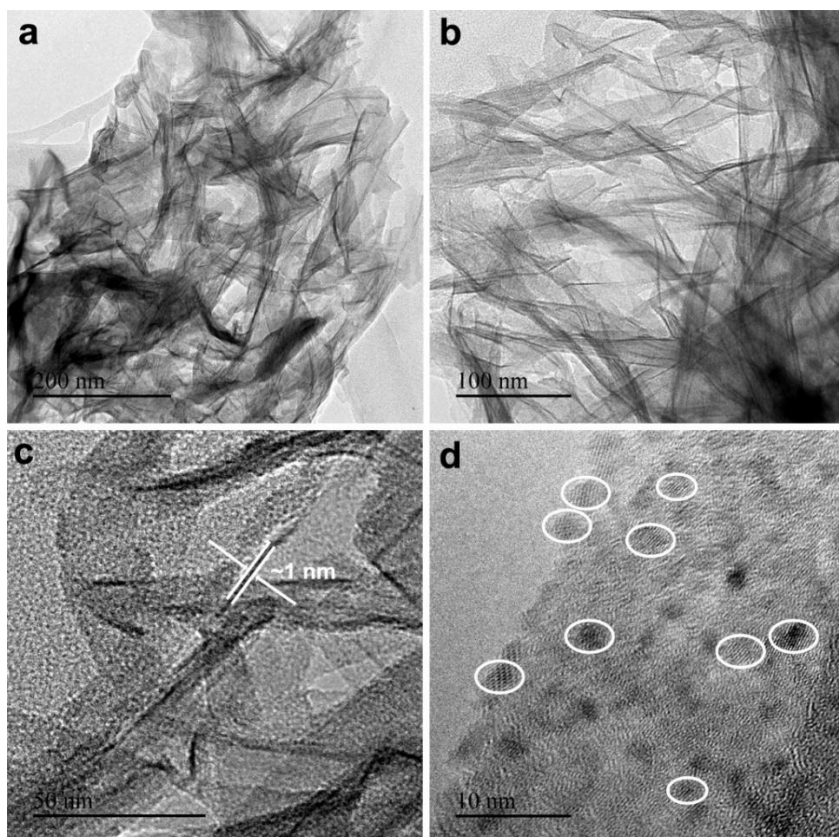
Figure 9.4. TEM images of $Co(OH)_2$/C nanosheets. (a, b) Low-magnification

TEM images of ultrathin two-dimensional Co(OH)$_2$/C composite nanosheets. (c) The thickness of the Co(OH)$_2$/C nanosheets is ca. 1 nm. (d) When the nearly amorphous nanosheets is irradiated by the electron beam for 1 min, the Co(OH)$_2$ will be transformed into small Co$_3$O$_4$ nanoparticles.
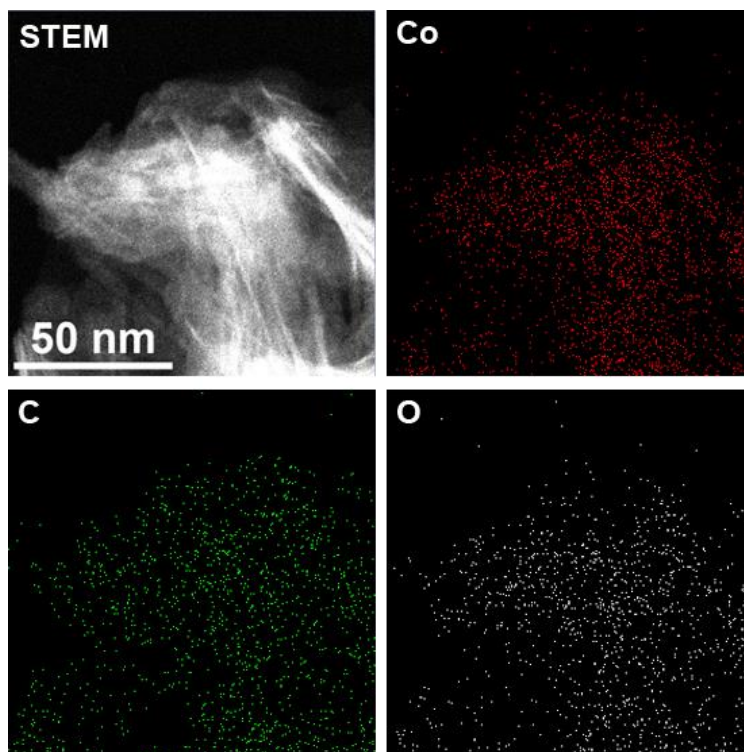
Figure 9.5. Elemental mapping of two-dimensional Co(OH)$_2$/C nanocomposites. Co, C and O are well overlapped in the elemental mapping images.

XRD pattern of Co@C NPs is shown in **Figure 9.3**. Only the diffraction pattern of metallic Co including cubic Co (*fcc* type, PDF code 96-900-8467) and hexagonal Co (*hcp* type, PDF code 96-900-8493) can be observed. The morphology of Co@C NPs was characterized by TEM, and as shown in **Figure 9.6a**, Co NPs are dispersed on thin carbon films with good dispersion. The crystal lattice fringes corresponding to metallic Co can be observed in the high-resolution TEM images (see **Figure 9.6b**). In addition, the Co NPs are partially

covered by thin carbon layers. Those thin carbon layers can protect from over oxidation by air, avoiding the deep oxidation of Co NPs. Nevertheless, some CoOx patches can also be found in the Co@C NPs, which should come from re-oxidation of the surface of metallic Co NPs after preparation and exposure to air (see **Figure 9.7**). The presence of CoOx and the disordered carbon layers coated on Co nanoparticles are also confirmed by Raman spectroscopy (see **Figure 9.8**). For comparison, Co_3O_4 nanoparticles were directly reduced by H_2 at 450 ^{o}C to get metallic Co nanoparticles (the sample is denoted as Co_3O_4-R). As shown in **Figure 9.9**, compared with Co@C sample, the Co_3O_4-R shows larger particle size and much higher percentage of CoOx species, suggesting that the introduction of carbon layers to Co nanoparticles can effectively protect the metallic Co nanoparticles from deep oxidation by air.
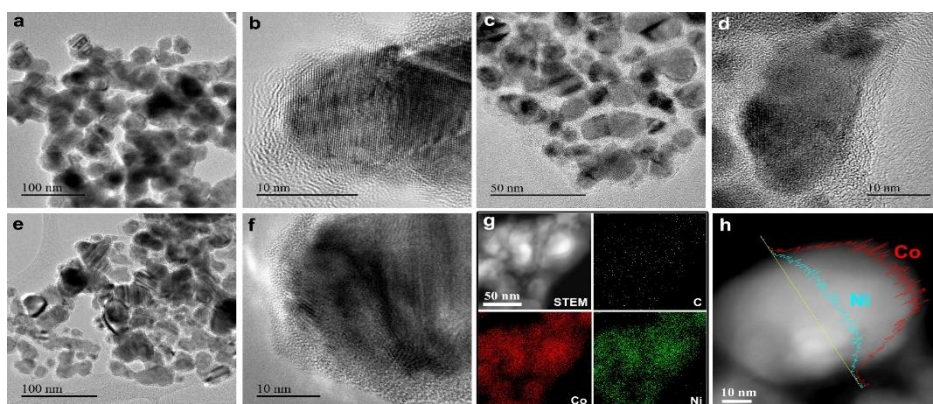
Figure 9.6. (a, b) TEM images of Co@C NPs, (c, d) TEM images of Ni@C NPs, (e, f) TEM images of CoNi@C NPs, (g) elemental mapping of Co, Ni and C in the CoNi@C sample and (h) linescan of the relative amount of Ni and Co in a single CoNi@C nanoparticle.
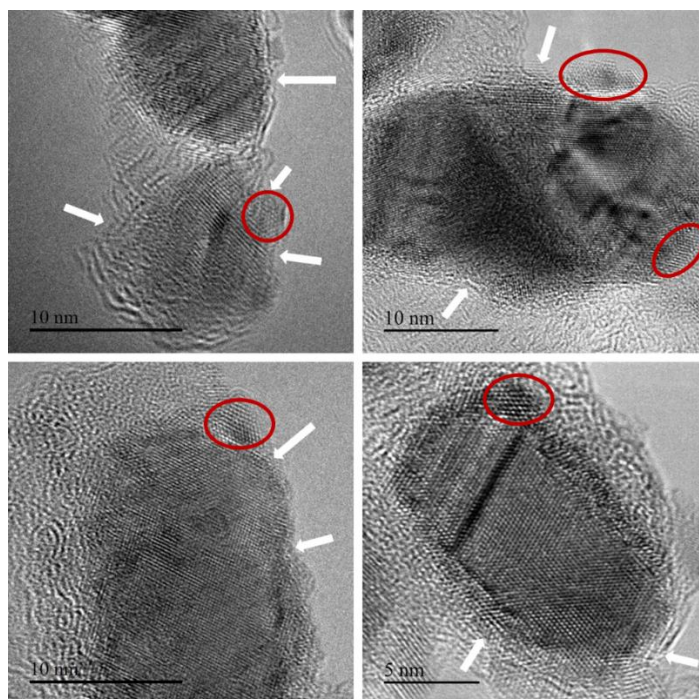
Figure 9.7. More high-resolution TEM images of Co@C NPs. The cracks of the thin carbon layers are indicated by white arrows. The CoOx patches are indicated by red circles.
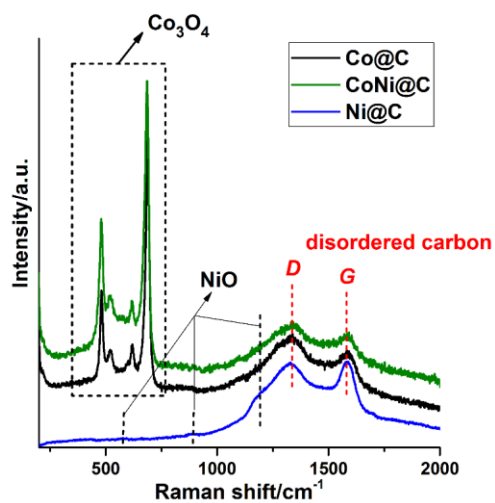
Figure 9.8. Raman spectra of Co@C, CoNi@C and Ni@C NPs. In Co@C and

CoNi@C samples, strong Raman bands corresponding to Co_3O_4 can be observed. In the Ni@C, several bands with weak intensity corresponding to NiO are also observed. In all the three samples, *D* band and *G* band associated with disordered carbon are observed.
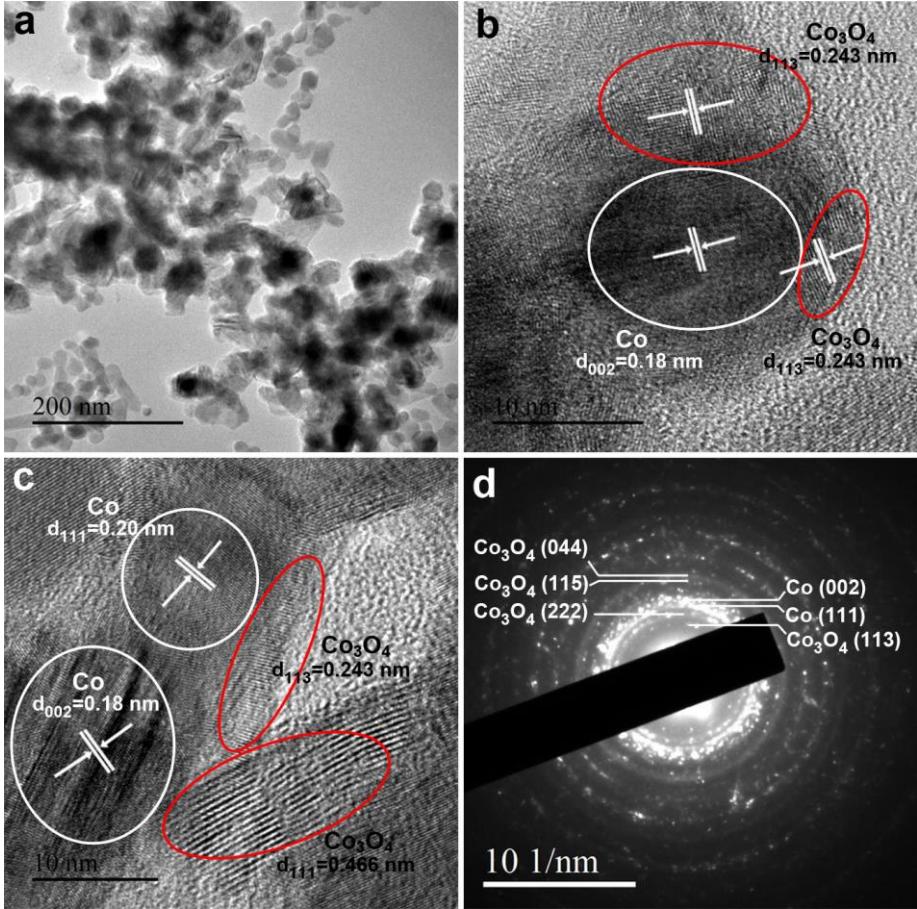
Figure 9.9. (a) TEM image, (b, c) high-resolution TEM images of Co_3O_4-R sample. (d) Selected-area electron diffraction pattern of Co_3O_4-R sample.
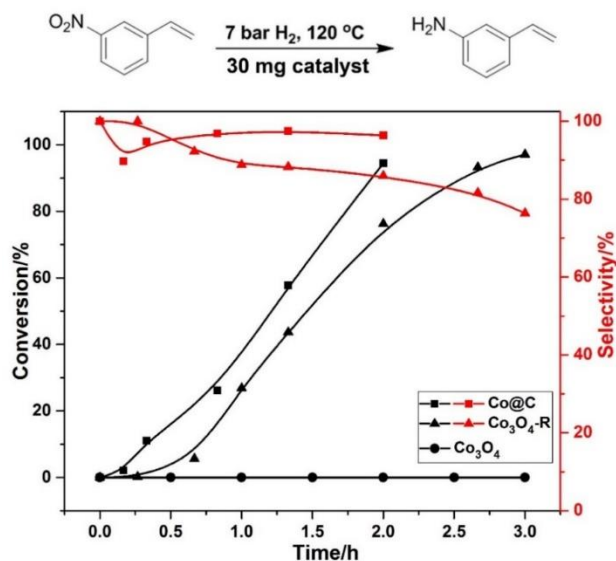
Figure 9.10. Catalytic performances of Co@C, Co$_3$O$_4$-R and Co$_3$O$_4$ nanoparticles in chemoselective hydrogenation of 3-nitrostyrene to 3-aminostyrene. Reaction conditions: 0.5 mmol 3-nitrostyrene, 30 mg Co@C NPs as the catalyst, 2 mL toluene as solvent, 40 μL dodecane as the internal standard. The black legends and red legends correspond to conversion and selectivity, respectively. The bi-product is mainly the full hydrogenation product, 3-ethylaniline.
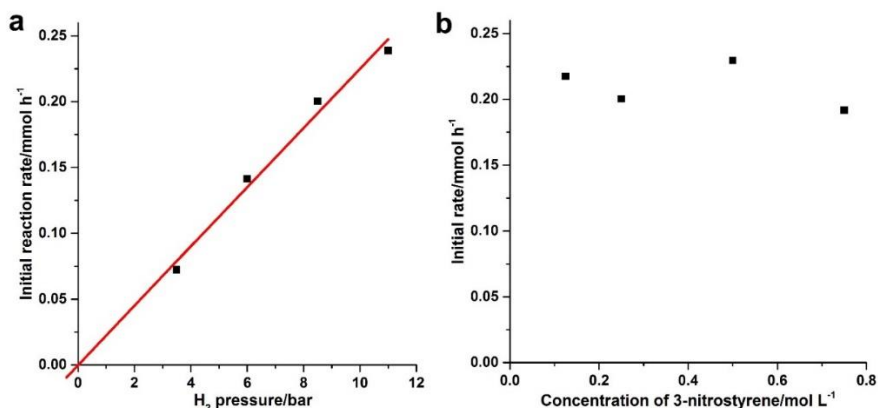
Figure 9.11. Study the limiting step of hydrogenation of 3-nitrostyrene with Co@C NPs. Reaction conditions: 0.5 mmol 3-nitrostyrene, 15 mg Co@C NPs

as the catalyst, 2 mL toluene as solvent, 120 $^{\circ}$C. The catalyst has been pre-reduced by H_2 at 160 $^{\circ}$C.

To show the effects of carbon-coating process on the catalytic properties of Co NPs, the chemoselective hydrogenation of 3-nitrostyrene was chosen as the model reaction. As it can be seen in **Figure 9.10**, both Co@C and Co_3O_4-R samples show hydrogenation activity. For Co@C sample, the hydrogenation of 3-nitrostyrene occurs very rapidly without obvious induction period (ca. 10 min), whereas, Co_3O_4-R sample shows an induction period of about 30 min, which is due to the in-situ reduction of CoOx patches in the sample. [15] Notably, Co@C NPs show higher selectivity to 3-aminostyrene than Co_3O_4-R sample. These results are consistent with our previous works, showing that the role of carbon layers is to protect the non-noble metal NPs from deep oxidation by air and promote the in situ reduction of CoOx patches in the Co@C NPs under reaction conditions.[15]

The kinetics for the hydrogenation of 3-nitrostyrene with Co@C sample was studied and results are presented in **Figure 9.11**. It can be seen that the initial reaction rate for hydrogenation increases linearly with the partial pressure of H_2 while remains practically no affected when changing the concentration of 3-nitrostyrene. The direct conclusion from the above results would be that, with Co@C catalyst, the reaction is controlled by H_2 dissociation or hydrogen addition. It has been shown that in the case of Au/TiO$_2$, the reaction rate of hydrogenation of nitroarenes was significantly improved by introducing a small amount of Pt to Au/TiO$_2$ catalyst, which can dissociate H_2 much more rapidly than solely Au nanoparticles.[16] On those basis and aiming to prepare an active and selective NNM catalyst, we decide to prepare bimetallic CoNi@C NPs. It is expected that the presence of Ni should improve the rate of H_2 dissociation and still maintain the high chemoselectivity. For preparing such a bimetallic catalyst, we started from a sample of Ni-doped Co_3O_4 NPs as precursor. After the coating of glucose through hydrothermal reaction and annealing at 600 $^{\circ}$C, CoNi@C bimetallic NPs (the molar ratio of Co/Ni in this sample is 77/23) covered by thin carbon layers can be prepared. As can be seen in **Figure 9.12**, XRD pattern of the starting Ni-Co_3O_4 nanoparticles is similar to that of Co_3O_4 nanoparticles. The homogeneous dispersion of Ni species in Co_3O_4

nanoparticles is also confirmed by STEM elemental mapping (see **Figure 9.13**). XRD pattern of CoNi@C NPs is shown in **Figure 9.14**. Only diffraction peaks corresponding to *fcc*-type of CoNi alloys can be seen. The structures of CoNi@C NPs are investigated by TEM. As shown in **Figure 9.6e**, the particle size of bimetallic CoNi@C NPs is ranging from 20 to 100 nm and lattice fringes with spacing of 0.21 nm corresponding to CoNi alloy can also be observed in high-resolution TEM image. Similarly, the CoNi NPs are also covered by thin carbon layers (see **Figure 9.6f**). The distribution of Co and Ni in bimetallic CoNi@C NPs are studied by EDS elemental mapping. As it can be seen in **Figure 9.6g**, the spatial distribution of Co, Ni and C overlap very well, indicating that Co and Ni have formed fully alloyed structures. Nevertheless, the alloy structure of CoNi@C NPs is also confirmed by EDS line-scan profile of a single CoNi NP, as presented in **Figure 9.6h**.
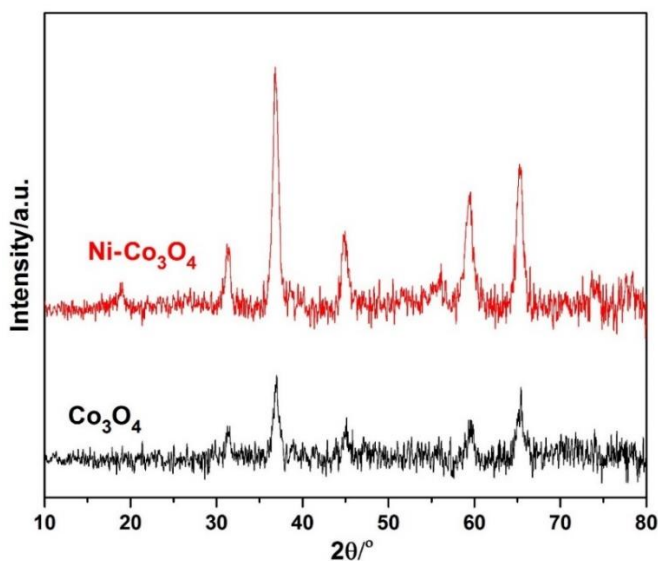
Figure 9.12. XRD patterns of Co_3O_4 and $Ni-Co_3O_4$ nanoparticles.
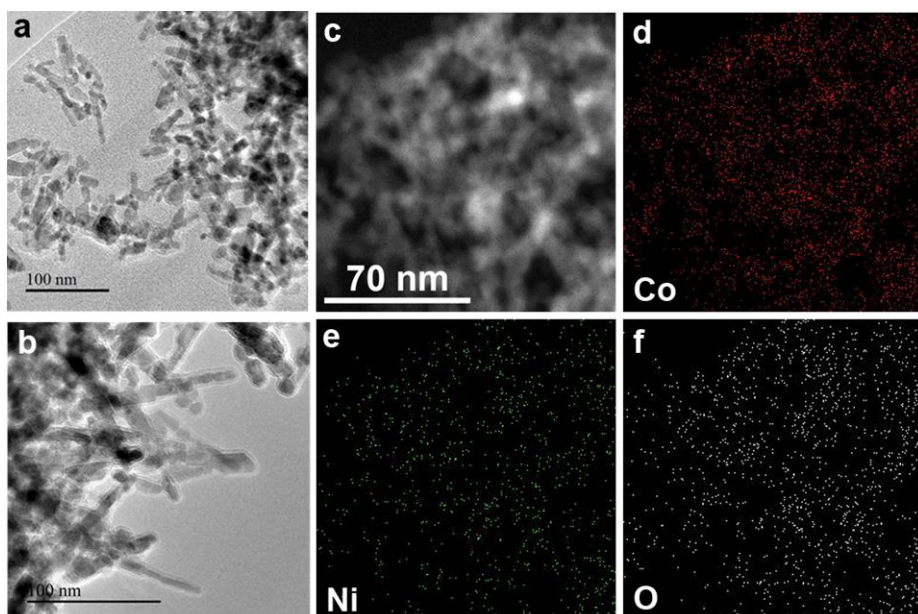
Figure 9.13. (a, b) TEM images of Ni-Co_3O_4 nanoparticles with similar morphology to Co_3O_4 nanoparticles.
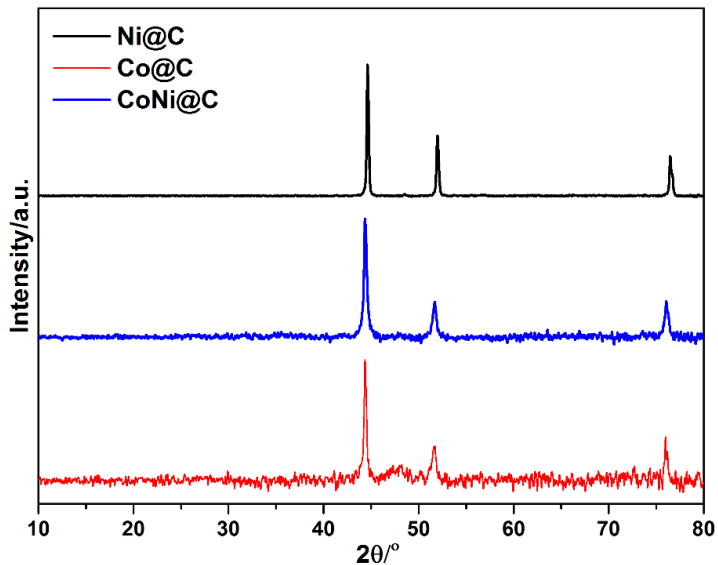
Figure 9.14. XRD patterns of Ni@C, Co@C and CoNi@C NPs.
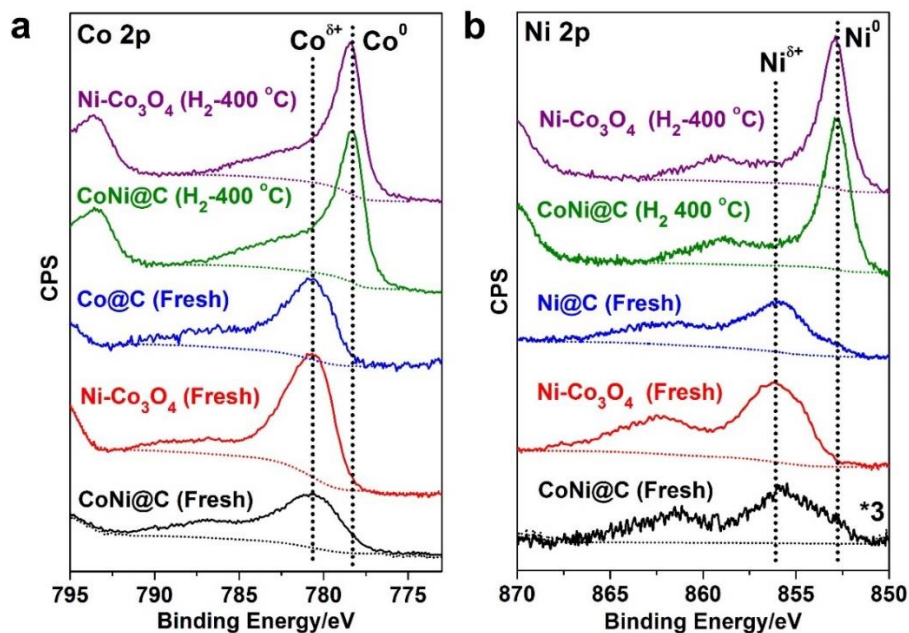
Figure 9.15. (a) Co 2p and (b) Ni 2p regions of the XPS spectra of fresh Co@C, Ni@C, CoNi@C and Ni-Co₃O₄ samples and the samples after reduction by H₂ at 400 °C.
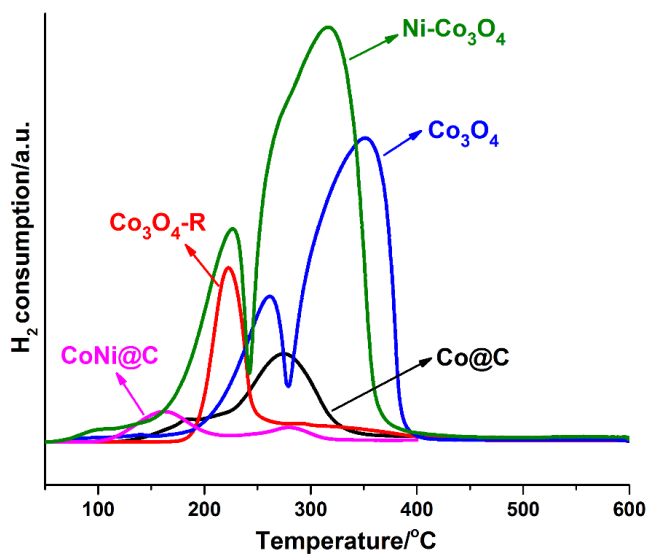
Figure 9.16. TPR profile of CoNi@C and Ni-Co₃O₄ samples.

3.2 Characterizations of NNM@C NPs

The surface properties of Co@C, Ni@C and bimetallic CoNi@C NPs were studied by XPS (see **Figure 9.15a and 15b**). For the fresh Co@C NPs, due to the re-oxidation by air after the synthesis, only CoOx without metallic Co^0 can be detected by XPS. Metallic Co^0 can only be detected by reducing the sample by H_2 in a high-pressure reactor connected to the XPS chamber.[17] However, in the CoNi@C sample, without any pre-treatments, metallic Co^0 can be seen clearly in the Co 2p region, indicating that Ni can contribute to stabilize the active metallic Co^0. In our previous work[15], it has been shown that metallic Co is the active phase for hydrogenation of nitroarenes. Therefore, the introduction of Ni into Co@C NPs can contribute to the stabilization of metallic Co, while increasing the role of H_2 dissociation.

As shown in the morphological characterizations, those carbon-coated transition metal nanoparticles (NNM@C NPs) will be re-oxidized by air, resulting in formation of oxide patches on the surface. Therefore, an in-situ reduction of those metal oxide patches on the surface on NNM@C NPs will occur at the beginning stage of hydrogenation reaction. The redox property of NNM@C NPs can be studied by temperature-programmed reduction (TPR). As it can be seen in **Figure 9.16**, the two metal oxide samples show high H_2 consumption, while three reduced sample show low H_2 consumption. Notably, the CoNi@C sample shows low reduction onset temperature and lowest H_2 consumption among all the samples, suggesting that the percentage of metal oxide patches in CoNi@C is lower than that in Co@C, and the introduction of Ni into Co@C NPs can promote the reducibility of CoOx by H_2.[18]

3.3 Catalytic properties of NNM@C NPs
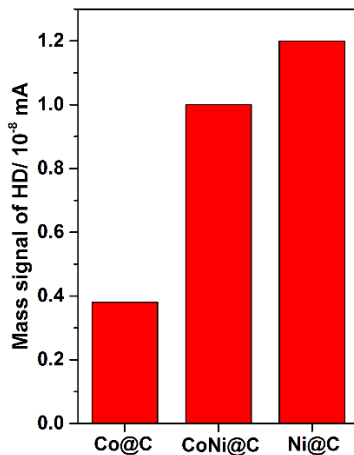
Figure 9.17. H_2-D_2 exchange experiments on Co@C (a), CoNi@C (b) and Ni@C (c) NPs. All the three samples are pre-reduced by H_2 before the H_2-D_2 exchange experiments.

The activity of the as-prepared CoNi@C and Co@C NPs for H_2-D_2 exchange was measured and the results are presented in **Figure 9.17**. It can be seen that with the bimetallic CoNi@C NPs show a more than two-fold improved rate for H_2 dissociation than Co@C NPs, and Ni@C NPs show the highest activity. Furthermore, the catalytic performance of three samples (Co@C, Ni@C and CoNi@C) have also been tested for the hydrogenation of 3-nitrostyrene under mild conditions (120 °C and 7 bar of H_2). The initial reaction rates normalized to the mass of metal catalysts are shown in **Figure 9.18**. Ni@C sample shows the highest activity and CoNi@C shows 4-fold higher activity than Co@C, which is in line with the H_2-D_2 exchange results. The selectivity to the desired 3-aminostyrene product at high conversion (> 95%) of three catalysts are presented in **Figure 9.18b**. Co@C and CoNi@C NPs show excellent selectivity (> 97%) for the hydrogenation of 3-nitrostyrene while Ni@C shows lower chemoselectivity (~80%) towards 3-aminostyrene (see the distributions of products in **Figure 9.19**), which is consistent with previous results from ours and other groups.[19-21] The synergistic effect between Co and Ni contributes the high activity and selectivity of CoNi@C NPs.[22] Moreover, Compared with Co@C NPs prepared by thermal decomposition of Co-EDTA complex, Co@C

NPs generated by the carbon-coating method show much higher activity for hydrogenation of 3-nitrostyrene (see **Figure 9.20**). H_2-chemisorption shows that, the percentage of exposed Co atoms in Co@C from carbon-coating method is much higher, which is probably responsible for the different catalytic activities observed.
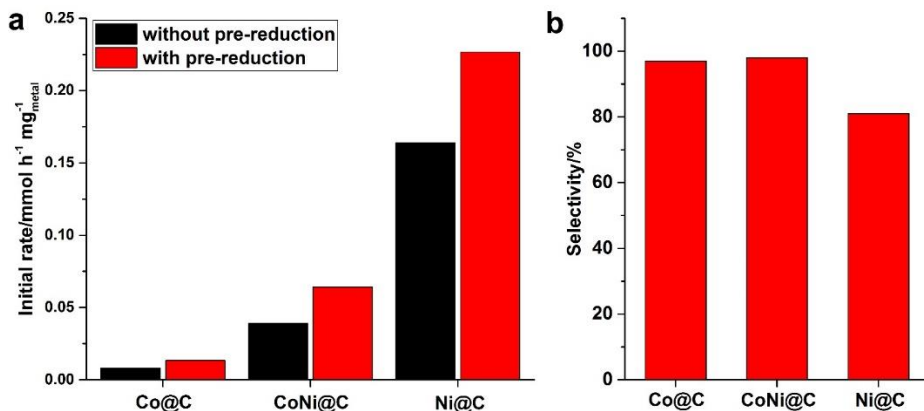
Figure 9.18. Catalytic performances of Co@C, CoNi@C and Ni@C NPs in selective hydrogenation of 3-nitrostyrene. (a) The initial reaction rates are calculated when the conversion of 3-nitrostyrene is below 20%. (b) The selectivity to 3-aminostyrene when the conversion reaches >90% on three catalysts under the same condition.
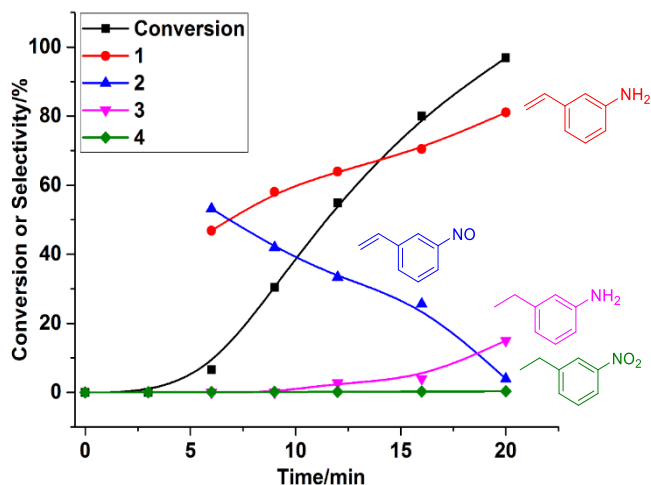
Figure 9.19. Time profile of the conversion of the distribution of products in the hydrogenation of 3-nitrostyrene using Ni@C as the catalyst. As it can be

seen, 3-nitrosostyrene can be observed during the hydrogenation reaction as intermediate. When the reaction reach high conversion (> 95%), 3-ethylaniline is the major bi-product.
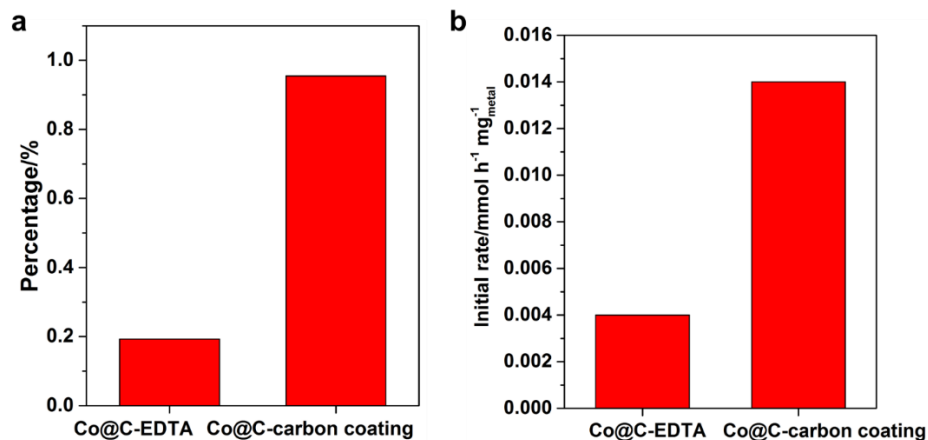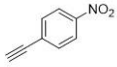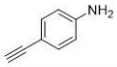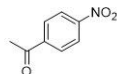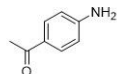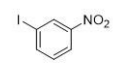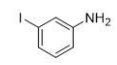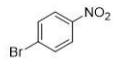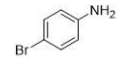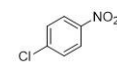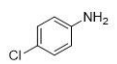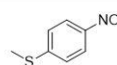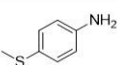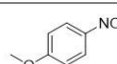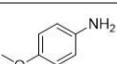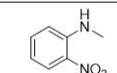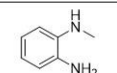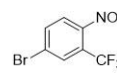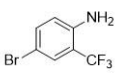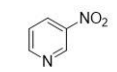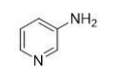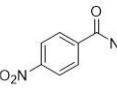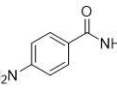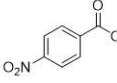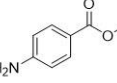

Figure 9.20. (a) Percentage of exposed surface metal atoms in Co@C NPs prepared by thermal decomposition of Co-EDTA complex (Co@C-EDTA) and Co@C NPs prepared by carbon-coating method described (Co@C-carbon coating) in this work. (b) Initial reaction rate of Co@C-EDTA and Co@C-carbon coating in hydrogenation of 3-nitrostyrene.

Table 9.1. Scope study of chemoselective hydrogenation of nitroarenes catalyzed by CoNi@C NPs.

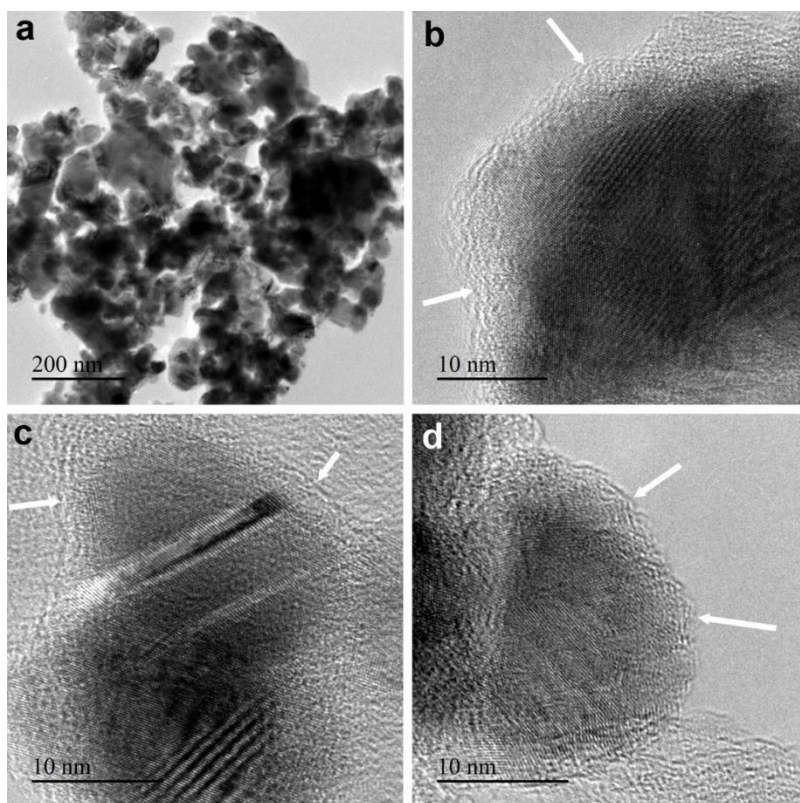| Entry	Substrate	Product	Time (h)	H₂ pressure (bar)	Temp. (°C)	Con.	Sel.
1			0.75	7	120	93%	95%
2			1	10	120	97%	97%
3			0.8	10	120	97%	98%
4			0.8	10	120	95%	98%
5			0.8	10	120	97%	98%
6			1	10	120	99%	95%
7			1	10	120	97%	97%
8			1	10	120	95%	95%
9†			1	10	120	98%	97%
10			1	10	120	97%	97%
11†			1	10	120	97%	99%
12			1	10	120	98%	99%

Figure 9.21. TEM images of CoNi@C NPs after the hydrogenation of 3-nitrostyrene. The thin carbon layers covered on CoNi NPs are still preserved after the reaction, as indicated by white arrows.
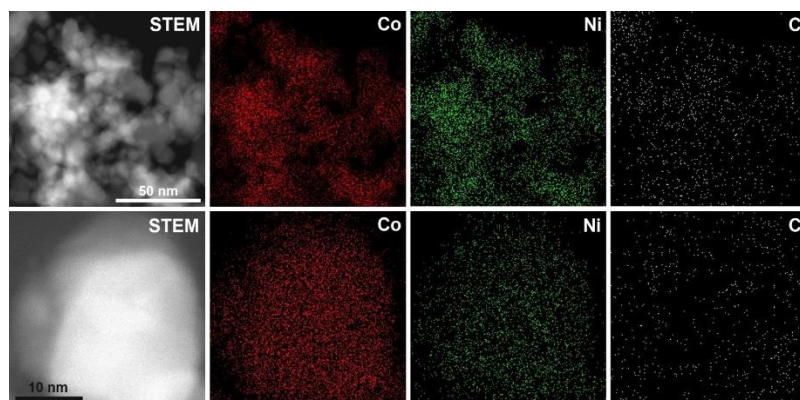

Figure 9.22. Elemental mapping of CoNi@C NPs after the hydrogenation of

3-nitrostyrene. The distribution of Ni, Co and C in both a large area with lots of CoNi@C NPs and a single CoNi@C NP are presented.
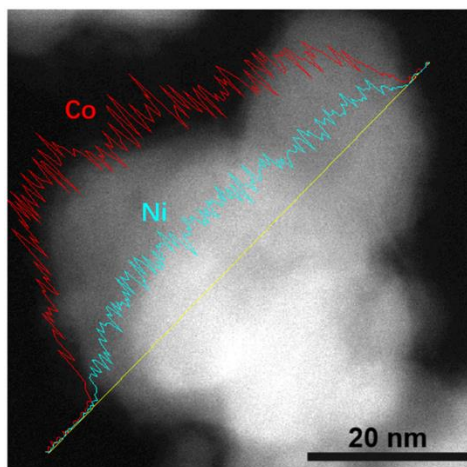

Figure 9.23. Linescan of the content of Ni (green)and Co (red) in bimetallic CoNi@C NPs after the hydrogenation of 3-nitrostyrene.
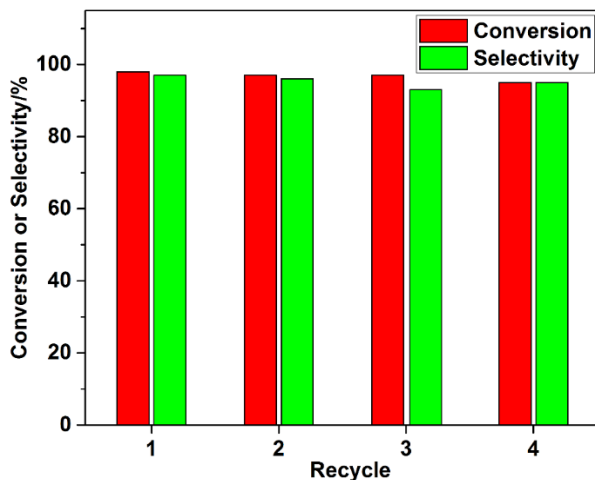

Figure 9.24. Stability tests of CoNi@C NPs. The catalytic performances of recycled Co@C NPs in hydrogenation of 3-nitrostyrene. Reaction conditions: 15 mg CoNi@C catalyst, 0.5 mmol of 3-nitrostyrene, 2 mL toluene, 40 μL of dodecane as internal standard, 120 °C and 7 bar of H_2. After each test, the CoNi@C catalyst are recycled by the magnetic bar and wash with acetone and toluene.
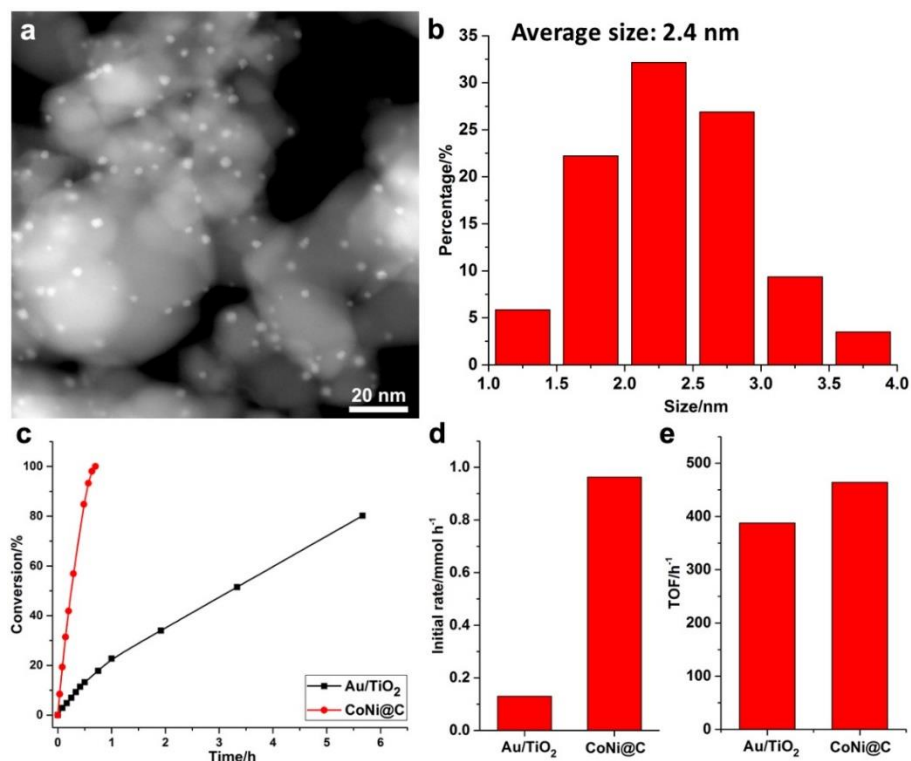
Figure 9.25. (a) STEM image of the commercial Au/TiO_2 catalyst (from AURO*lite*, with 1.0 wt.% of Au). (b) Size distribution of Au nanoparticles in the Au/TiO_2 sample, showing the average size of Au nanoparticles is ca. 2.4 nm. (c) Comparison between Au/TiO_2 and CoNi@C in hydrogenation of 3-nitrostyrene. Reaction conditions: 15 mg solid catalyst, 7 bar of H_2, 120 $^\circ$C, 0.5 mmol of 3-nitrostyrene and 2 mL toluene as solvent. (d) Comparison of the initial reaction rate based on the same amount of Au/TiO_2 and CoNi@C solid catalysts. (e) Comparison of the turnover frequency (TOF) based on the amount of surface atoms in Au/TiO_2 and CoNi@C catalysts. The amount of surface Au atoms in Au/TiO_2 are calculated based on the particle size distribution while the amount of exposed surface atoms in CoNi@C sample is calculated according to the H_2 chemisorption.

The structure of CoNi@C NPs after the hydrogenation of 3-nitrostyrene was also investigated by TEM. As shown in **Figure 9.21**, the particle size

distribution of CoNi NPs is similar to the fresh catalyst and they are still covered by the thin carbon layers, indicating the stability of CoNi NPs. As displayed in **Figure 9.22** and **Figure 9.23**, the alloyed structures of CoNi bimetallic NPs are preserved after the hydrogenation reaction. No obvious phase separation between Ni and Co can be observed, which further confirms that the carbon layers can effectively promote the chemical stability of bimetallic nanoparticles. The good stability of CoNi@C NPs is also reflected by its good recyclability for the selective hydrogenation of 3-nitrostyrene (see **Figure 9.24**).

It should be remarked that the scope of the bimetallic CoNi@C NPs is very good as can be seen from results given in **Table 9.1**. At this point, it can be concluded that a facile method to synthesize stable, active and selective non-noble metal catalysts for chemoselective hydrogenation of nitroarenes has been developed.

Substituted anilines were obtained from the corresponding nitroarenes with high chemoselectivity using noble metal catalysts, such as Au/TiO_2, Au-Pt/TiO_2.[23] As shown in **Figure 9.25**, CoNi@C sample shows much higher reaction rate than Au/TiO_2 when the same amount of solid catalyst is used for the reaction. Nevertheless, the turnover frequency (TOF) based on surface metal atoms were also calculated and compared. As it can be seen in **Figure 9.25d and Figure 9.25e**, regardless how the catalytic performance is compared (initial reaction rate with the same amount of solid catalyst or TOFs based on exposed surface metal atoms), CoNi@C sample is clearly more active than Au/TiO_2, indicating that non-noble bimetallic NPs can serve as promising substitute for noble metal catalysts.
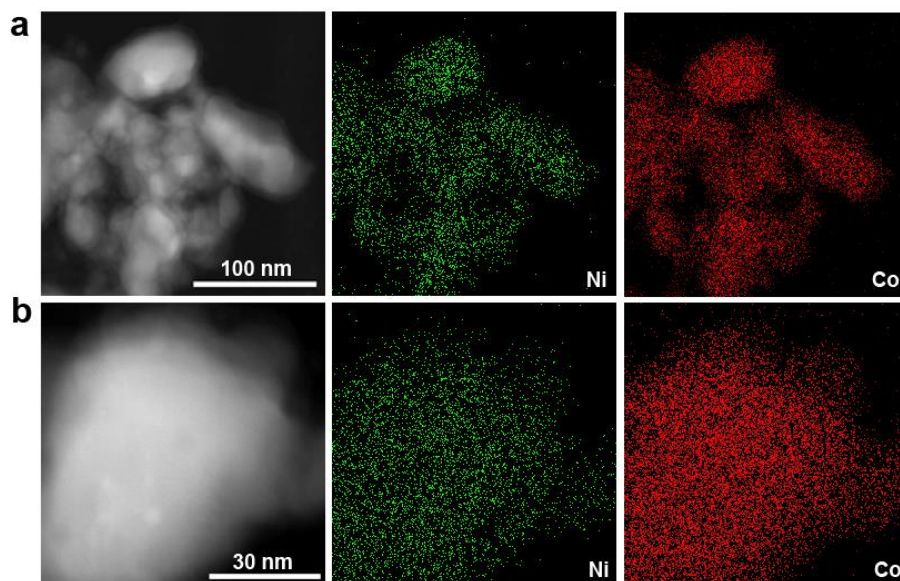
Figure 9.26. Elemental mapping of CoNi@C sample prepared in N_2 atmosphere in different areas, showing the fully alloyed structure of bimetallic CoNi nanoparticles.
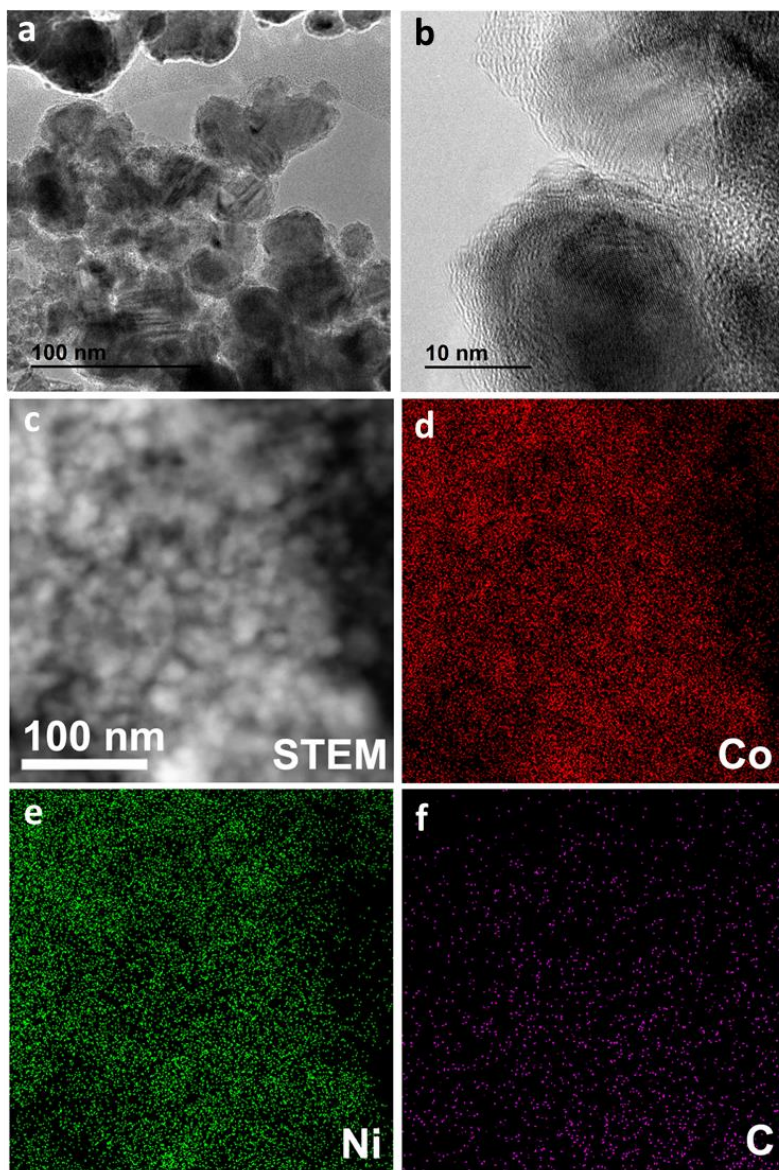
Figure 9.27. (a, b) TEM and HRTEM images and (c-f) Elemental mapping of CoNi@C sample prepared in Ar atmosphere in different areas, showing the fully alloyed structure of bimetallic CoNi nanoparticles covered by nitrogen-free thin carbon layers.
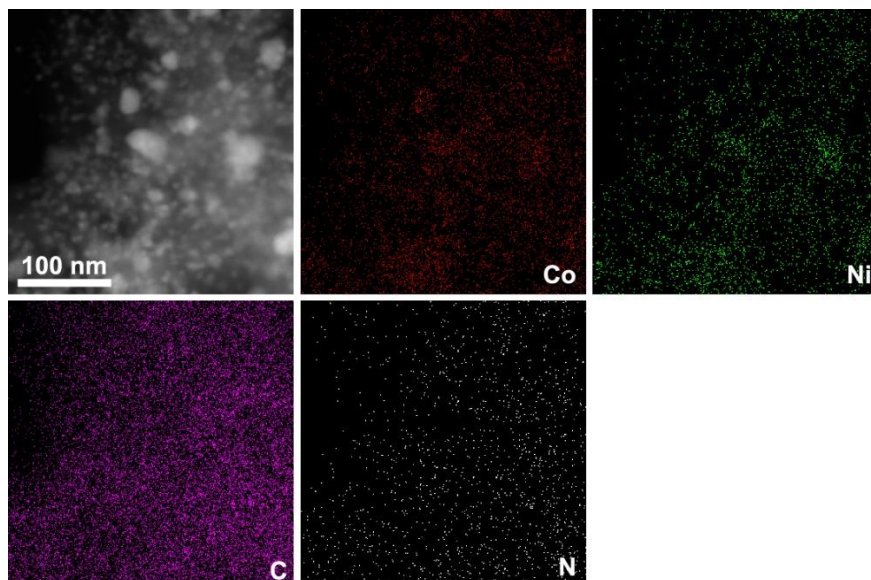
Figure 9.28. Elemental mapping of CoNi@C sample prepared with N-doping in carbon matrix. These results show the homogeneous dispersion of Co and Ni in bimetallic CoNi nanoparticles and the presence of N in the carbon matrix.
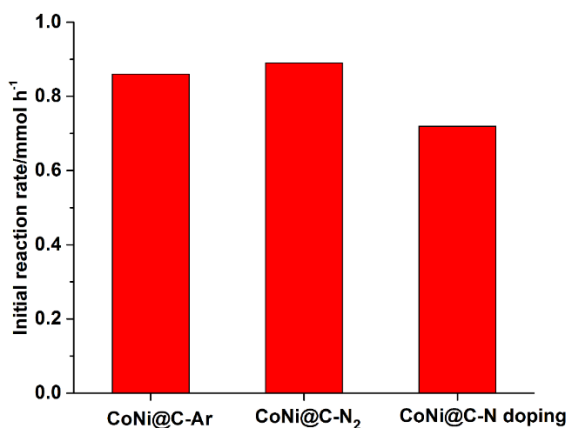

Figure 9.29. Initial reaction rates of bimetallic CoNi@C NPs prepared by calcination in Ar and N_2 atmosphere as well as the CoNi@C sample with nitrogen doping. Reaction conditions: 0.5 mmol 3-nitrostyrene, 15 mg solid sample as the catalyst, 2 mL toluene as solvent, 120 °C. The catalyst has been pre-reduced by H_2 at 160 °C.

3.4 Possible role of nitrogen for NNM hydrogenation catalysts

In some reported catalysts, it is claimed that the introduction of nitrogen into the carbon matrix plays a key role to give non-noble metal nanoparticles with high activity.[10,24] However, in our preparation method, though N-containing ligand was not used, we have still achieved high catalytic activity for the chemoselective hydrogenation of nitroarenes. Nevertheless, for the aforementioned samples, they were prepared by calcination in N_2, which may introduce tiny amount of N species into the sample at high temperature. In fact, we observed a nitrogen/metal ratio of ~0.3 in the CoNi@C sample by XPS, which is much lower than those samples prepared in the presence of N-containing ligands in the literature (with a nitrogen/metal ratio around 4).[10,12,13] Nevertheless, to check the possible influences of nitrogen present in the sample, we have also prepared CoNi@C NPs by calcination in Ar instead of N_2. In that case, no nitrogen was detected in the final sample by XPS. Morphological characterizations (see **Figure 9.26** and **Figure 9.27**) show that the sample obtained by calcination in N_2 and Ar have very similar morphology and both samples contain alloyed CoNi bimetallic nanoparticles covered by thin carbon layers. Besides, we have also prepared a sample with nitrogen-doping in the carbon matrix by introducing urea in the synthesis as nitrogen source. As shown in **Figure 9.28**, in that sample, bimetallic CoNi NPs are covered by N-doped carbon (named as CoNi@C-N doping). The catalytic performances of these three samples were tested for hydrogenation of 3-nitrostyrene. As can be seen in **Figure 9.29**, CoNi@C-Ar and CoNi@C-N_2 sample show practically the same activity while the CoNi@C-N sample shows a slightly lower activity.
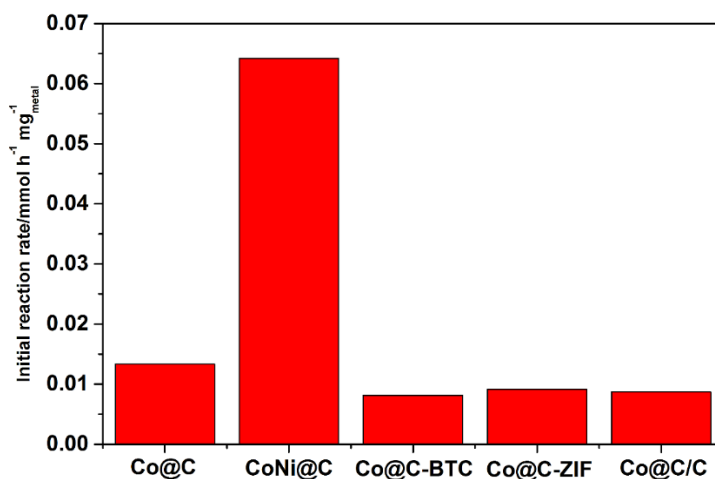
Figure 9.30. Comparison of the mass activity of non-noble metal NPs (NNM@C) prepared from different methods. The initial reaction rate is calculated at low conversion. The reaction condition is the same for all tests: 0.5 mmol 3-nitrostyrene, 120 °C, 2 mL toluene as solvent and 7 bar of H_2.
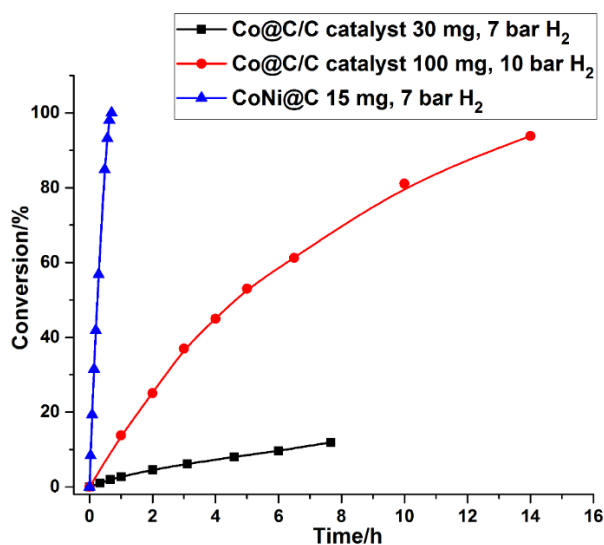

Figure 9.31. Comparison between Co@C and CoNi@C NPs prepared by carbon-coating method and supported Co@C/C prepared according to the literature. In all the tests, the catalysts have been pre-reduced by H_2 at 160 °C.

(a) The profiles of conversion with reaction time, (b) initial reaction rate normalized based on the mass of metal in the catalyst.
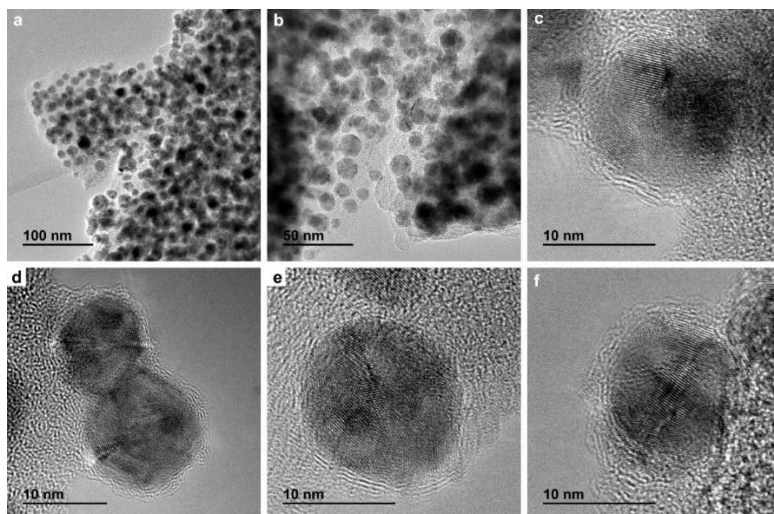

Figure 9.32. TEM and HRTEM images of Co@C NPs (named as Co@C-BTC) prepared from the thermal decomposition of Co-BTC metal-organic framework. Most of Co nanoparticles are covered by thin carbon layers.
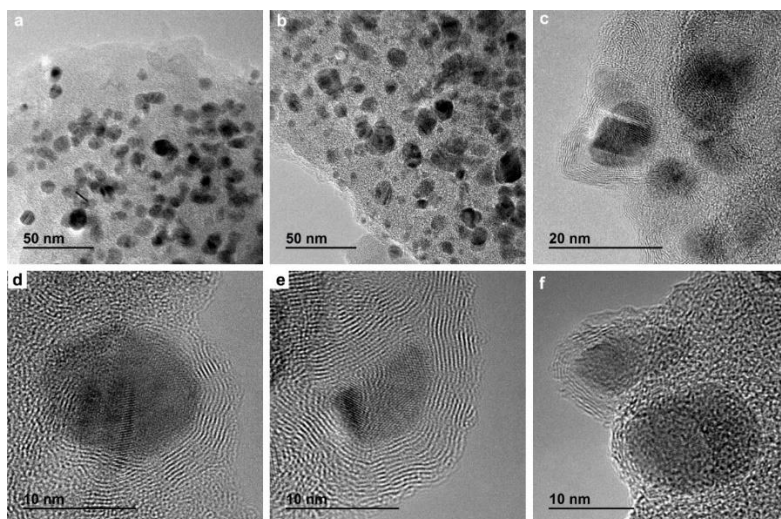

Figure 9.33. TEM and HRTEM images of Co@C NPs (named as Co@C-ZIF) prepared from the thermal decomposition of Co-ZIF metal-organic framework. Most of Co nanoparticles are covered by thin carbon layers.

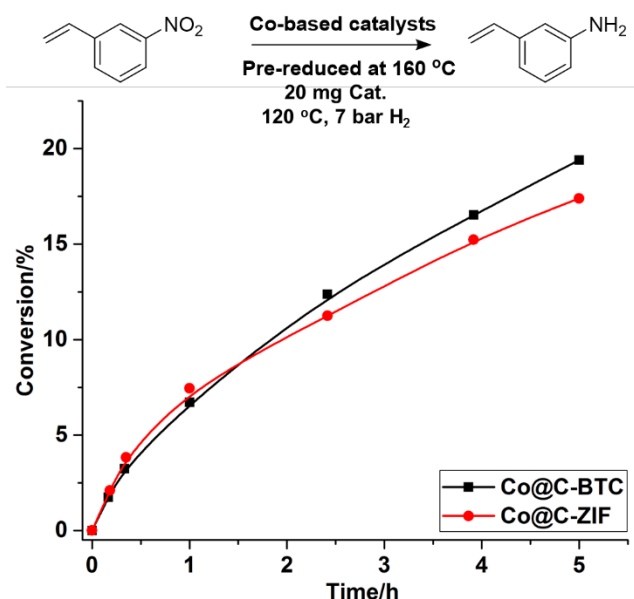**Figure 9.34.** Catalytic tests of Co@C-BTC and Co@C-ZIF samples. Both samples are pre-reduced by H_2 at 160 °C before the catalytic tests.
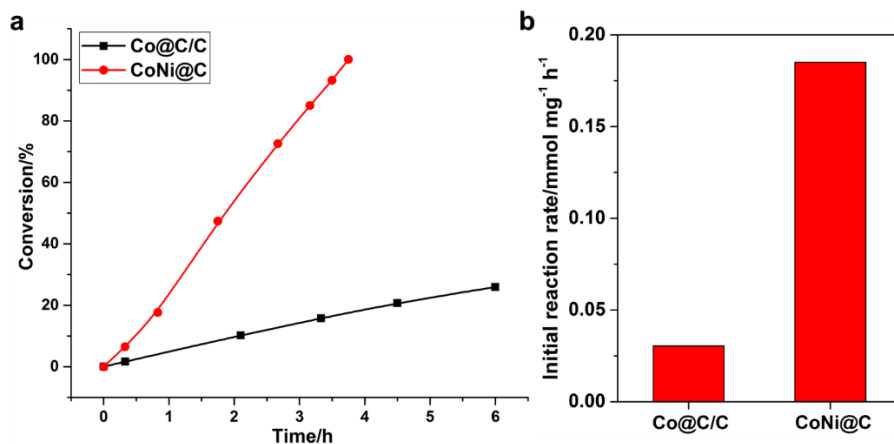

Figure 9.35. Selective hydrogenation of 3-nitrostyrene with CoNi@C and Co@C/C catalysts under the same conditions. Reaction conditions: 2 mL THF and 100 µL H_2O as solvent, 110 °C, 10 bar of H_2, substrate/metal=40. The catalyst has been pre-reduced by H_2 at 150 °C.

Table 9.2. Comparison between CoNi@C NPs and the catalysts in previous works for hydrogenation of nitrostyrene.

Catalyst	Substrate/ metal Catalyst	Temp./°C	Solvent	Time/h	H_2/bar	Yield/%	Reference
Co@C/C	100	110	$THF-H_2O$	6	50	91	Ref. 1
CoNi@C	40	110	$THF-H_2O$	3.75	10	95	This work
Co@C/SiO$_2$	20	110	$THF-H_2O$	15	50	82	Ref. 2
Co@C/CNT	12.5	110	Ethanol	12	30	98	Ref. 3
Co@C/C	10	120	THF	4	30	95	Ref. 4

References in Table 9.2.

[1] Westerhaus, F. A.; Jagadeesh, R. V.; Wienhofer, G.; Pohl, M. M.; Radnik, J.; Surkus, A. E.; Rabeah, J.; Junge, K.; Junge, H.; Nielsen, M.; Bruckner, A.; Beller, M. *Nature Chem.* **2013**, *5*, 537.

[2] Schwob, T.; Kempe, R. *Angew. Chem. Int. Ed.* **2016**, *55*, 15175.

[3] Wei, Z.; Wang, J.; Mao, S.; Su, D.; Jin, H.; Wang, Y.; Xu, F.; Li, H.; Wang, Y. *ACS Catal.* **2015**, *5*, 4783.

[4] Chen, B.; Li, F.; Huang, Z.; Yuan, G. *ChemCatChem* **2016**, *8*, 1132.

3.5 Comparison of non-noble metal catalysts prepared by different methods

Nevertheless, since it has recently been reported that a heterogeneous Co catalyst prepared from decomposition of metal-organic complexes is active and selective for the hydrogenation of 3-nitrostyrene,[10,25] we have prepared those catalysts following the reported procedure. It is important to remark that, in the reported works, high pressure of H_2 (50 bar) and $THF-H_2O$ as solvent were required, while our catalysts already work with 7 bar of H_2 in toluene. Moreover, we have also prepared Co nanoparticles supported on carbon (named as Co@C/C) according to the reported work and its activity and selectivity has been tested under the milder conditions required by our catalysts. Though the crystalline sizes of metal nanoparticles in the samples prepared according to literature are smaller than those prepared by our methodology, we have

compared the activity on the basis of mass of metal weight introduced in the catalytic test, knowing that the TOFs of our catalysts will be underevaluated.

As it is shown in **Figure 9.30**, Co@C and CoNi@C NPs prepared by our carbon-coating method give higher activity than other previously reported Co@C/C catalyst (also see **Figure 9.31**). For further comparison, we have also prepared here two Co@C catalysts by decomposition of a metal-organic framework (MOF) precursor (i.e. Co@C-BTC without N-containing organic linkers in the MOF precursor and Co@C-ZIF with N-containing organic linkers in the MOF precursor).[23,26] From TEM and HRTEM images (see **Figure 9.32** and **Figure 9.33**), it can be seen that, those Co NPs are encapsulated in the carbon matrix. As shown in **Figure 9.34**, both Co@C-BTC and Co@C-ZIF show low activity for hydrogenation of 3-nitrostyrene under the same conditions as Co@C NPs prepared in this work by carbon-coating method. And the similar performance of Co@C-BTC and Co@C-ZIF samples indicates that the introduction of N in the carbon matrix doesn't show obvious advantage for improving the activity of Co@C NPs.

After presenting that the CoNi@C was more active under our reaction conditions, we also tested CoNi@C NPs with a high substrate/catalyst ratio for hydrogenation of 3-nitrostyrene using similar conditions to the previously reported works. As shown in **Figure 9.35**, CoNi@C sample still gives ca. 6 times higher activity than the reported Co@C/C catalyst under the same reaction conditions (110 °C, 10 bar of H_2 in THF-H_2O solvent) with the same loading amount of metal catalyst (molar ratio substrate/metal is 40). In summary, the bimetallic catalyst prepared with the present carbon-coating methodology shows a significant advantage for performing the chemoselective hydrogenation under milder conditions (much lower pressure and shorter reaction time) than any of the catalysts reported before (see **Table 9.2**), without requiring the so-claimed metal-N interaction to achieve high activity and selectivity.
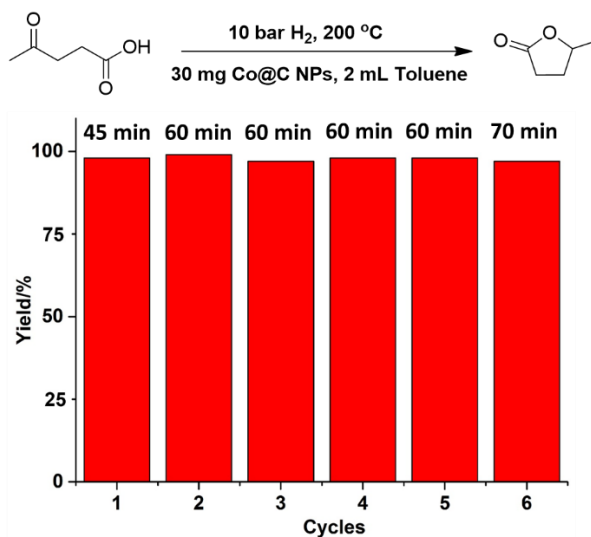
Figure 9.36. Hydrogenation of levulinic acid to γ-valerolactone by Co@C NPs and the stability tests. Reaction conditions: 1.0 mmol γ-valerolactone, 200 ºC, 2 mL toluene as solvent and 10 bar of H₂.
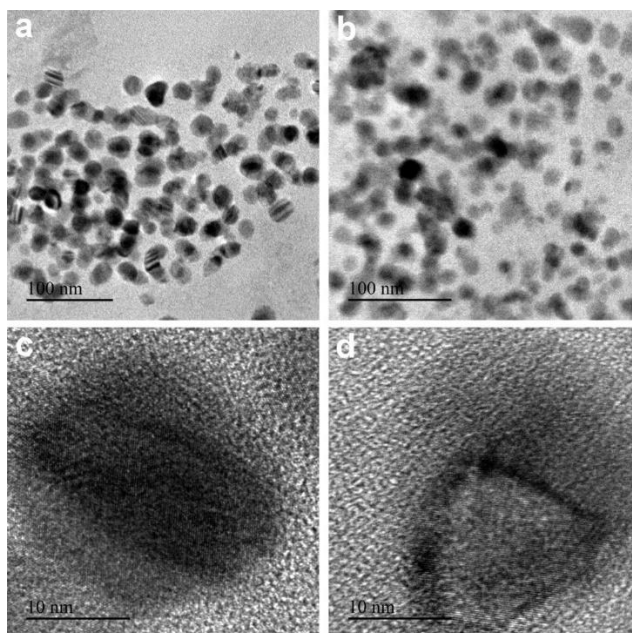

Figure 9.37. TEM images of Co@C NPs after hydrogenation of levulinic acid.

379

3.6 Application of Co@C NPs for hydrogenation of levulinic acid

The catalytic behavior of NNM@C NPs was also studied for hydrogenation of levulinic acid to γ-valerolactone, which is an important model reaction in the field of biomass to chemicals. As can be seen in **Figure 9.36**, the Co@C NPs can work at 200 °C with 10 bar of H_2, which are milder than those reports using Au-, Ru- and Cu-based catalysts.[27-29] Over 98% yield of γ-valerolactone was obtained within 45 min in the first run. The stability of non-noble metal catalysts is an important issue for the hydrogenation of levulinic acid. A significant leaching of Cu into the solution can be observed on supported Cu catalysts.[30] Besides, Shimizu et al. reported the application of Ni-MoOx/C catalyst for the hydrogenation levulinic acid under mild conditions.[31] However, the reported Ni-MoOx/C catalyst deactivated after the first use. In the case of Co@C NPs, after the first use, the solid catalyst can be easily recycled and used again after simply washing with acetone and toluene. Although the reaction rate decrease, 98% yield can still be obtained when prolonging reaction time to 1 h. Further recycle tests show that the activity can be further maintained for at least 5 cycles without obvious deactivation. The morphology of Co@C NPs after the hydrogenation of levulinic acid reaction is also checked by TEM. As one can see in **Figure 9.37**, monodispersed Co NPs are preserved after the reaction, indicating the chemical stability of Co@C NPs during the hydrogenation of levulinic acid. Future works on developing more efficient and stable mono and bimetallic NNM NPs for hydrogenation of levulinic acid and other reactions are undergoing in our laboratory.

4   Conclusions

In this work, we demonstrate a facile method to prepare monometallic and bimetallic NPs via a simple carbon coating process. Bimetallic CoNi NPs show significantly higher activity than monometallic Co and maintain high selectivity in chemoselective hydrogenation of nitroarenes. In addition, we also show that these materials can be promising catalyst for other reactions like hydrogenation of levulinic acid to γ-valerolactone. Our new method can also be a general method to prepare non-noble metal nanoparticles for heterogeneous catalytic applications and the results presented here also provide

new insights for rational design of non-noble metal nanoparticulate catalysts as substitute of noble metal catalysts.

References

(1) Principles and Practice of Heterogeneous Catalysis, 2nd Edition, Thomas, J.M.; Thomas, W.J. (Eds.), Wiley-VCH, 2014.

(2) Singh, S. K.; Singh, A. K.; Aranishi, K.; Xu, Q. *J. Am. Chem. Soc.* **2011,** *133*, 19638-19641.

(3) Wang, M.-Q.; Yang, W.-H.; Wang, H.-H.; Chen, C.; Zhou, Z.-Y.; Sun, S.-G. *ACS Catal.* **2014,** *4*, 3928-3936.

(4) Shown, I.; Hsu, H. C.; Chang, Y. C.; Lin, C. H.; Roy, P. K.; Ganguly, A.; Wang, C. H.; Chang, J. K.; Wu, C. I.; Chen, L. C.et al. *Nano Lett.* **2014,** *14*, 6097-6103.

(5) Wu, L.; Li, Q.; Wu, C. H.; Zhu, H.; Mendoza-Garcia, A.; Shen, B.; Guo, J.; Sun, S. *J. Am. Chem. Soc.* **2015,** *137*, 7071-7074.

(6) Iablokov, V.; Beaumont, S. K.; Alayoglu, S.; Pushkarev, V. V.; Specht, C.; Gao, J.; Alivisatos, A. P.; Kruse, N.; Somorjai, G. A. *Nano Lett.* **2012,** *12*, 3091-3096.

(7) Galvez, N.; Valero, E.; Ceolin, M.; Trasobares, S.; Lopez-Haro, M.; Calvino, J. J.; Dominguez-Vera, J. M. *Inorg. Chem.* **2010,** *49*, 1705-1711.

(8) Alayoglu, S.; Beaumont, S. K.; Melaet, G.; Lindeman, A. E.; Musselwhite, N.; Brooks, C. J.; Marcus, M. A.; Guo, J.; Liu, Z.; Kruse, N.et al. *J. Phys. Chem. C* **2013,** *117*, 21803-21809.

(9) Beaumont, S. K.; Alayoglu, S.; Pushkarev, V. V.; Liu, Z.; Kruse, N.; Somorjai, G. A. *Faraday Discussions* **2013,** *162*, 31.

(10) Westerhaus, F. A.; Jagadeesh, R. V.; Wienhofer, G.; Pohl, M. M.; Radnik, J.; Surkus, A. E.; Rabeah, J.; Junge, K.; Junge, H.; Nielsen, M.et al. *Nat. Chem.* **2013,** *5* (6), 537-543.

(11) Zhong, W.; Liu, H.; Bai, C.; Liao, S.; Li, Y. *ACS Catal.* **2015,** *5*, 1850-1856.

(12) Jagadeesh, R. V.; Surkus, A. E.; Junge, H.; Pohl, M. M.; Radnik, J.; Rabeah, J.; Huan, H.; Schunemann, V.; Bruckner, A.; Beller, M. *Science* **2013,** *342*, 1073-1076.

(13) Liu, W.; Zhang, L.; Yan, W.; Liu, X.; Yang, X.; Miao, S.; Wang, W.; Wang, A.; Zhang, T. *Chem. Sci.* **2016,** *7*, 5758-5764.

(14) Xie, X.; Li, Y.; Liu, Z. Q.; Haruta, M.; Shen, W. *Nature* **2009,** *458*, 746-749.

(15) Liu, L.; Concepción, P.; Corma, A. *J. Catal.* **2016,** *340*, 1-9.

(16) Serna, P.; Concepción, P.; Corma, A. *J. Catal.* **2009,** *265*, 19-25.

(17) Biesinger, M. C.; Payne, B. P.; Grosvenor, A. P.; Lau, L. W. M.; Gerson, A. R.; Smart, R. S. C. *Appl. Surf. Sci.* **2011,** *257*, 2717-2730.

(18) Andonova, S.; de Ávila, C. N.; Arishtirova, K.; Bueno, J. M. C.; Damyanova, S. *Appl. Catal. B: Environ.* **2011,** *105*, 346-360.

(19) Corma, A.; Serna, P.; Concepcion, P.; Calvino, J. J. *J. Am. Chem. Soc.* **2008,** *130*, 8748-8753.

(20) Pisiewicz, S.; Formenti , D.; Surkus, A.-E.; Pohl, M.-M.; Radnik, J.; Junge, K.; Topf, C.; Bachmann, S.; Scalone, M.; Beller, M. *ChemCatChem* **2016,** *8*, 129-134.

(21) Hahn, G.; Ewert, J.-K.; Denner, C.; Tilgner, D.; Kempe, R. *ChemCatChem* **2016,** *8*, 2461-2465.

(22) Hermannsdorfer, J.; Friedrich, M.; Miyajima, N.; Albuquerque, R. Q.; Kummel, S.; Kempe, R. *Angew. Chem. Int. Ed.* **2012,** *51*, 11473-11477.

(23) Serna, P.; Corma, A. *ACS Catal.* **2015,** *5*, 7114-7121.

(24) Wang, X.; Li, Y. *J. Mol. Catal. A: Chem.* **2016,** *420*, 56-65.

(25) Schwob, T.; Kempe, R. *Angew. Chem. Int. Ed.* **2016,** *55*, 15175-15179.

(26) Shen, K.; Chen, X.; Chen, J.; Li, Y. *ACS Catal* **2016,** *6*, 5887-5903.

(27) Xu, Q.; Li, X.; Pan, T.; Yu, C.; Deng, J.; Guo, Q.; Fu, Y. *Green Chem.* **2016,** *18*, 1287-1294.

(28) Luo, W.; Sankar, M.; Beale, A. M.; He, Q.; Kiely, C. J.; Bruijnincx, P. C.; Weckhuysen, B. M. *Nat. Commun.* **2015,** *6*, 6540.

(29) Jones, D. R.; Iqbal, S.; Ishikawa, S.; Reece, C.; Thomas, L. M.; Miedziak, P. J.; Morgan, D. J.; Edwards, J. K.; Bartley, J. K.; Willock, D. J.et al. *Catal. Sci. Technol.* **2016,** *6*, 6022-6030.

(30) Hengne, A. M.; Rode, C. V. *Green Chem.* **2012,** *14* (4), 1064.

(31) Shimizu, K.-i.; Kanno, S.; Kon, K. *Green Chem.* **2014,** *16* (8), 3899.

Chapter 10

Directing the chemoselective hydrogenation of nitroarenes into the corresponding aromatic azoxy and azo compounds with non-noble metal catalysts
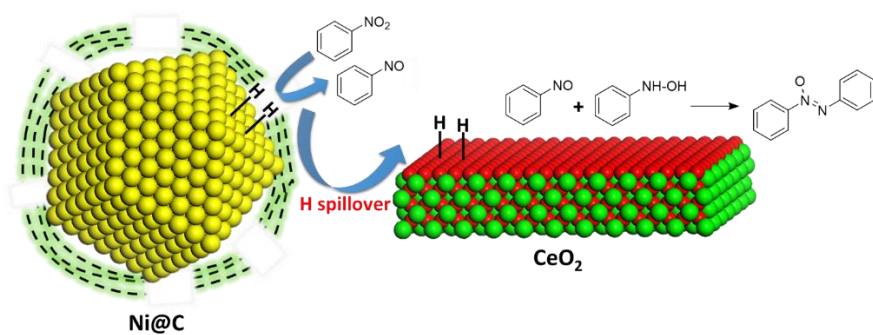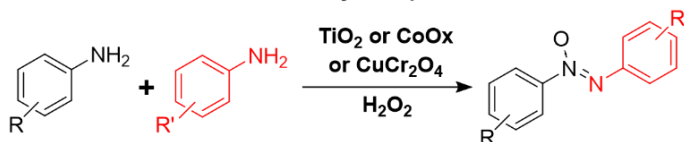
Abstract

   The hydrogenation of nitroaromatics is an important reaction for fine chemistry. Various products can be obtained, depending on the catalyst and reaction conditions. Among the products, aromatic azoxy compounds have wide applications and they can be prepared by stoichiometric reactions or catalytic reactions with H_2O_2 or N_2H_4 as oxidant or reductant. In this work, we will present a new reaction pathway different to previously found on noble metals (such as Au, Pt, etc.) for the hydrogenation of nitroaromatics on Ni nanoparticles by combining theoretical calculations and experimental results. It has been found that, nitrosobenzene is formed as a primary reaction intermediate, and the rate determining step of the process is the hydrogen transfer to the highly stable Ph-N species. Following that discovery, we have designed a bifunctional catalyst for the direct chemoselective hydrogenation of nitroarenes into aromatic azoxy compounds under base-free mild conditions with the combination of non-noble Ni@C nanoparticles and CeO_2. The catalytic performance of Ni@C-CeO_2 catalyst surpasses the state-of-art Au/CeO_2 catalyst for the direct production of azoxybenzene from nitrobenzene. By means of kinetic and spectroscopic results, a bifunctional mechanism is proposed for the reaction on the Ni@C-CeO_2 catalyst with the above catalytic system, the hydrogenation of nitrobenzene can be stopped on the formation of azoxybenzene with >95% conversion and >93% selectivity, or can be further driven to the formation of azobenzene with >85% selectivity. It is therefore shown that, by making a bifunctional catalyst with a non-noble metal, one can achieve chemoselective hydrogenation of nitroarenes not only to anilines, but also to corresponding azoxy and azo compounds.
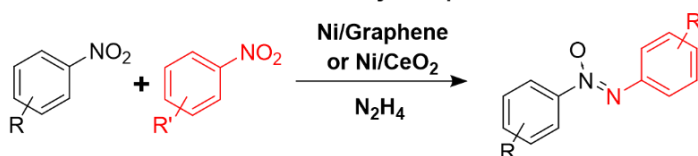
1. Introduction

   Selecting the desired reaction pathway among several possible ones is a key objective for heterogeneous catalysis.[1-3] It has been demonstrated in the literature that, by tuning the adsorption properties of molecules on catalyst surface and the formation of reaction intermediates, it is possible to achieve unique chemoselectivities by solid catalysts.[4-7] Moreover, by preparation of multifunctional catalysts, transformations which require multiple steps can be

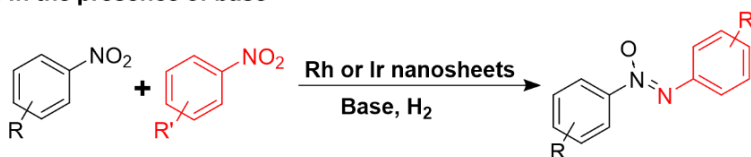achieved in one-pot process, which can reduce the energy consumption and improve the efficiency of the global process.[8-10]
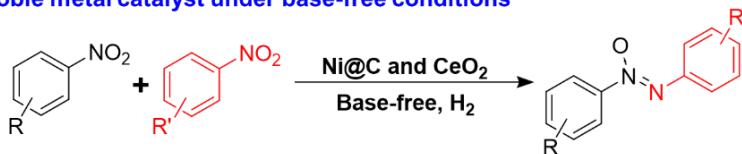

Figure 10.1. Catalytic routes for the preparation of aromatic azoxy compounds by different approaches, including selective oxidation of anilines with H_2O_2 (a), reduction of nitroarenes with N_2H_4 (b), hydrogenation of nitroarenes with H_2 by noble metal catalysts in the presence of base (c) and direct hydrogenation of nitroarenes with H_2 by non-noble metal catalysts under base-free conditions (d).

Aromatic azoxy compounds are important intermediate compounds with wide application as chemical stabilizers, polymerization inhibitors, dyes, pigments, as well as precursors for materials used in electronic displays and pharmaceuticals.[11,12] Moreover, aromatic azoxy compounds can be further transformed into hydroxyazo compounds through the Wallach rearrangement.[13] Conventionally, aromatic azoxy compounds are prepared by stochiometric

reactions (such as the condensation between hydroxylamine and nitrosobenzene), which is less atom-economic and may produce hazardous bi-products.[14] Therefore, In the last decade, some catalytic processes have been developed and aromatic azoxy compounds can be obtained by the oxidative coupling of anilines using metal oxides as the catalyst and H_2O_2 as the oxidant (Figure 10.1a).[15,16] Recently, it has also been reported that aromatic azoxy compounds can also be obtained through the reduction of nitroarenes by hydrazine (see Figure 10.1b).[17,18] Compared with conventional processes by stochiometric reactions, these heterogeneous catalytic processes are more efficient and sustainable. However, the use of reactants, such as H_2O_2 and hydrazine, is still required.
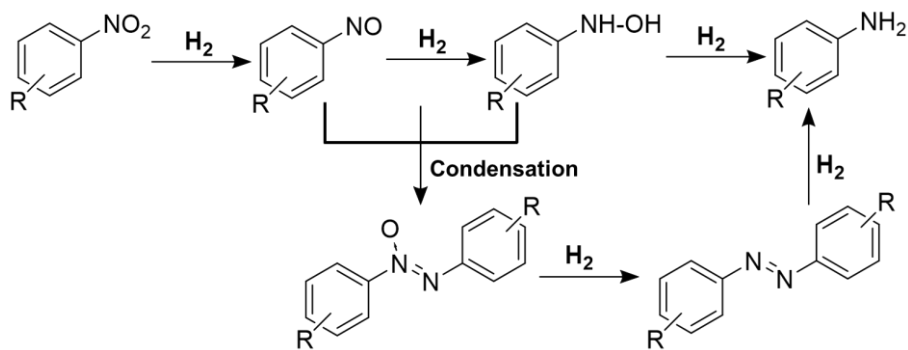

Figure 10.2. Catalytic hydrogenation of nitroarenes into different products via different routes.

Considering the reaction pathways for hydrogenation of nitroarenes into different products (see Figure 10.2), it should be possible to achieve the formation of azoxy and azo products if the reaction goes through the condensation route (shown in Figure 10.2). Indeed, in the presence of a base, the intermediates formed during the hydrogenation of nitroarenes can be transformed into azoxy and azo products through the condensation route, as has been reported for the hydrogenation of nitrobenzene to azoxybenzene in the presence of n-butylamine as base (see Figure 10.1c).[19]

In recent years, the development of non-noble metal catalysts as the substitutes for noble metal catalysts is emerging in the field of heterogeneous catalysis.[20] For chemoselective hydrogenation reactions, it has been reported

that Co-, Fe- and Ni-based catalysts show promising catalytic performances for hydrogenation of nitroarenes to anilines.[21-23] Recently, by studying the reaction mechanism and identification of the active sites, non-noble monometallic and bimetallic NPs have been prepared and show better catalytic performance than the state-of-art heterogeneous Au catalysts under the same reaction conditions for chemoselective hydrogenation of nitroarenes to corresponding anilines.[24,25] In this work, we show that by combining Ni@C NPs and CeO_2 NPs, a bifunctional catalytic system can be prepared for the direct chemoselective hydrogenation of nitroarenes into corresponding azoxy compounds with high yields under base-free mild conditions. By means of kinetic and spectroscopic studies, we discuss the role of the two components in the Ni@C-CeO_2 bifunctional catalyst and how they can interplay. It is of most interest that, based on the nanoparticulate Ni@C catalyst, it is possible to chemoselectively direct the hydrogenation of nitroarenes into corresponding azoxy, azo or aniline products.

2. Experiments

2.1 Synthesis of non-noble metal nanoparticles

Co@C and Ni@C nanoparticles were synthesized by a carbon-coating method, which was described in our recent work.[25]

CeO_2@C nanoparticles were prepared by a similar carbon-coating approach. 1.0 g of CeO_2 nanoparticles, 720 mg of glucose and 20 mL distilled water was mixed to a suspension with the help of ultrasonication. The suspension was then transferred to an autoclave and placed in an oven at 175 °C for 18 h. After the hydrothermal treatment, the solid product was collected by filtration and washed with water and acetone. The dried solid was then annealed in flow N_2 at 600 °C for 2 h with a ramp rate of 10 °C/min from room temperature to 600 °C. After the high-temperature annealing, the sample was cooled down to room temperature in N_2 flow and stored in a glass vial in ambient environment.

Synthesis of Cu@C and Fe@C nanoparticles.

We have also tried to prepare Cu@C and Fe@C nanoparticles by the above-mentioned carbon-coating process. However, that method is not applicable to

Cu and Fe. Only bulk Cu and Fe (with particle size larger than 1 μm) were obtained. Therefore, Cu@C and Fe@C nanoparticles were synthesized by reducing metal-EDTA complex, which was described in our recent work.[24] The Cu-EDTA complex were prepared through a hydrothermal process. First, 6.98 g $Cu(NO_3)_2$, 4.47 g Na_2EDTA and 0.96 g NaOH are dissolved in 20 mL H_2O. Then, 10 mL methanol was added to the mixed aqueous solution temperature under stirring at room temperature. After the formation of a homogeneous solution, 23 mL of the purple solution was transferred into a 35 mL stainless steel autoclave followed by static hydrothermal processing at 200 °C for 24 h. After cooling to room temperature, the generated precipitates were filtered and washed with deionized water and acetone several times followed by drying at 100 °C in air for 16 h. The obtained complex was denoted as Co-EDTA. Then, Cu@C NPs were prepared by reduction of Co-EDTA in H_2 (50 mL/min) at 450 °C for 2 h with a ramp rate of 10 °C/min from room temperature to 450 °C. After the H_2 reduction process at 450 °C, the sample was cooled down to room temperature in H_2 atmosphere. Then the black solid product was stored in a glass vial in ambient environment.

Fe-EDTA complex was prepared by the similar method. $Fe(NO_3)_3 \cdot 9H_2O$ was used as the precursor. The other experimental procedure is the same.

Synthesis of Ni-CeO$_2$-C nanocomposites.

The Ni-CeO$_2$-C nanocomposites can be prepared by the carbon-coating process in the presence of CeO_2 nanoparticles. 1.0 g CeO_2 nanoparticles, 720 mg of glucose, 0.5 g of Ni precipitate (obtained from the precipitation of $Ni(Ac)_2$ and sodium carbonate in glycol) was mixed with 20 mL water to form a homogeneous suspension with the help of ultrasonication. The suspension was then transferred to an autoclave and placed in an oven at 175 °C for 18 h. After the hydrothermal treatment, the solid product was collected by filtration and washed with water and acetone. The dried solid was then annealed in flow N_2 at 600 °C for 2 h with a ramp rate of 10 °C/min from room temperature to 600 °C. After the high-temperature annealing, the sample was cooled down to room temperature in N_2 flow and stored in a glass vial in ambient environment.

2.2 Characterizations

Powder X-ray diffraction (XRD) was performed with a HTPhilips X'Pert MPD diffractometer equipped with a PW3050 goniometer using Cu Kα radiation and a multisampling handler.

Raman spectra were recorded at ambient temperature with a 785 nm HPNIR excitation laser on a Renishaw Raman Spectrometer ("Reflex") equipped with an Olympus microscope and a CCD detector. The laser power on the sample was 15mW and a total of 20 acquisitions were taken for each spectra.

Samples for electron microscopy studies were prepared by dropping the suspension of solid sample in CH_2Cl_2 directly onto holey-carbon coated copper grids. All the measurements were performed in a JEOL 2100F microscope operating at 200 kV both in transmission (TEM) and scanning-transmission modes (STEM). STEM images were obtained using a High Angle Annular Dark Field detector (HAADF), which allows Z-contrast imaging.

The amount of exposed surface Ni atoms in the Ni@C catalyst was determined by H_2 chemisorption at 100 °C in an ASAP 2010C Micromeritics equipment by extrapolating the total gas uptakes in the adsorption isotherms at zero pressure. Prior to the measurements the sample was reduced under flowing pure H_2 at 400 °C. The percentage of exposed Ni atoms in the Ni@C NPs was estimated from the total amount of chemisorbed H_2 assuming an adsorption stoichiometry H_2/Ni of 1.

The FTIR spectra were collected with a Bruker Vertex 70 spectrometer equipped with a DTGS detector (4 cm^{-1} resolution, 32 scans). An IR cell allowing in situ treatments in controlled atmosphere and temperature from 25 to 500 ºC has been connected to a vacuum system with gas dosing facility. Self-supporting pellets (ca. 10 mg cm^{-2}) were prepared from the sample powders and treated at 200 ºC in hydrogen flow (20 ml min^{-1}) for 2 h followed by evacuation at 10^{-4} mbar at 250 ºC for 1h. In the case of the CeO_2 sample only activation under vacuum at 120ºC have been performed. After activation the samples were cooled down to 25 ºC under dynamic vacuum conditions followed by nitrobenzene dosing at 1.5 mbar. Once the physically absorbed and/or gas phase nitrobenzene was removed in evacuation at 25 ºC, H_2 was co-adsorbed at pressures between 0.4 mbar and 40 mbar. The IR spectra were recorded after 35 min at a specific reaction temperature (from 25 to 150 ºC).

Additional experiments were performed at different reaction times (from 20 min to 180 min) at each temperature.

X-ray photoelectron spectra of the catalysts were recorded with a SPECS spectrometer equipped with a Phoibos 150MCD-9 multichannel analyzer using non-monochromatic AlKα (1486.6 eV) irradiation. Spectra were recorded using analyser pass energy of 30 eV, an X-ray power of 100W and under an operating pressure of 10^{-9} mbar. The sample was pre-reduced by H_2 in a pre-treatment chamber at 120 or 200 °C and then transferred to analysis chamber for the XPS measurements. Peak intensities have been calculated after nonlinear Shirley-type background subtraction and corrected by the transmission function of the spectrometer. During data processing of the XPS spectra, binding energy (BE) values were referenced to C1s peak (284.5 eV) for the Ni@C samples and to the Ce3d5/2 peak at 882.8eV for the Ni@C-CeO$_2$ samples. CasaXPS software has been used for spectra treatment.

2.3 Catalytic tests

The chemoselective hydrogenation of nitroarenes was performed in batch reactors. The reactant, internal standard (hexadodecane), solvent (toluene), powder catalyst as well as a magnetic bar were added into the batch reactor. After the reactor was sealed, air was purged out from the reactor by flushing two times with 10 bar of hydrogen. Then the autoclave was pressurized with H_2 to the corresponding pressure. The stirring speed is kept at 1100 rpm and the size of the catalyst powder is below 0.05 mm to avoid either external or internal diffusion limitation. Finally, the batch reactor was heated to the target temperature. For the kinetic studies, 50 μL of the mixture was taken out for GC analysis at different reaction times. The products were identified by GC-MS.

In some cases, the catalyst was pre-reduced by H_2 at an elevated temperature (150 °C) for a certain time and then cooled down to room temperature. Then nitrobenzene was injected into the batch reactor and the temperature was raised to 120 °C again for the hydrogenation reaction test.

3. Results and Discussions
3.1 Theoretical calculations on the reaction mechanism on Ni

We have investigated the reaction pathways of hydrogenation of nitrobenzene and nitrostyrene on Ni surface by DFT calculations. This part of work has already been published in a recent paper.[26] The calculation results (see **Figure 10.3** and **Figure 10.4**) indicate that the reduction of nitrobenzene on Ni(111) follows a four step pathway that includes the formation of nitrosobenzene C_6H_5-NO as a primary reaction intermediate, its subsequent deoxygenation yielding a stable Ph-N species, and two consecutive hydrogen transfers to N to finally produce aniline that are the most energy demanding steps of the reaction. This proposed mechanism implies that the two oxygen atoms initially present in nitrobenzene and detached from the nitro group during the reaction are released to the Ni surface, and they should be removed to close the catalytic cycle and avoid catalyst oxidation and/or deactivation.

The hydrogenation of styrene and nitrobenzene, as substrate models for the reduction of vinyl and nitro groups in nitrostyrene, respectively, have been exhaustively investigated using DFT methods. The first remarkable conclusion obtained is that nitrobenzene hydrogenation follows different pathways on noble and non-noble metals. On Pt(111), hydrogen transfer steps are easier than NO bond breaking and therefore the preferred pathway is Ph-NO_2 → Ph-NOOH → Ph-N(OH)$_2$ → Ph-NOH → Ph-NHOH → Ph-NH → Ph-NH_2, with the selectivity to substituted anilines being usually low due to the instability of the vertical adsorption orientation. In contrast, the oxophylic character of non-noble metals like Ni strongly facilitates the dissociation of the N-O bond, so that the preferred pathway for nitrobenzene reduction on Ni(111) is Ph-NO_2 → Ph-NO → Ph-N → Ph-NH → Ph-NH_2. Nitrosobenzene is formed as a primary reaction intermediate, and the rate determining step of the process is the hydrogen transfer to the highly stable Ph-N species. Both statements have been experimentally confirmed using Ni@C particles as catalyst.
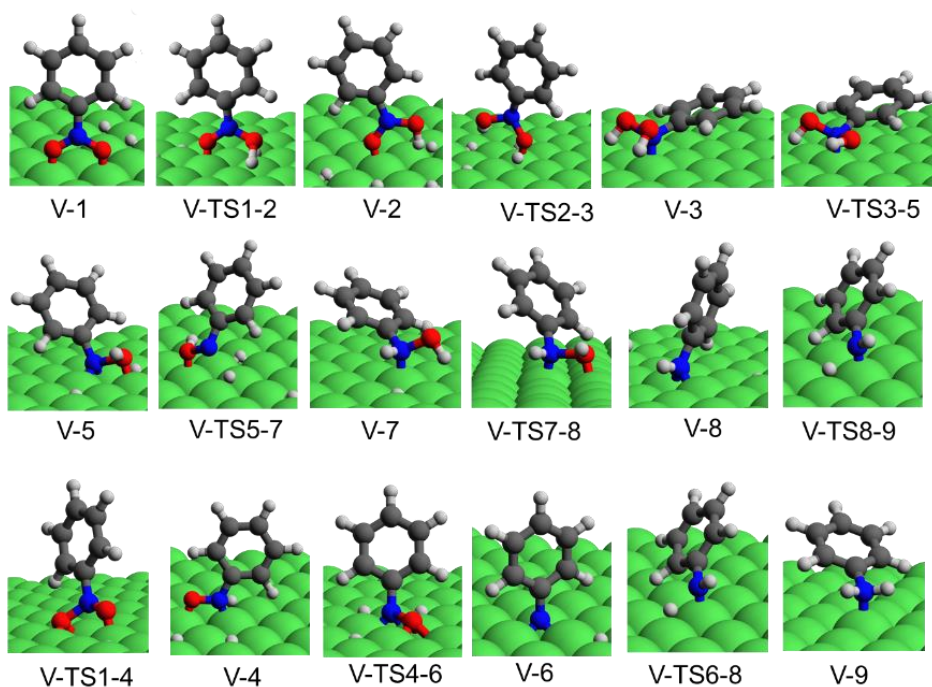
Figure 10.3. Optimized structures of minima and transition states involved in the vertical mechanism of nitrobenzene reduction over Ni(111) surface.
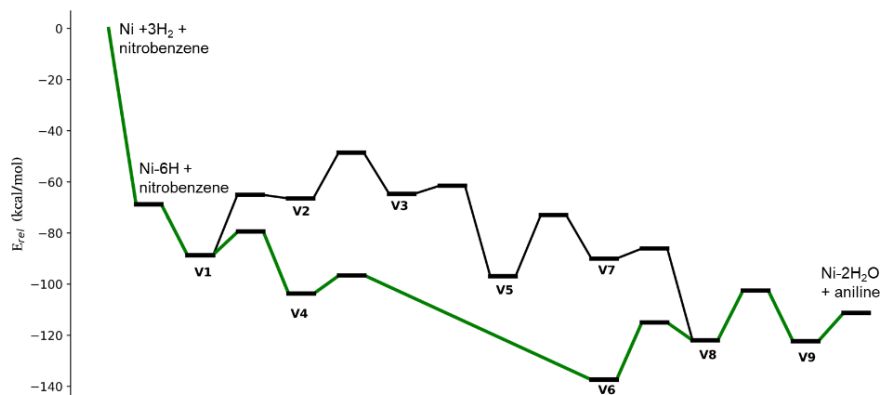

Figure 10.4. Calculated energy profile for the vertical pathways for nitrobenzene reduction over Ni(111) surface. The zero-energy level corresponds to the sum of the ZPE-corrected energies of the Ni slab+3H$_2$+Nitrobenzene.

The theoretical study of the reaction mechanism also shows that the oxygen atoms initially present in nitrobenzene are released to the Ni surface during the reaction. Afterwards, those oxygen atoms absorbed on Ni surface are removed by means of water formation through reaction with activated H_2. Notably, the removal of those surface oxygen species towards formation of water is energy demanding. This provokes a partial oxidation of the Ni surface which, in turn, favors the vertical adsorption of the nitro compound, thus hindering the hydrogenation of other reducible groups present in substituted nitroaromatics and improving the selectivity to substituted anilines. A similar positive effect on selectivity, but detrimental on activity, is caused by the presence of the highly stable Ph-N intermediate, which blocks part of the catalyst surface and makes difficult the parallel adsorption of reactants.

The above calculation results clearly suggest that, the hydrogenation of nitrobenzene follows a different reaction pathway on Ni surface, when compared to that on conventional noble metal surface (Au, Pt, etc).
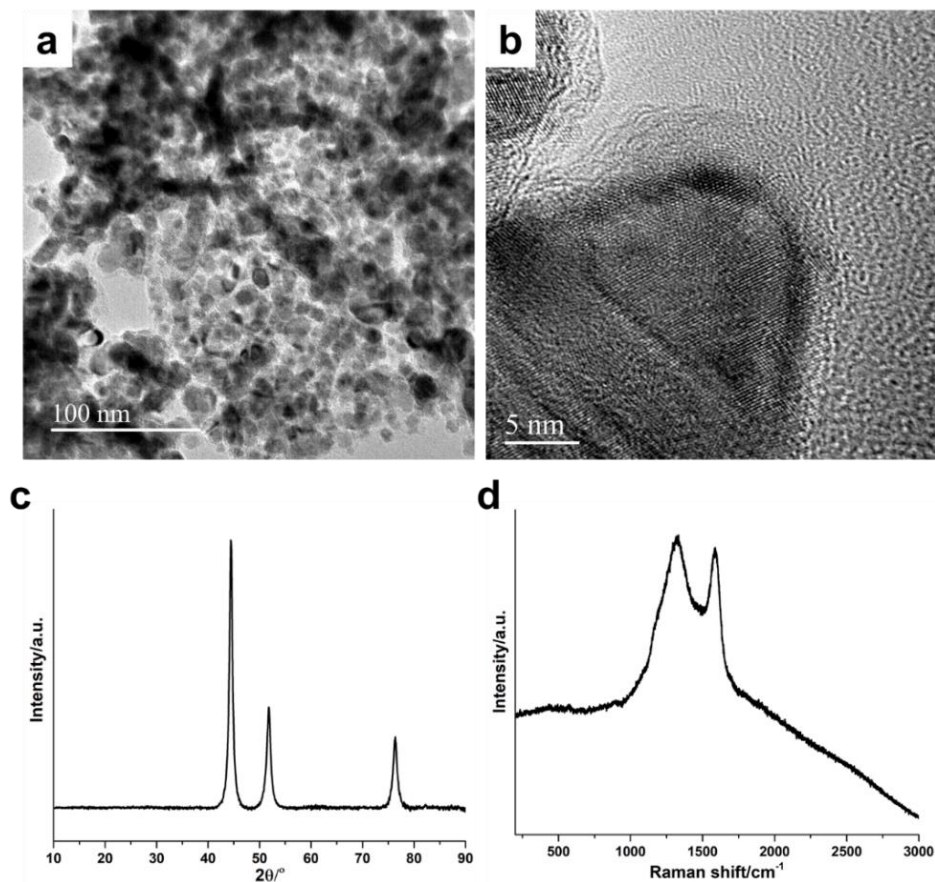
Figure 10.5. **Structural characterization of Ni@C nanoparticles.** (a, b) TEM and high-resolution TEM image. (c) XRD pattern of Ni@C nanoparticles, being the typical diffraction pattern of metallic Ni, without peaks corresponding to NiO or other speices. (d) Raman spectrum of Ni@C nanoparticles, showing the presence of Raman bands corresponding to disordered carbon.

To confirm the proposed mechanism and the trends predicted by the theoretical study, Ni@C nanoparticles are prepared according to the method described in our previous works. As shown in **Figure 10.5**, Ni NPs with average size of ~10 nm are covered by thin carbon layers. Structural characterizations (XRD and Raman) show that the as-prepared sample contains metallic Ni NPs with disorder carbon surrounding them.
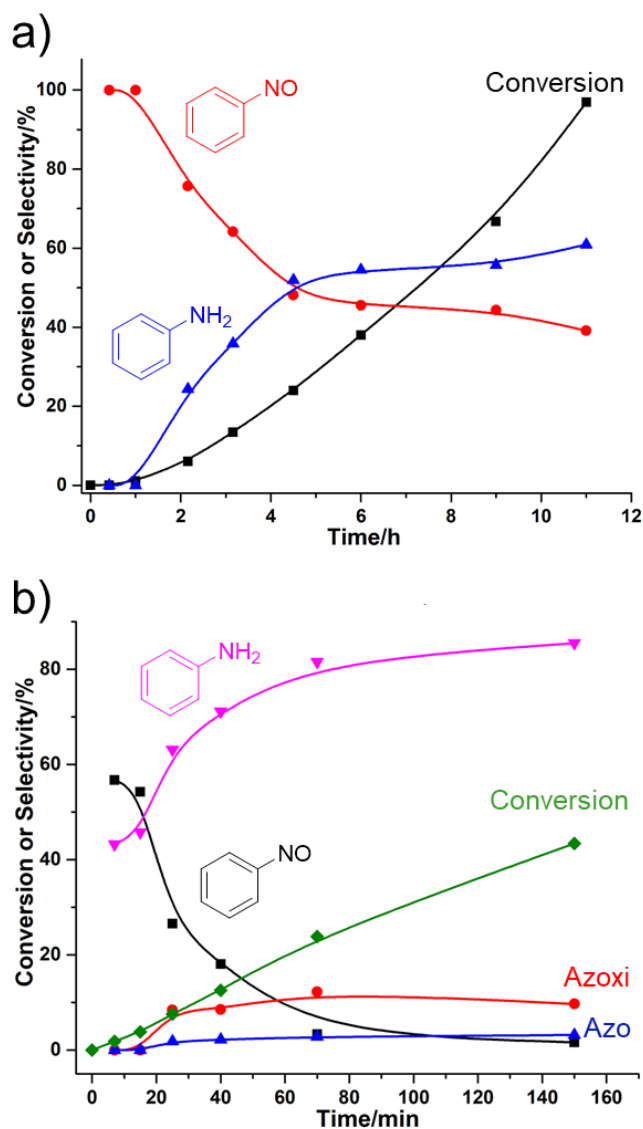
Figure 10.6. Hydrogenation of nitrobenzene with Ni@C catalysts at a) 20 ℃ and b) 120 ℃. Reaction conditions: 5 mg (a) and 1.5 mg (b) Ni@C as catalyst, 1 mmol 3-nitrostyrene, 2 mL toluene as solvent, 10 bar H_2.

The catalytic performance of these Ni@C NPs for hydrogenation of nitrobenzene was measured under different reaction conditions as described in

the Experimental Section. At 20 ºC nitrobenzene reacts slowly producing exclusively nitrosobenzene as a primary product (see **Figure 10.6a**) which, after a period of about one hour, starts to be converted into aniline, as proposed by the DFT study. At full nitrobenzene conversion the selectivity to aniline is only 60%, which means that 40% of nitrosobenzene initially formed has not reacted yet, in agreement with the higher activation barriers obtained for the final hydrogenation steps leading to aniline. Raising the reaction temperature to 120 ºC (see **Figure 10.6b**) accelerates the process (notice the different amount of catalyst used at 20ºC, 5mg, and at 120ºC, 1.5 mg, see caption of Figure 10.8), and the selectivity to nitrosobenzene during the first ten minutes does not exceed 60% while that of aniline is above 40%. Nitrosobenzene is then rapidly converted into aniline, so that at 45% nitrobenzene conversion the concentration of the primary product nitrosobenzene is negligible, and the selectivity to aniline is above 85%. After 7 hours reaction, at full nitrobenzene conversion, the selectivity to aniline is 100% (not shown in the plot in **Figure 10.6b**).

Noticeably, the presence of a non-negligible amount (~10% selectivity at 45% nitrobenzene conversion) of the azoxy compound formed as intermediate in the condensation route (see Scheme 1) is also observed. The observation of a low amount of this compound only at high temperature is in line with the previous indication that the direct route is the preferred, but not the only, pathway for nitrobenzene hydrogenation on Ni(111) surface. This finding allows us to predict that Ni based catalysts could be adequate for producing the most difficult to obtain azoxy compounds in higher selectivity, and those results will be shown later in this Chapter.

3.2.2. Kinetic Study

A kinetic study was performed to determine the rate controlling step of the process and check the hypothesis proposed from the theoretical study. For this purpose, initial reaction rates for nitrobenzene hydrogenation on Ni@C were measured at different H_2 pressures (**Figure 10.7a**) and at different nitrobenzene concentrations (**Figure 10.7b**) working at conversion levels below 15%. According to the Hougen-Watson/Langmuir-Hinselwood formalism, the kinetic behavior of heterogeneously catalyzed reactions can be described by

different reaction rate equations depending on the rate-limiting step of the process. In the case of nitrobenzene hydrogenation on a catalyst containing just one type of active site, and assuming that both reactants adsorb on the catalyst surface before reacting, three different kinetic equations are obtained. If the rate determining step is H_2 dissociation, the reaction rate is described by:

$$r = \frac{k_{H_2} \cdot P_{H_2}}{(1 + K_{NB} \cdot C_{NB})^2}$$

When nitrobenzene adsorption or activation is the step controlling the global process, then the reaction rate equation is:

$$r = \frac{k_{NB} \cdot C_{NB}}{(1 + \sqrt{K_{H_2} \cdot P_{H_2}})}$$

Finally, if the rate determining step is a surface reaction between the two reactants adsorbed on the catalyst, the kinetic equation describing the reaction rate is:

$$= \frac{k \cdot k_{NB} \cdot k_{H_2} \cdot C_{NB} \cdot P_{H_2}}{\left(1 + K_{NB} \cdot C_{NB} + \sqrt{K_{H_2} \cdot P_{H_2}}\right)^3}$$

where P_{H_2} is the H_2 pressure, C_{NB} is the concentration of nitrobenzene, k_{H_2}, k_{NB} and k are the kinetic constants of H_2 dissociation, NB adsorption and surface reaction, respectively, and K_{H_2} and K_{NB} are the equilibrium adsorption constants of H_2 and NB. The graphical representation of these three equations is plotted in **Figure 10.8**.

A non-linear correlation between initial reaction rate and H_2 pressure is observed in **Figure 10.7a**, while **Figure 10.7b** shows an initial fast increase in the reaction rate with increasing NB concentration followed by a slow decrease at higher NB concentration. Comparison of the experimental results in **Figure 10.7** with the graphs in **Figure 10.8** clearly indicate that the rate determining step of the reaction is not H_2 dissociation nor NB adsorption or activation, but a hydrogenation step involving the surface reaction of hydrogen with some adsorbed intermediate. These results agree with the mechanism proposed by the theoretical study, according to which the rate determining step is the hydrogen transfer to the Ph-N intermediate adsorbed on the Ni surface.
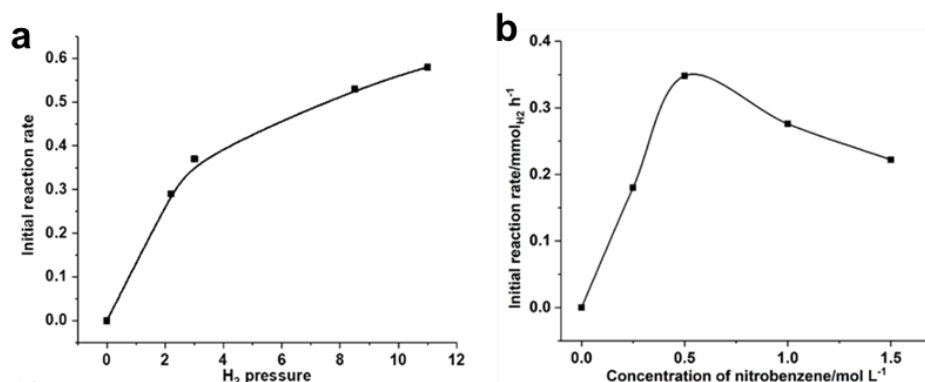
Figure 10.7. Kinetic studies on hydrogenation of nitrobenzene with Ni@C nanoparticles. (a) Initial reaction rate at different H_2 pressure and 1 mmol nitrobenzene. (b) Initial reaction rate at different concentration of nitrobenzene and 11 bar of H_2. Reaction conditions: 5 mg Ni@C as catalyst, 2 mL toluene as solvent, 20ºC. The catalyst was pre-reduced at 150 ºC with 10 bar of H_2 and then cooled down to 20ºC temperature before injecting the nitrobenzene to the batch reactor.

Table 10.1. Kinetic equations describing the reaction rate of nitrobenzene hydrogenation assuming different elementary steps as the rate-determining step of the process.[a]
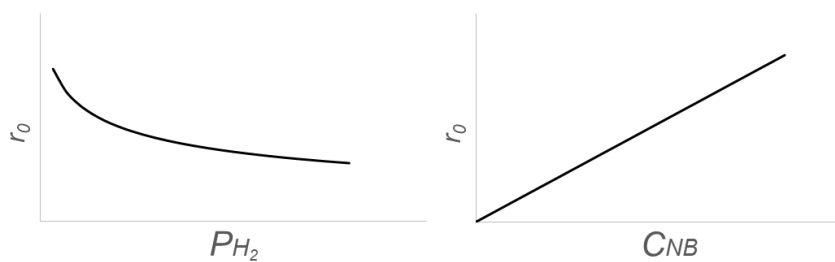
Rate determining step	reaction rate equation
H_2 dissociation	$r = \dfrac{k_{H_2} \cdot P_{H_2}}{(1 + K_{NB} \cdot C_{NB})^2}$
NB adsorption/activation	$r = \dfrac{k_{NB} \cdot C_{NB}}{(1 + \sqrt{k_{H_2} \cdot P_{H_2}})}$
surface reaction	$r = \dfrac{k \cdot k_{NB} \cdot k_{H_2} \cdot C_{NB} \cdot P_{H_2}}{\left(1 + K_{NB} \cdot C_{NB} + \sqrt{k_{H_2} \cdot P_{H_2}}\right)^3}$

[a]Kinetic equations obtained from ref. [39] in the manuscript.

a) H$_2$ dissociation
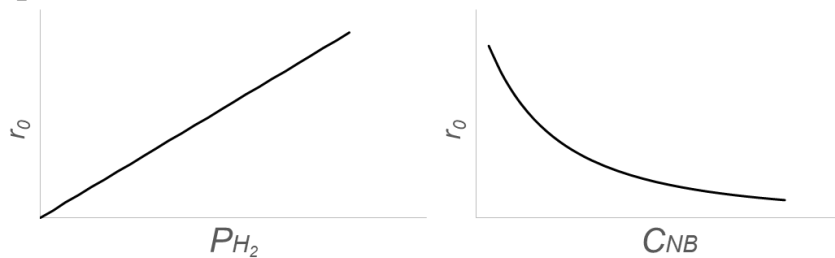
b) NB adsorption/activation
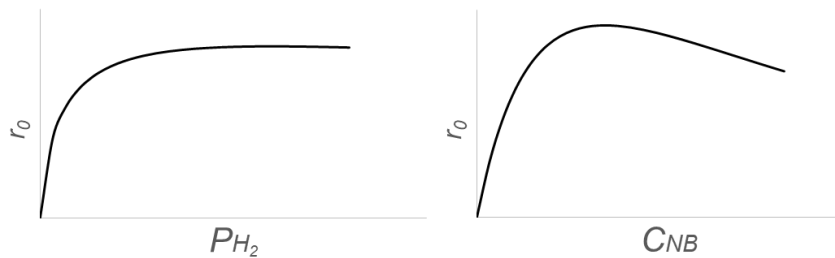

c) Surface reaction

Figure 10.8. Graphical representation of the kinetic equations shown in **Table 1** based on reaction mechanisms assuming different elementary steps as the rate-determining step of the process.
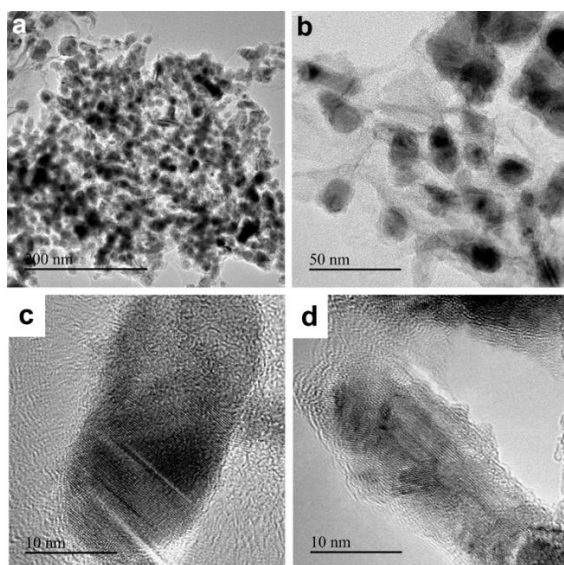
Figure 10.9. Structural characterization of Co@C nanoparticles. (a, b) Low-magnification TEM images of Co@C nanoparticles prepared through the carbon coating and graphitization process. (c, d) High-resolution TEM images of Co@C nanoparticles.
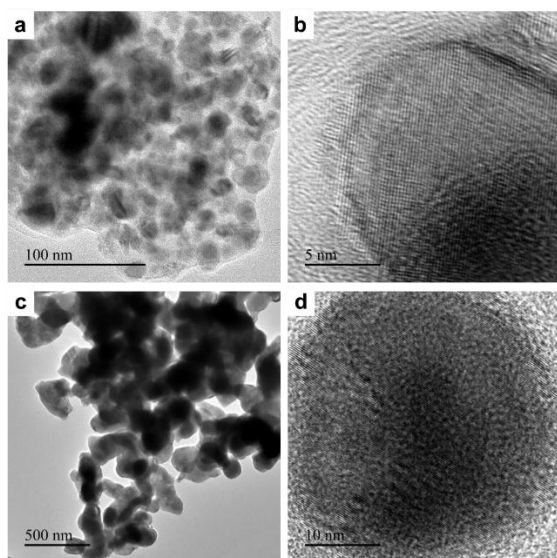

Figure 10.10. Structural characterization of Cu@C and Fe@C nanoparticles. (a, b) Low-magnification TEM image and high resolution TEM

image of Cu@C nanoparticles. (c, d) Low-magnification TEM image and high resolution TEM image of Fe@C nanoparticles.

Table 10.2. Catalytic performance of various non-noble metal catalysts for hydrogenation of nitrobenzene.[a]

Sample	Time/min	Conversion/%	Selectivity to Azoxy (1b)	Selectivity to Azo (1c)	Selectivity to Aniline (1d)
Ni@C	150	43.4	9.7	3.2	85.5
Co@C	210	9.1	-	-	>99.0
Cu@C	240	<3	-	-	-
Fe@C	240	<3	-	-	-
Ni@C+CeO$_2$	50	100	94.1	4.1	1.8
CeO$_2$	300	<2	-	-	-
Ni/CeO$_2$	840	5.9	75.6	6.2	18.3
Ni/CeO$_2$-in situ reduced	150	35.1	94.5	0.9	4.6
Ni@C+Al$_2$O$_3$	110	83.7	10.7	5.6	83.8
Ni@C+TiO$_2$	145	45.7	-	15.9	84.1
Ni@C+SiO$_2$	150	44.7	-	1.6	98.4
Ni@C+Hydrotalcite	75	84.8	6.5	5.6	74.3
Co@C+CeO$_2$	360	13.3	77.8	-	22.2
Cu@C+CeO$_2$	360	<5	-	-	-
Fe@C+CeO$_2$	360	<2	-	-	-

[a] Reaction conditions: 1 mmol of nitrobenzene, 2 mL toluene as solvent, 120 °C and 10 bar of H$_2$. 1.5 mg of metal nanoparticles and 10 mg of metal oxide as co-catalyst. The yields of different products are calculated based on hexadecane as internal standard. For Ni/CeO$_2$, 20 mg of the solid catalyst was used as catalyst.

Besides Ni@C, we have also prepared Co@C, Cu@C and Fe@C NPs, as shown in **Figure 10.9** and **Figure 10.10**. Firstly, we have studied the catalytic behavior of several types of non-noble metal NPs (Co@C, Ni@C, Fe@C and Cu@C NPs) for hydrogenation of nitrobenzene under mild conditions (120 °C and 10 bar of H$_2$). As shown in **Table 10.2**, Fe@C and Cu@C NPs show poor activity for hydrogenation of nitrobenzene while Co@C and Ni@C NPs can

work. Furthermore, Ni@C sample achieves 42% conversion after reaction for 150 min and gives aniline as the major product (~90% selectivity) and azoxybenzene (~9% selectivity) as byproduct. However, in the case of Co@C, very high selectivity to aniline is observed.
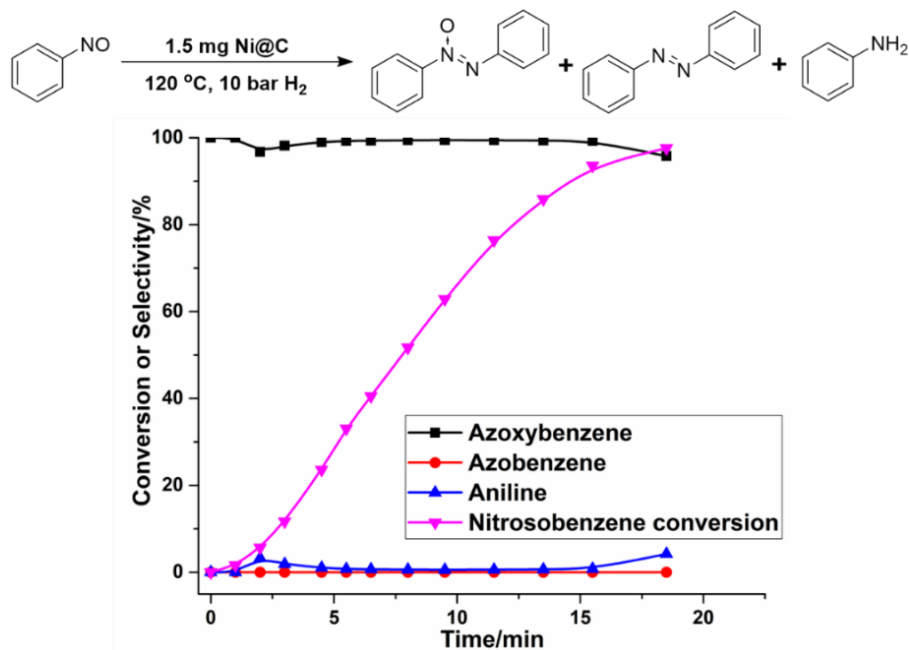

Figure 10.11. Conversion and selectivity for different products versus reaction time in hydrogenation of nitrosobenzene by Ni@C NPs. Reaction conditions: 1 mmol of nitrosobenzene, 1.5 mg of Ni@C, 2 mL toluene as solvent, 120 °C and 10 bar of H_2. As it can be seen, the selectivity to azoxybenzene was very high (>95%) and the reaction rate was much faster than that for hydrogenation of nitrobenzene. When the conversion of nitrosobenzene reach >93%, the selectivity to aniline started to increase.

Since a small amount of azoxybenzene and azobenzene was obtained with Ni@C NPs, this encourages us to study the kinetic profiles for hydrogenation of nitrobenzene on this catalyst. As shown in **Figure 10.6b**, nitrosobenzene can be observed at the starting stage, which comes from a new reaction pathway on Ni nanoparticles, being different to that reported on noble metal catalysts.[26] The selectivity to nitrosobenzene decreases with reaction time and aniline becomes

the major product when conversion is >20%. From these results, we thought that the nitrosobenzene formed as a primary product would be rapidly hydrogenated to aniline and the formation of azoxybenzene would not be kinetically favorable on this catalyst. However, when we reacted nitrosobenzene on Ni@C NPs (see **Figure 10.11**), azoxybenzene was obtained with high yield and aniline only starts to form when the conversion of nitrosobenzene was >90%. Then, according to the reaction network and the catalytic results shown in **Figure 10.11** and **Figure 10.12**, one can think that, a catalyst in where the rate of hydrogenation of nitrosobenzene to aniline is decreased and nitrosobenzene is allowed to accumulate, will be able to achieve the direct hydrogenation of nitrobenzene to azoxybenzene. Therefore, we thought that, in order to achieve high selectivity for hydrogenation of nitrobenzene to azoxybenzene, it would be critical to stabilize the nitrosobenzene or phenylhydroxylamine intermediates, and then transform them into azoxybenzene.

Considering that the involved intermediates (nitrosobenzene and phenylhydroxylamine) in the condensation reaction route (see **Figure 10.2**) can be stabilized and condensed in a basic environment, we thought that the selectivity to the azoxybenzene product should be improved in the presence of a solid catalyst with suitable basicity. After screening a combination of Ni@C and metal oxides with varying acid-base properties (see **Table 10.2**), it is found that the combination of Ni@C and CeO_2 NPs gives high selectivity to azoxybenzene (94%) at full conversion of nitrobenzene, though CeO_2 alone is not active for this reaction. We have also noticed that, other metal oxides with different acid-base properties such as Al_2O_3, TiO_2, SiO_2 or hydrotalcite (Mg/Al=4) give much lower selectivity to azoxybenzene.
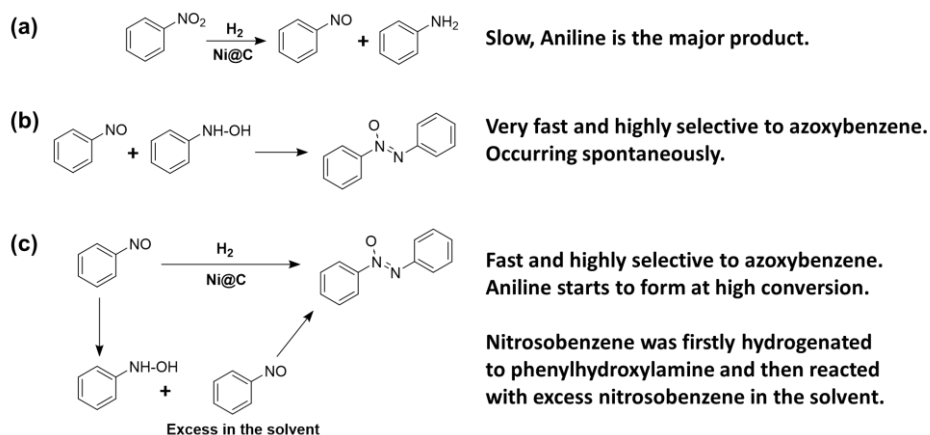
Figure 10.12. Reaction schemes of hydrogenation of nitrobenzene (a), condensation between nitrosobenzene and phenylhydroxylamine (b) and hydrogenation of nitrosobenzene (c) by Ni@C NPs.
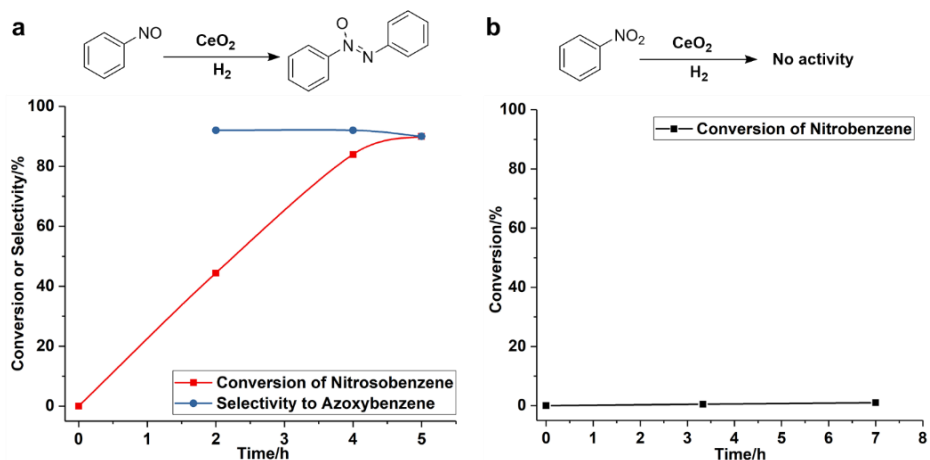

Figure 10.13. CeO_2 as the catalyst for hydrogenation reactions. (a) Hydrogenation of nitrosobenzene with CeO_2. Reaction conditions: 120 °C, 10 bar of H_2 and 20 mg CeO_2 as catalyst. High selectivity to azoxybenzene can be obtained, although the reaction rate is much lower than $Ni@C+CeO_2$. (b) Hydrogenation of nitrobenzene with CeO_2. Reaction conditions: 120 °C, 10 bar of H_2 and 20 mg CeO_2 as catalyst. CeO_2 is not active for hydrogenation of nitrobenzene.
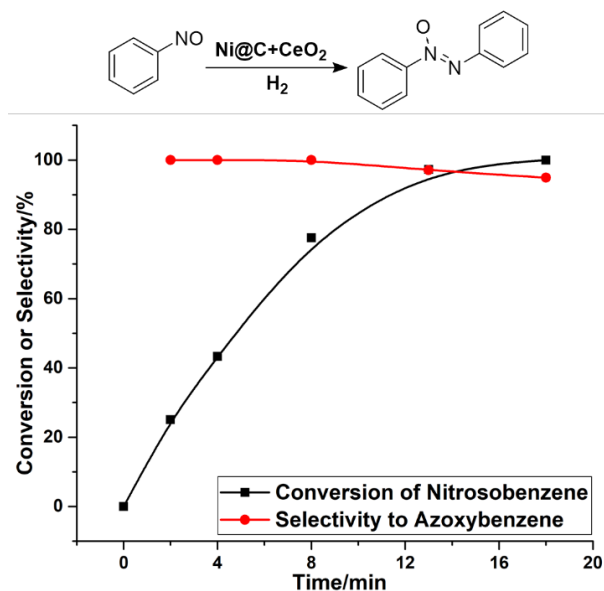
Figure 10.14. Hydrogenation of nitrosobenzene with Ni@C and CeO$_2$ nanoparticles. Reaction conditions: 1 mmol of nitrosobenzene, 1.5 mg of Ni@C, 10 mg of CeO$_2$, 2 mL toluene as solvent, 120 °C and 10 bar of H$_2$.
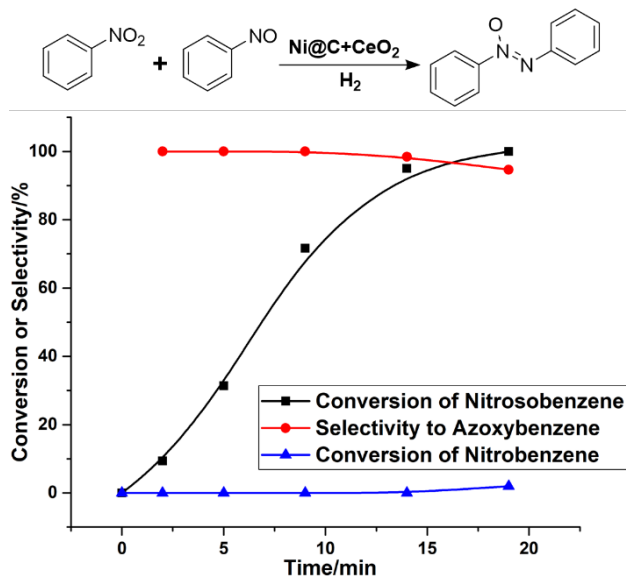

Figure 10.15. Hydrogenation of mixture of nitrosobenzene and nitrobenzene with Ni@C and CeO$_2$ nanoparticles. Reaction conditions: 1 mmol of

nitrosobenzene, 1 mmol of nitrobenzene, 1.5 mg of Ni@C, 10 mg of CeO_2, 2 mL toluene as solvent, 120 $^{\circ}$C and 10 bar of H_2. As it can be seen, nitrosobenzene was selectively hydrogenated into azoxybenzene while hydrogenation of nitrobenzene didn't occur until nitrosobenzene was consumed.
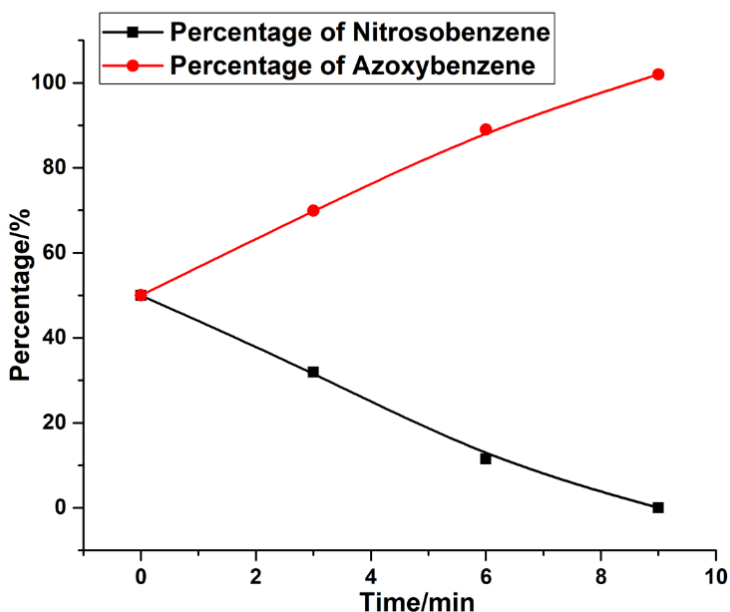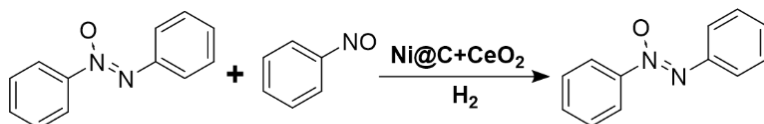

Figure 10.16. Hydrogenation of mixture of nitrosobenzene and azoxybenzene with Ni@C and CeO_2 nanoparticles. Reaction conditions: 0.5 mmol of nitrosobenzene, 0.25 mmol of azoxybenzene, 1.5 mg of Ni@C, 10 mg of CeO_2, 2 mL toluene as solvent, 120 $^{\circ}$C and 10 bar of H_2. As it can be seen, nitrosobenzene was selectively converted into azoxybenzene while azoxybenzene was not hydrogenated into azobenzene or aniline.
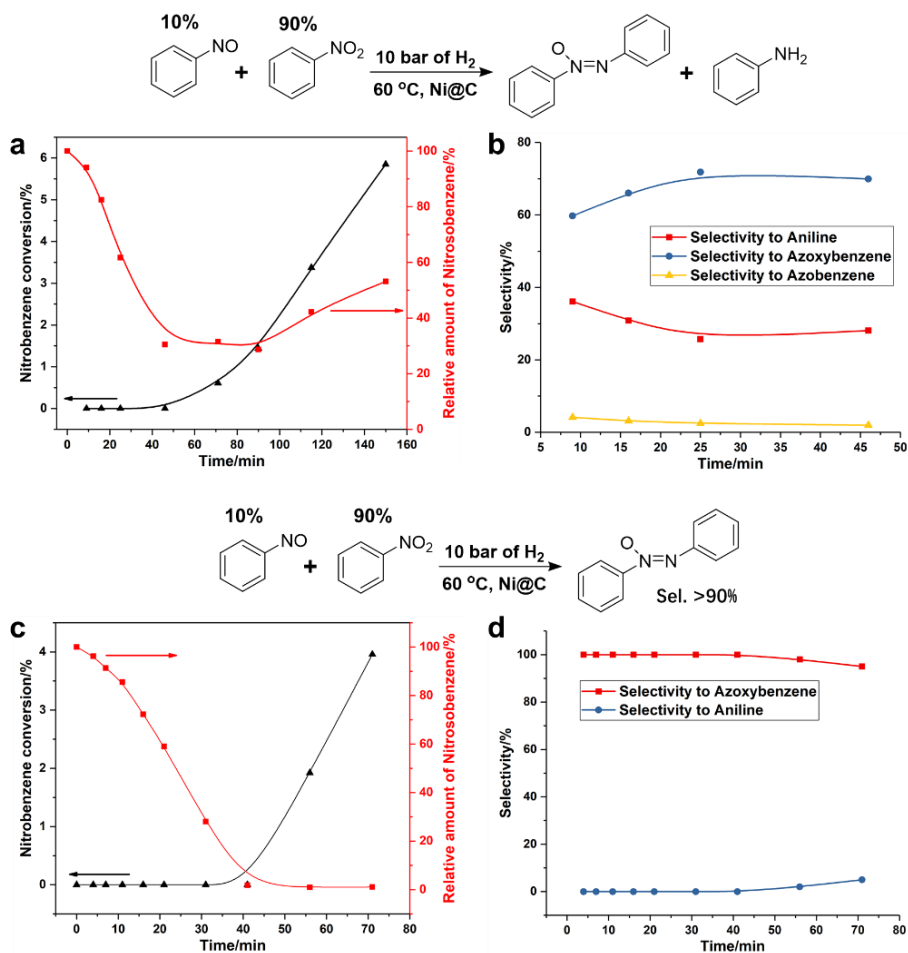
Figure 10.17. (a, b) Competitive hydrogenation of nitrosobenzene and nitrobenzene with Ni@C. Reaction conditions: 0.1 mmol nitrosobenzene, 0.9 mmol nitrobenzene, 2 mL toluene as solvent, 1.5 mg of Ni@C nanoparticles as catalyst. The reaction was carried out at 60 $^{\circ}$C to decrease the reaction rate in order to follow the amount of reactants. Both azoxybenzene and aniline were observed in the products. (c, d) Competitive hydrogenation of nitrosobenzene and nitrobenzene with Ni@C+CeO$_2$. Reaction conditions: 0.1 mmol nitrosobenzene, 0.9 mmol nitrobenzene, 2 mL toluene as solvent, 1.5 mg of Ni@C nanoparticles and 10 mg of CeO$_2$ as catalyst. The reaction was carried out at 60 $^{\circ}$C to decrease the reaction rate in order to follow the amount of reactants. Azoxybenzene is the major product with a selectivity >90%.

Figure 10.18. Influence of agitation on the initial reaction rate for hydrogenation of nitrobenzene to azoxybenzene with bifunctional Ni@C-CeO$_2$ catalyst. In these tests, the initial reaction rate was measured when the conversion of nitrobenzene is <20%. The amount of CeO$_2$ (10 mg) is excess, therefore, the selectivity to azoxybenzene is >95% in all cases. As shown in this figure, when the stirring rate is higher than 900 rpm, the initial reaction rate almost reaches the maximum value.
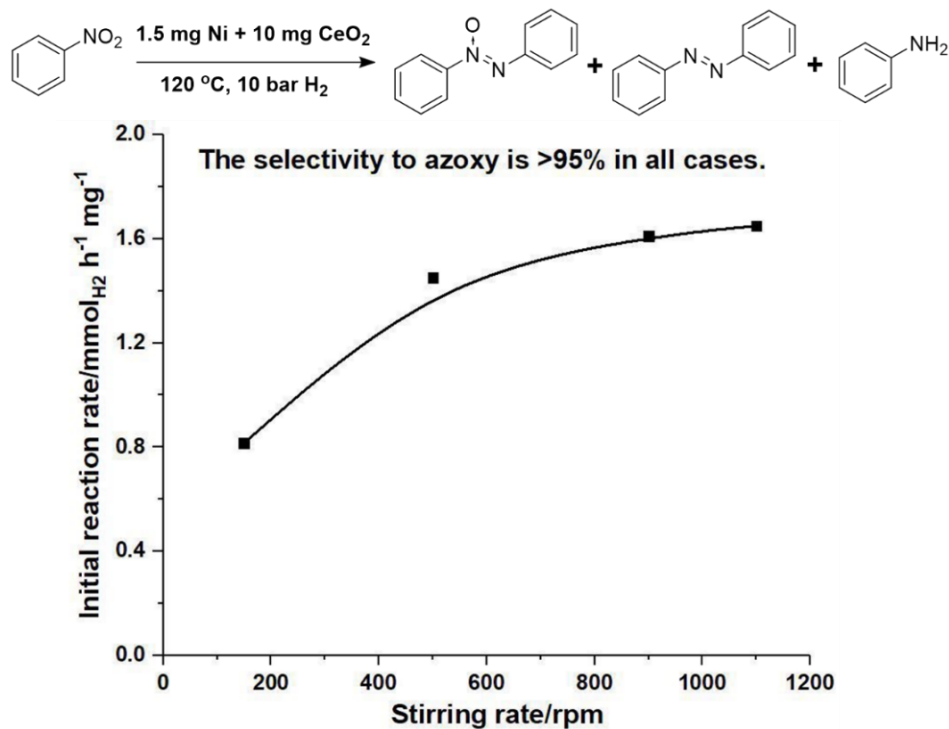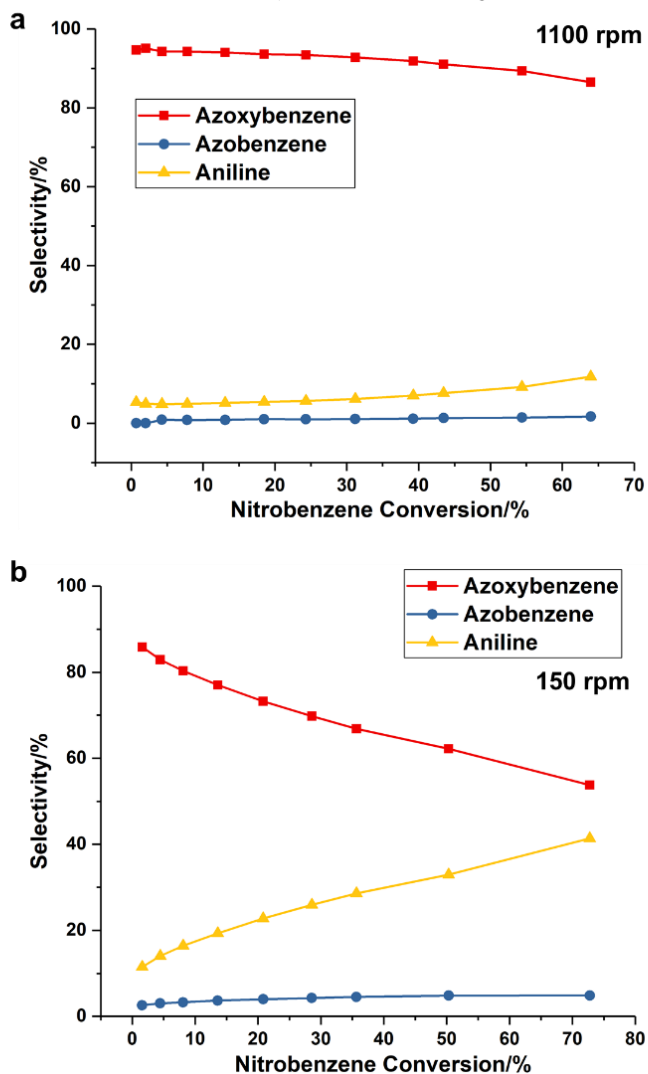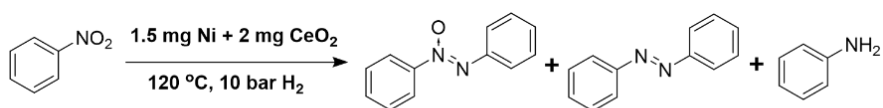
Figure 10.19. Influence of agitation on the selectivity for the hydrogenation of nitrobenzene to azoxybenzene with bifunctional Ni@C-CeO$_2$ as the catalyst. The selectivity to azoxybenzene at different conversion of nitrobenzene are given in each panel under 1100 rpm (a) and 150 rpm (b), respectively.
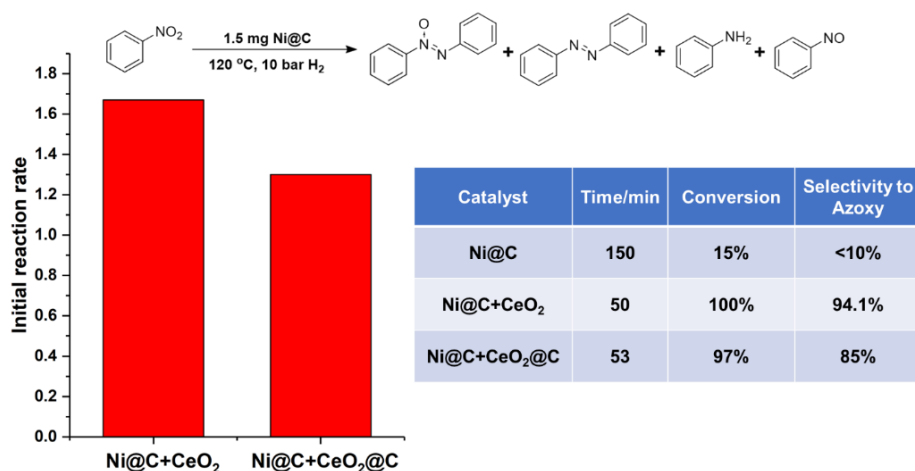
Figure 10.20. Use of CeO_2@C as co-catalyst with Ni@C nanoparticles for hydrogenation of nitrobenzene. The initial reaction rate of Ni@C+CeO_2@C is lower than that of Ni@C+CeO_2. More importantly, the selectivity to azoxybenzene is also lower. Reaction conditions: 1.5 mg Ni@C, 10 mg CeO_2@C, 1 mmol nitrobenzene, 2 mL toluene as solvent, 120 ºC and 10 bar H_2.

At this point, we assume that a bifunctional catalyst prepared by supporting Ni on CeO_2 NPs should work for the hydrogenation of nitrobenzene to azoxybenzene. Following that assumption, a supported Ni/CeO_2 catalyst (with 5 wt% of Ni on CeO_2) by wet impregnation and it was then reduced by H_2 at 450 ºC and passivated by air at room temperature after the H_2 reduction treatment. As it can be seen, the as-prepared Ni/CeO_2 catalyst shows poor activity for hydrogenation of nitrobenzene, which is probably caused by the re-oxidation of Ni when exposed to air. Indeed, when the Ni/CeO_2 catalyst was reduced in the reactor before the catalytic test, the activity improved significantly, implying that metallic Ni is the active component for hydrogenation of nitroarenes. Hou et al. has studied the chemical states of Ni particles supported on CeO_2.[18] The XPS results show that, only part of the Ni can be reduced by H_2 even after treatment at 500 ºC. Therefore, at our current reaction temperature (120 ºC), only a small amount of Ni particles in the Ni/CeO_2 catalyst can be reduced. The thin carbon layers in the Ni@C NPs can protect Ni from deep oxidation by air and promote the reduction of Ni under

reaction conditions. Therefore, the Ni@C-CeO$_2$ catalyst in where Ni nanoparticles with a high reduction degree are mixed with CeO$_2$ is more active than the Ni/CeO$_2$ in where only a small part of Ni is reduced.

To figure out the reaction mechanism of Ni@C-CeO$_2$ for direct conversion of nitrobenzene to azoxybenzene, we have performed the following experiments. Firstly, we have found that, bare CeO$_2$ NPs can catalyze the hydrogenation of nitrosobenzene to azoxybenzene but with a slow reaction rate (see **Figure 10.13a**). However, bare CeO$_2$ is not active for hydrogenation of nitrobenzene (see **Figure 10.13b**), inferring that the initial activation of nitrobenzene should be related with Ni@C NPs. Afterwards, it is shown in **Figure 10.14** that nitrosobenzene can be selectively hydrogenated into azoxybenzene by Ni@C-CeO$_2$ with high reaction rate. Furthermore, we have also studied the competitive reactivity between nitrosobenzene and other reactants by co-feeding nitrosobenzene with nitrobenzene or azoxybenzene for the hydrogenation reaction. As shown in **Figure 10.15** and **Figure 10.16**, only hydrogenation of nitrosobenzene was observed during the competitive hydrogenation tests with nitrobenzene and azoxybenzene.

Since the concentration of nitrosobenzene as intermediate in the reaction mixture can be very low during the hydrogenation of nitrobenzene, we have also carried out a competitive hydrogenation experiment with a mixture of 90% nitrobenzene and 10% of nitrosobenzene. As shown in **Figure 10.17a**, when only Ni@C was used as the catalyst, nitrosobenzene was firstly hydrogenated to both azoxybenzene and aniline while nitrobenzene was not converted until nearly most of the nitrosobenzene was consumed. Indeed, when the conversion of nitrosobenzene reaches ~70%, the hydrogenation of nitrobenzene started to occur, implying a competitive adsorption between nitrosobenzene and nitrobenzene on the surface of Ni@C nanoparticles. When Ni@C-CeO$_2$ was used as the catalyst (see **Figure 10.17b**), nitrosobenzene was also firstly selectively hydrogenated to azoxybenzene with a higher reaction rate and >90% selectivity to azoxybenzene. More importantly, hydrogenation of nitrobenzene only occurs when all the nitrosobenzene in the reaction mixture was completely converted. These results infer that, hydrogenation of nitrobenzene on Ni@C is more preferable when the concentration of nitrosobenzene is low, and that the presence of CeO$_2$ can accelerate the selective conversion of nitrosobenzene to

azoxybenzene, which explains the higher reactivity and selectivity of Ni@C-CeO$_2$. Since nitrosobenzene is not observed as the intermediate when using Ni@C-CeO$_2$ as the catalyst, it implies that nitrosobenzene may be preferentially absorbed by the CeO$_2$ and converted further to azoxybenzene. The role of CeO$_2$ in the catalytic process is to adsorb and convert the low-concentration nitrosobenzene rapidly to avoid the over-hydrogenation reaction to aniline on Ni@C nanoparticles. However, for doing that, nitrosobenzene formed on the Ni@C NPs should diffuse and adsorb on the CeO$_2$ NPs. For effective hydrogenation of the nitrosobenzene, the H$_2$ activated on the Ni@C NPs should also reach the CeO$_2$ NPs. Then, it will be on the surface of the CeO$_2$ NPs, where the azoxybenzene is produced. Nevertheless, the presence of Ni@C NPs is the key to produce the nitrosobenzene and to activate H$_2$.

Since the model described above requires the diffusion of intermediate products from one catalyst particle to another, mass transportation should be maximized to achieve maximum efficiency. Therefore, we study the influence of stirring speed in the reactor on the rate of reaction. The results presented in **Figure 10.18** show that the initial reaction rate increases when increasing the stirring rate up to 900 rpm. After that, further increasing the stirring speed has no effects on the initial reaction rate. Nevertheless, in the presence of 10 mg of CeO$_2$, high selectivity to azoxybenzene is always high. To show the influence of agitation on the selectivity for azoxybenzene, the amount of CeO$_2$ is decreased to 2 mg, which will cause less contact between Ni@C and CeO$_2$ NPs. The catalytic results presented in **Figure 10.19** show that the selectivity to azoxybenzene also decreases with the stirring rate, which should be caused by the insufficient diffusion of nitrosobenzene from the Ni@C to CeO$_2$ nanoparticles.

In another experiment, the surface of CeO$_2$ is partially blocked by the carbon coating treatment and then used as the co-catalyst with Ni@C for hydrogenation of nitrobenzene. As can be seen in **Figure 10.20**, the initial reaction rate decreases slightly compared to the naked CeO$_2$. More importantly, the selectivity to azoxybenzene also decreases, which further confirms the participation of CeO$_2$ for achieving high selectivity to azoxybenzene.
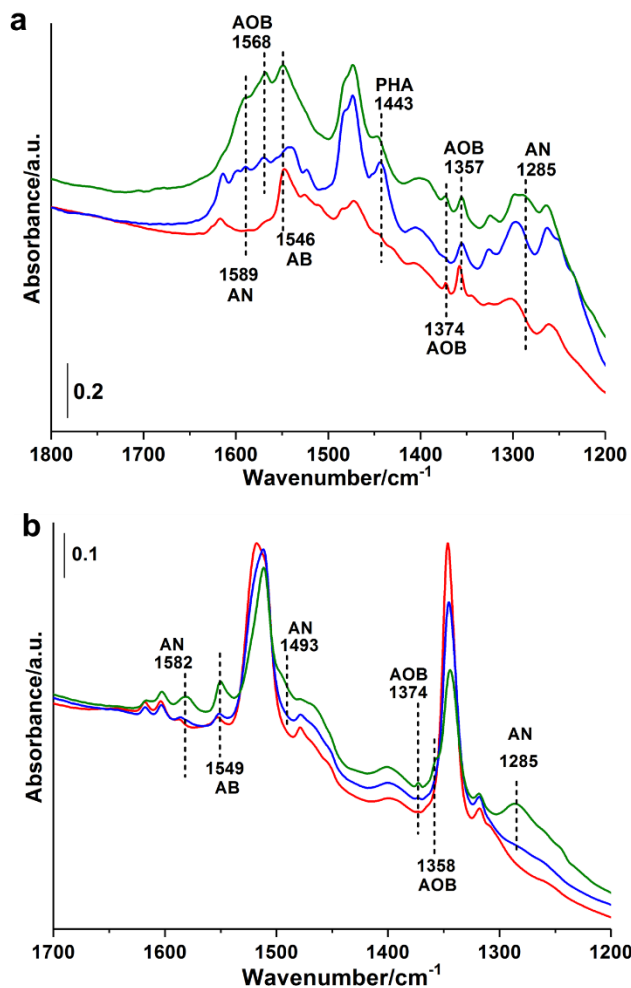
Figure 10.21. (a) *In situ* IR spectra of hydrogenation of nitrosobenzene on CeO$_2$ at 10 mbar H$_2$ and at temperatures of 25 ºC (red), 70 ºC (blue) and 120 ºC (green) (b). *In situ* IR spectra of hydrogenation of nitrobenzene on CeO$_2$ at 10mbar H$_2$ and at temperatures of 25 ºC (red), 70 ºC (blue) and 120 ºC (green) at 10 mbar H$_2$. IR spectra have been acquired after 35 min at each temperature. AN, aniline; AOB, azoxybenzene; AB, azobenzene; PHA, phenylhydroxylamine.
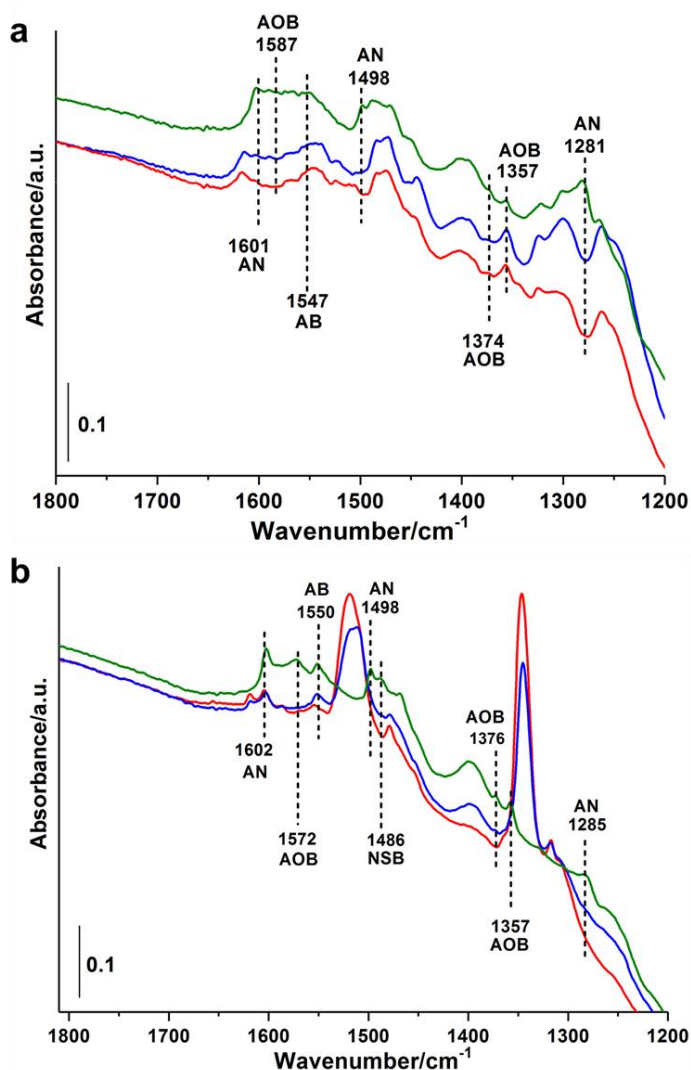
Figure 10.22. (a) *In situ* IR spectra of hydrogenation of nitrosobenzene on Ni@C+CeO$_2$ at 10 mbar H$_2$ and at temperatures of 25 ºC (red), 70 ºC (blue) and 120 ºC (green). (b) *In situ* IR spectra of hydrogenation of nitrobenzene on Ni@C+CeO$_2$ at 10 mbar H$_2$ and at temperatures of 25 ºC (red), 70 ºC (blue) and 120 ºC (green). IR spectra have been acquired after 35min at each temperature AN, aniline; AOB, azoxybenzene; AB, azobenzene; NB, nitrobenzene; NSB, nitrosobenzene.
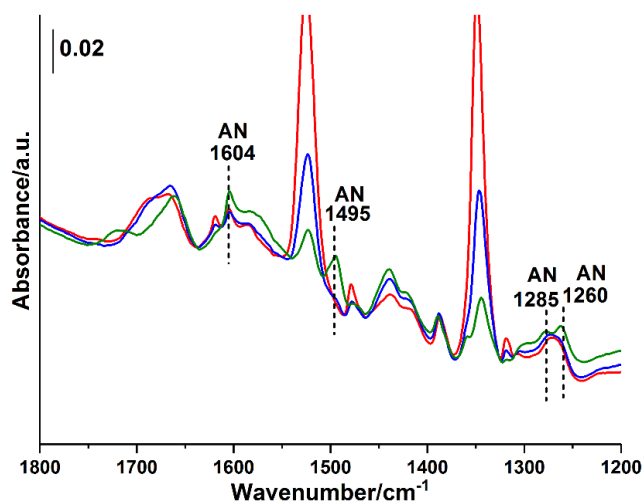
Figure 10.23. *In situ* IR spectra of hydrogenation of nitrobenzene on Ni@C+TiO$_2$. Only aniline can be observed as product in the IR spectra.

To further study the interaction of the reactants and intermediates with the surface of the catalyst, we have also performed the *in situ* IR studies on the CeO$_2$ NPs and Ni@C-CeO$_2$ catalyst. As shown in **Figure 10.21a**, when CeO$_2$ was used alone as catalyst after pre-activation in vaccum at 120 ^{o}C before the *in situ* IR experiments, nitrosobenzene was adsorbed on CeO$_2$ and the hydrogenation of nitrosobenzene was observed. Several reaction products were observed in the IR spectra, including phenylhydroxylamine (1443 cm^{-1}), azoxybenzene (1568, 1374 and 1357 cm^{-1}), azobenzene (1546 cm^{-1}) and aniline (1589, 1285 cm^{-1}). Interestingly, the conversion of nitrosobenzene during the *in situ* IR experiments is high, suggesting the activity of CeO$_2$ for hydrogenation reaction.[27] When the reactant was changed to nitrobenzene, the formation of small amounts of azoxybenzene (1374 and 1357cm^{-1}), azobenzene (1549 cm^{-1}) , and aniline (1582, 1493 and 1285 cm^{-1}) was still observed (see **Figure 10.21b**).[28,29] However, the conversion of nitrobenzene is much lower than that of nitrosobenzene, implying that CeO$_2$ alone is not active enough for hydrogenation of nitrobenzene, probably due to its low activity for H$_2$ activation. Furthermore, the hydrogenation of nitrobenzene and nitrosobenzene on Ni@C-CeO$_2$ has also been followed by *in situ* IR. As shown in **Figure 10.22**,

high conversion of nitrosobenzene and nitrobenzene can be observed together with the formation of azoxybenzene (1572,1376 and 1357 cm^{-1}), azobenzene (1550 cm^{-1}), nitrosobenzene (1486 cm^{-1}) as well as aniline (1602, 1498 and 1280 cm^{-1}) are also confirmed according to the IR bands. For comparison, we have also followed the hydrogenation of nitrobenzene on Ni@C+TiO$_2$ catalyst presented above. As can be seen in **Figure 10.23**, only IR bands corresponding to aniline are observed in the IR spectra, which is in line with the catalytic results (see **Table 10.1**). The IR results indicate that, nitrosobenzene can be further hydrogenated to phenylhydroxylamine and then form azoxybenzene on CeO$_2$. The role of Ni@C NPs may contribute to the activation of H$_2$ and production of nitrosobenzene as the primary intermediate. As a result of the synergistic effects of Ni@C and CeO$_2$, nitrobenzene can be firstly hydrogenated to nitrosobenzene and then to azoxybenzene.

The pristine Ni@C NPs and the sample after H$_2$ pre-reduction treatment have been measured by XPS. As shown in **Figure 10.24a**, 40.7% of metallic Ni can be observed in the pristine Ni@C NPs. After pre-reduction by H$_2$ at 120 ^{o}C, the percentage of metallic Ni increases to 54.2%. However, even after pre-reduction treatment at 200 ^{o}C, the amount of metallic Ni is just 65.6%, suggesting the difficulty to achieve fully reduced Ni nanoparticles under our current reaction conditions for hydrogenation of nitrobenzene in batch reactor. Interestingly, after being physically mixed with CeO$_2$, the amount of metallic Ni in the Ni@C NPs decreases and the NiO species become more difficult to be reduced by H$_2$ (see **Figure 10.24b**). These results refer interaction between Ni@C and CeO$_2$ NPs, which modulates the redox properties of Ni@C NPs. During our catalytic tests, we have observed that, the mixture of Ni@C and CeO$_2$ in the solvent (toluene) can form a magnetic composite. As shown in **Figure 10.25**, after stirring and heating at 60 ^{o}C for a short time, the physical mixture of Ni@C and CeO$_2$ was absorbed by the magnetic bar, implying that some interaction may occur between the Ni@C and CeO$_2$ nanoparticles. It is already known that, there are a number of –OH, –C=O and –COOH groups in the thin carbon layers in the Ni@C NPs, which can interact with the surface of CeO$_2$ nanoparticles.
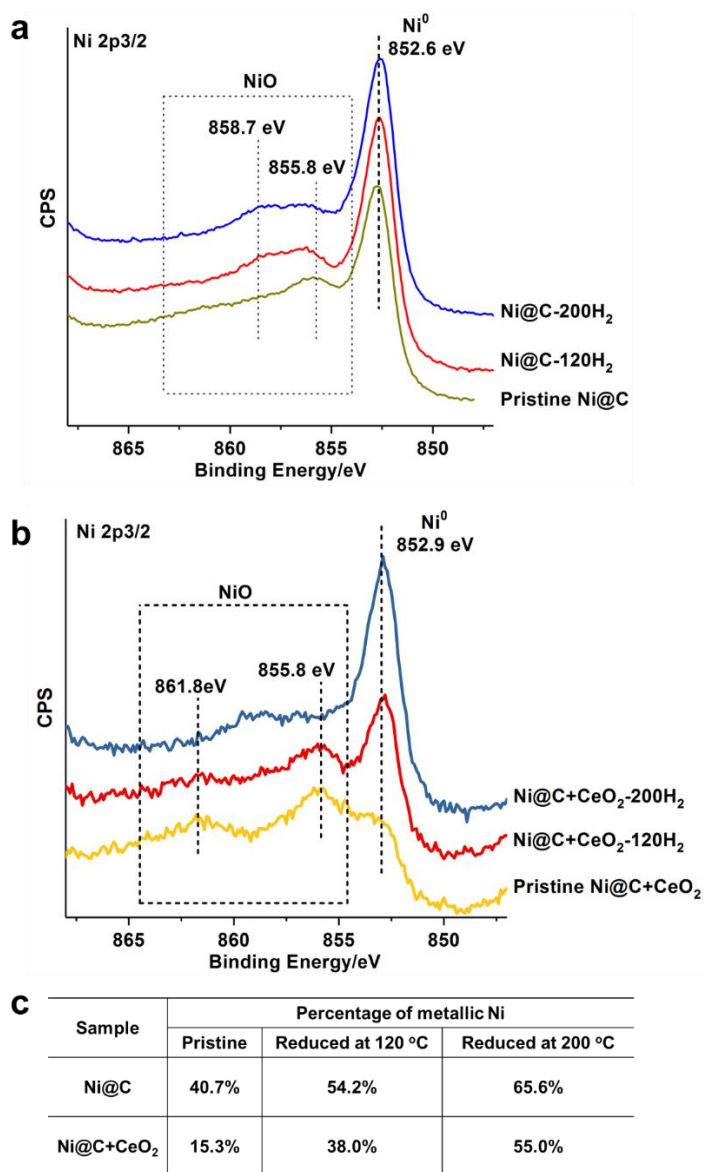
Figure 10.24. (a) XPS of Ni 2p3/2 region of the pristine Ni@C nanoparticles and the spectra acquired after ex-situ H_2 reduction treatment at 120 and 200 ºC. (b) XPS of Ni 2p3/2 region of the pristine Ni@C+CeO_2 and the spectra acquired after ex-situ H_2 reduction treatment at 120 and 200 ºC. (c) The percentage of metallic Ni in the two samples according to the fitting of XPS spectra.
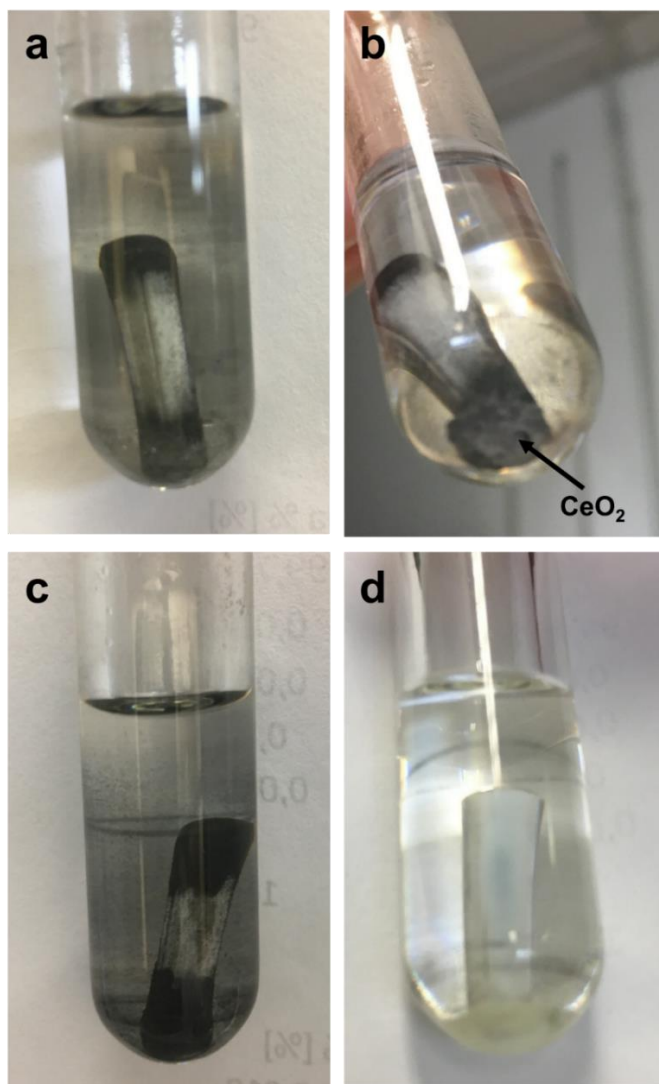
Figure 10.25. Photograph of the Ni@C, CeO$_2$ and the mixture of Ni@C and CeO$_2$ nanoparticles in toluene. (a) Ni@C nanoparticles in toluene. The magnetic bar absorbs the black nanoparticles. (b) After adding CeO$_2$ nanoparticles into the solvent, they are at the bottom of the tube. (c) After stirring and 2 min of heating at 60 $^{\circ}$C, both CeO$_2$ and Ni@C nanoparticles are absorbed by the magnetic bar. (d) CeO$_2$ nanoparticles in toluene. In the absence of Ni@C nanoparticles, the CeO$_2$ nanoparticles are at the bottom of the tube.
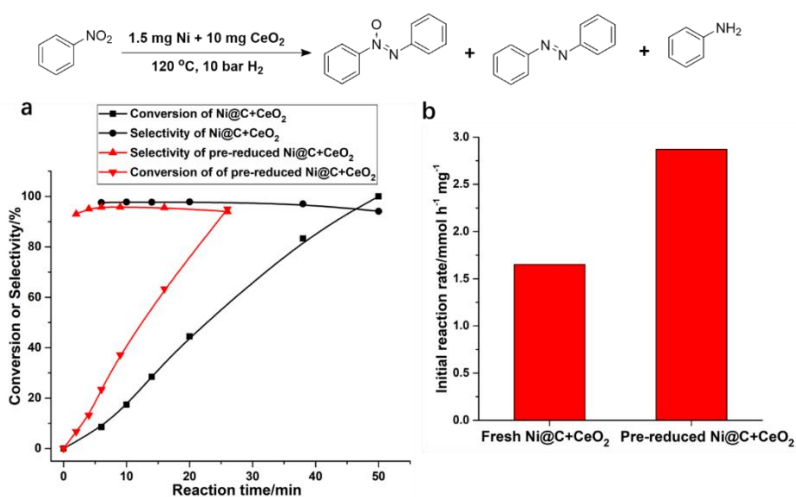
Figure 10.26. (a) Hydrogenation of nitrobenzene to azoxybenzene with pristine Ni@C+CeO$_2$ catalyst and the pre-reduced Ni@C+CeO$_2$ catalyst. In the pre-reduction treatment, the Ni@C+CeO$_2$ catalyst was reduced by 10 bar of H$_2$ at 150 °C in the batch reactor. Then 1 mmol nitrobenzene was injected and the reaction was started with 10 bar of H$_2$ at 120 °C. (b) The initial activity based on the mass of Ni@C NPs for hydrogenation of nitrobenzene on pristine Ni@C+CeO$_2$ and the pre-reduced Ni@C+CeO$_2$ catalysts.

To further clarify the active sites in Ni@C NPs, we have also pre-reduced the catalyst in the reactor before the hydrogenation reaction and then tested the catalytic behavior of the pre-reduced catalyst. As shown in **Figure 10.26**, the pre-reduced catalyst shows significantly higher initial activity for hydrogenation of nitrobenzene. More importantly, the high selectivity to azoxybenzene is preserved after the pre-reduction treatment. These results indicate that metallic Ni is the active phase in the Ni@C NPs and the presence of NiOx in the Ni@C NPs can decrease the activity but has no influence on the chemoselectivity. It should also be noted that, since the Ni@C NPs are not fully reduced under our current conditions, the nitrosobenzene intermediate formed on Ni@C can be transferred to CeO$_2$. According to our previous work,[26] on the fully reduced Ni surface, the nitrosobenzene can be further hydrogenated to aniline directly before the desorption from the surface of Ni@C NPs in the presence of abundant hydrogen.
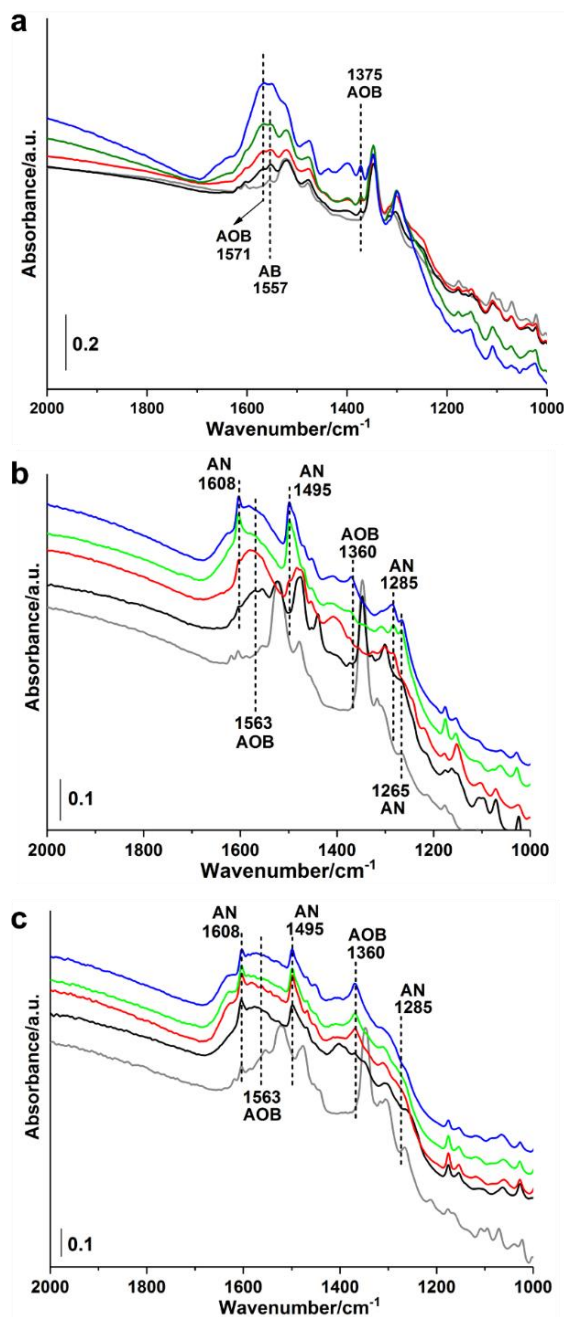
419

Figure 10.27 In situ IR spectra of adsorption of H_2 and nitrobenzene on Ni@C-CeO$_2$ catalyst under different H_2 pressures. (a) 0.4 mbar of H_2, (b) 10

mbar of H_2 and (c) 40 mbar of H_2. IR spectra are taken at 90ºC for 20 min (black), 80 min (red), 156 min (green) and at 120 ºC for 100 min (blue). AN, aniline; AOB, azoxybenzene; AB, azobenzene; NB, nitrobenzene.

We have investigated the influence of reaction conditions by *in situ* IR spectroscopy. As displayed in **Figure 10.27a**, when nitrobenzene is co-absorbed with low-pressure H_2 (0.4 mbar) on pre-reduced Ni@C-CeO$_2$ catalyst, aniline is not observed. When the H_2 pressure is increased to 10 or 40 mbar (**Figure 10.27b** and **Figure 10.27c**), aniline appears in the IR spectra. By comparing the product distributions in **Figure 10.19a** and **Figure 10.29b**, it can be seen that, after pre-reduction treatment, the selectivity to azoxybenzene decreases from ~85% to ~60% when using 1.5 mg of Ni@C and 2 mg of CeO$_2$ as the catalyst for hydrogenation of nitrobenzene. Therefore, the surface properties of Ni@C NPs and their ability for the activation of H_2 can also be a factor that influence the product distributions in the hydrogenation of nitrobenzene with bifunctional Ni@C-CeO$_2$ catalyst, although it is not so clear under our current reaction conditions in the batch reactor.
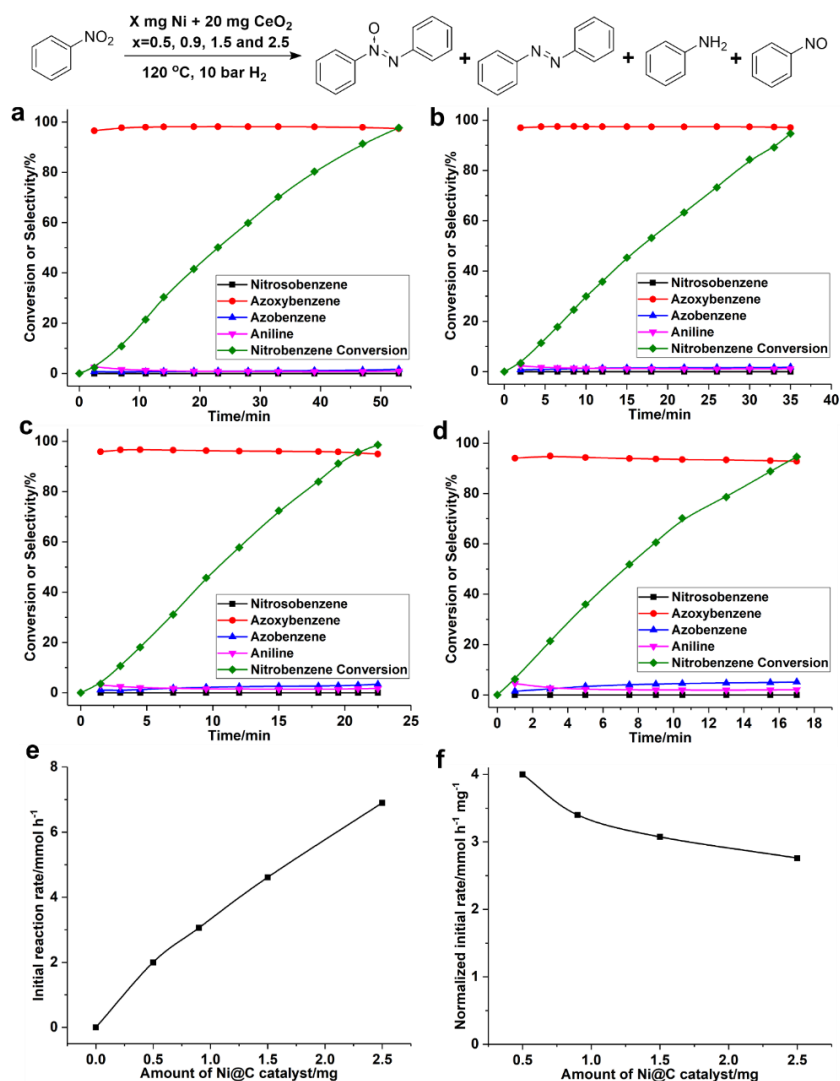
Figure 10.28. Hydrogenation of nitrobenzene with different amount of Ni@C NPs and 20 mg of CeO$_2$. (a) 0.6 mg Ni@C NPs and 20 mg CeO$_2$, (b) 0.9 mg Ni@C NPs and 20 mg CeO$_2$, (c) 1.5 mg Ni@C NPs and 20 mg CeO$_2$, (d) 2.5 mg Ni@C NPs and 20 mg CeO$_2$. (e) Relationship between initial reaction rate and the amount of Ni@C in the catalyst. (f) Normalized initial reaction rate. All the catalysts were pre-reduced by 10 bar of H$_2$ at 150 °C. In all cases, the selectivity to azoxybenzene is >93%.
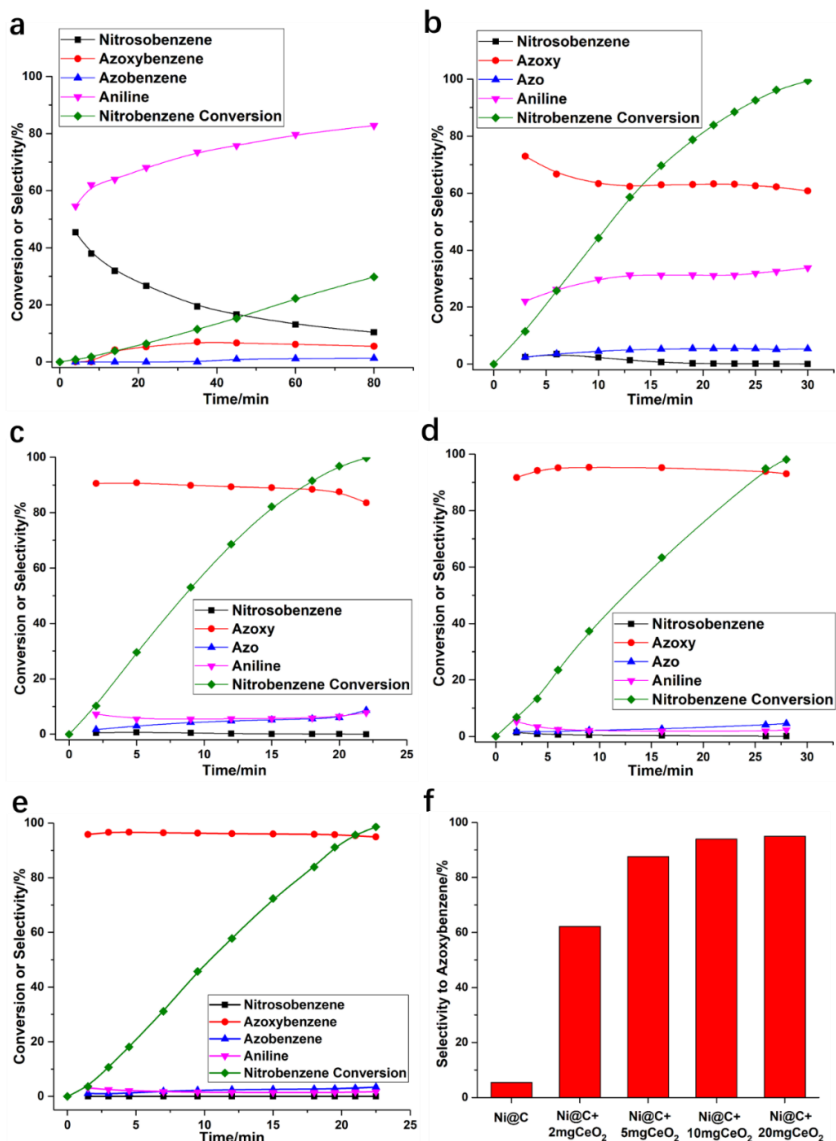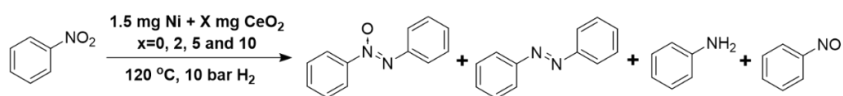
Figure 10.29. Hydrogenation of nitrobenzene by Ni@C+CeO$_2$ catalysts with different amount of CeO$_2$. (a) 1.5 mg Ni@C NPs, (b) 1.5 mg Ni@C NPs and 2 mg CeO$_2$, (c) 1.5 mg Ni@C NPs and 5 mg CeO$_2$, (d) 1.5 mg Ni@C NPs and 10 mg CeO$_2$ and (e) 1.5 mg Ni@C NPs and 20 mg CeO$_2$. (f) Selectivity to

azoxybenzene in the above four tests. All the catalysts were pre-reduced by 10 bar of H_2 at 150 °C. The selectivity to azoxybenzene with Ni@C catalyst corresponds to 30% conversion of nitrobenzene. The selectivity for the other Ni@C+CeO_2 catalysts correspond to conversion of >95%.

To further prove the role of Ni@C, the hydrogenation of nitrobenzene has been performed with the same amount of CeO_2 (20 mg) while varying the amount of Ni@C (0.5 to 2.5 mg). As presented in **Figure 10.28**, high selectivity to azoxybenzene has been obtained in all the catalytic tests. The initial reaction rate increases when increasing the amount of Ni@C catalyst and the selectivity to azoxybenzene remains high.

The influence of the amount of CeO_2 on the catalytic behavior of Ni@C has also been studied. As shown in **Figure 10.29**, addition of just 2 mg of CeO_2 as co-catalyst can dramatically improve the activity for hydrogenation of nitrobenzene. The selectivity to azoxybenzene is also improved from <10% to ~60%. Further increasing the amount of CeO_2 to 5 mg will lead to >80% selectivity. When 20 mg of CeO_2 is used as the co-catalyst, >95% selectivity to azoxybenzene can be achieved.

The above results indicate that at low mass ratios of CeO_2/Ni@C (5 mg/1.5 mg), the process for the formation of the azoxybenzene is controlled by the condensation step between the intermediates (nitrosobenzene and phenylhydroxylamine) and reduction step on the CeO_2. However, with a mass ratio of CeO_2/Ni@C higher than (20 mg/2.5 mg), the reaction is controlled by the transformation of nitrobenzene to nitrosobenzene, and reactivity is promoted by increasing the amount of Ni@C. In other words, and as it occurs within any bifunctional catalysts, both components should be optimized to maximize the overall activity and selectivity.[30-32]

In conventional supported metal catalysts (such as Au/TiO_2, Pt/TiO_2, etc.), spectroscopic results and theoretical calculations have proved that nitrobenzene is adsorbed at the metal-oxide interface.[33,34] H_2 is activated and dissociated on metal nanoparticles and then transfer to the metal-oxide interface for hydrogenation reaction (see **Figure 10.30a**). In this work, Ni@C interact with CeO_2 nanoparticles through inter-particle interaction, which is different to conventional supported metal catalysts.

As we have mentioned before, the evolution of the intermediates during the hydrogenation of nitrobenzene with Ni@C or Ni@C-CeO$_2$ catalyst (as shown in **Figure 10.6** and **Figure 10.17**) indicates that the presence of CeO$_2$ can immediately transform nitrosobenzene into azoxybenzene once it is formed. Therefore, it is highly likely that, nitrosobenzene can be preferentially absorbed on CeO$_2$. Considering the above catalytic and IR results, we propose that reaction intermediate species and activated H$_2$ are transported not only on a single catalyst particle, but between catalyst particles. As shown in **Figure 10.30b**, H$_2$ is activated on Ni@C NPs and the activated H species hydrogenate nitrobenzene into nitrosobenzene, which is a rate-limiting step in the reaction. Meanwhile, activated H can transfer to CeO$_2$ through inter-particle spillover, and convert nitrosobenzene into phenylhydroxylamine and making the condensation between nitrosobenzene and phenylhydroxylamine for azoxybenzene.[35-37] As discussed before, the interfacial interaction between Ni@C and CeO$_2$ NPs lead to the formation of a Ni@C-CeO$_2$ interface, which facilitate the inter-particle H spillover from Ni@C to CeO$_2$ NPs. Therefore, by employing Ni@C as the active sites for H$_2$ activation and nitrobenzene hydrogenation and employing CeO$_2$ as a co-catalyst for stabilization and further transformation of nitrosobenzene, the direct hydrogenation of nitrobenzene to azoxybenzene can be achieved under base-free mild conditions with high activity and selectivity.

It should be mentioned that, in the above proposed mechanism, the hydrogenation of nitrobenzene and hydrogenation of nitrosobenzene occurs on two separated sites. However, it is also possible that, nitrobenzene is absorbed on CeO$_2$ and then converted into azoxybenzene in the presence of activated H from the Ni@C nanoparticles. According to our above experimental results, we cannot rule out the above possibility. However, since we have observed the influence of agitation on the chemoselectivity for hydrogenation of nitrobenzene (see **Figure 10.19**), the intimate contact between Ni@C and CeO$_2$ NPs is important to achieve high selectivity to azoxybenzene, implying the transfer of reaction intermediate from one site to another. Thus, we prefer the mechanism that involves two separated reactive sites for hydrogenation of nitrobenzene to nitrosobenzene and then to azoxybenzene.
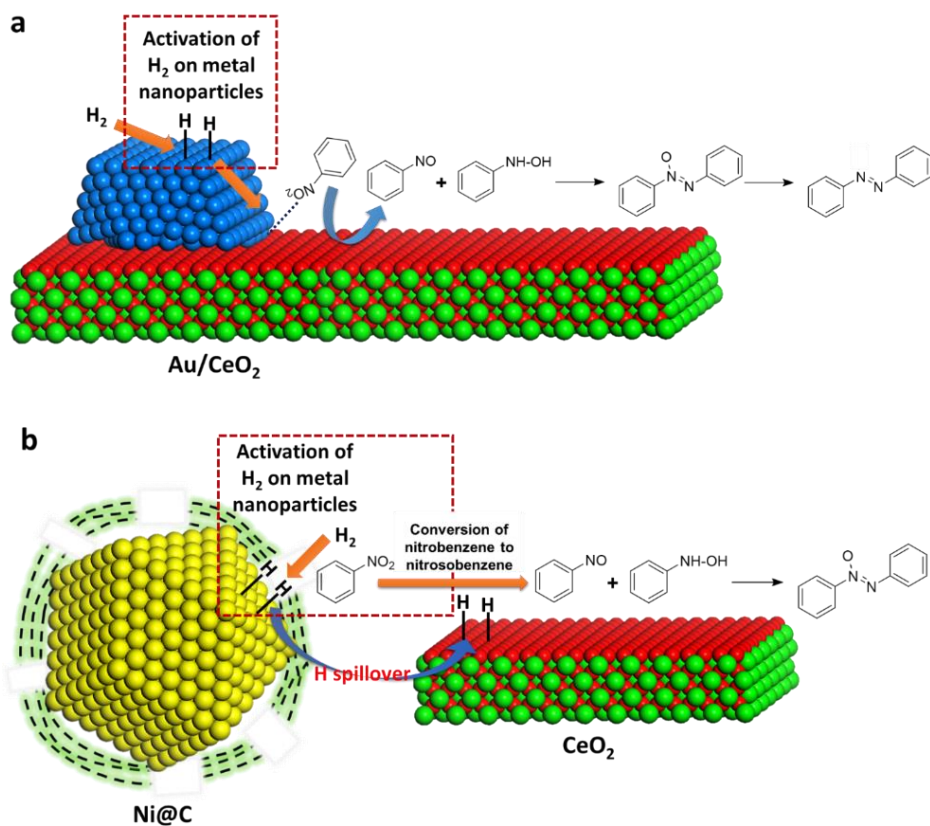
Figure 10.30. (a) Schematic illustration of direct hydrogenation of nitrobenzene to azoxybenzene and then to azobenzene on Au/CeO$_2$ catalyst. H$_2$ molecules are activated on Au nanoparticles and then transfer to the Au-CeO$_2$ interface to catalyze the hydrogenation of nitrobenzene. Nitroso and phenylhydroxylamine are the intermediates during the transformation. (b) Schematic illustration of direct chemoselective hydrogenation of nitrobenzene to azoxybenzene with Ni@C-CeO$_2$ catalyst. H$_2$ molecules are activated on Ni@C nanoparticles and then hydrogenate nitrobenzene to nitrosobenzene. Then, activated H species transfer to CeO$_2$ nanoparticles through hydrogen spillover and further convert nitrosobenzene to phenylhydroxylamine and then to azoxybenzene.
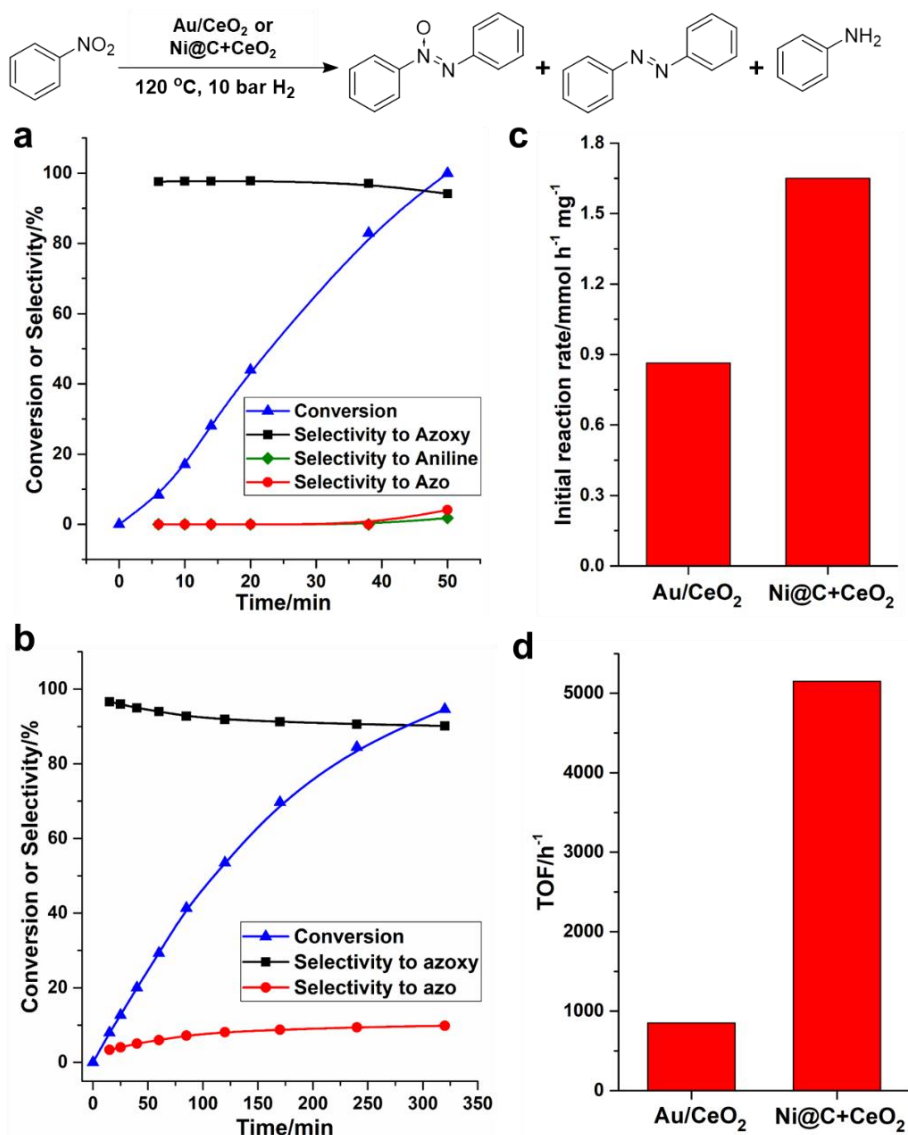
Figure 10.31. Comparison between commercial Au/CeO₂ (1 wt% of Au, from Johnson Matthey) and Ni@C-CeO2 for hydrogenation of nitrobenzene under the same conditions. (a) Catalytic result of Ni@C-CeO2 for hydrogenation of nitrobenzene to azoxybenzene. Small amount of azobenzene and aniline were obtained as by-products. Reaction conditions: 1 mmol of nitrobenzene, 2 mL toluene as solvent, 1.5 mg Ni@C and 10 mg of CeO₂ as catalyst, 120 °C and 10

bar of H_2. (b) Catalytic result of Au/CeO$_2$ for hydrogenation of nitrobenzene. Both azoxybenzene and azobenzene were observed in the products. Reaction conditions: 1 mmol of nitrobenzene, 2 mL toluene as solvent, 50 mg of Au/CeO$_2$ containing 0.5 mg of Au as catalyst, 120 $^{\circ}$C and 10 bar of H_2. (c) Initial reaction rates (mmol$_{H2}$·h^{-1}·mg^{-1}) normalized to the mass of metal of Au/CeO$_2$ and Ni@C-CeO$_2$ catalysts for hydrogenation of nitrobenzene. (d) Initial TOF values of Au/CeO$_2$ and Ni@C-CeO$_2$ for hydrogenation of nitrobenzene, calculated based on the surface atoms of Au and Ni in both systems. The amount of surface Au atoms in the Au/CeO$_2$ sample is calculated according to the size distribution of Au nanoparticles. In the case of Ni@C-CeO$_2$ catalyst, the amount of exposed surface Ni atoms is calculated based on the chemisorption measurement using CO as probe molecules.

We have compared the catalytic performance of Ni@C-CeO$_2$ with the state-of-art Au/CeO$_2$ for hydrogenation of nitrobenzene under the same conditions. As shown in **Figure 10.31**, with a higher amount of solid catalyst (50 mg of Au/CeO$_2$ vs. 1.5 mg of Ni@C+10 mg of CeO$_2$), Au/CeO$_2$ showed a much lower reaction rate. More importantly, Au/CeO$_2$ gives 90% selectivity to azoxybenzene at 94% conversion while Ni@C-CeO$_2$ gives 94% selectivity of azoxybenzene at 100% conversion. More importantly, Ni@C-CeO$_2$ catalyst can achieve full conversion of nitrobenzene with a much shorter reaction time than Au/CeO$_2$, especially if considering the lower quantity of solid catalyst used with Ni@C-CeO$_2$. The initial reaction rates normalized to the mass of metal catalysts and the initial turnover frequencies (TOFs) have also been calculated based on the exposed surface atoms in the Au/CeO$_2$ and Ni@C-CeO$_2$ catalysts. Ni@C-CeO$_2$ shows better performance than Au/CeO$_2$, indicating that the combination of Ni@C and CeO$_2$ is a good catalyst for the above-mentioned process.
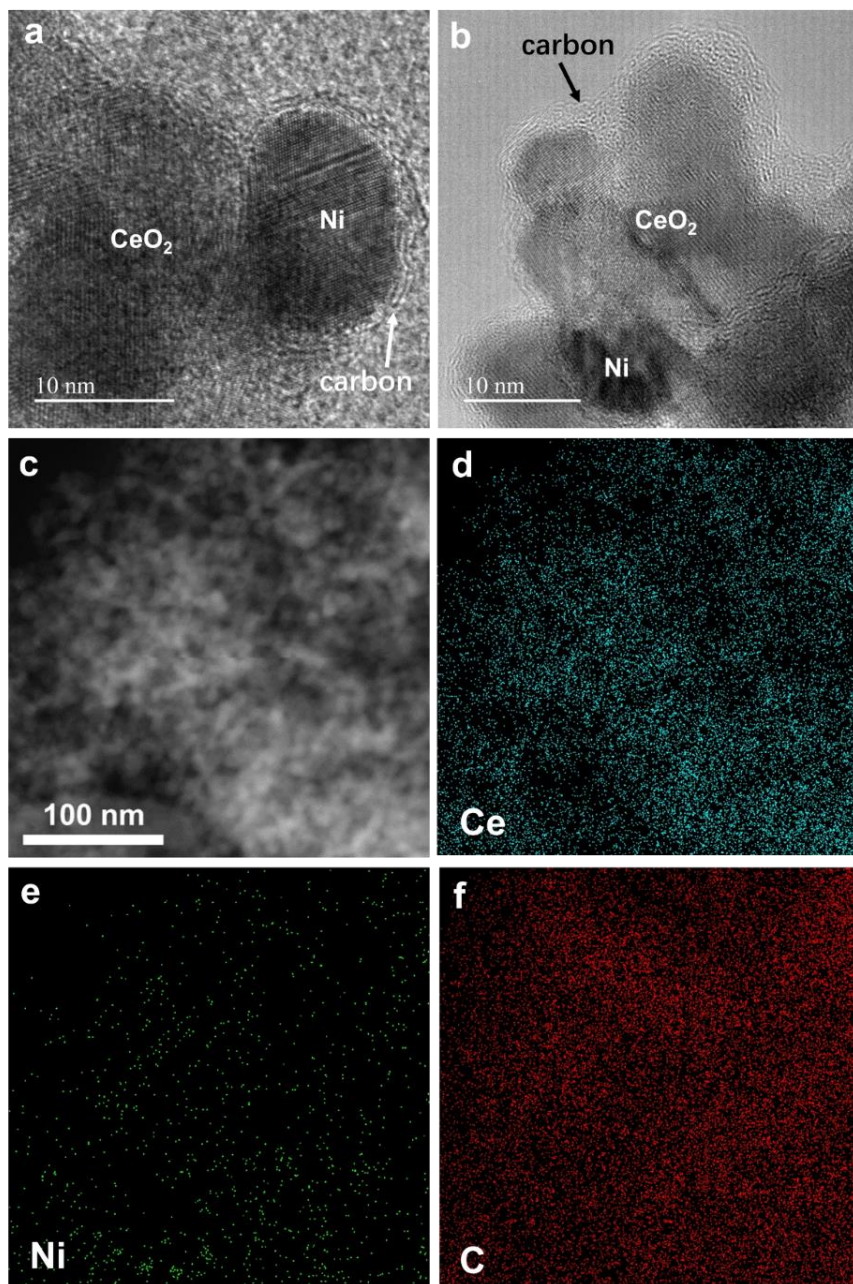
Figure 10.32. (a, b) High-resolution TEM images of the Ni-CeO$_2$-C catalyst, showing the presence of Ni nanoparticles and CeO$_2$ nanoparticles with thin

carbon layers surrounding them. (c-f) STEM image and the corresponding elemental mapping of that area.

Table 10.3. Catalytic performance of Ni-MOx-C catalyst prepared by one-pot hydrothermal synthesis for hydrogenation of nitrobenzene.[a]
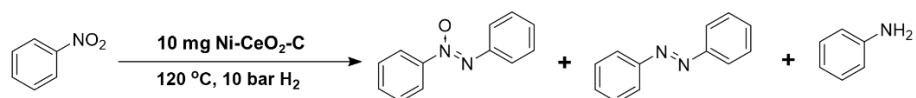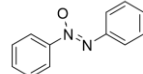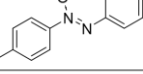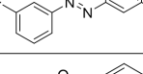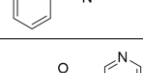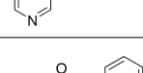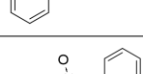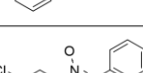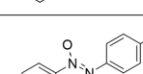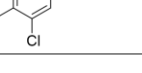

Sample	Time/min	Conversion/%	Selectivity to Azoxy	Selectivity to aniline	Selectivity to azo
Ni-CeO$_2$-C	35	97.1	92.4	4.9	2.7
Ni-TiO$_2$-C	190	38.2	-	>99	-
Ni-Al$_2$O$_3$-C	195	58.9	1.3	91.3	7.4
Ni-ZrO$_2$-C	190	19.8	21.9	78.1	0

[a] Reaction conditions: 1 mmol of nitrobenzene, 2 mL toluene as solvent, 120 °C and 10 bar of H$_2$. 10 mg of solid catalyst. The amount of Ni in the Ni-MOx-C catalysts is ca. 15 wt%. The yield of different products are calculated based on hexadecane as internal standard.

From a practical point of view, it will be more convenient for the application of this Ni@C-CeO$_2$ bifunctional system if the separated components can be merged into a single solid catalyst. To achieve that aim, we have prepared a Ni-CeO$_2$-C catalyst by one-pot hydrothermal synthesis and post-annealing treatment in N$_2$ at 600 °C (see experimental section for details). As shown in **Figure 10.32**, the Ni-CeO$_2$-C sample is consisted with Ni nanoparticles and carbon layers covered on Ni and CeO$_2$ particles. The catalytic results shown in **Table 10.3** indicate that, Ni-CeO$_2$-C sample is also active and selective for the hydrogenation of nitrobenzene to azoxybenzene. The activity of Ni-CeO$_2$-C is higher than the Ni@C-CeO$_2$ catalyst, which can be attributed the intimate contact between Ni and CeO$_2$ in the Ni-CeO$_2$-C nanocomposites. However, if CeO$_2$ is replaced with other metal oxides, the selectivity to azoxybenzene drops dramatically, which is similar to the results obtained with separated Ni@C and metal oxides.

Table 10.4. Scope study on direct hydrogenation of nitroarenes into corresponding aromatic azoxy products.[a]

Reactant	Product	Yield/%
		94%
		88%
		95%
		92%
		91%
		58%
		98%
		92%
		84%
		88%

[a] Reaction conditions: 1 mmol of nitrobenzene, 2 mL toluene as solvent, 120 °C and 10 bar of H_2. 2.0 mg of Ni@C nanoparticles and 20 mg of CeO_2 as co-catalyst. The yield of different products are calculated based on hexadecane as internal standard.

Table 10.5. Scope study on direct hydrogenation of nitroarenes into unsymmetrical azoxy compounds.[a]
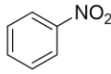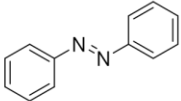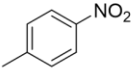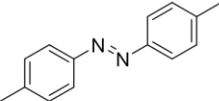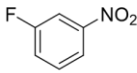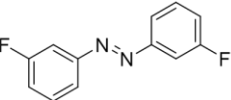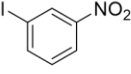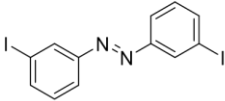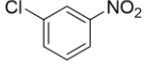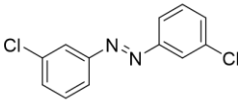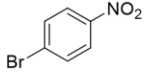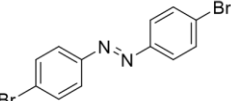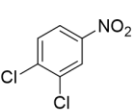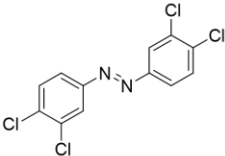
R₁-NO₂	R'-NO₂	Product	Yield/%
			58%
			63%
			65%
			75%
			45%
			31%
			58%
			64%

[a] Reaction conditions: 0.75 mmol of nitrobenzene, 0.25 mmol of R'-NO₂, 2 mL toluene as solvent, 90 °C and 12 bar of H_2. 2.0 mg of Ni@C nanoparticles and 20 mg of CeO_2 as co-catalyst. The yields of unsymmetric azoxy compounds were calculated based on the consumption of R'-NO₂. The yield of different products are calculated based on hexadecane as internal standard.

We have also studied the scope for direct hydrogenation of nitroarenes into corresponding azoxy compounds. As shown in **Table 10.4** and **Table 10.5**, high selectivity can be achieved for a variety of nitroarenes with different functional groups. Notably, 3-iodonitrobenzene can be selectivity hydrogenated into corresponding azoxy compounds, which cannot be achieved by supported Au catalysts. Therefore, it can be concluded that the combination of Ni@C NPs and CeO_2, azoxy compounds can be obtained with high chemoselectivity by direct hydrogenation of nitroarenes under mild conditions.

From the reaction scheme shown in **Figure 10.2**, in principle, azoxybenzene can be further hydrogenated into azobenzene.[28,38] After achieving high yield of azoxybenzene from nitrobenzene with Ni@C-CeO_2 catalyst, the hydrogenation reaction is continued and to our delight, azobenzene can be obtained with yield of 87%. Moreover, we have also studied the scope of Ni@C-CeO_2 catalyst for direct hydrogenation of various nitroarenes into corresponding azo compounds through azoxy compounds as intermediates. As shown in **Table 10.6**, several substituted azo compounds can be obtained from moderate to good yields under bass-free mild conditions.[39] Especially, it is possible to prepare aromatic azo compounds with iodo-substituted group with Ni@C-CeO_2 catalyst, which is not possible with Au-based catalysts. At this point, based on the above results and taking into consideration of the high reactivity and low cost of Ni@C-CeO_2 catalyst, it can work as promising substitute for Au/CeO_2 catalyst. Combining the results shown in this work and our previous works, it can be concluded that, nitroarenes can be selectively converted into different products (azoxy, azo or aniline) by various nanoparticulate non-noble metal catalysts.[21-25] As described in **Figure 10.33**, by tuning the reaction conditions and reaction time, it is possible to control the product distributions.

Table 6. Scope study on direct hydrogenation of nitroarenes into corresponding azo compounds.

Reactant	Product	Yield/%
		87%
		68%
		58%
		62%
		91%
		71%
		70%

[a] Reaction conditions: 1 mmol of nitrobenzene, 2 mL toluene as solvent, 90 °C and 10 bar of H_2. 2.0 mg of Ni@C nanoparticles and 20 mg of CeO_2 as co-catalyst. The yield of different products are calculated based on hexadecane as internal standard.
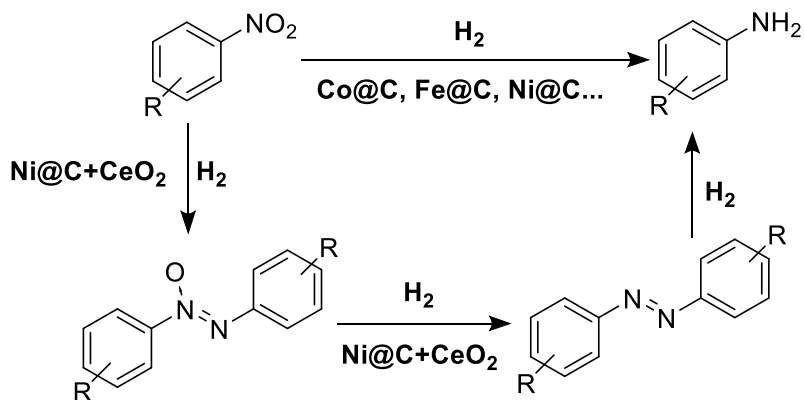
Figure 10.33. Chemoselective hydrogenation of nitroarenes to different products with non-noble metal catalysts. By choosing different catalysts and co-catalysts, it is possible to obtain various products (azoxy, azo and aniline) by tuning the reaction conditions and reaction time.

4. Conclusions

Bifunctional non-noble Ni@C-CeO$_2$ catalyst is found to be a highly active and selective catalyst for direct hydrogenation of nitroarenes into corresponding azoxy or azo products under mild conditions. Notably, the Ni@C-CeO$_2$ catalyst surpasses the performance of state-of-art Au/CeO$_2$ catalyst for direct transformation of nitroarenes to azoxy compounds. According to the kinetic and spectroscopic results, it is proposed that H$_2$ is activated on Ni@C nanoparticles and then transfer to CeO$_2$ through inter-particle hydrogen spillover and then catalyze the chemoselective hydrogenation of nitrobenzene to azoxybenzene. The Ni@C-CeO$_2$ catalyst enables us to obtained different products (azoxy, azo or aniline compound) by controlling the reaction time. This work brings new insights on the design and application of non-noble metal catalysts as promising substitutes to noble metal catalysts for chemoselective hydrogenation reactions. Considering the hydrogenation spillover mechanism proposed in this work, it will be possible to tuning the catalytic properties of metal nanoparticles by different combination of metal-oxide(or other co-catalysts) for various chemoselective hydrogenation reactions.

References

(1) Corma, A. *Angew. Chem. Int. Ed.* **2016,** *55*, 6112-6113.

(2) Ye, R.; Hurlburt, T. J.; Sabyrov, K.; Alayoglu, S.; Somorjai, G. A. *Proc. Natl. Acad. Sci. USA* **2016,** *113*, 5159-5166.

(3) Schlogl, R. *Angew. Chem. Int. Ed.* **2015,** *54*, 3465-3520.

(4) Serna, P.; Corma, A. *ACS Catal.* **2015,** *5*, 7114-7121.

(5) Filice, M.; Palomo, J. M. *ACS Catal.* **2014,** *4*, 1588-1598.

(6) Climent, M. J.; Corma, A.; Iborra, S.; Sabater, M. J. *ACS Catal.* **2014,** *4*, 870-891.

(7) Szőllősi, G. *Catal. Sci. Technol.* **2018,** *8*, 389-422.

(8) Lipshutz, B. H.; Isley, N. A.; Fennewald, J. C.; Slack, E. D. *Angew. Chem. Int. Ed.* **2013,** *52*, 10952-10958.

(9) Sheldon, R. A. *Green Chem.* **2017,** *19*, 18-43.

(10) Leyva-Perez, A.; Garcia-Garcia, P.; Corma, A. *Angew. Chem. Int. Ed.* **2014,** *53*, 8687-8690.

(11) Bigelow, H. E. *Chem. Rev.* **1931**, *9*, 117-167.

(12) Russew, M. M.; Hecht, S. *Adv. Mater.* **2010,** *22*, 3348-3360.

(13) Buncel, E. *Acc. Chem. Res.* **1975**, *8*, 132-139.

(14) Sakaue, S.; Tsubakino, T.; Nishiyama, Y.; Ishii, Y. *J. Org. Chem.* **1993,** *58*, 3633-3638.

(15) Acharyya, S. S.; Ghosh, S.; Bal, R. *ACS Sustainable Chem. Eng.* **2014**, *2*, 584-589.

(16) Tumma, H.; Nagaraju, N.; Reddy, K. V. *Appl. Catal. A: Gen.* **2009**, *353*, 54-60.

(17) Pahalagedara, M. N.; Pahalagedara, L. R.; He, J.; Miao, R.; Gottlieb, B.; Rathnayake, D.; Suib, S. L. *J. Catal.* **2016,** *336*, 41-48.

(18) Hou, T.; Wang, Y.; Zhang, J.; Li, M.; Lu, J.; Heggen, M.; Sievers, C.; Wang, F. *J. Catal.* **2017,** *353*, 107-115.

(19) Zhang, Z. P.; Wang, X. Y.; Yuan, K.; Zhu, W.; Zhang, T.; Wang, Y. H.; Ke, J.; Zheng, X. Y.; Yan, C. H.; Zhang, Y. W. *Nanoscale* **2016,** *8*, 15744-15752.

(20) Liu, L.; Corma, A. *Chem. Rev.* **2018,** *118*, 4981-5079.

(21) Westerhaus, F. A.; Jagadeesh, R. V.; Wienhofer, G.; Pohl, M. M.; Radnik, J.; Surkus, A. E.; Rabeah, J.; Junge, K.; Junge, H.; Nielsen, M.et al. *Nat. Chem.* **2013,** *5*, 537-543.

(22) Jagadeesh, R. V.; Surkus, A. E.; Junge, H.; Pohl, M. M.; Radnik, J.; Rabeah, J.; Huan, H.; Schunemann, V.; Bruckner, A.; Beller, M. *Science* **2013,** *342*, 1073-1076.

(23) Hahn, G.; Ewert, J.-K.; Denner, C.; Tilgner, D.; Kempe, R. *ChemCatChem* **2016,** *8*, 2461-2465.

(24) Liu, L.; Concepción, P.; Corma, A. *J. Catal.* **2016,** *340*, 1-9.

(25) Liu, L.; Gao, F.; Concepción, P.; Corma, A. *J. Catal.* **2017,** *350*, 218-225.

(26) Millán, R.; Liu, L.; Boronat, M.; Corma, A. *J. Catal.* **2018,** *364*, 19-30.

(27) Vile, G.; Bridier, B.; Wichert, J.; Perez-Ramirez, J. *Angew. Chem. Int. Ed.* **2012,** *51*, 8620-8623.

(28) Combita, D.; Concepción, P.; Corma, A. *J. Catal.* **2014,** *311*, 339-349.

(29) Richner, G.; van Bokhoven, J. A.; Neuhold, Y. M.; Makosch, M.; Hungerbuhler, K. *Phys. Chem. Chem. Phys.* **2011**, *13*, 12463-12471.

(30) Jiao, F.; Li, J.; Pan, X.; Xiao, J.; Li, H.; Ma, H.; Wei, M.; Pan, Y.; Zhou, Z.; Li, M.et al. *Science* **2016,** *351*, 1065-1068.

(31) Zecevic, J.; Vanbutsele, G.; de Jong, K. P.; Martens, J. A. *Nature* **2015,** *528*, 245-248.

(32) Kong, X.; Zhu, Y.; Zheng, H.; Li, X.; Zhu, Y.; Li, Y.-W. *ACS Catal.* **2015,** *5*, 5914-5920.

(33) Boronat, M.; Concepcion, P.; Corma, A.; Gonzalez, S.; Illas, F.; Serna, P. A *J. Am. Chem. Soc.* **2007,** *129*, 16230-16237.

(34) Corma, A.; Serna, P.; Concepcion, P.; Calvino, J. J. *J. Am. Chem. Soc.* **2008,** *130*, 8748-8753.

(35) Prins, R. *Chem. Rev.* **2012,** *112*, 2714-2738.

(36) Lee, S.; Lee, K.; Im, J.; Kim, H.; Choi, M. *J. Catal.* **2015,** *325*, 26-34.

(37) Karim, W.; Spreafico, C.; Kleibert, A.; Gobrecht, J.; VandeVondele, J.; Ekinci, Y.; van Bokhoven, J. A. *Nature* **2017,** *541*, 68-71.

(38) Liu, X.; Li, H. Q.; Ye, S.; Liu, Y. M.; He, H. Y.; Cao, Y. *Angew. Chem. Int. Ed.* **2014,** *53*, 7624-7628.

(39) Liu, W.; Zhang, L.; Yan, W.; Liu, X.; Yang, X.; Miao, S.; Wang, W.; Wang, A.; Zhang, T. *Chem. Sci.* **2016,** *7*, 5758-5764.

This chapter is reused from the following publication:

Sunlight-assisted hydrogenation of CO_2 into ethanol and C2+ hydrocarbons by sodium-promoted Co@C nanocomposites, **L. Liu**, A. V. Puga, J. Cored, P. Concepción, V. Pérez-Dieste, H. García and A. Corma *Applied Catalysis B: Environmental*, 2018, 235, 186-196.

Chapter 11

Sunlight-assisted Hydrogenation of CO_2 into ethanol and C2+ Hydrocarbons by Sodium-promoted Co@C Nanocomposites

Abstract

The hydrogenation of CO_2 into hydrocarbons promoted by the action of sunlight has been studied on Co nanoparticles covered by thin carbon layers. In particular, nearly 100% selectivity to hydrocarbons is obtained with increased selectivities towards C2+ hydrocarbons and alcohols (mainly ethanol) when using nanostructured materials comprising metallic cobalt nanoparticles, carbon layers, and sodium as promoter (Na-Co@C). In the contrary, larger amount of CH_4 and lower selectivities to C2+ hydrocarbons and alcohols were obtained in the conventional thermal catalytic process. When using Co@C nanoparticles in the absence of Na or bare Co_3O_4 as catalyst, methane is essentially the main product (selectivity >96%). Control experiments in the presence of methanol as a hole scavenger suggest the role of light in generating charges by photon absorption as promoting factor. The reaction mechanism for photoassisted CO_2 hydrogenation on the Co-based catalysts was investigated by near ambient-pressure X-ray photoelectron (AP-XPS) and *in situ* Raman spectroscopies, which provided information on the role of light and Na promoter in the modulation of product distribution for CO_2 hydrogenation. Spectroscopic studies suggested that surface CO_2 dissociation to CO, the stabilization of CO adsorbed on the surface of Na-Co@C catalyst and the easy desorption of reaction products is a key step for photothermal CO_2 hydrogenation to ethanol and C2+ hydrocarbons.

1. Introduction

Photocatalytic CO_2 reduction is one of the most challenging issues in chemical research.[1] In numerous investigations in this area, CO_2 reduction is coupled with the splitting of H_2O for the production of solar fuels, a process which is commonly referred to as artificial photosynthesis.[2,3] However, with heterogeneous photocatalysts, reaction rates for the transformation of CO_2/H_2O mixtures are usually in the order of micromoles per hour, which is too far from any practical application.[4-7] Moreover, the major products in most of the reports dealing with artificial photosynthesis are frequently CH_4 or CO. It appears that with the heterogeneous catalytic systems reported so far, it is very difficult to achieve carbon chain growth to go beyond CH_4 and to produce significant amounts of more valuable C2+ hydrocarbons during the photocatalytic

reduction of CO_2.

As an alternative to the reduction of CO_2 by H_2O, in the past few years, our research group has reported the photoassisted hydrogenation of CO_2 to CH_4 on Ni (or NiO) nanoparticles under solar light irradiation.[8,9] The formation rate of CH_4 was as high as mmol/h, which is about three orders of magnitude higher than for typical CO_2+H_2O reactions. However, only CH_4 was selectively produced using Ni, NiO or other supported Group VIII catalysts.[10] In a recent work, Ozin and his co-workers reported that hydride-terminated Si nanoparticles can catalyze the reverse water-gas shift (RWGS) reaction leading to the formation of CO under photo-thermal conditions.[11] Iron nanoparticles encapsulated in carbon can also be efficient catalyst for the photoassisted RWGS reaction, as reported by Ye and co-workers.[12] However, in most of previous works, the selectivity to C2+ products are usually quite low. In a recent work, Zhang *et al.* have reported the application of CoFe@C bimetallic nanoparticles for CO_2 hydrogenation to hydrocarbons by a photothermal process.[13] It has been claimed that solar light irradiation can increase the temperature of the catalyst surface, which further enhance the activity. However, the influence of solar light irradiation on the reaction mechanism for CO_2 hydrogenation is not clear.[14,15]

The lack of photoassisted processes generating C2+ hydrocarbons contrasts with conventional heterogeneous catalysis, whereby mixtures of CO_2 and H_2 can be transformed into CO or CH_4, but interestingly, also into other C2+ hydrocarbons, depending on the catalyst.[16-20] For instance, metal nanoparticles (including Ni, Co and Ru materials) are active catalysts for CO_2 methanation, converting CO_2 to CH_4.[21-23] This reaction requires temperatures above 250 °C, giving rise to a large amount of CO (in some cases, selectivity to CO can be as high as 80%) as by-product. Moreover, metal nanoparticles (including Fe, Co and Ru materials) can also serve as active catalysts for Fischer-Tropsch synthesis (FTS), transforming CO/CO_2 and H_2 into hydrocarbons and oxygenates, though FTS is usually performed at high pressure.[24] Recently, it has also been reported that Ni-NiOx nanocomposites can catalyze the CO hydrogenation into hydrocarbons by a photoassisted process.[25]

In this work, we report the photothermal hydrogenation of CO_2 into hydrocarbons (CH_4 together with a high proportion of C2+ hydrocarbons and

ethanol) using Na-promoted Co@C nanocomposites as catalysts under solar light and near-atmospheric pressure. The reaction rate of this process is in the order of mmol $g_{cat}^{-1} h^{-1}$ and the selectivity to ethanol is 6.5% at 37% CO_2 conversion and >30% selectivity to C2+ hydrocarbons at nearly 100% CO_2 conversion. It will also be shown that the analogous thermal reaction with the same catalyst behaves differently and produces larger amounts of CH_4 and much less alcohols. The effect of light irradiation on the reaction mechanism has been studied by ambient-pressure X-ray photoelectron spectroscopy (AP-XPS) and *in situ* Raman spectroscopy. The results indicate that light has a clear effect on the formation and stabilization of intermediates for the production of ethanol and the C-C chain growth process for the production of C2+ hydrocarbons.

2. Experiments

2.1 Catalyst preparation.

Preparation of Na-Co@C. The sodium-promoted Co@C nanocomposites were prepared through the reduction of cobalt-sodium-ethylenediaminetetraacetate (Co-Na-EDTA) complexes by H_2. The Co-EDTA complex was prepared through a hydrothermal process. Firstly, Na_2EDTA (4.47 g) and NaOH (0.96 g) were dissolved in H_2O (20 mL) at room temperature. $Co(NO_3)_2$ (6.98 g) was added to the above solution under strong stirring, resulting in formation of homogeneous solution. Then, methanol (10 mL) was added to the aqueous solution. A portion of the resulting purple homogeneous solution (ca. 23 mL) was transferred into a 35 mL stainless steel autoclave and kept in an oven at 200 °C for 24 h. After cooling to room temperature, the solid precipitates were collected by filtration and washed with deionized water and acetone, followed by drying at 60 °C to yield the Co-EDTA complex. Then, the sodium-promoted Co@C nanocomposite (Na-Co@C) was obtained by reduction of Co-EDTA complex with H_2 at 450 °C for 2 h with a ramp rate of 10 °C/min from room temperature to 450 °C.

Preparation of Co@C. In the first step, Co_3O_4 nanoparticles were prepared as precursor for Co@C. $Co(OAc)_2$ (4.94 g) was dissolved in ethylene glycol (100 mL) under stirring at 160 ºC. When $Co(OAc)_2$ was totally dissolved in ethylene

glycol, an aqueous Na_2CO_3 solution (mixture of 4.24 g of Na_2CO_3 and 160 mL distilled water) was added drop by drop. It took 1.5~2 h to finish the process, and then, the suspension was aged for another 1 h at 160 °C before cooling down to room temperature. A purple solid product was obtained after the filtration of the suspension and washing with water and acetone. After drying in an oven at 60 °C for 16 h, the solid product was submitted to calcination in static air at 450 °C for 3 h with a ramp rate of 1 °C/min from room temperature to 450 °C, resulting in formation of Co_3O_4 nanoparticles. In the second step, Co@C sample was prepared through a carbon coating process using the Co_3O_4 nanoparticles as precursor. Glucose (360 mg) was dissolved in distilled water (20 mL). Then Co_3O_4 (0.5 g) was dispersed in the glucose aqueous under ultra-sonication. The black suspension was transferred into autoclave and kept at 175 °C for 18 h. After cooling down to room temperature, the solid product was washed with water and acetone and dried in oven at 60 °C, resulting in the formation of $Co(OH)_2$/C composites. The Co@C nanoparticles were obtained by annealing the $Co(OH)_2$/C composites in N_2 at 600 °C for 2 h at a ramp rate of 10 °C/min from room temperature to 600 °C. After being kept at 600 °C for 2 h, the sample was cooled down in N_2 flow to room temperature and stored in glass vial in the ambient environment.

2.2 Structural characterization techniques.

Samples for electron microscopy studies were prepared by dropping the suspension of the powder sample using CH_2Cl_2 as the solvent directly onto holey-carbon coated nickel or copper grids. All the measurements were performed in a JEOL 2100F microscope operating at 200 kV both in transmission (TEM) and scanning-transmission modes (STEM). STEM images were obtained using a High Angle Annular Dark Field detector (HAADF), which allows Z-contrast imaging. Powder X-ray diffraction (XRD) was performed using a HTPhilips X'Pert MPD diffractometer equipped with a PW3050 goniometer using Cu Kα radiation and a multisampling handler.

2.3 Ambient-pressure X-ray photoelectron spectra (XPS).

The AP-XPS experiments were performed at the CIRCE beamline of the ALBA synchrotron. CIRCE is an undulator beamline with a photon energy range 100-

2000 eV. The beam spot size at the sample is 100×30 μm^2. The AP-XPS endstation, equipped with a PHOIBOS 150 analyzer from SPECS, is described elsewhere. [26] The data were acquired with an instrumental energy resolution better than 0.3 eV, PE 20 eV and exit slit 20 μm. The sample (10 mg) was pelletized and mounted onto the sample holder using a resistive bottom heater for sample heating. The temperature was monitored during all experiments with a K-type thermocouple in direct contact with the sample. For the photothermal studies a solar simulator (Newport®, Oriel Instruments, model 69921, same as for the catalytic studies) was placed outside on top of a viewport front to the sample. CO_2 and H_2 were fed into the analysis chamber using two leak valves maintaining a constant pressure of 0.1 mbar CO_2 and 0.5 mbar H_2 inside the chamber. The AP-XP spectra were acquired using two different photon energies, 510 and 1000 eV. XPS data were analyzed using the CASA software. The atomic fraction of each element was obtained from the peak areas, calibrated for the incident photon flux and the corresponding cross sections.

2.4 *Operando* Raman studies.

Raman spectra were recorded at ambient temperature with a 785 nm HPNIR excitation laser on a Renishaw Raman Spectrometer ("Reflex") equipped with an Olympus microscope and a CCD detector. The laser power on the sample was 15 mW and a total of 20 acquisitions were taken for each spectrum. For the *operando* Raman experiments 20mg of sample was loaded into a quartz cell adequate for "in situ" Raman studies. After evacuating the cell (P< 10 mbar), CO_2, N_2 and H_2 in a 1:1:5 molar ratios were introduced up to a total pressure of ~1 bar. In the photothermal studies, the catalytic cell was irradiated using a solar simulator (Newport®, Oriel Instruments, model 69921). Light irradiation was stopped at specific times where Raman spectra were acquired. For the thermal studies the catalytic cell was introduced in a heating plate at 235 ºC. Raman spectra were acquired under reaction conditions at specific times.

2.5 CO$_2$ hydrogenation tests.

Photothermal CO_2 hydrogenation under simulated sunlight irradiation in the presence of the catalyst solid powders (75 mg) were carried out in a purpose-designed quartz cell (V=50 cm^3). After evacuating the cell (P<10 mbar),

appropriate amounts of CO_2, N_2 and H_2 (typically, 20, 20 and 100 cm^3 as standard conditions) were introduced with a final pressure of ~2.8 bar. Simulated sunlight irradiations of the solids were carried out using a solar simulator (Newport®, Oriel Instruments, model 69921) equipped with a Xe lamp (1000 W) coupled with an AM1.5 filter that provides simulated concentrated sunlight. Unless otherwise noted, the irradiance at the surface of the solids was *ca.* 24 kW m^{-2}.

The initial reaction rates of Na-Co@C sample under thermal or photothermal conditions were measured in a photoreactor composed of a quartz tube (V = 300 cm^3) and a built-in heating plate, using the same gaseous mixture as described above, at a total pressure of *ca.* 100 kPa. The reactor body is made of aluminium to favor heat transfer to the environment and no special cooling system was used. The temperature and pressure inside the photoreactor were measured by an internal thermocouple and a manometer, respectively.

The time-profile conversion of the reactions was followed by analyzing samples (ca. 2.5 cm^3) taken from the gas phase periodically on a two-channel chromatograph (Agilent 490 Micro GC, carrier gas: Ar) equipped with thermal conductivity detectors (TCD), and a MS 5Å column (first channel) for the quantification of H_2, N_2 and CO, and a PoraPLOT Q column (second channel) for the quantification of CO_2 and hydrocarbons. The analysis of C2+ hydrocarbons and oxygenates was performed with a SCION-456 GC with FID detector. The selectivity to different products is calculated based on the carbon.

3. Results and discussion

3.1 Synthesis and structural characterization of Na-promoted Co@C

Na-promoted Co@C nanocomposites (denoted as Na-Co@C) were prepared by thermal decomposition of cobalt-sodium-ethylenediaminetetraacetate (Co-Na-EDTA) complexes at 450 °C (see Experimental section below) in H_2 atmosphere.[27] As shown in **Figure 11.1**, the X-ray diffraction (XRD) pattern of this sample only shows the diffraction peaks corresponding to metallic cobalt, being *fcc* (PDF code: 96-900-8467) and *hcp* phases (PDF code: 96-900-8493) as the predominant and minor phases present, respectively. Moreover, the Raman spectrum (see **Figure 11.2**) reveals that CoO_x species (Co_3O_4) are also detectable in the sample together with disordered carbon. To gain further

understanding on the structure of Na-Co@C, the sample was studied by electron microscopy. As shown in **Figure 11.4a-b**, Na-promoted Co@C nanocomposites consist of nanoparticles with sizes ranging from 15 to 150 nm (see **Figure 11.3** for more typical images and particle size distribution of the Na-Co@C sample). The high-resolution transmission electron microscopy (HRTEM) images in **Figure 11.4c** and **4d** show that Co nanoparticles are surrounded by thin carbon layers. Lattice fringes corresponding to metallic Co and Co_3O_4 can be observed in this sample, suggesting that, either part of the Co^{2+} species maintained their oxidation state, or part of the metallic Co was oxidized when exposed to air after the preparation. It is interesting to note that the core of the nanoparticles consisted of metallic cobalt, whereas Co_3O_4 patches are present on their surfaces below the carbon layers. Due to the presence of thin carbon layers, Co nanoparticles are protected from deep oxidation by air. Elemental mapping indicates that Co, C, O as well as Na are regularly dispersed in the nanocomposites **(Figure 11.4f-j)**. The Na-Co@C sample contains *ca.* 95 wt.% of Co and 2 wt.% of Na. An analogous Co@C sample free of Na has been also prepared (see the experimental section for synthesis procedure).[28] Similar to the Na-promoted sample, HRTEM of the Co@C sample shows the presence of Co nanoparticles surrounded by thin carbon layers (see **Figure 11.5**), with CoOx patches on the surface and metallic Co as the core. The XRD pattern of the Co@C sample is also similar to Na-Co@C, showing the typical diffraction pattern of *fcc* metallic Co and a small proportion of *hcp* Co.
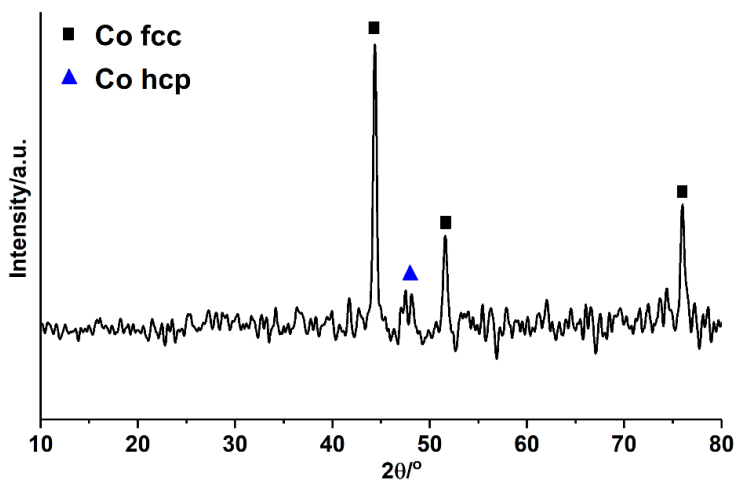
Figure 11.1. XRD pattern of Na-Co@C. In this sample, due to the good encapsulation of Co nanoparticles by thin carbon layers, only diffraction peaks corresponding to metallic Co can be observed.
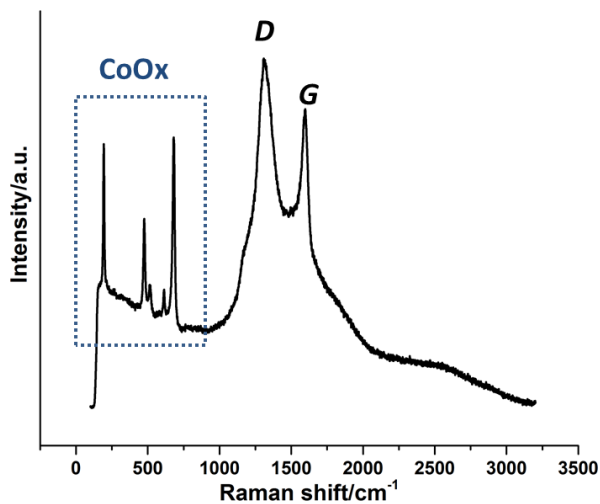
Figure 11.2. Raman spectrum of Na-Co@C. Raman bands corresponding to both Co_3O_4 and disordered carbon can be observed.
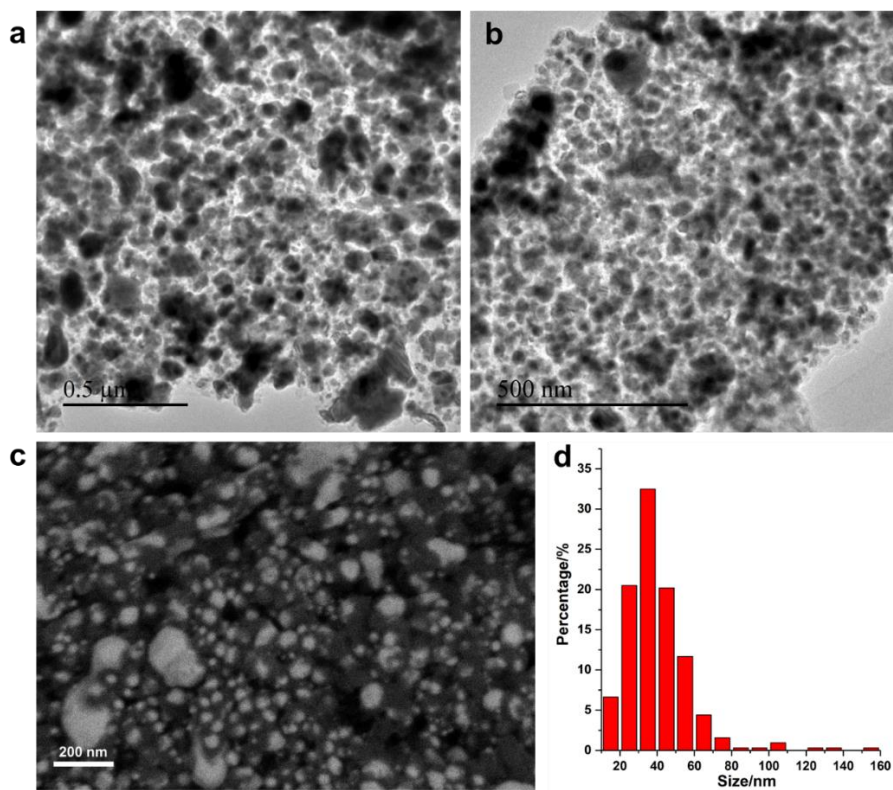
Figure 11.3. (a, b) Typical TEM images of Na-Co@C sample. (c) Typical FESEM image of Na-Co@C sample obtained by ESB mode. (d) Size distribution of Co nanoparticles in the Na-Co@C sample.
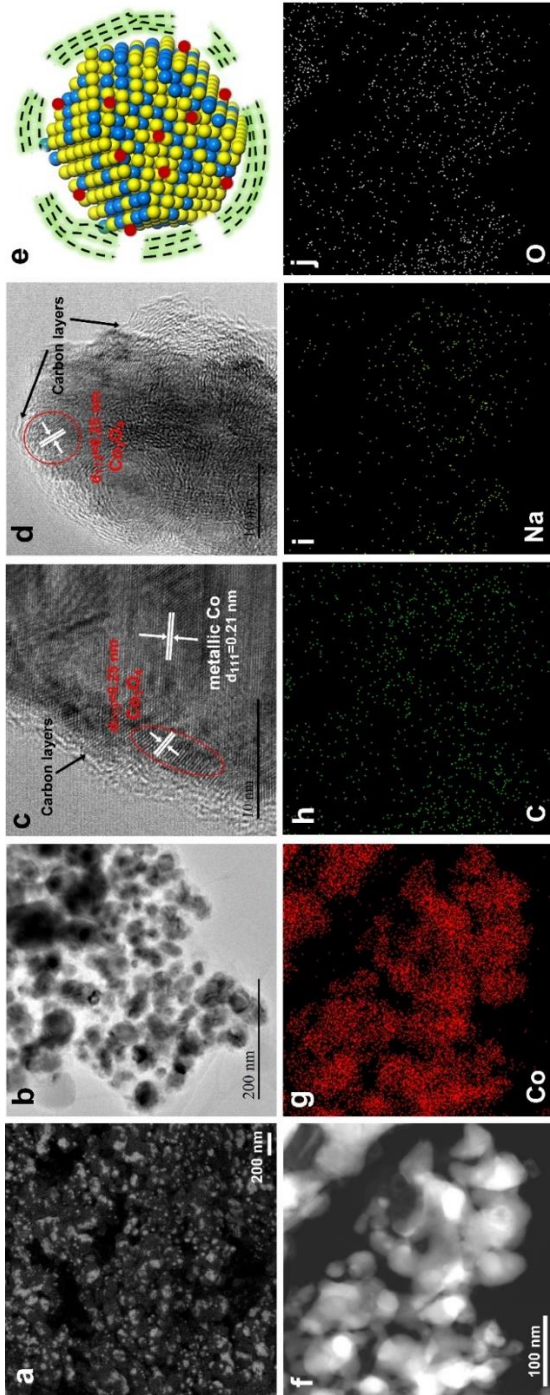
Figure 11.4. Structural characterization of Na-Co@C sample. (a) Field-emission scanning electron microscopy (FESEM) image, (b) transmission electron microscopy (TEM) images, and (c, d) high-resolution transmission electron microscopy (HRTEM) images of Na-Co@C sample. (e) A schematic illustration of one Na-Co@C nanoparticle. Co, CoO$_x$ and sodium are represented by yellow, blue and red balls, respectively, while the carbon layers are represented as shaded dashed lines. (f) Scanning transmission electron microscopy (STEM) image and (g-j) corresponding elemental mapping of different elements in the Na-Co@C sample.
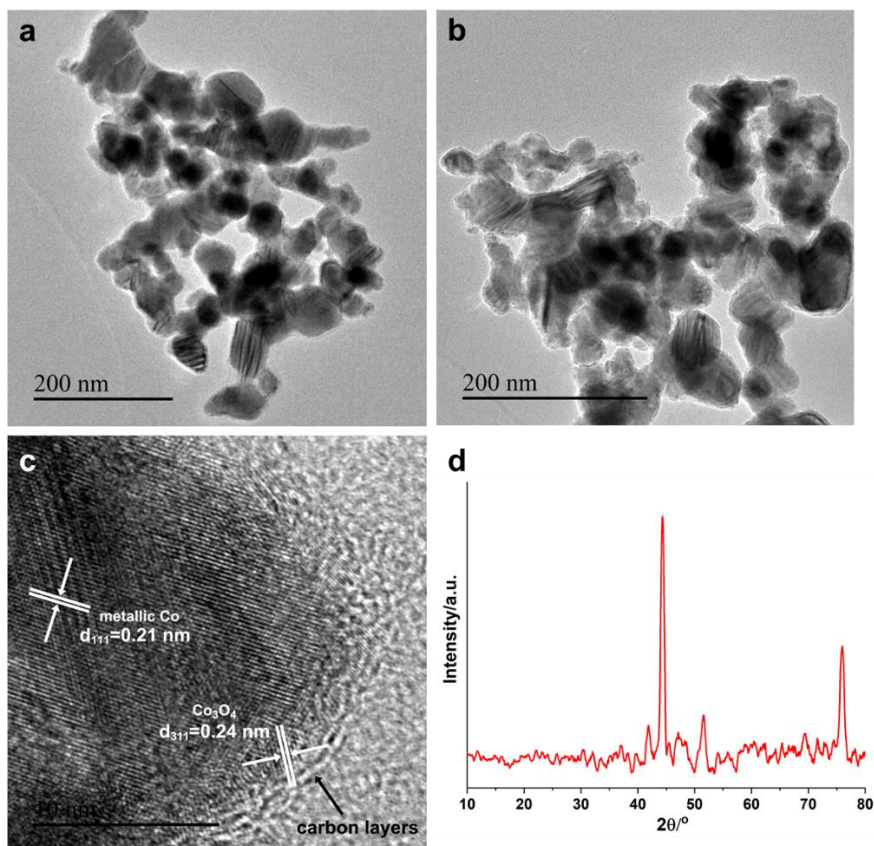
Figure 11.5. TEM images of Co@C sample. The sizes of Co nanoparticles are similar to those in the Na-Co@C sample. In this sample, Co nanoparticles are also covered by thin carbon layers. CoO_x patches can also be found on the surface of metallic Co.

3.2 Photothermal hydrogenation of CO_2

Table 1. Photothermal and thermal CO_2 hydrogenation on different cobalt catalysts.

Sample	Conversion/%	Selectivity[c]/%								
		CH$_4$	CO	Ethanol	C2	C3	C4	C5	C6	Other products
Na-Co@C-photothermal[a]	97.0	62.7	-	0.6	16.5	12.5	4.8	2.0	0.6	0.3
Co@C-photothermal[a]	98.8	92.6	-	-	4.4	1.8	0.7	0.3	0.1	-
Na-Co@C-photothermal[a]	**37.0**	**50.2**	**4.8**	**6.5**	**13.0**	**12.7**	**5.2**	**3.3**	**2.0**	**2.3**
Co$_3$O$_4$-photothermal[a]	96.9	98.2	-	-	1.8	-	-	-	-	-
Na-Co@C-thermal[b]	91.5	67.4	-	0.4	11.9	10.4	5.1	2.7	1.3	0.6
Na-Co@C-thermal[b]	38.0	63.2	2.4	0.71	12.1	11.4	5.1	2.9	1.4	0.8

[a] Reaction conditions for photoassisted CO_2 hydrogenation reaction: mixture of CO_2 (20 mL), H_2 (100 mL), and N_2 (20 mL); catalyst mass, 75 mg; irradiation source, solar simulator. Blank controls in the absence of any solid catalyst or the reaction in the dark without heating did not lead to any product. The temperature of the sample (235 $^{\circ}$C) under the photothermal conditions was measured by a thermocouple placed in close contact with the upper surface of the powdered solid. [b] The thermal reaction was performed at the same temperature as the photothermal process without the presence of solar light irradiation. [c]The selectivity to different products are normalized to carbon.
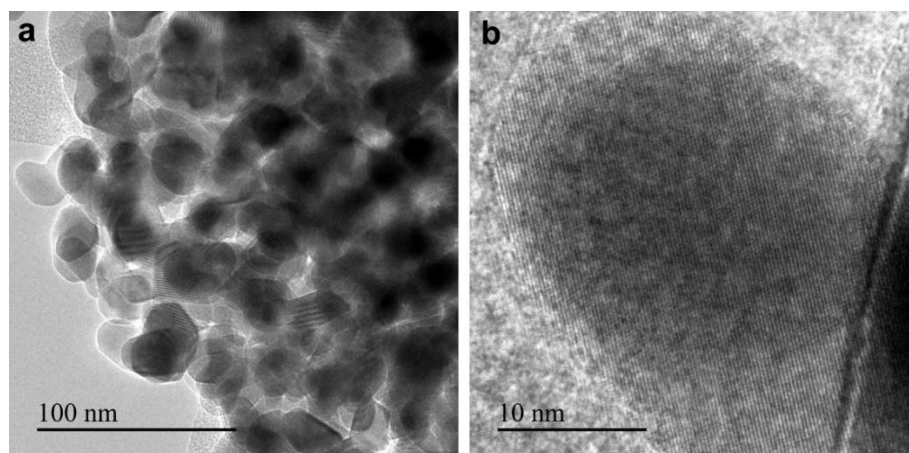
Figure 11.6. TEM image of commercial Co$_3$O$_4$ nanoparticles.

Table 11.2. Product distributions for CO_2 hydrogenation with Na-Co@C catalyst under thermal and photothermal process.

	CO_2 conversion	CH_4	C2=	C2	C3=	C3	C4=	C4	Ethanol	C5	C6	CO	C6=	C7=	1-pentanol
	38.7	63.02	0.03	12.09	0.29	11.11	0.60	4.53	0.71	2.95	1.45	2.36	0.59	0.32	0.08
Na-Co@C-thermal	55.2	63.27	0.03	12.35	0.30	11.66	0.70	4.88	0.70	3.16	1.55	0.54	0.59	0.32	0.08
	73.9	64.52	0.02	12.18	0.21	11.33	0.65	4.93	0.29	3.04	1.53	0.48	0.60	0.32	0.03
	91.5	67.38	0.00	11.88	0.00	10.45	0.67	4.43	0.43	2.69	1.33	0.00	0.52	0.28	0.08
Na-Co@C-photothermal	37.1	50.01	0.21	12.84	1.64	11.03	0.37	4.81	6.55	3.34	2.05	4.79	0.52	0.28	0.83
	58	54.80	0.10	13.79	0.82	11.82	0.37	5.06	3.14	3.59	2.07	2.53	0.51	0.25	0.60
	97	62.73	0.00	16.51	0.00	12.50	0.49	4.32	0.60	2.01	0.60	0.00	0.23	0.05	0.12
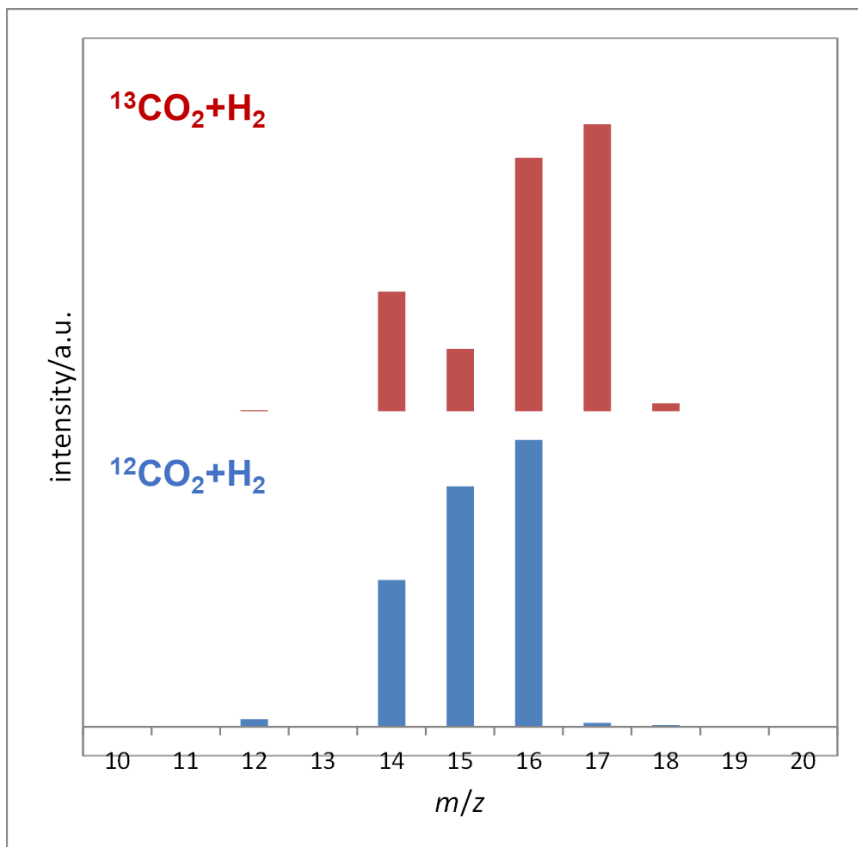
Figure 11.7. Mass spectrum of the methane product obtained with $^{13}CO_2+H_2$ and $^{12}CO_2+H_2$, respectively. red: Mass spectrum of the reaction product between $^{13}CO_2$ and H_2 on Na-Co@C, showing that $^{13}CH_4$ was a product of the reaction, as revealed by the peak at $m/z = 17$ (further fragmentation results in peaks at $m/z = 16$, $m/z = 15$). Bottom, blue: Mass spectra of a sample of the reaction between $^{12}CO_2$ and H_2 on Na-Co@C, where the peak at $m/z = 17$ is

insignificant and the main peak is shifted down one m/z unit, that is $m/z = 16$ as compared to the $^{13}CO_2$ reaction product. The relatively intense peak at $m/z = 14$ on the top spectrum (blue) is due to N^+ ion fragments from N_2, used as internal standard in the reaction. Instrument: Agilent 5973 GC-MS, electronic ionization, positive mode.
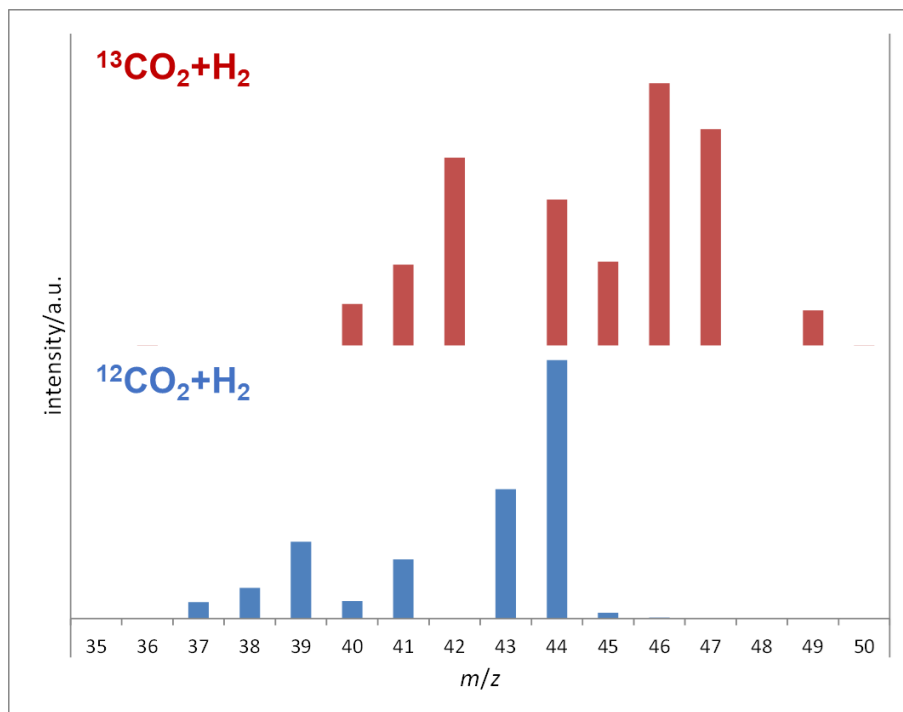
Figure 11.8. Mass spectrum of the C3 reaction products obtained with $^{13}CO_2+H_2$ and $^{12}CO_2+H_2$, respectively. red: Mass spectra of a sample of the reaction between $^{13}CO_2$ and H_2 on Na-Co@C, showing that $^{13}C_3H_8$ was a product of the reaction, as revealed by the peak at $m/z = 47$ (further fragmentation results in peaks at $m/z = 46$, $m/z = 45$ and so on). Bottom, blue: Mass spectra of a sample of the reaction between $^{12}CO_2$ and H_2 on Na-Co@C, where the peak at $m/z = 47$ is insignificant and the main peak is shifted down of three m/z units ($m/z = 44$), as compared to the $^{13}CO_2$ reaction product. The relatively intense peak at $m/z = 44$ on the top spectrum is due to CO_2^+ ion fragments from residual CO_2; otherwise, the fragmentation patterns are similar

and as expected for $^{13}C_3H_8$ and $^{12}C_3H_8$ for top and bottom spectra, respectively. Instrument: Agilent 5973 GC-MS, electronic ionization, positive mode.

The performance of three Co-based nanoparticulate catalysts for the photothermal hydrogenation of CO_2 under simulated sunlight is shown in **Table 11.1**. For comparison, the activity of commercial Co_3O_4 nanoparticles supplied by Sigma-Aldrich (the TEM images of commercial Co_3O_4 nanoparticles are shown in **Figure 11.6**) and Co@C nanoparticles (without Na) was also measured under the same conditions. As can be seen (**Table 11.1, entry 4**), Co_3O_4 was able to catalyze the hydrogenation of CO_2, and CH_4 was the major product (>98% selectivity). The formation of the hydrocarbons from CO_2 has been confirmed by ^{13}C labeling experiments. As shown in **Figure 11.7** and **Figure 11.8**, products such as $^{13}CH_4$ and $^{13}C_3H_8$ coming from $^{13}CO_2$ are observed in mass spectrum, suggesting that the hydrogenation products in the catalytic tests indeed come from CO_2, not from the decomposition of carbon layers. In the case of Co@C catalyst, CH_4 also appeared as the dominant product and low selectivity to ethane (4.4%) was also observed. When Na-Co@C was used as the catalyst (**Table 11.1, entry 1**), CH_4 selectivity was markedly lower (62.7%), and more importantly, C2+ hydrocarbons and ethanol were also formed. These results suggest that the presence of Na is crucial for the production of C2+ hydrocarbons during the photothermal hydrogenation of CO_2, which is in line with classic heterogeneous catalytic systems favoring the formation of hydrocarbon chains.[29]

The reaction equations of the reactions involved in the photoassisted CO_2 hydrogenations are listed in equation (1-3).

$$CO_2 + 4\ H_2 \rightarrow CH_4 + 2\ H_2O \qquad\qquad (1)$$
$$n\ CO_2 + (3n+1)\ H_2 \rightarrow C_nH_{2n+2} + 2n\ H_2O \qquad (2)$$
$$n\ CO_2 + 3n\ H_2 \rightarrow C_nH_{2n} + 2n\ H_2O \qquad\qquad (3)$$
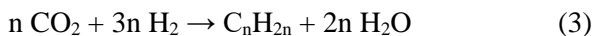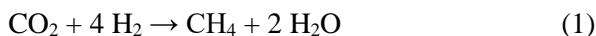
The oxidation half reaction in the CO_2 hydrogenation reaction should be the oxidation of H_2 to water. It is clear in the above reactions that, as in either CO_2+H_2 or $CO+H_2$ to hydrocarbons, the ratio consumed H_2/CO_2 should be between 3 and 4 as a global situation. In our catalytic tests, the ratio of H_2/CO_2 in the feed gas is 5, which means H_2 is always excess. For instance, for the **entry 1** in **Table 11.1**, H_2 conversion quantified by GC is 73.7%, corresponding

to a H_2/CO_2 ratio of ~3.6, which is in line with the theoretical value.

We also tested Na-Co@C under thermal conditions without sunlight irradiation at the same temperature measured under photothermal conditions (235 $^{\circ}$C). As shown in **Table 11.1**, the selectivity to C2+ hydrocarbons is lower than that obtained under photothermal conditions and a small amount of ethanol is also observed at high CO_2 conversion. The difference between the photothermal and thermal catalysis with Na-Co@C catalyst is more evident when the CO_2 conversion is below 40%. More C2+ hydrocarbons as well as ethanol are formed, suggesting that the light irradiation has significant influence on the product selectivity of Na-Co@C catalyst, which is different to previously reported works.[13]
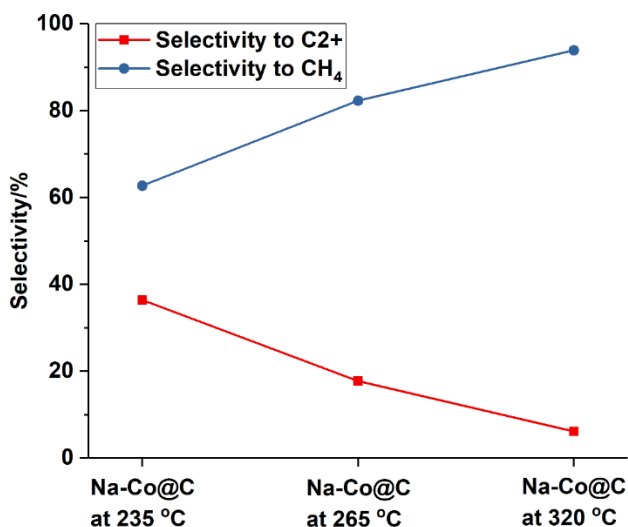
Figure 11.9. Influence of the reaction temperature on the photothermal CO_2 hydrogenaton catalyzed by Na-Co@C catalyst. The selectivity to CH_4 and C2+ hydrocarbons (obtained at >97% conversion of CO_2) are shown in this Figure. As shown in this Figure, when the reaction is performed at higher temperature, the selectivity to C2+ decreases while the selectivity to CH_4 increases.

It has been claimed that solar light irradiation can increase the temperature of the catalyst surface, which further enhances the activity while does not influence the selectivity [12,13]. In our case, we have also tested the Na-Co@C catalyst for CO_2 hydrogenation under photothermal conditions at different

temperature. As shown in **Figure 11.9**, at similar CO_2 conversion (>97%), the selectivity to C2+ hydrocarbons decreased with the temperature and more CH_4 was produced at higher temperature, suggesting that the improved selectivity to C2+ hydrocarbons is not caused by the thermal effects under the photothermal conditions.

Since various of products were observed on Na-Co@C sample under both photothermal and thermal conditions, the product distributions obtained at different CO_2 conversion were followed and given in **Figure 11.10**. Under both photothermal and thermal conditions, the small amounts of CO formed initially were gradually consumed, and eventually could not be observed among the products (see **Figure 11.10a** and **Figure 11.10b**). This leads to conclude that CO was produced as a reaction intermediate, which then evolved towards the formation of higher hydrocarbons and alcohols through CO dissociation or a CO insertion mechanism respectively.[30] Notably, the selectivity to CO under photothermal conditions is slightly higher than under thermal conditions while selectivity to CH_4 is lower under photothermal conditions.

Furthermore, the variations of hydrocarbons and ethanol along the CO_2 hydrogenation were also followed. As presented in **Figure 11.10c**, under photothermal conditions, the selectivity to ethanol and C2+ hydrocarbons is 6.5% and 36.3% respectively, when the CO_2 conversion is 37%. With the increase of CO_2 conversion, the selectivity to ethanol decreases, which could be caused by the photocatalytic reforming of ethanol with CO_2. According to the catalytic results, the chain growth probability factor (α) for hydrocarbon result in 0.55 at 37-58% CO_2 conversion and decreases to 0.38 at 97% CO_2 conversion.

It is clearly shown that, the yield of ethanol (<0.8%) on Na-Co@C sample under thermal conditions is significantly lower than under photothermal process. Nevertheless, the selectivity to light olefins is also lower under thermal conditions (see **Table 11.2**). In the thermal process, the chain growth probability factor α is ~0.55 at all CO_2 conversion, which is similar to values reported in the literature for the CO_2 hydrogenation on cobalt-based catalysts.[31] The above catalytic results clearly indicate that, the solar light irradiation has significant influences on the product distribution during CO_2 hydrogenation. With the help of sunlight irradiation, the selectivity to C2+ hydrocarbons and

ethanol is promoted, especially at medium CO_2 conversion (<50%).
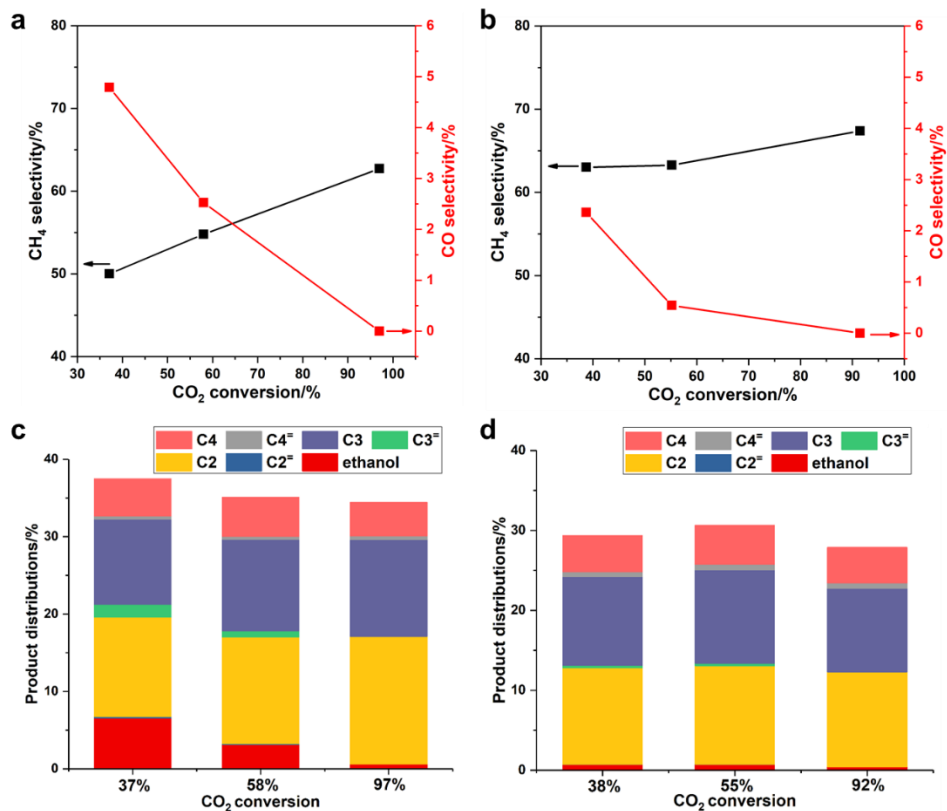
Figure 11.10. Evolution of the products during CO_2 hydrogenation with Na-Co@C under photothermal and thermal conditions. (a) Selectivity to CH_4 and CO at different CO_2 conversion under photothermal conditions. (b) Selectivity to CH_4 and CO at different CO_2 conversion under thermal conditions. (c) Selectivity to C2+ hydrocarbons and ethanol under photothermal conditions at different CO_2 conversion. (d) Selectivity to C2+ hydrocarbons and ethanol under thermal conditions at different CO_2 conversion.
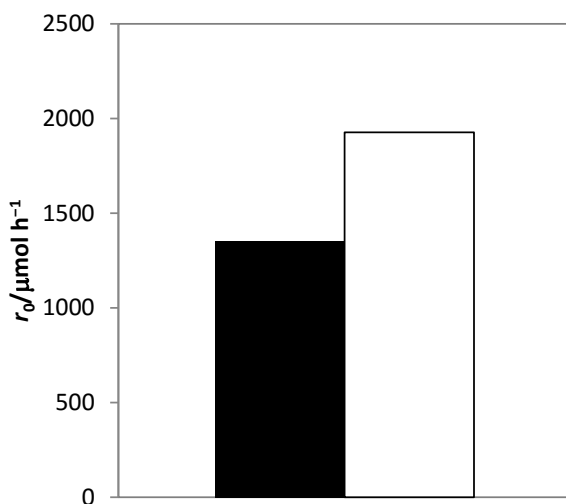
Figure 11.11. Comparison of the initial reaction rates (expressed as micromoles of CO_2 converted per unit of time) under either thermal (black column) or photothermal (white column) conditions. The reactions were performed in a photoreactor composed of a quartz tube (V = 300 cm^3) and a built-in heating plate using a mixture of CO_2, N_2 and H_2 (molar ratio ≈ 1:1:5, total pressure ≈ 100 kPa); catalyst mass, 200 mg; irradiation source, solar simulator. Thermal conditions correspond to the experiment performed in the absence of irradiation, whereas photothermal conditions imply that the sample was heated and irradiated simultaneously. In both cases, the temperature of the catalyst was carefully controlled by a thermocouple placed in close contact with the upper surface of the powdered solid. Irradiation during the photothermal experiment was carried out using a water filter (quartz cell filled with deionized water) between the light source and the photoreactor, in order to block the infrared radiation and thus avoid overheating, being the rest of the set-up identical to the typical photoassisted experiments (see Experimental section in the main text); the incident irradiance under such conditions was 19 kW m^{-2}, as measured by means of a photodiode.
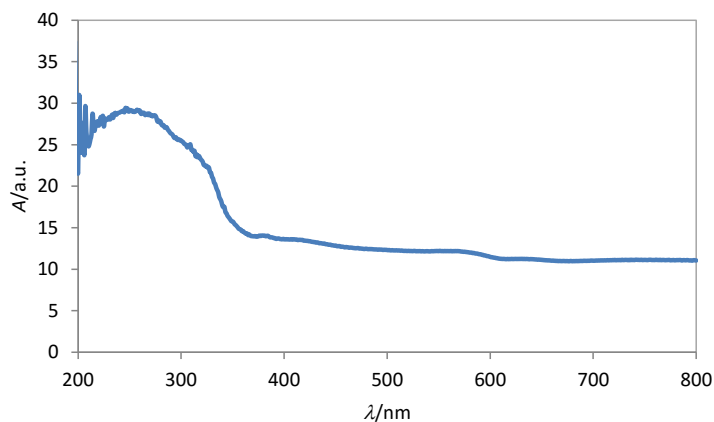
Figure 11.12. Diffuse reflectance UV-vis spectrum of Na-Co@C. The absorption is intense throughout the entire UV-vis spectrum, especially in the UV region below 350 nm.
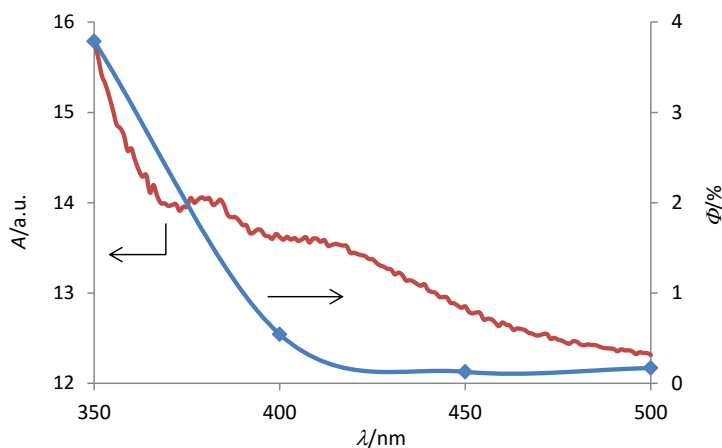
Figure 11.13. Apparent quantum yields (Φ) for the reduction of CO_2 by H_2 on Na-Co@C, as compared to the absorption spectrum of the material. The measurements were carried out using a 150 W Xe lamp adapted to a Czerny-Turner monochromator. The intensity of the light to determine the quantum yield was measured with a calibrated diode. It is clear from the photo-action spectrum that light can promote the reaction in a noticeable fashion only in the UV range (< 400 nm). These results are in line with a recent study on the use of carbon-coated iron nanoparticles in a similar process, whereby hot electrons

generated by absorption of UV light were suggested to promote the activation of CO_2.
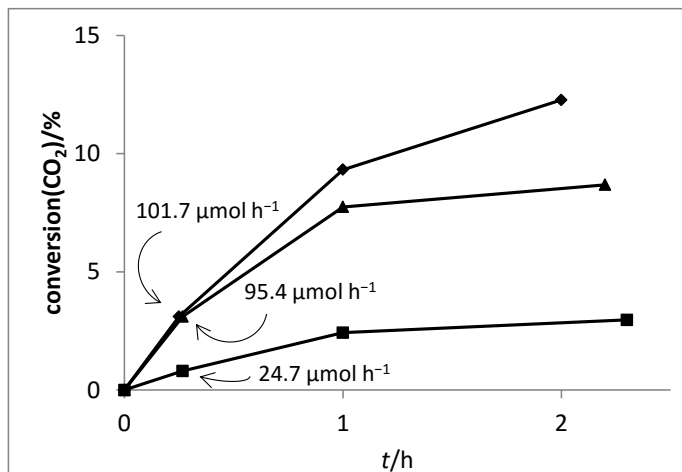
Figure 11.14. Conversion profiles for irradiations using concentrated simulated sunlight ($I = 19$ kW m^{-2}) of gaseous mixtures containing CO_2, H_2 and N_2 (20:100:20 cm^3, N_2 as internal standard) on Na-Co@C, in the absence (diamonds), or in the presence of methanol (50 or 120 mg, triangles and squares, respectively). The reactions were performed under relatively mild conditions ($T = 200$°C, $I = 19$ kW m^{-2}, milder than the conditions used in the standard tests, as shown in **Table 1**) in order to slow down the initial reaction rate. Conversions of CO_2 were recorded at short reaction times, and the initial reaction rates (as moles of CO_2 converted per unit of time at conversion below 10%) were calculated, and are shown for each reaction in the graph. The introduction of a small amount of methanol vapour in the cell leads to a slight decrease in the initial reaction rates: from 101.7 to 95.4 μmol h^{-1} for the reaction without methanol and for the analogous experiment in the presence of 50 mg of the alcohol as hole scavenger. At higher conversions (longer reaction times), the differences become more significant, that is, the reaction is clearly slower in the presence of methanol. By increasing the amount of methanol introduced (120 mg), the reaction rate decreases to a significantly greater extent (24.7 μmol h^{-1}), thus confirming that the presence of a hole scavenger has detrimental effects in the sunlight-induced CO_2 hydrogenation process.

3.3 Effect of light on the catalytic performance

In previous works, it has been reported that CO_2 hydrogenation can be enhanced under solar light irradiation.[12,32] Herein, we have also observed that the initial reaction rate of the CO_2 hydrogenation on Na-Co@C under thermal conditions was lower than for the analogous process performed under photothermal conditions (see **Figure 11.11**). The Na-Co@C nanomaterials show an intense light absorption profile throughout the entire UV-vis spectrum (see **Figure 11.12**). In order to investigate on which wavelengths might be responsible for the activation of CO_2 hydrogenation, irradiations were performed using monochromatic light of selected frequencies (see **Figure 11.13**). Light in the UV range (<400 nm) was observed to promote the reaction in a noticeable way.[33] Therefore, it can be deduced that photo-generation of charges (electron-hole pairs) on Co@C nanoparticles may participate in the CO_2 hydrogenation reaction. A recent study on the use of carbon-coated iron nanoparticles in a similar process suggested that hot electrons generated by absorption of UV light were responsible for activating CO_2.[12]

In the present system, we considered the hypothesis of direct participation of the photo-generated charges, which would be transferred to appropriate adsorbed species and then involved in CO_2 hydrogenation reaction. Therefore, control experiments by adding a hole scavenger in the reaction system were designed to check whether consumption of photo-generated charges had any effect on activity. A series of sunlight-assisted experiments in the absence or in the presence of methanol as a hole scavenger were performed (see **Figure 11.14**). The introduction of a small amount of methanol vapor in the cell leads to a slight decrease in the initial reaction rates. A further increase in the amount of methanol leads to a significantly greater decrease of the initial activity. Based on the aforementioned evidences, it is proposed here that the photothermal CO_2 hydrogenation on Na-Co@C nanocomposites is to some extent activated by the UV light.

4. Mechanistic studies based on *in situ* spectroscopy

Due to the complexity of the CO_2 hydrogenation reaction, characterizations of the catalyst under working conditions at molecular level have been carried

out to identify the nature of active sites and establish correlations between structure and catalytic reactivity. Thus, near-ambient pressure X-ray photoelectron spectroscopy (AP-XPS) and *in situ* Raman studies have been performed providing useful information on the nature of surface intermediate species involved in the reaction mechanism and the chemical states of the catalyst surface in the presence of CO_2/H_2 mixture. A detailed analysis of surface species under reaction conditions will allow to shed light on the role of light irradiation and the promoting effect of sodium on the catalytic behavior of Na-Co@C sample for CO_2 hydrogenation.
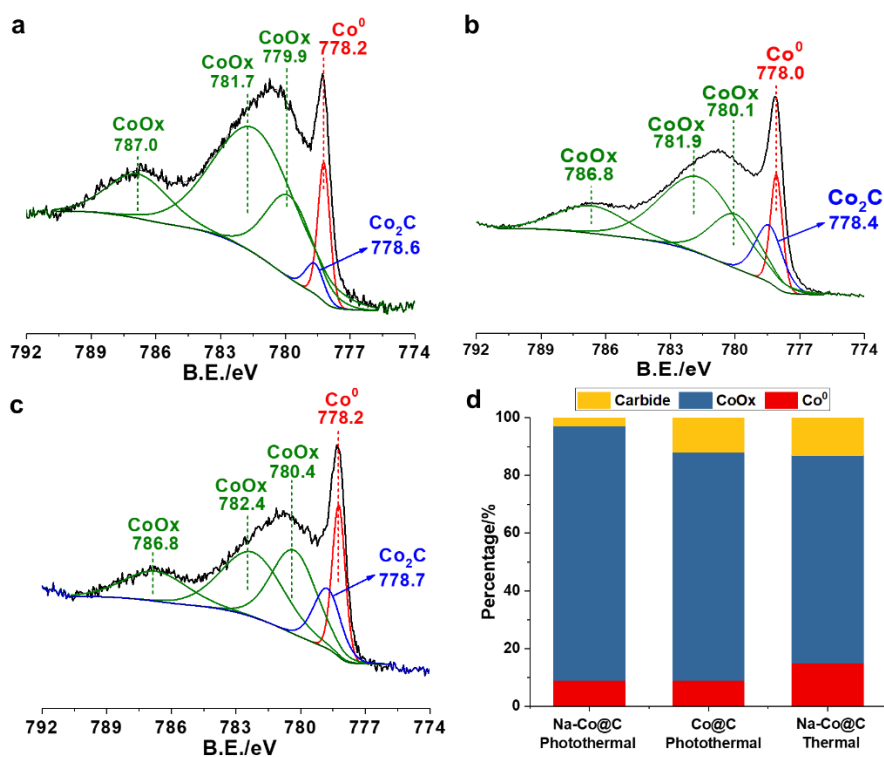
Figure 11.15. AP-XPS spectra of Co2p$_{3/2}$ region obtained at 250 °C with incident X-ray energy of 1000 eV. (a) Na-Co@C under photothermal conditions, (b) Co@C under photothermal conditions and (c) Na-Co@C under thermal conditions. (d) Percentage of cobalt carbide, CoOx and metallic Co^0 in different Co-based catalysts based on the AP-XPS spectra.

4.1 AP-XPS studies on the surface properties of Co-based catalysts

In contrast to the Na-Co@C sample, a different catalytic behavior has been observed on the Na-free Co@C sample under photoassisted reaction conditions (see **Table 1**). The role of sodium in FTS cobalt based catalysts has extensively been discussed in the literature. It has been proposed that sodium can stabilize cobalt carbide species which serve as active sites for the formation of oxygenates.[34,35] In some other works, it is suggested that cobalt carbides can suppress the hydrogenation of C=C bonds and facilitate the desorption of olefins, leading to higher selectivity to olefin.[36] However, it has also been proposed that cobalt carbides can decrease the reducibility of cobalt oxide and/or block active sites, resulting in lower catalytic activity for FTS.[37,38]

As shown in **Figure 11.15a**, carbide species have been detected on the Na-Co@C sample in the $Co2p_{3/2}$ spectra under light irradiation. At the reaction temperature (250 ºC), Co2p3/2 peak fitting shows the co-existence of Co^0 (9%), CoO (88%) and Co_2C (3%) species. Notably, the formation of carbide species is rather low, leading us to question their participation in the formation of alcohols under our reaction conditions. The low reducibility of cobalt species under reaction conditions should also be noted. On the other hand, under light irradiation and in the absence of Na, Co2p3/2 peak fitting shows the presence of Co^0 (9%), CoO (79%) and Co_2C (12%) at 250 ºC (**Figure 11.15b**). A higher amount of cobalt carbide is observed on the Co@C sample while the amount of metallic Co is similar to Na-Co@C sample, implying that the promotion effect of Na does not seem to relate with either the increase of reducibility or stabilization of carbide. Nevertheless, the $Co2p_{3/2}$ peak fitting of the Na-Co@C sample under thermal condition (see **Figure 11.15c**) shows the presence of Co^0 (15%), CoO (72%) and Co_2C (13%), suggesting that sunlight irradiation can suppress the formation of cobalt carbide.

The abovementioned XPS results of $Co2p_{3/2}$ region indicate that, higher selectivity to C2+ hydrocarbons and ethanol on Na-Co@C sample under photothermal conditions is probably not related with cobalt carbide species. Moreover, considering the similar percentage of metallic Co in the above three cases, it seems that the observed different catalytic behavior is not related with the reducibility of the Co catalyst.
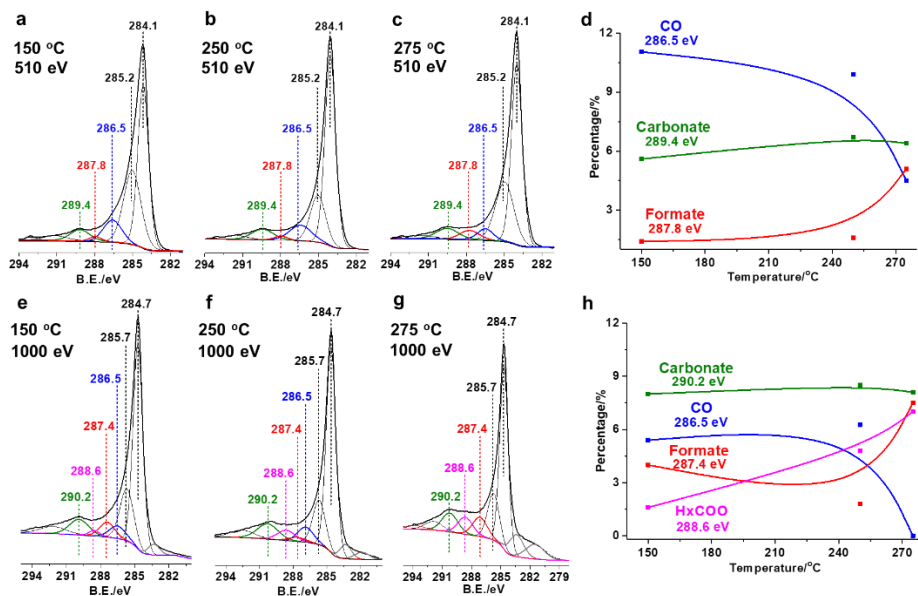
Figure 11.16. Ambient-pressure XPS spectra of Na-Co@C sample during CO$_2$ hydrogenation reaction conditions (P$_{CO2}$= 0.1 mbar and P$_{H2}$= 0.5 mbar) under photothermal conditions. (a-c) C1s spectra obtained with incident X-ray energy of hv=510 eV. (d) Percentage of different types of carbon species at different temperature according to the spectra obtained at hv=510 eV. (e-g) Spectra obtained with incident X-ray energy of hv=1000 eV. (h) Percentage of different types of carbon species at different temperature according to the spectra obtained at hv=1000 eV.
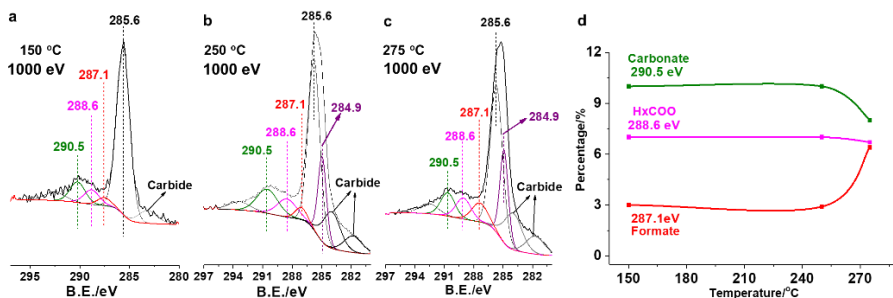
Figure 11.17. Ambient-pressure XPS spectra of Na-Co@C sample during CO$_2$ hydrogenation reaction conditions (P$_{CO2}$= 0.1 mbar and P$_{H2}$= 0.5 mbar)

under thermal conditions. (a-c) C1s AP-XPS spectra of Na-Co@C sample under thermal conditions obtained with incident X-ray energy of hv=1000 eV. (d) Percentage of different types of carbon species at different temperature according to the spectra obtained at hv=1000 eV.
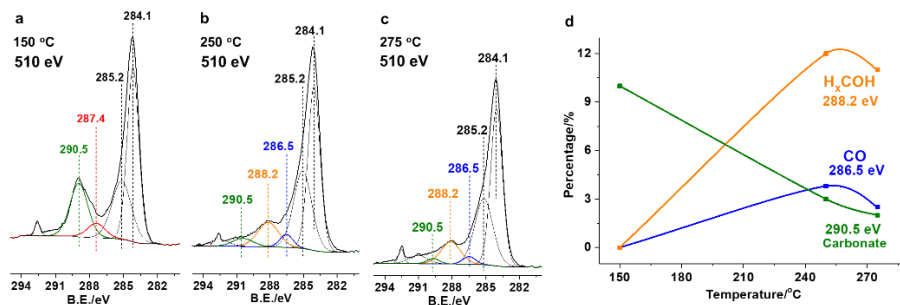
Figure 11.18. Ambient-pressure XPS spectra of Co@C sample during CO$_2$ hydrogenation reaction conditions (P_{CO2}= 0.1 mbar and P_{H2}= 0.5 mbar) under photothermal conditions. (a-c) C1s AP-XPS spectra of Co@C sample under photothermal conditions obtained with incident X-ray energy of hv=510 eV. (d) Percentage of different types of carbon species at different temperature according to the spectra obtained at hv=510 eV.
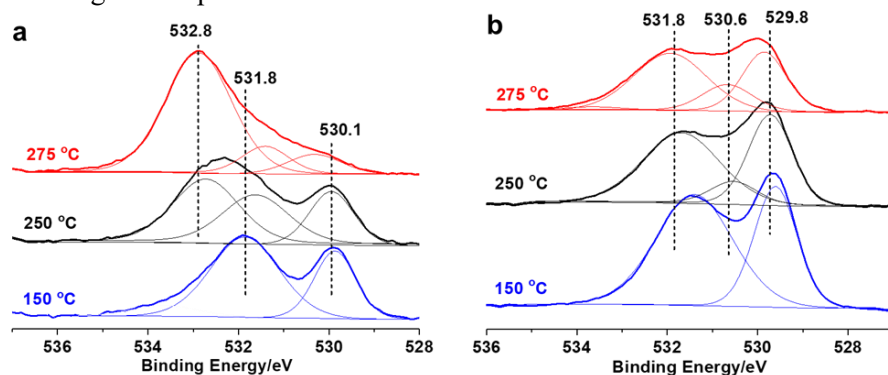
Figure 11.19. AP-XPS spectra of O1s region of Na-Co@C (a) and Co@C (b) samples under photothermal CO$_2$ hydrogenation conditions at P_{CO2}= 0.1 mbar and P_{H2}= 0.5 mbar. These spectra were obtained with incident X-ray of hv=1000 eV. The peak at BE 529.8-530.1 eV corresponds to surface cobalt oxide species and the peak at BE=531.8eV corresponds to adsorbed CO species. The significant decrease in intensity of the component at 530.1 eV on the Na-Co@C

sample under photothermal conditions at 275 ºC is associated with the reduction of cobalt oxide species to Co^0, which is not observed on the Na-free Co@C sample at the same temperature.

4.2 AP-XPS studies on the surface carbon species

Though several reaction paths have been proposed for the CO_2 hydrogenation reaction, the starting point is the activated $CO_2^{\delta-}$ specie which can either dissociate into CO+O or undergo direct hydrogenation [39]. The *in situ* formed CO can be further hydrogenated or dissociate into C and O ad-atoms, resulting in the formation of different surface species, like for instance formyl (HCO), hydroxycarbene (HCOH), hydroxymethyl (H_2COH), methyl (CH_3), methylene (CH_2), methylidyne (CH) and hydroxymethylidyne (COH). Chain growth takes place by a surface polymerization condensation reaction process resulting in the formation of paraffins, olefins and oxygenates. The types of the surface carbon species can be used as fingerprint for reaction pathways towards different products. Therefore, we firstly have studied the surface carbon species by AP-XPS to follow their evolution on Co-based catalysts.

The C1s core levels of the Na-Co@C and Co@C samples in presence of CO_2 and H_2, under thermal and photothermal reaction conditions, are shown in **Figure 11.16** to **Figure 11.18**, where XPS spectra have been acquired at two photon energies, *hv*=510 eV and *hv*=1000 eV, in order to analyze at different depths of the sample. Firstly, the Na-Co@C sample has been studied. Two C1s peaks at BE 285.2-285.6 and 284.1-284.7 eV have been observed in the Na-Co@C sample under light irradiation, corresponding to carbon layers covered on Co nanoparticles. Moreover, the C1s spectra (**Figure 11.16a-16c**) under light irradiation and working at *hv*=510 eV, show predominately CO (BE 286.5 eV) as main component in addition to formate (BE 287.8 eV) and carbonate species (BE 289.4 eV).[40-42] When working at higher photon energy (1000 eV) (**Figure 11.16e-16g**), besides CO (BE 286.5 eV), formate (BE 287.4 eV) and carbonate species (BE 290.2 eV), an additional component at 288.6 eV is observed. In the O1s region (**Figure 11.19a**), a new component at 532.8 eV appears when increasing the reaction temperature, showing similar behavior to the C1s component at BE 288.6 eV. Based on the high BE of both species and

their parallel growing, we can tentatively assign both components to some type of hydrogen-carbonate intermediate specie, i.e HxCOO*. Peak areas of each component according to the fitting results of C1s spectra, and their evolution as a function of the temperature, are given in **Figure 11.16d** and **Figure 11.16h**. Taking into consideration that CO is predominantly observed at low photon energy (being high surface sensitive conditions) and Co nanoparticles are covered by thin carbon layers, the XPS results indicate that CO is stabilized on the surface carbon layers of the Na-Co@C sample. At higher photon energy (hv=1000 eV), the contribution of formate and HxCOO* in the C1s peak increases, indicating their stronger interaction with Co surface covered by the carbon layers. Based on **Figure 11.16d and 16h**, it can be observed that when increasing reaction temperature, the signal intensity of the surface CO decreases, while formate species and HxCOO* increase. Meanwhile carbonate like species remains practically stable with the temperature. This behavior indicates that CO, formate and HxCOO* behave as intermediate species while carbonate species, stabilized either on cobalt surface or on the carbon layer, are not involved in the reaction pathways.
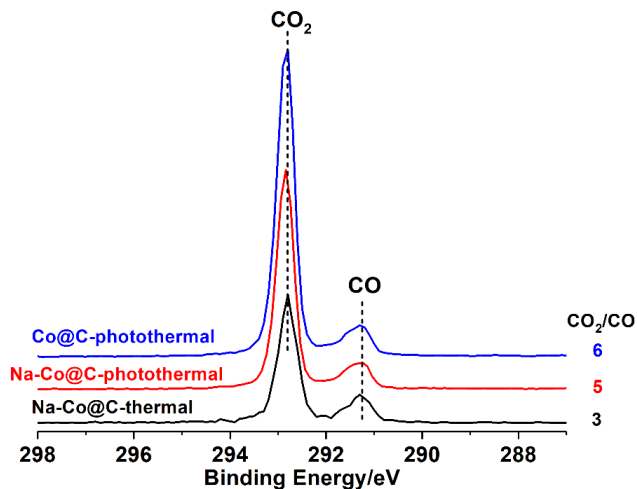
Figure 11.20. C1s gas phase spectra acquired at 250 ºC in the presence of of 0.1 mbar CO_2 and 0.5 mbar H_2 under photothermal conditions on Co@C (blue) and Na-Co@C (red) and under thermal conditions on Na-Co@C (black). These spectra were acquired at hv=510 eV.

The CO_2 hydrogenation on Na-Co@C sample under thermal conditions has also been studied by AP-XPS. As shown in **Table 1** and **Figure 11.10**, the product distribution under thermal conditions with Na-Co@C for CO_2 hydrogenation is similar to the situation under photothermal conditions, although selectivity to C2+ hydrocarbons and ethanol were lower under thermal conditions. Based on the AP-XPS studies (**Figure 11.17a-17c**), CO (BE 286.7 eV) is not detected on the catalyst surface under thermal conditions, while it is detected in the gas phase (**Figure 11.20**), suggesting that CO interacts weakly with the catalyst surface under thermal conditions. Since the stabilization of CO on catalyst surface is a key for the formation of oxygenates during CO_2 hydrogenation, the absence of CO on Na-Co@C under thermal conditions can explain its low selectivity to ethanol. Besides, carbonate (BE 290.5 eV), formate (BE 287.1 eV) and HxCOO* (BE 288.6 eV), are also predominantly observed in the C1s spectra. Notoriously carbide species with BE 283.7 and 281.6 eV (also observed in the Na-Co@C sample under light irradiation) and graphitic carbon species and/or CHx species with BE at 284.9 eV are also detected, which is in line with the higher amount of cobalt carbide as observed in **Figure 11.15** for the Na-Co@C sample under thermal conditions. This difference implies that the sunlight irradiation can suppress the deposition of carbon on cobalt.

Considering our previous hypothesis where UV light plays an important role in the CO_2 activation through the formation of electron hole pairs, a support for this hypothesis can be found from the AP-XPS studies. As we have mentioned before, two C1s peaks at BE 285.2-285.6 and BE 284.1-284.7 eV have been observed in the Na-Co@C sample under light irradiation (**Figure 11.16**). The first ones corresponding to carbon are also observed in the Na-Co@C sample without sunlight irradiation (**Figure 11.17**), while the later ones are only observed on irradiated samples. The low BE of the C1s peak at BE 284.1-284.7 eV may account for electron-rich carbon species from the carbon layer formed under light irradiation, which can play an important role in the activation of CO_2 to $CO_2^{\delta-}$, enhancing the CO_2 dissociation to CO and O. These results can explain the higher initial reaction rate for CO_2 hydrogenation on Na-Co@C sample under sunlight irradiation.

In order to explain the ~92% CH_4 selectivity observed in the Co@C catalyst,

and in an attempt to find out why and how Na plays an effect of the product distribution, the evolution of carbon intermediate species at different reaction temperatures has been followed by AP-XPS studies (**Figure 11.18**). Surprisingly, a different reaction intermediate is observed in the non-promoted Co@C catalyst, where a new component at BE 288.2 eV, not observed in the Na-Co@C sample, is predominant. In addition, CO (BE 286.5 eV) is also formed together with surface carbonate species (BE 290.5 eV). Formate species (BE 287.4 eV) are only detected at low temperature (**Figure 11.18a-c**). Based on the growth of a parallel new component at BE 530.6 eV in the O1s peak (**Figure 11.19b**), associated to hydroxyl groups, we can assign the peak at BE 288.2 eV to enol like species (HxCOH). These enol like species are unstable on Co surface, and further C-OH scission would lead to formation of CHx species, which can be further hydrogenated into CH_4, as detected in the catalytic studies.

Combining the above AP-XPS results, it can be concluded that, under light irradiation, the promoting effect of sodium on the production of C2+ hydrocarbons and oxygenate cannot be ascribed to any of the effects described previously in the literature.[43-45] The effect of Na in our system is probably related with the modulation of the surface intermediates during the catalytic process of CO_2 hydrogenation, resulting in different product distributions. Meanwhile, we have observed that light plays an important role in the reaction mechanism, by modulating the types of intermediates species and their stability (especially CO) on the surface of Co nanoparticles.
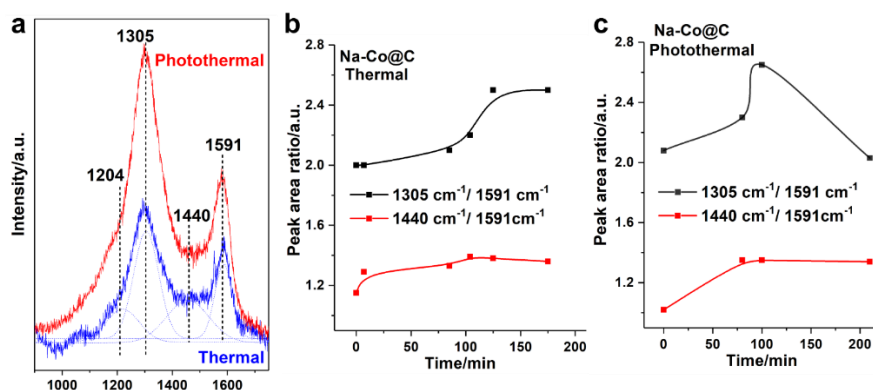
Figure 11.21. *In situ* Raman spectra of Na-Co@C under thermal and photothermal conditions for CO_2 hydrogenation. (a) Raman spectra

obtained with Na-Co@C sample after 100 min reaction under photothermal (red curve) and thermal (blue curve) conditions for CO_2 hydrogenation. (b) Peak area ratio of the Raman bands at different reaction time under photothermal and thermal conditions for CO_2 hydrogenation.

4.3 *In situ* Raman Studies on the surface carbon species

The formation of carbon species in the CO_2 hydrogenation process, already detected in the AP-XPS studies, has also been analyzed by operando Raman studies. As shown before in **Figure 11.15**, the amount of cobalt carbide formed on Na-Co@C under thermal conditions is more than under photothermal conditions. The high sensitivity of Raman spectroscopy to carbonaceous species, and the possibility to work under more realistic reaction conditions (1 bar in Raman versus 0.6 mbar in AP-XPS) enables us to obtain more realistic information about the formation of carbon species and their evolution under operando conditions.

Peak fitting of the Raman spectra of the Na-Co@C catalyst, shows several bands at 1204, 1305, 1440 and 1591 cm^{-1} associated to different carbon species (see **Figure 11.21**), which can be ascribed to disordered graphite, capillary carbon or defects in graphite, amorphous carbon and graphite like carbon, respectively.[46,47] Under thermal CO_2 hydrogenation conditions, an increase in the amount of amorphous carbon (1.15 to 1.39) and capillary carbon (2.08 to 2.5) is observed with reaction time. Under photothermal conditions, the amount of capillary carbon species increases in the first 100 min from 2.08 to 2.65 and then decreases to 2.03, while amorphous carbon increases and remains practically constant (1.02 to 1.35). Thus, the *in situ* Raman results infer that sunlight irradiation suppress the carbon deposition on Na-Co@C catalyst. Such effect may cause the low percentage of cobalt carbide formed on the Na-Co@C catalyst under photothermal conditions.
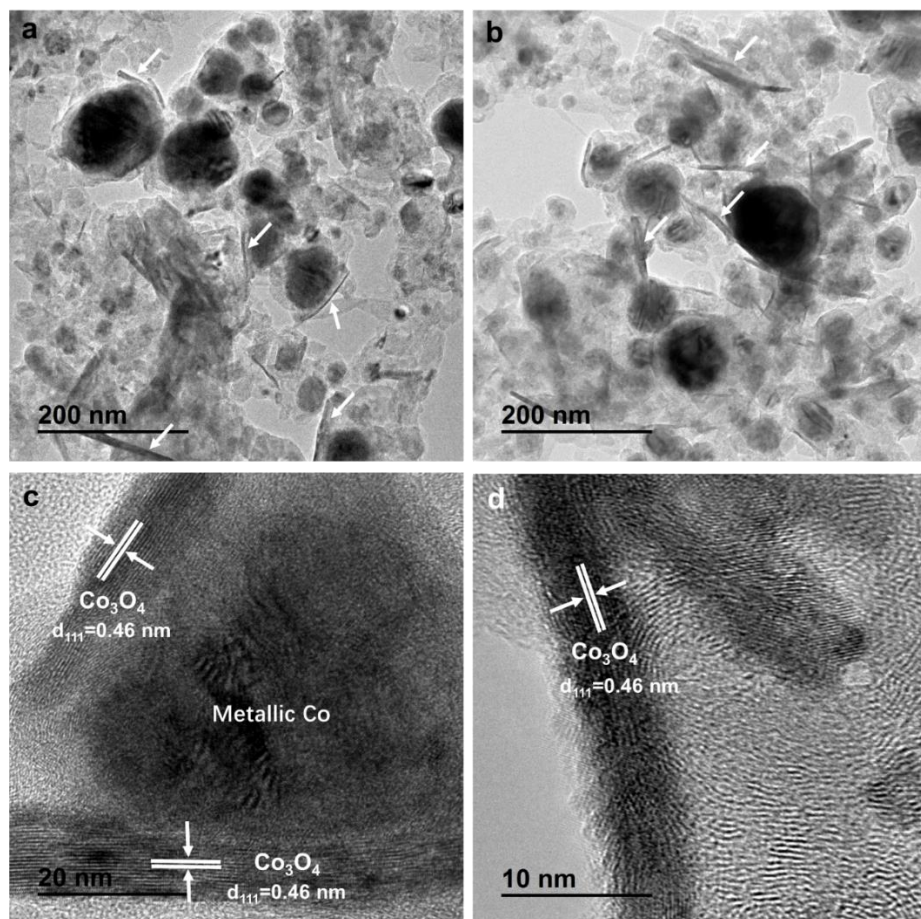
Figure 11.22. TEM images of Na-Co@C after CO_2 hydrogenation reaction under photothermal conditions. Compared with the fresh Na-Co@C (shown in **Figure 11.1**), the morphology of the Na-promoted Co@C nanoparticles changed after the photoassisted CO_2 hydrogenation. Rod-like particles can be observed in the used catalyst. High-resolution images confirm that, these rod-like structures are Co_3O_4 nanoparticles.
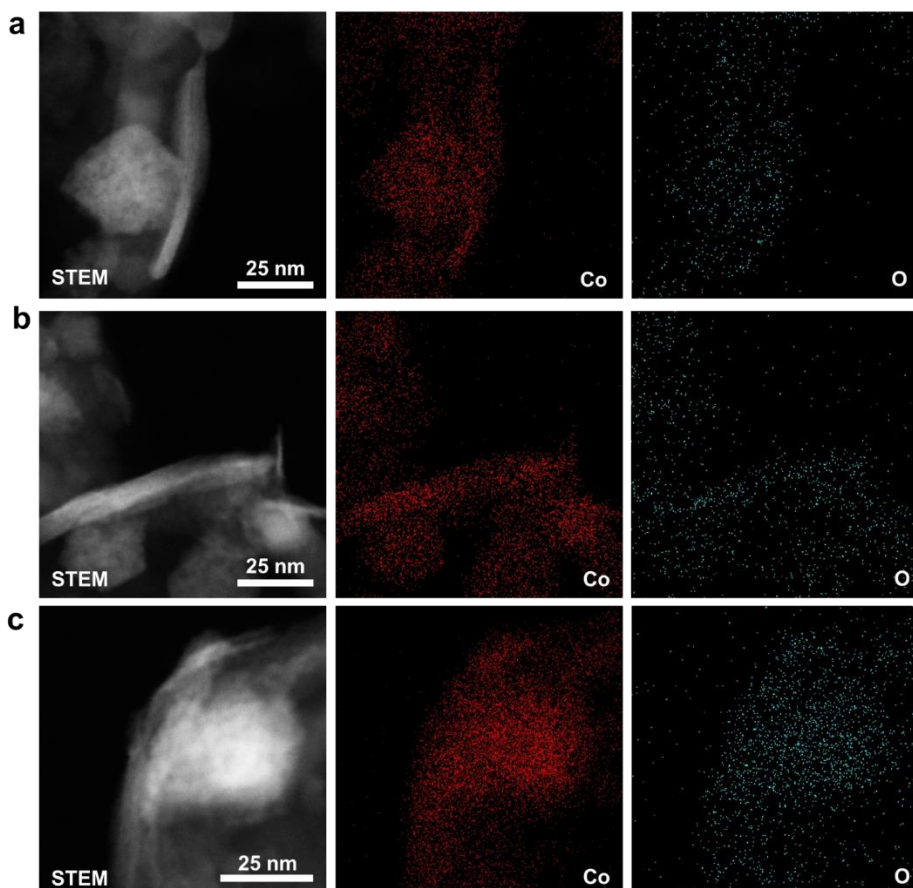
Figure 11.23. Elemental mapping of the used Na-Co@C catalyst after photothermal CO_2 hydrogenation reaction. From the mapping results in three different areas, it is confirmed that, the rod-like structures are consisted by both Co and O.
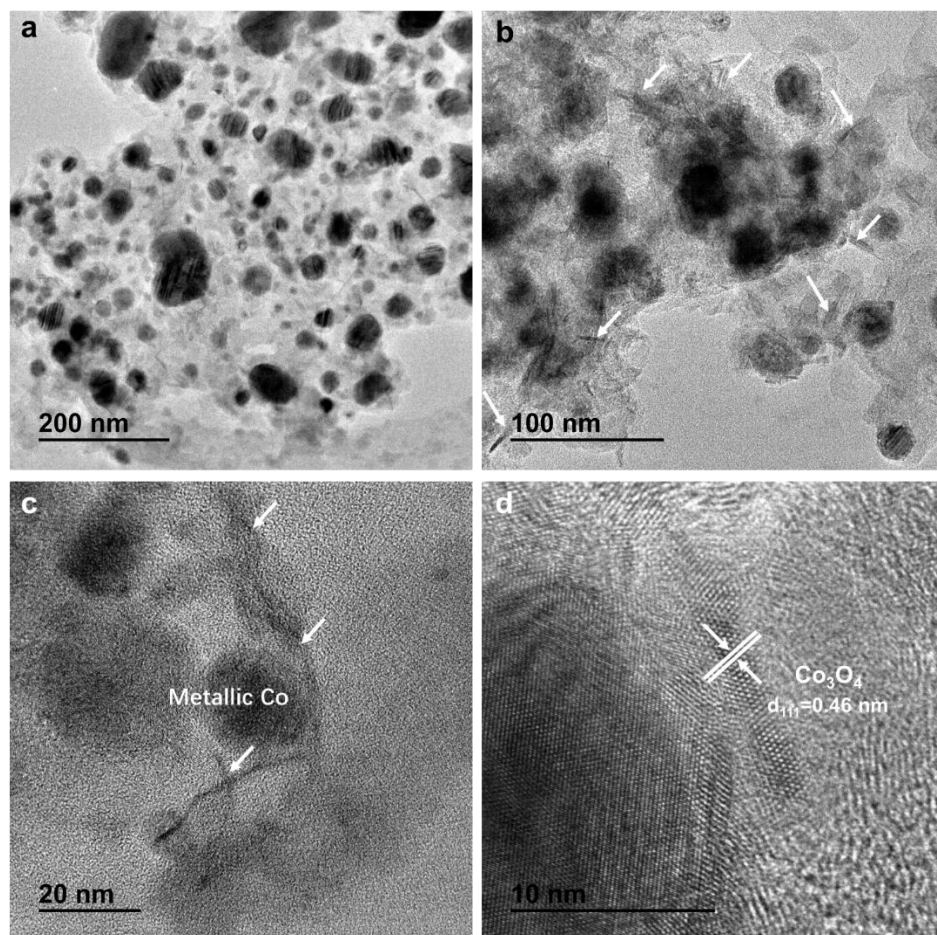
Figure 11.24. TEM images of Na-Co@C after CO_2 hydrogenation reaction under thermal conditions. Compared with the fresh Na-Co@C (shown in **Figure 11.1**), the morphology of the Co@C nanoparticles changed after the CO_2 hydrogenation under thermal conditions, which is similar to the situation of used Na-Co@C catalyst after CO_2 hydrogenation under photothermal conditions. Rod-like particles can be observed in the used catalyst. High-resolution images confirm that, these rod-like structures are Co_3O_4 nanoparticles.
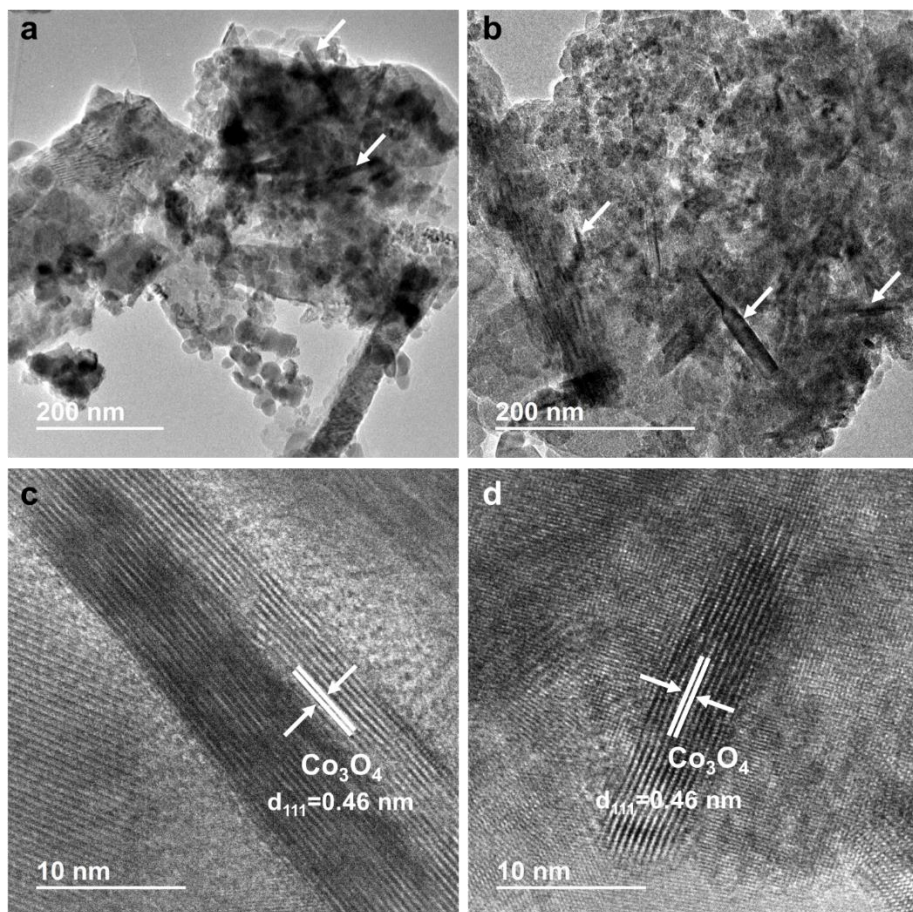
Figure 11.25. TEM images of commercial Co_3O_4 nanoparticles after CO_2 hydrogenation reaction under photothermal conditions. Compared with the fresh Co_3O_4 nanoparticles (shown in **Figure 11.S4**), the morphology of the Co_3O_4 nanoparticles changed dramatically after the photoassisted CO_2 hydrogenation. Rod-like particles can be observed in the used catalyst and their sizes are larger than those observed in the Na-Co@C sample. High-resolution images confirm that, these rod-like structures are Co_3O_4 nanoparticles.
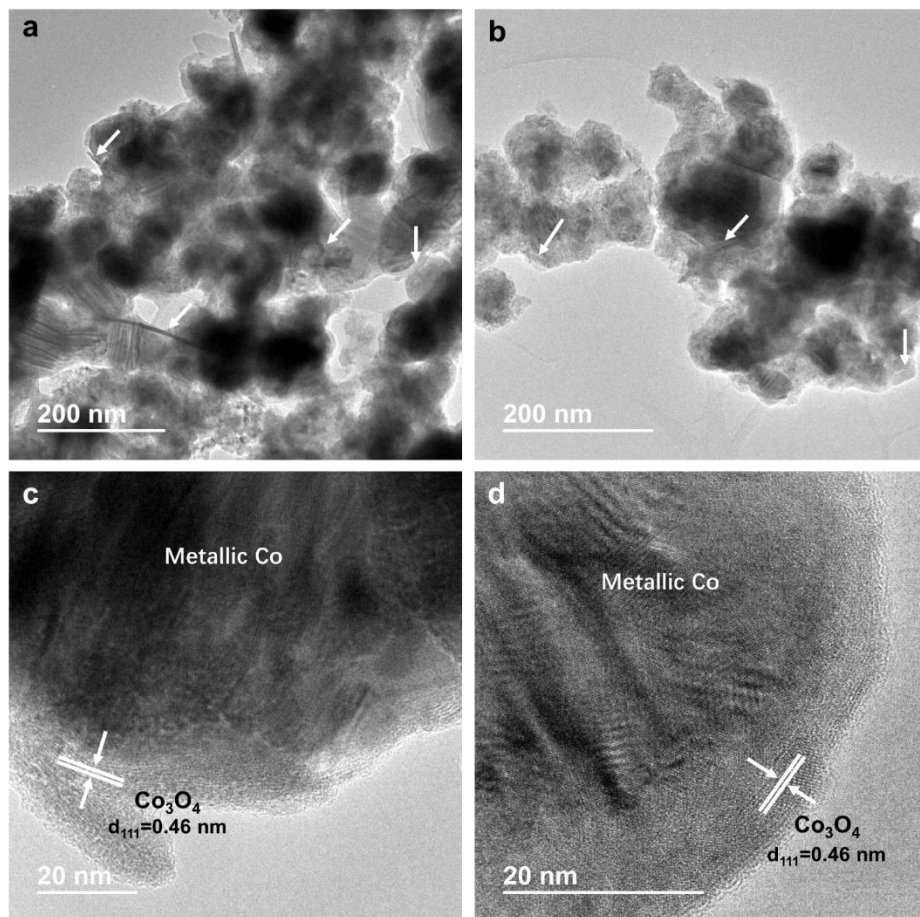
Figure 11.26. TEM images of Co@C after CO_2 hydrogenation reaction under photothermal conditions. Compared with the fresh Co@C (shown in **Figure 11.S3**), the morphology of the Co@C nanoparticles changed after the photoassisted CO_2 hydrogenation, which is similar to the situation of Na-Co@C sample. Rod-like particles can be observed in the used catalyst. High-resolution images confirm that, these rod-like structures are Co_3O_4 nanoparticles.
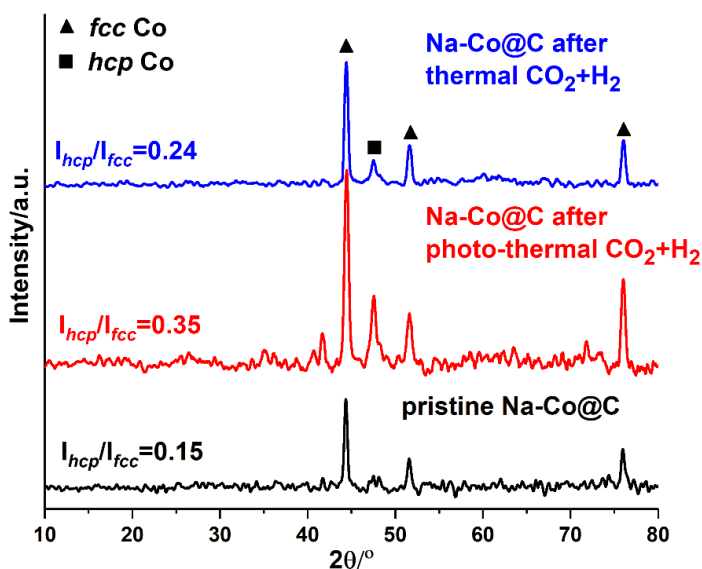
Figure 11.27. XRD patterns of pristine Na-Co@C sample and the samples after thermal and photothermal CO_2 hydrogenation reactions. The values I_{hcp} and I_{fcc} correspond to the intensities (peak heights, a.u.) of the **hcp** and **fcc** reflection peaks at $2\theta = 47.6$ and 44.2 °, respectively.

5. Influence of sunlight irradiation on the structure of the Co-based catalysts

The morphologies of Co-based catalysts after CO_2 hydrogenation reactions under thermal and photothermal conditions have been studied by TEM. As shown in **Figure 11.22** the morphology of Na-Co@C after photothermal CO_2 hydrogenation is different to the pristine sample. Rod-like structures are formed along the spherical Co nanoparticles. Elemental mapping (see **Figure 11.23**) results show that, those rod-like structures contains Co, suggesting that structural reconstruction occurred during the CO_2 hydrogenation reaction under photothermal conditions. Furthermore, HRTEM images indicate that, those rod-like structures corresponding to Co_3O_4. However, those Co_3O_4 species may come from the re-oxidation of metallic Co^0 or Co_2C species after contact with air during preparation of the samples for TEM measurements. Besides, we have also measured the other Co catalysts after CO_2 hydrogenation reactions. As shown in **Figure 11.24** to **Figure 11.26**, rod-like structures can be observed in

all the cases, suggesting the structural reconstruction is a common phenomenon in Co catalysts for CO_2 hydrogenation reaction.[48] Catalyst reconstruction could be also reflected from the AP-XPS data where the number of exposed cobalt surface sites increases under reaction conditions (**Table 11.3**). It should be noted that, the size of the rod like structures formed in Co_3O_4 nanoparticles are larger than those formed in either Na-Co@C or Co@C, which may be related with the absence of carbon layers on the Co nanoparticles.

In addition, in conventional Fischer-Tropsch processes, the presence of the Co^0 ***hcp*** phase plays an important role during the growth of carbon chain for producing higher hydrocarbons.[49-51] As shown in **Figure 11.27**, the percentage of the Co^0 ***hcp*** phase increases significantly in the Na-Co@C sample after the photothermal reaction. For comparison purposes, the XRD pattern of the Na-Co@C sample after only-thermal catalytic hydrogenation of CO_2 was also measured. The percentage of ***hcp*** phase Co also increased in this case, but not as much as after the photothermal reaction, implying that solar light irradiation during the CO_2 hydrogenation reaction can promote the transformation of Co species into the ***hcp*** phase, which may have influence on the catalytic behavior.
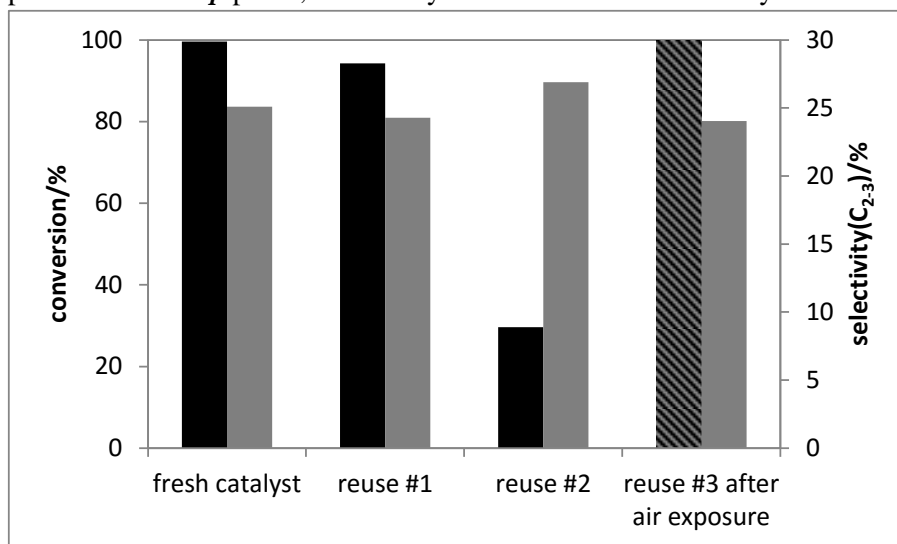
Figure 11.28. Recyclability tests on Na-Co@C for photothermal CO_2 hydrogenation reaction. Conversion: black bars; selectivity to C_{2-3}: grey bars. During the first two reuses, the sample was kept in the reactor without contact with air, the final reaction gas mixture evacuated under reduced pressure, and

then fresh reaction gas mixtures were added. Between the second and third reuses, the sample was exposed to air at atmospheric pressure and room temperature and the catalytic performance was recovered.

Table 11.3. Chemical surface composition determined from AP-XPS studies at an X-ray energy of 1000 eV.

Sample	treatment	Co:C:O (atomic ratio)
Na-Co@C	fresh	2: 80: 18
Co@C	fresh	11: 69: 20
Na-Co@C	Photoassisted CO_2/H_2 reaction 250 ºC	4: 79: 17
Na-Co@C	Thermal CO_2/H_2 reaction 250 ºC	7: 82: 11
Co@C	Photoassisted CO_2/H_2 reaction 250 ºC	11: 72: 17

As shown in **Figure 11.28**, excellent activity and high selectivity towards C2 and C3 hydrocarbons was observed during the first reuse of the catalyst. However, significant deactivation of the catalyst became apparent during the second reuse. It should be noted that, the catalyst was always kept in reductive atmosphere during the first and second reuse. According to the spectroscopic characterizations in this work and the literature, it seems that, the formation of cobalt carbide or graphitic carbon on the catalyst surface may contribute to the loss of activity.[52,53] Since cobalt carbide can be oxidized by air, then the blocked surface sites by cobalt carbide or graphitic carbon can be recovered after mild oxidation treatment. In fact, after exposing the reused catalyst to air at ambient temperature and pressure, the high activity and selectivity of Na-Co@C was again recovered (see **Figure 11.28**).
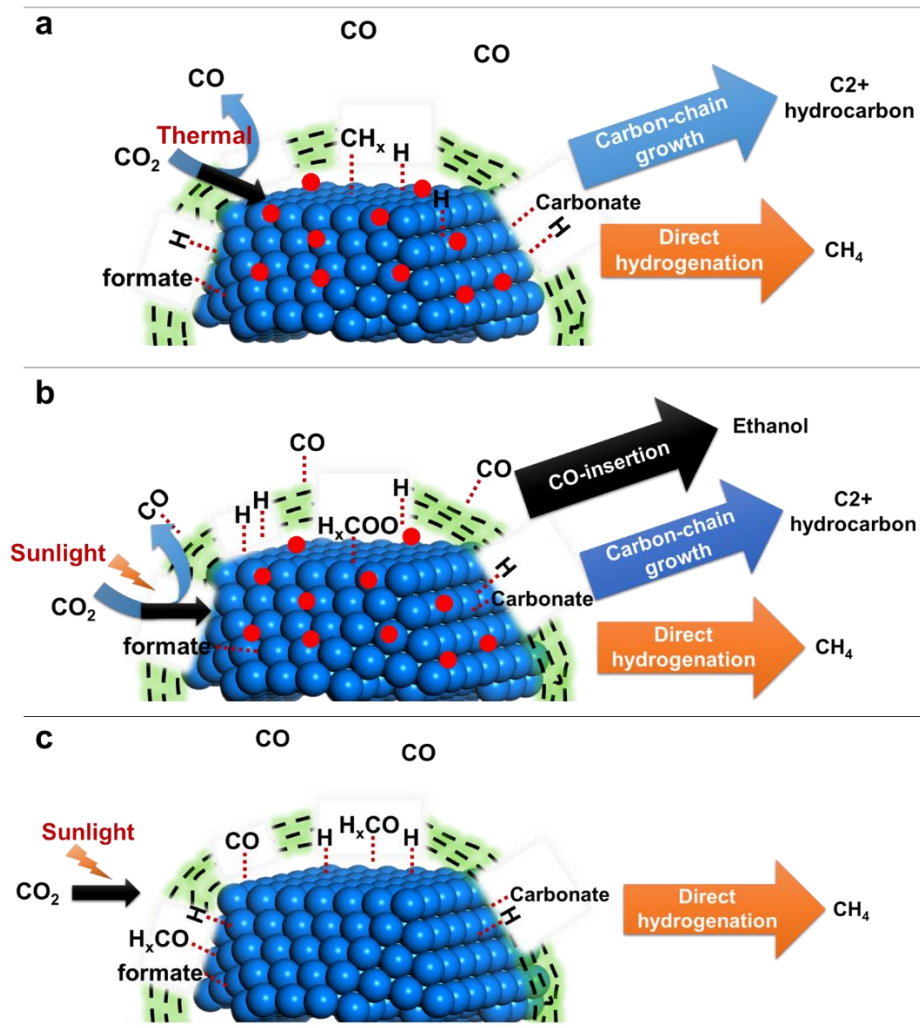
Figure 11.29. Schematic illustration of the CO_2 hydrogenation on Na-Co@C and Co@C catalysts under thermal and photothermal conditions. Sodium is shown with red circles. (a) Under thermal conditions, Na-Co@C catalyst mainly produce CH_4 and C2+ hydrocarbons. (b) Under photothermal conditions, ethanol is also produced as well as C2+ hydrocarbon and CH_4. (c) Under photothermal conditions, CH_4 is the predominant product on Co@C sample, due to the fast hydrogenation of the intermediates instead of C-C coupling reaction.

6. Proposed reaction mechanism

Based on the above spectroscopic studies, we can conclude that light irradiation plays an important role in the CO_2 activation mechanism, favoring the RWGS reaction ($CO_2 + H_2 \rightarrow CO + H_2O$) and the stabilization of CO on the catalyst surface. The direct role of light has been ascribed to an electronic effect where electrons generated by absorption of UV light are responsible for activating CO_2 to $CO_2^{\delta-}$, promoting CO_2 dissociation into CO, and the stabilization of CO on the catalyst surface (as shown in **Figure 11.29**). The stabilization of CO contributes to a higher selectivity toward ethanol by a CO insertion mechanism. Moreover, a clear effect of light on the chain growth process can also be deduced according to the different surface intermediates observed by AP-XPS. This can be reflected from the catalytic results where under light irradiation the ASF hydrocarbon distribution differs from the thermal process, with a higher selectivity to C2-C3 hydrocarbons and ethanol. The higher selectivity to C_2H_6 and C_3H_8 under light irradiation can be related to a lower concentration of surface C species, or to low metal-C adsorption strength promoting hydrocarbon desorption. At this point, and based on our spectroscopic data, it has been observed that sunlight irradiation can reduce the metal-carbon interaction. Indeed, the amount of carbide species observed in the AP-XPS spectra is markedly lower in the presence of light than under thermal conditions. Nevertheless, we have also observed the influence of light irradiation on the phase structure of Co catalysts, which show higher amount of Co *hcp* phase under sunlight irradiation. Finally, and in agreement to literature data, sodium plays an important role on the C-C formation by influencing the nature of intermediate species on the catalyst surface. In the absence of sodium, enol species seem to be stabilized, and the C-OH scission favors the formation of CH_4.

7. Conclusions

In summary, we report the application of Na-Co@C nanocomposites for photocatalytic hydrogenation of CO_2 to C2+ hydrocarbons and ethanol. Under photothermal conditions the Na-promoted Co@C sample shows almost 100% selectivity to hydrocarbons as well as high selectivity to C2 and C3 products (16.5% and 12.5% respectively) at >97% CO_2 conversion. Photo-generation of

charges on Co@C nanoparticles upon UV light absorption, in addition to the favored formation of active ***hcp*** phases under such conditions, proved the activating role of sunlight irradiation in the photothermal process. Control experiments confirm the participation of photo-generated charges in the catalytic process. In addition, AP-XPS studies have shown a direct role of light irradiation on the formation of electron rich carbon species on the surface of Na-Co@C nanoparticles. These species are involved in CO_2 activation to $CO_2^{\delta-}$, promoting CO_2 dissociation into CO. Moreover, CO is stabilized by interaction with the carbon layers on the catalyst surface, enabling the formation of ethanol via a CO insertion mechanism. Based on spectroscopic studies, this work shows how the light irradiation can influence the surface intermediate species during CO_2 hydrogenation reaction, leading to different reaction pathways.

References

(1)   Ozin, G. A. *Adv. Mater.* **2015,** *27*, 1957-1963.

(2)   Lewis, N. S.; Nocera, D. G. *Proc. Natl. Acad. Sci. USA* **2006,** *103*, 15729-15735.

(3)   Nocera, D. G. The artificial leaf. *Acc. Chem. Res.* **2012,** *45*, 767-776.

(4)   Liu, L.; Gao, F.; Zhao, H.; Li, Y. *Appl. Catal. B: Environ.* **2013,** *134-135*, 349-358.

(5)   Sun, Z.; Fischer, J. M. T. A.; Li, Q.; Hu, J.; Tang, Q.; Wang, H.; Wu, Z.; Hankel, M.; Searles, D. J.; Wang, L. *Appl. Catal. B: Environ.* **2017,** *216*, 146-155.

(6)   Habisreutinger, S. N.; Schmidt-Mende, L.; Stolarczyk, J. K. *Angew. Chem. Int. Ed.* **2013,** *52*, 7372-7408.

(7)   Corma, A.; Garcia, H. *J. Catal.* **2013,** *308*, 168-175.

(8)   Sastre, F.; Puga, A. V.; Liu, L.; Corma, A.; Garcia, H. *J. Am. Chem. Soc.* **2014,** *136*, 6798-6801.

(9)   Puga, A. V. *Top. Catal.* **2016,** *59*, 1268-1278.

(10) Meng, X.; Wang, T.; Liu, L.; Ouyang, S.; Li, P.; Hu, H.; Kako, T.; Iwai, H.; Tanaka, A.; Ye, J. *Angew. Chem. Int. Ed.* **2014,** *53*, 11478-11482.

(11) Sun, W.; Qian, C.; He, L.; Ghuman, K. K.; Wong, A. P.; Jia, J.; Jelle, A. A.; O'Brien, P. G.; Reyes, L. M.; Wood, T. E.et al. *Nat. Commun.* **2016,** *7*, 12553.

(12) Zhang, H.; Wang, T.; Wang, J.; Liu, H.; Dao, T. D.; Li, M.; Liu, G.; Meng, X.; Chang, K.; Shi, L.et al. *Adv. Mater.* **2016,** *28* (19), 3703-3710.

(13) Chen, G.; Gao, R.; Zhao, Y.; Li, Z.; Waterhouse, G. I. N.; Shi, R.; Zhao, J.; Zhang, M.; Shang, L.; Sheng, G.et al. *Adv. Mater.* **2018,** *30*, 1704663.

(14) Lanzafame, P.; Abate, S.; Ampelli, C.; Genovese, C.; Passalacqua, R.; Centi, G.; Perathoner, S. *ChemSusChem* **2017,** *10*, 4409-4419.

(15) Navarrete, A.; Centi, G.; Bogaerts, A.; Martín, Á.; York, A.; Stefanidis, G. D. *Energy Technol.* **2017,** *5*, 796-811..

(16) Dorner, R. W.; Hardy, D. R.; Williams, F. W.; Willauer, H. D. *Energy Environ. Sci.* **2010,** *3*, 884.

(17) Porosoff, M. D.; Yan, B.; Chen, J. G. *Energy Environ. Sci.* **2016,** *9*, 62-73.

(18) Centi, G.; Quadrelli, E. A.; Perathoner, S. *Energy Environ. Sci.* **2013,** *6*, 1711.

(19) Khodakov, A. Y.; Chu, W.; Fongarland, P. *Chem. Rev.* **2007,** *107*, 1692-1744.

(20) Wang, W.; Wang, S.; Ma, X.; Gong, J. *Chem. Soc. Rev.* **2011,** *40*, 3703-3727.

(21) Iablokov, V.; Beaumont, S. K.; Alayoglu, S.; Pushkarev, V. V.; Specht, C.; Gao, J.; Alivisatos, A. P.; Kruse, N.; Somorjai, G. A. *Nano Lett.* **2012,** *12*, 3091-3096.

(22) Andersson, M. P.; Abild-Pedersen, F.; Remediakis, I. N.; Bligaard, T.; Jones, G.; Engbæk, J.; Lytken, O.; Horch, S.; Nielsen, J. H.; Sehested, J. *J. Catal.* **2008,** *255*, 6-19.

(23) Gao, J.; Liu, Q.; Gu, F.; Liu, B.; Zhong, Z.; Su, F. *RSC Adv.* **2015,** *5*, 22759-22776.

(24) Khodakov, A. Y.; Chu, W.; Fongarland, P. *Chem. Rev.* **2007,** *107*, 1692-1744.

(25) Zhao, Y.; Zhao, B.; Liu, J.; Chen, G.; Gao, R.; Yao, S.; Li, M.; Zhang, Q.; Gu, L.; Xie, J.et al. *Angew. Chem. Int. Ed.* **2016,** *55*, 4215-4219.

(26) Pérez-Dieste, V.; Aballe, L.; Ferrer, S.; Nicolàs, J.; Escudero, C.; Milán, A.; Pellegrin, E. Near Ambient Pressure XPS at ALBA. *J. Phys. Conference Series* **2013,** *425*, 072023..

(27) Liu, L.; Concepción, P.; Corma, A. *J. Catal.* **2016,** *340*, 1-9.

(28) Liu, L.; Gao, F.; Concepción, P.; Corma, A. *J. Catal.* **2017,** *350*, 218-225..

(29) Riedel, T.; Claeys, M.; Schulz, H.; Schaub, G.; Nam, S.-S.; Jun, K.-W.; Choi, M.-J.; Kishan, G.; Lee, K.-W. *Appli. Catal. A: Gen.* **1999,** *186*, 201-213.

(30) Ojeda, M.; Nabar, R.; Nilekar, A. U.; Ishikawa, A.; Mavrikakis, M.; Iglesia, E. *J. Catal.* **2010,** *272*, 287-297.

(31) Fischer, N.; Claeys, M. *Catal. Today* **2016,** *275*, 149-154.

(32) Jia, J.; Wang, H.; Lu, Z.; O'Brien, P. G.; Ghoussoub, M.; Duchesne, P.; Zheng, Z.; Li, P.; Qiao, Q.; Wang, L.et al. *Advanced science* **2017,** *4*, 1700252.

(33) Simon, G.; Meziane, L.; Courty, A.; Colomban, P.; Lisiecki, I. *J. Raman Spectroscopy* **2016,** *47*, 248-251.

(34) Deng, X.; Verdaguer, A.; Herranz, T.; Weis, C.; Bluhm, H.; Salmeron, M. *Langmuir* **2008,** *24*, 9474-9478.

(35) Roiaz, M.; Monachino, E.; Dri, C.; Greiner, M.; Knop-Gericke, A.; Schlogl, R.; Comelli, G.; Vesselli, E. *J. Am. Chem. Soc.* **2016,** *138*, 4146-4154.

(36) Gnanamani, M. K.; Jacobs, G.; Keogh, R. A.; Shafer, W. D.; Sparks, D. E.; Hopps, S. D.; Thomas, G. A.; Davis, B. H. *Appl. Catal. A: Gen.* **2015,** *499*, 39-46.

(37) Dai, Y.; Yu, F.; Li, Z.; An, Y.; Lin, T.; Yang, Y.; Zhong, L.; Wang, H.; Sun, Y. *Chinese J. Chem.* **2017,** *35*, 918-926.

(38) Zhai, P.; Xu, C.; Gao, R.; Liu, X.; Li, M.; Li, W.; Fu, X.; Jia, C.; Xie, J.; Zhao, M.et al. *Angew. Chem. Int. Ed.* **2016,** *55*, 9902-9907.

(39) Yates, I. C.; Satterfield, C. N. *Energy Fuels* **1991,** *5*, 168-173.

(40) Weatherbee, G. Hydrogenation of CO2 on group VIII metals II. *J. Catal.* **1982,** *77*, 460-472.

(41) Neatu, S.; Macia-Agullo, J. A.; Concepcion, P.; Garcia, H. *J. Am. Chem. Soc.* **2014,** *136*, 15969-15976.

(42) Wu, C. H.; Eren, B.; Bluhm, H.; Salmeron, M. B. *ACS Catal.* **2017,** *7*, 1150-1157.

(43) Ishida, T.; Yanagihara, T.; Liu, X.; Ohashi, H.; Hamasaki, A.; Honma, T.; Oji, H.; Yokoyama, T.; Tokunaga, M. *Appl. Catal. A: Gen.* **2013,** *458*, 145-154.

(44)   Khobragade, M.; Majhi, S.; Pant, K. K. *Appl. Energy* **2012,** *94*, 385-394.

(45)   Blanchard, M.; Derule, H.; Canesson, P. *Catal. Lett.* **1989,** *2*, 319-322.

(46)   Cats, K. H.; Weckhuysen, B. M. *ChemCatChem* **2016,** *8*, 1531-1542..

(47)   Ferrari, A. C.; Robertson, J. Resonant Raman spectroscopy of disordered, amorphous, and diamondlike carbon. *Phys. Rev. B* **2001,** *64*, 075414.

(48)   Prieto, G.; Martínez, A.; Concepción, P.; Moreno-Tost, R. *J. Catal.* **2009,** *266*, 129-144.

(49)   Sadeqzadeh, M.; Karaca, H.; Safonova, O. V.; Fongarland, P.; Chambrey, S.; Roussel, P.; Griboval-Constant, A.; Lacroix, M.; Curulla-Ferré, D.; Luck, F.et al. *Catal. Today* **2011,** *164*, 62-67.

(50)   Paterson, J.; Peacock, M.; Ferguson, E.; Purves, R.; Ojeda, M. *ChemCatChem* **2017,** *9*, 3463-3469.

(51)   Gnanamani, M. K.; Jacobs, G.; Shafer, W. D.; Davis, B. H. *Catal. Today* **2013,** *215*, 13-17.

(52)   Tsakoumis, N. E.; Rønning, M.; Borg, Ø.; Rytter, E.; Holmen, A. *Catal. Today* **2010,** *154*, 162-182.

(53)   Saib, A. M.; Moodley, D. J.; Ciobîcă, I. M.; Hauman, M. M.; Sigwebela, B. H.; Weststrate, C. J.; Niemantsverdriet, J. W.; van de Loosdrecht, J. *Catal. Today* **2010,** *154*, 271-282.

Chapter 12

Perspectives

It has been presented along the thesis that, in the case of metal catalysts, and even more so with supported metal catalysts, the number of variables that can have an effect on the catalytic behavior is quite high. Among them, we can highlight: size and shape of the metal particles, the nature of the support and metal-support interaction, the presence of the other metals, from impurities to defined bimetallic or multimetallic particles, and the chemical states of the surface. However, among all, we would like to point out two of them: a) the intrinsic electronic difference and binding capacities when going from single atoms to clusters and to nanoparticles; b) the dynamic characteristics of the catalytic process which is directed by the metal-reactant and/or metal-solvent interaction. In this later case, the size, shape and electronic properties can be even dramatically modified by such interactions. These changes can be for the good or for the bad from a catalytic point of view, and it shows how difficult is to get sensible structure-reactivity correlations by combining catalytic results, catalyst characterizations and molecular modelling, unless the dynamic characteristics of the catalyst during the reaction are considered.

When nanoparticles become smaller and specially, metal clusters with less than 20 atoms or even single atoms supported on solid carriers, the size, shape and electronic properties of the metal will also depend on the electronic structure and surface arrangement of the support. The extreme situation occurs with single metal atoms in where the "ligands" of those will be atoms from the support. Then, the presence and the number of vacancies, the oxidation state of the atoms of the solid carrier and the characteristics of their frontier orbital and potential overlapping with those of the metal species, not only will mark the final electronic properties of the "single" atom and their reactivity for catalysis, but also the metal sintering and/or metal leaching. Therefore, in the case of supported "single atoms", the real active site, in where reactants are activated and transition states are stabilized, will be the "single metal atom" but the "ligand" atoms of the support will play an important role.

It has been proposed recently that, heterogeneous single-atom catalysts can work as an analogous to homogeneous catalysts. Despite their difference on electronic structures, in our opinion, the geometric factor can be a significant difference between them. In the case of homogeneous catalysis, the metal centers are coordinated by ligands and/or the reactants and the geometric

structure of such complexes are quite flexible. The metal center can be accessible to large molecules and can adjust the coordination configuration between the metal and reactant during the catalytic cycles. However, in the case of supported single atoms, their geometric structures are partially restricted by the support, especially for those supported on inorganic solid carriers. Consequently, the catalytic applications of single-atom catalysts in the literature are mainly related with activation of small molecules, at least up to date. It has been reported that, when Rh single atoms are stabilized by polymers, they can serve as stable and active sites for hydroformylation reactions. Considering the flexible geometric structure of polymers, it maybe a possible approach to overcome the geometric restriction of conventional inorganic solid carriers, making single-atom catalysts closer to its homogeneous counterpart. However, the stability and the potential leaching of single atoms should also be considered under those circumstances.

All the abovementioned factors may be key issues for preparing a successful single-atom catalyst. In the case of metal clusters, the nature of the support and the metal-support interaction will dictate the shape of the supported clusters, their stability, the atomic structure of metal-cluster interface and electronic interactions between the support and the metal clusters. The fact that the number of variables and their interdependence is so large in the case of subnanometric metal catalysts, has made that many of the studies presented appear phenomenological and "specific" for a given catalyst-reaction system. Nevertheless, there are already some general lessons that could be extracted from the studies reported up to now.

First of all, the important role that single atoms and small clusters can play in catalysis. While this could be intuitively deduced from older work, it is now possible to "see" those metal entities on supports and solution with the development of new catalyst preparation techniques and the development of aberration-corrected TEM and MALDI-TOF techniques. Furthermore, the direct observation of those subnanometric metal species leads to better discussions on their stability and catalytic role. All of the above together with the advances in molecular modelling have boosted our understanding of the catalytic behavior at the molecular level on those highly dispersed species.

It should be emphasized that, the theoretical calculations and molecular

modeling should match the experimental conditions as much as possible to obtained reasonable interpretation on experimental results. Currently, in many works, the modeling of active sites in heterogeneous catalysts and the computational methods are still far away from the realistic working catalyst.[576] With unrealistic parameters for theoretical calculations, the output results may be useless for understanding the behavior and reaction mechanism of heterogeneous catalysts. On the other hand, with suitable modeling on the experimental basis, the theoretical calculations and modeling can be very helpful to understand experimental phenomena and can even be used for predictions. It can be expected in the near future that, with the development of better hardware resources and especially with the help of new concepts from machine learning and artificial intelligence, the accuracy of theoretical calculations for heterogeneous catalytic reactions will be improved greatly.

It should be noticed that, we normally build "static" models of the catalytic phenomena, while those catalysts are dynamic under reaction conditions. So, today we are still missing more deepness on this aspect. Therefore, in situ surface techniques such as XAS, XPS, XRD and TEM that allow following catalyst evolution during reaction will be most helpful. It is true that in situ TEM studies on metal nanoparticles has been already performed and has provide new insights on the atomic structures of metal particles when they interact with reactants. However, nanoparticles of 2-10 nm are already quite stable, and the critical issue is to apply such technique for catalysts based on single atoms and subnanometric clusters. As was said in the thesis, the first steps along this direction are now being given.

If we want to go beyond the study of particular cases, we should work to establish a unified theory that will envelope and explain all the casuistic in metal catalysis, regardless if that is based on homogeneous or heterogeneous chemical, photochemical, electrochemical or photoelectrochemical catalysts. At the end, all of them are based on electronic interactions and, to achieve global explanations, we can make use of the knowledge generated by the physicists and chemists on solid state chemistry, physical chemistry of surface and chemical reactivity. It is also true that if we attempt to achieve this global and unifying knowledge on catalysis, we will require more than just quick catalytic experiments. We should combine more and more "realistic" operando

characterizations with high-quality adsorption, reaction kinetics, isotopic studies as well as theoretical work. In other words, we should generate a deeper molecular mechanistic knowledge involving dynamic transformations of metal catalysts and molecular interactions at the gas/liquid-solid interface to deal with the complications introduced when going from molecular catalysis to heterogeneous catalysis with metal catalysts.

Abstract

Metal species with different size (single atoms, nanoclusters and nanoparticles) show different catalytic behavior for various heterogeneous catalytic reactions. It has been shown in the literature that, many factors including the particle size, shape, chemical composition, metal-support interaction, metal-reactant/solvent interaction, can have significant influences on the catalytic properties of metal catalysts. The recent developments of well-controlled synthesis methodologies and advanced characterization tools allow to correlate the relationships at molecular level.

In this thesis, I have carried out studies on metal catalysts from single atoms to nanoclusters and nanoparticles. By developing new synthesis methodologies, the size of metal species can be modulated and used as model catalysts to study the size effect on the catalytic behavior of metal catalysts for CO oxidation, selective hydrogenation, selective oxidation and photocatalysis. It has been found that, singly dispersed metal atoms and subnanometric metal clusters may agglomerate into larger nanoclusters or nanoparticles under reaction conditions. To improve the stability of subnanometric metal catalysts, I have developed a new strategy for the generation of single atoms and clusters in zeolites. Those subnanometric metal species are stable in oxidation-reduction treatments at 550 ºC. Following this new synthesis methodology, this new type of materials can serve as model catalyst to study the evolution of subnanometric metal species under reaction conditions. The structural transformation of subnanometric Pt species has been studied by in situ transmission electron microscopy. It has been shown that the size of Pt species is strongly related with the reaction conditions, which provide important insights for understanding the behavior of subnanometric metal catalysts under reaction conditions.

In the other research line for non-noble metal catalysts, I have developed several general strategies to obtain non-noble metal catalysts either supported on metal oxides or protected by thin carbon layers. These materials show excellent performance for several important reactions, such as chemoselective hydrogenation of nitroarenes, even when compared with conventional noble metal catalysts. In some cases, non-noble metal catalysts can even achieve selectivities to unfeasible products which has not been possible to achieve on

conventional noble metal catalysts, which is caused by the different reaction pathway on non-noble metal catalysts. In some other cases (e.g. CO_2 hydrogenation), selectivity to alcohols and C2+ hydrocarbons can be modulated through light irradiation (as evidenced by ambient-pressure X-ray photoelectron spectroscopy) which opens a new possibility for tuning the catalytic behavior of metal catalysts.

Based on the above works from different aspects related with heterogeneous metal catalysts, perspectives on the future directions towards better understanding on the catalytic behavior of different metal entities (single atoms, nanoclusters and nanoparticles) in a unifying manner have also been given in this thesis.

Resumen

Las especies de metal con diferentes tamaños (átomos individuales, nanocristales y nanopartículas) muestran un comportamiento catalítico diferente para diversas reacciones catalíticas heterogéneas. Se ha demostrado en la bibliografía que muchos factores que incluyen el tamaño de partícula, la forma, la composición química, la interacción metal-soporte, la interacción metal-reactivo / disolvente, pueden tener influencias significativas sobre las propiedades catalíticas de los catalizadores metálicos. Los desarrollos recientes de metodologías de síntesis bien controladas y herramientas de caracterización avanzada permiten correlacionar las relaciones a nivel molecular.

En esta tesis, he llevado a cabo estudios sobre catalizadores metálicos desde átomos individuales hasta nanoclusters y nanopartículas. Al desarrollar nuevas metodologías de síntesis, el tamaño de las especies metálicas puede modularse y usarse como catalizadores modelo para estudiar el efecto del tamaño sobre el comportamiento catalítico de los catalizadores metálicos para la oxidación del CO, la hidrogenación selectiva, la oxidación selectiva y la fotocatálisis. Se ha encontrado que, los átomos metálicos dispersados por separado y los grupos subnanométricos de metal pueden aglomerarse en nanoclusters o nanopartículas más grandes en condiciones de reacción. Para mejorar la estabilidad de los catalizadores subnanométricos de metal, he desarrollado una nueva estrategia para la generación de átomos individuales y clusters en zeolitas. Esas especies subnanométricas de metales son estables en tratamientos de oxidación-reducción a 550 ºC. Siguiendo esta nueva metodología de síntesis, este nuevo tipo de materiales puede servir como catalizador modelo para estudiar la evolución de especies subnanométricas de metales en condiciones de reacción. La transformación estructural de las especies subnanométricas de Pt ha sido estudiada mediante microscopía electrónica de transmisión in situ. Se ha demostrado que el tamaño de las especies de Pt está fuertemente relacionado con las condiciones de reacción, que proporcionan importantes conocimientos para comprender el comportamiento de los catalizadores de metales subnanométricos en condiciones de reacción.

En la otra línea de investigación para catalizadores de metales no nobles, he desarrollado varias estrategias generales para obtener catalizadores de metales

no nobles, ya sea soportados sobre óxidos metálicos o protegidos por capas delgadas de carbono. Estos materiales muestran un rendimiento excelente para varias reacciones importantes, como la hidrogenación quimioselectiva de nitroarenos, incluso cuando se comparan con los catalizadores de metales nobles convencionales. En algunos casos, los catalizadores de metales no nobles pueden incluso alcanzar selectividades para productos inviables que no ha sido posible conseguir en catalizadores de metales nobles convencionales, que es causado por la diferente ruta de reacción en catalizadores de metales no nobles. Sin embargo, la espectroscopía fotoelectrónica de rayos X a presión ambiente ha revelado que la irradiación de la luz puede modular la selectividad a los alcoholes y los hidrocarburos C2 +, lo que abre una nueva posibilidad para ajustar el comportamiento catalítico de los catalizadores metálicos.

Con base en los trabajos anteriores de diferentes aspectos relacionados con catalizadores metálicos heterogéneos, las perspectivas sobre las direcciones futuras hacia una mejor comprensión del comportamiento catalítico de diferentes entidades metálicas (átomos individuales, nanoagrupamientos y nanopartículas) de una manera unificadora también se han dado en esta tesis.

Resum

Les espècies metàl·liques de diferents dimensions (àtoms individuals, nanoclusters i nanopartícules) mostren diferents comportaments catalfics per a diverses reaccions catalfiques heterogènies. S'ha demostrat a la literatura que, molts factors que inclouen la mida de la partícula, la forma, la composició química, la interacció amb el suport metàl·lic, la reacció metàl·lica i la interacció amb dissolvents poden tenir influències significatives sobre les propietats catalfiques dels catalitzadors metàl·lics. Els desenvolupaments recents de metodologies de síntesi ben controlades i eines de caracterització avançada permeten relacionar les relacions a nivell molecular.

En aquesta tesi, he realitzat estudis sobre catalitzadors metàl·lics d'àtoms únics a nanoclústers i nanopartícules. Mitjançant el desenvolupament de noves metodologies de síntesi, la mida de les espècies metàl·liques es pot modular i utilitzar com a catalitzadors model per estudiar l'efecte de mida sobre el comportament catalfic dels catalitzadors metàl·lics per a l'oxidació de CO, hidrogenació selectiva, oxidació selectiva i fotocatàlisi. S'ha trobat que, els àtoms metàl·lics dispersos individualment i els clústers metàl·lics subnanomètrics poden aglomerar-se en nanoclústeres o nanopartícules més grans en condicions de reacció. Per millorar l'estabilitat dels catalitzadors subnanomètrics de metall, he desenvolupat una nova estratègia per a la generació d'àtoms i racimos en zeolites. Aquestes espècies metàl·liques subnanomètricas són estables en tractaments de reducció d'oxidació a 550 oC. Després d'aquesta nova metodologia de síntesi, aquest nou tipus de materials poden servir com a model de catalitzador per estudiar l'evolució de les espècies metàl·liques subnanomètricas en condicions de reacció. La transformació estructural de l'espècie Pn subnanomètrica ha estat estudiada per microscòpia electrònica de transmissió in situ. S'ha demostrat que la mida de les espècies de Pt està fortament relacionada amb les condicions de reacció, que proporcionen idees importants per comprendre el comportament dels catalitzadors de subnanometria en condicions de reacció.

En l'altra línia de recerca dels catalitzadors de metalls no nobles, he desenvolupat diverses estratègies generals per obtenir catalizadors de metalls no nobles recolzats en òxids metàl·lics o protegits per capes de carboni primes.

Aquests materials presenten un excel·lent rendiment per a diverses reaccions importants, com la hidrogenació quimioelectiva de nitroarenes, fins i tot quan es comparen amb els catalitzadors convencionals de metall noble. En alguns casos, els catalitzadors de metalls no nobles poden fins i tot aconseguir selectivitats a productes no factibles que no s'han pogut assolir en catalitzadors de metall noble convencionals, que es deuen a la via de reacció diferent en catalitzadors de metalls no nobles. No obstant això, s'ha observat una espectroscòpia de fotoelèctria de raigs X amb pressió d'atmosfera que la irradiació lleugera pot modular la selectivitat als alcohols i hidrocarburs C2 +, la qual cosa obre una nova possibilitat per sintonitzar el comportament catalífic dels catalitzadors metàl·lics.

A partir d'aquests treballs de diferents aspectes relacionats amb els catalitzadors metàl·lics heterogenis, també s'ha donat en aquesta tesi perspectives sobre les futures orientacions cap a una millor comprensió del comportament catalífic de diferents entitats metàl·liques (àtoms individuals, nanoclústers i nanopartícules).

Lichen Liu

Instituto de Tecnología Química, Universitat Politècnica de València, Av. de los Naranjos, s/n 46022, Valencia, España

E-mail: lichenliu1991@gmail.com

Education

BS in Chemistry, Nanjing University
09/2008—06/2012

Master in Sustainable Chemistry, Universitat Politècnica de València   09/2013—07/2014
Supervisor: Prof. Avelino Corma

PhD student in Sustainable Chemistry, Universitat Politècnica de València   09/2014—present
Supervisor: Prof. Avelino Corma

Research

During my PhD period in ITQ, my research is mainly focused on the generation, stabilization and evolution of subnanometric metal species (single atoms and clusters) in zeolites and developing non-noble metal catalysts as substitutes to noble metal catalysts for selective hydrogenation and oxidation reactions.
Review:
1. Metal Catalysts for Heterogeneous Catalysis: From Single Atoms to Nanoclusters and Nanoparticles, *Chemical Reviews*, <u>L. Liu</u> and A. Corma, 2018, *118*, 4981-5079.

Research works related with single atoms and metal clusters:
2. Generation of subnanometric platinum with high stability during transformation of a 2D zeolite into 3D. <u>L. Liu</u>, U. Díaz, R. Arenal, G.

Agostini, P. Concepción and A. Corma, *Nature Materials*, 2017, 16, 132-138.

3. Evolution and stabilization of subnanometric metal species in confined space by in situ TEM, **L. Liu**, D.N. Zakharov, R. Arenal, P. Concepcion, E.A. Stach and A. Corma, *Nature Communications*, 2018, 9, 574.

4. Stabilized naked sub-nanometric Cu clusters within a polymeric film catalyze C–N, C–C, C–O, C–S, and C–P bond-forming reactions, J. Oliver-Messeguer, **L. Liu**, S. García-García, C. Canós-Giménez, I. Domínguez, R. Gavara, A. Doménech-Carbó, P. Concepción, A. Leyva-Pérez and A. Corma, *Journal of the American Chemical Society*, 2015,137, 3894-3900.

5. Generation of Gold Nanoclusters Encapsulated in MCM-22 Zeolite for Aerobic Oxidation of Cyclohexane. **L. Liu**, R. Arenal, D. Motta and Avelino Corma, *Submitted*.

Research works related with non-noble metal nanoparticles:

6. A new strategy to transform mono and bimetallic non-noble metal nanoparticles into highly active and chemoselective hydrogenation catalysts, **L. Liu**, F. Gao, P. Concepcion and A. Corma, *Journal of Catalysis*, 2017, 350, 218-225.

7. Non-noble metal catalysts for hydrogenation: A facile method for preparing Co nanoparticles covered with thin layered carbon, **L. Liu**, F. Gao, P. Conception and A. Corma, *Journal of Catalysis*, 2016, 340, 1-9.

8. Facile synthesis of surface-clean monodispersed CuOx nanoparticles and their catalytic properties for oxidative coupling of alkynes, **L. Liu**, T. Matsushita, P. Concepción, A. Leyva-Pérez and A. Corma, *ACS Catalysis*, 2016, 6, 2211-2221.

9. A new molecular pathway allows the chemoselective reduction of nitroaromatics on non-noble metal catalysts, R. Millán, **L. Liu**, M. Boronat, and A. Corma, *Journal of Catalysis*, 2018, 364, 19-30.

10. Sunlight-assisted hydrogenation of CO_2 into ethanol and C2+ hydrocarbons by sodium-promoted Co@C nanocomposites, **L. Liu**, A. V. Puga, J. Cored, P. Concepción, V. Pérez-Dieste, H. García and A.

Corma *Applied Catalysis B: Environmental*, 2018, 235, 186-196.

11. Directing the chemoselective hydrogenation of nitroarenes into the corresponding aromatic azoxy and azo compounds with non-noble metal catalysts. **L. Liu**, P. Concepcion and A. Corma, *Submitted*.

Other collaboration publications:

12. Complete photocatalytic reduction of CO_2 to methane by H_2 under solar light irradiation, F. Sastre, A.V. Puga, **L. Liu**, A. Corma and H. García, *Journal of the American Chemical Society*, 2014,136, 6798-6801.

13. Nanolayered Co–Mo–S Catalysts for the Chemoselective Hydrogenation of Nitroarenes, I. Sorribes, **L. Liu** and A. Corma, *ACS Catalysis*, 2017, 7, 2698-2708.

14. Nanolayered Cobalt-Molybdenum Sulfides as Highly Chemo- and Regioselective Catalysts for the Hydrogenation of Quinoline Derivatives, I. Sorribes, **L. Liu**, A. Doménech-Carbó and A. Corma, *ACS Catalysis*, 2018, 8, 4545-4557.

Participation in Academic Conferences

2015   ACS National Spring Meeting, Denver. (Oral)

2016   16th International Congress of Catalysis, Beijing. (Oral)

2017   13th European Congress of Catalysis, Florence. (Oral)

2018   18th International Symposium on Relationships between Heterogeneous and Homogeneous Catalysis. (Short Oral, Poster)

2018   International Symposium on Advancement and Prospect of Catalysis Science & Technology (Oral)

2018   7th EuCheMS, Livepool. (Oral)

Honors & Awards

2018   European Young Chemist Award (Silver)

2018   *ACS Catalysis* Award for Early Career Researcher

2018   Poster Prize, 18th International Symposium on Relationships between Heterogeneous and Homogeneous Catalysis.

2017   Chinese Government Award for Outstanding Self-Finance Students Abroad

2013   Distinguish Student Award, Nanjing University

2011-2012   Jiang Wenruo Scholarship, Nanjing University.

2011-2012   Dai Anbang & Gao Jiyu Scholarship, Nanjing University.